Journal of
Marine Science and Engineering

Selected Papers from the 15th Estuarine and Coastal Modeling Conference

Edited by
Richard P. Signell

Printed Edition of the Special Issue Published in
Journal of Marine Science and Engineering

www.mdpi.com/journal/jmse

MDPI

Selected Papers from the 15th Estuarine and Coastal Modeling Conference

Selected Papers from the 15th Estuarine and Coastal Modeling Conference

Special Issue Editor

Richard P. Signell

MDPI • Basel • Beijing • Wuhan • Barcelona • Belgrade

Special Issue Editor
Richard P. Signell
United States Geological Survey
USA

Editorial Office
MDPI
St. Alban-Anlage 66
4052 Basel, Switzerland

This is a reprint of articles from the Special Issue published online in the open access journal *Journal of Marine Science and Engineering* (ISSN 2077-1312) from 2018 to 2019 (available at: https://www.mdpi.com/journal/jmse/special_issues/ECM15)

For citation purposes, cite each article independently as indicated on the article page online and as indicated below:

LastName, A.A.; LastName, B.B.; LastName, C.C. Article Title. *Journal Name* **Year**, *Article Number*, Page Range.

ISBN 978-3-03921-269-9 (Pbk)
ISBN 978-3-03921-270-5 (PDF)

Contents

About the Special Issue Editor

Richard P. Signell holds the position of research oceanographer at the US Geological Survey in Woods Hole, MA, USA. He earned his doctorate in physical oceanography from the MIT/Woods Hole Oceanographic Institution Joint Program in 1989. He has over 30 years of experience in coastal ocean modeling and geoinformatics. He is the author or co-author of more than 100 refereed articles and was the chair of the 2011 Gordon Research Conference on Coastal Ocean Modeling. He was also the chair of the 13th, 14th, and 15th Estuarine and Coastal Modeling conferences.

Preface to "Selected Papers from the 15th Estuarine and Coastal Modeling Conference"

This Special Issue contains selected papers from the 15th International Conference on Estuarine and Coastal Modeling (ECM15), held on 25–27 June 2018 in Seattle, Washington, USA. The conference brings modelers from academic institutions, government, and private industry together to present and discuss the latest developments in the field of marine environmental modeling. Begun in 1989 by Dr. Malcolm Spaulding, the conference is held every other year in a retreat-like setting with a maximum of about 125 people to encourage interaction and help strengthen ties between modeling communities. A wide range of modeling issues are discussed, including advances in physical understanding, numerical algorithm development, model applications, and better tools. A wide range of modeling topics are discussed as well, including storm surge, eutrophication, larval transport, search and rescue, oil spills, fisheries issues, coastal erosion, and sediment transport

The 21 papers presented here cover a broad spectrum of topics, including the development of regional forecast systems, storm surge impacts, improved numerical techniques, water quality, methods for distributing model output, and regional modeling applications.

Richard P. Signell
Special Issue Editor

Journal of
Marine Science and Engineering

MDPI

Article

Analysis and Visualization of Coastal Ocean Model Data in the Cloud

Richard P. Signell [1,*] and Dharhas Pothina [2]

[1] Woods Hole Coastal and Marine Science Center, U.S. Geological Survey, Woods Hole, MA 02543, USA
[2] U.S. Army Engineer Research and Development Center, Vicksburg, MS 39180, USA; dharhas.pothina@erdc.dren.mil
* Correspondence: rsignell@usgs.gov; Tel.: +1-508-457-2229

Received: 6 March 2019; Accepted: 1 April 2019; Published: 19 April 2019

Abstract: The traditional flow of coastal ocean model data is from High-Performance Computing (HPC) centers to the local desktop, or to a file server where just the needed data can be extracted via services such as OPeNDAP. Analysis and visualization are then conducted using local hardware and software. This requires moving large amounts of data across the internet as well as acquiring and maintaining local hardware, software, and support personnel. Further, as data sets increase in size, the traditional workflow may not be scalable. Alternatively, recent advances make it possible to move data from HPC to the Cloud and perform interactive, scalable, data-proximate analysis and visualization, with simply a web browser user interface. We use the framework advanced by the NSF-funded Pangeo project, a free, open-source Python system which provides multi-user login via JupyterHub and parallel analysis via Dask, both running in Docker containers orchestrated by Kubernetes. Data are stored in the Zarr format, a Cloud-friendly n-dimensional array format that allows performant extraction of data by anyone without relying on data services like OPeNDAP. Interactive visual exploration of data on complex, large model grids is made possible by new tools in the Python PyViz ecosystem, which can render maps at screen resolution, dynamically updating on pan and zoom operations. Two examples are given: (1) Calculating the maximum water level at each grid cell from a 53-GB, 720-time-step, 9-million-node triangular mesh ADCIRC simulation of Hurricane Ike; (2) Creating a dashboard for visualizing data from a curvilinear orthogonal COAWST/ROMS forecast model.

Keywords: ocean modeling; cloud computing; data analysis; geospatial data visualization

1. Introduction

Analysis, visualization, and distribution of coastal ocean model data is challenging due to the sheer size of the data involved, with regional simulations commonly in the 10GB–1TB range. The traditional workflow is to download data to local workstations or file servers from which the data needed can be extracted via services such as OPeNDAP [1]. Analysis and visualization take place with environments like MATLAB®and Python running on local computers. Not only are these datasets becoming too large to effectively download and analyze locally, but this approach requires acquiring and maintaining local hardware, software, and personnel to ensure reliable and efficient processing. Archiving is an additional challenge for many centers. Effective sharing with collaborators is often limited by unreliable services that cannot scale with demand. In some cases, a subset of analysis and visualization tools are made available through custom web portals (e.g., [2,3]). These portals can satisfy the needs of data dissemination to the public but don't have the suite of scientific analysis tools needed for collaborative research use. In addition, the development and maintenance of these portals require dedicated web software developers and is out of the reach of most scientists. The traditional method of data access and use is becoming time and cost inefficient.

The Cloud and recent advances in technology provide new opportunities for analysis, visualization, and distribution of model data, overcoming these problems [4]. Data can be stored in the Cloud efficiently in object storage which allows performant access by providers or end users alike. Analysis and visualization can take place in the Cloud, close to the data, allowing efficient and cost-effective access, as the only data that needs to leave the Cloud are graphics and text returned to the browser. As these tools have matured, they have lowered the barrier of entry and are poised to transform the ability of regular scientists and engineers to collaborate on difficult research problems without being constrained by their local resources.

The Pangeo project [5–7] was created to take advantage of these advances for the scientific community. The specific goals of Pangeo are to: "(1) Foster collaboration around the open source scientific Python ecosystem for ocean/atmosphere/land/climate science. (2) Support the development with domain-specific geoscience packages. (3) Improve scalability of these tools to handle petabyte-scale datasets on HPC and Cloud platforms." It makes progress toward these goals by building on open-source packages already widely used in the Python ecosystem, and supporting a flexible and modular framework for interactive, scalable, data-proximate computing on large gridded datasets. Here we first describe the essential components of this framework, then demonstrate two coastal ocean modeling use cases: (1) Calculating the maximum water level at each grid cell from a 53 GB, 720 time step, 9 million node triangular mesh ADCIRC [8] simulation of Hurricane Ike; (2) creating a dashboard for visualizing data from the curvilinear orthogonal COAWST/ROMS [9] forecast model.

2. Framework Description

Pangeo is a flexible framework which can be deployed in different types of platforms with different components, so here we describe the specific framework we used for this work, consisting of:

- Zarr [10] format files with model output for cloud-friendly access
- Dask [11] for parallel scheduling and execution
- Xarray [12] for working effectively with model output using the NetCDF/CF [13,14] Data Model
- PyViz [15] for interactive visualization of the output
- Jupyter [16] to allow user interaction via their web browser (Figure 1).

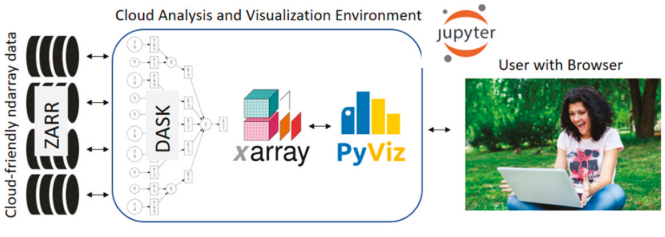

Figure 1. The Pangeo Cloud framework used here: Zarr for analysis ready data, on distributed, globally accessible storage; Dask for managing parallel computations; Xarray for gridded data analysis, PyViz for interactive visualization and; Jupyter for user access via a web browser. The framework works with any Cloud provider because it uses Kubernetes, which orchestrates and scales a cluster of Docker containers.

We will briefly describe these and several other important components in more detail.

2.1. Zarr

Zarr is a Cloud-friendly data format. The Cloud uses object storage. Access to NetCDF files (the most commonly used format for model data) in object storage is poor, due to the latency of object requests and the numerous small requests involved with accessing data from a NetCDF file. Therefore,

we converted the model output from NetCDF format to Zarr format which was developed specifically to allow Cloud-friendly access to n-dimensional array data. With Zarr, the metadata is stored in JSON format, and the data chunks are stored as separate storage objects, typically with chunk sizes of 10–100 mb, which enables concurrent reads by multiple processors. The major features of the HDF5 and NetCDF4 data models are supported: Self-describing datasets with variables, dimensions and attribute, supporting groups, chunking, and compression. It is being developed in an open community fashion on GitHub, with contributions from multiple research organizations. Currently, only a Python interface exists, but it has a well-documented specification and other language bindings are being developed. The Unidata NetCDF team is working on the adoption of Zarr as a back-end to the NetCDF C library. Data can be converted from NetCDF, HDF5 or other n-dimensional array formats to Zarr using the Xarray library (described below).

2.2. Dask

Dask is a component that facilitates out-of-memory and parallel computations. Dask arrays allow handling very large array operations using many small arrays known as "chunks". Dask workers perform operations in parallel, and dask worker clusters can be created on local machines with multiple CPUs, on HPC with job submission, and on the Cloud via Kubernetes [17] orchestration of Docker [18] containers.

2.3. Xarray

Xarray is a component which implements the NetCDF Data model, with the concept of a dataset that contains named shared dimensions, global attributes, and a collection of variables that have identified dimensions and variable attributes. It can read from a variety of sources, including NetCDF, HDF, OPeNDAP, Zarr and many raster data formats. Xarray automatically uses Dask for parallelization when the data are stored in a format that uses chunks, or when chunking is explicitly specified by the user.

2.4. PyViz

PyViz is a coordinated effort to make data visualization in Python easier to use, easier to learn, and more powerful. It is a collection of visualization packages built on top of a foundation of mature, widely used data structures and packages in the scientific Python ecosystem. The functions of these packages are described separately below along with the associated EarthSim project that is instrumental in advancing and extending PyViz capabilities.

2.5. EarthSim

EarthSim [19,20] is a project that acts as a testing ground for PyViz workflows specifying, launching, visualizing and analyzing environmental simulations such as hydrologic, oceanographic, weather and climate modeling. It contains both experimental tools and example workflows. Approaches and tools developed in this project often are incorporated into the other PyViz packages upon maturity. Specifically, key improvements in the ability to represent large curvilinear mesh and triangular mesh grids made the PyViz tools practical for use by modelers, e.g., TriMesh and QuadMesh.

2.6. PyViz: Datashader

Datashader [21] renders visualizations of large data into rasters, allowing accurate, dynamic representation of datasets that would otherwise be impossible to display in the browser.

2.7. PyViz: HoloViews

HoloViews [22] is a package that allows the visualization of data objects through annotation of the objects. It supports different back-end plotting packages, including Matplotlib, Plotly, and Bokeh.

The Matplotlib backend provides static plots, while Bokeh generates visualizations in JavaScript that are rendered in the browser and allow user interaction such as zooming, panning, and selection. We used Bokeh here, and the visualizations work both in Jupyter Notebooks and deployed as web pages running with Python backends. A key aspect of using HoloViews for large data is that it can dynamically rasterize the plot to screen resolution using Datashader.

2.8. PyViz: GeoViews

GeoViews [23] is a package that layers geographic mapping on top of HoloViews, using the Cartopy [24] package for map projections and plotting. It also allows a consistent interface to many different map elements, including Web Map Tile Services, vector-based geometry formats such as Shapefiles and GeoJSON, raster data and QuadMesh and TriMesh objects useful for representing model grids.

2.9. PyViz HvPlot

HvPlot [25] is a high-level package that makes it easy to create HoloViews/GeoViews objects by allowing users to replace their normal object .plot() commands with .hvplot(). Sophisticated visualizations can therefore be created with one plot call, and then if needed supplemented with additional lower-level HoloViews information for finer-grained control.

2.10. PyViz: Panel

Panel [26] is a package that provides a framework for creating dashboards that contain multiple visualizations, control widgets and explanatory text. It works within Jupyter and the dashboards can also be deployed as web applications that work dynamically with Dask-powered Python backends.

2.11. JupyterHub

JupyterHub [27] is a component that allows multi-user login, with each user getting their own Jupyter server and persisted disk space. The Jupyter server runs on the host system, and users interact with the server via the Jupyter client, which runs in any modern web browser. Users type code into cells in a Jupyter Notebook, which get processed on the server and the output (e.g., figures and results of calculations) return as cell output directly below the code. The notebooks themselves are simple text files that may be shared and reused by others.

2.12. Kubernetes

Kubernetes [17] is a component that orchestrates containers like Docker, automating deployment, scaling, and operations of containers across clusters of hosts. Although developed by Google, the project is open-source and Cloud agnostic. It allows JupyterHub to scale with the number of users, and individual tasks to scale with the number of requested Dask workers.

2.13. Conda: Reproducible Software Environment

Utilizing both Pangeo and PyViz components, the system contains 300+ packages. With these many packages, we need an approach that minimizes the possibility of conflicts. We use Conda [28], "an open source, cross-platform, language agnostic package manager and environment management system". Conda allows installation of pre-built binary packages, and providers can deliver packages via channels at anaconda.org. To provide a consistent and reliable build environment, the community has created conda-forge [29], a build infrastructure that relies on continuous integration to create packages for Windows, macOS, and Linux. We specify the conda-forge channel only when we create our environment, and use specific packages from other channels only when absolutely necessary. For example, currently, over 90% of the 300+ packages we use to build the Pangeo Docker containers are from conda-forge.

2.14. Community

The Pangeo collaborator community [30] plays a critical role in making this framework deployable and usable by domain scientists like ocean modelers. The community discusses technical and usage challenges on GitHub issues [31], during weekly check-in meetings, and in a blog [32].

3. System Application

3.1. Deployment on Amazon Cloud

We obtained research credits from the Amazon Open Data program [33] to deploy and test the framework on the Amazon Cloud. The credits were obtained under the umbrella of the Earth System Information Partners (ESIP) [34], of which USGS, NOAA, NASA, and many other federal agencies are partners. Deploying the environment under ESIP made access possible from government and academic collaborators alike.

3.2. Example: Mapping Maximum Water Level During a Storm Simulation from an Unstructured Grid (Triangular Mesh) Model

A common requirement in the analysis is to compute the mean or other property over the entire grid over a period of simulation. Here we illustrate the power of the Cloud to perform one of these calculations in 15 s instead of 15 min by using 60 Dask workers instead of just one, describing a notebook that computes and visualizes the maximum water level over a one week simulation of Hurricane Ike for the entire model mesh (covering the US East and Gulf Coasts).

The notebook workflow commences with a specification of how much processing power is desired, here requesting 60 Dask workers utilizing 120 CPU cores (Figure 2). The next step is opening the Zarr dataset in Xarray, which simply reads the metadata (Figure 3). We see we have water level variable called zeta, with more than 9 million nodes, and 720 time steps. We can also see data is arranged in chunks that each contain 10 time steps and 141,973 nodes. The chunk size was specified when the Zarr dataset was created, using Xarray to convert the original NetCDF file from Clint Dawson (University of Texas), and using the Amazon Web Services command line interface to upload to Amazon S3 object storage.

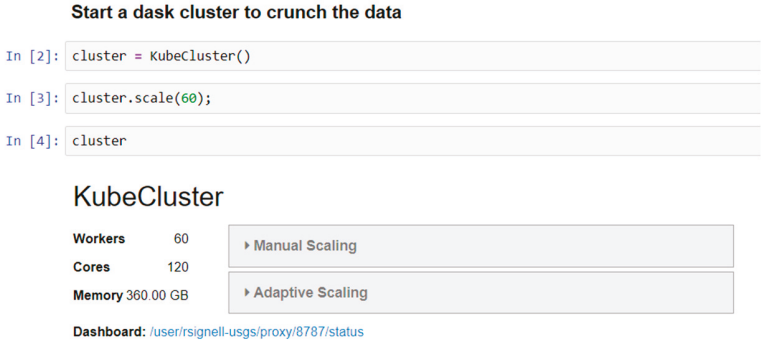

Figure 2. Starting up a Dask cluster with KubeCluster, which use Kubernetes to create a cluster of Docker containers. A Dashboard link is also displayed, which allows users to monitor the work done by the cluster in a separate browser window.

```
In [8]: if pangeo=='ESIP-AWS-S3':
            import s3fs
            fs = s3fs.S3FileSystem(anon=True)
            map = s3fs.S3Map('esip-pangeo/pangeo/adcirc/ike', s3=fs)

In [9]: ds = xr.open_zarr(map)

In [10]: ds['zeta']

Out[10]: <xarray.DataArray 'zeta' (time: 720, node: 9228245)>
         dask.array<shape=(720, 9228245), dtype=float64, chunksize=(10, 141973)>
         Coordinates:
           * time     (time) datetime64[ns] 2008-09-05T12:00:00 ... 2008-09-10T11:50:00
             x        (node) float64 dask.array<shape=(9228245,), chunksize=(141973,)>
             y        (node) float64 dask.array<shape=(9228245,), chunksize=(141973,)>
         Dimensions without coordinates: node
         Attributes:
             location:       node
             long_name:      water surface elevation above geoid
             mesh:           adcirc_mesh
             standard_name:  sea_surface_height_above_geoid
             units:          m
```

Figure 3. Reading a Zarr dataset from s3 storage in Xarray. Note the data looks as if it were read from a local NetCDF file or an OPeNDAP service, with the defined data type, shape, dimensions, and attributes.

After inspecting the total size that zeta would take in memory (58 GB), we calculate the maximum of zeta over the time dimension (Figure 4), and Dask automatically creates, schedules and executes the parallel tasks over the workers in the Dask cluster. The progress bar shows the parallel calculations that are taking place, in this case reading chunks of data from Zarr, computing the maximum for each chunk, and assembling each piece into the final 2D field.

```
In [12]: ds['zeta'].nbytes/1.e9

Out[12]: 53.1546912

In [13]: max_var = ds['zeta'].max(dim='time').persist()
         progress(max_var)
```

Figure 4. Calculating the maximum value zeta (water level) over the time dimension. The "persist" command tells Dask to leave the data on the workers, for possible future computations. The progress command creates progress bars that give the user a visual indicator of how the parallel computation is progressing. Here was see for example that 4813 Zarr reading commands were executed.

Once the maximum water level has been computed, we can display the results using the GeoViews TriMesh method, which when combined with the rasterize command from Datashader, dynamically renders and rasterizes the mesh to the requested figure size (here 600 × 400 pixels) (Figure 5). The controls on the right side of the plot allow the user to zoom and pan the visualization, which triggers additional rendering and rasterization of the data (Figure 6). In this way, the user can see investigate the full resolution of the model results. Even with this 9 million node grid, rendering is fast, taking less than 1 s. This will become even faster with PyViz optimizations soon to be implemented.

```
In [25]: tiles = gv.WMTS('https://maps.wikimedia.org/osm-intl/{Z}/{X}/{Y}@2x.png')

In [26]: value = 'max water level'
         label = '{} (m)'.format(value)
         trimesh = gv.TriMesh((tris, points), label=label)
         mesh = dshade.rasterize(trimesh).opts(
                    cmap='rainbow', colorbar=True, width=600, height=400)

In [27]: tiles * mesh

Out[27]:
```

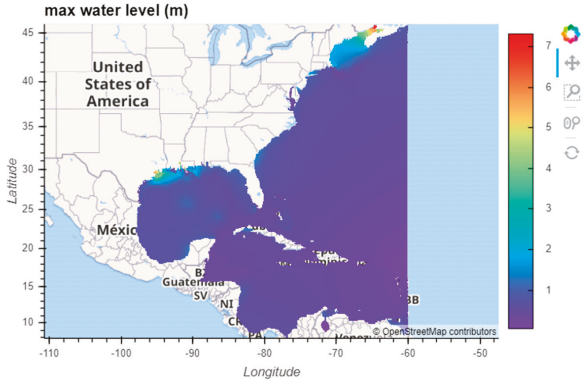

Figure 5. The TriMesh method from GeoViews is used to render the 9 million node mesh, and Datashader rasterizes the output to the requested width and height.

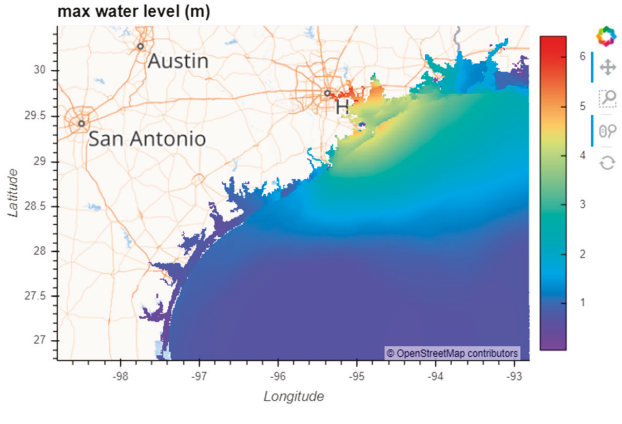

Figure 6. Using the controls on the right, the user has selected pan and wheel_zoom, which enables dynamic exploration of the maximum water level result in a region of interest (here the Texas Coast).

The notebook is completely reproducible, as it accesses public data on the Cloud, and the software required to run the notebook is all on the community Conda-Forge channel. The notebook is available on GitHub [35], and interested parties can not only download it for local use, but launch it immediately on the Cloud using Binder [36].

3.3. Example: Creating a Dashboard for Exploring a Structured Grid (Orthogonal Curvilinear Grid) Model

In addition to dynamic visualization of large grids, the PyViz tools hvPlot and Panel allow for easy and flexible construction of dashboards containing both visualization and widgets. In fact, hvPlot creates widgets automatically if the variable to be mapped has more than two dimensions. We can demonstrate this functionality with the forecast from the USGS Coupled Ocean Atmosphere Wave and

Sediment Transport (COAWST) model [9]. In Figure 7, a simple dashboard is shown that allows the user to explore the data by selecting different time steps and layers. This was created by the notebook code cell shown in Figure 8. The curvilinear orthogonal grid used by the COAWST model is visualized using the QuadMesh function in GeoViews. As with the TriMesh example, the user has the ability to zoom and pan, which Datashader re-renders the data (within a second) and then delivers the result to the browser (Figure 9). This notebook is also available on GitHub [34], where it can be examined, downloaded, or run on the Cloud (using the "launch Binder" button).

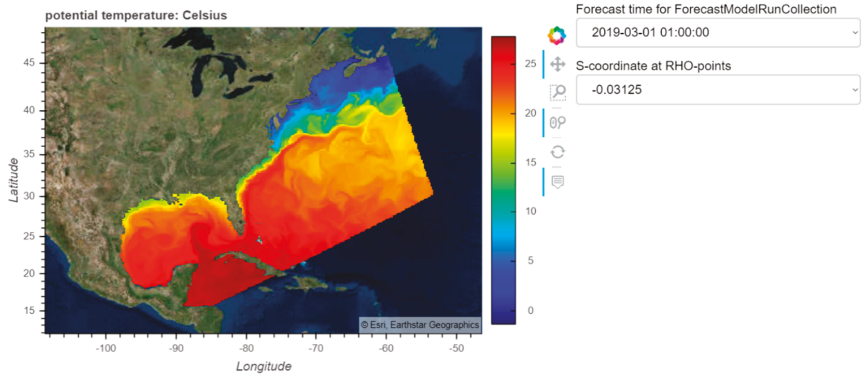

Figure 7. Simple dashboard for interactive, dynamic visualization of model results (here from the curvilinear orthogonal grid COAWST forecast model).

```
var = 'temp'
title = f'{ds[var].long_name}: {ds[var].units}'
mesh = ds[var][-24:,:].hvplot.quadmesh(x='lon_rho',y='lat_rho',crs=crs,title=title,cmap='jet',
                          rasterize=True,groupby=['time','s_rho'],width=600,height=400)
overlay = (gvts.EsriImagery * mesh).opts(active_tools=['wheel_zoom', 'pan'])
widgets = {'time': pn.widgets.Select, 's_rho': pn.widgets.Select}
dashboard = pn.holoviews.HoloViews(overlay, widgets=widgets).layout
```

Figure 8. Notebook cell that generates the dashboard in Figure 7. COAWST uses a curvilinear grid, we specify that HvPlot use the QuadMesh method to visualize the potential temperature, that we want to rasterize the result, and that by the GroupBy option, to create widgets for the time and vertical layers. We then specify that we want to use the ESRI Imagery tile service for a basemap, and overlay the visualization on top. Finally, we change widgets to type Select, which provide a dropdown list of values (instead of the default slider).

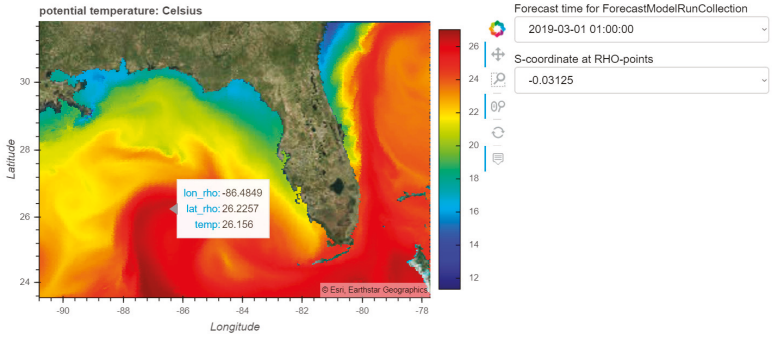

Figure 9. Zooming into the Gulf of Mexico on the COAWST forecast temperature, using the pan and wheel zoom controls. The hover control is also selected, which allows data values to be displayed along with their coordinates.

4. Discussion

The Pangeo framework demonstrated here works not only on the Cloud, but can run on HPC or even on a local desktop. On the local desktop, however, data needs to be downloaded for analysis by each user, and parallel computations are limited to the locally available CPUs. On HPC, there may be access to more CPUs, but the data still needs to be downloaded to the HPC center. On the Cloud, however, anyone can access the data without it having to be moved and have virtually unlimited processing power available to them. On the Cloud, Pangeo allows similar functionality to Google Earth Engine [37], allowing computation at a scale close to the data, but can be run on any Cloud, and with any type of data. Let us review the advantages of the Cloud in more detail:

Data access: Data in object storage like S3, can be accessed directly from a URL without the need of a special data service like OPeNDAP. This prevents the data service from being a bottleneck on operations, or data access failing because the data service has failed. It also means that data storage on the Cloud is immediately available for use by your collaborators or users. While data services like OPeNDAP can become overwhelmed by too many concurrent requests, this doesn't happen with access from object storage. Object storage is also extremely reliable, 99.999999999% with default storage on Amazon, which means if 10,000 objects are stored, you may lose one every 10 million years. Finally, data in object storage are not just available for researchers to analyze, but are also available for Cloud-enabled web applications to use. This includes applications that have been developed by scientists as PyViz dashboards, then published using Panel as dynamic web applications with one additional line of code.

Computing on demand: On the Cloud, costs accrue per hour for each machine type in use. It costs the same to run 60 CPUs for 1 min as it does to run 1 CPU for 60 min, and because nearly instantaneous access is available, with virtually unlimited numbers of CPUs, big data analysis tasks can be conducted interactively instead of being limited to batch operations. The Pangeo instance automatically spins up and down Cloud instances based on computational demands.

Freedom from local infrastructure: Because the data, analysis, and visualization are on the Cloud, buying or maintaining local computer centers, high power computer systems, or even fast internet connections is not necessary. Researchers and their colleagues can analyze and visualize data from anywhere with a simple laptop computer and the WiFi from a cell phone hotspot.

We have demonstrated the Pangeo framework for coastal ocean modeling here, but the framework is flexible and is being used increasingly by a wide variety of research projects, including climate scale modeling [38] and remote sensing [39]. While the framework clearly benefits the analysis and visualization of large datasets, it is useful for other applications as well. For example, the AWS Pangeo instance we deployed was used by the USGS for two multi-day machine learning workshops that each had 40 students from various institutions with a diversity of computer configurations, operating systems, and versions. The students were able to do the coursework on the Cloud using their web browsers, avoiding the challenges encountered when the course computing environment needs to be installed on a number of heterogeneous personal computers.

While there are numerous benefits to this framework, there are also some remaining challenges [40,41]. One important challenge is cost. The Cloud often appears expensive to researchers because much of the true cost of computing is covered by local overhead (e.g., the physical structure, electricity, internet costs, support staff). Gradual adoption, training, and subsidies for Cloud computing are some of the approaches that can help researchers and institutions make the transition to the Cloud more effectively. Another challenge is cultural: Scientists are accustomed to having their data local, and some do not trust storage on the Cloud, despite the reliability. Security issues are also a perceived concern with non-local data. Finally, converting the large collection of datasets designed for file systems to datasets that work well on object storage is a non-trivial task even with the tools discussed above.

Once these challenges are overcome, we can look forward to a day when all model data and analysis takes place on the Cloud, with all data directly accessible and connected by high-speed networks (e.g., Internet 2) and common computing environments can be shared easily. This will lead

to unprecedented levels of performance, reliability, and reproducibility for the scientific community, leading to more efficient and effective science.

Several agencies have played key roles in the development of these open-source tools that support the entire community: DARPA (U.S. Defense Advanced Research Projects Agency) provided significant funding for Dask, and ERDC (U.S. Army Engineer Research and Development Center) has provided significant funding through their EarthSim project for developing modeling-related functionality in the PyViz package. We hope that more agencies will participate in this type of open source development, accelerating our progress on expanding this framework to more use cases and more communities.

5. Conclusions

Pangeo with PyViz provides an open-source framework for interactive, scalable, data-proximate analysis and visualization of coastal ocean model output on the Cloud. The framework described here provides a glimpse of the scientific workplace of the future, where a modeler with a laptop and a modest internet connection can work interactively at scale with big data on the Cloud, create interactive visual dashboards for data exploration, and generate more reproducible science.

Author Contributions: Conceptualization, R.P.S.; methodology, software and writing, R.P.S. and D.P.

Funding: This research benefited from National Science Foundation grant number 1740648, and EarthSim project was funded by ERDC projects PETTT BY17-094SP and PETTT BY16-091SP. This project also benefited from research credits granted by Amazon.

Acknowledgments: Thanks to Ryan Abernathy, Joe Hamman, Matthew Rocklin, and rest of the Pangeo team for creating the community and tools that made this work possible. Thanks to Clint Dawson at the University of Texas for providing the ADCIRC simulation, and to John Warner from USGS for the COAWST forecast. Thanks to Jacob Tomlinson from the British Met Office, Joe Flasher from Amazon, John Readey from the HDF Group and Annie Burgess from ESIP for making our Pangeo deployment on AWS possible. Thanks to Filipe Fernandes for help building Conda-Forge packages for this project. Thanks to CollegeDegrees360 for the "Girl Using Laptop in Park" photo [42]. Any use of trade, product, or firm names is for descriptive purposes only and does not imply endorsement by the U.S. Government.

Conflicts of Interest: The authors declare no conflict of interest.

References

1. Hankin, S.C. NetCDF-CF-OPeNDAP: Standards for Ocean Data Interoperability and Object Lessons for Community Data Standards Processes. *OceanObs09* **2010**, 450–458.
2. MARACOOS OceansMap. Available online: http://oceansmap.maracoos.org/ (accessed on 26 February 2019).
3. AOOS Model Explorer. Available online: http://p.axds.co/?portal_id=16 (accessed on 26 February 2019).
4. Committee on Future Directions for NSF Advanced Computing Infrastructure to Support U.S. Science in 2017–2020. In *Future Directions for NSF Advanced Computing Infrastructure to Support U.S. Science and Engineering in 2017–2020*; National Academies Press: Washington, DC, USA, 2016. [CrossRef]
5. Abernathey, R.; Paul, K.; Hamman, J.; Rocklin, M.; Lepore, C.; Tippett, M.; Henderson, N.; Seager, R.; May, R.; Del Vento, D. Pangeo NSF Earthcube Proposal. *Figshare*, 2017.
6. Pangeo Project Web Page. Available online: https://pangeo.io (accessed on 28 February 2019).
7. Ennard-Bontemps, G.; Abernathey, R.; Hamman, J.; Ponte, A.; Rath, W. The Pangeo Big Data Ecosystem and its use at CNES. In *Proceedings of the 2019 Conference on Big Data from Space, 19-21, Munich, Germany*; Soille, P., Loekken, S., Albani, S., Eds.; Publications Office of the European Union: Luxembourg, 2019; pp. 49–52. [CrossRef]
8. ADCIRC Model Web Page. Available online: https://adcirc.org (accessed on 28 February 2019).
9. Warner, J.C.; Armstrong, B.; He, R.; Zambon, J.B. Development of a Coupled Ocean–Atmosphere–Wave–Sediment Transport (COAWST) Modeling System. *Ocean Model.* **2010**, *35*, 230–244. [CrossRef]
10. Zarr format web page. Available online: https://zarr.readthedocs.io/en/stable (accessed on 28 February 2019).
11. Dask project web page. Available online: https://dask.org (accessed on 28 February 2019).
12. Xarray project web page. Available online: http://xarray.pydata.org (accessed on 28 February 2019).
13. NetCDF format web page. Available online: https://www.unidata.ucar.edu/software/netcdf/ (accessed on 28 February 2019).

14. CF Metadata web page. Available online: http://cfconventions.org (accessed on 28 February 2019).
15. PyViz project web page. Available online: http://pyviz.org (accessed on 28 February 2019).
16. Jupyter project web page. Available online: https://jupyter.org (accessed on 28 February 2019).
17. Kubernetes web page. Available online: https://kubernetes.io (accessed on 28 February 2019).
18. Docker web page. Available online: https://www.docker.com (accessed on 28 February 2019).
19. EarthSim project web page. Available online: https://earthsim.pyviz.org (accessed on 28 February 2019).
20. Pothina, D.; Rudiger, P.; Bednar, J.; Christensen, S.; Winters, K.; Pevey, K.; Ball, C.; Brener, G. EarthSim: Flexible Environmental Simulation Workflows Entirely Within Jupyter Notebooks. *SciPy* **2018**, 48–55. [CrossRef]
21. Datashader project web page. Available online: http://datashader.org (accessed on 28 February 2019).
22. HoloViews project web page. Available online: https://holoviews.org (accessed on 28 February 2019).
23. GeoViews project web page. Available online: https://geoviews.org (accessed on 28 February 2019).
24. Cartopy project web page. Available online: https://scitools.org.uk/cartopy (accessed on 28 February 2019).
25. HvPlot project web page. Available online: https://hvplot.pyviz.org (accessed on 28 February 2019).
26. Panel project web page. Available online: https://panel.pyviz.org (accessed on 28 February 2019).
27. JupyterHub project web page. Available online: https://jupyterhub.readthedocs.io (accessed on 28 February 2019).
28. Conda web page. Available online: https://conda.io (accessed on 28 February 2019).
29. Conda-Forge web page. Available online: https://conda-forge.org (accessed on 28 February 2019).
30. Pangeo collaborators web page. Available online: https://pangeo.io/collaborators.html (accessed on 28 February 2019).
31. Pangeo issues web page. Available online: https://github.com/pangeo-data/pangeo/issues (accessed on 28 February 2019).
32. Pangeo blog web page. Available online: https://medium.com/pangeo (accessed on 28 February 2019).
33. Open Data on AWS web page. Available online: https://aws.amazon.com/opendata/ (accessed on 28 February 2019).
34. Earth System Information Partners Federation (ESIP) web page. Available online: https://www.esipfed.org (accessed on 28 February 2019).
35. Reproducible Jupyter Notebooks. Available online: https://github.com/reproducible-notebooks (accessed on 28 February 2019).
36. Binder Service Web Page. Available online: https://mybinder.org (accessed on 28 February 2019).
37. Gorelick, N.; Hancher, M.; Dixon, M.; Ilyushchenko, S.; Thau, D.; Moore, R. Google Earth Engine: Planetary-Scale Geospatial Analysis for Everyone. *Remote Sens. Environ.* **2017**, *202*, 18–27. [CrossRef]
38. Busecke, J.J.; Abernathey, R.P. Ocean Mesoscale Mixing Linked to Climate Variability. *Sci. Adv.* **2019**, *5*, eaav5014. [CrossRef] [PubMed]
39. Cloud Native Geoprocessing of Earth Satellite Data with Pangeo. Available online: https://medium.com/pangeo/cloud-native-geoprocessing-of-earth-observation-satellite-data-with-pangeo-997692d91ca2 (accessed on 28 February 2019).
40. Olanrewaju, R.F.; Burhan ul Islam, K.; Mueen Ul Islam Mattoo, M.; Anwar, F.; Nurashikin Bt. Nordin, A.; Naaz Mir, R.; Noor, Z. Adoption of Cloud Computing in Higher Learning Institutions: A Systematic Review. *Indian J. Sci. Technol.* **2017**, *10*, 1–19. [CrossRef]
41. Vance, T.C.; Wengren, M.; Burger, E.F.; Hernandez, D.; Kearns, T.; Merati, N.; O'Brien, K.M.; O'Neil, J.; Potemra, J.; Signell, R.P.; et al. From the Oceans to the Cloud: Opportunities and Challenges for Data, Models, Computation and Workflows. *Frontiers Marine Sci.* **2019**, *6*, 211. [CrossRef]
42. "Girl Using Laptop in Park" Photo from Flickr Photo-Sharing Web Site. Available online: https://www.flickr.com/photos/83633410@N07/7658165122 (accessed on 28 February 2019).

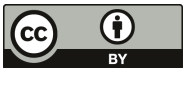

Journal of
Marine Science and Engineering

MDPI

Article

Modeling Tidal Datums and Spatially Varying Uncertainty in the Texas and Western Louisiana Coastal Waters

Wei Wu [1,*], Edward Myers [1], Lei Shi [1], Kurt Hess [1], Michael Michalski [2] and Stephen White [3]

[1] Office of Coast Survey, Coast Survey Development Laboratory, Silver Spring, MD 20910, USA; edward.myers@noaa.gov (E.M.); l.shi@noaa.gov (L.S.); kurt.hess@noaa.gov (K.H.)
[2] Center for Operational Oceanographic Products and Services, Silver Spring, MD 20910, USA; michael.michalski@noaa.gov
[3] National Geodetic Survey, Remote Sensing Division, Silver Spring, MD 20910, USA; stephen.a.white@noaa.gov
* Correspondence: wei.wu@noaa.gov; Tel.: +1-240-847-8258

Received: 30 September 2018; Accepted: 22 December 2018; Published: 9 February 2019

Abstract: Tidal datums are key components in NOAA's Vertical Datum transformation project (VDatum), which enables effective vertical transformation of the water level between tidal, orthometric, and ellipsoid -based three-dimensional reference systems. An initial application of modeling tidal datums was developed for the coastal waters of Texas and western Louisiana in 2013. The goals of the current work include: (1) updating the tidal model by using the best available shoreline, bathymetry, and tide station data; (2) implementing a recently developed statistical interpolation method for interpolating modeled tidal datums and computing tidal datum uncertainties; and (3) using modeled tidal datums to upgrade non-tidal polygons for enhancing the quality of the VDatum marine grid population. The updated tidal model outperformed the previous tidal model in most cases. The statistical interpolation method is able to limit the interpolated tidal datums to within a user-defined model error (0.01 m in this work) and produce a spatially varying uncertainty field for each interpolated tidal datum field. The upgraded non-tidal polygons enhanced the quality of the VDatum marine grid population. This paper will introduce the detailed procedures of this modeling work, present and discuss the obtained results, share the effective methods used for improving model performance and lessons learned in the model assessments, and analyze the improvement of the current tidal model in comparison with the previous tidal model.

Keywords: coastal and estuarine modeling; ADCIRC; water level time series; VDatum; tidal datums; statistical interpolation; spatially varying uncertainty; non-tidal zones; marine grid population; Texas; western Louisiana; Gulf of Mexico

1. Introduction

Tidal datums are one type of the three vertical datums (ellipsoid-based datums, orthometric datums, and tidal datums) that are used for referencing the elevation of any specific point on the Earth's surface. A tidal datum is calculated from the average of high or low tidal heights (tidal extrema). This vertical reference surface is derived from water level measurements recorded along coastlines, estuaries, and tidal rivers, and is fundamental to the determination of the spatial coordinates of latitude, longitude, and elevation relative to mean sea level [1,2].

Tidal datums are mainly used to determine horizontal boundaries and to provide accurate vertical references for bathymetry and topography. Some examples include the legal determinations of private and public lands, state owned tide lands, state submerged lands, U.S. Navigable Waters,

U.S. Territorial Sea, Contiguous Zone, and Exclusive Economic Zone, as well as the High Seas or international waters [2]. The establishment of tidal datums and their reference to the geodetic control network is important for broad applications. As pointed out in [2], navigation in harbors, shipping channels, and intracoastal waterways (ICW) requires an accurate knowledge of the depth of the ocean and submerged hazards at the low-water phase of the tidal cycle. Passage underneath bridges requires knowledge of the clearance at the high water phase of the tide. Coastal construction and engineering require knowledge of the tidal cycle, in addition to significant wave heights, periods, and directions; the heights of storm surges or tsunami waves; and the frequency and horizontal extent of flooding in the coastal zone.

Tidal datums are key components in NOAA's Vertical Datum transformation software tool (VDatum) [3–5]. This free VDatum software tool allows users to vertically transform geospatial data among a variety of three-dimensional ellipsoidal, orthometric, and tidal datum reference systems. The VDatum database is crucial to coastal applications that rely on vertical accuracy in bathymetric, topographic, and coastline datasets. For example, using inconsistent datums from multiple data sources can cause artificial discontinuities [3,4], which can be problematic, especially when accurate maps are needed by federal, state, and local authorities to make informed decisions. In this case, applying VDatum to merge multiple data sources into one entire data set by using a common vertical datum reference system can be particularly useful.

The goal of the VDatum project is to develop a seamless nationwide utility that would facilitate more effective sharing of vertical data and also complement a vision of linking such data through national elevation and shoreline databases [3,4]. The VDatum software tool is currently available in the coastal regions covering the continental United States, Puerto Rico, and the U.S. Virgin Islands [1]. Several regions are undergoing model upgrades to update foundational geodetic and tidal datum data. The updated VDatum software will eventually cover all of the U.S. coastal waters from the landward navigable reaches of estuaries and charted embayments out to 75 nautical miles offshore, including all tidal datum and sea surface topography transformations over the water and all transformations between the ellipsoidal and orthometric datums over the water and the land [5]. The availability of VDatum nationwide enables bathymetric, topographic, and shoreline data to be easily transformed and assembled in a manner that complements dissemination through national databases [3].

In support of the VDatum development, a tidal model for the coastal waters of Texas (TX) and western Louisiana (LA) was initially developed in 2013 for the products of modeled tidal datums and associated uncertainties [6,7]. The previous modeling work includes: (1) creating unstructured triangular model grids with bathymetry assigned; (2) running a two-dimensional barotropic version of the ADvanced Circulation (ADCIRC) hydrodynamic model [8–11]; (3) conducting sensitivity tests for determining optimal model parameters; (4) calculating and analyzing tidal datums using modeled water level time series; (5) analyzing and correcting the model errors by comparing modeled and observed tidal datums; and (6) producing a VDatum marine grid population for the final VDatum products. Note that ADCIRC is an advanced hydrodynamic model which has been developed since the early 1990s [9–11]. The model has been demonstrated to be effective in modeling ocean, coastal, and estuarine processes and thus has been widely used in the modeling community. The initial development of modeling tidal datums in the TX and western LA coastal waters was important for a basic understanding of tidal datum characteristics in the model regions.

Shoreline and bathymetry change with time due to numerous physical processes. For example, severe weather events such as hurricanes and tropical storms can dramatically change the structure of a shoreline and bathymetry. The archives at the National Hurricane Center reveal that hurricanes and tropical storms occurred in the western Gulf of Mexico every year in the past two decades [12]. Dredging, sediment transport, land subsidence, and sea level rise are also common factors of bathymetry or shoreline changes.

Considering the potential changes in the shoreline and bathymetry and the availability of new observations (shoreline, bathymetry, and tides), it is necessary to update this tidal model to ensure

the quality of the VDatum products. For example, the previous tidal model for the TX and western LA coastal waters used the National Ocean Service (NOS) bathymetry data which were collected in the hydrographic surveys from 1885 to 2005 (available at that time); meanwhile, we used additional NOS bathymetry data which were collected in hydrographic surveys from 2005 to 2015 for the model update. The additional 11 years of new data represent the most current bathymetry information from NOS hydrographic surveys, enhancing the accuracy of model bathymetry. Detailed information on the data used for the model update will be introduced in Section 2.

The current work on updating the tidal model and the modeled tidal datums is part of the VDatum project, in support of the development of updated nationwide VDatum products and the VDatum software tool. Six tidal datums were involved in the update: (1) Mean Higher High Water (MHHW): the average of all the daily higher high water heights; (2) Mean High Water (MHW): the average of all the daily high water heights; (3) Mean Low Water (MLW): the average of all the daily low water heights; (4) Mean Lower Low Water (MLLW): the average of all the daily lower low water heights; (5) Diurnal Tidal Level (DTL): the average of MHHW and MLLW; and (6) Mean Tidal Level (MTL): the average of MHL and MLW. Here "daily" refers to "each tidal day."

The goals of the current work include: (1) updating the tidal model and modeled tidal datums by incorporating the best available shoreline, bathymetry, and tide station data; (2) implementing a Spatially Varying Uncertainty (SVU) statistical interpolation method [13] to interpolate the modeled tidal datums and compute associated spatially varying uncertainties; and (3) upgrading the existing observationally-based estimates of non-tidal polygons by incorporating modeled non-tidal grids. Note that "non-tidal" is defined as MHW minus MLW (the mean tidal range) less than 0.09 m [14]. Thus, if a model grid satisfied the condition that the difference between MHW and MLW was less than 0.09 m, we marked the model grid as a non-tidal grid. The non-tidal threshold was established by NOAA's Center for Operational Oceanographic Products and Services (CO-OPS) for masking areas with negligible tides from the determination of tidal datums since it is difficult to identify and tabulate regular daily high and low tides in those areas [14]. Physically, a non-tidal area represents an area where a periodic tide is present and consistent, but the mean tidal range is negligible.

For the current work, we first extended model mesh grids to include new tide stations, and updated shoreline and bathymetry using the best available data. Next, we ran the updated tidal model to attain modeled water level time series at each model grid point. The modeled water level time series were then used to compute modeled tidal datums. Modeled tidal datums were compared with observed tidal datums at the 75 tide stations available in this model domain. Large (>0.10 m) model biases were reduced by adjusting the tidal model, as we will detail later in Section 3.2. After that, a statistical interpolation method (the SVU method) was implemented to interpolate the modeled tidal datums and compute associated spatially varying uncertainties. Further, the modeled non-tidal grids were incorporated to upgrade the existing non-tidal zones, which were estimated by CO-OPS based on observations. Finally, the tidal datum marine grid population was produced for the final VDatum products.

As we will show and discuss later in Section 3, the updated tidal model outperformed the previous tidal model statistically. The statistical interpolation method limits the interpolated tidal datums to within a user-defined model error (0.01 m in this work). The statistical interpolation method was demonstrated to reduce the model bias and model errors in comparison with the previous deterministic approach, according to the previous study [13]. The statistical interpolation also produces a spatially varying uncertainty field for each interpolated tidal datum field. This offers the spatially varying characteristics of the uncertainty field, which is an improvement from the previous single-value model uncertainty over an entire VDatum region. The upgrade of the non-tidal polygons enhanced the quality of the VDatum marine grid population.

Section 2 introduces details of the hydrodynamic model and its configuration; the model domain update; the coastline/bathymetry/observed tidal datum datasets used for the model update; and the methodologies used in the calculations of observed and modeled tidal datums and the statistical

interpolation, and in the estimation of non-tidal grids. Section 3 presents and discusses the obtained results, including: (1) the observed and modeled tidal datums; (2) the assessment of modeled tidal datums and the techniques used for improving model performance, and lessons learned in model assessment; (3) the statistically interpolated tidal datums and associated spatially varying uncertainties; (4) statistics regarding the observed tidal datums, the modeled tidal datums, the modeled tidal datums after the statistical interpolation, and associated spatial varying uncertainties; (5) upgraded non-tidal polygons and their effect on the VDatum marine grid population; and (6) the assessment of tidal model improvements. Section 4 briefly summarizes the entire work.

2. Model, Data, and Methods

2.1. Hydrodynamic Model and Its Configuration

As mentioned in Section 1, ADCIRC is an advanced hydrodynamic model and has been widely used in the ocean, coastal, and estuarine modeling community. ADCIRC applications cover a wide range of topics, such as wave-current-surge interactions [15], storm surges [16,17], and surge and tide predictions [18,19]. In this work, we use the two-dimensional depth-integrated barotropic version of the ADCIRC hydrodynamic model (version 51.52.34, released in January 2016) [8] to simulate the time series of tidal elevation at each model grid point.

2.1.1. Model Configuration

The key model parameter settings are similar to the previous model [6,7], except for (as described below) the open ocean boundary forcing setting:

(1) nonlinear quadratic bottom friction with a spatially constant bottom friction coefficient of 0.002;
(2) a spatially constant horizontal eddy viscosity of 5.0 m^2/s for the momentum equations;
(3) wetting and drying process enabled with a minimum water depth of 0.05 m as a wet node/element criterion;
(4) a spatially uniform Generalized Wave-Continuity Equation (GWCE) weighting factor of 0.02;
(5) advective terms were included;
(6) no atmospheric forcing and river flow were imposed;
(7) tidal potential body force of eight principal tidal constituents (K1, O1, P1, Q1, M2, S2, N2, and K2) was included;
(8) water elevations from the same eight principal tidal constituents: K1, O1, P1, Q1, M2, S2, N2, and K2 were used at the open ocean boundary. That is, open ocean boundary forcing equals the sum of the elevations of the eight tidal harmonic constituents, which were extracted from the EC2015 tidal database [20,21].

    Note that the open ocean boundary forcing setting in the previous model is different. The previous model examined the ADCIRC EC2001 database [22], Oregon State University's (OSU's) TPXO (the OSU TOPEX/Poseidon Global Inverse Solution) global tide prediction model [23], and OSU's regional tide prediction model in the Gulf of Mexico region (OSU-GOM) [24], and then chose the OSU-GOM to extract open ocean boundary forcing for the ADCIRC model run [6,7];

(9) a total of 67 days of the ADCIRC model run. A hyperbolic tangent ramp function was specified, and the beginning six days were used to ramp up ADCIRC forcings from zero. The time step for the ADCIRC model run is 3 s. The output from the ADCIRC model run is the 6-min water level time series at each model grid point from the final 60-day run, which were used for computing tidal datums at each model grid point.

2.1.2. Model Domain

The model domain spans from the coast of San José de los Leones, Mexico [97.71° W, 24.25° N], about 198 km south of the US-Mexico border from Brownsville in the southwest of the model domain to the intersection of east of Caillou Bay and west of Lake Pelto [91.12° W, 29.22° N] in LA (Figure 1). The model domain was first extended to include new tide stations using a commercial software package called Surface-water Modeling System© [25] (SMS version 12.2.7). The major extension areas are in the western LA coastal region (Figure 2). Four new tide stations in the western LA coastal region were included through the extension. Two minor extension areas are in the middle of the TX coast to include two new tide stations (shown in the right panel of Figure 2): one is a shallow-water area in the southwest of Aransas River, and the other is a shallow and short water channel between Redfish Slough and Mustang Lake. It is worthwhile to note that the scope of the extension was determined by the judgment that water bodies in the extended areas were connected to the existing model grids and bathymetry was available.

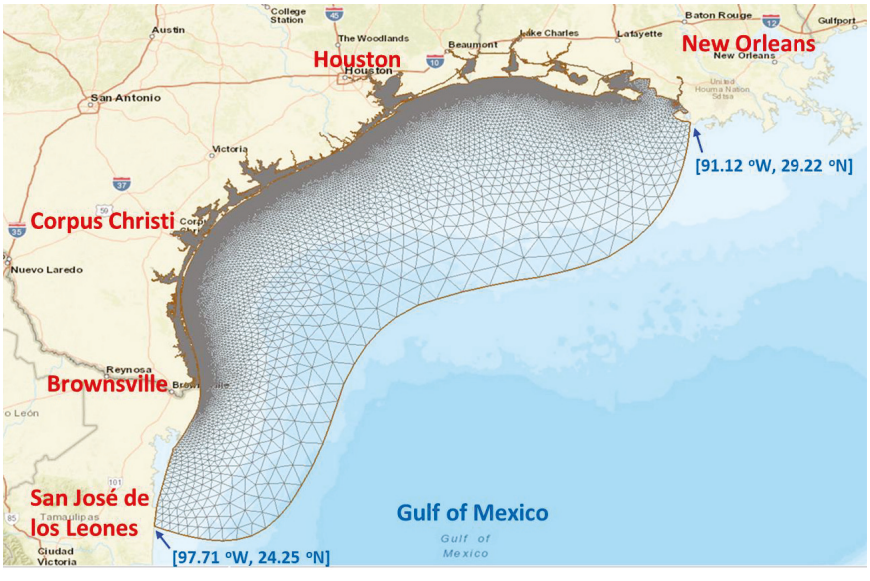

Figure 1. Model domain for the TX and western LA coastal regions.

NOAA's shoreline dataset (Continually Updated Shoreline Product—CUSP [26]) was used as a reference for determining the model boundary when extending the model domain. Section 2.2.1 will give a brief introduction on the CUSP dataset and how we used the dataset.

The spatial resolution of the model grids ranges from 14.38 m in the coastal region to 28.58 km near the open ocean boundary. The updated model domain includes a total of 297,227 nodes and 542,936 elements. The grid resolution increases from the open ocean boundary to the coasts and embayments to better represent the complexity in the shorelines and shallow water tidal dynamics. The best available bathymetry data were used to update the model bathymetry. Model grid bathymetry ranges from 0.13 m to 2090.40 m. The shallowest bathymetry occurs in the lakes and the deepest bathymetry is located at the open ocean boundary. Section 2.2.2 will briefly describe the bathymetry datasets used for the update and their priorities.

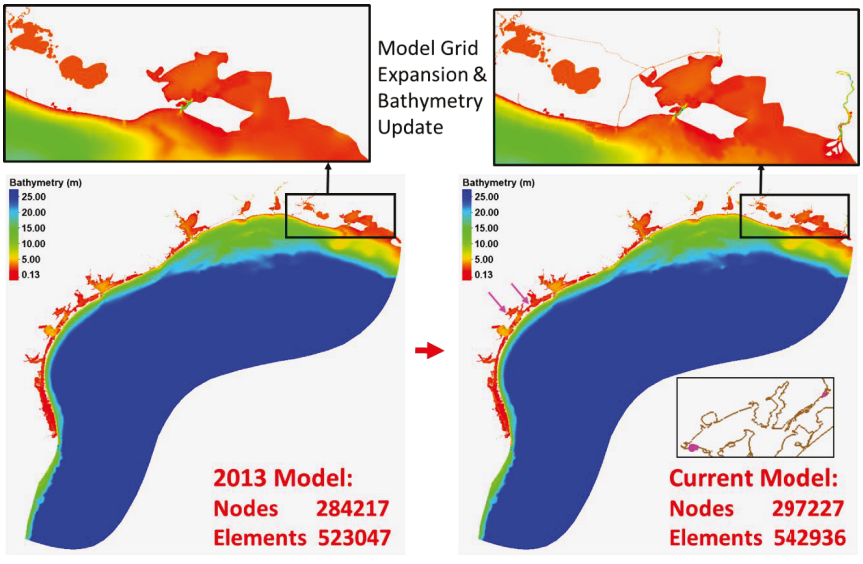

Figure 2. Model grid extension into smaller rivers and the Intracoastal Waterway (ICW) with updated bathymetry: before (**left**) and after (**right**) the model update. The two pink arrows in the right panel show the two areas with a minor extension of model grids in the middle of the TX coast. The extended model grid points in the two areas are shown as pink dots in the enlarged plot in the right lower corner of the right panel.

2.2. Data

2.2.1. NOAA's Continually Updated Shoreline Product (CUSP)

The shoreline represents a dynamic interface between land and water and it changes with time, as mentioned in Section 1. CUSP provides the most current shoreline representation of the U.S. and its territories, available online [26,27]. The CUSP shoreline dataset was created to deliver a continuous shoreline with frequent updates to support various applications, such as developing coastal and marine spatial plans; managing resources; mitigating hazard events; and conducting coastal environmental analyses for federal agencies, coastal state and local organizations, academic institutions, and private companies.

CUSP is built upon National Geodetic Survey's (NGS's) National Shoreline data and it uses all national shorelines that have been verified by contemporary imagery and shorelines from other non-NOAA sources including lidar, imagery, and shoreline vectors. The shoreline vector only includes shoreline and alongshore features that represent the shoreline (groins, breakwaters, and jetties). Individual national shoreline projects are edge matched using contemporary imagery as a guide. Single-line alongshore features and alongshore features where water passes underneath are not included. CUSP references a MHW shoreline based on vertical modeling or image interpretation using both water level stations and/or shoreline indicators if applicable. The decision to compile features is based on the ability to extract a proxy MHW line considering water level, image date, resolution, accuracy, and shoreline slope. CUSP covers the continental U.S., with portions of Hawaii, the Pacific Islands, Alaska, Puerto Rico, and the U.S. Virgin Islands.

We used the CUSP shoreline dataset as a reference to: (1) determine the model boundary when extending the model domain; and (2) update the coastline data file for producing the VDatum marine grid population.

2.2.2. Bathymetry Data

Several bathymetry datasets were used to update the bathymetry for the model grids. Bathymetry data were applied by priority. The more reliable and more recent bathymetry data have a higher priority. For example, the most recent hydrographic survey data have the highest priority. The datasets used are listed below:

Priority 1. NOAA/NOS best available hydrographic survey data from 2005 to 2015, processed and provided by the data team at NOAA/NOS/OCS (Office of Coast Survey)/CSDL (Coast Survey Development Laboratory)/GADB (Geospatial Applications Development Branch). Note that NOAA/NOS older hydrographic survey data from 2001, 2002, and 1935 were also used for the extended waterways near Weeks Bay and Atchafalaya River (Figure 3), where no recent-year hydrographic survey data were available.

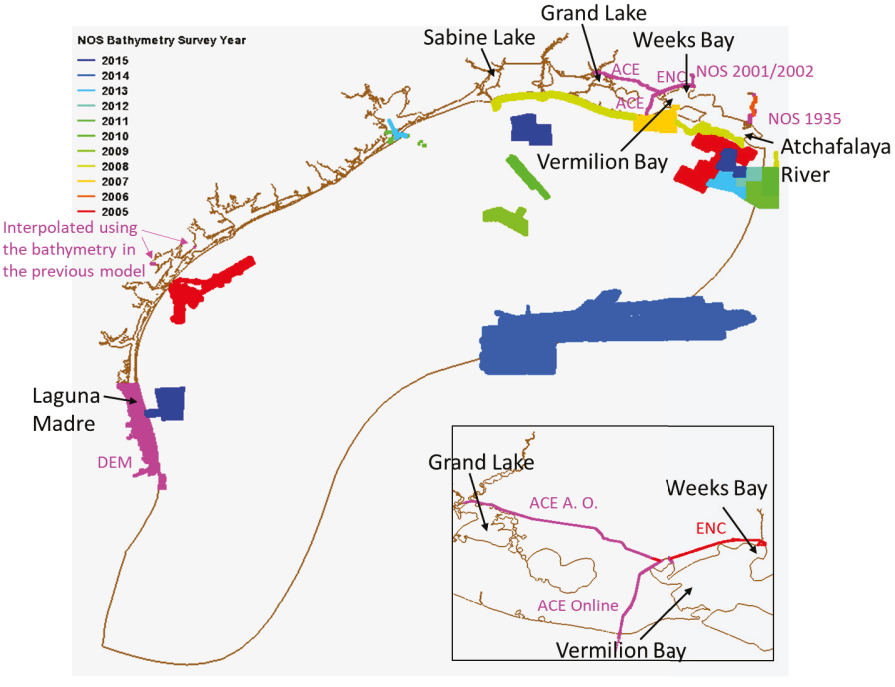

Figure 3. The locations, types, and years of the new bathymetry data used for the model update. The areas with a pink color represent data other than NOS bathymetry. The region with the extended water paths in the western LA's ICW area is enlarged in the box in the lower right corner to show details. "A. O." represents data provided by ACE's Andrew Oakman.

Priority 2. The U.S. Army Corps of Engineers (ACE) hydrographic survey data in the extended southern LA's Freshwater Bayou area [28] and in the extended western LA's ICW between Grand Lake and Vermilion Bay (Figure 3) (the 10-year accumulated bathymetry data in the area were kindly provided by ACE's Andrew Oakman). No NOS hydrographic survey data were available in those areas.

Priority 3. NOAA's Electronic Navigational Chart (ENC, Chart #11345) data [29] were used for interpolating bathymetry in the extended western LA ICW between Vermilion Bay and Weeks Bay where no hydrographic survey data were available.

Priority 4. NOAA's National Geophysical Data Center (NGDC) High-Resolution Digital Elevation Model (DEM) data in the southwestern TX coastal area where no bathymetry data were available

from the abovementioned three resources. The DEM bathymetry used for the model update is "South_Padre_TX_1/3_arc_second_DEM_MHW.asc" [30].

Priority 5. The previous model's bathymetry dataset (the model input file "fort.14") [7], which was created by using NOAA/NOS hydrographic survey data from 1885 to 2005, NOAA's ENCs for Sabine Lake and southern Laguna Madre (Figure 3), and ACE bathymetry data (for major shipping channels and ICW in the previous model grids).

Figure 3 shows the locations, types, and years of the new bathymetry data used for the model update.

2.2.3. Observed Tidal Datums and Associated Root-Mean-Square (RMS) Errors

The observed tidal datums (MHHW, MHW, MLW, and MLLW) and associated RMS errors were calculated using observed water level time series at tide stations by CO-OPS [2,31]. The calculation method will be briefly introduced in Section 2.3.1. We used the observed tidal datums for assessing model performance, and used both the observed tidal datums and associated RMS errors for the statistical interpolation.

A total of 75 tide stations have valid greater-than-zero observed tidal datums within the model domain [98° W to 91° W, 24° N to 31° N]. Sixteen out of the 75 tide stations do not have the observed RMS error data, so we used the average of the RMS errors at the remaining 59 tide stations to represent the RMS errors in the 16 tide stations for the statistical interpolation. The locations of the tide stations will be shown later in Section 3.1 when we discuss the distributions of the observed tidal datums.

2.3. Methods

This section describes the methods used in the calculations of observed and modeled tidal datums, the SVU statistical interpolation, and the estimates of non-tidal zones. Figure 4 shows a schematic diagram which depicts the detailed workflow of the model update, with the statistical interpolation step enclosed within the box.

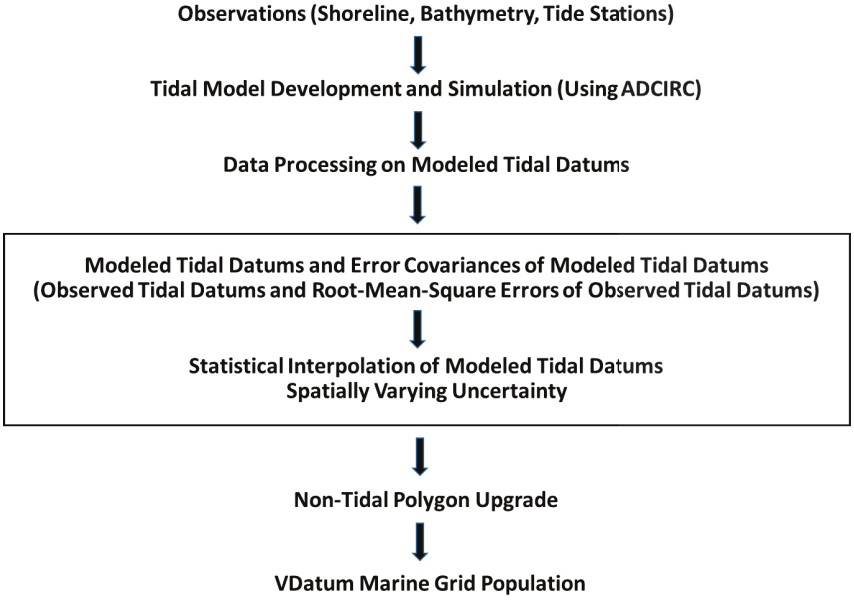

Figure 4. A schematic diagram of the workflow of the model update with the SVU statistical interpolation step enclosed within the box.

2.3.1. Calculation of Observed Tidal Datums

Detailed information about NOS observed datum computation procedures can be found in "CO-OPS's Tidal datums and their Applications" [2,31]. NOS collects raw data at 6-min intervals from tide stations. The collected raw data were first processed for quality control. After that, the tabulation process with quality control was carried out, including the generation of hourly heights, high and low waters, and monthly means, and the selection of higher high and lower low waters. A specific 19-year period designated as a National Tidal Datum Epoch (NTDE) was used to compute tidal datums. The NTDE is used as the fixed period of time for the determination of tidal datums because it includes all significant tidal periods, it is long enough to average out the local meteorological effects on sea level, and specifying the NTDE can ensure a uniform approach to apply to the tidal datums for all stations. The current NOS observed tidal datums were computed with reference to the current tidal epoch of 1983–2001 NTDE.

Tidal datums at control stations are computed by an arithmetic mean method for a specific length of record over a tidal epoch. The input for the procedure requires the monthly mean values for a tidal epoch. Tidal datums at secondary stations are generally computed by a comparison of monthly means between subordinate and control stations. Tidal datums at tertiary stations are computed by a comparison of monthly means or comparison of simultaneous high and low waters (if no calendar month of data) between the tertiary station and a control station, or with an acceptable secondary station. The input for this procedure is the simultaneous means from the control and subordinate stations in a region of similar tidal characteristics to produce an equivalent datum at the subordinate station with an adjustment to 19-year values. More details about observed datum computation can also be found in [2,31–34].

2.3.2. Calculation of ADCIRC Tidal Datums

Detailed procedures about how modeled datums were computed by using the 6-min ADCIRC modeled water level time series can be found in "Standard Procedures to Develop and Support NOAA's Vertical Datum Transformation Tool" [5].

First, modeled water level time series are checked for several conditions, including too small a signal, drying or ponding, and repeated values. For example, if a model node goes dry (i.e., its water depth drops below some specified value h0), the model code automatically substitutes a default value for the output elevation. Thus, the first check is for water level values below a user-defined level h99. If this situation has occurred, the analysis is skipped and the output values of the datums are set to be a default value.

After that, the averaged water levels for each half-hourly period (centered on the hour and half-hour) are computed to estimate the times of tidal peaks by following a specific approach and by using the method of singular value decomposition [5]. Peaks are then put into chronological order and any repeated peaks are eliminated.

Next, the peaks are screened and those pairs that do not fit separation criteria are eliminated. CO-OPS' criteria are that the amplitudes must differ by at least delhr in time (hours) and delamp in amplitude (meters), where the nominal values delhr = 2.0 h and delamp = 0.03 m were used in this work. First, extrema pairs are screened and those too close in time are eliminated. Then, in the standard procedures, the mean tidal range, which is computed as the difference between the mean of the high waters minus the mean of the low waters, is checked. If this range is lower than a user-specified value rangemin, datums for that time series are set to be a default value. Then, extrema pairs are screened and those too close in amplitude are eliminated. Then, another check of the mean tidal range is made.

Following this, the highs and lows are separated into higher highs, lower highs, higher lows, and lower lows by applying the '25 h algorithm' developed by CO-OPS. For example, three successive highs in a 25-h window are examined to determine the maximum value. The window is then centered on this peak, which becomes the higher high; the peaks ahead and behind become lower highs. Finally, in the last step, all the higher highs are averaged to determine the Mean Higher High Water (MHHW),

all the daily lower highs are averaged to determine the Mean Lower High Water (MLHW), and all the peaks are averaged to become the Mean High Water (MHW). The calculations for low water are analogous. The Mean Tide Level (MTL) is the mean of MHW and MLW, and the Diurnal Tide Level (DTL) is the mean of MHHW and MLLW. Note that modeled Mean Sea Level (MSL) is the mean of the 6-min modeled water levels. The MSL was deducted from the six tidal datums for a comparison with the observed tidal datums which have also deducted the observed MSL.

2.3.3. Statistical Interpolation of Tidal Datums and Their Associated Spatially Varying Uncertainties

Once the ADCIRC modeled tidal datums are derived from the 6-min modeled water level time series, a tidal datum analysis field f is calculated by blending the modeled tidal datum with observed tidal datum using a statistical interpolation method [13].

As described in "Statistical Interpolation of Tidal Datums and Computation of Its Associated Spatially Varying Uncertainty" [13], the method was developed based on the variational principle. We first constructed a cost function $J(f)$ according to the statistical characteristics (error covariance) of the observed and modeled tidal datums as

$$J(f) = \frac{1}{2}(f - f_m)^T P^{-1}(f - f_m) + \frac{1}{2}(f_0 - Hf)^T \left(W^{-\frac{1}{2}}\right)^T R^{-1} W^{-\frac{1}{2}}(f_0 - Hf) \quad (1)$$

where f is a new $n \times 1$ tidal datum analysis field at model mesh nodes, f_m is a size $n \times 1$ discrete modeled tidal datum field, f_0 is a size $m \times 1$ observed tidal datum field at CO-OPS station locations, H (size $m \times n$) is the interpolation matrix projecting the modeled field to the observed data locations, and W (size $m \times m$) is a diagonal weight matrix that adjusts how much the final product f differs from the observed values at the station locations. It is assumed the model and observation fields are unbiased, and both f_m and f_0 follow a normal distribution, where $\mathrm{Var}(f_m) = P$ and $\mathrm{Var}(f_0) = R$, respectively. Then, we derived a blended tidal datum field f that minimizes the cost function $J(f)$ as

$$f = f_m + G(f_0 - Hf_m) \quad (2)$$

where $G = PH^T[W^{\frac{1}{2}} R \left(W^{\frac{1}{2}}\right)^T + HPH^T]^{-1}$ is the gain matrix and f is the unbiased estimate of the true tidal datum field. In the final step, as a by-product, the associated uncertainty (e.g., the posterior error covariance matrix P_a) is calculated for the blended tidal datum field f by

$$P_a = Var(f) = (I - GH)P(I - GH)^T + GRG^T \quad (3)$$

where I is the identity matrix.

Note that the model error covariance matrix is estimated as $P_{ij} = var(f_{n_1}, f_{n_2}) = \sigma_{n_1}\sigma_{n_2} corr(f_{n_1}, f_{n_2})$, ($1 \le i, j \le n$, in unit of m^2). σ_{n_1} and σ_{n_2} are the standard deviations of the model errors at nodes n_1 and n_2, respectively, and are assumed to be constant at all the model nodes which were equal to the standard deviation of the modeled errors at all the tide stations. The correlation between two points is calculated using a three-day moving average tidal datum time series. Here, the covariance is adjusted and decreases exponentially over the distance between nodes n_1 and n_2. Also, the weight matrix W determines the weight of R in the computation of the analysis field f. The diagonal element w_{ii} ($0 \le w_{ii} \le 1$, $1 \le i \le m$) is the weight of the observation error variance r_{ii} at station i in the determination of analysis field f. The weight matrix W was determined through iteration following the predetermined constraint; that is, the discrepancy between the analysis field and the observations at all tide stations is equal to or less than 1 cm or the CO-OPS's uncertainty value (observed rms error), whichever is less.

As demonstrated in [13], the statistical interpolation has a few advantages over the traditional deterministic correction method: (1) it provides a spatially varying uncertainty; (2) it provides a framework to assimilate future data streams with known uncertainty to improve the quality of the

final tidal datum product; and (3) it reduces model bias, maximum absolute model error, mean absolute model error, and root mean square of the model errors in comparison with the traditional deterministic approach.

The traditional method for correcting modeled tidal datums, called "Tidal Constituent and Residual Interpolation (TCARI)", was based on the application of Laplace's Equation [5,35–37]. The TCARI method numerically creates a tidal datum correction field at all the model grid points by using the modeled tidal datum errors at tide stations. The modeled tidal datums after TCARI corrections closely match the observed tidal datums at tide stations. The accuracy (uncertainty) of the modeled tidal datums after TCARI corrections was assessed by computing the root mean square of the differences between the observed value and the TCARI-interpolated value over an entire interested model domain, which was obtained by using a jackknifing approach and the TCARI method. A detailed explanation of the estimation of the VDatum uncertainty can be found in [5,38].

It is worth pointing out that the RMS error of the observed tidal datum at each tide station is the same for all the tidal datums. The difference in tidal datums' spatially varying uncertainties mainly comes from the difference in the covariance of the modeled tidal datum errors, which is different for different tidal datums.

2.3.4. Estimates of Non-Tidal Zones and VDatum Marine Grid Population

As mentioned in Section 1, CO-OPS established the "non-tidal" zones, which represent areas where a periodic tide is present and consistent in the observations, but the mean tidal range is negligible (MHW minus MLW is less than 0.09 m) [14]. Likewise, a model grid point referred to a modeled non-tidal grid if its modeled MHW minus MLW was less than 0.09 m. Modeled non-tidal grids were incorporated for upgrading the existing non-tidal polygons (detailed in Section 3.4).

The upgraded non-tidal polygons were used for the VDatum marine grid population (the last step of the workflow, as shown in Figure 4) to ensure the areas with valid tidal datums have valid populated tidal datums at marine grids, while the areas without valid tidal datums (non-tidal areas) have invalid populated tidal datums at marine grids. The VDatum marine grid population includes two steps [5]: First, a uniformly spaced marine grid field was generated with a spatial resolution of 0.001 (one thousandth) degree in longitude and latitude (see an example in Section 3.4). The marine grid field distinguishes between points that represent land and those that represent water, using a coastline and bounding polygon file to make the determination. Then, the marine grids were populated using modeled tidal datums.

The accuracy of non-tidal polygons is thus crucial to the quality of the VDatum marine grid population. The important role of non-tidal polygons in the VDatum marine grid population will be explained in Section 3.4. In this work, we incorporated the modeled non-tidal grids to upgrade the existing non-tidal polygons for enhancing the quality of the VDatum marine grid population.

3. Results and Discussion

3.1. Observed Tidal Datums

Figure 5 shows the four major tidal datums from observations at the 75 available tide stations in this model domain. The observed tidal datums are referenced to the local MSL at each station. As introduced in Section 1, MHHW/MHW/MLW/MLLW respectively refer to the average of the higher high water height each tidal day, the average of all the high water heights each tidal day, the average of all the low water heights each tidal day, and the average of the lower low water height each tidal day.

As shown in this figure, the maximum value of the observed tidal datums in the model domain is less than 0.40 m. The observed tidal datums show relatively larger values from the Houston area to the east: MHHW and MHW are greater than 0.10 m, and MLW and MLLW are deeper than −0.20 m. The area from Houston to the west shows relatively smaller tidal datums.

Figure 6 shows the mean tidal ranges from the 75 tide stations, ranging from 0.10 m to 0.49 m. The mean tidal range from Houston to the east is much larger than that from Houston to the west. The averaged value of the observed mean tidal ranges equals 0.33 m for the region from Houston to the east (blue polygon) and 0.23 m for the region from Houston to the west (red polygon). It is worthwhile to mention that the Gulf of Mexico is characterized as a region with a small tidal range. This is mainly because: (1) the Gulf of Mexico has a narrow connection with the Atlantic Ocean; and (2) the Gulf of Mexico is a diurnal-tide dominant ocean basin, but the diurnal tides are small in the Atlantic Ocean since the Atlantic Ocean is too small to produce resonant sloshing with a diurnal-tide period [39].

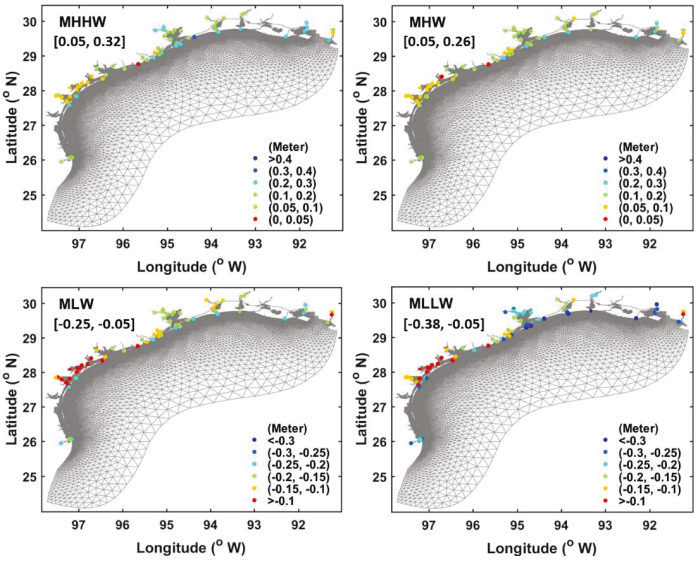

Figure 5. Observed tidal datums with minimum and maximum values listed in the brackets.

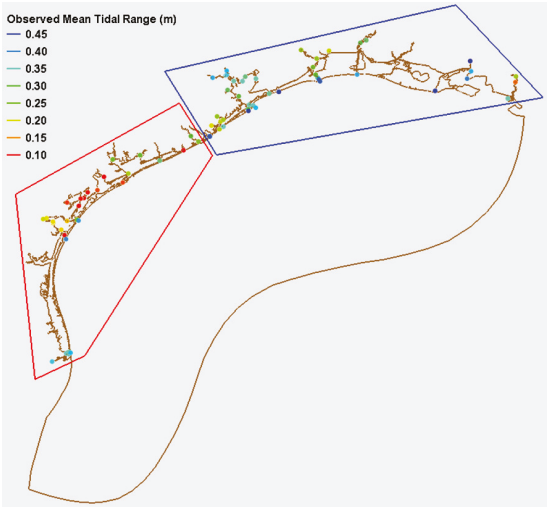

Figure 6. The mean tidal ranges from the 75 tide stations. The blue polygon includes 43 tide stations from Houston to the east (with a mean tidal ranges of 0.33 m), and the red polygon includes 32 tide stations from Houston to the west (with a mean tidal ranges of 0.23 m).

3.2. The Assessment and Improvement of ADCIRC Modeled Tidal Datums

Figure 7a shows a comparison between the ADCIRC modeled tidal datums and the observed tidal datums. The modeled tidal datums at four tide stations have greater than 0.10 m model errors. The 0.10 m threshold set was determined by considering this region's small tidal range, the experience of the previous model, and the magnitude of the observed RMS errors in this region.

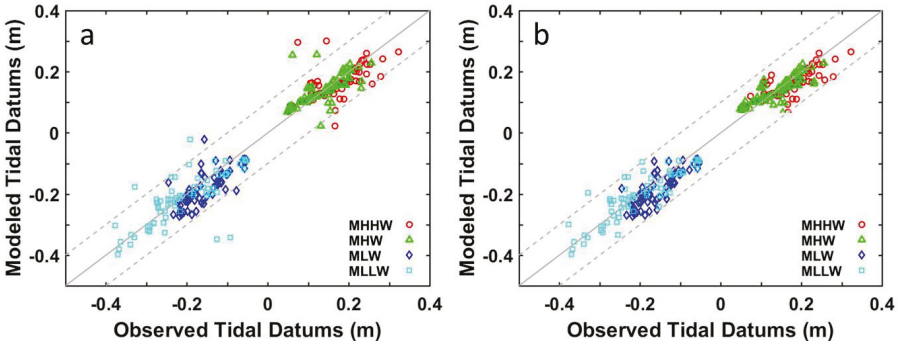

Figure 7. Modeled tidal datums vs observed tidal datums before (**a**) and after (**b**) model adjustments. The dashed lines represent 0.10 m error limits.

According to the geographic characteristics of the four tide stations, sensitivity tests were conducted and the model performance was significantly improved after model adjustments (Figure 7b). The effective techniques used for model improvement include: (1) extending the river length in the upper streams (for fixing model overestimation); (2) refining the model grid near a river's entrance, for example, enhancing model grid resolution and removing land patches from a model element (for fixing model overestimation); (3) increasing the model grid resolution along rivers (for fixing model underestimation); (4) enhancing the width of a narrow river (for fixing model underestimation); and (5) correcting bathymetry near a river's entrance (for fixing model underestimation).

An important lesson learned from the model assessment is that the accuracy of a station's coordinates is critical. As an example, Figure 8 shows the model errors of the four major tidal datums at one specific tide station before (left) and after (right) the station coordinates were corrected.

In the left panel, the model errors are greater than 0.10 m for MHHW and MLLW, and the station's coordinates [92°18.3′ W, 29°33.3′ N] correspond to a land location (inaccurate). After correction, the true station's coordinates (the right panel) are [92°18.315720′ W, 29°33.105300′ N]. Although the errors from the coordinates are small: delta (longitude) = −0.01572′ W and delta (latitude) = 0.1947′ N, which yield a distance of about 350 m in between, the true model errors of the tidal datums reveal much smaller values (<0.10 m), as shown in the right panel. The accuracy of the station's coordinates is essential to making an effective model assessment and thus to producing accurate modeled tidal datums. Discussions on the significance of the Earth surface coordinates' accuracy to ensure good-quality nautical, navigational, and geospatial products are also given in [40].

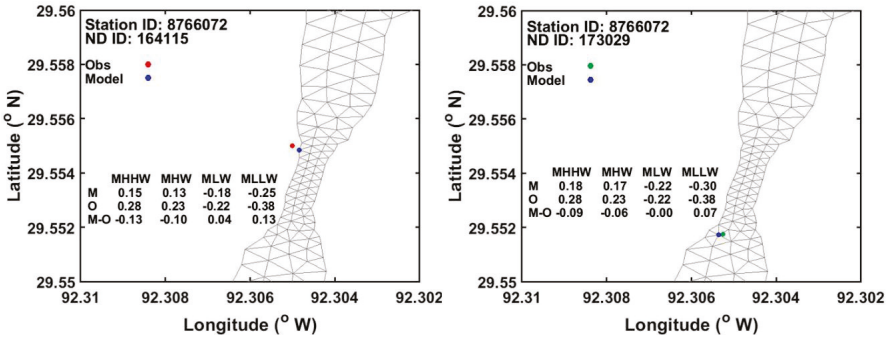

Figure 8. Modeled and observed tidal datums (in units of meters) at Station #8766072 before (**left**) and after (**right**) correcting the station's coordinates. "Obs" and "O" refer to "Observation". "M" refers to "Model". "ND ID" refers to "model node (grid point) identification".

3.3. Statistical Interpolation of Modeled Tidal Datums and Associated Uncertainties

ADCIRC modeled tidal datums, and the modeled tidal datums after the SVU statistical interpolation and their associated SVU spatially varying uncertainties of MHHW/MHW, MLW/MLLW, and DTL/MTL are shown in Figures 9–11, respectively. Modeled non-tidal grid points in the figures are marked as pink dots. As we will show later, the modeled non-tidal grid points in general agree with the CO-OPS estimated non-tidal zones.

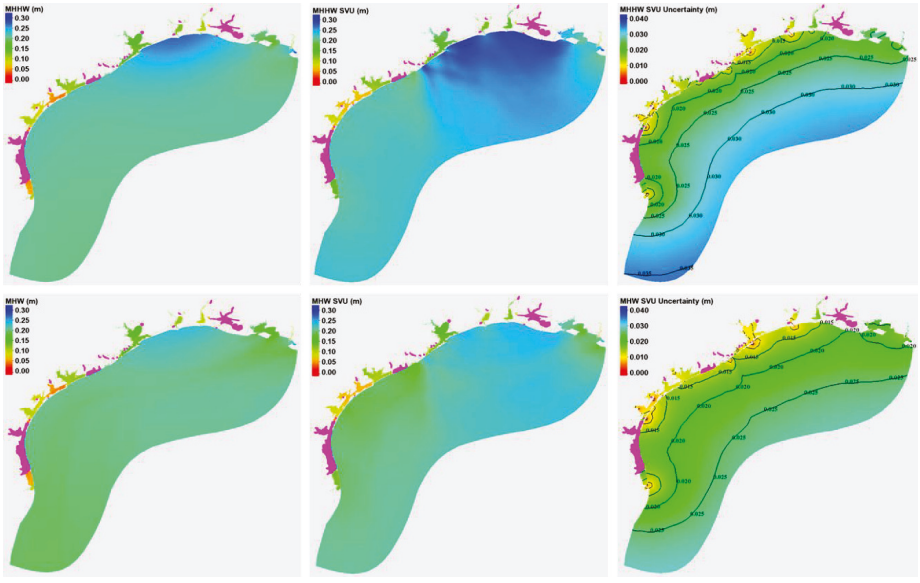

Figure 9. Modeled MHHW (**upper row**) and MHW (**lower row**) tidal datums. The first column shows ADCIRC modeled tidal datums; the second column shows the tidal datums after the SVU statistical interpolation; the third column shows the associated SVU spatially varying uncertainties. Model grid points in pink represent the modeled non-tidal grid points (modeled MHW-MLW < 0.09 m).

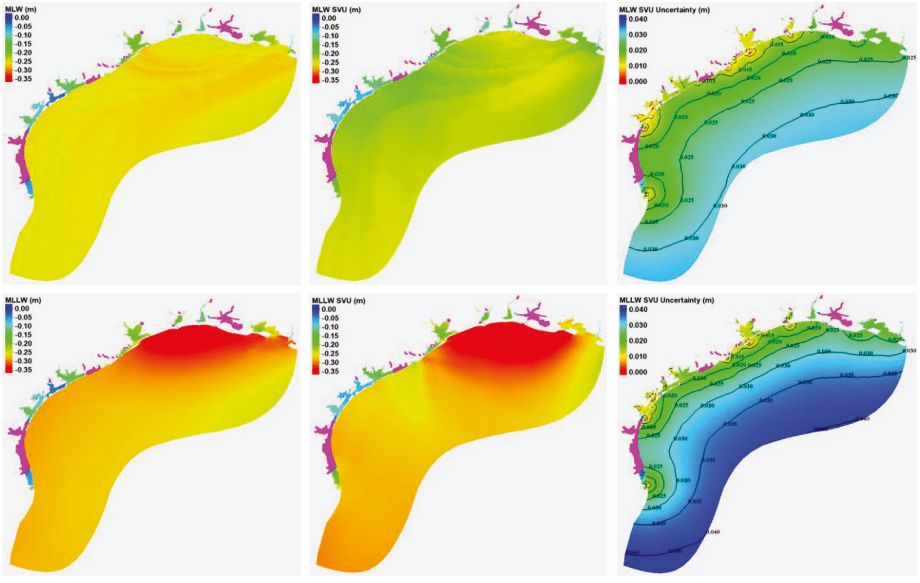

Figure 10. Modeled MLW (**upper row**) and MLLW (**lower row**) tidal datums. The first column shows ADCIRC modeled tidal datums; the second column shows the tidal datums after the SVU statistical interpolation; the third column shows the associated SVU spatially varying uncertainties. Model grid points in pink represent the modeled non-tidal grid points (modeled MHW-MLW < 0.09 m).

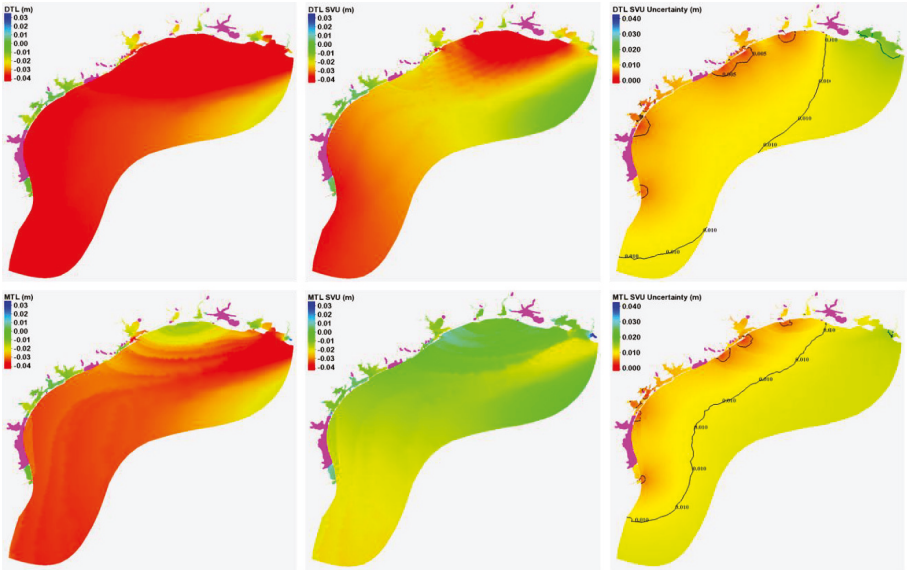

Figure 11. Modeled DTL (**upper row**) and MTL (**lower row**) tidal datums. The first column shows ADCIRC modeled tidal datums; the second column shows the tidal datums after the SVU statistical interpolation; the third column shows the associated SVU spatially varying uncertainties. Model grid points in pink represent the modeled non-tidal grid points (modeled MHW-MLW < 0.09 m).

Similar to the observed tidal datums, the modeled tidal datums (except for MLW and DTL with relatively uniform distributions) show relatively larger values in the eastern coastal region than in the western coastal region. The distributions of the modeled MHHW, MLLW, and MTL are qualitatively consistent with the characteristics of the observed proportion of tidal current energy to total energy (Figure 3 of [41]) and of the observed mean amplitude of tidal current energy (Figure 16 of [41]) from the same eight principal tidal constituents (K1, O1, P1, Q1, M2, S2, N2, and K2); that is, a rapid increase in magnitude from about 130 km offshore to the northern Texas-Louisiana shelf and from the Houston area to the east, within [95.5° W to 92.3° W, 28.5° N to 29.8° N]. It is worthwhile to mention that the analyzed tidal current observations were limited to only offshore stations; that is, no tidal current observations are close to the shore. Both the abovementioned distributions of the modeled tidal datums and the characteristics of the tidal current observations show roughly uniform patterns across the southern Texas shelf west of Houston, with a minor decrease in magnitude farther offshore. Similar patterns were also found in the previous modeled tidal datums, as shown in Figure 10 of [7]. The concave geographic shape of the basin and the large water body with shallow bathymetry (Figure 12) in the northern Texas-Louisiana shelf (within the black box) could be one of the major triggers of the relatively larger tidal datums and tidal current energy, in addition to the dominant loop currents in the Gulf of Mexico, as shown in Figure 1 of [42].

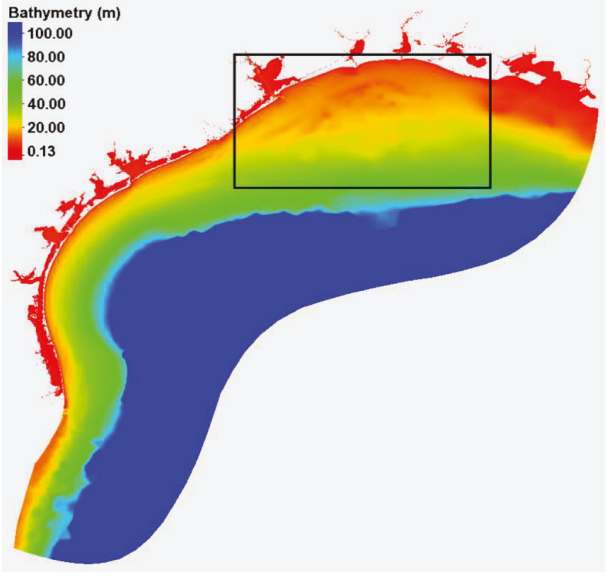

Figure 12. The concave geographic shape and shallow bathymetry characteristics of the northern Texas-Louisiana shelf within the black box.

Figures 9 and 10 show that the spatially varying uncertainty of the four major tidal datums computed by the SVU statistical interpolation method is the largest for MLLW, the second largest for MHHW, the third largest for MLW, and the smallest for MHW. The spatially varying uncertainty was smaller at nodes close to the coastal lines and tide stations, and was relatively larger otherwise. The largest uncertainties were located near the open ocean boundary, where no tide stations existed and the distance to the available tide stations was the greatest. As stated in Section 2.3.3, the RMS errors of the observed tidal datums at each tide station were the same for all the tidal datums. The difference among tidal datums' spatially varying uncertainties was mainly determined by the difference in the model error covariance $\sigma_{n_1}\sigma_{n_2}corr(f_{n_1}, f_{n_2})$, which was different for different tidal datums. Note that

σ_{n_1} and σ_{n_2} were the standard deviations of the model errors at nodes n_1 and n_2, respectively, and were assumed to be constant at each node and equal to the standard deviation of the modeled errors at all the tide stations. Here, the covariance was adjusted and decreases exponentially over the distance between nodes n_1 and n_2, as mentioned in Section 2.3.3. Thus, the MLLW has the greatest uncertainty, mainly because it has the largest model background error (the standard deviation σ_n of the model errors at all the tide stations). The standard deviation σ_n of the model errors at tide stations (from the largest to the smallest) is 0.0417 m (MLLW), 0.0347 m (MHHW), 0.0327 m (MLW), or 0.0281 m (MHW). Also, because the covariance was adjusted and decreases exponentially over the distance between nodes n_1 and n_2, the greater the distance from a node to tide stations, the larger the SVU uncertainty at the node, which explains why the greatest uncertainty was located near the open ocean boundary.

The statistical values of the observed, ADCIRC modeled, and SVU statistical interpolated MHHW/MHW/MLW/MLLW tidal datums and associated SVU uncertainties are listed in Table 1. "Max", "Min", "Mean", and "Std" represent the maximum, minimum, mean, and standard deviation, respectively. "Abs" refers to an absolute value. "ADCIRC-SVU" refers to the modeled tidal datums after SVU statistical interpolation, and "SVU uncertainty" refers to the spatially varying uncertainty values. Tidal datums are in a 2-decimal form, errors/standard deviations are in a 3-decimal form, and all are in the units of meters.

Table 1. Statistical values of observed and modeled tidal datums and the associated SVU spatially varying uncertainties (in meters). Model errors from observations are given in parentheses when applicable; note that errors do not necessarily correspond to the categorical value reported next to them (e.g., min, max, mean), but are instead the categorical error over the entire model domain. For example, the maximum model error (0.063) next to the maximum value of ADCIRC modeled MHHW (0.28) refers to the maximum model error of ADCIRC modeled MHHW in comparison with the observations at the 75 tide stations. Note also: Model errors refer to modeled tidal datums minus observed tidal datums; "Mean Value" of ADCIRC model errors refers to Mean (Abs(ADCIRC model error)); "Mean Value" of ADCIRC-SVU model errors refers to Mean (Abs(ADCIRC-SVU model error)); "STD" stands for Standard Deviation.

Data Type	MHHW	MHW	MLW	MLLW
		Maximum Value		
Observation	0.32	0.26	−0.25	−0.38
ADCIRC	0.28 (0.063)	0.24 (0.067)	−0.31 (0.072)	−0.43 (0.132)
ADCIRC-SVU	0.31 (0.010)	0.25 (0.010)	−0.27 (0.010)	−0.45 (0.010)
SVU Uncertainty	0.036	0.033	0.034	0.046
		Minimum Value		
Observation	0.05	0.05	−0.05	−0.05
ADCIRC	0.03 (−0.010)	0.03 (−0.088)	−0.03 (−0.093)	−0.03 (−0.089)
ADCIRC-SVU	0.03 (−0.010)	0.03 (−0.010)	0.00 (−0.010)	−0.03 (−0.010)
SVU Uncertainty	0	0	0	0
		Mean Value		
Observation	0.16	0.14	−0.15	−0.20
ADCIRC	0.16 (0.028)	0.15 (0.021)	−0.18 (0.035)	−0.21 (0.032)
ADCIRC-SVU	0.17 (0.005)	0.15 (0.005)	−0.16 (0.005)	−0.22 (0.005)
SVU Uncertainty	0.015	0.013	0.015	0.018
		STD		
Observation	0.066	0.052	0.053	0.090
ADCIRC	0.066 (0.035)	0.056 (0.028)	0.074 (0.033)	0.102 (0.042)
ADCIRC-SVU	0.069 (0.006)	0.055 (0.006)	0.057 (0.007)	0.095 (0.006)
SVU Uncertainty	0.004	0.004	0.005	0.006

Table 1 reveals the small tidal datums in this model domain. The observed tidal datums (located only in coastal regions) are less than 0.38 m, the ADCIRC modeled tidal datums (in the entire model domain) are less than 0.43 m, and the tidal datums after the SVU interpolation are less than 0.45 m. The spatially varying uncertainties of the tidal datums after the SVU statistical interpolation are less

than 0.046 m. It is worth mentioning that the MLW and MLLW datums are negative and thus the minimum values of the MLW and MLLW datums refer to the shallowest MLW and MLLW datums.

The magnitude of the ADCIRC model error is the greatest for the MLLW datum and the smallest for the MHHW datum. The mean absolute ADCIRC model error is the greatest for the MLW datum and the smallest for the MHW datum.

The modeled tidal datums after the SVU statistical interpolation are close to the observed tidal datums at all the tide stations to less than 0.010 m. The mean value of the SVU uncertainty is the greatest for the MLLW datum and the smallest for the MHW datum. Likewise, the maximum value of the SVU uncertainty is the greatest for the MLLW datum and the smallest for the MHW datum.

3.4. Non-Tidal Polygon Upgrade and VDatum Marine Grid Population

Modeled non-tidal grids were incorporated for upgrading existing observationally-based estimates of non-tidal polygons produced by CO-OPS (shown in the left panel of Figure 13). The non-tidal polygons after the upgrade are shown in the right panel of Figure 13. As shown in the figure (the left panel), the ADCIRC modeled non-tidal zones (pink dots) in general agree with the CO-OPS estimated non-tidal polygons (closed black lines).

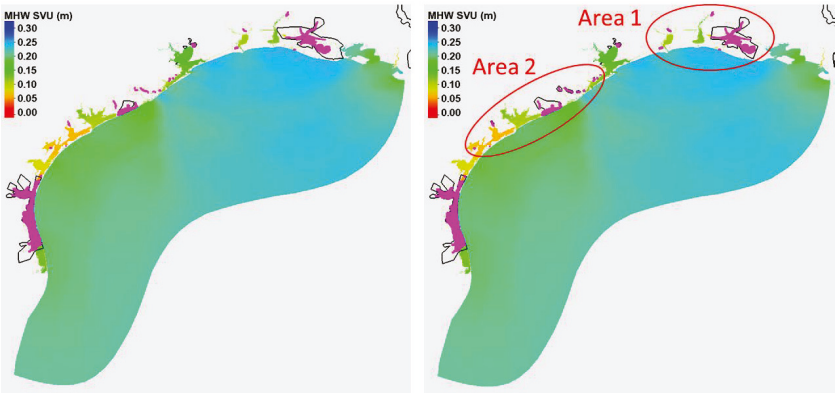

Figure 13. Non-tidal polygons (closed black lines) before (**left**) and after (**right**) the upgrade. Modeled non-tidal grid points are marked as pink dots. Area 1 and Area 2 (within the closed red lines) are the two areas which had major adjustments in the non-tidal upgrade.

For upgrading the CO-OPS estimated non-tidal polygons, modeled non-tidal grids were incorporated in the areas without or lacking tidal observations, such as the western LA coastal region (Area 1) and the middle TX coastal region (Area 2). We kept the CO-OPS estimated non-tidal polygons unchanged for areas where CO-OPS has tidal observations or references, but the model missed predicting non-tidal information, such as part of the Houston coastal region (the non-tidal polygons between Area 1 and Area 2) and part of the southwestern TX coastal region.

The major adjustments include: (1) a significant reduction in non-tidal area and four new small non-tidal areas in the western LA coastal region (Area 1); and (2) a significant extension in non-tidal area and several new non-tidal areas in the middle TX coastal region (Area 2).

The accuracy of non-tidal polygons directly influences the quality of the final VDatum marine grid population. Figure 14 shows an example of the VDatum marine grid population for the modeled MHHW after the SVU interpolation in the western LA coastal region by using the non-tidal polygons before (Figure 14a) and after (Figure 14b) the upgrade. As can be seen, the populated MHHW does not have any values inside the polygons. Using the existing non-tidal polygons causes several areas with valid tidal datums to be excluded in the final valid VDatum product. This is because the existing non-tidal polygons cover part of the region with valid tidal datums that prohibits the

generation of a complete picture of the VDatum marine grid population. On the contrary, the upgraded polygons enable the VDatum marine grid population to reveal a complete picture of the datum. Thus, the upgrade of the non-tidal polygons enhanced the quality of the VDatum marine grid population.

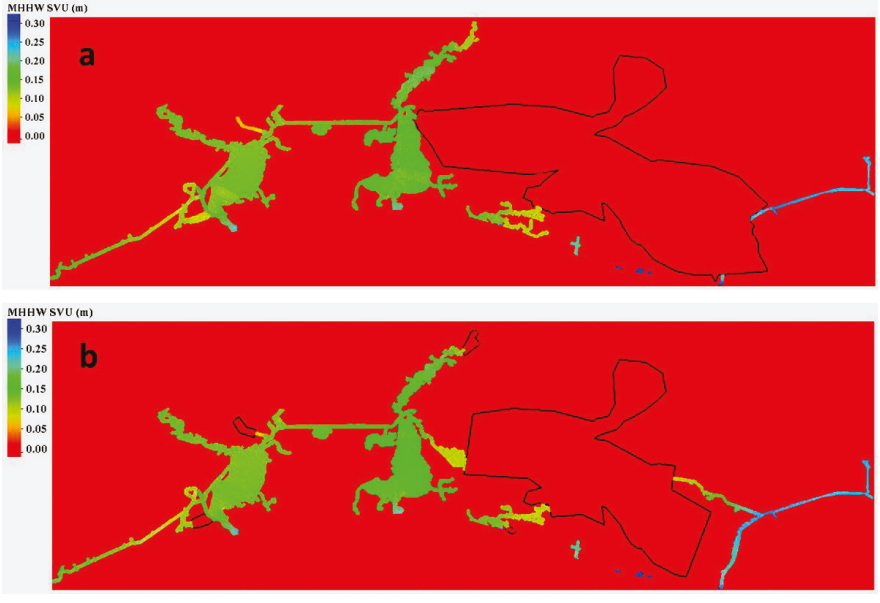

Figure 14. An example of the marine grid population for the modeled MHHW after the SVU interpolation in the western LA coastal region by using the non-tidal polygons before (**a**) and after (**b**) the upgrade.

It is worthwhile to mention that five water layers were artificially added landward from the shoreline in the marine grid generation, equivalent to a total distance of about 500 m or greater in this model domain, as shown in Figure 15. The five artificially added water layers allow datums to extend artificially to land for people who need the datum information.

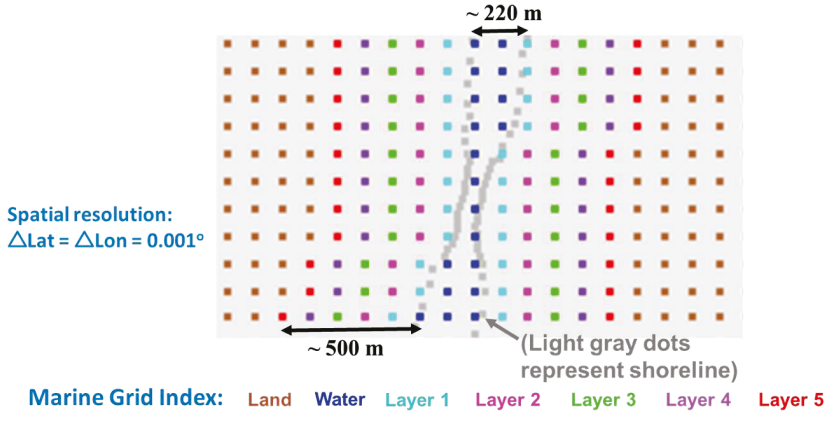

Figure 15. An example of the detailed marine grid field surrounding a narrow water path (light gray dots). The marine grids at land and in water are marked in brown and blue, respectively. The artificially added water layers 1 to 5 are marked in cyan, pink, green, purple, and red, respectively.

3.5. Comparisons of the Updated Tidal Model with the Previous Tidal Model

The major improvement of the model update comes from the work including: (1) model grid extension to include new tide stations; (2) the incorporation of the best available data (shoreline, bathymetry, and tide stations); (3) the implementation of a better version of the ADCIRC model; (4) the implementation of the most recently developed tidal database EC2015; and (5) the implementation of the SVU statistical interpolation method. In this section, we will compare the statistical values of the ADCIRC model errors between the updated tidal model and the previous tidal model to understand the overall model improvement.

First, let us focus on the area with the major model grid extension in the western LA region, as shown in Figure 16. Three tide stations in this region were included in both the current and previous model domains. We used the current CO-OPS data of observed tidal datums and modeled tidal datums from the current and previous tidal models to analyze how much the updated tidal model improves the modeled tidal datums in this model area.

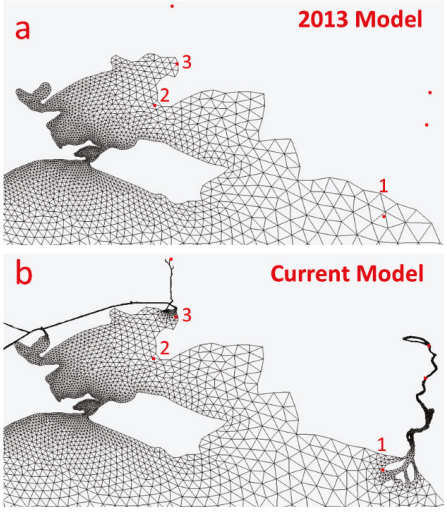

Figure 16. The locations of the three tide stations ("1", "2", and "3") in the western LA region, which were included in both the previous (**a**) and current (**b**) tidal model domains. The coordinates of the tide stations 1, 2, and 3 are [91.3381° W, 29.4496° N], [−91.8800° W, 29.7134° N], and [−91.8800° W, 29.7134° N], respectively. The red dots are the tide stations in the CO-OPS tidal datum data used for this work.

Table 2 lists the statistical values of the model errors from the current and previous tidal models. The values outside the parentheses are from the current tidal model, while the values inside the parentheses are from the previous tidal model. The values in bold indicate that the model errors in the previous tidal model are greater than those in the current model. Based on Table 2, the updated model improved the modeled MHW at all the three stations, improved the modeled MHHW/MLLW at two of the three tide stations, and improved MLW only at Station 2. That is, the updated model outperformed the previous model in simulating MHHW/MHW/MLLW in this model area. The mean absolute errors indicate that statistically the updated model outperformed the previous model in the modeled MHW the most, MLLW the second most, and MHHW the third most, but underperformed the previous model in the modeled MLW.

Table 2. The statistical values of the model errors from the current and previous tidal models (in meters).

Tide Station	MHHW (M-O)	MHW (M-O)	MLW (M-O)	MLLW (M-O)
1	−0.011 (0.009)	0.009 (**0.032**)	−0.093 (−0.022)	−0.078 (**−0.090**)
2	−0.057 (**−0.063**)	−0.029 (**−0.046**)	−0.001 (**0.013**)	0.050 (0.049)
3	−0.025 (**−0.030**)	−0.016 (**−0.030**)	−0.012 (0.005)	0.037 (**0.038**)
Mean |Error|	0.031 (**0.034**)	0.018 (**0.036**)	0.035 (0.013)	0.055 (**0.059**)

Note: "M" represents "Model", and "O" represents "Observation". The values outside the parentheses are from the current tidal model. The values inside the parentheses are from the previous tidal model. "Mean |Error|" refers to "the average of the absolute model errors" over the three tide stations. The values in bold indicate that the model errors in the previous tidal model are greater than in the current tidal model.

Next, a similar statistical analysis was conducted in the entire model domain at all the 69 tide stations which were included in both the current and previous model domains; that is, the six out of the 75 tide stations that were included in the current model domain by model grid extension but were not included in the previous tidal model domain, were excluded in the statistical analysis. We obtained similar results as in the abovementioned analysis over the three stations. The updated tidal model outperformed the previous tidal model in simulating MHHW (39 out of the 69 tide stations), MHW (36 out of the 69 tide stations), and MLLW (38 out of the 69 tide stations), but underperformed the previous model in simulating MLW (54 out of the 69 tide stations). The difference of the mean absolute errors over the 69 stations between the previous tidal model and the current tidal model (the mean absolute errors of the previous tidal model minus the mean absolute errors of the current tidal model) is: 0.002 m (MHHW), 0.003 m (MHW), −0.013 m (MLW), and 0.003 m (MLLW). This indicates that statistically, the updated tidal model outperformed the previous tidal model in simulating MHHW/MHW/MLLW, but underperformed the previous tidal model in simulating MLW over the entire model domain.

4. Summary

This paper introduces the procedures and the methodologies used in updating the tidal model and the modeled tidal datums in the TX and western LA coastal waters, presents and discusses the obtained results, shares effective techniques used for improving the hydrodynamic model performance and lessons learned in the model assessment, and statistically analyzes the model improvement in simulating the tidal datums.

The updated tidal model statistically outperformed the previous tidal model in most cases. The SVU statistical interpolation method interpolated the modeled tidal datums to within a user-defined error (0.01 m in this work), which was demonstrated to reduce the model biases and model errors in comparison with the previous deterministic approach (TCARI) based on the previous study [13]. The statistical interpolation also produced the spatially varying uncertainty field for each interpolated tidal datum, which offers the spatial characteristics of the uncertainty field, much better than the previous single-value model uncertainty over an entire VDatum model domain. The upgraded non-tidal polygons enhanced the quality of the VDatum marine grid population and thus the final tidal datum products.

The accuracy of a tide station's coordinates was shown to significantly influence the outcome and thus the quality of the model assessment, which should be an important lesson for the modeling community in general.

Author Contributions: W.W. and E.M. conceived and designed the experiments; W.W. performed the experiments and data analysis, and drafted the manuscript; E.M. supervised the VDatum SVU project and organized bi-weekly group meetings on the VDatum SVU project; L.S. supported the SVU code; K.H. supported the tidal datum data and code, as well as the marine grid population code; M.M. supported the tidal datum data and non-tidal polygon data and upgrade; S.W. supported coordinating the VDatum SVU project and organizing monthly review meetings on the VDatum SVU project. All the authors reviewed and approved the final manuscript.

Funding: This research was supported by NOAA's VDatum Program Funding.

Acknowledgments: The authors would like to thank the Editor Stephen Parks and his team for their great support, and thank the three anonymous reviewers for their constructive comments and suggestions, which significantly enhanced the manuscript. The authors would also like to thank for support from the NOAA NOS's NGS/CO-OPS/OCS VDatum project tri-office management. Special thanks to CSDL management support from Edward J Van Den Ameele, Julia Powell, and Neeraj Saraf. Special thanks also to Yuji Funakoshi for support on ADCIRC model, to Kurt Nelson, Cuong Hoang, Alison Carisio, Chris Libeau, Andrew Oakman, Tim Osborn, Jonathan Brazzell, Jiangtao Xu, Corey Allen, Laura Rear-McLaughlin, and Russell Quintero for support on bathymetry data; to Alan Zundel for support on SMS software techniques; and to Greg Seroka, Neil Weston, and John Kelley for carefully reading, editing, and commenting on the manuscript. The lead author would like to thank Steven DiMarco (Texas A&M University) for his discussions and constructive comments and suggestions; and the colleagues and friends who are not listed in the acknowledgment but provided invaluable discussions during the course of this work.

Conflicts of Interest: The authors declare no conflict of interest.

References

1. NOAA/NOS VDatum Website. Available online: https://vdatum.noaa.gov/ (accessed on 6 February 2019).
2. Gill, S.; Schultz, J. *Tidal Datums and Their Applications*; NOAA Special Publication NOS CO-OPS 1: Silver Spring, MD, USA, 2000. Available online: http://www.tidesandcurrents.noaa.gov/publications/tidal_datums_and_their_applications.pdf (accessed on 6 February 2019).
3. Myers, E.P. Review of progress on VDatum, a vertical datum transformation tool. In Proceedings of the OCEANS 2005 MTS/IEEE, Washington, DC, USA, 17–23 September 2005; pp. 974–980.
4. Myers, E.; Hess, K.; Yang, Z.; Xu, J.; Wong, A.; Doyle, D.; Woolard, J.; White, S.; Le, B.; Gill, S.; et al. VDatum and strategies for national coverage. In Proceedings of the OCEANS 2007, Vancouver, BC, Canada, 29 September–4 October 2007; pp. 1–8.
5. Hess, K.; Kenny, K.; Myers, E. *Standard Procedures to Develop and Support NOAA's Vertical Datum Transformation Tool, VDATUM (Version 2010.08.03)*; NOAA NOS Technical Report; NOAA NOS: Silver Spring, MD, USA, 2012.
6. Xu, J.; Myers, E. Modeling tidal dynamics and tidal datums along the coasts of Texas and Western Louisiana. In Proceedings of the 11th International Conference on Estuarine and Coastal Modeling, Seattle, WA, USA, 4–6 November 2009.
7. Xu, J.; Myers, E.P.; Jeong, I.; White, S.A. *VDatum for the Coastal Waters of Texas and Western Louisiana: Tidal DAtums and Topography of the Sea Surface*; NOAA: Silver Spring, MD, USA, 2013.
8. ADCIRC Users Manuals. Available online: https://adcirc.org/home/documentation/users-manuals-compile-options-faqs-wiki/ (accessed on 6 February 2019).
9. Luettich, R.A., Jr.; Westerink, J.J.; Scheffner, N.W. *ADCIRC: An Advanced Three-Dimensional Circulation Model for Shelves, Coasts, and Estuaries. Report 1. Theory and Methodology of ADCIRC-2DDI and ADCIRC-3DL*; Coastal Engineering Research Center: Vicksburg, MS, USA, 1992.
10. Westerink, J.J.; Luettich, R., Jr.; Scheffner, N. *ADCIRC: An Advanced Three-Dimensional Circulation Model for Shelves, Coasts, and Estuaries. Report 3. Development of a Tidal Constituent Database for the Western North Atlantic and Gulf of Mexico*; Coastal Engineering Research Center: Vicksburg, MS, USA, 1993. Available online: https://apps.dtic.mil/dtic/tr/fulltext/u2/a268685.pdf (accessed on 6 February 2019).
11. Westerink, J.; Luettich, R., Jr.; Blain, C.; Scheffner, N.W. *ADCIRC: An Advanced Three-Dimensional Circulation Model for Shelves, Coasts, and Estuaries. Report 2. User's Manual for ADCIRC-2DDI*; Army Engineer Waterways Experiment Station: Vicksburg, MS, USA, 1994. Available online: file:///C:/Users/Wei.Wu/Downloads/ADCIRC_An_Advanced_Three-Dimensional_Circulation_M%20(1).pdf (accessed on 6 February 2019).
12. National Hurricane Center Tropical Cyclone Report. Available online: https://www.nhc.noaa.gov/data/tcr/ (accessed on 6 February 2019).
13. Shi, L.; Myers, E. Statistical Interpolation of Tidal Datums and Computation of Its Associated Spatially Varying Uncertainty. *J. Mar. Sci. Eng.* **2016**, *4*, 64. [CrossRef]
14. Gill, S.; Michalski, M. *Classification of a Water Level Station as Non-Tidal*; NOAA SOP # 7.3.A.1; NOAA: Silver Spring, MD, USA, 2016.
15. Mao, M.; Xia, M. Dynamics of wave–current–surge interactions in Lake Michigan: A model comparison. *Ocean Model.* **2017**, *110*, 1–20. [CrossRef]

16. Akbar, M.K.; Luettich, R.A.; Fleming, J.G.; Aliabadi, S.K. CaMEL and ADCIRC Storm Surge Models—A Comparative Study. *J. Mar. Sci. Eng.* **2017**, *5*, 35. [CrossRef]
17. Vinogradov, S.; Myers, E.; Funakoshi, Y.; Moghimi, S.; Calzada-Morrero, J. Real-Time Storm Surge Forecasting Systems Research, Design, and Development. In Proceedings of the 98th American Meteorological Society Annual Meeting, Austin, TX, USA, 7–11 January 2018. Available online: https://ams.confex.com/ams/98Annual/webprogram/Paper327250.html (accessed on 6 February 2019).
18. Funakoshi, Y.; Feyen, J.C.; Aikman, F.; van der Westhuysen, A.J.; Tolman, H.L. *The Extratropical Surge and Tide Operational Forecast System (ESTOFS) Atlantic Implementation and Skill Assessment*; NOAA Technical Report NOS CS 32; NOAA: Silver Spring, MD, USA, 2013; 147p.
19. Xu, J.; Feyen, J.C. *The Extra Tropical Surge and Tide Operational Forecast System for the Eastern North Pacific Ocean (ESTOFS-Pacific): Development and Skill Assessment*; NOAA Technical Report NOS CS 36; NOAA: Silver Spring, MD, USA, 2016; 153p.
20. ADCIRC EC2015 Tidal Database. Available online: http://adcirc.org/products/adcirc-tidal-databases/ (accessed on 9 February 2019).
21. Szpilka, C.; Dresback, K.; Kolar, R.; Feyen, J.; Wang, J. Improvements for the Western North Atlantic, Caribbean and Gulf of Mexico ADCIRC Tidal Database (EC2015). *J. Mar. Sci. Eng.* **2016**, *4*, 72. Available online: https://doi.org/10.3390/jmse4040072 (accessed on 6 February 2019). [CrossRef]
22. Mukai, A.Y.; Westerink, J.J.; Luettich, R.A., Jr.; Mark, D. *Eastcoast 2001, a Tidal Constituent Database for Western North Atlantic, Gulf of Mexico, and Caribbean Sea*; Engineer Research and Development Center Vicksburg Ms Coastal and Hydraulicslab: Technical Report, ERDC/CHL TR-02-24; US Army Engineer Research and Development Center, Coastal and Hydraulics Laboratory: Vicksburg, MS, USA, 2002; 201p. Available online: https://coast.nd.edu/reports_papers/2001-Mukai-TR-02-24.pdf (accessed on 6 February 2019).
23. Egbert, G.D.; Svetlana, Y.E. The OSU TOPEX/Poseidon Global Inverse Solution TPXO. Available online: http://volkov.oce.orst.edu/tides/global.html (accessed on 6 February 2019).
24. Egbert, G.D.; Svetlana, Y.E. OTIS Regional Tidal Solutions. Available online: http://volkov.oce.orst.edu/tides/Mex.html (accessed on 6 February 2019).
25. SMS—The Complete Surface-water Solution. Available online: https://www.aquaveo.com/software/sms-surface-water-modeling-system-introduction (accessed on 6 February 2019).
26. NOAA Shoreline Website—NOAA Continually Updated Shoreline Product (CUSP). Available online: https://www.ngs.noaa.gov/CUSP/ (accessed on 6 February 2019).
27. NOAA's Continually Updated Shoreline Product (CUSP). Available online: https://www.ngs.noaa.gov/INFO/OnePagers/CUSP_One-Pager.pdf (accessed on 6 February 2019).
28. The U.S. Army Corps of Engineers (USACE) Hydrographic Survey Data. Available online: http://www.mvn.usace.army.mil (accessed on 6 February 2019).
29. NOAA's Electronic Navigational Chart (ENC, Chart #11345). Available online: http://www.charts.noaa.gov/OnLineViewer/11345.shtml (accessed on 6 February 2019).
30. NOAA's National Geophysical Data Center (NGDC) High-Resolution Digital Elevation Model (DEM) Data. Available online: https://www.ngdc.noaa.gov/ (accessed on 6 February 2019).
31. CO-OPS. *Computational Techniques for Tidal Datums Handbook*; NOAA Special Publication NOS CO-OPS 2; NOAA: Silver Spring, MD, USA, 2003. Available online: https://www.tidesandcurrents.noaa.gov/publications/Computational_Techniques_for_Tidal_Datums_handbook.pdf (accessed on 6 February 2019).
32. Parker, B. *Tidal Analysis and Prediction*; NOAA Special Publication NOS CO-OPS 3, 2007. Available online: https://tidesandcurrents.noaa.gov/publications/Tidal_Analysis_and_Predictions.pdf (accessed on 6 February 2019).
33. Gill, S.; Hovis, G.; Kriner, K.; Michalski, M. Implementation of Procedures for Computation of Tidal Datums in Areas with Anomalous Trends of Relative Mean Sea Level. NOAA Technical Report NOS CO-OPS 068; 2014. Available online: https://tidesandcurrents.noaa.gov/publications/NOAA_Technical_Report_NOS_COOPS_68.pdf (accessed on 6 February 2019).
34. Gill, S.; Hubbard, J.; Dingle, G. Tidal Characteristics and Datums of Laguna Madra, Texas. NOAA Technical Memorandum NOS OES 008; 1995. Available online: https://tidesandcurrents.noaa.gov/publications/Noaa_Technical_Memorandum_NOS_OES_008.pdf (accessed on 6 February 2019).

35. Hess, K.; Schmalz, R.; Zervas, C.; Collier, W. *Tidal Constituent and Residual Interpolation (TCARI): A New Method for the Tidal Correction of Bathymetric Data*; NOAA Technical Report NOS CS 4; NOAA: Silver Spring, MD, USA, 1999.
36. Hess, K.W. Spatial Interpolation of Tidal Data in Irregularly-shaped Coastal Regions by Numerical Solution of Laplace's Equation. *Estuar. Coast. Shelf Sci.* **2002**, *54*, 175–192. Available online: https://doi.org/10.1006/ecss.2001.0838 (accessed on 6 February 2019). [CrossRef]
37. Hess, K. Water level simulation in bays by spatial interpolation of tidal constituents, residual water levels, and datums. *Cont. Shelf Res.* **2003**, *23*, 395–414. [CrossRef]
38. NOAA/NOS Vertical Datums Transformation, Estimation of Vertical Uncertainties in VDatum. 2016. Available online: https://vdatum.noaa.gov/docs/est_uncertainties.html (accessed on 6 February 2018).
39. Stewart, R. Introduction to Physical Oceanography (Version 2008). Available online: https://www.colorado.edu/oclab/sites/default/files/attached-files/stewart_textbook.pdf (accessed on 6 February 2019).
40. Weston, N. Benefits and Impacts to Nautical Charting by Adopting a New Reference. 2018. Available online: https://www.eiseverywhere.com/ehome/chc-nsc2018/home/ (accessed on 6 February 2019).
41. DiMarco, S.F.; Reid, R.O. Characterization of the principal tidal current constituents on the Texas-Louisiana shelf. *J. Geophys. Res. Ocean.* **1998**, *103*, 3093–3109. Available online: https://doi.org/10.1029/97JC03289 (accessed on 6 February 2019). [CrossRef]
42. Oey, L.-Y.; Ezer, T.; Lee, H.-C. Loop Current, rings and related circulation in the Gulf of Mexico: A review of numerical models and future challenges. In *Circulation in the Gulf of Mexico: Observations and Models*; Sturges, W., Lugo-Fernandez, A., Eds.; Geophysical Monograph Series; Geophysical Monograph-American Geophysical Union: Washington, DC, USA, 2005; Volume 161, pp. 31–56. Available online: http://www.ccpo.odu.edu/~{}tezer/PAPERS/2005_AGU_GOM.pdf (accessed on 6 February 2019).

Journal of
Marine Science and Engineering

MDPI

Article

Lateral Circulation in a Partially Stratified Tidal Inlet

Linlin Cui *, Haosheng Huang, Chunyan Li and Dubravko Justic

Department of Oceanography and Coastal Sciences, College of the Coast and Environment, Louisiana State University, Baton Rouge, LA 70803, USA; hhuang7@lsu.edu (H.H.); cli@lsu.edu (C.L.); djusti1@lsu.edu (D.J.)

* Correspondence: lcui2@lsu.edu; Tel.: +1-225-578-5117

Received: 30 September 2018; Accepted: 3 December 2018; Published: 19 December 2018

Abstract: Using a three-dimensional, hydrostatic, primitive-equation ocean model, this study investigates the dynamics of lateral circulation in a partially stratified tidal inlet, the Barataria Pass in the Gulf of Mexico, over a 25.6 h diurnal tidal cycle. Model performance is assessed against observational data. During flood tide, the lateral circulation exhibits the characteristics similar to those induced by differential advection, i.e., lateral flow consists of two counter-rotating cells and is convergent at the surface. The analysis of momentum balance indicates that, in addition to the pressure gradient and vertical stress divergence, nonlinear advection and horizontal stress divergence are also important contributors. During ebb phase, the lateral circulation is mostly toward the right shoal (when looking into the estuary) for the whole water column and persisting for almost the whole period. The surface divergence suggested by the differential advection mechanism lasts for a very short period, if it ever exists. The main momentum balance across most of the transect during ebb is between the along-channel advection of cross-channel momentum and pressure gradient. The sectional averaged lateral velocity magnitude during ebb is comparable to that during flood, which is different from the idealized numerical experiment result.

Keywords: estuarine modeling; lateral circulation; tidal currents; momentum balance

1. Introduction

The lateral circulation in tidally dominant estuaries can be driven by various mechanisms. Nunes and Simpson [1] identified the effect of differential advection on the generation of secondary circulation. They pointed out that due to frictional retardation, the along-channel velocity is stronger in the channel than over the shoals. When acting upon an along-channel density gradient, it results in greater (smaller) density at the thalweg than at the shoals during flood (ebb) tides. This produces a cross-channel pressure gradient toward the channel (shoals) on the surface and a pressure gradient toward the shoals (channel) at the bottom during flood (ebb) tides. Thus, the lateral flows are convergent (divergent) at the surface over the deep channel and divergent (convergent) at the bottom during flood (ebb) tides. However, the surface axial convergence was only observed during flood tides in Nunes and Simpson's work.

In an idealized, narrow straight channel with weak stratification, Lerczak and Geyer [2] confirmed that secondary circulation was driven by differential advection. Differential rotation of tidal ellipse was also identified as a mechanism for axial convergence fronts [3]. Interactions between barotropic pressure gradient and bathymetry can generate convergence of lateral flow, producing flows rotating toward the channel from the shoals [4,5]. In curved estuaries, an alternative driving mechanism for lateral circulation is the centrifugal acceleration [6–8] and advection [9]. Winds can enhance or degrade the local-curvature-induced, two-layer flow and can drive three-layer flow [10]. Ekman-forced lateral circulation varies with the Ekman number. When the boundary layer is comparable to the channel depth (large Ekman number), lateral flow is a single circulation cell; while for thin tidal boundary

layer (small Ekman number), lateral flow is complex and varies over the tidal cycle [2]. Boundary mixing on a no-flux boundary layer was confirmed to be one of the driving mechanisms of lateral circulation [2,11]. Cheng et al. [12] investigated the lateral circulation during stratified ebb tides due to the lateral baroclinic pressure gradient, which is generated by differential diffusion caused by a lateral asymmetry in vertical mixing.

In the same idealized numerical experiment, Lerczak and Geyer [2] found that lateral flow is about four times stronger during flood tides than during ebb tides. They attributed it to the interaction between the along-channel tidal currents and nonlinear advective processes over a tidal cycle. This flood–ebb asymmetry in the lateral circulation strength was also observed by Scully et al. [13] in the Hudson River estuary, where stronger lateral flows were observed during flood tides while lateral flows were suppressed during ebb tides. However, in the numerical modeling of James River Estuary, Li et al. [14] found flood–ebb asymmetry during neap tides with stronger lateral circulation on ebb, while flood–ebb asymmetry was reduced during spring tides.

Lateral circulation plays an important role in estuarine dynamics. Many observational and numerical simulation results [2,7,12,15,16] have demonstrated the existence of secondary currents, and discussed its dependence and feedback on density stratification [7,12,17,18], streamwise momentum budget [2], estuarine circulation [12,13], as well as its impacts on sediment transport and geomorphology [19–21]. In Barataria Pass, the area of focus for this study, observations showed that there existed a distinct asymmetry in stratification within the diurnal cycle [22]. However, in that analysis no consideration was given to the contribution of the lateral circulation to density stratification.

In this study, we use a three-dimensional (3-D), high-resolution hydrodynamic model to examine the lateral circulation structure in the partially stratified tidal inlet, Barataria Pass, which connects Barataria Bay with the continental shelf in the southeastern Louisiana. The objectives of this study are to elucidate the tidal evolution of lateral circulation and determine its driving mechanisms. The remainder of this paper is organized as follows: Section 2 describes the study area, and the configuration of the 3-D finite volume numerical ocean model. Section 3 presents the validation of the numerical model and the temporal evolution of lateral circulation over a 25.6 h diurnal tidal cycle. In Section 4, we quantify the 2-D and 3-D momentum balance and examine the driving forcing for lateral circulation. Flood–ebb variations in lateral circulation pattern are also discussed in Section 4. Finally, conclusions are given in Section 5.

2. Materials and Methods

2.1. Study Area

Barataria Bay (Figure 1) is located at the southeastern Louisiana, on the western side of the Mississippi Birdfoot Delta. It is connected to the Gulf of Mexico through several tidal inlets including Barataria Pass, which is between two barrier islands, Grand Isle Island and Grand Terre Island (Figure 1b). The most significant freshwater source inside the Barataria Bay is the Davis Pond freshwater diversion. The maximum diversion discharge is ~300 m^3 s^{-1} [23]. Barataria Pass is an 800 m wide narrow channel. It is one of the four main tidal passes of Barataria Bay, accounting for ~66% of total water exchange [24]. Tidal currents account for ~85% of the total flow variance in the inlet, with equal contributions from the O_1 and K_1 constituents. Tidal amplitudes for both O_1 and K_1 constituents are about 0.5 m s^{-1} [25]. Maximum tidal currents reach as high as 2 m s^{-1} during tropic tides.

Barataria Bay is composed of broad shallow waters (average depth of 2 m), islands and a 5 m deep main shipping channel, the Barataria Waterway. The shipping channel ends at Barataria Pass. Around Barataria Pass the main channel has an average depth of ~20 m and is being periodically dredged, causing a depression of ~50 m deep close to the inlet (Figure 2). A cross-sectional view of the Barataria Pass, along which all analyses are performed, is shown in Figure 1c. Bathymetrically this transect has one 20 m deep channel in the center bordered by extensive shoal regions. The shoal at the left-hand side (looking upstream) is ~2 m deep and 250 m wide, while that at the right-hand side is ~3 m deep and 100 m wide.

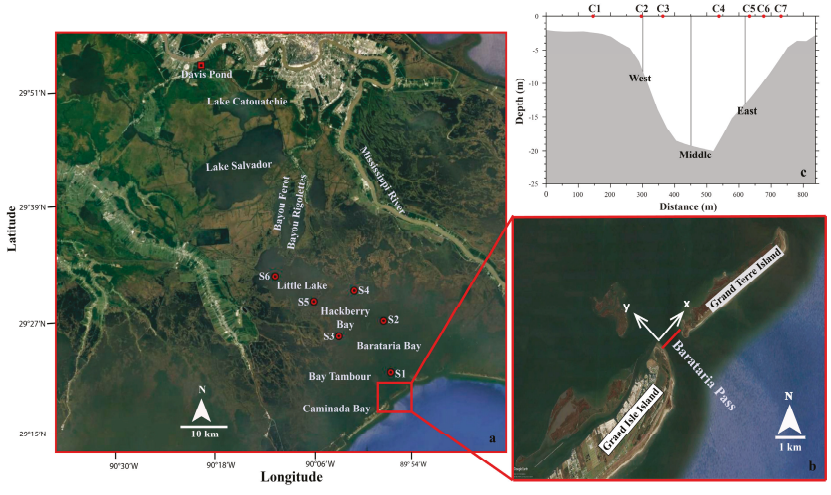

Figure 1. (**a**) Geographic location of the Barataria Estuary. S1–S6 are USGS stations. (**b**) Location of Barataria Pass. The coordinate is defined as positive x to the eastern bank, positive y to the upstream. The red line indicates the cross-section shown in (**c**) and is used in later analysis. (**c**) Cross-sectional view of Barataria Pass. The black lines indicate CTD measurements. C1–C7 are locations used for 2-D momentum equation analysis.

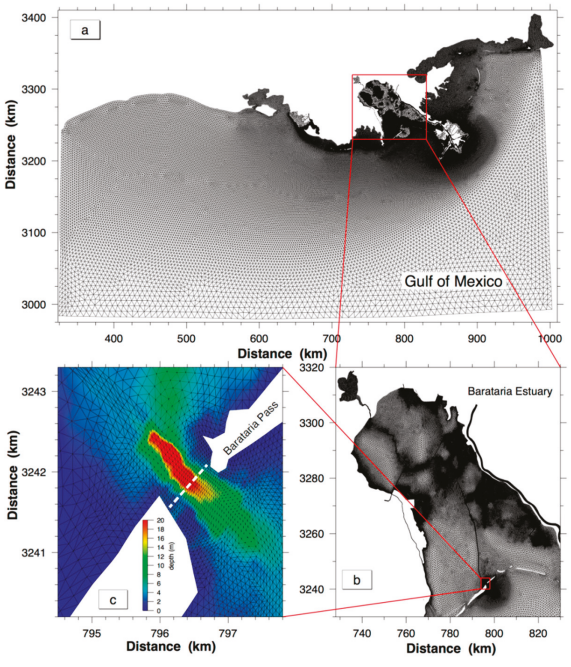

Figure 2. Unstructured grid configured for the Finite Volume Coastal Ocean Model (FVCOM) Barataria Pass model: (**a**) whole computational domain; (**b**) local domain of Barataria Estuary; (**c**) local domain of Barataria Pass, with horizontal resolution ~50 m in the cross-channel direction and 30 m in the along-channel direction. Contours are interpolated bathymetry. White dash line indicates cross section in this study.

2.2. Model Description and Configuration

The Finite Volume Coastal Ocean Model (FVCOM) is used in this study to simulate the hydrodynamics of the Barataria Basin and adjacent continental shelf. FVCOM is a 3-D, hydrostatic, free surface, primitive-equation ocean model [26,27]. In the finite volume method, the computational domain is discretized using a mesh of non-overlapping triangles in the horizontal and sigma-coordinate (σ-coordinate) in the vertical. The governing equations are solved in their integral forms in each individual control volume. The triangular grid in the horizontal can resolve complex coastal and bathymetric geometries. It uses a cell-vertex-centered (similar to the finite-difference *C*-grid) method, which facilitates the enforcement of mass conservation in tracer advection and tracer open boundary conditions. Vertical mixing uses modified Mellor and Yamada level 2.5 turbulence model [28,29] and horizontal diffusion uses Smagorinsky eddy parameterization [30]. The model employs mode split approaches (barotropic 2D (external) mode and baroclinic 3D (internal) mode) to solve the momentum equations with second-order accuracy. The bottom boundary conditions apply an exact form of the no flux boundary conditions.

A flooding–drying scheme is implemented in FVCOM to simulate motions in intertidal zones and wetlands. If vertical water column thickness at the cell center is less than a criterion value (typically 5 cm), then the cell is designated as a dry cell and its velocity is set to zero. Whenever the vertical water column thickness exceeds the criterion value, the cell becomes wet and water level and velocity are computed from control equations. The advantage of triangular mesh to accurately represent complex bathymetry and coastlines makes FVCOM ideally suited for Barataria Pass study.

A high-resolution FVCOM Barataria Pass model was developed by configuring FVCOM version 2.6 to the Northwestern Gulf of Mexico continental shelf region with inclusion of the intertidal zones inside the Barataria Bay. The computational domain extends longitudinally from Mobile Bay (Alabama) to west of Galveston Bay (Texas) and offshore to about 27° N (Figure 2). It consists of 146,266 triangular nodes and 283,721 triangular cells. The horizontal grid resolution varies from about 10 m in the upper estuary to about 8 km near the open boundary. Near Barataria Pass, grid cells are fine enough to ensure that the 800 m wide inlet cross section is resolved by ~20 triangles (Figure 2c). Vertically FVCOM employs 19 uniform sigma layers, which is ~0.1 m over the shoal and ~1 m in the central depression of the tidal inlet. Computational time steps are 0.2 s and 2.0 s for the external and internal modes, respectively. Model results are saved every 10 min for further diagnostic analysis.

Model bathymetry was obtained from various sources. Using an inverse distance weighted interpolation method, a 5 m by 5 m resolution digital elevation model constructed from Light Detection and Ranging (LIDAR) measurement was interpolated into model wetland region. The water depth in channels, bayous, and lakes was interpolated from Coastal Louisiana Ecosystem Assessment and Restoration Report (CLEAR), US Army Corp Survey, and NOAA nautical charts. Shelf and open ocean water depth was interpolated from a coarse resolution ADCIRC model bathymetry. The water depth values in the inlet were obtained by vessel-based surveys [22,31].

Since temperature difference is minute across much of our modeling region during summer time [32], salinity is considered to be the most important factor that influences water density and vertical stratification in Barataria Bay and adjacent coastal oceans in this study. Thus it is the only prognostic tracer variable in FVCOM simulations. Temperature is kept as a spatial and temporal constant (20 °C). The coefficients for horizontal viscosity and diffusivity are both set to be 0.4 m^2 s^{-1}. The conventional quadratic bottom friction formulation is applied, with drag coefficient C_d determined by matching a logarithmic bottom boundary layer velocity to that of the numerical model at the lowest sigma-layer height. However, bottom drag coefficient over the wetlands is defined as five times greater than that in the estuarine channels, mimicking the vegetation damping effect [33].

2.3. Model Forcing, Initial, and Boundary Conditions

FVCOM is driven by winds at the surface, sea level elevation at the open boundary, and freshwater inflows from various Mississippi River and Atchafalaya River passes, and the Davis Pond Diversion.

It is initialized on 1 October 2007 and run until 31 December 2008. We use 3-hourly wind data from NOAA National Centers for Environmental Prediction (NCEP) North American Regional Reanalysis (NARR) products and interpolate it onto the entire computational domain. The initial values of sea level elevation and velocity are specified as zero throughout the computational domain. The initial salinity field over the continental shelf is interpolated from HYCOM Gulf of Mexico $1/25^{\circ}$ reanalysis product, while salinity inside the Barataria Bay is interpolated from observations at the United States Geological Survey (USGS) stations. Experiments show that this technique gives more accurate salinity simulation result than that with linear interpolation from estuarine head to the mouth. At the open boundary, the 6-min interval sea level time series at four stations are downloaded from NOAA tides and currents website. Time series of Dauphin Island, Southwest Pass, Freeport, and Galveston Pier 21 are directly used to prescribe sea surface elevations at the easternmost node, the southeastern node, the southwestern node, and the westernmost node, respectively. Sea level elevation at other open boundary nodes are piecewise linearly interpolated from these four nodes. Observed 15-min freshwater discharge at four locations, Mississippi River at Belle Chasse, David Pond diversion, Atchafalaya River at Morgan City, and Wax Lake Outlet, are injected into the computational domain with flux boundary conditions of zero salinity and specified volume and momentum. All model forcing functions are ramped up from zero over a period of 10 days.

2.4. Observations

Simulated water elevation, velocity and salinity are compared with in situ observations. Water elevation data is obtained from National Water Information System of USGS shown in Figure 1, including six stations, Barataria Bay near Grand Terre Island (S1), Barataria Bay North of Grand Isle (S2), Hackberry Bay near NW of Grand Isle (S3), Barataria Waterway (S4), Little Lake near Bay Dosgris (S5), and Little Lake near Bay Cutoff (S6). The unit of water elevation is converted to meter and vertical datum is adjusted to mean sea level in order to be compared with model results. Velocity and salinity data are from the field observations conducted at Barataria Pass from 11:30 31 July to 11:10 1 August 2008 UTC (see Li et al. [31] for details about field observation and data processing).

2.5. Analysis Methods

The vertically averaged cross- and along-channel momentum equations are written as:

$$\underbrace{\frac{1}{D}\frac{\partial \overline{u}D}{\partial t}}_{DDT} = \underbrace{-\frac{1}{D}\left(\frac{\partial \overline{u}^2 D}{\partial x}+\frac{\partial \overline{u}\,\overline{v}D}{\partial y}\right)}_{ADV} + \underbrace{f\overline{v}}_{COR} \underbrace{-g\frac{\partial \zeta}{\partial x}}_{DPBP} \underbrace{-\frac{g}{\rho_0}\left[\int_{-1}^{0}\frac{\partial}{\partial x}\left(D\int_{\sigma}^{0}\rho d\sigma'\right)d\sigma+\frac{\partial D}{\partial x}\int_{-1}^{0}\sigma\rho d\sigma\right]}_{DPBC} + \underbrace{\frac{\tau_{sx}}{D\rho_0}}_{WIND} \underbrace{-\frac{\tau_{bx}}{D\rho_0}}_{FRIC} + \underbrace{\widetilde{F}_x}_{HDIF} + \underbrace{\frac{1}{D}G_x}_{AV2D} \quad (1)$$

$$\underbrace{\frac{1}{D}\frac{\partial \overline{v}D}{\partial t}}_{DDT} = \underbrace{-\frac{1}{D}\left(\frac{\partial \overline{u}\,\overline{v}D}{\partial x}+\frac{\partial \overline{v}^2 D}{\partial y}\right)}_{ADV} \underbrace{-f\overline{u}}_{COR} \underbrace{-g\frac{\partial \zeta}{\partial y}}_{DPBP} \underbrace{-\frac{g}{\rho_0}\left[\int_{-1}^{0}\frac{\partial}{\partial y}\left(D\int_{\sigma}^{0}\rho d\sigma'\right)d\sigma+\frac{\partial D}{\partial y}\int_{-1}^{0}\sigma\rho d\sigma\right]}_{DPBC} + \underbrace{\frac{\tau_{sy}}{D\rho_0}}_{WIND} \underbrace{-\frac{\tau_{by}}{D\rho_0}}_{FRIC} + \underbrace{\widetilde{F}_y}_{HDIF} + \underbrace{\frac{1}{D}G_y}_{AV2D} \quad (2)$$

where $(\overline{u}, \overline{v})$ are the vertical integrated cross- and along-axis velocity components. The positive u is pointed to the eastern bank, the positive v to the upstream. Terms from the left to the right are local acceleration (DDT), nonlinear advection (ADV), Coriolis force (COR), barotropic pressure gradient (DPBP), baroclinic pressure gradient (DPBC), wind stress (WIND), bottom friction (FRIC), horizontal diffusion (HDIF), and difference between nonlinear terms of vertically-averaged 2-D variables and vertical integration of 3-D variables (AV2D). The expressions for HDIF and AV2D can be referred to [26,27]. Consistent with 3-D currents converted to cross- and along-channel directions,

all terms in Equations (1) and (2) are rotated from the original FVCOM computation x-y coordinates (see Appendix A for details).

A 3-D FVCOM momentum equation analysis was used to identify the mechanisms that drive lateral circulation. The equation is written as:

$$\underbrace{\frac{1}{D}\frac{\partial uD}{\partial t}}_{} = \underbrace{-\frac{1}{D}\frac{\partial u^2D}{\partial x}}_{} \underbrace{-\frac{1}{D}\frac{\partial uvD}{\partial y}}_{} \underbrace{-\frac{1}{D}\frac{\partial u\omega}{\partial \sigma}}_{} + \underbrace{fv}_{} \underbrace{-g\frac{\partial \zeta}{\partial x}}_{} \underbrace{-\frac{g}{\rho_0}\left[\frac{\partial}{\partial x}\left(D\int_{\sigma}^{0} d\sigma' + \sigma\rho\frac{\partial D}{\partial x}\right)\right]}_{} + \underbrace{\frac{1}{D^2}\frac{\partial}{\partial \sigma}\left(K_m\frac{\partial u}{\partial \sigma}\right)}_{} + \underbrace{F_x}_{} \quad (3)$$

$$\underbrace{\frac{1}{D}\frac{\partial vD}{\partial t}}_{DDT} = \underbrace{-\frac{1}{D}\frac{\partial uvD}{\partial x}}_{ADVU} \underbrace{-\frac{1}{D}\frac{\partial v^2D}{\partial y}}_{ADVV} \underbrace{-\frac{1}{D}\frac{\partial v\omega}{\partial \sigma}}_{ADVW} \underbrace{-fu}_{COR} \underbrace{-g\frac{\partial \zeta}{\partial y}}_{DPBP} \underbrace{-\frac{g}{\rho_0}\left[\frac{\partial}{\partial y}\left(D\int_{\sigma}^{0} d\sigma' + \sigma\rho\frac{\partial D}{\partial y}\right)\right]}_{DPBC} + \underbrace{\frac{1}{D^2}\frac{\partial}{\partial \sigma}\left(K_m\frac{\partial v}{\partial \sigma}\right)}_{VDIF} + \underbrace{F_y}_{HDIF} \quad (4)$$

where (u, v) are cross- and along-channel velocity components. The advection terms are moved to the same side of the pressure gradient, and each term in Equations (3) and (4) is calculated with its corresponding sign (e.g., $-\partial(u^2D)/D\partial x$).

3. Results

3.1. Two-Month Water Elevation Comparisons

We use the Pearson correlation coefficient [34] as evaluation metrics. Two-month (1 July to 31 August 2008) time series of water elevation for both observation and model simulation are shown in Figure 3. The model reproduces the observed tidal variations, including tropic-equatorial modulation, as well as wind-driven water level set-up and set-down with all correlation coefficients above 0.9.

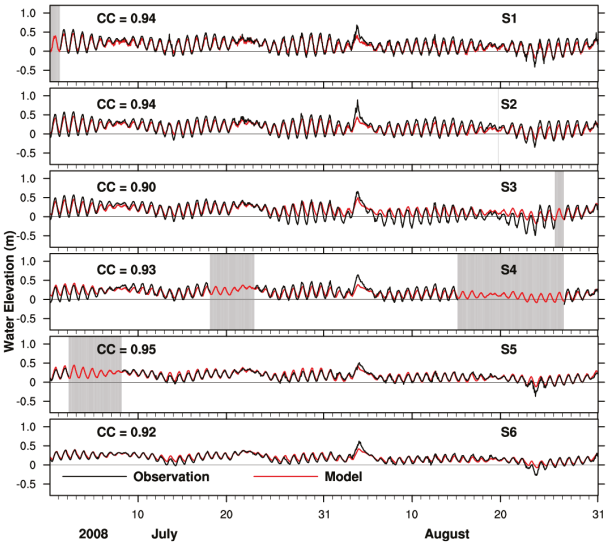

Figure 3. Water elevation comparison between USGS observations (black) and model simulation (red) from 1 July to 31 August 2008. Grayed areas represent missing data.

3.2. Velocity

Similar to the treatment in Li et al. [22], the x- and y-velocity components were counterclockwise rotated by 52.7° from the east and north direction to obtain the cross- and along-channel velocity components (Figure 1b), which are shown in Figure 4. Positive along-channel velocity is flood current. As shown in Figure 4a, the observed along-channel velocity has a stronger tidal signal, with maximum magnitude of ~1.5 m s^{-1}, than the model simulated velocity, which has a maximum magnitude of ~1.0 m s^{-1}. The tidal phase is in agreement with the observations. Both observed and modeled cross-channel velocities (Figure 4b) are much smaller and noisier, and the tidal signal is not clear compared to the along channel velocity component. The discrepancy between the observed and modeled velocity is, in part, due to the fact that observed velocity data points were chosen along a 530 m long transect within a 90 m band (45 m on each side [22]), while modeled velocity data points are exactly along the chosen transect.

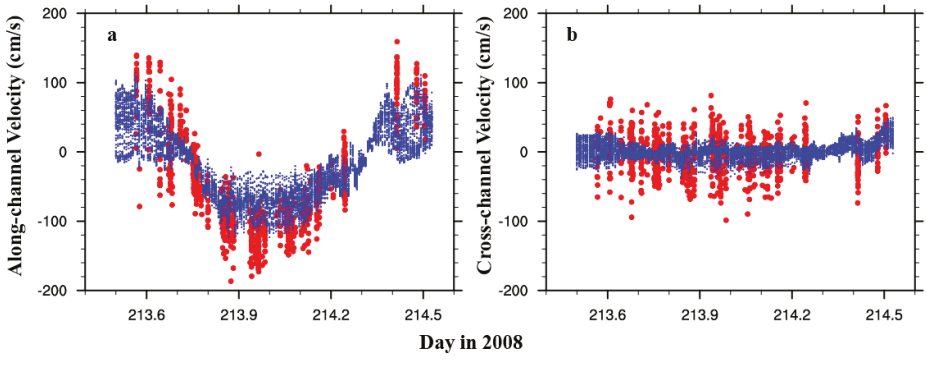

Figure 4. (**a**) Along-channel velocity at 1.32 m below the surface for observed (red dot) and modeled (blue dot) data; (**b**) Cross-channel velocity at 1.32 m below the surface for observed (red dot) and modeled (blue dot) data.

3.3. Vertical Salinity Profile

A seabird Electronics Conductivity, Temperature, and Depth Sensor (CTD) was used for vertical profiles of salinity. A total of 28 CTD casts were made between 31 July and 1 August 2008 over a 25.6 h period (see Table 1 in Li et al. [31] for details). Vertical salinity profiles from FVCOM simulation at three locations, eastern, middle, and western side of the channel (see Figure 1c for station locations), are compared with the CTD measurements in Figure 5. The magnitude of observed salinity ranges between 19 and 28.5. The maximum vertical salinity difference is about 5.5. The magnitude of the simulated salinity varies between 15 and 27. Generally, the model underestimates salinity, perhaps partially due to the neglect of evaporation. However, the model successfully captures characteristic features in salinity vertical profile. For example, cast 6 (Figure 5a), which was made 4 h after maximum flood, has a weak stratification at the top of the water column and well-mixed state at the bottom. Our model captures this feature. Other casts, such as casts 19, 26, 18, 8, and 16, have similar vertical profiles with the simulation. The temporal evolution of modeled salinity is also consistent with the observations. For example, the sequence of cast numbers (from low to high) for both the observation and the model show that the salinity tends to decrease in Figure 5f (ebb tide, west station). This gives us confidence to apply the model to do further qualitative dynamic analysis.

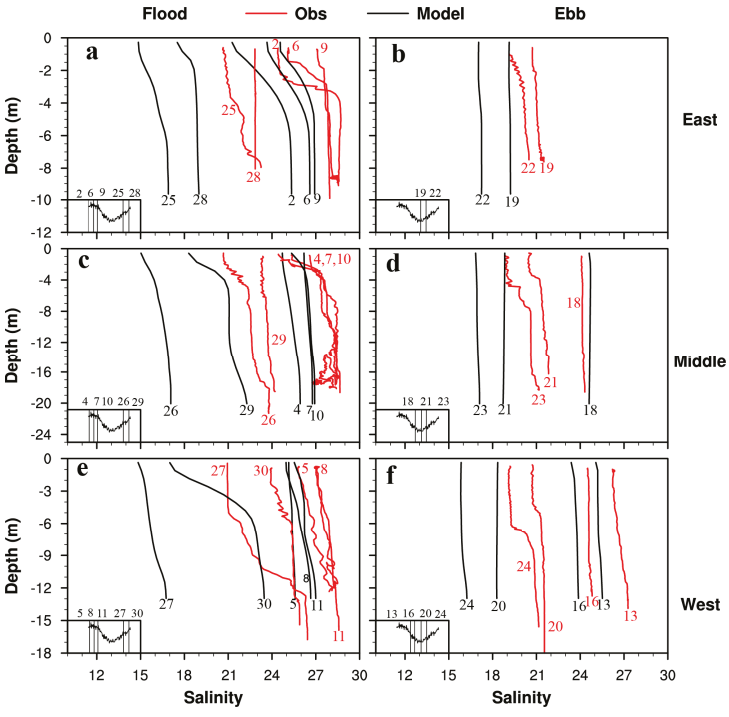

Figure 5. Vertical profiles of salinity comparison between in situ observation (red) and simulation (black). The numbers in the plot represent the sequence of CTD casts. Left panels are for flood tides (**a**,**c**,**e**), while right panels for ebb tides (**b**,**d**,**f**). **Top**, **middle**, and **bottom** row are at the eastern (**a**,**b**), middle (**c**,**d**), and western (**e**,**f**) side of the channel, respectively. Water level elevation in the deep channel is shown in the bottom-left small panel, with vertical lines showing casting times.

3.4. Temporal Variation of Stratification in the Barataria Pass

In order to study the variation of stratification over a diurnal cycle, a 25.6 h time series from the FVCOM simulation, starting from 06:00 31 July to 07:40 1 August 2008, was chosen to perform further analysis. Time series of water level, depth-averaged along-channel velocity and salinity difference between bottom and surface at three cross-channel locations are shown in Figure 6. The water elevation and depth-averaged velocity are not in-phase. Based on the deep channel station, flood tide lasts for ~12 h with maximum vertically averaged flood velocity ~0.8 m/s, while ebb tide lasts for ~13.6 h and maximum vertically averaged ebb velocity ~1.2 m/s. This tidal asymmetry is mainly caused by upstream Davis Pond diversion discharge, which is ~200 m^3/s during this period of time. Stratification evolution at these three locations shows distinct cross-channel variation. Within 2 h of early flood tides, stratification at all three locations decreases and reaches a well-mixed condition. Then stratification starts increasing. First the station at the western shoal quickly reaches the maximum (Figure 6a), followed by the deep channel station (Figure 6b). The station at the eastern shoal has a more moderate increase rate (Figure 6c). During the remaining period of flood tide, the western shoal experiences variation between well-mixed and stratified conditions. The deep channel and the eastern shoal are always stratified, and the latter has the largest stratification except near the end of flood. During ebb tide stratification at the western shoal is the weakest and remains almost well-mixed for the whole ebb tide. Stratification at the deep channel and eastern shoal have similar evolution, decreasing in the beginning, reaching well-mixed condition 5–6 h after ebbing, and increasing again 3 h before the slack water.

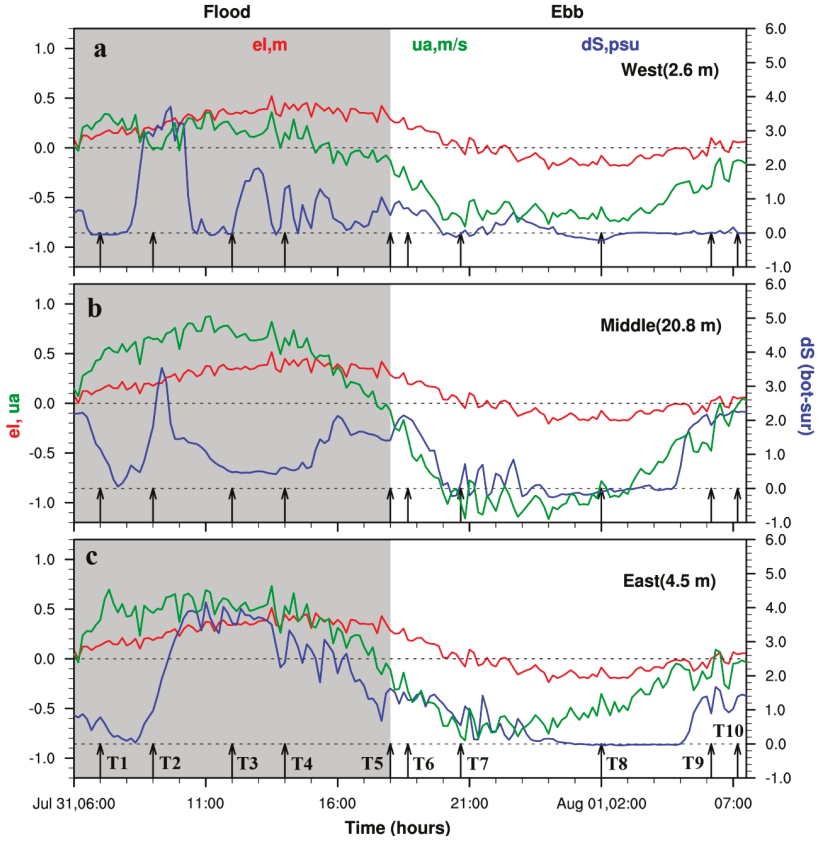

Figure 6. Time series (06:00 31 July to 07:40 1 August 2008) of water level elevation (red), depth-averaged along-channel velocity (green), and bottom-top salinity difference at (**a**) western shoal, (**b**) deep channel, and (**c**) eastern shoal. Shaded area represents flood tide. Arrows show different stages during a tidal cycle.

3.5. Residual Currents in the Barataria Pass over One Tidal Cycle

Tidal, ebb-, and flood- averaged along-channel velocities for the same 25.6 h time period are shown in Figure 7. The location of the transect is shown in Figure 1b and the western shoal is on the left side of Figure 7. The magnitude of cross-sectionally averaged ebb tides is −0.46 m/s, and that of cross-sectionally averaged flood tides is 0.33 m/s. The transverse structure of the along-channel residual current differs significantly between ebb and flood tides. For ebb tide, the maximum outflow is at the surface near the western shoal, inclining against the western bank of the deep channel. For flood tide, the maximum inflow is near the mid-depth in the central deep channel. Vertical velocity shear is much larger along the eastern bank than along the western bank. The magnitude of spatially averaged residual current during the 25.6 h period is −0.09 m/s, which is in the ebb direction. The maximum residual current is near the western shoal with the magnitude close to −0.3 m/s.

Using idealized numerical experiments, Cheng and Valle-Levinson [35] studied the sensitivity of estuarine exchange flow pattern on two nondimensional parameters, the Rossby number R_0 (U/fB, where U is the estuarine circulation velocity, f is the Coriolis parameter, and B is the width of the channel) and the Ekman number E_k (A_z/fH^2, where A_z is the vertical eddy viscosity, H is water depth, and f is the Coriolis parameter). They demonstrated that the exchange flow is vertically sheared

at large R_0, and horizontally sheared at large E_k. In our case ($R_0 \approx 1.72,\ E_k \approx 2.06$), the residual current is both vertically and horizontally sheared, which is similar to their case shown in Figure 5c ($R_0 = 2.63,\ E_k = 1$) of [35]. For a triangular shaped cross section, Wong [36] showed that the estuarine circulation is outward at the surface and inward at the bottom of the deep channel due to the interaction between baroclinic force and triangular bathymetry. Field observations at Barataria Pass captured this characteristics [31], in which the inflow is very weak. Our model also reproduces a weak inflow near the bottom of the eastern slope (Figure 7c). The asymmetry of estuarine–ocean exchange, i.e., inflow tending to the right side of the channel and outflow to the left side (when looking up-estuary) may be attributed to the Coriolis force [37].

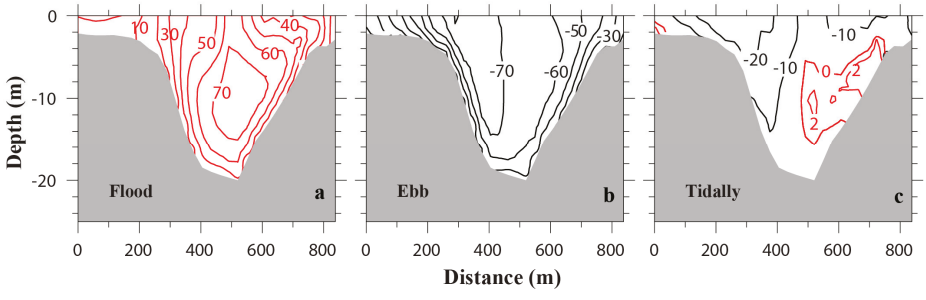

Figure 7. Transverse distribution of (**a**) flood-, (**b**) ebb-, and (**c**) tidally-averaged along-channel velocities, looking up-estuary (unit: cm/s). Red isolines represent flood velocities, while black isolines ebb velocities.

The transverse structure of cross-channel residual current also differs significantly between ebb and flood tides. The maximum flood-averaged and ebb-averaged velocity can reach 0.2 m/s and 0.16 m/s, respectively. The ebb-averaged velocity exhibits no horizontal divergence or convergence in the deep channel (Figure 8b,e), while the flood-averaged velocity shows a strong convergence close to the surface in the mid-channel (Figure 8a,d). However, no closed cell circulation exists for the flood average (Figure 8d), which is different from that described in Nunes and Simpson [1]. The tidally averaged cross-channel velocity is relatively weaker (Figure 8c), and it displays a clockwise circulation cell in the western channel and an even weaker counterclockwise cell in the eastern channel (Figure 8f).

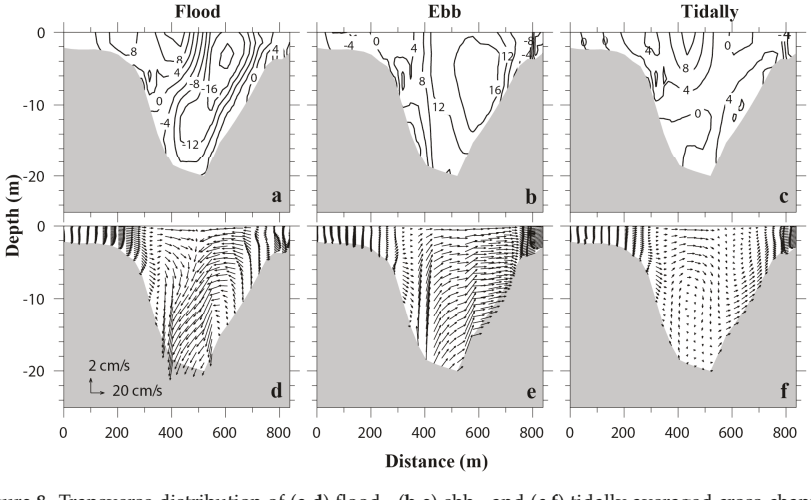

Figure 8. Transverse distribution of (**a**,**d**) flood-, (**b**,**e**) ebb-, and (**c**,**f**) tidally averaged cross-channel velocities (unit: cm/s, positive is eastward, negative is westward) and lateral circulation.

3.6. Time Series of Cross-Sectional Salinity and Currents Structures

Figure 9 shows the temporal evolution of along-channel velocity, lateral circulation, salinity, and turbulent vertical eddy viscosity for the Barataria Pass transect during flood tide. Each row represents a time instance indicated by an arrow in Figure 6. One hour after the flood starts (T1 in Figure 6), stratification is weak (bottom-top salinity difference ~1) across the deep channel and eastern shoal, and the western shoal is almost well-mixed (Figure 9c). Strong lateral circulation mainly occurs in the mid-depth with a convergence zone below 10 m in the deep channel (Figure 9b). The along-channel velocity is ~0.4 m/s, extending almost the whole deep channel. Thus, vertical and lateral velocity shear is weak. The vertical eddy viscosity is mostly smaller than 0.005 m^2/s, probably due to the small flood current magnitude and its shears.

Two hours later (T2 in Figure 6), the whole water column becomes more or less well-mixed across the deep channel and eastern shoal, while in the western shoal a sharp salinity stratification develops with bottom-top salinity difference ~3 in 2 m water column (Figure 9g). The distribution of salinity, and thus density, in the cross-channel direction is such that lateral baroclinic pressure gradients are directed from the central part of the deep channel towards the shoals. This is similar to the situation pointed out in Nunes and Simpson [1]. Based on their theory, such pressure gradient force will induce a lateral circulation with convergence at the surface and divergence near the bottom. This indeed occurs in our numerical results. Surface lateral flow at the west half of the channel changes from ~0.1 m/s westward to ~0.2 m/s eastward between T1 and T2. A pair of counter-rotating circulations can be clearly seen at T2 with strong convergence 2 m below the surface. Contrast to the idealized case in Lerczak and Geyer [2], the two circulation cells are not closed at this time. The maximum along-channel tidal velocity reaches ~0.8 m/s, confined at the mid-depth of the central channel (Figure 9e). The vertical shear in along-channel velocity is relatively weak, while the horizontal shear is great, which is, over the western slope, ~0.6 m/s within 200 m distance. It follows that Nunes and Simpson's argument is also applicable here in that differential advection of along-channel current is at least one of the mechanisms to generate the lateral salinity gradient. Strong vertical mixing (maximum eddy viscosity ~0.05 m^2/s, Figure 9h) occurs at the mid-depth and bottom boundary layer, where either tidal currents or bottom friction are strong (Figure 9e). Strong turbulence mixing tends to destratify the water column, which explains the relatively uniform salinity distribution in the deep channel and east shoal (Figure 9g).

At the maximum flood (T3), the along-channel velocities intensify. Maximum along-channel velocity, located at channel thalweg, reaches ~1.2 m/s and extends to the surface (Figure 9i), which is quite different from T2 (Figure 9e). The lateral shear of along-channel velocity, i.e., differential advection, is 1.0 m/s across 300 m distance on both sides. However, salinity distribution changes drastically. The western shoal is completely well-mixed at this time, while the eastern shoal and part of the east channel have surface stratification with a salinity difference of ~3 within 5–6 m depth (Figure 9k). The stratification in the deep channel, especially below 10 m, is weak, because the tidal mixing is relatively high (vertical eddy viscosity ~0.03 m^2/s) at the bottom boundary (Figure 9l). The lateral circulation pattern is similar to that at T2, but with intensified strength. The convergent zone rises to the ocean surface and the right circulation cell is now a complete circle (Figure 9j).

Four hours before the end of flood (T4), differential advection still persists, although the maximum along-channel tidal current has reduced to ~1 m/s and lowered below the surface (Figure 9m). Turbulence mixing weakens (Figure 9p). Hence, a weak stratification (bottom–surface salinity difference ~1.5) develops at the western shoal (Figure 9o). The salinity distribution shows a more symmetric pattern relative to the axis of the channel compared with T1, T2, and T3. As a result, the counter-rotating lateral circulation cells are more symmetric and fully developed (Figure 9n).

At the flood slack (T5), the surface water column becomes stratified in the upper 6 m (salinity difference ~1) while the deep channel is almost well-mixed (Figure 9s). The lateral circulation almost completely disappears in the deep channel (Figure 9r).

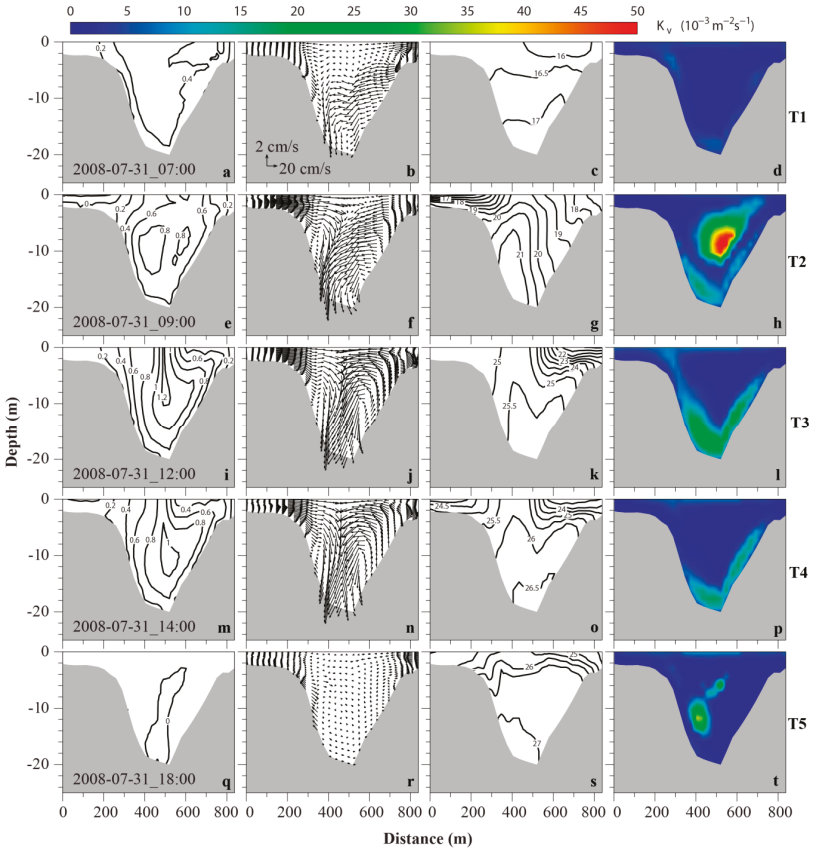

Figure 9. Cross-sectional profiles of currents (u, v, w), salinity and vertical viscosity during flood tide. The first column (**a**,**e**,**i**,**m**,**q**) is along-channel velocity, the second column (**b**,**f**,**j**,**n**,**r**) secondary circulation, the third column (**c**,**g**,**k**,**o**,**s**) salinity, and the last column (**d**,**h**,**l**,**p**,**t**) vertical viscosity. The velocity contour interval is 0.2 m/s, positive is up-estuary. The salinity contour interval is 0.5. Each row corresponds to a time instance indicated by an arrow in Figure 6.

At the beginning of ebb tide (T6), although the along-channel ebb current increases to ~0.4 m/s (Figure 10a), the salinity distribution and vertical stratification (Figure 10c) are almost the same as that of T5. There is a weak (less than 0.1 m/s) eastward lateral flow below 6 m (Figure 10b).

Two hours later (T7), the along-channel ebb current reaches above 1.0 m/s, locating mostly on the western slope and reaching the sea surface. The magnitude of along-channel velocity across the majority of the cross section is ~0.8 m/s (Figure 10e), which induces large tidal mixing (maximum vertical eddy viscosity ~0.16 m^2/s, Figure 10h). Thus, the whole water column is vertically well-mixed (Figure 10g). However, a horizontal salinity gradient exists, with higher salinity located near the channel axis, fresher water on both shoals. The western shoal is fresher than the eastern shoal (Figure 10g). This is because freshwater is flushed out of the estuary through the western shoal, as shown in Figure 7b,c. The lateral circulation shows mostly eastward currents in the deep channel across the whole water column, while the eastern shoal has a convergence area (Figure 10f).

During the next five hours, this cross section is always vertically well-mixed and salinity decreases constantly due to freshwater outflow. The turbulence mixing remains intense in the deep channel during this period. The maximum vertical eddy viscosity can reach up to 0.2 m^2/s, which results in the water

column in the east half of the channel vertically and horizontally well-mixed (Figure 10k, T8). The water column in the west half of the channel is also vertically well-mixed, but has a weak (~1) horizontal salinity decrease westward. The structure of lateral circulation and along-channel velocity remains the same, although the maximum ebb velocity has decreased from 1.0 m/s at T7 to 0.8 m/s at T8.

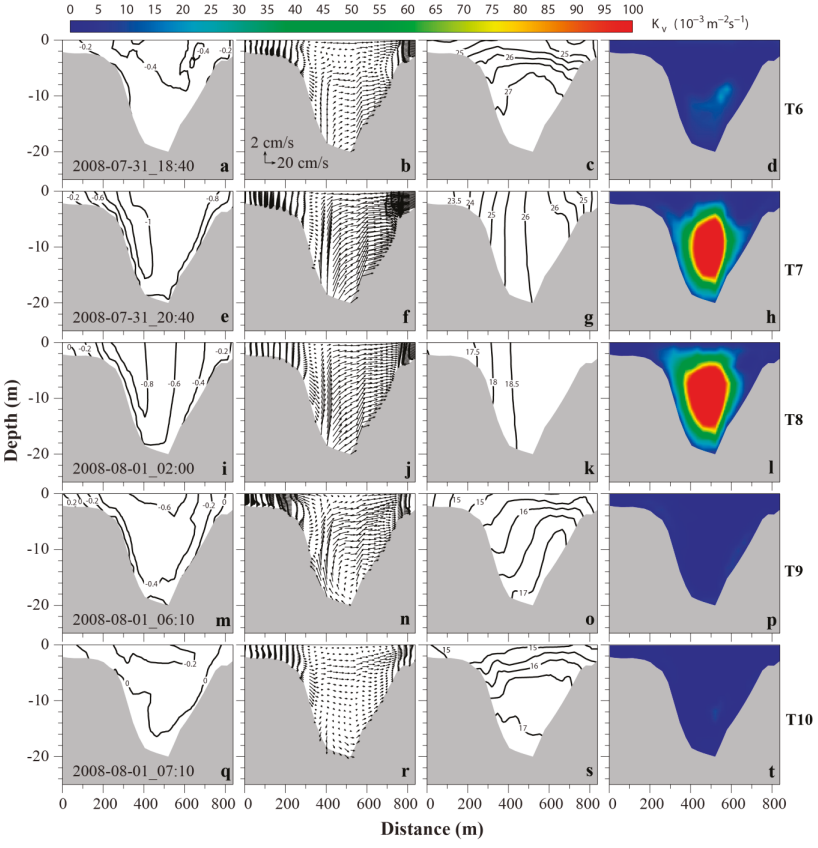

Figure 10. Cross-sectional profiles of currents (u, v, w), salinity and vertical viscosity during ebb tide. The first column (**a**,**e**,**i**,**m**,**q**) is along-channel velocity, the second column (**b**,**f**,**j**,**n**,**r**) secondary circulation, the third column (**c**,**g**,**k**,**o**,**s**) salinity, and the last column (**d**,**h**,**l**,**p**,**t**) vertical viscosity. The velocity contour interval is 0.2 m/s, positive is landward. The salinity contour interval is 0.5. Each row corresponds to a time instance indicated by an arrow in Figure 6.

Later during the ebb period (T9), the vertical stratification returns (Figure 10o), probably due to greatly reduced turbulence vertical eddy viscosity (Figure 10p). The vertical salinity difference is ~2 in the deep channel and on the eastern shoal. Lateral circulation shows a weak flow divergence close to the surface near the western slope (Figure 10n). The maximum along-channel ebb current moves to the surface central channel and its magnitude decreases to 0.6 m/s (Figure 10m).

At the ebb slack (T10), salinity distribution go back to similar to T1 situation. The western shoal is almost vertically uniform. Strong stratification (salinity difference ~2 over 6 m depth) occurs in the upper water column of the deep channel and on the eastern shoal. The lower water column in the deep channel has a weak stratification (Figure 10s). Lateral circulation is greatly reduced compared to other time instances of the ebb tide (Figure 10r).

4. Discussion

4.1. Depth-Averaged Momentum Balance

The Coriolis force, wind stress, and horizontal diffusion in Equations (1) and (2) are at least one order of magnitude smaller than the other terms during the 25.6 h period. Thus, these three terms are not shown. Figure 11 shows time series of six terms (DDT, ADV, DPBP, DPBC, FRIC, and AV2D) in Equations (1) and (2) at seven locations across the channel (Figure 1c). The momentum balance across this narrow channel is very complex, as various locations have different characteristics.

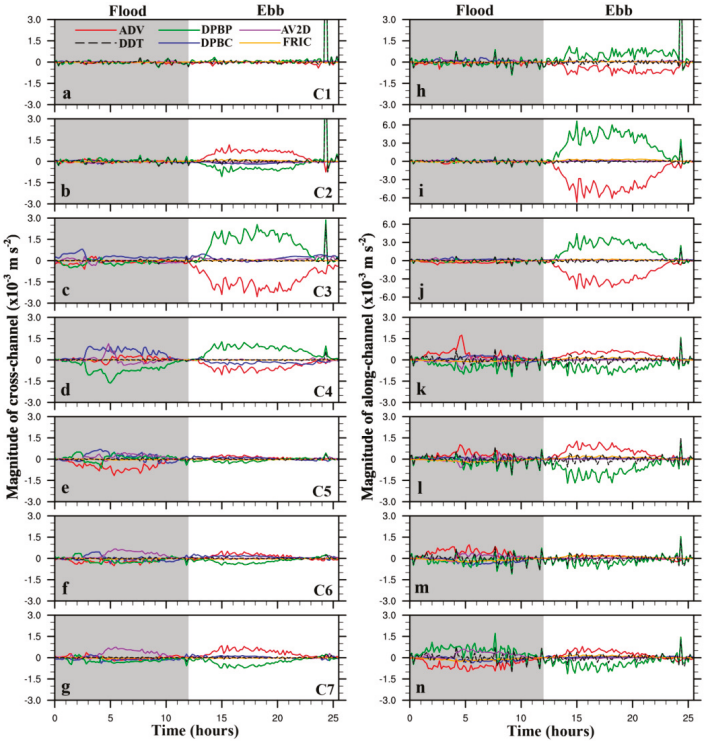

Figure 11. Time series of vertically averaged momentum equation terms in the cross- (**a**–**g**) and along-channel (**h**–**n**) directions during the same 25.6 h tidal cycle. The left column is for the cross-channel direction. The right column is for the along-channel direction. DDT (dash black) represents the local acceleration, AVD (red) the non-linear advection, COR (pink) the Coriolis force, DPBP (green) the barotropic pressure gradient, DPBC (blue) the baroclinic pressure gradient, AV2D (purple) the difference between 2-D and 3-D nonlinear terms, FRIC (orange) the bottom friction, and HDIF (yellow) the horizontal diffusion. Shaded areas indicate flood tide. Stations (C1–C7) from top to bottom are located from the west to the east shown in Figure 1c. Note that the y-axis scales for Figure (**i**,**j**) are different from others.

In the along-channel momentum balance, the dominant balance is between the barotropic pressure gradient and the nonlinear advection, especially during ebb tide. The magnitudes of these two terms for stations on the western side (C2 and C3, Figure 11i,j) of the channel are at least twice as greater as that of other stations. This is because maximum ebb currents flush out of the Barataria Bay near these two stations. The sign of barotropic pressure and nonlinear advection at stations on the west channel (C1–C3, Figure 11h–j) is opposite to those on the east channel (C4–C7, Figure 11k–n). There is a

spike during ebb tide, similar to that in Huang et al. [33]. The reason for this spike is not clear. During flood tide, the magnitudes of all terms at stations in the western channel (C1–C3, Figure 11h–j) are relatively small. This is because the sign of terms in the upper layer is opposite to that of the lower layer during flood tide. They offset each other after integrating over depth. The balance is among the DDT, nonlinear advection, barotropic pressure gradient, baroclinic pressure gradient, and the AV2D.

In the cross-channel momentum balance, the characteristics are similar to that of along-channel, i.e., the dominant balance is between advection term and the barotropic pressure gradient. Excluding station C1, the signs of advection and barotropic pressure terms at the westmost station (C2, Figure 11b) and the eastmost station (C7, Figure 11g) are the same, but opposite to the stations of the deep channel (C3, C4, Figure 11c,d). During flood tides, the balance is among the DDT, nonlinear advection, barotropic pressure gradient, baroclinic pressure gradient, and the AV2D. Note that, the baroclinic pressure is great at stations in the deep channel, and the magnitude is larger than that of along-channel. This indicates the lateral salinity gradient play an important role in momentum balance.

4.2. Driving Mechanism of Lateral Circulation

Lerczak and Geyer [2] pointed out that lateral advection plays an important role in the estuarine dynamics when lateral flows are strong enough to advect water parcels relative to 0.5 times the breadth of the channel ($4|v|/\sigma B \geq 1$, where $|v|$ is the absolute value of lateral velocity amplitude, σ is the semidiurnal tidal frequency, and B is the channel width) in a tidal cycle. As shown in previous results, lateral circulation in the Barataria Pass is strong both during maximum flood and maximum ebb. Thus, lateral advection is expected to be an important term in the momentum balance. The 3-D momentum Equations (3) and (4) are used to explore the generation mechanisms of the lateral circulation.

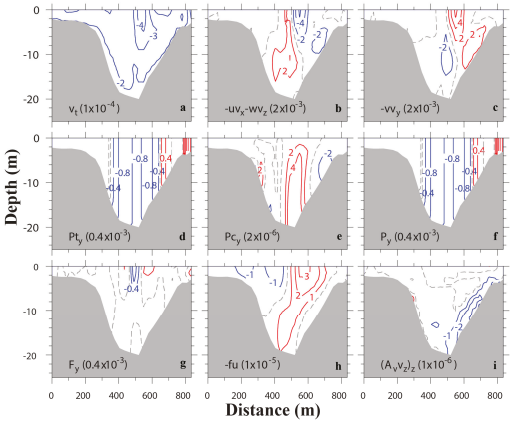

Figure 12. Transverse distributions of terms (m/s^2) in along-channel momentum equation at flood (T3). Terms include (**a**) local acceleration, (**b**) lateral advection, (**c**) along-channel advection, (**d**) barotropic pressure gradient, (**e**) baroclinic pressure gradient, (**f**) total pressure gradient, (**g**) horizontal stress divergence, (**h**) Coriolis force, and (**i**) vertical stress divergence. Red isolines represent positive values, while blue isolines negative values. Dash line shows contour 0. The contour intervals are shown in parenthesis.

Transverse distributions of various momentum terms of along- and cross-channel components at T3 (flood tide) are shown in Figures 12 and 13, respectively. In the along-channel momentum equation, baroclinic pressure gradient (Figure 12e), Coriolis force (Figure 12h) and vertical stress divergence (Figure 12i) are at least two orders of magnitude less than other terms at this time, thus are less important. The total pressure gradient comes from the barotropic pressure gradient (Figure 12d), and the largest terms are the nonlinear advection terms (Figure 12b,c). Lateral advection of along-channel momentum (Figure 12b, $-uv_x - wv_z$) is one of the largest terms in the momentum

balance. This term has a similar pattern but opposite sign with the along-channel momentum advection ($-vv_y$). The main force balance at this time is between non-linear advection and the barotropic pressure gradient, which is consistent with the result in 2-D momentum analysis.

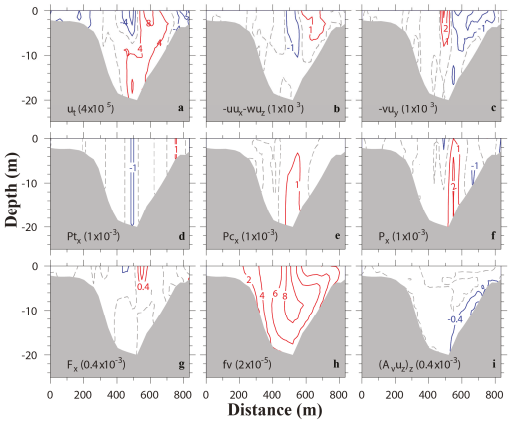

Figure 13. Transverse distributions of terms (m/s^2) in cross-channel momentum equation at flood (T3). Terms include (**a**) local acceleration, (**b**) lateral advection, (**c**) along-channel advection, (**d**) barotropic pressure gradient, (**e**) baroclinic pressure gradient, (**f**) total pressure gradient, (**g**) horizontal stress divergence, (**h**) Coriolis force, and (**i**) vertical stress divergence. Red isolines represent positive values, while blue isolines negative values. Dash line shows contour 0. The contour intervals are shown in parenthesis.

In the cross-channel momentum balance, Coriolis force (Figure 13h), although small, has exactly the same pattern as the transverse distribution of along-channel velocity (Figure 9i). Differential advection of the flood current at this time is clearly shown in the picture. The baroclinic pressure gradient (Figure 13e) has almost the same magnitude as the barotropic pressure gradient (Figure 13d), especially near the bottom, due to its magnitude increasing with depth. The baroclinic pressure gradient is mostly positive in the whole channel, except near the eastern shoal. Combining with the salinity distribution at the transect (Figure 9k), it indicates that the conceptual model of cross-channel baroclinic pressure gradient induced by differential advection is applicable here. However, the simple diagnostic model proposed by Nunes and Simpson [1] to explain the mechanism of lateral circulation generation, in which the momentum balance is between cross-channel pressure gradient and vertical stress divergence, seems to be oversimplified. Our numerical experiment shows that vertical stress divergence is mostly confined to the near bottom layer of the eastern slope (Figure 13i). Several other terms—nonlinear advection (Figure 13b,c) and horizontal stress divergence (Figure 13g)—are as important as the terms suggested in [1].

During ebb tide (i.e., at T7), the main momentum balance in the along-channel direction is among the nonlinear advection terms and the barotropic pressure gradient (Figure 14), which is the same as during the flood tide (Figure 12).

In the cross-channel momentum balance, the barotropic pressure gradient (Figure 15d) dominates the baroclinic pressure gradient (Figure 15e). Thus, contour lines of the total cross-channel pressure gradient (Figure 15f) are very similar to that of the former. It seems that at this time the main momentum balance is between along-channel advection of cross-channel momentum (Figure 15c) and pressure gradient (Figure 15f) over most of the cross-section area, both of which have alternative positive and negative vertical stripes and, when added together, almost cancel out each other. At the eastern shoal, all terms, excluding Coriolis force (Figure 15h) and baroclinic pressure gradient (Figure 15e), are needed in order to balance the cross-channel momentum equation. Because of the insignificant contribution from the baroclinic pressure gradient, no obvious convergence or divergence occurs in

this transect during the ebb period (Figure 10, second column). This is in clear contrast to the near surface convergence that happens during flood tide (Figure 9, second column).

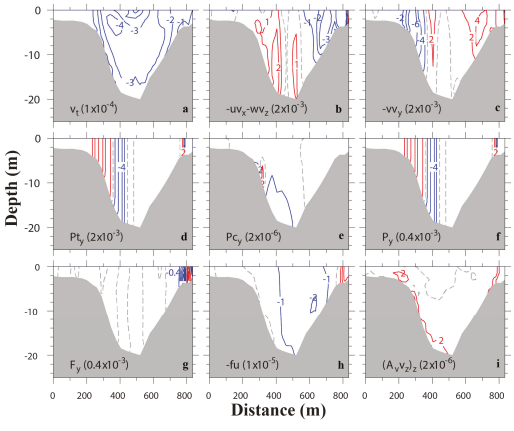

Figure 14. Transverse distributions of terms (m/s^2) in along-channel momentum equation at ebb (T7). Terms include (**a**) local acceleration, (**b**) lateral advection, (**c**) along-channel advection, (**d**) barotropic pressure gradient, (**e**) baroclinic pressure gradient, (**f**) total pressure gradient, (**g**) horizontal stress divergence, (**h**) Coriolis force, and (**i**) vertical stress divergence. Red isolines represent positive values, while blue isolines negative values. Dash line shows contour 0. The contour intervals are shown in parenthesis.

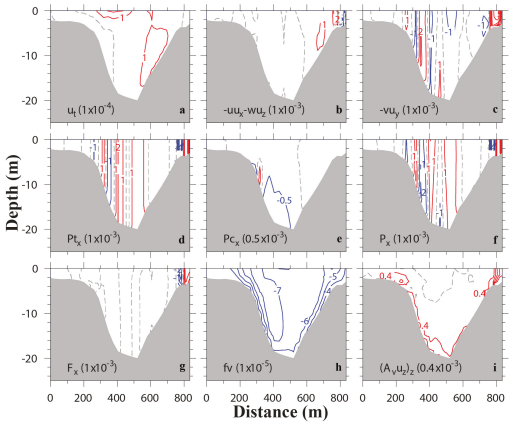

Figure 15. Transverse distributions of terms (m/s^2) in cross-channel momentum equation at ebb (T7). Terms include (**a**) local acceleration, (**b**) lateral advection, (**c**) along-channel advection, (**d**) barotropic pressure gradient, (**e**) baroclinic pressure gradient, (**f**) total pressure gradient, (**g**) horizontal stress divergence, (**h**) Coriolis force, and (**i**) vertical stress divergence. Red isolines represent positive values, while blue isolines negative values. Dash line shows contour 0. The contour intervals are shown in parenthesis.

4.3. Flood–Ebb Asymmetry

Here, we follow Lerczak and Geyer [2] using the cross-channel average of depth-averaged velocity amplitude $< |u| > = \frac{1}{A} \iint |u| dA$ ($|u|$ is the absolute value of depth-averaged cross-channel velocity, A is the cross-channel area) to represent the strength of the lateral flow. The result is shown in Figure 16. The maximum $< |u| >$ during flood is 0.32 m/s, while the maximum during ebb is 0.34 m/s. Generally, cross-channel current amplitude during ebb is comparable, even slightly greater than that during

flood, which is different from the idealized case [2], in which lateral circulation is about four times stronger during flood tides than during ebb tides. However, this inconsistence is also observed in James River estuary [14], where the lateral circulation shows no flood–ebb asymmetry during spring tides, and a reversed asymmetry during neap tides, that is stronger during ebb than during flood. Li et al. [14] attribute negligible flood–ebb variations during spring tides to turbulent mixing, which in their numerical experiment was simulated via a turbulence closure model. It reduces the vertical shear and the flood–ebb asymmetry in the vorticity generation. In comparison, the idealized case of Lerczak and Geyer [2] used a constant eddy viscosity. In our numerical experiment, turbulent mixing is simulated using the Mellor-Yamada 2.5 turbulence closure model and the 25.6 h diurnal tidal cycle is close to tropic tide. Maximum turbulent vertical viscosity is twice as great during ebb (Figure 10, last column) as during flood (Figure 9, last column). Therefore, our simulation result is more similar to Li et al. [14] than to Lerczak and Geyer [2].

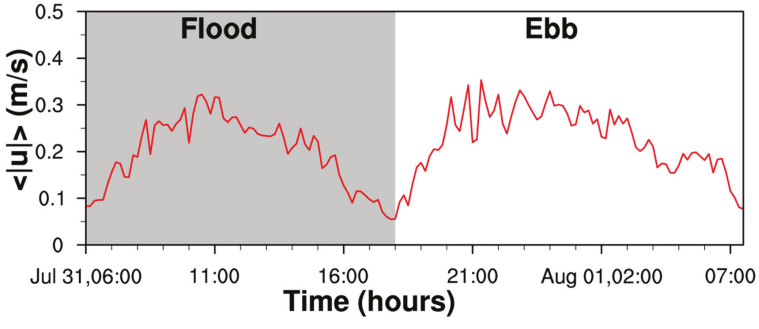

Figure 16. Cross-sectional average of lateral velocity magnitude for the 25.6 h diurnal tidal period.

During flood tide, lateral circulation shows asymmetry across the section (Figure 9f,j,n). The counterclockwise circulation on the east side is stronger, which is due to the presence of lower salinity water close to and over the eastern shoal (Figure 9k,o). This fresher water increases the lateral baroclinic pressure gradient on the east side, and thus enhances the strength of the lateral circulation cell at this side. The low salinity water is from the Mississippi River plume based on analyses of in-situ observational data and numerical simulation result [22].

Another asymmetry between flood and ebb tides lies in that maximum flood currents are always located, more or less, at the central part of the deep channel (Figure 9, first column), while maximum ebb currents, when they are greater than 0.8 m/s, are located closer to the western shoal or over the western slope (Figure 10e,i). Only when maximum ebb currents are below 0.6 m/s, they move back to the middle of the channel (Figure 10a,m,q).

5. Conclusions

Barataria Pass is a tidal inlet that connects the Barataria Bay to the continental shelf. Previous investigation has introduced the tidal straining effect on density stratification during the same 25.6 h period along the same transect [22]. In this study, we conduct a numerical model simulation and illustrate that the lateral variations in the salinity and velocity fields are comparable to or even larger than the vertical variations within a diurnal tidal cycle.

The density distribution within any estuary is a result of both advective and mixing processes. In Barataria Pass, the turbulent mixing is closely related to the magnitude of ebb/flood current and the strength of the tidal bottom boundary layer. Characteristics of horizontal advection processes in the inlet are that maximum flood currents are located at the central part of the deep channel for a large part of the flood period. This differential advection [1], when acting upon the along-channel density gradient, produces a distinct density difference between the shoal and channel waters. In addition,

the advection of Mississippi River water to the eastern channel during part of the flood period further enhances the density difference. On the contrary, maximum ebb currents swing between the western slope and central surface of the channel during the ebb. When maximum ebb flows are at the western slope, the differential advection mechanism does not work. When they go back to the channel center, the salinity contour lines are mostly horizontal due to weak vertical turbulence mixing. Thus, both situations are not favorable to produce an extreme density near the middle of the channel.

During flood period, when density distribution is high near the channel center and low at both shoals, the horizontal pressure gradient drives a lateral circulation with two counter-rotating cells and surface or near surface convergence. This result from the Barataria Pass is similar to that reported by Nunes and Simpson [1]. However, detailed analysis of momentum equations indicates that, in addition to the pressure gradient and vertical stress divergence, nonlinear advection and horizontal stress divergence are also important terms.

During ebb period, the lateral circulation is mostly eastward for the whole water column and persisting for almost the whole period. The surface divergence suggested by the differential advection mechanism is either non-existent or lasting for a very short period. The main momentum balance across most of the transect is between the along-channel advection of cross-channel momentum and pressure gradient. In addition, the sectional averaged lateral velocity magnitude during ebb is comparable to that during flood, which is different from the idealized numerical experiment [2].

Interactions among lateral circulation, along-channel tidal currents, and density stratification are complex processes. Lateral circulation can play a critical role in the dynamics of estuaries. It can act as a driving term for the estuarine exchange flow [2], and thus alter the along-channel momentum budget [38]. During flood tide, lateral circulation transported near-bed sediment out of the channel toward the shoal [37]. During ebb tide, it created a convergence in suspended sediment at the transition between channel and shoal [39]. Trapping by lateral circulation alters the lateral distribution of bed sediment. The idealized numerical experiment with constant eddy coefficients [2] demonstrated that the lateral circulation can be significantly different over a spring-neap cycle and density stratification can inhibit lateral circulation. Our study can be a starting point for further investigations of interactions among lateral circulation, estuarine circulation, and estuarine stratification in the partially stratified tidal inlet, the Barataria Pass.

Supplementary Materials: FVCOM simulation data are publicly available through the Gulf of Mexico Research Initiative Information and Data Cooperative (GRIIDC) at https://data.gulfresearchinitiative.org (DOI: 10.7266/n7-1qe9-mg27).

Author Contributions: Conceptualization, L.C. and H.H.; Investigation, L.C., H.H., C.L.; Writing-Original Draft Preparation, L.C.; Writing-Review & Editing, H.H., C.L., D.J.; Visualization, L.C.; Funding Acquisition, D.J., H.H.

Funding: This research was made possible in part by a grant from The Gulf of Mexico Research Initiative. L.C. was also funded by the Economic Development Assistantship from the Graduate School, Louisiana State University.

Acknowledgments: Portions of this research were conducted with high performance computational resources provided by Louisiana State University (http://www.hpc.lsu.edu) and the Louisiana Optical Network Initiative (http://www.loni.org).

Conflicts of Interest: The authors declare no conflict of interest.

Appendix A. Decomposition of Vectors into Along- and Cross-Channel Directions

In x-y-σ coordinates, where x-direction is defined to the east and y-direction to the north, the FVCOM x- and y-axis 3-D momentum equations are written as:

$$\underbrace{\frac{\partial uD}{\partial t}}_{DUDT} = \underbrace{-\frac{\partial u^2 D}{\partial x}}_{ADVUX} \underbrace{-\frac{\partial uvD}{\partial y}}_{ADVVX} \underbrace{-\frac{\partial u\omega}{\partial \sigma}}_{ADVWX} + \underbrace{fvD}_{CORX} \underbrace{-gD\frac{\partial \zeta}{\partial x}}_{DPBPX} \underbrace{-\frac{gD}{\rho_0}\left[\frac{\partial}{\partial x}\left(D\int_{\sigma}^{0} d\sigma' + \sigma\rho\frac{\partial D}{\partial x}\right)\right]}_{DPBCX} + \underbrace{\frac{1}{D}\frac{\partial}{\partial \sigma}\left(K_m\frac{\partial u}{\partial \sigma}\right)}_{VVISCX} + \underbrace{F_x}_{HVISCX} \tag{A1}$$

$$\underbrace{\frac{\partial vD}{\partial t}}_{DVDT} = \underbrace{-\frac{\partial uvD}{\partial x}}_{ADVUY} \underbrace{-\frac{\partial v^2 D}{\partial y}}_{ADVVY} \underbrace{-\frac{\partial v\omega}{\partial \sigma}}_{ADVWY} \underbrace{-fuD}_{CORY} \underbrace{-gD\frac{\partial \zeta}{\partial y}}_{DPBPY} \underbrace{-\frac{gD}{\rho_0}\left[\frac{\partial}{\partial y}\left(D\int_{\sigma}^{0} d\sigma' + \sigma\rho\frac{\partial D}{\partial y}\right)\right]}_{DPBCY} + \underbrace{\frac{1}{D}\frac{\partial}{\partial \sigma}\left(K_m\frac{\partial v}{\partial \sigma}\right)}_{VVISCY} + \underbrace{F_y}_{HVISCY} \tag{A2}$$

where (u, v) are the velocity components in the (x, y) directions, σ is the vertical coordinate.

In order to quantify along- and cross-channel momentum balance, we choose the along-channel direction (y') to be aligned with the channel. It is positive when pointing into the estuary. The cross-channel direction (x') is defined to be positive when pointing to the eastern boundary (Figure A1). The relationship between (u', v') and (u, v), $(x', y\prime)$ and (x, y) are as following:

$$u' = ucos\theta + vsin\theta \tag{A3}$$

$$v' = -usin\theta + vcos\theta \tag{A4}$$

$$x' = (x - x_0)cos\theta + (y - y_0)sin\theta \tag{A5}$$

$$y' = -(x - x_0)sin\theta + (y - y_0)cos\theta \tag{A6}$$

where θ is the angle between the x'-direction (cross-channel) and the x-direction.

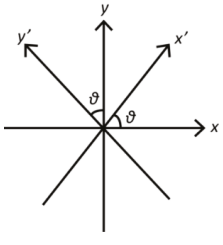

Figure A1. Illustration of x-y coordinate transformed to x'-y' coordinate.

In x'-y' coordinates, the momentum equations are written as:

$$\underbrace{\frac{\partial u'D}{\partial t}}_{DUDT'} = \underbrace{-\frac{\partial u'^2 D}{\partial x'}}_{ADVUX'} \underbrace{-\frac{\partial u'v'D}{\partial y'}}_{ADVVX'} \underbrace{-\frac{\partial u'\omega}{\partial \sigma}}_{ADVWX'} + \underbrace{fv'D}_{CORX'} \underbrace{-gD\frac{\partial \zeta}{\partial x'}}_{DPBPX'} \underbrace{-\frac{gD}{\rho_0}\left[\frac{\partial}{\partial x'}\left(D\int_{\sigma}^{0} d\sigma' + \sigma\rho\frac{\partial D}{\partial x'}\right)\right]}_{DPBCX'} + \underbrace{\frac{1}{D}\frac{\partial}{\partial \sigma}\left(K_m\frac{\partial u\prime}{\partial \sigma}\right)}_{VVISCX'} + \underbrace{F_{x\prime}}_{HVISCX'} \tag{A7}$$

$$\underbrace{\frac{\partial v'D}{\partial t}}_{DVDT'} = \underbrace{-\frac{\partial u'v'D}{\partial x'}}_{ADVUY'} \underbrace{-\frac{\partial v'^2 D}{\partial y'}}_{ADVVY'} \underbrace{-\frac{\partial v'\omega}{\partial \sigma}}_{ADVWY'} \underbrace{-fu'D}_{CORY'} \underbrace{-gD\frac{\partial \zeta}{\partial y'}}_{DPBPY'} \underbrace{-\frac{gD}{\rho_0}\left[\frac{\partial}{\partial y'}\left(D\int_{\sigma}^{0} d\sigma' + \sigma\rho\frac{\partial D}{\partial y'}\right)\right]}_{DPBCY'} + \underbrace{\frac{1}{D}\frac{\partial}{\partial \sigma}\left(K_m\frac{\partial v\prime}{\partial \sigma}\right)}_{VVISCY'} + \underbrace{F_{y\prime}}_{HVISCY'} \tag{A8}$$

To project the momentum equations into the cross- and along-channel directions, we treat each term in the momentum equations as a vector in the (x, y) direction and then apply the same

decomposition as Equations (A3) and (A4). Thus terms in x'-y' coordinates can be calculated by corresponding terms in x-y coordinates as follows:

$$\begin{aligned} DUDT' = \frac{\partial u'D}{\partial t} &= \frac{\partial(ucos\theta+vsin\theta)D}{\partial t} = \frac{\partial uD}{\partial t}cos\theta + \frac{\partial vD}{\partial t}sin\theta \\ &= DUDTcos\theta + DVDTsin\theta \end{aligned}$$

$$\begin{aligned} DVDT' = \frac{\partial v'D}{\partial t} &= \frac{\partial(-usin\theta+ucos\theta)D}{\partial t} = -\frac{\partial uD}{\partial t}sin\theta + \frac{\partial vD}{\partial t}cos\theta \\ &= -DUDTsin\theta + DVDTcos\theta \end{aligned}$$

Terms ADVUX'+ADVVX', ADVUY'+ADVVY', ADVWX', ADVWY', CORX', CORY', DPBPX', DPBPY', DPBCX', DPBCY', VVISCX', VVISCY', HVISCX', and HVISCY' can be calculated with the same method. While ADVUX', ADVVX', ADVUY', and ADVVY' should be calculated by the finite volume difference. For example, ADVUX' can be calculated as:

$$\iint \frac{\partial u'^2D}{\partial x'}dx'dy' = \oint u'u'Ddy' = \oint UIJ' \times \begin{pmatrix} UIJ1' \\ UIJ2' \end{pmatrix} \times DIJ \times dy' \tag{A9}$$

where UIJ, $UIJ1'$ and $UIJ2'$ are shown in Figure A2.

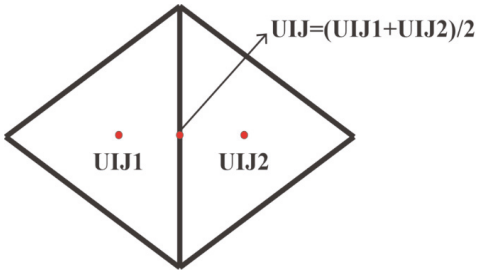

Figure A2. Illustration of local coordinate used to calculate the horizontal advection terms.

With Equations (A3)–(A6), we have:

$$dy' = -sin\theta + cos\theta dy \tag{A10}$$

$$UIJ' = UIJcos\theta + VIJsin\theta \tag{A11}$$

$$UIJ'^1_2 = UIJ^1_2 \times cos\theta + VIJ^1_2 \times sin\theta \tag{A12}$$

Substituting Equations (A10)–(A12) into Equation (A9),

$$\begin{aligned} ADVUX' &= \frac{\partial u'^2D}{\partial y'} = \frac{\partial u^2D}{\partial y}sin\theta cos^2\theta + \frac{\partial uvD}{\partial y}sin^2\theta cos\theta + \frac{\partial vuD}{\partial y}sin^2\theta cos\theta \\ &+ \frac{\partial v^2D}{\partial y}sin^3\theta + \frac{\partial u^2D}{\partial x}cos^3\theta + \frac{\partial uvD}{\partial x}sin\theta cos^2\theta + \frac{\partial vuD}{\partial x}sin\theta cos^2\theta + \frac{\partial v^2D}{\partial x}sin^2\theta cos\theta \end{aligned}$$

With the same method, $ADVVX'$, $ADVUY'$, and $ADVVY'$ are given as:

$$\begin{aligned} ADVVX' &= \frac{\partial u'v'D}{\partial y'} = -\frac{\partial u^2D}{\partial y}sin\theta cos^2\theta - \frac{\partial uvD}{\partial y}sin^2\theta cos\theta + \frac{\partial vuD}{\partial y}cos^3\theta \\ &+ \frac{\partial v^2D}{\partial y}sin\theta cos^2\theta + \frac{\partial u^2D}{\partial x}sin^2\theta cos\theta + \frac{\partial uvD}{\partial x}sin^3\theta - \frac{\partial vuD}{\partial x}sin\theta cos^2\theta - \frac{\partial v^2D}{\partial x}sin^2\theta cos\theta \end{aligned}$$

$$\begin{aligned} ADVUY' &= \frac{\partial u'v'D}{\partial x'} = -\frac{\partial u^2D}{\partial y}sin^2\theta cos\theta + \frac{\partial uvD}{\partial y}sin\theta cos^2\theta - \frac{\partial vuD}{\partial y}sin^3\theta \\ &+ \frac{\partial v^2D}{\partial y}sin^2\theta cos\theta - \frac{\partial u^2D}{\partial x}sin\theta cos^2\theta + \frac{\partial uvD}{\partial x}cos^3\theta - \frac{\partial vuD}{\partial x}sin^2\theta cos\theta + \frac{\partial v^2D}{\partial x}sin\theta cos^2\theta \end{aligned}$$

$$ADVVY' = \frac{\partial v'^2 D}{\partial y'} = \frac{\partial u^2 D}{\partial y} sin^2\theta cos\theta - \frac{\partial uvD}{\partial y} sin\theta cos^2\theta - \frac{\partial vuD}{\partial y} sin\theta cos^2\theta + \frac{\partial v^2 D}{\partial y} cos^3\theta - \frac{\partial u^2 D}{\partial x} sin^3\theta + \frac{\partial uvD}{\partial x} sin^2\theta cos\theta + \frac{\partial vuD}{\partial x} sin^2\theta cos\theta - \frac{\partial v^2 D}{\partial x} sin\theta cos^2\theta$$

References

1. Nunes, R.A.; Simpson, J.H. Axial convergence in a well-mixed estuary. *Estuar. Coast. Shelf Sci.* **1985**, *20*, 637–649. [CrossRef]
2. Lerczak, A.J.; Geyer, W.R. Modeling the lateral circulation in straight, stratified estuaries. *J. Phys. Oceanogr.* **2004**, *34*, 1410–1428. [CrossRef]
3. Li, C. Axial convergence fronts in a barotropic tidal inlet—Sand shoal inlet, VA. *Cont. Shelf Res.* **2002**, *22*, 2633–2653. [CrossRef]
4. Li, C.; Valle-Levinson, A. A two-dimensional analytic tidal model for a narrow estuary of arbitrary lateral depth variation: The intratidal motion. *J. Geophys. Res. Oceans* **1999**, *104*, 23525–23543. [CrossRef]
5. Valle-Levinson, A.; Li, C.; Wong, K.-C.; Lwiza Kamazima, M.M. Convergence of lateral flow along a coastal plain estuary. *J. Geophys. Res. Oceans* **2000**, *105*, 17045–17061. [CrossRef]
6. Chant, R.J.; Wilson, R.E. Secondary circulation in a highly stratified estuary. *J. Geophys. Res. Oceans* **1997**, *102*, 23207–23215. [CrossRef]
7. Lacy, J.R.; Monismith, S.G. Secondary currents in a curved, stratified, estuarine channel. *J. Geophys. Res. Oceans* **2001**, *106*, 31283–31302. [CrossRef]
8. Pein, J.; Valle-Levinson, A.; Stanev, E.V. Secondary Circulation Asymmetry in a Meandering, Partially Stratified Estuary. *J. Geophys. Res. Oceans* **2018**, *123*, 1670–1683. [CrossRef]
9. Li, C.; Chen, C.; Guadagnoli, D.; Georgiou Ioannis, Y. Geometry-induced residual eddies in estuaries with curved channels: Observations and modeling studies. *J. Geophys. Res. Oceans* **2008**, *113*, C01005. [CrossRef]
10. Wargula, A.; Raubenheimer, B.; Elgar, S. Curvature- and Wind-Driven Cross-Channel Flows at an Unstratified Tidal Bend. *J. Geophys. Res. Oceans* **2018**, *123*, 3832–3843. [CrossRef]
11. Chen, S.-N.; Sanford, L.P. Lateral circulation driven by boundary mixing and the associated transport of sediments in idealized partially mixed estuaries. *Cont. Shelf Res.* **2009**, *29*, 101–118. [CrossRef]
12. Cheng, P.; Wilson, R.E.; Flood, R.D.; Chant, R.J.; Fugate, D.C. Modeling influence of stratification on lateral circulation in a stratified estuary. *J. Phys. Oceanogr.* **2009**, *39*, 2324–2337. [CrossRef]
13. Scully, E.M.; Geyer, W.R.; Lerczak, A.J. The influence of lateral advection on the residual estuarine circulation: A numerical modeling study of the Hudson River Estuary. *J. Phys. Oceanogr.* **2009**, *39*, 107–124. [CrossRef]
14. Li, M.; Liu, W.; Chant, R.; Valle-Levinson, A. Flood-ebb and spring-neap variations of lateral circulation in the James River estuary. *Cont. Shelf Res.* **2017**, *148*, 9–18. [CrossRef]
15. Geyer, W.R. Three-dimensional tidal flow around headlands. *J. Geophys. Res. Oceans* **1993**, *98*, 955–966. [CrossRef]
16. Vennell, R.; Old, C. High-resolution observations of the intensity of secondary circulation along a curved tidal channel. *J. Geophys. Res. Oceans* **2007**, *112*, C11008. [CrossRef]
17. Lacy, J.R.; Stacey, M.T.; Burau, J.R.; Monismith, S.G. Interaction of lateral baroclinic forcing and turbulence in an estuary. *J. Geophys. Res. Oceans* **2003**, *108*, 3089. [CrossRef]
18. Nidzieko, N.J.; Hench, J.L.; Monismith, S.G. Lateral circulation in well-mixed and stratified estuarine flows with curvature. *J. Phys. Oceanogr.* **2009**, *39*, 831–851. [CrossRef]
19. Brocchini, M.; Calantoni, J.; Postacchini, M.; Sheremet, A.; Staples, T.; Smith, J.; Reed, A.H.; Braithwaite, E.F.; Lorenzoni, C.; Russo, A.; et al. Comparison between the wintertime and summertime dynamics of the Misa River estuary. *Mar. Geol.* **2017**, *385*, 27–40. [CrossRef]
20. Hunt, S.; Bryan, K.R.; Mullarney, J.C. The influence of wind and waves on the existence of stable intertidal morphology in meso-tidal estuaries. *Geomorphology* **2015**, *228*, 158–174. [CrossRef]
21. Van Maren, D.S.; Hoekstra, P. Seasonal variation of hydrodynamics and sediment dynamics in a shallow subtropical estuary: The Ba Lat River, Vietnam. *Estuar. Coast. Shelf Sci.* **2004**, *60*, 529–540. [CrossRef]
22. Li, C.; Swenson, E.; Weeks, E.; White, J.R. Asymmetric tidal straining across an inlet: Lateral inversion and variability over a tidal cycle. *Estuar. Coast. Shelf Sci.* **2009**, *85*, 651–660. [CrossRef]

23. Das, A.; Justic, D.; Inoue, M.; Hoda, A.; Huang, H.; Park, D. Impacts of mississippi river diversions on salinity gradients in a deltaic Louisiana estuary: Ecological and management implications. *Estuar. Coast. Shelf Sci.* **2012**, *111*, 17–26. [CrossRef]
24. Marmer, H.A. *The Currents in Barataria Bay*; The Texas A.&M. Research Foundation Project 9; Texas A.&M.: College Station, TX, USA, 1948; p. 30.
25. Snedden, G.A. River, Tidal, and Wind Interactions in a Deltaic Estuarine System. Ph.D. Thesis, Louisiana State University, Baton Rouge, LA, USA, 2006; p. 116.
26. Chen, C.; Beardsley, R.C.; Cowles, G.; Qi, J.; Lai, Z.; Gao, G.; Stuebe, D.; Xu, Q.; Xue, P.; Ge, J.; et al. *An Unstructured Grid, Finite-Volume Community Ocean Model FVCOM User Manual*, 3rd ed.; Rep. 06-0602; SMAST/UMASSD: New Bedford, MA, USA, 2011.
27. Chen, C.; Liu, H.; Beardsley, R.C. An unstructured grid, finite-volume, three-dimensional, primitive equations ocean model: Application to coastal ocean and estuaries. *J. Atmos. Ocean. Technol.* **2003**, *20*, 159. [CrossRef]
28. Mellor, G.L.; Yamada, T. Development of a turbulence closure model for geophysical fluid problems. *Rev. Geophys.* **1982**, *20*, 851–875. [CrossRef]
29. Galperin, B.; Kantha, L.H.; Hassid, S.; Rosati, A. A Quasi-equilibrium turbulent energy model for geophysical flows. *J. Atmos. Sci.* **1988**, *45*, 55–62. [CrossRef]
30. Smagorinsky, J. General circulation experiments with the primitive equations. *Mon. Weather Rev.* **1963**, *91*, 99–164. [CrossRef]
31. Li, C.; White, J.R.; Chen, C.; Lin, H.; Weeks, E.; Galvan, K.; Bargu, S. Summertime tidal flushing of Barataria Bay: Transports of water and suspended sediments. *J. Geophys. Res. Oceans* **2011**, *116*, C04009. [CrossRef]
32. Walker, N.D.; Wiseman, W.J.; Rouse, L.J.; Babin, A. Effects of River Discharge, Wind Stress, and Slope Eddies on Circulation and the Satellite-Observed Structure of the Mississippi River Plume. *J. Coast. Res.* **2005**, *21*, 1228–1244. [CrossRef]
33. Huang, H.; Justic, D.; Lane, R.R.; Day, J.W.; Cable, J.E. Hydrodynamic response of the Breton Sound estuary to pulsed Mississippi River inputs. *Estuar. Coast. Shelf Sci.* **2011**, *95*, 216–231. [CrossRef]
34. Willmott, C.J. On the validation of models. *Phys. Geogr.* **1981**, *2*, 184–194. [CrossRef]
35. Cheng, P.; Valle-Levinson, A. Influence of lateral advection on residual currents in microtidal estuaries. *J. Phys. Oceanogr.* **2009**, *39*, 3177–3190. [CrossRef]
36. Wong, K.-C. On the nature of transverse variability in a coastal plain estuary. *J. Geophys. Res. Oceans* **1994**, *99*, 14209–14222. [CrossRef]
37. Geyer, W.R.; Signell, R.P.; Kineke, G.C. Lateral trapping of sediment in partially mixed estuary. In *Physics of Estuaries and Coastal Seas*; AA Balkema: Brookfield, VT, USA, 1998; pp. 115–124.
38. Geyer, W.R.; Trowbridge, J.H.; Bowen, M.M. The dynamics of a partially mixed estuary. *J. Phys. Oceanogr.* **2000**, *30*, 2035–2048. [CrossRef]
39. Ralston, D.K.; Geyer, W.R.; Warner, J.C. Bathymetric controls on sediment transport in the Hudson River estuary: Lateral asymmetry and frontal trapping. *J. Geophys. Res.* **2012**, *117*, C10013. [CrossRef]

Journal of
Marine Science and Engineering

MDPI

Article

Storm Surge Propagation and Flooding in Small Tidal Rivers during Events of Mixed Coastal and Fluvial Influence

Liv Herdman *, Li Erikson and Patrick Barnard

Pacific Coastal and Marine Science Center, United States Geological Survey, Santa Cruz, CA 95060, USA; lerikson@usgs.gov (L.E.); pbarnard@usgs.gov (P.B.)
* Correspondence: lherdman@usgs.gov; Tel.: +1-831-460-7464

Received: 28 September 2018; Accepted: 12 November 2018; Published: 17 December 2018

Abstract: The highly urbanized estuary of San Francisco Bay is an excellent example of a location susceptible to flooding from both coastal and fluvial influences. As part of developing a forecast model that integrates fluvial and oceanic drivers, a case study of the Napa River and its interactions with the San Francisco Bay was performed. For this application we utilize Delft3D-FM, a hydrodynamic model that computes conservation of mass and momentum on a flexible mesh grid, to calculate water levels that account for tidal forcing, storm surge generated by wind and pressure fields, and river flows. We simulated storms with realistic atmospheric pressure, river discharge, and tidal forcing to represent a realistic joint fluvial and coastal storm event. Storm conditions were applied to both a realistic field-scale Napa river drainage as well as an idealized geometry. With these scenarios, we determine how the extent, level, and duration of flooding is dependent on these atmospheric and hydrologic parameters. Unsurprisingly, the model indicates that maximal water levels will occur in a tidal river when high tides, storm surge, and large fluvial discharge events are coincident. Model results also show that large tidal amplitudes diminish storm surge propagation upstream and that phasing between peak fluvial discharges and high tide is important for predicting when and where the highest water levels will occur. The interactions between tides, river discharge, and storm surge are not simple, indicating the need for more integrated flood forecasting models in the future.

Keywords: storm surge; coastal storm; flooding; compound events

1. Introduction

Coastal and inland flooding damage property and endanger lives, with the losses from inland flooding averaging $7.96 billion in damages and 82 fatalities per year over the 30 years prior to 2014, in the United States alone [1]. Inland and coastal flooding are expected to worsen in the future. Many locations (including the US) around the world are experiencing increases in heavy precipitation events, with this trend expected to accelerate with climate change [2]. Coastal flooding is becoming more frequent and expensive with sea level rise (SLR). Studies show that in the future there will be increases in the frequency of nuisance flooding [3], and that flooding frequencies will double in decades in some locations from both SLR and storm and wave frequency changes [4]. More frequent flooding will have significant socioeconomic impacts. In coastal regions near rivers, such as San Francisco Bay, both fluvial-driven flooding and oceanic flooding can cause significant damage. Events like the winter storms in February 1998 (part of an El Niño weather pattern) caused 9 m waves off the coast of California and large rainfall in coastal watersheds, both of which caused flooding [5]. This weather pattern is an example of one storm that can be the cause of both coastal and fluvial flooding, and there is evidence that this occurs for smaller storm systems as well. The changing nature of these events

with climate change makes it necessary to have both short-term and long-term predictive models for these floods.

The economic impacts of coincident flooding can be exacerbated by the fact that historical settlement patterns have favored settlement along rivers in locations where coastal/tidal dynamics still play a role. This zone of mixed fluvial and coastal influences was a good place to settle since it often represents a location with access to fresh water, rich estuarine food resources, and a navigable channel [6]. However, the benefits of being in a zone of mixed fluvial and coastal influence mean that it is susceptible to flooding from both coastal and fluvial causes. This paper focuses on the Napa River watershed which is emblematic of this development pattern as the downtown of the largest city in the region is located at the head of the tide in the river. Traditionally, there is not a significant amount of communication between the agencies responsible for flood prediction on the coast and those that predict flooding in rivers. Most forecast models that are currently in use do not incorporate the forcings necessary to represent these mixed events. Separation of these communities is evident in that, there are many papers on coastally driven flooding (e.g., [7,8]) and many papers on fluvial flooding (e.g., [9]) but relatively few that consider the compound impact of the two. Given the concentration of people residing in these regions, our aim is to better understand these compound flooding events and understand the utility of short-term predictive models for these types of events.

While storm events have not been specifically studied, the dynamics of rivers with coastal influence have been studied, especially, with regard to the interactions of tidal propagation in rivers. LeBlond [10] found that in the tidally influenced St Lawrence river, the main momentum balance was between friction and the free surface gradient except during the brief periods of slack tide when velocity and thus the friction term becomes zero leaving the unsteady inertia term to balance the free surface gradient. LeBlond [11] also reported that the subtidal wave (i.e., spring-neap variability) is amplified as it progresses upstream. Work in other large rivers like the Amazon ([12,13], Yangtze [14–16], and Columbia Rivers [17,18] has made similar findings, indicating that spring-neap variations penetrate farther upstream in a tidal river than the daily tidal oscillation. These rivers differ from the varied small tributaries in San Francisco Bay in that they are much larger in width and depth, have larger flow rates, and the region of tidal influence extends for hundreds of km upstream of the coast instead of tens of kilometers. In these larger rivers, understanding the physics of variable discharges has been pursued by frequency-based analysis because the large basins create discharge hydrographs that occupy distinct frequency space from that of the tidal motions. For example, Sassi and Hoitink [19] found that the tidal damping that occurs during the rising limb is different from the damping that occurs during the falling limb of a discharge curve. In smaller rivers with typical hydrograph durations near the dominant tidal frequency (12.42 h) it is not clear if the duration of the discharge relative to the tidal phase is long enough to produce similar interactions.

Storm surge has been widely studied but primarily with a focus on coastal areas, not extending farther up into rivers. A number of factors contribute to storm surge, including atmospheric pressure gradients, wind speed [20], and storm propagation speed [21]. The local bathymetry and land use also plays an important role in predicting local water levels. Sabatino et al. [22] found that funneling can create higher storm surges as one progresses up a narrowing estuary. Land use changes such as wetland restorations can also have an important impact on total water levels in storm surge propagation [23,24]. Condon and Sheng [25] found that coastal inundation predicted by sea level rise creates an overestimate in flooding relative to the same water level increase from storm surge because land dissipation is neglected. A similar result was found by Wang et al., [26] who showed that a storm surge of short enough duration can dissipate before reaching the maximum inland water levels. All of these studies find that once atmospheric forcing sets the storm surge coastal water levels, the propagation in inland bays and channels is primarily affected by interaction with local bathymetry and topography. Few studies extend the domain to include the propagation of storm surge up smaller river channels, likely because it requires a significant change in the model resolution.

The work that has been done considering the compound effects of tides, storm surge, and fluvial discharge has found that timing is a complicating factor in understanding the severity of coastal storms and rainfall-induced flooding. The timing of the arrival of the peak of the storm hydrograph to the coastal region is influenced by the spatial distribution of the rain in the watershed, and the shape, size, slope, soil type, and level of urbanization in the watershed [27]. The storm surge is linked via the fact that it is primarily driven by atmospheric forcing (wind and pressure) which is linked to the distribution of rainfall. Occurring separately from the storm are the astronomical tides that can also drive large variations in coastal water levels. Zheng et al. [27] found that the timing of river discharge phasing relative to tidal forcing is of great importance in predicting total water levels. Moreover, Zheng et al. [28] found that different locations have different probabilistic interdependences between rainfall intensity and storm surge. This interaction of storm surge with fluvial discharge is, of course, more likely to cause flooding in locations where atmospheric forcing and local watershed characteristics create a strong interdependence between coastal wind and pressure and overland rainfall.

In this work, we investigate the dynamics relevant for predicting water levels in smaller tidal rivers for relatively short time-scales and explicitly consider the effects of storm surge in addition to tides. Our primary interest is in how the storm surge changes the flows in the river and resultant flooding from the interaction of oceanic and fluvial drivers. Not only are we examining the impacts of storm surge, but additionally we focus on a smaller river size than has been examined in the past (e.g., Puget Sound WA, US; Chesapeake Bay, MD, US; Severn Estuary, UK; and Moreton Bay, AU). Our focus area is San Francisco Bay, into which numerous small rivers drain and extensive critical infrastructure (roads, airports, wastewater treatment systems) and large populations align the coast and are at risk of mixed oceanic and fluvial flooding. In this paper, we first provide background on the location and relevant physics, then describe our modeling set up and the scenarios. Lastly, we show the relative impacts of each of the forcings: fluvial, tidal, and storm surge, and how their interactions change flooding potentials.

1.1. Study Area: Hydrodynamic Characteristics

San Francisco Bay is an urbanized estuary which opens to the ocean at the narrow mouth of the Golden Gate (37.8° N, 122.5° W) and extends inland to connect to the Sacramento and San Joaquin Delta and rivers. The open coast at the mouth is subject to swell from the entire Pacific Ocean, thus it can be a fairly energetic environment with the mean annual significant wave height (H_s) of 2.5 m with the annual maximum H_s typically exceeding 8 m [29]. The water level at the Golden Gate can be raised significantly by the wave conditions as well as global-scale climate patterns like the El Niño Southern Oscillation and the Pacific Decadal Oscillation. The tides at the Golden Gate are mixed semi-diurnal with a diurnal tidal range of 1.78 m (mean lower low water to mean higher high water, MLLW-MHHW). The Bay is at a maximum depth near the opening of the Golden Gate (113 m) and shallows as the channel goes inland to San Pablo Bay (with channel depths of 11 to 24 m). The tidally driven currents range from just above 2 m/s in Central Bay to as high as 1 m/s in the shallower channel reaches [30] The Napa River drains into a narrow straight, between two sub embayments where currents regularly reach 1.5 m/s during peak flood and ebb.

1.2. Study Area: Hydrologic Characteristics

There are 483 watersheds draining into the San Francisco Bay landward of the Golden Gate bridge. Of these, 482 of them are relatively small. The Sacramento and San Joaquin Rivers account for 95% of the total watershed areas that drain into the Bay, with the remaining 482 watersheds accounting for only 5% of the total. Although a small percentage of the total watershed, the many small tributaries are located in the nine urbanized counties and are home to 7.151 million people [31]. The Napa River watershed is among the larger of the remaining 482 watersheds at 1100 km^2 and is a mix of urban (9%), agricultural (35%), grassland (15%), and forests (40%) with the area adjacent to the Bay being restored to a wetland habitat. It extends from the Mayacamas Mountains to the north and empties into the Bay

west of the Carquinez straight [6]. The watershed is bounded by relatively steep terrain surrounding the long narrow valley that is 43 km long and 8 km wide at its widest point. The city of Calistoga is in the northern end of the watershed and the city of Napa sits at the southern, tidally influenced end, with Vallejo, CA located on the eastern side of the river where it meets the Bay, as shown in Figure 1.

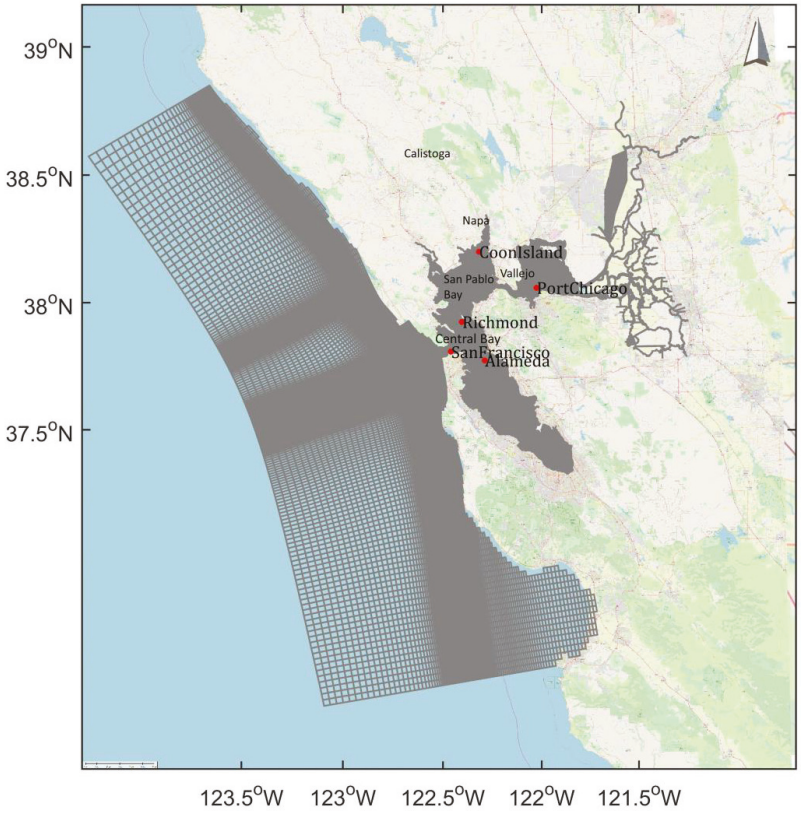

Figure 1. Map of San Francisco Bay, including the Napa River watershed and model grid. Gray mesh is grid. Red dots indicate locations with water level records. Map is from openstreetmap.org.

1.3. Study Area: Geology

The Central and San Pablo Bays have been filled since 5 ka with the fringing saltmarshes being developed ~4.7 ka. Over the last two centuries, human activity has significantly altered the sediment system. Gold mining activity led to a deposition of ~350 million m^3 of sediment between 1856 and 1887. In the 20th century, dams, reservoirs, flood control bypasses, and bank protection systems have reduced the delivery of sediment to the bay. In the current era, direct sediment removal occurs regularly via dredging, aggregate mining, and borrow pit mining [30].

Current bed conditions vary spatially throughout the bay. The Golden Gate inlet is comprised of bedrock. The strait that the Napa River drains just west of is 35 m deep and flanked by rock. San Pablo Bay has an 11–24 m-deep channel with a mostly sandy bed, whereas 80% of the San Pablo Bay consists of mud-dominated tidal flats [32]. The river channel itself is made up of coarse to fine sands on the bay side with gravel deposits and cobble in the most upstream reaches of the study area. Cohesive alluvial fan sediments, as well as tidally transported cohesive bay muds, flank the river banks. The marsh plains at the mouth of the river have been shown to accrete between 5 to 50 mm/year while the

river flood plains accrete 0 to 39 mm/year, with any accretion rates greater than 30 mm/year being extremely localized [33].

1.4. Study Area: Human and Natural Pressures

Historically, the Napa River and the adjacent bay region have been vulnerable to floods from both coastal and fluvial influences. Since 1862, there have been at least 27 flood events on the river with the most recorded damage occurring in February 1986 when 7000 residents were forced to evacuate, resulting in three deaths and $100 million dollars in damage [34]. The most recent flooding along the river occurred in 2017, although it was to a much lesser extent than it might have been without the completion of a major flood project along the river corridor in 2016 at the cost of $565 million dollars. Among other things, this project widened the floodplain and added a flood bypass channel to the oxbow portion of the river, significantly increasing the throughput of water in high-flow conditions and protecting downtown Napa. The flood bypass was designed to maintain the existing energy slope, thus maintaining the longitudinal sediment equilibrium. This project also increased the tidal prism downstream of downtown Napa, decreasing the amount of tidal flow penetration upstream [33].

There is significant infrastructure in these regional floodways, including Highway 37. This highway serves 38,000–40,000 drivers a day [35], crosses the Napa River mouth and follows along the bay shoreline to the north. The highway's proximity to bay wetlands makes it susceptible to nuisance flooding when there are high coastal water levels. The most recent closure due to flooding was in February 2017 for at least a week [36]. There are also records of at least four other road closures from flooding since 1999, with the longest duration of closure being for 21 days in January 2005 [37]. By the year 2060, there is a 40–65% likelihood that SLR will reach or exceed 30 cm in the bay [38] which would only exacerbate this problem. In some regions of the bay, the effective SLR will be higher due to subsidence and the consolidation of sediments, although this is less of an issue in the Napa River region.

2. Materials and Methods

We used the hydrodynamic modeling software DFlow FlexibleMesh from Deltares (version 1.4.6, Delft, The Netherlands) which implements a finite volume method of conservation of mass and conservation of momentum on a staggered unstructured grid. We ran both a realistic field simulation, that includes a true to life representation of the geometry of the bay system, and an idealized simulation that represents the river with simplified geometries. The realistic setup is to ground our modeled behavior in reality and give us the ability to compare to observations. The idealized setup runs more quickly and allows us to identify which physics might be more generalizable and not merely a function of the specific river geometry (e.g., a particular bend or sill).

2.1. Realistic Field-Scale Model

For the realistic field cases, the domain extends 90 km offshore of the Golden Gate and to Point Arena in the north and Monterey in the south (300 km). There are 202,842 grid cells in the domain with the size of the grid cells ranging from 4 km at the ocean side to as small as 5 m in the coastal region near the Napa watershed, see Figures 1 and 2. The bathymetry in the model is determined by averaging the depth points from a 2-m digital elevation model contained in each grid cell [39–42]. In the horizontal direction, the grid follows the river channel as closely as possible. The Napa River abruptly shifts from ~250 m wide to only ~100 m wide and stays less than 150 m wide as one progresses upstream with it, gradually narrowing to a shallow 50 m-wide stream. Along the lower portion of the Napa River, there are mudflats that are submerged by ~0.3 m of water at MLLW. The model grid captures these features, creating a very irregular channel both due to the variation in depth, see Figure 2, and the sinuousness of the natural channel. Fixed weirs are used to represent regional levees [43]. Fixed weirs are defined at the velocity points and block flow between the two adjacent computational cells when water levels are below the specified height of the fixed weir without reducing the total wet surface

and the volume of the model. This allows us to represent levees which have sub-grid dimensions but are large enough to change flow patterns and flood extents. Flooding extents and depths are determined by interpolating water levels from each model grid cell onto a 2-m resolution grid and differencing the Digital Elevation Model (DEM). This very high-resolution DEM does not cover the northernmost reaches of the channel, so the main channel slope is extrapolated with a constant slope for the last kilometer of river channel, while the side channels are flat. The bed friction in the model is based on roughness defined by manning's n. A background value of 0.023 is used with some locations having different values that were calibrated to best match the observed water levels. There is no special treatment for vegetated wetland areas. The water level at the ocean boundary is forced by astronomic tidal constituents (Topex/Poseidon 7.2 [44]). Major river discharges are, unless noted, set to typical winter (November through March) values, see Table 1. Water levels are initialized from a non-storm condition.

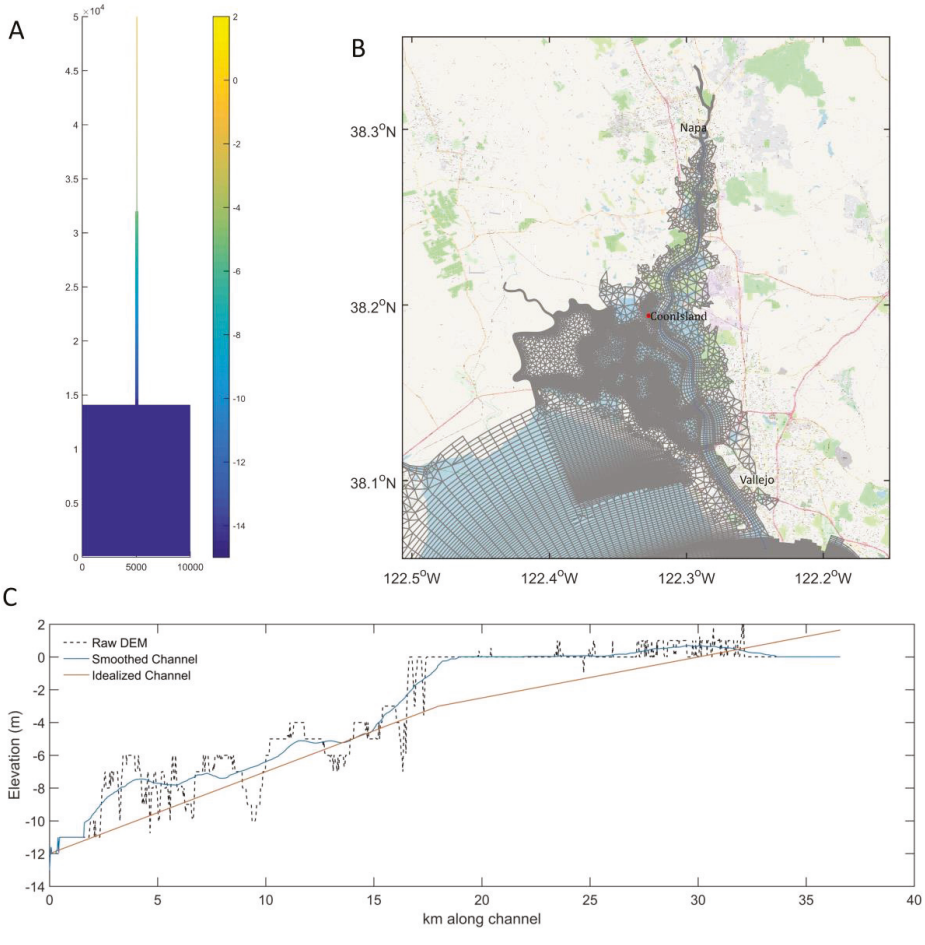

Figure 2. Comparison of the realistic field-scale and idealized models. (**A**) Birds-eye view of the idealized model grid colored by depth. (**B**) Realistic field-scale grid zoomed in on Napa, with the blue line showing the location of the river channel center. (**C**) Thalweg elevations of the Napa River channel (minimum elevations extracted from the digital elevation model and within 100 m of the channel center (dashed black line), smoothed elevations (blue solid line), and the idealized model grid (red dots)).

Table 1. Typical winter river discharges applied to river inlets.

Freshwater Source	Non-Storm Discharges (m^3 s^{-1})
Sacramento River	500
American River	45
Arcade Creek	0.02
Napa River	5
Petaluma River	5
Corte Madera Creek	2
San Joaquin River	60
San Francisquito Creek	0.5
Matadero Creek	0.05
Coyote Creek	3
Guadalupe River	2

2.2. Idealized Model

The idealized model consists of fewer grid cells (14,718 compared to >200,000 of the more geometrically accurate field model) and idealized forcing. The idealized model consists of a 10 km × 14 km bay, similar to the size of San Pablo Bay, with a channel extending northward from the center. The idealized rectangular channel is 300 m wide with a slope of 0.0005 for the first 18 km and is 100 m wide and twice as steep for the final 18 km, resulting in a total length of 36 km for the river channel. This set up roughly mimics the Napa River which gets narrower and steeper approximately 16 km upstream of the mouth (at Edgerly Island). The idealized rectangular channel more closely resembles the upper reaches of the river which have much steeper sides, often levees or other structures to protect the infrastructure adjacent to the river.

2.3. Scenarios

In order to investigate the effect of different drivers on the coastal flooding of the region, we devised a number of scenarios with a range of oceanic and discharge conditions, see Table 2. For each scenario, we ran the simulation for at least 6 days, 2 days of spin-up time and 4 days of the varying storm conditions. Both spring and neap tides were simulated, as were scenarios for which tides were not included. Napa River discharge conditions were set to equal either a background flow with a discharge of 5 m^3/s or a storm discharge represented with a December 2012 hydrograph, equivalent to a 5-year return period discharge event, with a peak discharge of 294 m^3/s. For this set of simulations, the peak discharge was translated on the time axis to occur on the 50th hour of the simulation and be coincident with high tide at the Golden Gate (for scenarios when tides were simulated). Ocean storm conditions are represented by applying spatially varying barometric pressure and wind fields from a 7-year return period storm (based on storm surge water levels at the Golden Gate) that occurred. These smaller magnitude storms were selected to represent events that were more likely to occur simultaneously and to assess how incorporating the interaction of relatively common coastal and fluvial events changes the nature of the event. The wind and pressure field time-series were translated so that the minimum barometric pressure occurred on the third day of the storm simulation. This means that the peak discharge occurs ~20 h before the peak storm surge at the Golden Gate. The pressure reaches a minimum on day 3, but the pressure contributes at least 12 cm of storm surge for the duration of the event and there are some local minima at 15 and 41 h (0.6 and 1.7 days). Although the winds and pressure are from a real storm event and thus create coherent atmospheric forcing, they are implemented separately in some scenarios in order to assess the individual impacts of pressure and winds. Since the addition/removal of wind forcing had little to no impact on the following results, the winds are neglected for most of the following discussion. The conditions used to generate these different flooding scenarios are shown in Figure 3. The complex nature of the forcing from real storms and the relative phasing of various components are part of what led us to create

an idealized scenario which allowed us to better characterize and investigate individual components and their phasing.

Table 2. Realistic model scenario titles and forcing included.

Scenario Name	Water Level	Pressure	Discharge
R1 (MSL-Q)	MSL (Mean Sea Level) Flat	Constant	Storm
R2 (MSL-P)	MSL Flat	Storm	Low Normal
R3 (MSL-W)	MSL Flat	Constant	Low Normal
R4 (MSL-P/W/Q)	MSL Flat	Storm	Storm
R5 (ST-Q)	Spring Tide	Constant	Storm
R6 (ST-P)	Spring Tide	Storm	Low Normal
R7 (ST-W)	Spring Tide	Constant	Low Normal
R8 (ST-P//W/Q)	Spring Tide	Storm	Storm
R9 (NT-Q)	Neap Tide	Constant	Storm
R10 (NT-P)	Neap Tide	Storm	Low Normal
R11 (NT, W)	Neap Tide	Constant	Low Normal
R12 (NT-P/W/Q)	Neap Tide	Storm	Storm

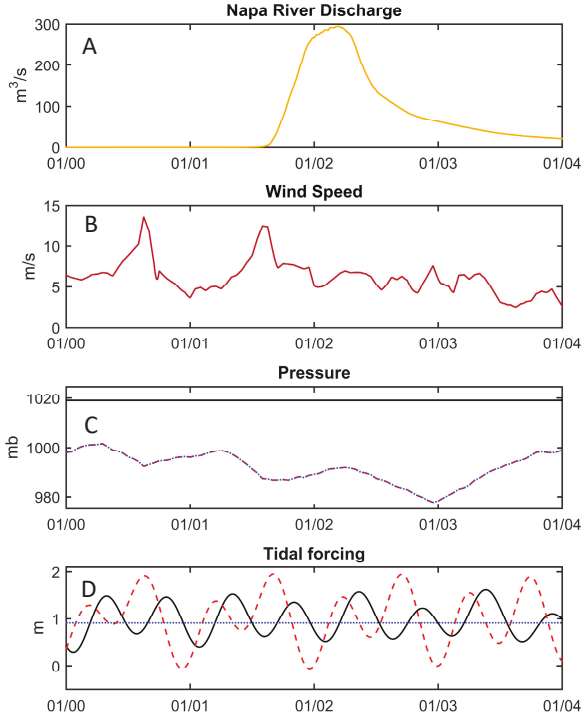

Figure 3. Realistic storm forcings. (**A**) Discharge at the head of Napa River (see Figure 1 for location). (**B**) Wind speed, (**C**) atmospheric pressure at sea level, for the storm (dashed red) and not storm case (solid black), and (**D**) water level variations due to astronomic tides at San Francisco (red dash is spring, solid black is neap, and small blue dash is water held at Mean Sea Level), see Figure 1 for location.

The forcings utilized for the idealized scenarios, as shown in Table 3, were simplified versions of the real cases, see Figure 4. The atmospheric conditions were idealized with a low pressure that lasted for 2 days starting with 1 day of background pressure levels and negligible (less than 20 cm/s) winds for a smooth transition. Spring and neap tides were simplified to tides with an M2 period of

2 m and 1 m amplitudes. The discharge curve remained the same for the idealized scenarios as in the real scenario. We tested the phasing of discharge relative to the tide in different cases [I22–I35]. The different parameters used for the large set of idealized scenarios are listed in Table 3.

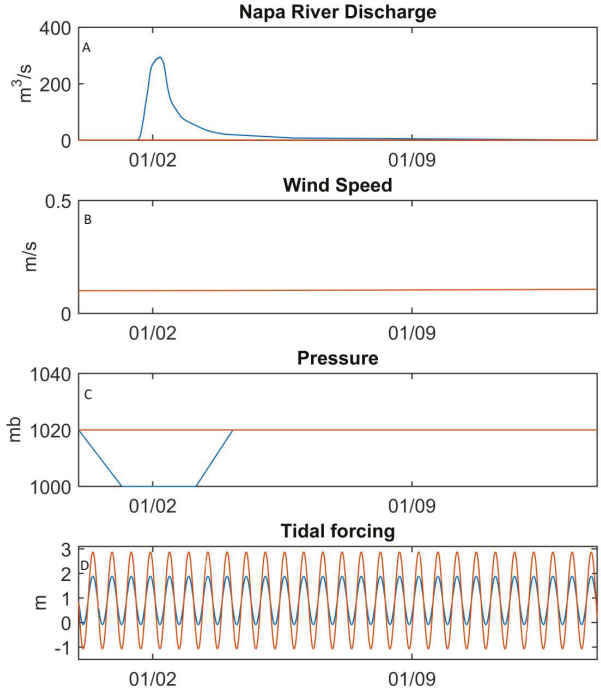

Figure 4. Idealized storm forcings (**A**) Discharge at head of Napa River. (**B**) Wind speed (spatially uniform over entire domain). (**C**) Atmospheric pressure (red is non-storm and blue is storm condition). (**D**) Tidal water level forced at southern bay boundary (red is 2-m M_2 tide and blue is 1-m M_2 tide).

Table 3. Idealized model runs and their forcings.

Scenario Name	Water Level	Pressure	Discharge
I1 (MSL-Q + 0)	MSL Flat	Constant	Storm
I2 (MSL-P0.2)	MSL Flat	0.2 m Storm	Low Normal
I3 (MSL)	MSL Flat	Constant	Low Normal
I4 (MSL-P0.2/Q + 0)	MSL Flat	0.2 m Storm	Storm
I5 (T2-Q + 0)	2 m M2	Constant	Storm
I6 (T2-P0.2)	2 m M2	0.2 m Storm	Low Normal
I7 (T2)	2 m M2	Constant	Low Normal
I8 (T2-P0.2/Q + 0)	2 m M2	0.2 m Storm	Storm
I9 (T1-Q + 0)	1 m M2	Constant	Storm
I10 (T1-P0.2)	1 m M2	0.2 m Storm	Low Normal
I11 (T1)	1 m M2	Constant	Low Normal
I12 (T1-P0.2/Q + 0)	1 m M2	0.2 m Storm	Storm
I13 (T2-P2)	2 m M2	2 m Storm	Low Normal
I14 (T2-P1)	2 m M2	1 m Storm	Low Normal
I15 (T2-P0.5)	2 m M2	0.5 m Storm	Low Normal
I16 (T2-P0.1)	2 m M2	0.1 m Storm	Low Normal
I17 (T0.2-P0.2)	0.2 m M2	0.2 m Storm	Low Normal
I18 (T1-P0.5)	1 m M2	0.5 m Storm	Low Normal

Table 3. *Cont.*

Scenario Name	Water Level	Pressure	Discharge
I19 (T0.5-P0.5)	0.5 m M2	0.5 m Storm	Low Normal
I20 (T0.2-P0.5)	0.2 m M2	0.5 m Storm	Low Normal
I21 (T0.1-P0.5)	0.1 m M2	0.5 m Storm	Low Normal
I22 (T2-Q − 7)	2 m M2	Constant	Storm − 7 h
I23 (T2-Q − 6)	2 m M2	Constant	Storm − 6 h
I24 (T2-Q − 5)	2 m M2	Constant	Storm − 5 h
I25 (T2-Q − 4)	2 m M2	Constant	Storm − 4 h
I26 (T2-Q − 3)	2 m M2	Constant	Storm − 3 h
I27 (T2-Q − 2)	2 m M2	Constant	Storm – 2 h
I28 (T2-Q − 1)	2 m M2	Constant	Storm − 1 h
I29 (T2-Q + 1)	2 m M2	Constant	Storm + 1 h
I30 (T2-Q + 2)	2 m M2	Constant	Storm + 2 h
I31 (T2-Q + 3)	2 m M2	Constant	Storm + 3 h
I32 (T2-Q + 4)	2 m M2	Constant	Storm + 4 h
I33 (T2-Q + 5)	2 m M2	Constant	Storm + 5 h
I34 (T2-Q + 6)	2 m M2	Constant	Storm + 6 h
I35 (T2-Q + 7)	2 m M2	Constant	Storm + 7 h

3. Results

3.1. Model Validation

The skill of the field-scale model was quantified by comparing predicted water levels at 3 NOAA tide stations, one at the mouth of the San Francisco Bay (NOAA/CO-OPS station 9414290), one just offshore of the city of Richmond (NOAA/CO-OPS station 9414863) and one east of the Carquinez straight near port Chicago (NOAA/CO-OPS station 9415144) [45]. The predicted water levels are compared to the observed water levels during two coastal storm events, one in January 2010 with a maximum surge of 65 cm, and one in March 2011 with a maximum surge of 45 cm, see Table 4. The wind and pressure fields are provided by an analysis of the 13-km resolution Rapid Update Cycle weather model from the National Center of Environmental Prediction. During the March 2011 event, ref. [46] had instrumentation measuring the water level at Coon Island in a marsh adjacent to the Napa River, see Figure 1. For each of these locations, model skill is assessed by the mean error, the Wilmott Skill Score [47], and where tidal predictions are available, a coefficient of efficiency [48] relative to tidal predictions.

The mean error is:

$$\frac{1}{N}\sum_{i=1}^{N}(M_i - O_i) \tag{1}$$

The Wilmott Skill Score is defined as:

$$D = 1.0 - \frac{\sum_{i=1}^{N}(O_i - M_i)^2}{\sum_{i=1}^{N}\left(|M_i - \overline{O}| + |O_i - \overline{O}|\right)^2} \tag{2}$$

where O_i and M_i refer to the ith of N total observed and modeled values, respectively, and the overbar indicates an average. This is a standardized measure of the degree of model prediction error. The values range from zero to 1, with zero meaning complete disagreement and a value of 1 indicating covariability of O and M about the true mean.

The coefficient of efficiency is defined as:

$$E = 1.0 - \frac{\sum_{i=1}^{N}(O_i - M_i)^2}{\sum_{i=1}^{N}(O_i - T_i)^2} \tag{3}$$

where T is the water level predicted by NOAA using the known harmonic tidal constituents for that location, and the other variables are as defined above. In other locations, this metric compares the difference between observations and modeled values (numerator) to the difference between observations and an average observation (denominator) as a way of indicating how much more information the model is able to provide relative to just predicting the mean value. The metric we use here is a modified efficiency where instead of using the mean as the comparison we use the known tidal water level as the baseline for comparison. This is a slightly more rigorous metric where our model must be more accurate than the known tidal values, i.e., running the model must be more efficient than simply using the tidal predictions. The values of the coefficient of efficiency can range from minus infinity to 1. A value of 0.0 indicates that the model performance is the same as the tidal prediction, $E < 0$ indicates that the model performs worse than the tidal predictions alone, and $E \approx 1$ indicates excellent predictions compared to measurements relative to using tidal predictions alone.

Table 4. Skill statistics comparing modeled and observed water levels.

Station	Observed Diurnal Range (m)	Mean Error (m)		Wilmott Skill Score (*D*)		Coeff. of Efficiency (*E*)	
		January 2010	March 2011	January 2010	March 2011	January 2010	March 2011
San Francisco	1.78	−0.04	−0.01	0.99	0.99	0.74	0.44
Richmond	1.85	−0.01	−0.05	0.99	0.98	0.73	0.43
Port Chicago	1.50	−0.05	−0.11	0.97	0.96	0.51	0.38
Coon Island	NA	NA	−0.15	NA	0.87	NA	0.72

Performance statistics, shown in Table 4, demonstrate good performance within the larger open regions and decreasing, but still acceptable, behaviors along the upper reaches of San Francisco Bay. Our model consistently performs better than merely utilizing tidal predictions for a location. The model performs a little less well after passing through the constriction at Carquinez straight, as indicated by the inferior skill indices at the Port Chicago station. However, the region of primary interest in this study is on the west side and should not be significantly affected by the errors east of the strait. The model assessment is relatively similar between the San Francisco and Richmond stations. At all the stations, the water level is lower than observed on average (as noted with the mean error); this is particularly noticeable during periods of low water. However, during the period of elevated water levels associated with storm surge, we observe that the model does much better than the tidal predictions.

3.2. Maximum Water Levels

Results indicate that the maximum water level (MXWL) is set by different forcings at different points along the channel. In Figure 5A, we show the MXWL along the river channel for all of the realistic scenarios that occur during the simulated 4-day storm. The highest water level occurs when there is a large discharge, a low atmospheric pressure generating a storm surge, as well as a spring tide (scenario R8(ST-P/W/Q)). The MXWL on the ocean side of the river (at 0 km in Figure 2C) is set by the maximum tidal water level plus any impacts from storm surge. The lowest water level on the ocean side is from scenario R1 (MSL-Q) where the ocean water level is held constant at ~1.0 m (local MSL referenced to NAVD88) and without atmospheric storm forcing. On the upstream side, MXWLs are strongly influenced by fluvial discharges. In the runs with a normal discharge, the MXWL is very closely related to the water level set by the ocean conditions. All runs with the fluvial storm discharge experienced higher water levels upstream and are nearly identical with the largest upstream value ranging from 3.70 m to 3.76 m, compared to 1.35–2.12 m for the low discharge scenarios. The upstream MXWL values from the scenarios with a fluvial storm discharge closely track each other from 36 km to

30 km upstream where the values then transition to the downstream value set by ocean conditions. The slope of this transition zone depends upon how different the upstream discharge-dominated water level is from the water level in the ocean. For most scenarios, this middle area where the fluvial discharge and coastal conditions meet is the area with the largest changes in MXWL (15–30 km).

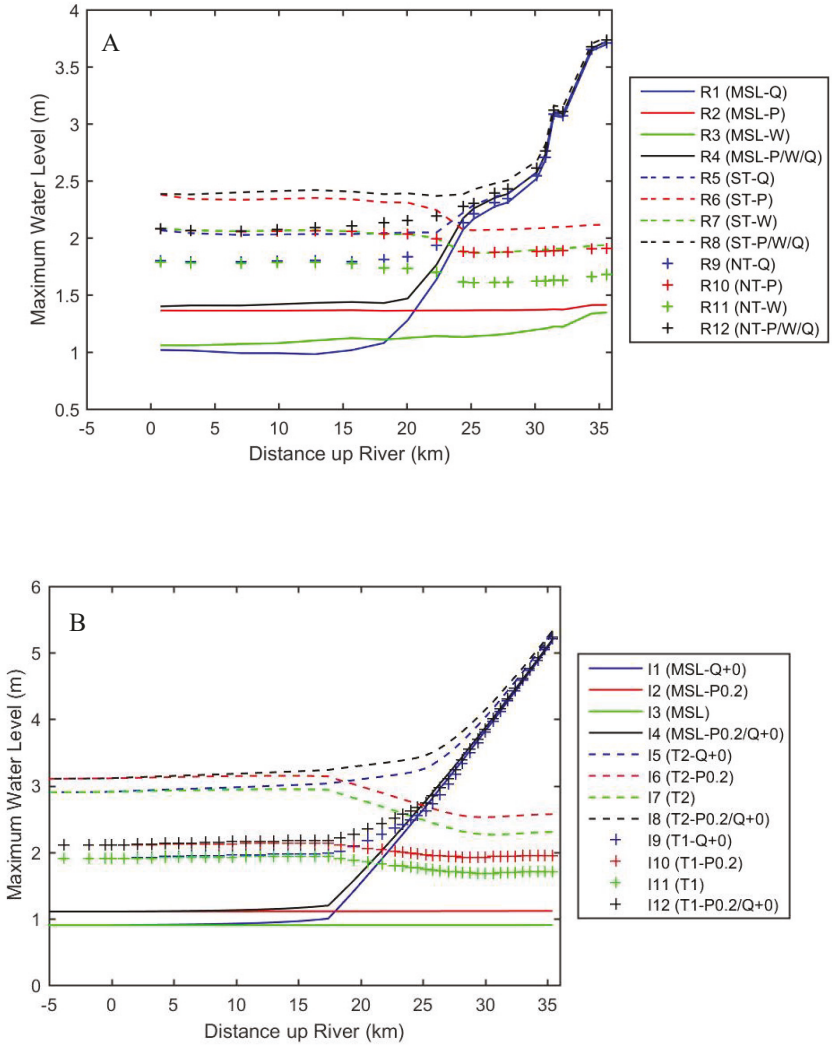

Figure 5. Maximum water level along river during a storm for (**A**) realistic and (**B**) idealized storms.

There are very similar MXWL patterns in the idealized scenarios, see Figure 5B. Again, we observe a discharge-dominated upstream region that relaxes to the MXWL set by the ocean as it approaches the river mouth. The slopes of the lines are more slowly varying and regular because of the reduced bathymetric complexity. Most of the differences between the idealized and real model occur because of the straight rectangular cross-section of the idealized model. This unwavering straight channel requires an unrealistically high friction coefficient (Manning's n = 0.1) compared to the field-scale model (n = 0.023) in order to achieve a similar amount of tidal damping. In the field-scale model,

the sinuosity of the channel causes significant damping of the tidal signal. In the idealized cases, the channel geometry is not only straight but also different because the width does not vary with depth (i.e., there are no flood plains). This means that the water level increases more in the idealized case because in the realistic scenario a higher discharge can create overbank flow. The combination of the greater coefficient and the unvarying channel cross-section with height creates a higher free surface height. For the same discharges, we observed the most-upstream water levels to range from 5.18 to 5.33 m, compared with 3.70–3.76 for the realistic field-scale case. We also see a small shift in the location where the MXWL is tidally dominated versus discharge dominated. The tidally dominant section extends farther inland in the field model compared to the idealized scenarios. However, the patterns seen in the MXWLs are very similar, showing similar transitions between the dominance of tides, river outflows, and pressure. Therefore, the idealized scenario, given its uncomplicated set up and quick runtime, created a good way to conduct numerous runs that allow us to more fully explore the parameter space. The simplified nature of the forcings also makes the interactions between the forcings simpler to analyze, thus in most of the following analyses, we focus on the results from the idealized simulations. Although the behavior is similar in the idealized and full field-scale simulations, the water levels cannot be directly compared to deduce flood- or other hazards.

3.3. Storm Surge Only

Under conditions of no tides and a normal fluvial discharge, as in runs R2 and I2, Figure 5A,B, the MXWL increases in amplitude as it propagates up the channel, indicating a small funneling effect. Fitting a piecewise line to the MXWL, we can estimate the rate of funneling or dissipation. This method indicates that the funneling of the storm surge creates an almost negligible increase in MXWL with upstream distance, at the rate of 0.018 cm/km in the wide channel and at 0.03 cm/km in the narrow channel. The tides alone (I7) have a net amplification in the wider portion of the channel of 0.18 cm/km, but the narrower channel is more frictional and has a net MXWL decay of −3.6 cm/km. When storm surge is added to these 2-m tidal scenarios, the decay rate in the narrow channel decreases to −3.3 cm/km. Having a larger tidal amplitude creates more dissipation of the storm surge amplitude since the rate of decay for the 1-m tide with (I10) and without storm surge (I11) was −1.2 cm/km and −1.0 cm/km, respectively.

Looking at the water levels in frequency space, see Figure 6, we can see that the largest changes in the water levels from the interaction of storm surge with tides occur in the very long period part of the spectra that is associated with the storm surge. In Figure 6A, with only tidal forcing, the largest peak in the spectra is at the M_2 tidal frequency and there are some smaller higher frequency peaks associated with tidal propagation in shallow waters, often called overtides. The spectra of water levels that are only forced with storm surge, shown in Figure 6B, have no peaks in these higher frequency (shorter period) regions and there is a broadly distributed energy over the long periods with little variability along the channel. In the idealized run where these two forcings interact (I6), there is a less than 1% change in the tidal frequencies for most of the channel, see Figure 6C. Near the river end of the channel, there are changes in the tidal spectral energy of nearly 5%, but this may be due to a boundary effect. However, the longer period energy (periods of 48 to 200 h) is reduced from 99% to 33% of the purely storm-surge case at all locations along the channel, with locations further upstream in the channel having larger reductions. The biggest reduction occurs farthest upstream from the ocean, indicating that the interaction between the storm surge and tidal wave progressively removes energy from the long period portion of the spectra as the storm surge propagates upstream.

It becomes clear upon examination of runs I8, I12, and I13–I21 that one of the relevant physical parameters is the relative amplitude of the storm surge to the tidal amplitude, as shown in Figure 7. The highest water levels on the offshore side occur when the sum of the storm surge and tidal amplitude are highest; it becomes more complicated on the upstream side because of the varying rates of dissipation, see Figure 7A. When the storm surge is five times bigger (I21) than the tidal amplitude, the small amplification of the storm surge (funneling) occurs in the wide channel, as in the case with no

tidal activity. The storm surge very slightly decreases in the narrower channel. The impact of the tide on such a large storm surge is fairly minimal, allowing the full storm surge to propagate all the way up the channel. The largest decrease in water level occurs in the case with the largest tidal amplitude relative to storm surge (I16). In this case, with a tidal amplitude 20 times the storm surge, the total water level is only 80% of the ocean water level upstream. However, the net decrease in water level does not only depend on the ratio of storm surge to tidal amplitude and there is a big range in the rate of decrease for a given ratio. For example, when there is an equal ratio of storm surge to tidal amplitude (I13, I17, I19) we observe a change in water level that corresponds to upstream levels of 98% to 103% of the ocean water level. Larger tidal amplitudes cause a larger decrease in MXWL for a given ratio.

The tides also slow down the propagation of the storm surge wave, leading to peak water levels occurring later during the storm than they would if no tides were present. The interactions between tides and storm surge result in an MXWL in the channel that is different to the sum of the two individual high water levels. It is also clear that the strength of the dissipation depends on the width of the channel, with the narrow channel lowering the water level more per unit length than the wide channel. For the higher values of storm surge, the amplification continues until the narrowest channel upstream is reached. The abruptness and magnitude of the transition from a wide to narrow channel do not directly correspond to the real scenarios but it highlights the importance of accurately knowing the channel geometry for representing the interaction between storm surge and tides.

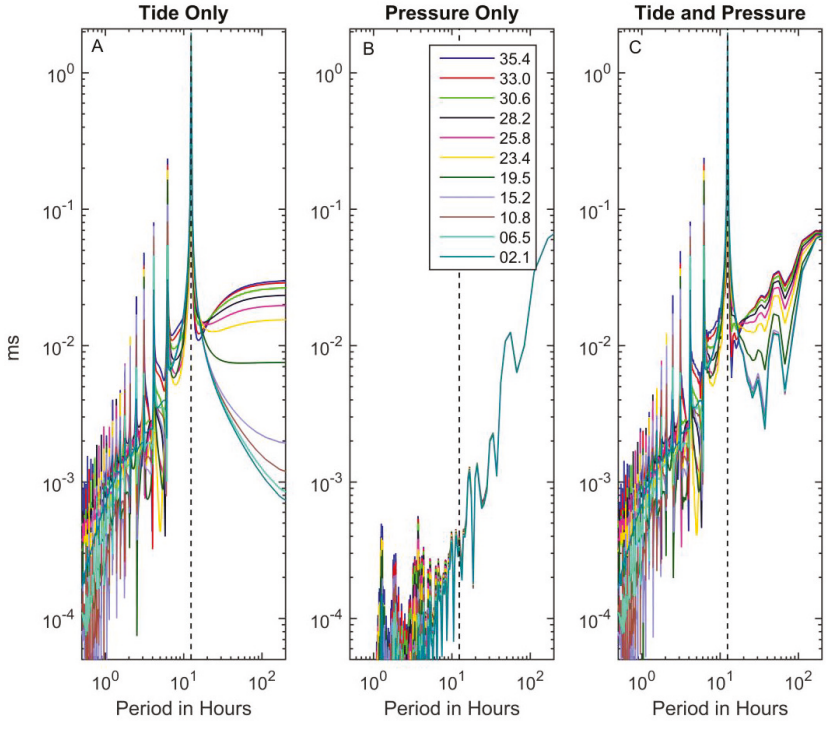

Figure 6. Spectra from Fourier transforms of selected idealized runs. (**A**) Spectra from I7 with different color lines for different locations along the channel. Legend indicates km upstream of river mouth. (**B**) Same as A but from I2. (**C**) Same as in A but for run I6. The black dashed line indicates M_2 tidal frequency.

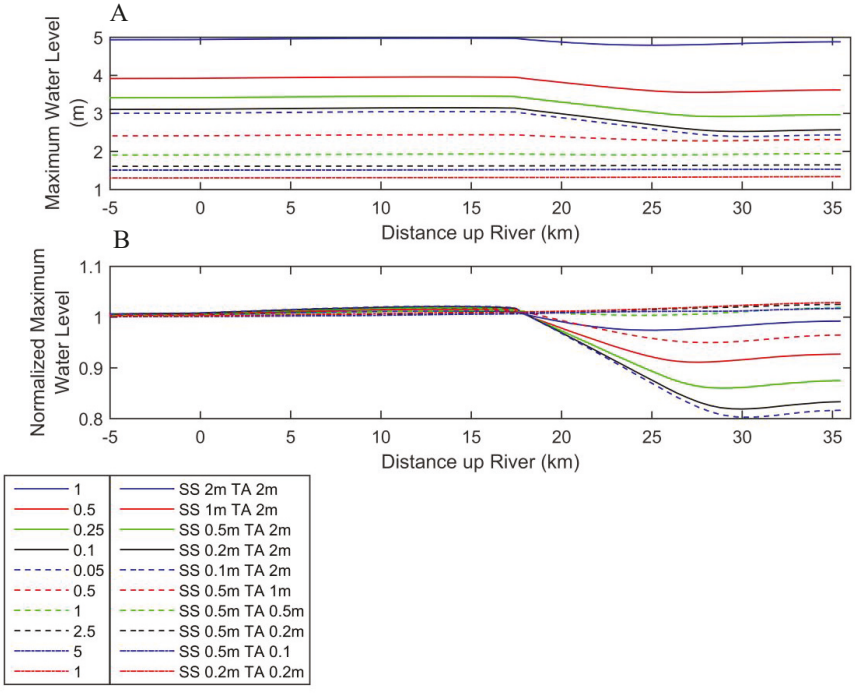

Figure 7. (**A**) Maximum water levels along the idealized river with varying storm surge (SS) and tidal amplitude (TA). The value for each simulation is shown in the legend. (**B**) The water level normalized by the maximum experienced at the open water boundary condition. The lines are the same as in the first figure; however, the legend indicates the ratio of SS to TA.

3.4. Discharge Only

In the idealized runs, that include fluvial storm discharge (Figure 5B, I1, I4, I5, I8, I9, and I12), we observe the discharge wave rapidly attenuating as it travels down the channel. The decrease in MXWL is at a fairly steady rate, regardless of downstream conditions, (20 to 25 cm/km) until reaching about 25 km. From 25 km to 16 km the rate of change of the MXWL depends largely on the tidal conditions. Once the channel widens, starting near 16 km, the attenuation of the peak water level occurs at a much slower rate of 0.5 to 1 cm/km. In both regions, the slower rates of attenuation occur in the runs with higher peak water levels and stronger tidal activity.

At the upstream end of the river, the bottom stress and velocity are lower with tides (runs I5 and I9) as compared to without (I1). This is because the water depth is higher with tidal activity, allowing the same total discharge with a lower depth-averaged velocity. In these first idealized cases (I1, I5, I9), the rising limb of the discharge is coincident in time with an ebb tidal current in the channel. This phasing means that the velocity is higher during the rising limb, allowing the discharge to continue downstream immediately. However, the main difference between with and without tide, is not due to the phasing of the discharge with the tide but is because the water depth is higher. The greater water depth allows for the same discharge with a lower velocity, and because the velocity is lower there is also less bottom stress to resist motion, further reducing the need to have a strong free-surface gradient.

The interaction between tides and discharge can be explored by looking at the same runs in frequency space, see Figure 8. We observe that there is a rapid attenuation in energy with progression downstream for the part of the spectrum associated with the discharge. Similar to the storm surge wave, the discharge wave has more energy at the longer periods than the tides only case. The energy

of the discharge wave is also evenly distributed, with no peaks, over the longer period region (greater than 15 h). However, unlike the storm surge case, there is a significant peak near the tidal period and there is more interaction between tides and discharge in frequency space. In the run with both discharge and tides, two new peaks occur in the channel at 17.7 and 28 h that did not exist in either the tide or discharge alone scenarios. Also, in the combined case there is a reduction from the tides-only case (near 10% for most channel locations) in the peaks at the overtide frequencies (8 h and below). There is a significant increase in the amount of energy found in the longer periods for the combined case relative to both the tide and discharge only cases.

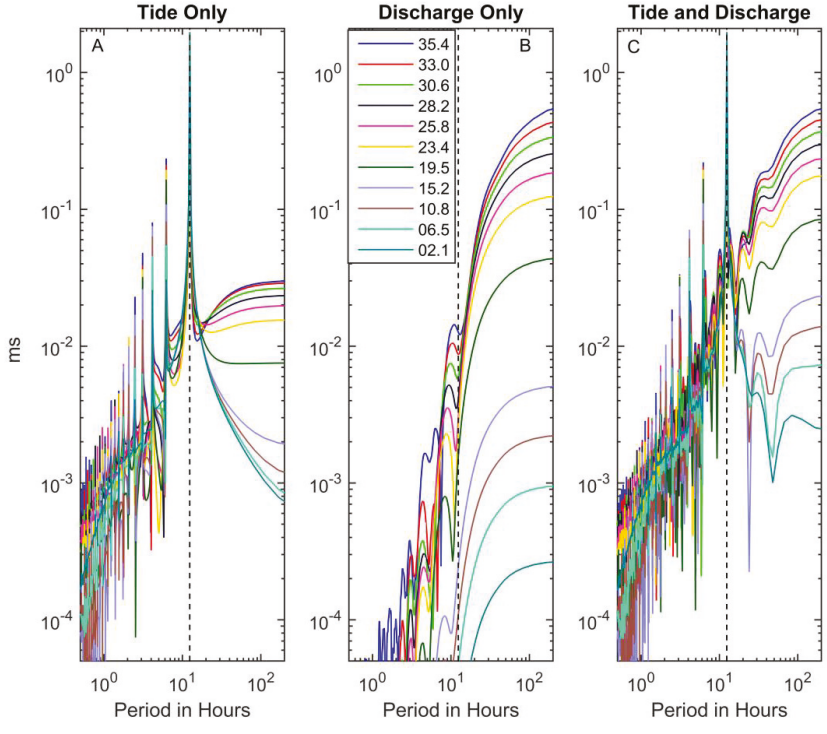

Figure 8. Spectra from Fourier transform of runs (**A**) I7, (**B**) I1, and (**C**) I5. Black dashed line indicates M_2 tidal frequency.

We also found that the phasing of the discharge with the tide is important in predicting the magnitude and location of the MXWL along the channel. Figure 9a shows the maximum water levels achieved over the course of the storm for the idealized scenario with discharge and a 2-m M2 tide, but with the discharge timing shifted by up to 7 h forward or back from the original release time (I22–I35). The water levels converge to the same value in the bay. The values at the head of the river range by nearly 30 cm (5.16 to 5.44 m). The variability in MXWL of ~0.5 m with different discharge timing persists through the narrow portion of the channel.

The timing of the MXWL is also most variable in the upstream portion of the channel. MXWL occurs at the discharge peak on the upstream side. Figure 9B shows that the peak water level occurs coincident with the peak discharge at the most upstream point, which is why the timing of each peak is lagged by about an hour. Upstream of 34 km, the peak water level is clearly set by the timing of the discharge peak. With progression downstream, the timing of the maximum water level begins to be influenced by the tide and the peak water level travels slower or faster depending on what phase of

the tide (and depth of water) it encounters. For the early release cases where the peak discharge water level encounters a flood tide, the peak water level further downstream is associated with the high tide that occurs before the peak discharge. When the discharge wave encounters an ebb tide and speeds up the propagation of the discharge wave, the peak water level is then associated with the high tide that follows the peak discharge. Where the interaction between the discharge wave and the tide has the most influence on MXWL timing and magnitude, is in the most downstream reach of the narrow channel ~30 km. The MXWL for a given location can vary by up to a half meter depending on the phasing of the discharge release. The interaction of the discharge wave with tides also impacts the net flow rate in the channel. If a flood tide occurs on the rising limb of the discharge wave, this lowers the discharge rate on the rising limb and compresses more flow into the peak discharge when tides are included. The peak discharge is then higher at every location in the domain a few cells downstream of the original downstream boundary condition. The phasing of the discharge release relative to the tide has a larger impact on the upstream water level than the amplitude of the tide, i.e., the variability in runs I22 to 135 is larger on the upstream side than between runs I1, I5, and I9.

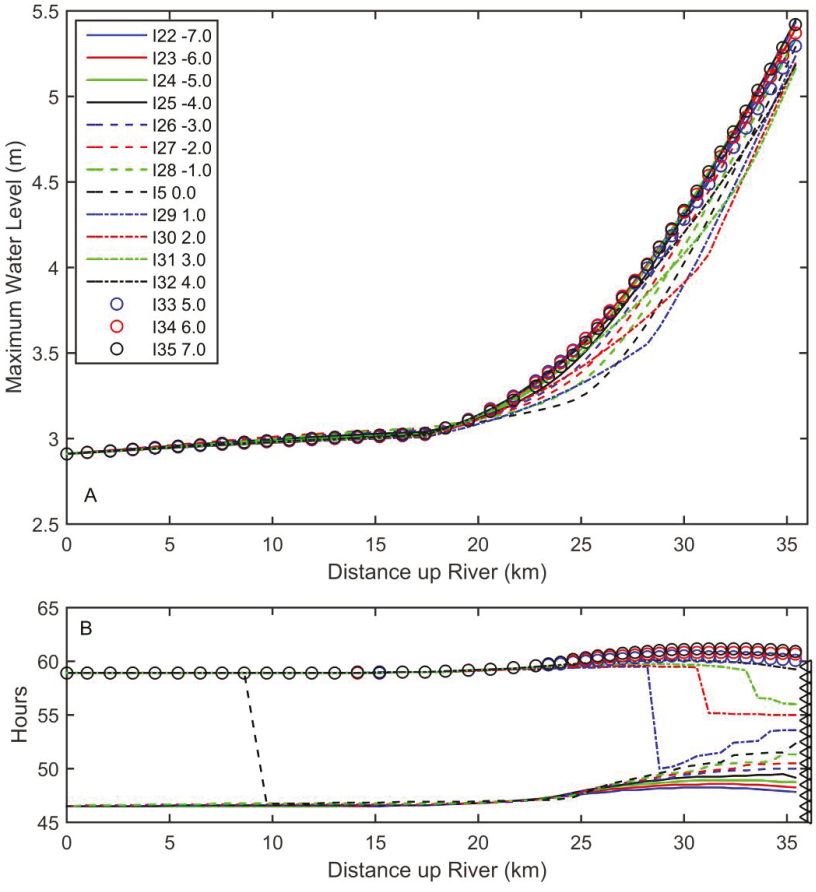

Figure 9. (**A**) Maximum water level along the river in cases with a 2-m M_2 tide and shifted discharge peaks. The legend indicates the hours of shift from the original discharge curve. (**B**) The time that the maximum water level occurs along the idealized river channel with triangles indicating the time of release at the head of the channel.

3.5. A Complete Storm

When both storm surge and discharge occur at once, the largest MXWL's occur; however, it is not as high as one would find from summing together the water level increases associated with each storm component. In Figure 10A, we can see the water level variation in time and space for the complete storm. The tidal lows and highs are clearly damped as they progress upstream and there is a slight arc to their progression as the wave speed decreases upon entering shallower water. The discharge peak interacts with multiple high tides elevating the tidal water levels in the upper reaches of the stream for the duration of the discharge and as the falling limb of the discharge occurs.

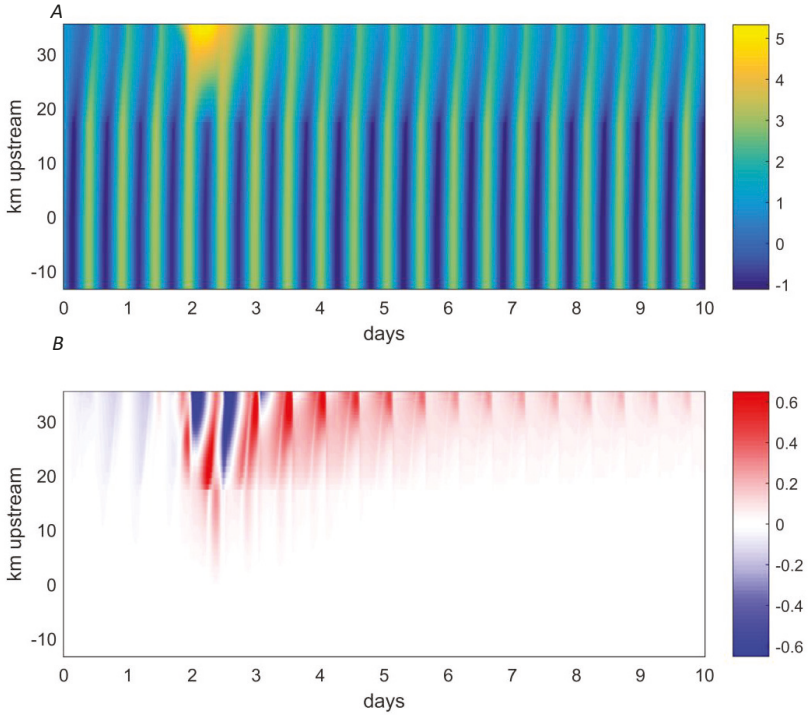

Figure 10. The sum of the parts is greater than the parts combined. (**A**) Water level in time (x-axis) and space (y-axis) with color indicating value in meters for model run I8, which has the highest water level of all the idealized scenarios. (**B**) The same x and y axes as in A. Color indicates the difference between I8 (the full storm) and the "simple prediction" referenced in the text.

If we estimate the water level in this storm event by adding up the relative water level increase associated with storm surge (from I2), discharge (from I1), and tides (from I7) we would overestimate the peak values by about 0.5 m and underestimate water levels downstream of the peak and in the tail of the discharge by a similar amount, see Figure 10b. This estimate of each component's contribution to the water level is found by subtracting the baseline situation (I3) from each of the identified scenarios that are storm surge only (I2), discharge only (I1) and tides only (I7). In the following discussion, we will call this sum of the components $((I2 - I3) + (I1 - I3) + (I7 - I3) + I3)$ the "simple prediction". At the beginning of this storm, we observe that the modeled water levels are lower than the simple prediction in the upstream reaches due to tidal damping of the storm surge. As the discharge increases (the rising limb), interaction with the tide causes a lowering and broadening of the peak water level relative to the simple prediction, causing the peaks to lower and

the troughs to become higher. The increase in background water level from the storm surge wave causes a smaller water level increase from the peak discharge and also lowers the slope of the falling limb. The interaction between storm surge and discharge is a much smaller impact relative to the tidal interactions for these amplitudes (0.2-m storm surge and 2-m tide). One can also observe that there is a significant discontinuity in the difference between the modeled water levels and the simple prediction at the locations the channel changes widths. There is almost no difference in the bay part of the simulation. What is extremely clear from comparing the combined event to the simple prediction is that the tides greatly slow the release of the discharge. The water levels are higher and tidal oscillations are muted in the upstream reaches of the channel for days after the storm surge has rescinded and the peak discharge has passed. The water level does not return to the normal tidally predicted value until day 14, which is 11 days after the peak discharge and 10 days after the storm surge has become zero.

4. Discussion

These results are consistent with our understanding of dynamics in larger tidal rivers. Although this system is much smaller than the previously studied systems, we still observe the strong interaction between discharge and tide. The discharge substantially changes the tidal propagation upstream and alters the in-channel velocity. This is consistent with our understanding that the nonlinearity in the friction term of the momentum balance is the primary mechanism for the generation of the shallow water tidal components. Therefore, the large change in velocity associated with a storm discharge will also cause substantial changes in the frequency term and interact with the tides to shift the frequency spectra. Other studies have also found this non-linear combination results in a lowering of peak water level [49]. However, one new observation is that the tide slows the release of the discharge maintaining elevated water levels (higher high- and low tides) for a much longer period after the discharge peak than the storm itself lasts. The length of this period of elevated water levels could be important when factoring in storms that occur subsequently. The fact that this effect is enhanced in the narrower portion of the channel means that it may be particularly relevant in smaller tributaries.

Previous studies have not considered the propagation of storm surge this far upstream. However, longer tidal waves (e.g., 28-day period waves associated with spring-neap variability) have been shown to propagate further upstream in rivers than the semi-diurnal and diurnal tidal constituents, and in some cases, have increased in amplitude [14]. Like the spring-neap variability, the storm surge consists of very long period energy and it is not associated with a substantial change in velocity. The primary influence of the storm surge is to increase the water level at all locations. Although unsurprising when comparing to other long period forcing, it is notable that the storm surge water elevation propagates further upstream than the head of the tide. However, storm surge does not impact velocity and thus there is no shift of energy between frequencies because it does not change the non-linearities in the friction term. The primary impact of increasing the water level with the storm surge is to allow for more discharge for a given free surface gradient, which means that the free-surface gradient does not have to be as high to permit the same flow rate.

In these simulations, we are currently neglecting the effects of waves, both offshore swell as well as locally generated wind waves on the water level. Previous studies have shown that offshore swell can increase storm surge by another 10–20 cm and locally generated winds can further increase the water level on the order of 20 cm in Northern San Francisco Bay [50]. We anticipate that this would result in a long wave signal similar to the pressure-created storm surge and could simply be considered as a case with additional height in the storm surge. Locally generated waves also increase the effective friction in the system and thus could further impact water levels by enhancing damping of the tide as it approaches the river mouth. However, most of this study is focused on water levels within the river channel, where local wave generation will be extremely fetch limited and thus not permit the significant development of wave activity in the channel. An increase in local wave generation would therefore not significantly change the results of the fluvial zone or the in-channel interactions but, due to increased bay water levels, could increase the amounts of flooding in the downstream regions.

We are also neglecting any changes to the underlying bathymetry. For an individual storm event, this is a reasonable assumption. The river channel has undergone significant flood control work over the last 20 years and the work was designed to maintain a sediment equilibrium and ensure that, exclusive of a 100-year return period fluvial event, deposition and accretion will not exceed 30 mm and these large changes are expected to be extremely localized [33]. The mechanisms of coastal sediment resuspension and transport are not significantly changed by the increase in the water level associated with storm surge. Storm surge is not associated with any increase in velocity at the bed that could lead to greater resuspension. In other estuaries, it has been found that large wind events, through the action of the locally generated wind waves, can significantly contribute to the total changes in bathymetry, although changes were never more than 50 mm during a 3-day storm event and more typically did not exceed 10 mm [51]. This magnitude of change is probably similar to the error inherent in the need to fit the bathymetry to the grid on which the hydrodynamic equations are solved. Also, the computational expense of including morphological dynamics is significant and would make use of this type of modeling for short-term flood forecasts prohibitively expensive. Although bathymetric changes will be important to the coastal circulation, given that the timing of the flooding is primarily driven by the short duration peak discharge, it is likely they would occur too slowly to significantly change the peak water levels. However, the changes from one event could very likely impact the next event. To account for these changes, a much more intense monitoring of coastal systems would need to be implemented.

Ultimately, what is important for predicting the expected hazard, is not just the water level but the total amount of flooded area and the length of time for which it is flooded. Returning to the more realistic scenarios, it is apparent that the difference between only accounting for river flows and including the effect of a coastal storm diminishes with distance from the coast, see Figure 11. Although the area flooded is very similar in the upstream reaches, there are differences in water depth. The differences in the maximum water level are negligible in the upstream regions primarily driven by discharge, becoming as small as 1 cm. In this relatively mild storm scenario (R1), when not much flooding is to be expected, the inclusion of the coastal storm and tides (R8) results in an additional flooding of ~6 km^2, see Figure 11C. The average depth of the extra flooding is 0.5 m with a few locations experiencing up to 2 m of water when, without the coastal storm, they would have remained dry. The duration of flooding is also significantly different between the two scenarios, with many more locations experiencing flooding for 40–72 h during this 72-h period. This represents an increase in duration of 10–30 h for many of these locations. We can also classify the change in flooding by integrating these two values to create a flood-hazard parameter F that we define as the integrated depth of water (h) over the duration of the simulation. It is calculated numerically as:

$$F = \sum_{t=0}^{t_n} h_n \Delta t_n \quad (4)$$

In our case, Δt was 30 min, as that was the time interval for which water levels were output in the model. The flood hazard change, F, can be large in situations for which the duration did not change but there was an increase in depth. It can also be large when there is a small change in depth but a large change in duration. Of course, changes in depth and duration are often related, although that relationship will be a complicated function of the local bathymetry. In Figure 12, we can see that there is a wide variety in response to the addition of the coastal forcing. Although, all the duration and depth values in Figure 12C are positive indicating that there are no locations that adding coastal flooding produces a shorter duration or lower elevation flood. Some locations merely show an increase in water depth, but inundation lasts for the same amount of time, while others show an increase in both depth and duration with the addition of the coastal storm. Relatively few locations experience an increase in duration with only a small change in water depth. These locations indicate places that will be more susceptible to "nuisance" flooding [3] which is a low water level that can persist for days.

Places with a short duration of flooding and deep water are closer to a "flash flood" which does not occur in this situation.

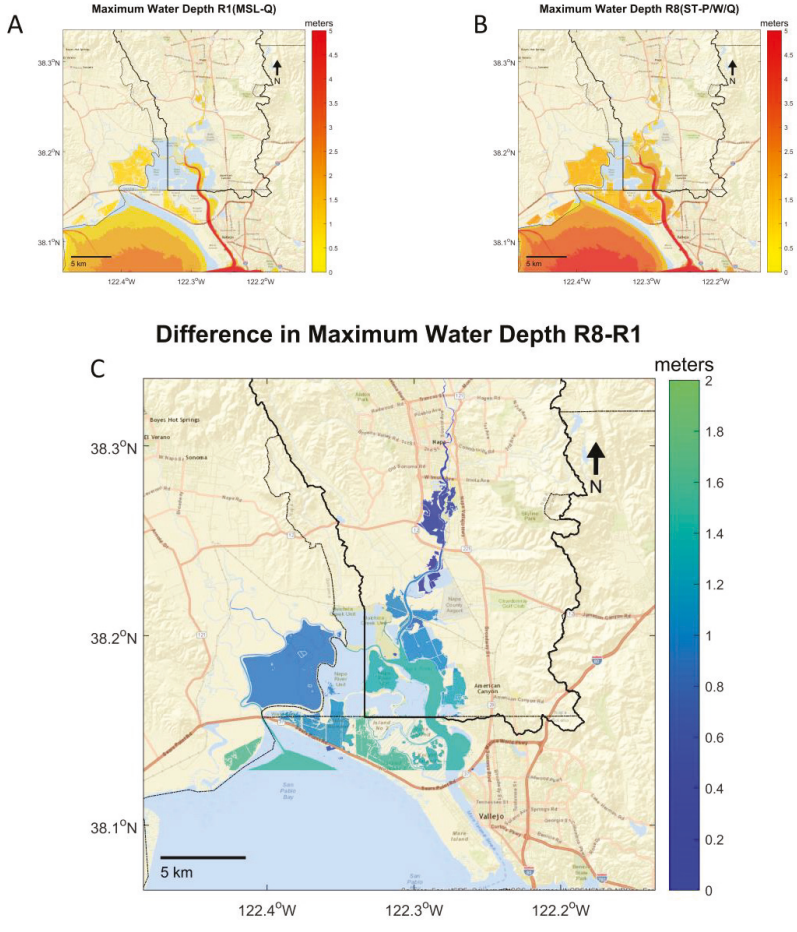

Figure 11. Comparison of modeled flood patterns accounting for river flows only and in combination with storm surge and tides. (**A**) Maximum water depth with a 5-year return period fluvial discharge and no tides (scenario R1). (**B**) Maximum water depth with a 5-year return fluvial discharge, 7-year return period coastally driven storm surge, and spring tides (scenario R8). (**C**) Increase in flood extent and water depth for scenario R8 relative to R1.

Under the modeled conditions, wetland regions experienced the biggest difference in flooded area, which is not associated with any danger to human life or property. However, ecosystem managers care about the relative frequency of these events and will need to incorporate both river discharge and storm surge to accurately understand the frequency, duration, and depth of flooding in the protected wetland areas. With sea level rise, it is anticipated that the region of coastal influence will progress inland by ~2 km [6] and this could mean that more urban areas begin to be impacted by the convergence of the two storm types (pluvial and oceanic). However, these results show that running a full hydrodynamic model would be the only way to predict flooding in the transition zone with this level of detail.

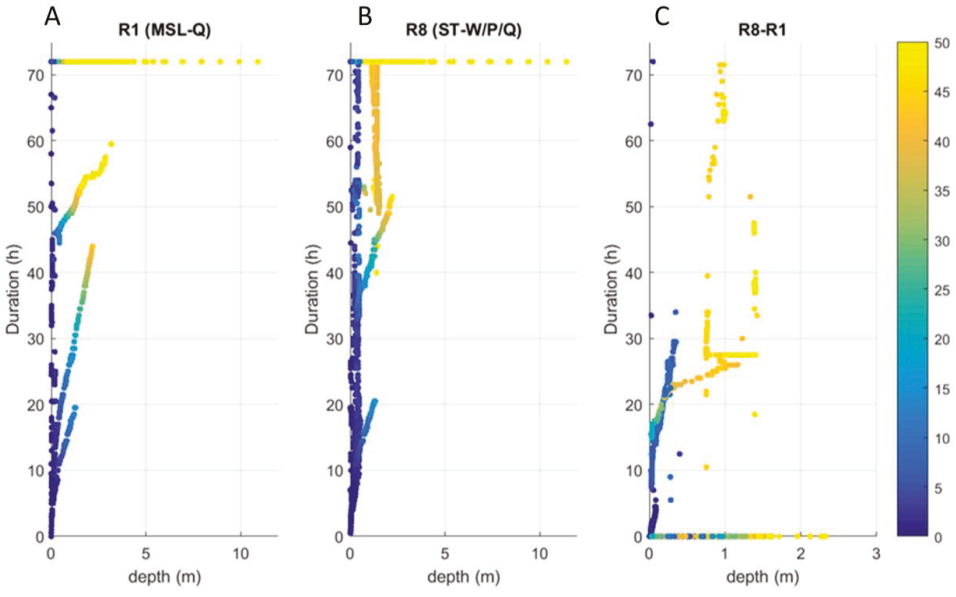

Figure 12. Changes in depth, duration, and hazard factor, *F*. Each point on the plot represents one 2-m grid cell in the Digital Elevation Model (DEM) and is positioned by the maximum water level (MXWL) experienced during the storm (x-axis) and the duration for which the cell was wet (y-axis). The plot is colored by the flood hazard factor (*F*). (**A**) Results shown for the modeled scenario account, R1 (5-year return period fluvial discharge). (**B**) Results shown for scenario R8 (same fluvial discharge in combination with a 7-year storm surge and spring tide). (**C**) The difference between scenarios R8 and R1.

These results indicate that the simplest estimate one can make by summing up the total impact from each of the contributing factors will likely overestimate the peak water level. However, this method can both over- and underestimate the total water levels for a given point in time and will be inaccurate in predicting the time evolution of water levels. For an area that does not have the resources to develop a fully coupled fluvial discharge and hydrodynamic model, this simple prediction could be a reasonable way to adjust peak water levels from a fluvial discharge model to account for coastal forcing and for management of regulated releases. However, to obtain accurate timing of the maximum water levels, a fully coupled model would be necessary. For example, the fact that the water levels remain elevated for so long after the peak discharge has occurred can have important implications for the duration of the flooding and the possibility of flooding occurring due to a secondary event that encounters these already elevated water levels. Also, this work highlights the importance of accurately knowing the timing of the peak discharge. Shifts of a few hours in peak discharge of the same magnitude can result in significant spatial and magnitude differences in peak water levels. Fluvial discharge forecasts are often not sufficiently accurate to predict the timing of the peak discharge on the hour accuracy [52], thus this indicates the need for improved peak discharge timing to accurately predict flooding levels near the coast where the discharge and tidal water level is also important.

The conditions modeled here focus on a system where the tidal range is substantially larger than the coastal storm surge, generally typical of San Francisco Bay. In other locations where storm surge can be larger and the tidal range is smaller, these results indicate that the impacts of storm surge will be felt much further upstream. For example, along the Gulf Coast of the United States, which is considered microtidal (tidal range <1 m) [53], hurricanes and tropical storms can create surges of 5 m or more (Hurricane Katrina had surges of 7–10 m [54]). In locations like this, we would anticipate

coastally driven water levels to propagate further up a tidal river, making the need for integrated modeling even more important than that of the San Francisco region. Indeed, some of the initial work on this topic has been done in regions susceptible to hurricanes, and they have found similar results in that there is a finite inland region where including both coastal and hydrological forcing is important for predicting total flooding [49,55]. Bilskie and Hagen [49] found the region in which it was necessary to account for coastal forcing ranged from 6 km up to almost 30 km from the coast, depending greatly on the underlying bathymetry/topography.

5. Conclusions

San Francisco Bay is an urbanized estuary with multiple flood drivers and therefore serves as an ideal location for developing a modeling approach to determine the risk of compound flooding along the bay-river interface. Due to the inherent non-linearities of these events, it was essential to apply a sophisticated numerical model to deterministically calculate water levels and flood extents that account for tidal forcing, storm surge generated by wind and pressure fields, and river flows. We utilized Delft3D-FM to efficiently capture these interactions along a sinuous estuarine shoreline, where rectilinear approaches would limit the resolution and accuracy of shallow water and nearshore interactions. We have shown that it is important to integrate both coastal and fluvial forcings during a storm event to accurately capture the time and duration of peak water levels. Maximal water levels will occur in a tidal river when high tides, storm surge, and large fluvial discharge events are coincident. However, the interaction between the coastal and fluvial forcings are complex and non-linear, making a simple linear superposition of forcing inadequate. For example, larger tidal amplitudes diminish the storm surge amplitude with propagation upstream. Also, the phasing between the peak fluvial discharges and the high tide is important in predicting when and where the highest water levels will occur. Finally, we found that relatively small coastal storms can create an extremely long duration of elevated upstream water levels. These findings demonstrate the need to utilize integrated flood forecasting models in the future to adequately capture the hazard of compound flooding in urbanized settings where community vulnerability is high.

Author Contributions: Conceptualization, L.H. and L.E.; Methodology, L.H. and L.E. Formal Analysis and Investigation and Writing Oriiginal Draft L.H., Writing-Review & Editing, L.H., P.B. and L.E.; Supervision, L.E. and P.B.; Funding Acquisition, P.B. Any use of trade, firm, or product names is for descriptive purposes only and does not imply endorsement by the US Government.

Funding: This research was funded by Sonoma County Water Agency (Agreement #18WSTAA175836).

Conflicts of Interest: The authors declare no conflict of interest.

References

1. *United States Flood Loss Report—Water Year 2014*; National Oceanographic and Atmospheric Administration: Silver Spring, MD, USA, 2014; p. 6. Available online: http://www.nws.noaa.gov/os/water/Flood%20Loss%20Reports/WY14%20Flood%20Loss%20Summary.pdf (accessed on 15 January 2018).
2. Easterling, D.R.; Meehl, G.A.; Parmesan, C.; Changnon, S.A.; Karl, T.R.; Mearns, L.O. Climate Extremes: Observations, Modeling, and Impacts. *Science* **2000**, *289*, 2068–2074. [CrossRef] [PubMed]
3. Moftakhari, H.R.; AghaKouchak, A.; Sanders, B.F.; Feldman, D.L.; Sweet, W.; Matthew, R.A.; Luke, A. Increased nuisance flooding along the coasts of the United States due to sea level rise: Past and future. *Geophys. Res. Lett.* **2015**, *42*, 9846–9852. [CrossRef]
4. Vitousek, S.; Barnard, P.L.; Fletcher, C.H.; Frazer, N.; Erikson, L.; Storlazzi, C.D. Doubling of coastal flooding frequency within decades due to sea-level rise. *Sci. Rep.* **2017**, *7*, 1399. [CrossRef] [PubMed]
5. Changnon, S.A. Impacts of 1997–98 EI Niño–Generated Weather in the United States. *Bull. Am. Meteorol. Soc.* **1999**, *80*, 1819–1828. [CrossRef]
6. Dusterhoff, S.D.; Beagle, J.; Collins, J.N.; Doehring, C. *Initial Protocol to Identify and Delineate the Head of Tide Zone in San Francisco Bay Tributaries*; No. 719; San Francisco Estuary Institute: Richmond, CA, USA, 2014; pp. 1–76.

7. Barnard, P.L.; van Ormondt, M.; Erikson, L.H.; Eshleman, J.; Hapke, C.; Ruggiero, P.; Adams, P.N.; Foxgrover, A.C. Development of the Coastal Storm Modeling System (CoSMoS) for predicting the impact of storms on high-energy, active-margin coasts. *Nat. Hazards* **2014**, *74*, 1095–1125. [CrossRef]
8. Zhang, J.; Liu, H. Modeling of waves overtopping and flooding in the coastal reach by a non-hydrostatic model. *Procedia IUTAM* **2017**, *25*, 126–130. [CrossRef]
9. Teng, J.; Jakeman, A.J.; Vaze, J.; Croke, B.F.W.; Dutta, D.; Kim, S. Flood inundation modelling: A review of methods, recent advances and uncertainty analysis. *Environ. Model. Softw.* **2017**, *90*, 201–216. [CrossRef]
10. LeBlond, P.H. On tidal propagation in shallow rivers. *J. Geophys. Res.* **1978**, *83*. [CrossRef]
11. LeBlond, P.H. Forced fortnightly tides in shallow rivers. *Atmosphere-Ocean* **1979**, *17*, 253–264. [CrossRef]
12. Kosuth, P.; Callède, J.; Laraque, A.; Filizola, N., Jr.; Guyot, J.-L.; Seyler, P.; Marie Fritsch, J.; Guimaraes, V. Sea-Tide Effects on Flows in the Lower Reaches of the Amazon River. *Hydrol. Process.* **2009**, *23*, 3141–3150. [CrossRef]
13. Guo, L.; van der Wegen, M.; Jay, D.A.; Matte, P.; Wang, Z.B.; Roelvink, D.; He, Q. River-tide dynamics: Exploration of nonstationary and nonlinear tidal behavior in the Yangtze River estuary. *J. Geophys. Res. Oceans* **2015**, *120*, 3499–3521. [CrossRef]
14. Pu, X.; Shi, J.Z.; Hu, G.-D.; Xiong, L.-B. Circulation and mixing along the North Passage in the Changjiang River estuary, China. *J. Mar. Syst.* **2015**, *148*, 213–235. [CrossRef]
15. Zhang, E.F.; Savenije, H.H.G.; Chen, S.L.; Mao, X.H. An analytical solution for tidal propagation in the Yangtze Estuary, China. *Hydrol. Earth Syst. Sci.* **2012**, *16*, 3327–3339. [CrossRef]
16. Jay, D.A.; Leffler, K.; Diefenderfer, H.L.; Borde, A.B. Tidal-Fluvial and Estuarine Processes in the Lower Columbia River: I. Along-Channel Water Level Variations, Pacific Ocean to Bonneville Dam. *Estuaries Coasts* **2015**, *38*, 415–433. [CrossRef]
17. Jay David, A.; Leffler, K.; Degens, S. Long-Term Evolution of Columbia River Tides. *J. Waterw. Port Coast. Ocean Eng.* **2011**, *137*, 182–191. [CrossRef]
18. Sassi, M.G.; Hoitink, A.J.F. River flow controls on tides and tide-mean water level profiles in a tidal freshwater river. *J. Geophys. Res. Oceans* **2013**, *118*, 4139–4151. [CrossRef]
19. van der Grinten, R.M.; de Vries, J.W.; de Swart, H.E. Impact of wind gusts on sea surface height in storm surge modelling, application to the North Sea. *Nat. Hazards* **2012**, *66*, 1313–1326. [CrossRef]
20. Rego, J.L.; Li, C. On the importance of the forward speed of hurricanes in storm surge forecasting: A numerical study. *Geophys. Res. Lett.* **2009**, *36*. [CrossRef]
21. Sabatino, A.D.; O'Hara Murray, R.B.; Hills, A.; Speirs, D.C.; Heath, M.R. Modelling sea level surges in the Firth of Clyde, a fjordic embayment in south-west Scotland. *Nat. Hazards* **2016**, *84*, 1601–1623. [CrossRef]
22. Bilskie, M.V.; Hagen, S.C.; Medeiros, S.C.; Passeri, D.L. Dynamics of sea level rise and coastal flooding on a changing landscape. *Geophys. Res. Lett.* **2014**, *41*, 927–934. [CrossRef]
23. Smolders, S.; Plancke, Y.; Ides, S.; Meire, P.; Temmerman, S. Role of intertidal wetlands for tidal and storm tide attenuation along a confined estuary: A model study. *Nat. Hazards Earth Syst. Sci.* **2015**, *15*, 1659–1675. [CrossRef]
24. Condon, A.J.; Peter Sheng, Y. Evaluation of coastal inundation hazard for present and future climates. *Nat. Hazards* **2011**, *62*, 345–373. [CrossRef]
25. Wang, R.-Q.; Herdman, L.M.; Erikson, L.; Barnard, P.; Hummel, M.; Stacey, M.T. Interactions of Estuarine Shoreline Infrastructure With Multiscale Sea Level Variability. *J. Geophys. Res. Oceans* **2017**, *122*, 9962–9979. [CrossRef]
26. Zheng, F.; Leonard, M.; Westra, S. Application of the design variable method to estimate coastal flood risk. *J. Flood Risk Manag.* **2017**, *10*, 522–534. [CrossRef]
27. Zheng, F.; Westra, S.; Leonard, M.; Sisson, S.A. Modeling dependence between extreme rainfall and storm surge to estimate coastal flooding risk. *Water Resour. Res.* **2014**, *50*, 2050–2071. [CrossRef]
28. Scripps Institute of Oceanography. *U.S.D. Coastal Data Information Program*; UC San Diego: La Jolla, CA, USA, 2017. Available online: http://cdip.ucsd.edu/?nav=historic&sub=data&units=metric&tz=UTC&pub=public&map_stati=1,2,3&stn=142&stream=p1 (accessed on 30 June 2017).
29. Bureau, U.S.C. 2010 Census. 2011. Available online: http://www.census.gov/2010census/data/ (accessed on 7 January 2018).

30. Barnard, P.L.; Erikson, L.H.; Elias, E.P.L.; Dartnell, P. Sediment transport patterns in the San Francisco Bay Coastal System from cross-validation of bedform asymmetry and modeled residual flux. *Mar. Geol.* **2013**, *345*, 72–95. [CrossRef]
31. Barnard, P.L.; Schoellhamer, D.H.; Jaffe, B.E.; McKee, L.J. Sediment transport in the San Francisco Bay Coastal System: An overview. *Mar. Geol.* **2013**, *345*, 3–17. [CrossRef]
32. Neary, V.S.; Wright, S.A.; Bereciartua, P. Case Study: Sediment Transport In Proposed Geomorphic Channel For Napa River. *J. Hydraul. Eng. ASCE* **2001**, *127*, 901–910. [CrossRef]
33. Goetting, J. Recalling 86 While Cleaning up from 05. In *Napa Valley Register*; Lee Enterprises: Napa, CA, USA, 2005. Available online: https://napavalleyregister.com/news/local/article_08baa217-9e06-5e01-8154-486c84403846.html (accessed on 8 June 2018).
34. Caltrans. *2016 Traffic Volumes on California State Highways*; US Department of Transportation: Sacramento, CA, USA, 2016. Available online: http://www.dot.ca.gov/trafficops/census/docs/2016_aadt_volumes.pdf (accessed on 10 June 2017).
35. Moore, D. Highway 37 Closure still causing headaches for motorists. In *The Press Democrat*; Press Democrat Media Company: Santa Rosa, CA, USA, 2017. Available online: http://www.pressdemocrat.com/news/6666970-181/highway-37-closure-still-causing?sba=AAS (accessed on 30 June 2017).
36. Vandever, J.; Sudhalkar, A.; May, K.; Villafranca, J.; Lightner, M.; Shilling, F. *State Route 37 Integrated Traffic, Infrastructure and Sea Level Rise Analysis*; Road Ecology Center, UC Davis: Davis, CA, USA, 2015; p. 87. Available online: http://hwy37.ucdavis.edu/files/upload/resource/Phase_II_SR_37_Stewardship_FinalReport_Task%202_Risk_Assessment.pdf (accessed on 11 November 2017).
37. Council, O.P. *State of California Sea Level Rise Guidance, 2018 Update*; Ocean Protection Council: Sacramento, CA, USA, 2018; p. 84.
38. Foxgrover, A.C.; Barnard, P.L. A seamless, high-resolution digital elevation model (DEM) of the north-central California coast. In *Data Series*; US Geological Survey: Reston, VA, USA, 2012. Available online: http://pubs.er.usgs.gov/publication/ds684 (accessed on 25 January 2017). [CrossRef]
39. Foxgrover, A.C.; Dartnell, P.; Jaffe, B.E.; Takekawa, J.Y.; Athearn, N.D. High-resolution bathymetry and topography of south San Francisco Bay, California. In *Scientific Investigations Map*; US Geological Survey: Reston, VA, USA, 2007. Available online: http://pubs.er.usgs.gov/publication/sim2987 (accessed on 20 July 2018). [CrossRef]
40. Foxgrover, A.C.; Finlayson, D.P.; Jaffe, B.E.; Fregoso, T.A. Bathymetry and digital elevation models of Coyote Creek and Alviso Slough, South San Francisco Bay, California. In *Open-File Report*; US Department of the Interior, US Geological Survey: Reston, VA, USA, 2018; p. 28. Available online: http://pubs.er.usgs.gov/publication/ofr20111315 (accessed on 20 July 2018). [CrossRef]
41. Foxgrover, A.C.; Finlayson, D.P.; Jaffe, B.E.; Takekawa, J.Y.; Thorne, K.M.; Spragens, K.A. 2010 bathymetric survey and digital elevation model of Corte Madera Bay, California. In *Open-File Report*; USGS: Reston, VA, USA, 2011; p. i-20. Available online: http://pubs.er.usgs.gov/publication/ofr20111217 (accessed on 20 July 2018). [CrossRef]
42. Institute, S.F.E. San Francisco Bay Shore Inventory: Mapping for Sea Level Rise Planning GIS Data. 2016. Available online: http://www.sfei.org/projects/SFBayShoreInventory (accessed on 30 April 2017).
43. Dushaw, B.D.; Egbert, G.; Worcester, P.F.; Cornuelle, B.D.; Howe, B.; Metzger, K. A TOPEX/POSEIDON Global Tidal Model (TPXO.2) and Barotropic Tidal Currents Determined from Long-Range Acoustic Transmissions. *Prog. Oceanogr.* **1997**, *40*, 337–367. [CrossRef]
44. Center for Operational Oceanographic Products and Services Tides and Currents. National Oceanic and Atmospheric Administration (NOAA). Silver Srping, Maryland. Available online: https://tidesandcurrents.noaa.gov (accessed on 8 August 2018).
45. Willmott, C.J. On The Validation of Models. *Phys. Geogr.* **1981**, *2*, 184–194. [CrossRef]
46. Thorne, K.M.; Dugger, B.D.; Buffington, K.J.; Freeman, C.M.; Janousek, C.N.; Powelson, K.W.; Gutenspergen, G.R.; Takekawa, J.Y. *Marshes to Mudflats—Effects of Sea-Level Rise on Tidal Marshes Along a Latitudinal Gradient in the Pacific Northwest*; U.S. Geological Survey Open-File Report: Sacramento, CA, USA, 2015. [CrossRef]
47. Nash, J.E.; Sutcliffe, J.V. River flow forecasting through conceptual models part I—A discussion of principles. *J. Hydrol.* **1970**, *10*, 282–290. [CrossRef]

48. Bilskie, M.V.; Hagen, S.C. Defining Flood Zone Transitions in Low-Gradient Coastal Regions. *Geophys. Res. Lett.* **2018**, *45*, 2761–2770. [CrossRef]
49. O'Neill, A.; Erikson, L.; Barnard, P. Downscaling wind and wavefields for 21st century coastal flood hazard projections in a region of complex terrain. *Earth Space Sci.* **2017**, *4*, 314–334. [CrossRef]
50. Ganju, N.K.; Suttles, S.E.; Beudin, A.; Nowacki, D.J.; Miselis, J.L.; Andrews, B.D. Quantification of Storm-Induced Bathymetric Change in a Back-Barrier Estuary. *Estuaries Coasts* **2017**, *40*, 22–36. [CrossRef]
51. Granato, G.E. *Estimating Basin Lagtime and Hydrograph-Timing Indexes Used to Characterize Stormflows for Runoff-Quality Analysis*; US Geological Survey: Reston, VA, USA, 2012; p. i-47. Available online: http://pubs.er.usgs.gov/publication/sir20125110 (accessed on 20 November 2018). [CrossRef]
52. Nichols, M.M.; Boon, J.D. Chapter 7 Sediment Transport Processes in Coastal Lagoons. In *Elsevier Oceanography Series*; Kjerfve, B., Ed.; Elsevier: New York, NY, USA, 1994; Volume 60, pp. 157–219.
53. Fritz, H.M.; Blount, C.; Sokoloski, R.; Singleton, J.; Fuggle, A.; McAdoo, B.G.; Moore, A.; Grass, C.; Tate, B. Hurricane Katrina storm surge distribution and field observations on the Mississippi Barrier Islands. *Estuar. Coast. Shelf Sci.* **2007**, *74*, 12–20. [CrossRef]
54. Silva-Araya, W.; Santiago-Collazo, F.; Gonzalez-Lopez, J.; Maldonado-Maldonado, J. Dynamic Modeling of Surface Runoff and Storm Surge during Hurricane and Tropical Storm Events. *Hydrology* **2018**, *5*, 13. [CrossRef]
55. Bacopoulos, P.; Tang, Y.; Wang, D.; Hagen, S.C. Integrated Hydrologic-Hydrodynamic Modeling of Estuarine-Riverine Flooding: 2008 Tropical Storm Fay. *J. Hydrol. Eng.* **2017**, *22*. [CrossRef]

Journal of
Marine Science and Engineering

MDPI

Article

An Assessment of Two Models of Wave Propagation in an Estuary Protected by Breakwaters

Amin Ilia * and James O'Donnell

Department of Marine Sciences, University of Connecticut, Groton, CT 06340, USA; james.odonnell@uconn.edu
* Correspondence: amin.ilia@uconn.edu; Tel.: +1-860-405-9152

Received: 26 July 2018; Accepted: 23 November 2018; Published: 27 November 2018

Abstract: Breakwaters influence coastal wave climate and circulation by blocking and dissipating wave energy. In a large harbor, these effects are combined with wave generation, refraction and reflection. Accurate representation of these processes is essential to the determination of coastal circulation and wave processes. MIKE21SW and SWAN are two third-generation spectral wave models which are used widely in coastal research and engineering applications. Recently improved versions of the models are able to consider the influence of breakwater structures. In this study, we used available observations to evaluate the accuracy of model simulations of waves in New Haven Harbor, Connecticut, USA, an estuary with three detached breakwaters near the mouth. The models were executed on their optimum unstructured triangular grid. The boundary conditions were derived from a bottom mounted Acoustic Doppler Current Profilers (ADCP) on the offshore side of the breakwaters. Wind forcing was applied using data from the Central Long Island Sound buoy. We found that both models were largely consistent with observations during storms. However, MIKE21SW predicted some of storm peaks slightly better. SWAN required the finer grid to achieve the optimum condition, but as it uses a fast, fully implicit algorithm, the computational times were similar. Also, the sensitivity analysis represents that wind forcing and the breakwaters have significant impact on the results.

Keywords: wave hindcast; breakwater; harbor; estuary; SWAN; MIKE21SW; unstructured grid

1. Introduction

Breakwaters are used to protect harbors and shorelines from waves and to limit coastal erosion. In harbors, breakwaters provide tranquility behind them to ease both navigation and berthing for vessels. Breakwaters influence coastal wave climate by breaking, reflecting, and diffracting wave energy. In a large harbor, the fetch may be sufficient for the local generation of waves to be important. Studying these influences in situ poses a challenge. In recent years, spectral wave models have become more widely used and are important in describing coastal wave behavior. However, the performance and precision of the spectral models in real harbors in the presence of the breakwaters has not been well examined.

SWAN, MIKE21SW, and Wavewatch III are three commonly used spectral wave models in coastal and ocean communities. Wavewatch III is mostly used for deep ocean and open sea applications and is not able to include breakwater structures. On the other hand, the recent versions of SWAN and MIKE21SW are equipped to handle breakwaters.

Although parabolic and elliptic mild slope models as well as Boussinesq models may be more appropriate for the simulation of waves in small harbors, where diffraction is the most important phenomenon, in large embayments and harbors wind-wave generation can be important and spectral models are useful. However, some circumstances should meet to use spectral for wave simulation in harbors [1,2].

In recent years, unstructured grid models have become more popular for modeling complex geometries and are an effective alternative to the grid nesting approach, [3,4]. In this study, we employ unstructured SWAN (v41.20) and MIKE21SW (v2017) to simulate the effects of three coastal breakwaters on the wave field in New Haven Harbor, Connecticut, and then assessed their accuracy and efficiency.

There have been previous comparisons of these models. Strauss et al. [5] compared simulations of waves on a narrow continental shelf in Gold Coast, Australia using SWAN and MIKE21SW. SWAN was executed in the fully spectral mode with a structured grid, while MIKE21SW was executed on a directional decoupled parametric mode with an unstructured grid. The results indicated that both models overestimated significant wave height. Moeini and Etemad-Shahidi [6] applied SWAN and MIKE21SW for hindcasting waves in Lake Erie. The study suggested SWAN simulated significant wave height better, while MIKE21SW simulated wave period and direction better. Conversely, Fonseca et al. [7] suggested that MIKE21SW, SWAN, and STWAVE models have similar behavior and precision when examining performance on the Portuguese coast. Hoque et al. [8] evaluated SWAN and MIKE21SW in the Mackenzie Delta in Beaufort Sea, Canada. They concluded that the results of the models were almost identical, but in water shallower than 7 m for wave height between 2 and 3 m, SWAN simulated the significant wave height better, though the peak period from MIKE21SW was more accurate.

In all previous studies, SWAN was executed on a structured grid and MIKE21SW on an unstructured grid. In this study, both SWAN and MIKE21SW were run on their optimum unstructured grids and evaluated inside New Haven Harbor which is separated from Long Island Sound by substantial breakwaters (Figure 1). The model results are compared to data from two bottom mounted Acoustic Doppler Current Profilers (ADCP) in the harbor for all storm events, and to one outside the harbor for storms with northerly winds. The sensitivity of the model results to characteristics of the wind forcing, and the representation of diffraction, reflection, and the breakwaters are discussed. The simulation skill and the efficiency of the models are summarized and possible explanations for their differences were discussed.

Figure 1. Locations of breakwater structures in front of New Haven Harbor are highlighted by white lines and ADCP locations inside and outside the harbor are identified by yellow boxes and labels. Image Source: "New Haven Harbor". 41° 15′03.79″ N and 72° 55′20.36″ W. Google Earth. 23 September 2017. 18 June 2018.

2. Model Descriptions

MIKE21SW is a proprietary model developed by DHI Company. It is one of the most widely used wave models in coastal and marine engineering projects around the world. It has a graphical user interface (GUI) that makes it simple to set up the model and visualize the results. SWAN is an open source model developed by the Delft University of Technology. It is often used in academic coastal research and has been integrated to community circulation models. For simplification and clarification, we introduce the models by summarizing their similarities and differences.

SWAN [9] and MIKE21SW [10] are both third generation fully spectral wave models. The models solve the wave action balance equation, described by Mei [11], Komen et al. [12], and Young [13]. In Cartesian coordinates, the wave action balance equation can be written as

$$\frac{\partial N}{\partial t} + \nabla.\left(\left(\vec{c}_g - U\right)N\right) = \frac{S}{\sigma} \quad (1)$$

where $N(x, \sigma, \theta, t)$ is the wave action density, $\vec{c}_g = (c_x, c_y, c_\sigma, c_\theta)$ is the wave group velocity, U is ambient current, σ is relative frequency, θ is wave direction, t is time, and S is the total source and sink terms which represent generation, dissipation, and redistribution of wave energy. ∇ is the four-dimensional differential operator with respect to $x, y, \sigma,$ and θ.

The source terms in both models are almost the same. Wave dissipation terms such as bed friction, wave breaking, whitecapping, nonlinear quadruplet interactions, nonlinear triad wave interactions, and diffraction are essentially the same. However, in some cases such as wind input, whitecapping and quadruplet wave interaction, SWAN provides a wider range of parameterizations and coefficients.

SWAN can be run on both structured and unstructured grids, while MIKE21SW only uses unstructured grids. The spatial discretization method differs between the models. SWAN's spatial discretization is based on a vertex-centered method while MIKE21SW uses a cell-centered method. This implies that wave action N is stored at the grid cell vertices in SWAN and at the cell center in MIKE21SW. Thus, the control volume in SWAN is a polygon, while in MIKE21SW it is triangular.

The numerical methods used in structured and unstructured SWAN are different. In the structured mode of SWAN, a first order upwind-space backward-time (BSBT) scheme, or a second order SORDUP scheme (default for stationary mode), and second order Stelling and Leendertse scheme (default for nonstationary mode) may be selected. In unstructured SWAN the only option is the BSBT scheme which is fast but diffusive [14]. MIKE21SW uses a first order upwind difference and second order accurate scheme in space. The first order scheme is usually sufficient for small-scale domains dominated by local wind. In the case of swell propagation, the second order scheme should be applied [10].

The major difference between the numerical methods is that SWAN uses a fully implicit method time integration whereas MIKE21SW is an explicit approach. Consequently, MIKE21SW avoids solving a large system of equations with the drawback that the temporal step is limited by the Courant number. SWAN's fully implicit scheme eliminates the stability constraint on the temporal step but requires a large system of equations must be solved to achieve a solution. To improve efficiency SWAN uses a point-by-point multi-directional Gauss-Seidel iteration technique that circumvents the need to construct and solve a large system of simultaneous equations as is typical in implicit methods [14]. This technique highly improves the computational efficiency of the SWAN model.

3. Methods

In this study, the model domain is New Haven Harbor, Connecticut, USA. New Haven Harbor is located in Long Island Sound, a large estuary on the northeast coast of the United States. There are three detached breakwaters in front of the harbor to reduce the effects of waves during extreme storms. The area is frequently affected by strong winds during winter, from January to March, and occasionally by hurricanes in the summer and early fall. The significant wave height in central Long Island Sound, where New Haven Harbor is located can exceed two meters. Also, the maximum distance from New

Haven breakwaters to end of estuary is 7 km, sufficient fetch for local wave generation to be important. This is the main reason that the spectral wave models, rather than mild slope or Boussinesq wave models, were employed in this study.

To observe the effect of breakwaters on waves in extreme storms, we deployed two ADCPs, one outside the harbor (NH1) and one inside (NH2), during the winter of 2015 from 21 January to 5 April. The wind data were gathered during the same period by the Central Long Island Sound Buoy (CLIS) which is located 25 km from New Haven. CLIS wind data are a good representative of New Haven wind, particularly when the winds are southerly. Northerly winds may be more influenced by the roughness of the land surrounding the harbor. However, the topography of the New Haven area does not contain features that could cause substantial influence on wind direction. Depths and locations of the observations can be found in Table 1, and Figure 1 illustrates the field site.

Table 1. Location and depth information for the observations used for modeling

Station ID	Latitude (N)	Longitude (W)	Depth (m)	Location
NH1	41°13.44′	72°53.15′	10.4	Outside Harbor
NH2	41°14.64′	72°56.96′	5.2	Inside Harbor
CLIS	41°8.28′	72°39.30′	27	Outside Harbor

Instead of applying a nesting approach, which uses results from a large-scale model to force the boundaries of the local wave model, we used the observed wave spectrum at NH1 to force the open boundary of the models. In this way, we reduce the uncertainty that arises from simulation of the large-scale wave field. The possible variation of the wave field along the boundary was neglected since Long Island Sound is fetch limited and the bathymetric variations near the study site were small. The models were also forced by a uniform wind stress over the domain at half-hour intervals using observation from the CLIS buoy. Mean sea level variations were prescribed in the simulation using observed water level data at the NH2 station.

For the results from the models to be comparable, both models were set up with the same forcing and the optimum time step and grid size for each model were determined by comparison to observations. In MIKE21SW, the user selects a range for time steps (the minimum and maximum) and the model automatically determines the optimum time step based on the grid size, wave propagation speed, and Courant number. The minimum time step must meet the Courant number restriction. In SWAN, the numerical scheme is unconditionally stable but it is critical to ensure that the solution has converged. Using a grid with the resolution range $dx_{max} = 350$ m and $dx_{min} = 35$ m, we found that a time step $dt = 60$ s provided the same solution as a range of smaller time steps, Figure 2a,b compare the solutions at the location of NH2 for two 24 h intervals together with the observations.

We also examined the effect of the grid generation choices. Using a grid converter, available in the MIKE21 package, and the grid generation software in the surface-water modeling system package (SMS v12) we created grids for the models using the same spatial smoothing ratio. Figure 2c,d shows the sensitivity of SWAN solutions for different grid sizes and time steps. As the grid size is decreased, the time step also must be decreased by the same factor to avoid accumulation of numerical computation errors. For the majority of storms, the grid size $dx_{max} = 350$ m and $dx_{min} = 35$ m was adequate (Figure 2c), but some storms required finer grid, (Figure 2d). Refining the grid size and time step by the factor of $\sqrt{2}$ increases the computational time at least by the factor of $\left(\sqrt{2}\right)^3 = 2.8$; therefore, it is vital that the optimum grid size be selected very carefully. The grid size $dx_{max} = 250$ m and $dx_{min} = 25$ m with time step $dt = 42$ s was found to provide the optimum condition for SWAN.

Figure 2e,f illustrates the sensitivity of the MIKE21SW solutions to grid size. Since MIKE21SW selects the optimum time step based on the grid size automatically, it is easier and faster to get to optimum condition by MIKE21SW. MIKE21SW also showed less sensitivity to grid size than SWAN, (Figure 2e,f). The result was converged for grid size with $dx_{max} = 500$ m and $dx_{min} = 50$ m.

The optimum unstructured triangular grid for each model is presented in Figure 3. The grids were smoothly refined around the breakwaters and inside the harbor.

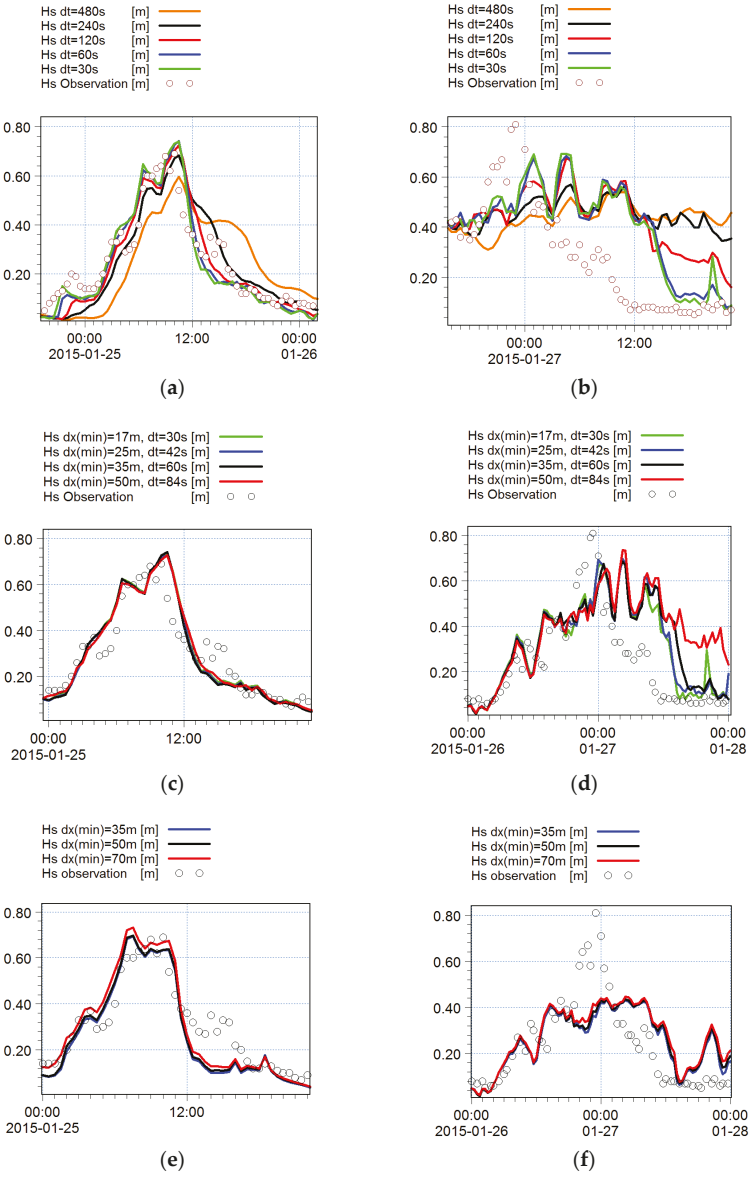

Figure 2. (**a**,**b**) Wave height at NH2 from SWAN time step sensitivity analysis using a grid size range $dx_{max} = 350$ m and $dx_{min} = 35$ m. The results indicate that solutions with time steps of 30 s (green) and 60 s (blue) are almost identical for this grid size. (**c**,**d**) SWAN solutions for grid size and time step sensitivity analysis, the solution for grid size less than $dx_{max} = 250$ m and $dx_{min} = 25$ m are almost indistinguishable. (**e**,**f**) MIKE21SW solutions is less sensitive to grid size and converge with larger grid size $dx_{max} = 500$ m and $dx_{min} = 50$ m.

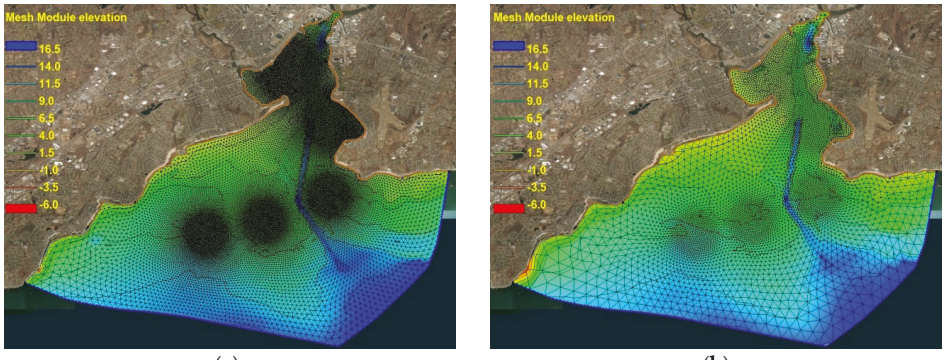

(**a**) (**b**)

Figure 3. The optimum unstructured triangulate grids used for (**a**) SWAN with $dx_{max} = 250$ m and $dx_{min} = 25$ m and (**b**) MIKE21SW with $dx_{max} = 500$ m and $dx_{min} = 50$ m; SWAN required a finer grid to reach the optimum condition. The spatial smoothing of the grids is the same. The grids were refined around the breakwaters, three densification zones, and in the harbor.

The models were calibrated using data from the period of 23 to 28 January. For each model, we tested settings and coefficients, and applied the set that achieved the best agreement with the observations. Both models were executed in third generation fully spectral and non-stationary mode. The same spectral discretization (25 frequencies and 16 directional discretizations) were applied to SWAN and MIKE21SW with a minimum frequency of 0.06 Hz and a maximum of 0.59 Hz.

The results of MIKE21SW were tested for both first and second order numerical scheme, and no significant difference was observed between the first order and second order schemes. Consequently, in order to save computational time, MIKE21SW was run on first order. As mentioned in Section 2, the only available numerical scheme in unstructured SWAN is first order BSBT.

Options for representing the wind input source and whitecapping dissipation functions are different in the models. SWAN is configured to use the wind input source function of Janssen [15,16], as implemented in WAM cycle 4 [17]; the method of Komen [18], as implemented in WAM cycle 3 [19]; and method of Yan [20]. MIKE21SW only supports Janssen's method. Dissipation through whitecapping is based on the development of Hasselmann [21] in both Janssen's and Komen's methods, however, the coefficients are different (see Komen [12,18]). Yan's wind input method is combined with saturation-based whitecapping as described in Van der Westhuysen [22,23]. Moeini and Etemad-Shahidi [6] suggested that Komen's method led to more accurate significant wave height than Janssen's method for Lake Erie. Hoque [8] indicated Westhuysen's formulation tends to have better significant wave height in the Mackenzie Delta. We tested all three methods with SWAN. We found that Janssen's method provides the best wave height simulations in the harbor. Therefore, Janssen's wind input method was used for both models with the tunable coefficients set as $C^*_{ds} = 4.5$ and $\delta = 0.5$.

Wave dissipation due to bottom friction was represented in both models by the empirical JONSWAP [24] approach. The friction coefficients introduced by Zijlema et al. [25] were used: $C_b = 0.038$ m^{2}s^{-3} for SWAN and $c_{fw} = 0.0077$ ms^{-1} for MIKE21SW.

Waves breaking in shallow water was taken into account in the models using the Battjes and Janssen [26] formulation with $\alpha = 1$ and $\gamma = 0.8$. Also, triad wave–wave interactions were enabled in both models. Triad interactions in MIKE21SW are calculated based on Eldeberky and Battjes [27] and in SWAN based on Eldeberky [28], a slightly modified version of the former. Quadruplet wave–wave interactions were also enabled in the models. In both models, the quadruplet wave–wave interactions are computed with the Discrete Interaction Approximation (DIA) as proposed by Hasselmann et al. [29].

When breakwaters are present in the model domain, diffraction computations become important. Diffraction is taken into account in the models using a phase-decoupled refraction-diffraction approximation proposed by Holthuijsen et al. [1]. Diffraction computation in the models is almost the same, but a wave field smoothing technique for the computation of the diffraction parameter that is not available in SWAN with an unstructured grid.

The reflection coefficients for breakwaters were calculated using the method proposed in the Coastal Protection Manual: Part VI, [30], and originally developed by Seeling [31], for non-overtopped slopping structures with the parameter values of Davidson [32]. The reflection coefficient for the type of structure and wave climate in the study area varied from 0.47 to 0.52. Therefore, the average reflection coefficient of 0.493 was selected.

Spectral wave models adequately simulate the effects of diffraction when breakwaters are far from the coastline and have a low reflection coefficient [1]. In addition, the breakwaters should not cover the down-wave view substantially, [1]. In New Haven harbor, the distance between the breakwaters and coastline varies 4 to 5.2 km, and the separation of the breakwaters is 700 m to 1000 m, which much larger than the threshold distance [2] of twice the dominant wavelength (here $2L \cong 100$ m, where L is wave length). Also, the rubble mound breakwaters with low reflection coefficient, 0.493, create incoherent wave reflection.

The spectral wave models such as SWAN simulate wave diffraction better for the wider directional spectrum of wind-waves than for swell [2]. The wave spectra for the important storms are shown in Figure 4. The wave spectra in the harbor are directionally broad, similar to those obtained in Long Island Sound. Therefore, New Haven harbor is considered a suitable case for simulating waves using the spectral models.

4. Results

The results of SWAN and MIKE21SW models were compared and assessed inside the harbor at NH2 during all storms and at NH1 for northerly storms. We divided the observations into five storm periods, detailed in Table 2. Each of these periods is discussed separately, and then the results are summarized. The statistical parameters used for data validation are

$$Bias = \frac{\sum_{i=1}^{n}(Y_i - X_i)}{n}, \tag{2}$$

$$RMS = \sqrt{\frac{\sum_{i=1}^{n}(Y_i - X_i)^2}{n}}, \tag{3}$$

$$m = slope\ of\ the\ best\ fitted\ line, \tag{4}$$

$$R^2 = 1 - \frac{\sum_{i=1}^{n}\left(Y_i - Y_i'\right)^2}{\sum_{i=1}^{n}\left(Y_i - \overline{Y}\right)^2}, \tag{5}$$

where Y_i, with mean $\overline{Y}$, are the observed values, X_i are the simulated values, and n is the number of data points. RMS is the root mean square error, R^2 is the fraction of the variance in the data explained by the model, Y_i' is the estimated value by regression, and $\overline{Y}$ is the mean of the observed values.

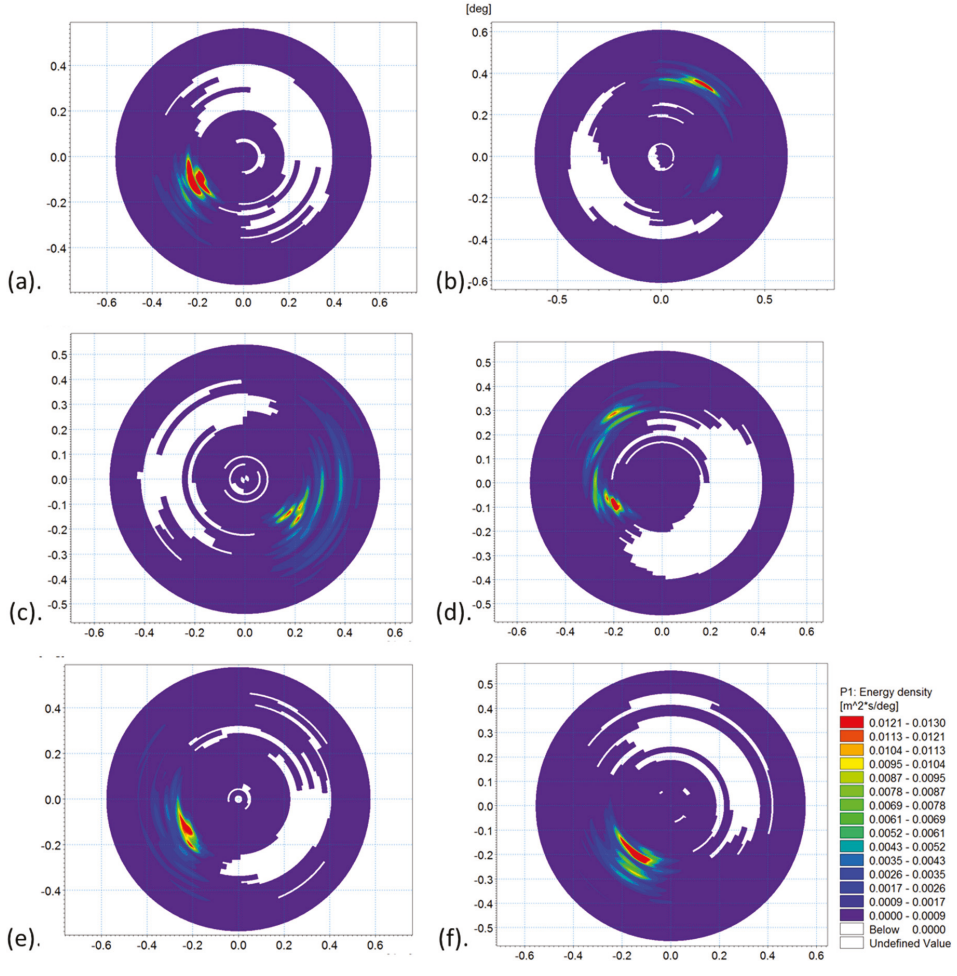

Figure 4. The two-dimensional wave spectra for important storms at NH1. As the majority of waves generates with local wind in central Long Island Sound, the spectrums are directionally wide. (**a**) 25 January; (**b**) 27 January; (**c**) 2 February; (**d**) 15 February; (**e**) 7 March; and (**f**) 2 April. The spectral wave models simulate wave diffraction for directionally wide spectrum better than directionally narrow spectrum, [2].

Table 2. Storm periods used for analyzing and assessing the models

No.	Storm Period
1	23 to 28 January
2	1 to 10 February
3	14 to 21 February
4	6 to 8 March
5	2 to 5 April

Three consecutive high wind intervals occurred during the first storm period, 23 to 28 January. Wave boundary condition and wind input data, as well as comparisons between observations and the model predictions of the significant wave height, peak wave period and wave direction for Storm

Period 1 are presented in Figure 5. The noise in observed wave periods and directions in low significant wave heights events were not included in the assessments. In this storm period, the first two storms had winds from the west and southwest. In the first storm, the predicted significant wave height (H_s) series were very similar to each other. Both missed the first part of the storm peak and under-predicted the second part by 5% (Figure 5b). Both models were able to simulate wave period and direction correctly (Figure 5c,d). In the second storm, both models reproduced the storm's entire wave height peak very well. Simulated wave period and direction for the second storm also agreed well with the observations. For the third storm, the models did not perform well. On 26 January, the storm caused easterly winds, then on 27 January, wind stress vectors suddenly turned by 90 degrees and a very strong wind (in excess of 15 m/s) blew from the north. This strong wind was adequate to generate wave in a very fetch limited area as New Haven estuary. The models showed different behavior during this storm. Simulated peak wave periods were in consistent with observations. Modeled wave directions for the first part of the storm completely agreed with observation, but after the wind vector rotated on 26 January 10 p.m., there was a 25 to 40 degrees difference between observed and simulated wave direction. The observation showed a wave direction from northeast (50 degrees), while simulated wave directions were from north. The statistical parameters show that SWAN results were slightly better than MIKE21SW for this period, (Table 3). The *Bias* in significant wave heights obtained from SWAN was 0.03 m less than that in MIKE21SW. R^2 for SWAN was 0.60 versus 0.57 for MIKE21SW. The *RMS* values were the same (0.13) and the slope of best fitted line was better for MIKE21SW (0.89) than SWAN (0.72).

Comparison of the results of the models and observations from Storm Period 2, 1 to 10 February, are shown in Figure 6. Both models showed similar behavior during this period though SWAN overestimated the strongest storm significant wave height on 2 February by 50% (Figure 6b). There was a high wind event from the north on 5 and 6 February (Figure 6a), and the models simulated the significant wave height very well (Figure 6b). In other storms, the models had very similar behavior, both missed some small oscillations and overestimated others. The models correctly simulated the peak wave period and mean wave direction, (Figure 6c,d). Statistical parameters for this period did not present any substantial preference of the models, *Bias* and R^2 were better for SWAN and *RMS* and *m* were better for MIKE21SW (Table 3).

Three storms occurred in the third period, from 14 to 21 February. As shown in Figure 7, the models accurately simulated the first storm. The second storm started with a wind from north to south and it then rotated to the east. MIKE21SW accurately simulated significant wave height in the first part of the storm but later produced overestimates. In contrast, SWAN overestimated significant wave height over the whole storm duration. Both models provide poor estimates of the wave period for the second part of the storm. For the third storm, both models successfully simulated the wave height, period, and direction, however, MIKE21SW slightly under-predicted the first part. Overall, *RMS* error was 0.03 lower, the slope of the best-fitted line was 0.11 higher, and R^2 was 0.01 higher for MIKE21SW. The magnitude of *Bias* values were the same (0.02) but with opposite signs, (Table 3). Therefore, MIKE21SW results were slightly more accurate than SWAN for this time period, mostly due to better simulation of the second storm.

In the fourth storm period, both models failed to correctly simulate significant wave height variations between 6 and 8 March, as shown in Figure 8. The storm includes two peaks in significant wave height, but the models underestimated both (Figure 8b). However, they correctly estimated wave periods and directions (Figure 8c) and the statistical parameters show similar model performance. There was two hours delay in storm growth in both models. The storm started at 3 March 03:00 p.m., according to observations, but 05:00 p.m. in the models. Also, there was no difference between wind speed at 03:00 and 05:00 p.m. (both around 5 m/s, Figure 8a). Some statistical parameters, such as R^2, were better for MIKE21SW and others, such as *Bias*, for SWAN (Table 3).

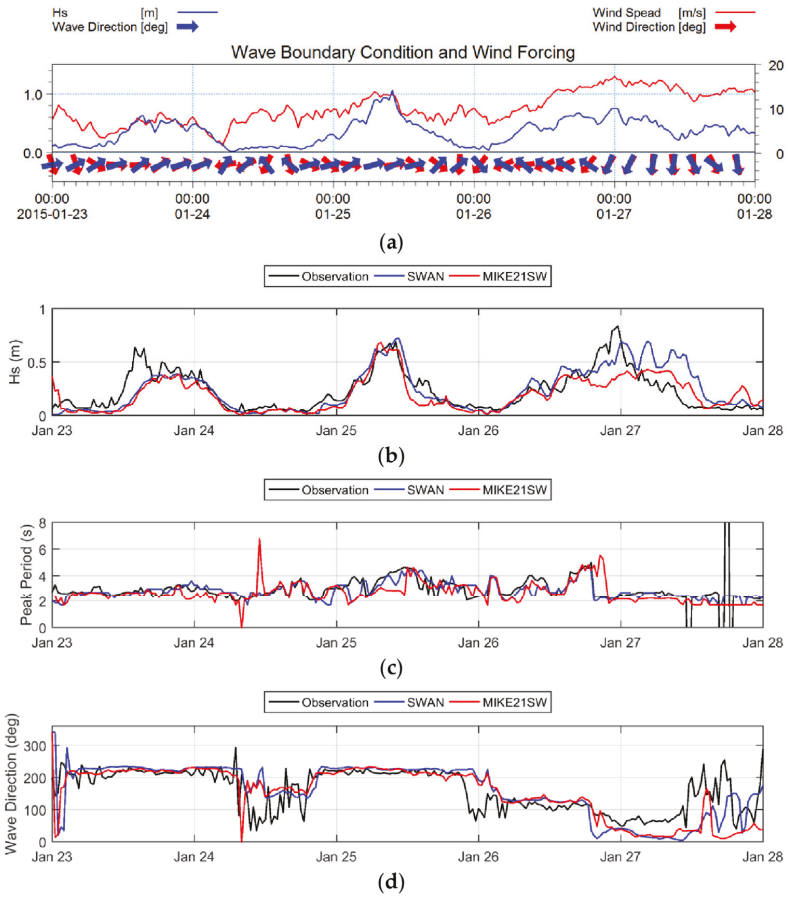

Figure 5. (**a**) Wave boundary condition and wind input for the time interval of 23 to 28 January. Blue: significant wave height (left axis), blue arrow: wave direction at the boundary, red: wind speed (right axis), red arrow: wind direction. (**b**–**d**) Comparison of SWAN (blue), MIKE21SW (red), and observation (black) at NH2 for the time interval of 23 to 28 January. (**b**) Significant wave height. (**c**) Peak wave period (**d**) Mean wave direction. The models had good performance for the first two southerly events but not for the third event which was from the north.

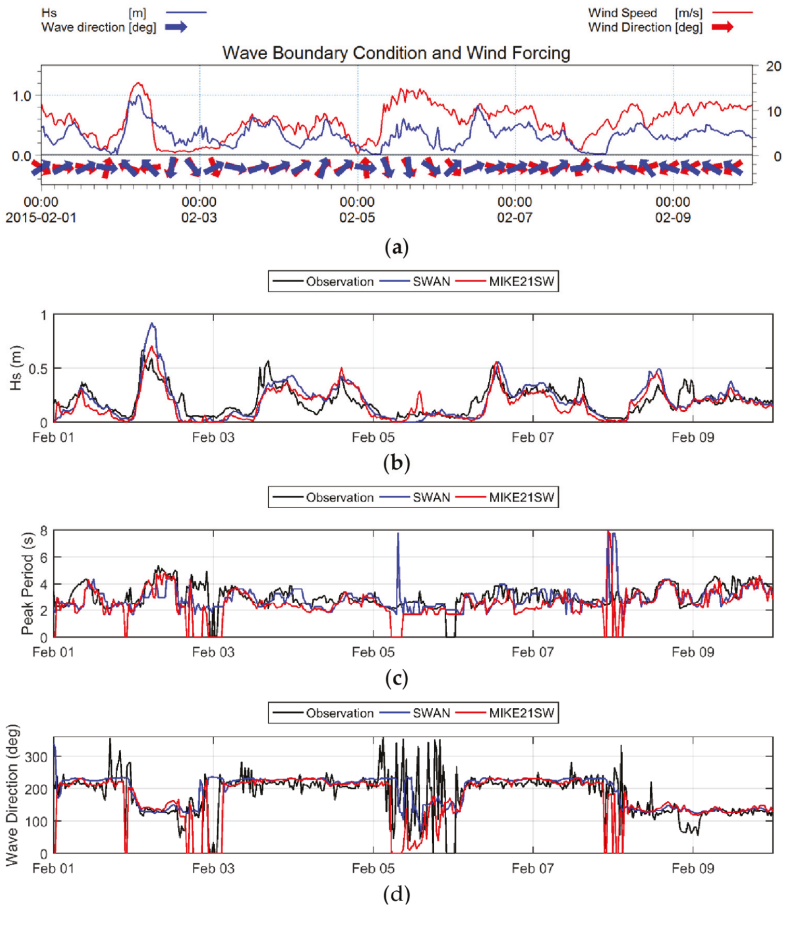

Figure 6. (**a**) Wave boundary condition and wind input for the time interval of 1 to 10 February. Blue: significant wave height (left axis), blue arrow: wave direction at the boundary, red: wind speed (right axis), red arrow: wind direction. (**b**–**d**) Comparison of SWAN (blue), MIKE21SW (red), and observation (black) at NH2 for the time interval of 1 to 10 February. (**b**) Significant wave height. (**c**) Peak wave period (**d**) Mean wave direction. The models had good performance for this period though SWAN overestimated the strongest storm on 2 February.

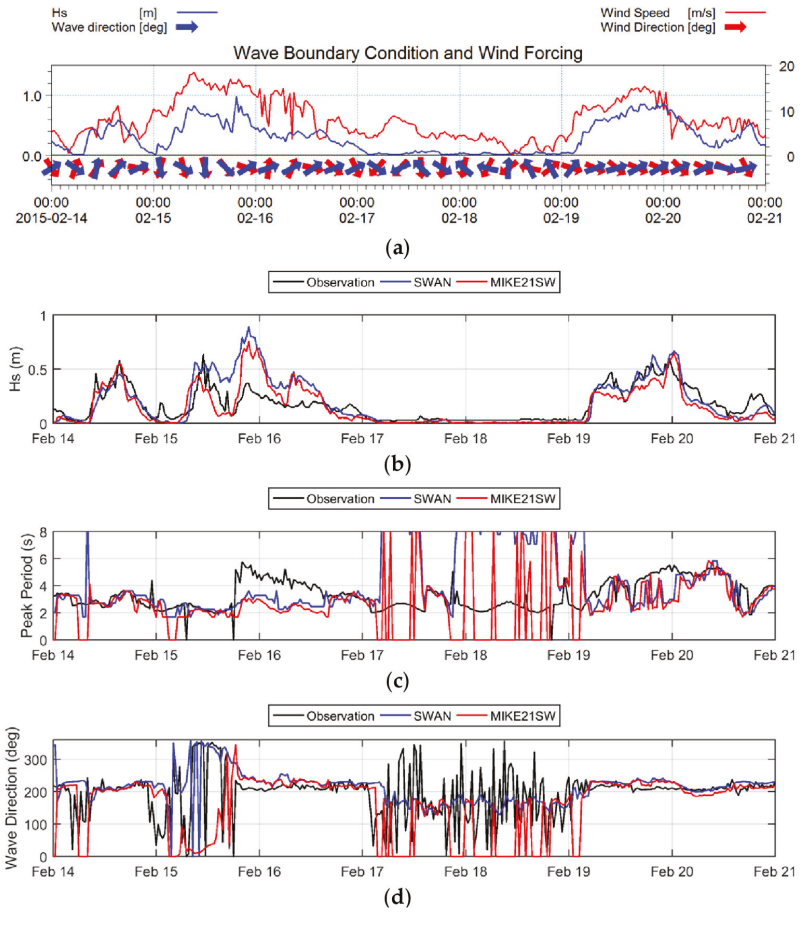

Figure 7. (**a**) Wave boundary condition and wind input for the time interval of 14 to 21 February. Blue: significant wave height (left axis), blue arrow: wave direction at the boundary, red: wind speed (right axis), red arrow: wind direction. (**b**–**d**) Comparison of SWAN (blue), MIKE21SW (red), and observation (black) at NH2 for the time interval of 14 to 21 February. (**b**) Significant wave height. (**c**) Peak wave period (**d**) Mean wave direction. During the second storm, when the wind direction changed from north to south to west to east, the simulations were poor.

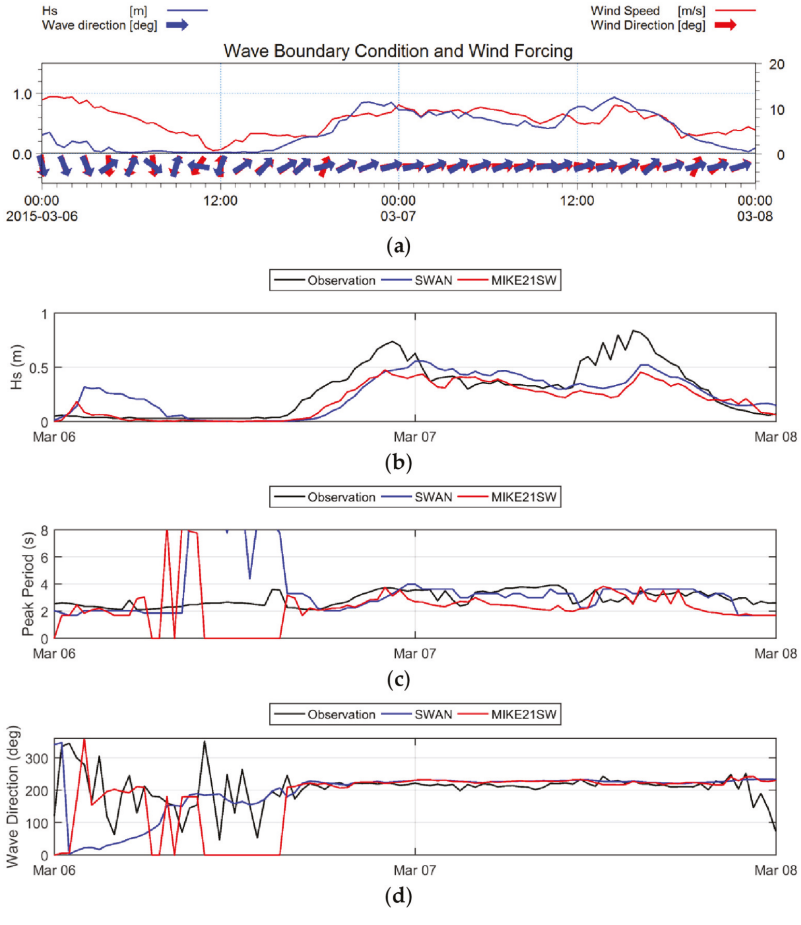

Figure 8. (**a**) Wave boundary condition and wind input for the time interval of 6 to 8 March. Blue: significant wave height (left axis), blue arrow: wave direction at the boundary, red: wind speed (right axis), red arrow: wind direction. (**b**–**d**) Comparison of SWAN (blue), MIKE21SW (red), and observation (black) at NH2 for the time interval of 6 to 8 March. (**b**) Significant wave height. (**c**) Peak wave period (**d**) Mean wave direction. Both models did not do well during this time interval. A two-hour delay in storm growth was significant in models results.

Results from Storm Period 5 are illustrated in Figure 9, showing the assessment of the models results during the storm took place on 2 and 3 April. MIKE21SW was able to catch the storms highest wave height and correctly computed wave period and direction during the storm. SWAN slightly underestimated the first part of the storm and there was a short delay in storm growth (Figure 9b). Statistical parameters were slightly better for MIKE21SW with R^2 = 0.81 versus SWAN results with R^2 = 0.77. *RMS* was better for MIKE21SW and the slope of best-fitted line was better for SWAN (Table 3).

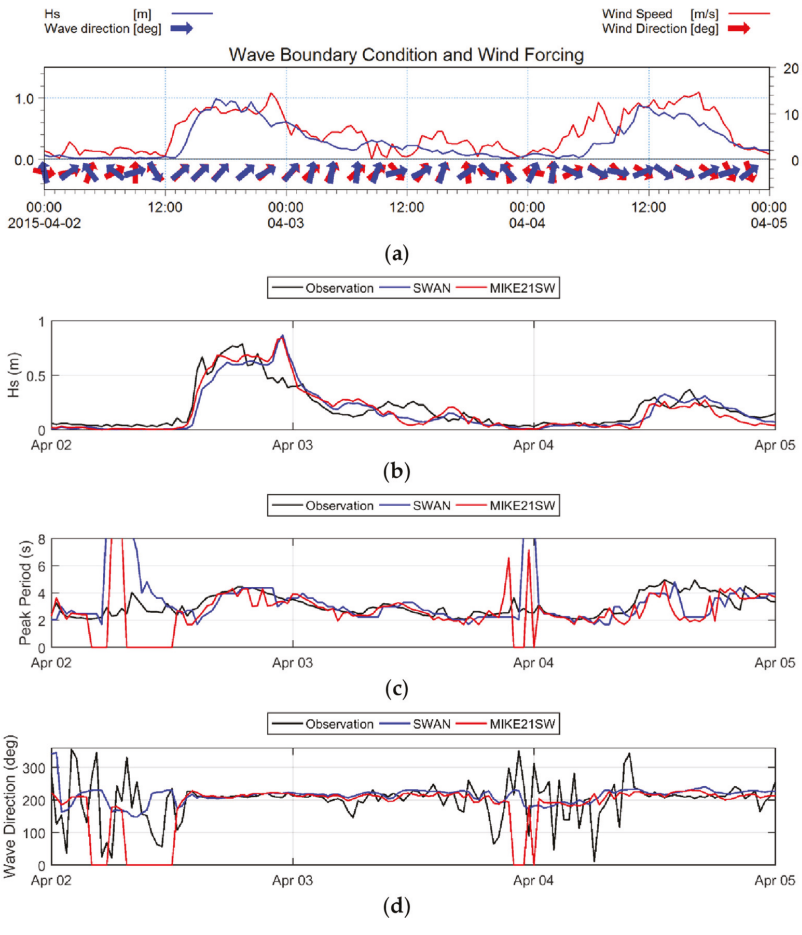

Figure 9. (**a**) Wave boundary condition and wind input for the time interval of 2 to 5 April. Blue: significant wave height (left axis), blue arrow: wave direction at the boundary, red: wind speed (right axis), red arrow: wind direction. (**b**–**d**) Comparison of SWAN (blue), MIKE21SW (red), and observation (black) at NH2 for the time interval of 2 to 5 April. (**b**) Significant wave height. (**c**) Peak wave period (**d**) Mean wave direction. Both models performed well for this storm period, but MIKE21SW was slightly better during the first part of the storm on 2 March.

We compare all storm simulations to data in Figure 10. *Bias* was better for SWAN. *RMS* of MIKE21SW was 0.01 lower than *RMS* obtained from SWAN results. The slope of best-fitted line for MIKE21SW was closer to one. R^2 of the models' results were almost the same, 0.61 for MIKE21SW versus 0.60 for SWAN. Therefore, the statistical parameters suggest the performance of both models were good and the models' results had a lot of similarity.

The model predictions did not agree with observation at NH2, inside the harbor, for two northerly storms, 27 January and 15 February. To assess whether the errors were due to the wind speed magnitude being too high, we compared the results of the models to data obtained at NH1, at the boundary of the model domain, (Figure 11). Note that since wave energy was propagating out of the domain during northerly wind the boundary observations were not influencing in the predictions. Both model results were biased high relative the observation at NH1 with the SWAN results having a larger bias (Figure 11a). However, both models were more correlated with observations at NH1

than at NH2. Both models did a better job for the second northerly event on 15 February. SWAN showed lower errors early in the simulation but both models overestimated the significant wave height later in the storm just as they did in the interior of the Harbor at NH2. This may be a consequence of overestimation of the wind stress, however, the reduced correlation in the model and data time series cannot be explained by the magnitude bias alone.

Table 3. Comparison of statically parameter between SWAN and MIKE21SW. Statistically, there was no substantial difference between the performances of the models. SWAN performance was better for the storm periods 23 to 28 January while MIKE21SW for 14 to 21 February and 2 to 5 April.

Storm Period	SWAN					MIKE21SW				
	n	*Bias*	*Rms*	*m*	R^2	*n*	*Bias*	*Rms*	*m*	R^2
23 to 28 January	241	−0.01	0.13	0.72	0.60	241	0.04	0.13	0.89	0.57
1 to 10 February	433	0.00	0.10	0.60	0.62	433	0.03	0.09	0.69	0.60
14 to 21 February	337	−0.02	0.14	0.55	0.60	337	0.02	0.11	0.66	0.61
6 to 8March	97	0.03	0.16	1.03	0.56	97	0.09	0.16	1.33	0.73
2 to 5 April	145	0.02	0.10	0.83	0.77	145	0.02	0.09	0.79	0.81
All Storms	1253	0.00	0.12	0.67	0.60	1253	0.03	0.11	0.79	0.61

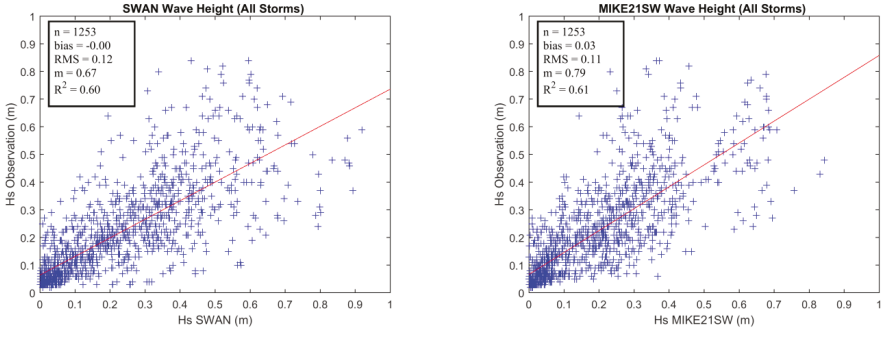

(a) (b)

Figure 10. Comparison of scatter plot and statically parameter between observed and simulated significant wave heights from SWAN (**a**) and MIKE21SW (**b**) for all storms. There was no substantial difference between the performance of the models. *Bias* was better for SWAN and *RMS*, the slope best fitted line and R^2 were better for MIKE21SW.

Figure 12 displays the variation of significant wave height over the model domain for three storms on 25 January (wind from the southwest), 27 January (wind from the north), and 2 February (wind from the southeast). Unfortunately, as the output format of the models were different, we were not able to plot them with the same tools, therefore, the color bars scales are slightly different. The models had similar behavior over the domain on the southern storms (Figure 12a,b), but different on the northern storm (Figure 12c,d). Also, it can be implied that MIKE21SW dissipates wave energy around the breakwaters more than SWAN, it may be the reason or the SWAN overestimation on 2 February.

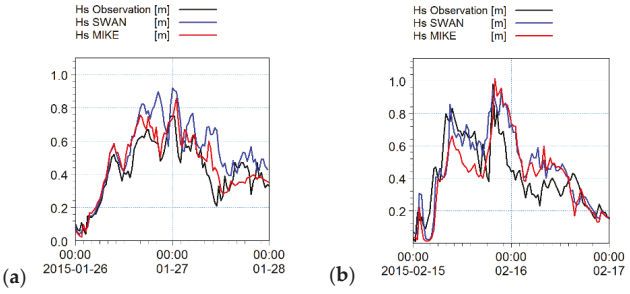

Figure 11. Comparison of significant wave height for two northerly storms at NH1 station outside the harbor. SWAN (blue), MIKE21SW (red), and observation (black) (**a**) 26 to 28 January. (**b**) 15 to 17 February.

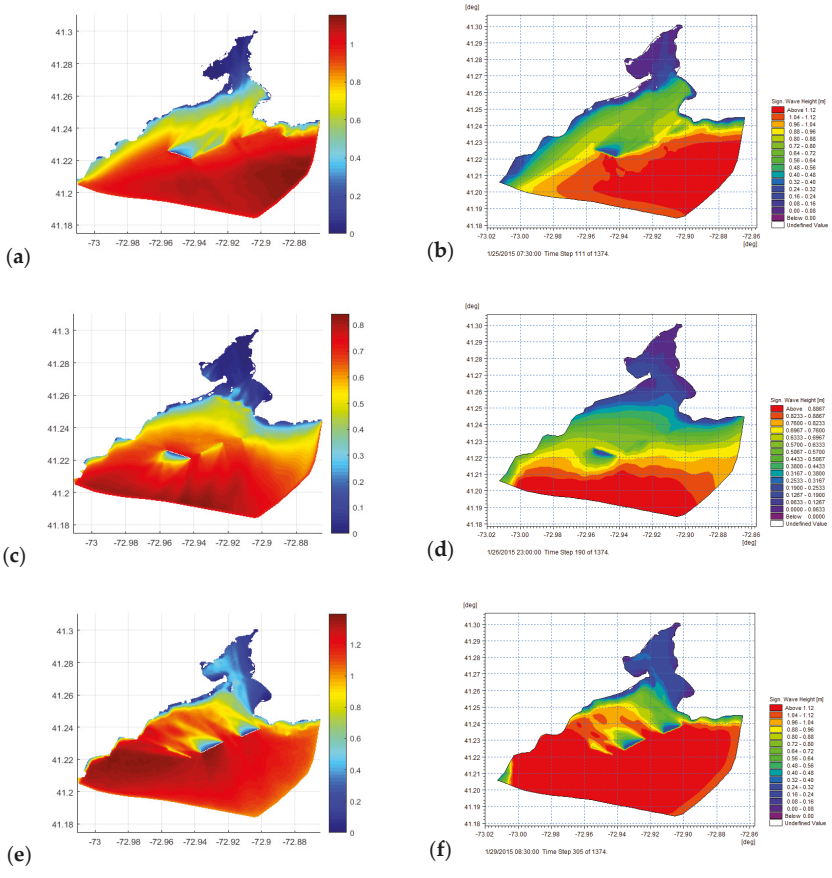

Figure 12. The variation of significant wave height over modeling domain for three main storms from the southwest, north, and southeast. (**a**) SWAN, 25 January, storm from the southwest; (**b**) MIKE21SW, 25 January, storm from the southwest; (**c**) SWAN, 27 January, storm from the north; (**d**) MIKE21SW, 27 January, storm from the north; (**e**) SWAN, 2 February, storm from the southeast; (**f**) MIKE21SW, 2 February, storm from the southeast. Note: the color bar scales are slightly different for SWAN and MIKE21SW, as they were plotted by different tools.

5. Discussion

In total, 14 storms occurred in New Haven harbor during the observation period in the winter of 2015 and the models simulated similar wave fields in most of them. Both models had very good statistical performance when storm winds blew from the south, when the breakwaters are most influential. SWAN predicted the peak significant wave height for one storm (on 18 February) better than MIKE21SW, while MIKE21SW simulated three storms (on 2 February, 15 February, and 3 April) better than SWAN. The worst performance during southerly wind storms was the SWAN results for 2 February when the model overestimated the peak significant wave height by 50%. Figure 12e suggest that the wave sensor was close to a region of high spatial gradient in the significant wave height during this storm and, therefore, slight differences in diffraction and propagation led to large differences in model solution values. The worst performance of MIKE21SW was on 18 February when the peak significant wave height was underestimated by 25%. In other storms the models had similar behavior. Notably, both models underestimated the storm peak on 7 March by 60%.

To further understand the sensitivity of the models results to different physical processes we ran the simulations with the wind forcing eliminated; zero reflection from the breakwaters; with diffraction disabled; and with the breakwaters entirely removed. Figure 13 shows the results of these simulations at NH2.

Figure 13a,d show the observations (+symbols) and solutions at NH2 for the 25 January storm with SWAN and MIKE21SW when the wind blew from the south. The agreement between the black lines and the +symbols shows that both models performed well. The differences between the black and blue lines shows that the influence of the wind over the harbor is significant and increases the peak significant wave height during the storm by 50%. Comparison of the black line to the magenta, green, and red lines show that the next most important process is the presence of the breakwaters. Eliminating them increases the peak significant wave height by approximately 15% in SWAN and 30% in MIKE21SW. Figure 13b,e shows the same properties for the 2 February storm period when the wind was from the south east. Since the performance of both models were not as good, due to high spatial gradients near the location of the wave sensor, the comparison of the result with (black line) and without local wind forcing (blue line) shows again that the local wind can increase the peak significant wave height by approximately 50%. Similarly, removing the breakwaters increases the peak wave heights as in Figure 13a,d, by comparable amounts. We note that the presence of breakwaters appears to be more significant in MIKE21SW than SWAN. The spatial distributions of wave height in Figure 12 also indicate this difference in model performance.

Comparison of the green and red lines with the black lines in Figure 13a,b,d,e illustrates that the effects of diffraction and reflection influenced the significant wave height at NH2 by less than 5 percent in both models. NH2 is approximately 2 km (or $40L$, where L is the dominant wave length) away from the breakwaters. This is consistent with [2] which concluded that reflection and diffraction effects are insignificant far away the breakwaters.

Figure 13c,f show the data and solutions for the 27 January storm when the wind was from the north. As expected, comparison of the black and blue lines shows that in the absence of wind forcing the significant wave height drops to zero. The other effects do not play a large role in the model predictions though reflection, also, has a maximum effect of 7%. These results highlight the importance of wind in this case study, which is a large harbor with fetch length varies from 5 km to 7 km.

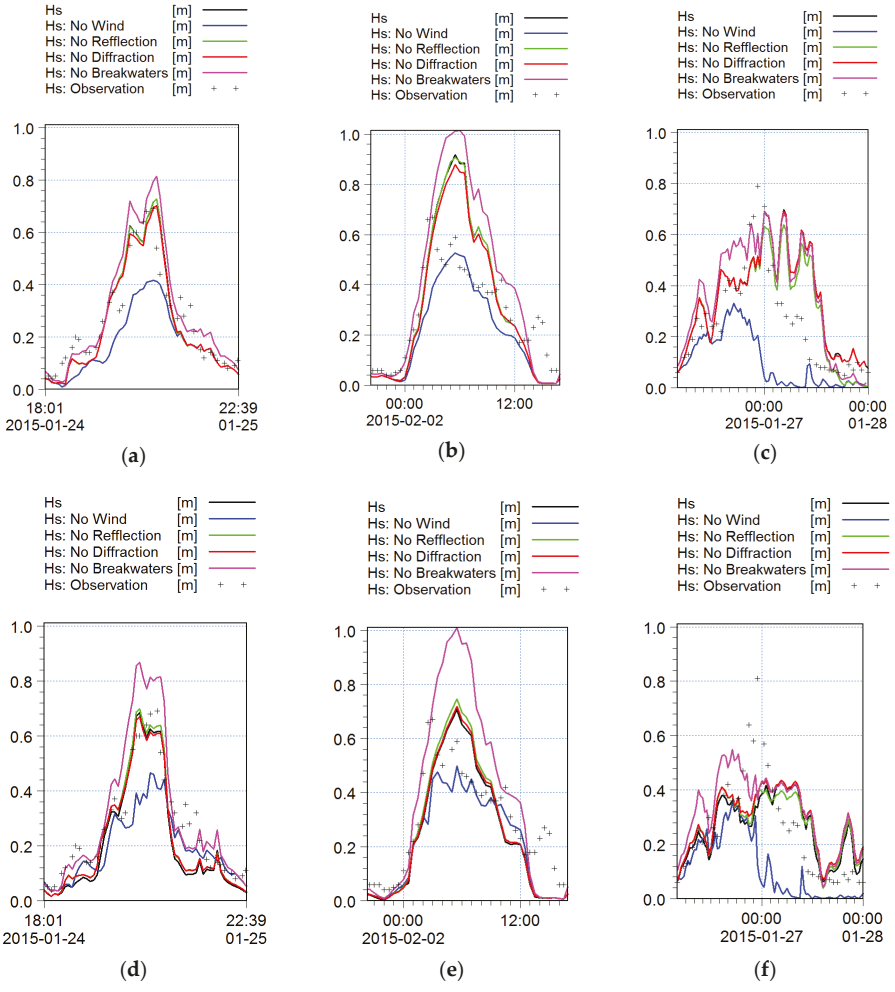

Figure 13. Sensitivity of the models to wind, reflection, diffraction module, and the breakwaters. Black: the model results considering all processes. Blue: The model results without wind forcing. Green: the model results without reflection from the breakwaters. Orange: the model results with disabling diffraction module. Pink: the model results with removing the breakwaters. (**a**) SWAN, 25 January; (**b**) SWAN, 2 February; (**c**) SWAN, 27 January; (**d**) MIKE21SW, 25 January; (**e**) MIKE21SW, 2 February; (**f**) MIKE21SW, 27 January.

In some events, such as 6 April and 6 March, a delay in the growth of the waves was observed in the models results, however, the delay in SWAN results was about one hour more than MIKE21SW results. There were three events (27 January, 5 February, and 15 February) with high winds from the north and the models did not deliver good simulations in two, 27 January and 15 February. These events were accompanied with 90-degree rotation of wind vectors during the storm. This inconsistency may be a consequence of the uncertainty in the difference between the wind observed at the buoy and that over the harbor. The wind observation station is located about 20 km away from the coastline. When wind blow from the coast (from the north), the wind boundary layer near the coastline become very complex. This complicity may not be observed at the wind station located 20 km away from the coastline. In addition, the significant wave height evaluation outside the harbor for northerly storms,

Figure 11, demonstrates that the models overestimate the significant wave height when winds were from the north. It implies that, for northern storms, winds at CLIS are more intensive than New Haven. Also, New Haven estuary has a complex geometry. Consequently, a small change in wind direction can change the fetch length drastically. For example, for NH2 station, a wind blowing from 10 degrees has more than double fetch length of the wind from the north, (Figure 1). The inconsistency of the models with observation for a very small fetch length with strong wind condition needs more investigation. This requires a local high frequency wind and wave observation to record precisely oscillation in wind speed and direction.

Another possible source of error is that a spectral wave model cannot simulate wave resonance due to reflected waves from the harbor edges and breakwaters. Figure 4b,d show spectra for 27 January and 15 February, when the models failed to accurately simulate the wave field, there were two waves, a low frequency wave from the south and high frequency waves propagating from the north. In this situation, reflection could have significant role. To observe these effects more accurately, multiple high frequency wave observation stations in the harbor would be required. The wave spectra shown in Figure 4 are not confined to a narrow range of directions and, in some events such as 2 February, the spectrum has multiple peaks. For this storm SWAN overestimated the wave height by 50%. Both models under-predicted significant wave heights during the storm on 7 March. In this event, the wave spectrum, also, have two peaks (Figure 4e). The models had good performance for the two-peak storm on 25 January, however, this storm had two peaks from the same direction but different frequency. The models may have lower accuracy in the events that the wave spectrum have multiple peaks at different directions, but that is not always the case as MIKE21SW well predicted the storm on 2 February with multiple spectrum peaks. Further investigation is required.

The influence of currents on waves was not considered in this study. Current can be considered in the modeling using a coupled hydrodynamic-wave models such as FVCOM-SWAVE, ADCIRC-SWAN, XBEACH [33,34], and MIKE21 Coupled Model. This effect should be considered in modeling in forthcoming studies. Another uncertainty in the results can be due to uncertainty in the model wave boundary condition. Though we used the observed wave spectra, instead of a model or parametrization, to prescribe the open boundary condition, it is possible that there are periods when there is variation in wave conditions along the boundary. Multiple wave sensors would be needed to assess that possibility and we hope to evaluate it in the future.

Besides the accuracy of the model, the efficiency and simplicity of the models are important in assessment of the model utility. SWAN is much more efficient computationally than MIKE21SW. SWAN executes the same model grid and configuration using the same computational engine much faster than MIKE21SW. Although SWAN is equipped with a fast-computational algorithm, the total computational time of the models in the optimum conditions was almost the same. SWAN requires much finer mesh to reach the optimum condition. In this study, the grid size of the mesh used for SWAN ($dx_{max} = 250$ m and $dx_{min} = 25$ m) was half of the grid size of the mesh used for MIKE21SW ($dx_{max} = 500$ m and $dx_{min} = 50$ m). Getting to the optimum condition with MIKE21SW was faster than SWAN. MIKE21SW automatically selects the optimum time step based on the grid size. User just needs to assign the minimum and maximum time steps. In addition, MIKE21SW showed less sensitivity to grid size than SWAN. Therefore, finding the optimum condition in MIKE21SW needs fewer number of sensitivity simulations than SWAN.

The time integration and spatial discretization method employed in SWAN and MIKE21SW play the main role in determining the differences in the results and efficiency. MIKE21SW uses an explicit Euler scheme for time integration with cell-centered finite volume when computing wave propagation while SWAN uses a fully implicit method for time integration with finite difference first order BSBT scheme. This study suggests that the method used in SWAN is computationally much faster but it is more sensitive to spatial resolution and requires much finer mesh.

The application of the spectral models for simulation of waves inside the harbor in the presence breakwater is questioned by some authors [1,2,35]. This implies that the spectral models are not suitable

for small ports with narrow connections to the ocean. However, in situations in which breakwaters have low reflection coefficients, are far enough the shoreline and do not shade a significant portion of the basin [1] spectral models may be useful as we have demonstrated in this work. In situ observations and sensitivity analyses are extremely valuable in assessing model effectiveness at all sites.

6. Conclusions

SWAN and MIKE21SW are two spectral wave models that solve the wave action balance equations. Although there are lots of similarities in both the main equations and wave source terms, they have some minor differences in the algorithms used to obtain solutions that impact both the results and efficiency of the models. SWAN and MIKE21SW were assessed on the unstructured grid and inside a harbor in the presence of three detached breakwaters. This study suggests the results of the models were consistent with observations during the storms which were affected by breakwaters. The R^2 was approximately 0.6 for both models. Considering the complexity of the modeling domain, the results are quite acceptable. The models behaved similarly in most events, MIKE21SW slightly better simulated significant wave height at storm peaks in some events. SWAN required the finer grid to get to the optimum condition, but as it uses the faster computational algorithm, the total computational time for their optimum condition was almost the same. MIKE21SW automatically selects the efficient time step based on grid size and it was less sensitive to grid size than SWAN. Therefore, the optimum condition of MIKE21SW was reached with fewer sensitivity simulations. Both models performed poorly for when high wind blew from the coast to sea. It is likely that this was a consequence of inadequate resolution of the wind field, though further observations and investigations will be required to fully understand that result. The sensitivity analysis demonstrates the wind effect was significant on the results due to large fetch length in the harbor. This is also the reason for using the spectral models for this case study. Also, it has been shown that, in MIKE21SW simulation, the breakwaters dissipate wave energy slightly more than the breakwaters in SWAN simulation.

Author Contributions: Conceptualization, A.I. and J.O.; Methodology, A.I.; Software, A.I..; Validation, A.I. and J.O.; Formal Analysis, A.I.; Investigation, A.I. and J.O.; Resources, A.I.; Writing—Original Draft Preparation, A.I.; Writing—Review & Editing, A.I. and J.O.; Visualization, A.I.; Supervision, J.O.; Project Administration, J.O.; Funding Acquisition, J.O.

Funding: The observations in this research were funded by NOAA and the Connecticut Department of Energy and Environmental Protection.

Acknowledgments: We are grateful to DHI for providing us with the MIKE21 package, and TU Delft for making SWAN open source. Connecticut Institute for Resilience and Climate Adaptation (CIRCA) supported the observations with funding from NOAA and the Connecticut Department of Energy and Environmental Protection. We are also grateful to Kay Howard-Strobel, Ale Cifuentes, and Molly James for valuable technical assistance.

Conflicts of Interest: The authors declare no conflict of interest.

References

1. Holthuijsen, L.H.; Herman, A.; Booij, N. Phase-decoupled refraction-diffraction for spectral wave models. *Coast. Eng.* **2003**, *49*, 291–305. [CrossRef]
2. Boshek, M.R. Reflection and Diffraction around Breakwaters. Master's Thesis, Delft University of Technology, Department of Hydraulic Engineering, Delft, The Netherlands, 2009.
3. Dietrich, J.C.; Tanaka, S.; Westerink, J.J.; Dawson, C.N.; Luettich, R.A., Jr.; Zijlema, M.; Holthuijsen, L.H.; Smith, J.M.; Westerink, L.G.; Westerink, H.J. Performance of the Unstructured-Mesh, SWAN+ADCIRC Model in Computing Hurricane Waves and Surge. *J. Sci. Comput.* **2012**, *52*, 468–497. [CrossRef]
4. Zijlema, M. Parallel, unstructured mesh implementation for SWAN. *Coast. Eng.* **2009**, *5*, 470–482. [CrossRef]
5. Strauss, D.; Mirferendesk, H.; Tomlinson, R. Comparison of two wave models for Gold Coast, Australia. *J. Coast. Res.* **2007**, *50*, 312–316.
6. Moeini, M.H.; Etemad-Shahidi, A. Application of two numerical models for wave hindcasting in Lake Erie. *Appl. Ocean Res.* **2007**, *29*, 137–145. [CrossRef]

7. Fonseca, R.B.; Gonçalves, M.; Guedes Soares, C. Comparing the Performance of Spectral Wave Models for Coastal Areas. *J. Coast. Res.* **2017**, *33*, 331–346. [CrossRef]
8. Hoque, M.A.; Perrie, W.; Solomon, S.M. Evaluation of two spectral wave models for wave hindcasting in the Mackenzie Delta. *Appl. Ocean Res.* **2017**, *62*, 169–180. [CrossRef]
9. Booij, N.; Ris, R.C.; Holthuijsen, L.H. A third-generation wave model for coastal regions: 1. model description and validation. *J. Geophys. Res. Oceans* **1999**, *104*, 7649–7666. [CrossRef]
10. DHI group. *MIKE 21 Spectral Wave Module. Scientific Documentation*; Danish Hydraulic Institute (DHI): Hørsholm, Denmark, 2017; 56p.
11. Mei, C.C. *The Applied Dynamics of Ocean Surface Waves*; Volume 1 of Advanced Series on Ocean Engineering; World Scientific: Singapore, 1989; ISBN 9971507897.
12. Komen, G.J.; Cavaleri, L.; Donelan, M.; Hasselmann, K.; Hasselmann, S.; Janssen, P.A.E.M. *Dynamics and Modelling of Ocean Waves*; Cambridge University Press: Cambridge, UK, 1994.
13. Young, I.R. *Wind Generated Ocean Waves, Elsevier Ocean Engineering Series*, 1st ed.; Bhattacharyya, R., McCormick, M.E., Eds.; Elsevier: Amsterdam, The Netherlands, 1999; Volume 2, ISBN 9780080433172.
14. SWAN team. *Swan Scientific and Technical Documentation*; Delft University of Technology: Delft, The Netherlands, 2018; 147p.
15. Janssen, P.A.E.M. Wave-Induced Stress and the Drag of Air Flow over Sea Waves. *J. Phys. Oceanogr.* **1989**, *19*, 745–754. [CrossRef]
16. Janssen, P.A.E.M. Quasi-linear Theory of Wind-Wave Generation Applied to Wave Forecasting. *J. Phys. Oceanogr.* **1991**, *21*, 1631–1642. [CrossRef]
17. Gunther, H.; Hasselmann, S.; Janssen, P.A.E.M. *The WAM Model Cycle 4 (Revised Version)*; Deutsch. Klim. Rechenzentrum, Techn. Rep. No. 4; Deutsches Klimarechenzentrum: Hamburg, Germany, 1992.
18. Komen, G.J.; Hasselmann, K.; Hasselmann, K. On the Existence of a Fully Developed Wind-Sea Spectrum. *J. Phys. Oceanogr.* **1984**, *14*, 1271–1285. [CrossRef]
19. WAMDI Group. The WAM Model—A Third Generation Ocean Wave Prediction Model. *J. Phys. Oceanogr.* **1988**, *18*, 1775–1810. [CrossRef]
20. Yan, L. *An Improved Wind Input Source Term for Third Generation Ocean Wave Modelling*; Scientific report WR-No 87-8; Royal Netherlands Meteorological Inst.: De Bilt, The Netherlands, 1984.
21. Hasselmann, K. On the spectral dissipation of ocean waves due to white capping. *Bound. Layer Meteorol.* **1974**, *6*, 107–127. [CrossRef]
22. Van der Westhuysen, A.J. Advances in the Spectral Modelling of Wind Waves in the Nearshore. Ph.D. Thesis, Delft University of Technology, Department of Civil Engineering, Delft, The Netherlands, 2007.
23. Van der Westhuysen, A.J.; Zijlema, M.; Battjes, J.A. Nonlinear saturation-based whitecapping dissipation in SWAN for deep and shallow water. *Coast. Eng.* **2007**, *54*, 151–170. [CrossRef]
24. Hasselmann, K.; Barnett, T.P.; Bouws, E.; Carlson, H.; Cartwright, D.E.; Enke, K.; Ewing, J.A.; Gienapp, H.; Hasselmann, D.E.; Kruseman, P.; et al. *Measurements of Wind-Wave Growth and Swell Decay during the Joint North Sea Wave Project (JONSWAP)*; Ergänzungsheft 8–12; Deutches Hydrographisches Institut: Hamburg, Germany, 1973.
25. Zijlema, M.; van Vledder, G.P.; Holthuijsen, L.H. Bottom friction and wind drag for wave models. *Coast. Eng.* **2012**, *65*, 19–26. [CrossRef]
26. Battjes, J.A.; Janssen, J.P.F.M. Energy loss and set-up due to breaking of random waves. In Proceedings of the 16th International Conference Coastal Engineering, Hamburg, Germany, 27 August–3 September 1978; pp. 569–587. [CrossRef]
27. Eldeberky, Y.; Battjes, J.A. Parameterization of triad interactions in wave energy models. In Proceedings of the Coastal Dynamics Conference '95, Gdansk, Poland, 4–8 September 1995; pp. 140–148.
28. Eldeberky, Y. Nonlinear Transformation of Wave Spectra in the Nearshore Zone. Ph.D. Thesis, Delft University of Technology, Department of Civil Engineering, Delft, The Netherlands, 1996.
29. Hasselmann, S.; Hasselmann, K.; Allender, J.H.; Barnett, T.P. Computations and Parameterizations of the Nonlinear Energy Transfer in a Gravity-Wave Specturm. Part II: Parameterizations of the Nonlinear Energy Transfer for Application in Wave Models. *J. Phys. Oceanogr.* **1985**, *15*, 1378–1391. [CrossRef]
30. U.S. Army Corps of Engineers. *Coastal Engineering Manual Part VI*; Books Express Publishing: Newbury, UK, 2012.

31. Seelig, W.N. Wave Reflection from Coastal Structures. In Proceedings of the Coastal Structures '83, Arlington, Virginia, 9–11 March 1983; American Society of Civil Engineers: Reston, VA, USA; pp. 961–973.
32. Davidson, M.A.; Bird, P.A.; Bullock, G.N.; Huntley, D.A. Wave Reflection: Field Measurements, Analysis and Theoretical Developments. In Proceedings of the Coastal Dynamics '94, Barcelona, Spain, 21–25 February 1994; American Society of Civil Engineers: Reston, VA, USA; pp. 642–655.
33. Sánchez-Arcilla, A.; García-León, M.; Gracia, V. Hydro morphodynamic modelling in Mediterranean storms: Errors and uncertainties under sharp gradients. *Nat. Hazards Earth Syst. Sci.* **2014**, *14*, 2993–3004. [CrossRef]
34. Gracia, V.; García-León, M.; Grifoll, M.; Sánchez-Arcilla, A. Breaching of a barrier under extreme events: The role of morphodynamic simulations. *J. Coast. Res.* **2013**, *65*, 951–956. [CrossRef]
35. Booij, N.; Holthuijsen, L.H.; de Lange, P.H.M. The penetration of short-crested waves through a gap. In Proceedings of the 23rd International Conference on Coastal Engineering, Venice, Italy, 4–9 October 1992; pp. 1044–1052.

Journal of
Marine Science and Engineering

MDPI

Article

Sediment Transport Model Including Short-Lived Radioisotopes: Model Description and Idealized Test Cases

Justin J. Birchler [1,2,*], Courtney K. Harris [1], Christopher R. Sherwood [3] and Tara A. Kniskern [1]

[1] Virginia Institute of Marine Science, College of William & Mary, Gloucester Point, VA 23062, USA; ckharris@vims.edu (C.K.H.); knista@vims.edu (T.A.K.)
[2] U.S. Geological Survey, Saint Petersburg, FL 33701, USA
[3] U.S. Geological Survey, Woods Hole, MA 02543, USA; csherwood@usgs.gov
* Correspondence: jbirchler@usgs.gov; Tel.: +1-727-502-8019

Received: 1 October 2018; Accepted: 24 November 2018; Published: 27 November 2018

Abstract: Geochronologies derived from sediment cores in coastal locations are often used to infer event bed characteristics such as deposit thicknesses and accumulation rates. Such studies commonly use naturally occurring, short-lived radioisotopes, such as Beryllium-7 (^{7}Be) and Thorium-234 (^{234}Th), to study depositional and post-depositional processes. These radioisotope activities, however, are not generally represented in sediment transport models that characterize coastal flood and storm deposition with grain size patterns and deposit thicknesses. We modified the Community Sediment Transport Modeling System (CSTMS) to account for reactive tracers and used this capability to represent the behavior of these short-lived radioisotopes on the sediment bed. This paper describes the model and presents results from a set of idealized, one-dimensional (vertical) test cases. The model configuration represented fluvial deposition followed by periods of episodic storm resuspension. Sensitivity tests explored the influence on seabed radioisotope profiles by the intensities of bioturbation and wave resuspension and the thickness of fluvial deposits. The intensity of biodiffusion affected the persistence of fluvial event beds as evidenced by ^{7}Be. Both resuspension and biodiffusion increased the modeled seabed inventory of ^{234}Th. A thick fluvial deposit increased the seabed inventory of ^{7}Be and ^{234}Th but mixing over time greatly reduced the difference in inventory of ^{234}Th in fluvial deposits of different thicknesses.

Keywords: numerical model; sediment transport; marine; short-lived radioisotopes

1. Introduction

Radioisotopic tracers, such as Beryllium-7 (^{7}Be) and Thorium-234 (^{234}Th) have been used to characterize sediment provenance, transport pathways, deposition, and biological mixing for numerous marine environments [1], including estuaries (e.g., [2–4]) and continental shelves adjacent to rivers (e.g., [5–7]). Both ^{7}Be and ^{234}Th are highly particle-reactive and therefore useful as tracers of sediment processes [8,9]. In river-dominated sedimentary environments, precipitation and subsequent river runoff can supply ^{7}Be-laden sediments to coastal waters, so researchers have inferred that seabed sediment with significant ^{7}Be activities contained recent terrestrial material [5,6,9–11]. Additionally, the decay profile of ^{7}Be has been used to infer seabed mixing coefficients [9,12]. Th-234 is continuously produced in the coastal ocean via decay of its parent Uranium-238 [6,13,14]. It has been used both as a tracer of biological mixing intensity [15,16] and an indicator of recent deposition of (re-)suspended material [6,13]. Given the short half-lives of ^{7}Be and ^{234}Th, 53.3 and 24.1 days, respectively, these radioisotopes provide useful indicators of processes that occurred over the last 100–250 days [9,11,13,14].

Several factors influence sediment bed profiles of radioisotopic tracers, including source terms; physical and biological mixing within the seabed; and time-scales of deposition, erosion, burial, and radioisotope decay [1,5,17]. For example, ^{7}Be deposition from the atmosphere depends on seasonality of both precipitation and atmospheric inventory [18]. Scavenging of ^{234}Th from the water column is more likely under high suspended sediment concentrations, such as during elevated river discharges or high wave energy, which both vary seasonally and with weather [6,19]. Sediment bed surface activities of ^{7}Be in continental shelf environments range from 1 to 10 disintegrations per minute per gram of sediment (dpm g^{-1}) and for ^{234}Th range from 10 to 80 dpm g^{-1} [5,6,19,20]. Specific activities of suspended sediments range from 0 to 50 dpm g^{-1} for ^{7}Be and 15 to 115 dpm g^{-1} for ^{234}Th under near oceanic salinities [2,3].

Bioturbation modifies the physical, chemical, and biological properties of sediment and can alter the radioisotope signal within surficial sediment deposits [12,16,17,21]. Upper continental shelf bioturbation rates are 10–100 cm^{2} yr^{-1} depending on water depth, seasonal conditions, location, and the specific radioisotope tracer used to infer them [12,17,22]. Many studies have estimated deposition and flood sediment budgets based on analysis of radioisotopic data (e.g., [6,7,9,23,24]). Additionally, deposition and mixing of seafloor sediment frequently occur at the same time, complicating the interpretation of radionuclide activity profiles within the seabed [17,23–26]. Although radioisotopes are useful tools for quantifying rates of biological mixing and short-term deposition, the complex combinations of processes can yield ambiguity in the interpretation of activity-depth profiles.

Numerical models have long promised to help improve our interpretations of radioisotopic profiles, but few models have directly represented the underlying physical and biological processes that shape activity-depth profiles. A previous study used a one-dimensional sedimentation–bioturbation model to estimate the fraction of the original unit volume of the seabed that retained its primary depositional fabric, defining this "the preservation quotient" [27]. The model included changes to the preservation quotient via depositional events and bioturbation processes, but neglected physical mixing, erosion, consolidation, and temporal variability [27]. Other researchers used a two-dimensional numerical model to represent gravity-driven sediment transport and deposition on the Waiapu shelf, New Zealand (NZ) [28]. The fluvial deposit thickness was multiplied by a decay factor to characterize a relative ^{7}Be activity within the simulated flood deposit, which was then compared to available ^{7}Be observations on the shelf [28,29]. Neither of these examples, however, directly modeled the seabed behavior of the radioisotopes.

More typically, three-dimensional sediment transport models simply calculate erosion and deposition, changes to sediment deposit thickness, and grain size distributions (e.g., [30–32]). Such calculations, however, are difficult to directly relate to radioisotopic records, even for cases where the models resolve both the temporal scales (i.e., event to seasonal timescales), and spatial scales (i.e., ~centimeter-scale sediment bed layers) at which the radioisotopic tracers are observed. For example, radioisotopic evidence of flood deposition for the Waipaoa shelf, NZ [7] was compared to model estimates for the same flood, but the modeled deposits were thinner than those inferred from the penetration depth of ^{7}Be [33]. The mismatch was attributed to uncertainties related to sampling resolution, spatial patchiness in deposition, and physical and biological mixing of the radioisotope in the seabed [33]. Similarly, ^{7}Be was used to identify flood deposit geometry and mass from Tropical Storm Lee in the Chesapeake Bay, and those observations compared favorably with model simulations of sediment dynamics for the event [34]. These modeled estimates of sediment reworking and deposition attempted to reproduce the observed scales of storm seabed-layer thickness subsequent to the peak storm erosion. However, there remains some ambiguity in the interpretation of observed seabed activity profiles because they also reflect downward mixing via physical reworking and biodiffusion that were unaccounted for in the model.

There is therefore a disconnect between the sediment transport models, which calculate sediment deposit thicknesses, and observations based on radioisotopic data which reflect deposition along with physical mixing and bioturbation. To our knowledge, no numerical sediment transport model

has incorporated radioisotopic tracers, which would provide an obvious direct comparison to field observations. Additionally, few numerical sediment transport models include seabed mixing via bioturbation, which is necessary to directly compare modeled tracer profiles with seabed observations. Incorporating these processes into a numerical sediment transport model would help strengthen the ability to directly compare the modeled values and observations.

We modified a coupled sediment-transport and hydrodynamic model to account for the transport and decay of radioisotopes that were represented as reactive tracers in the water column and seabed. This paper describes the implementation of reactive tracers in the sediment-transport model and demonstrates the representation of short-lived radioisotopes in one-dimensional test cases of fluvial deposition and wave resuspension.

2. Materials and Methods

Radioisotopes were represented as reactive tracers in the water column and on the seabed through modifications to the Community Sediment Transport Modeling System (CSTMS) [32]. This section describes the model and the modifications that account for short-lived radioisotopes. It then outlines the one-dimensional (vertical), idealized model of fluvial deposition and wave resuspension used to demonstrate the model's representation of short-lived radioisotopes.

2.1. Adding Reactive Tracers to the CSTMS

The CSTMS [32] operates as a module within the Regional Ocean Modeling System (ROMS; see [35,36]). Within the ocean modeling literature, a tracer refers to a dissolved or particulate scalar quantity that is transported by oceanic flows. Within ROMS, tracers are used to calculate the time-dependent, spatially varying fields of temperature and salinity. ROMS also uses tracers to track concentrations of sediment classes when the sediment module is used [32]; and biochemical constituents (oxygen, phytoplankton, etc.) when the biogeochemical module is used (e.g., [37]). These concentration fields are updated by solving mass balance equations that may include reactive terms for biogeochemical tracers [35,36]. Until recently, however, all implementations of the CSTMS assumed that the sediment classes acted as conservative tracers, so that their water-column concentrations were updated using the transport equation, with erosion and deposition terms for sources and sinks, and no reaction terms.

The sediment model uses tracers to account for a user-specified number of sediment classes (typically size classes) and represents grain size distributions on the seafloor using a user-specified number of sediment bed layers [32,38]. As a model run progresses, bed layer thicknesses and grain size distributions are adjusted to account for erosion and deposition. Additionally, changes to the thickness of the active transport layer, the layer of sediment at the seabed surface available for erosion [39], can modify the surficial bed characteristics. The non-cohesive sediment transport model used here [32] assumes that the active transport layer usually thickens during times of high excess bed shear stress [39], however, the parameter governing the thickness of the active transport layer is poorly constrained. The model also represents bed armoring, which occurs when the more mobile sediment (lower critical shear stresses and settling velocities) has been eroded; leaving the less mobile sediment (higher critical shear stresses and settling velocities) on the bed to form a lag layer that shelters underlying fine sediment from being entrained into the water column (e.g., [40]).

CSTMS applications commonly treat sediment as a conservative tracer, where the only sources and sinks of sediment are at open boundaries and the sediment bed [32]. Sediment resuspension can be stated as a one-dimensional (vertical) mass balance equation:

$$\frac{\partial c_{s,i}}{\partial t} = \frac{\partial}{\partial z}\left(w_{s,i}c_{s,i} - K_z\frac{\partial c_{s,i}}{\partial z}\right) + S_i, \quad (1)$$

where z is the vertical coordinate for height above the seafloor (m, positive upwards); K_z is eddy viscosity ($m^2\ s^{-1}$); $w_{s,i}$ is settling velocity ($m\ s^{-1}$); $c_{s,i}$ is the concentration ($kg\ m^{-3}$); and i designates the

sediment class (Figure 1). S_i accounts for external sources or sinks of sediment. Typically, S_i includes fluxes into and out of the bottom cell to account for erosion and deposition. Note that the actual mass balance equation used in ROMS is three-dimensional and discretized for the model coordinate system.

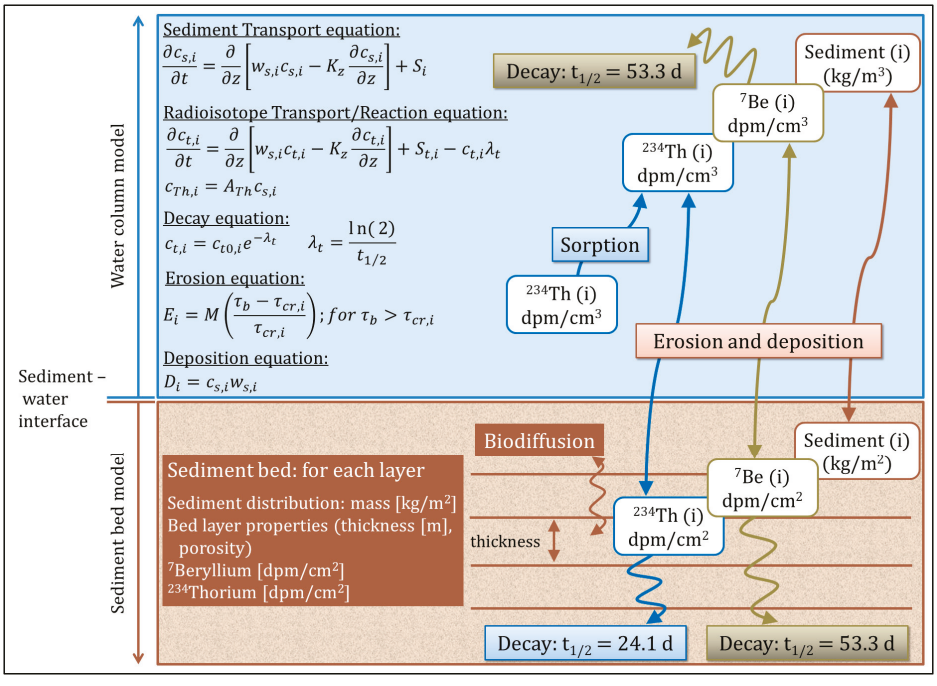

Figure 1. Schematics of the sediment transport and geochronology model. Water column layers (blue) overlie seabed layers (brown) of variable thickness. Shaded boxes indicate processes; white boxes indicate state variables (tracers).

The sediment transport model has recently been enhanced to include reactive tracers whose transport equation includes reaction terms that represent geochemical processes that change (or exchange) quantities in tracer classes [38,41]. Reactive tracer quantities are transported in the water column at the same rate as associated water parcels or sediment with equivalent settling and erosion properties, so they can shadow a water mass or specific sediment class. The sediment bed model was also modified so that reactive tracers could be stored on the sediment bed and undergo exchanges between the water column and seabed. A recent application has used reaction terms to account for both particulate and dissolved geochemically reactive tracers in the seabed and the water column to evaluate the role of resuspension in biogeochemical cycles [42]. Here, we use a similar approach to simulate the transport, deposition, and decay of ^{7}Be and ^{234}Th (Figure 1), as described in the next section.

The one-dimensional (vertical) activity balance equation for a radioisotope is:

$$\frac{\partial c_{t,i}}{\partial t} = \frac{\partial}{\partial z}\left[w_{s,i}c_{t,i} - K_z\frac{\partial c_{t,i}}{\partial z}\right] + S_{t,i} - c_{t,i}\lambda_t \quad (2)$$

where $c_{t,i}$ is suspended tracer concentration (dpm m^{-3}), $w_{s,i}$ is the settling velocity (m s^{-1}), K_z is eddy viscosity (m^2 s^{-1}), $S_{t,i}$ is the source/sink term of tracer concentration associated with the sediment class, and λ_t is the tracer decay constant (s^{-1}). The index, i, denotes the sediment class to which this tracer is associated; while the index, t, denotes the reactive tracer. Aside from decay, tracers were

assumed to remain associated with the sediment particles, due to the high particle-reactive nature of the tracers, so that desorption was neglected [1,8,9]. This behavior is consistent with previous studies in shelf environments (e.g., [8,43,44]). Because the transport terms ($w_{s,i}$, K_z, and S_i) act identically on the tracer class and the associated sediment class, this equation links the tracer activity to the mass concentration of the sediment class.

The boundary conditions for ^{7}Be and ^{234}Th were modified to represent their behavior in coastal environments. In our conceptual model, ^{7}Be on river-dominated shelves is associated with fresh sediment delivered by fluvial input and is not significantly influenced by local atmospheric fallout [5]. We represented this by initializing the numerical model with sediment in suspension, notionally delivered by a fluvial source, and assigning this sediment a user-specified ^{7}Be activity reflecting the fluvial provenance. As the model ran forward in time, ^{7}Be activities behaved according to Equation (2) as ^{7}Be-associated sediment settled, deposited, and possibly was resuspended. Th-234 was treated differently. Our conceptual model was that ^{234}Th is produced in seawater and scavenged by suspended particles [13,14]. We represented this in the numerical model by maintaining at a constant level the activity levels of ^{234}Th associated with suspended sediment. In our model, $c_{Th,i} = A_{Th}c_{s,i}$ (Figure 1); where A_{Th} was the assumed activity of suspended sediment (dpm kg^{-1}) and $c_{s,i}$ was the suspended sediment concentration (kg m^{-3}). This approach was equivalent to assuming that the activity of any sediment in suspension immediately equilibrates to the level driven by local seawater activity. This assumes that equilibration in the model occurs over much shorter timescales than the timescales of typical resuspension events and natural removal of ^{234}Th by sediment, which occurs on the order of days and is dependent on the amount of sediment resuspension [3,19,43]. Once sediment carrying ^{234}Th enters the sediment bed, activities begin to decay. Through these treatments of the activities of ^{7}Be and ^{234}Th, we can characterize their behavior in a coastal ocean environment with river input and episodic resuspension.

The model tracked sediment mass and reactive tracer activities in terms of concentration (kg m^{-3} and dpm m^{-3}) in each grid cell of the water column, and as layer-integrated quantities (km m^{-2} and dpm m^{-2}) in each sediment bed layer. Erosion and deposition had corresponding influences on the inventory of radioisotope tracers and associated sediment in the water column and sediment bed. During erosion, reactive tracers linked to sediment classes were removed from the surface sediment layer (i.e., the active transport layer) and added to the water column. During deposition, reactive tracers linked to sediment were removed from the water column and returned to the surface sediment bed layer.

When the bed shear stress (τ_b, Pascals, Pa) exceeds the critical shear stress ($\tau_{cr,i}$, Pa), the model estimates a sediment entrainment rate for each sediment class (i) proportional to the excess shear stress ($S = \tau_b - \tau_{cr,i}$) following the sediment entrainment equation [32]:

$$E_i = M\left(\frac{\tau_b - \tau_{cr,i}}{\tau_{cr,i}}\right), \quad (3)$$

where E_i is the entrainment rate (kg m^{-2} s^{-1}), M is the erosion rate parameter (kg m^{-2} s^{-1}), and i denotes the sediment class to which this tracer is associated. The model assumes simultaneous erosion and deposition (Figure 1), with the deposition equal to the settling flux [32]:

$$D_i = c_{s,i}w_{s,i}, \quad (4)$$

where D_i is the deposition rate (kg m^{-2} s^{-1}) and $c_{s,i}$ is the suspended-sediment concentration (kg m^{-3}) in the bottommost grid cell. Like most implementations of the CSTMS, we assumed that the hydrodynamic properties of sediment (i.e., settling velocity $w_{s,i}$ and critical shear stress for motion $\tau_{cr,i}$) remain fixed for each sediment class [32]. This neglects aggregation and disaggregation; settling velocities are fixed for each class because there is no exchange between sediment classes; though these have recently been included in other versions of the CSTMS [38].

We also modified the CSTMS sediment bed model to better represent stratigraphic processes that affect the distribution of radioisotopes in the seabed. The default sediment bed-layering scheme created new bed layers by dividing the bottom layer in half [32]. This can lead to having thick layers near the bed surface, and exponentially thinner layers with depth, so as in our recent work, we modified the scheme to form new layers by peeling off a thin layer from the bottom layer [38,41]. Additionally, we added biodiffusive mixing between bed layers of tracer concentrations and sediment types using a depth-dependent biodiffusion coefficient (see [38]). The biodiffusion coefficient, D_b, generally decreased with depth in the bed until it reached a small value specified in the input files.

Numerical solution of the tracer conservation equations was verified by comparison with the analytical equation for pure decay of initial activity (no erosion, deposition, or mixing) [45,46]. Using typical values for radioisotope activities and decay constants, burial rates, burial depths, and time scales; the model results were found to match analytical solutions [45,46] within 0.1 percent.

2.2. Idealized Test Case: Model Implementation

This paper presents simulations that explore behavior of the radioisotope tracers within a one-dimensional (vertical) model that represents the water column and underlying sediment bed (Figure 1). Configured similarly to a previously published model [38], our implementation included deposition of a thin fluvial layer and subsequent reworking via idealized storm forcing. Compared to the Standard Model Case, other runs varied parameters to explore sensitivity to the biodiffusion coefficient, resuspension intensity (maximum bed shear stress), and flood deposit thickness. For full details of the model implementation, model code, and input and output files, see the archive [47].

Specifically, the one-dimensional model represented a 20-m deep site using 30 water column layers. Several parameters were based on those used within a three-dimensional ROMS model for the northern Gulf of Mexico [48], including seabed porosity (0.8), and erosion rate parameter (M; 1×10^{-5} kg m^{-2} s^{-1}). The sediment model included three classes: fine (micro-floc), medium (macro-floc), and coarse (sand) with equivalent grain diameters of 15, 63, and 125 micrometers (μm), respectively. These sediment classes assumed a quartz density (2650 kg m^{-3}) and had critical shear stresses set to 0.03, 0.08, and 0.1 Pa; and settling velocities of 0.01, 0.1, and 1.0 cm s^{-1}, respectively. The two fine classes represented micro-flocs and macro-flocs, though this version of the model neglected flocculation processes; i.e., the hydrodynamic properties of each class remained fixed and mass was not exchanged between classes. Radioisotopes ^{7}Be and ^{234}Th were linked to the two fine classes and assigned decay constants of $\lambda_{Be} = 1.51 \times 10^{-7}$ s^{-1} and $\lambda_{Th} = 3.33 \times 10^{-7}$ s^{-1}. The radionuclide adsorption properties were assumed identical for the fine and medium classes.

The upper 10 cm of the sediment bed were represented using 40 sediment layers, most of which were ~5 mm thick. The initial sediment bed grain size distribution was assumed uniform with depth. Unless otherwise specified, biodiffusion occurred throughout the model runs. The biodiffusion coefficient was assumed to vary with depth [38]; for the Standard Case it was set to be 1 cm^2 yr^{-1} from the sediment–water interface to a depth of 3 cm, then decreased linearly between 3 to 6 cm below the sediment–water interface. Below 6 cm, it was held constant at 0.02 cm^2 yr^{-1}.

The water column initially carried suspended concentrations of 0.1 kg m^{-3} for each of the two finest sediment classes, which were tagged with radioisotopes having specific activities of both ^{7}Be and ^{234}Th of 5 dpm g^{-1}, a reasonable value for continental shelves (see Introduction). This material settled out of the water column within the first few days of the model, forming a flood deposit. The initial sediment bed had zero radioisotope inventories. The idealized model was configured to represent a situation where a single flood deposit is reworked by subsequent storm waves. Therefore, ^{7}Be was added only at the beginning of the model, and the ^{7}Be inventory subsequently decayed. In contrast, the model assumed that ^{234}Th activities associated with seabed sediment underwent decay, but that ^{234}Th was replenished upon sediment resuspension. To represent this, the activity of ^{234}Th on all suspended sediment was instantly reset to 5 dpm g^{-1}.

After the initial suspended sediment settled, the freshly-deposited fluvial layer was subjected to a 125-day idealized stormy period comprised of consecutive two-week intervals that each included a three-day storm and an eleven-day quiescent period (Figure 2a). Sediment was eroded under high bed shear stresses during the storms (2.7 Pa), and then settled and redeposited after bed stresses returned to background levels. The model neglected horizontal flux convergence or divergence, and therefore all sediment eroded during a storm redeposited when conditions subsided. The end of the model included a long quiescent period to evaluate model behavior (Figure 2a–c). Though idealized, the time-series for the wave forcing allows us to examine model behavior for a relatively simple case and has proved useful in past modeling studies [38].

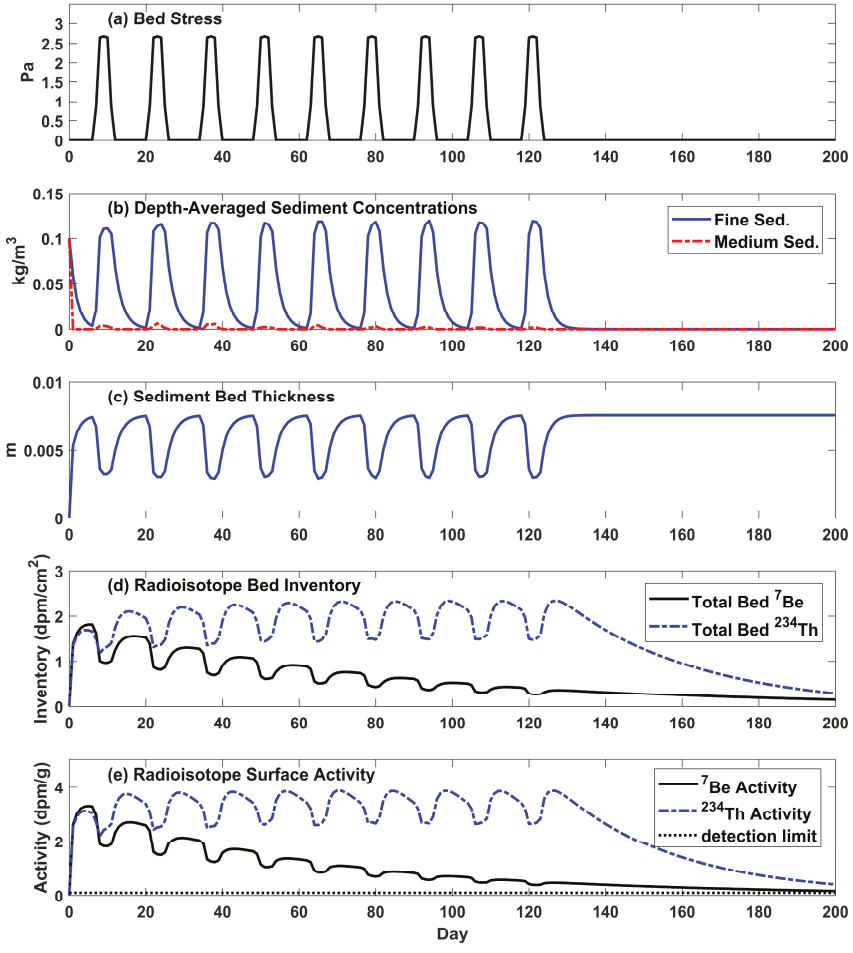

Figure 2. Time series for the Standard Case (Case 1) of (**a**) bed stress, (**b**) depth-averaged suspended sediment concentrations (see legend), (**c**) bed thickness relative to initial, (**d**) radioisotope bed inventories, and (**e**) radioisotope surface activities. Shows first 200 days of 365-day run. Conditions remained quiescent after Day 130.

Three sets of experiments used the idealized scenario described above to investigate the sensitivity of seabed radioisotope activities to biodiffusion, flood layer thickness, and resuspension intensity. The Standard Case (Case 1) used intermediate values; while Cases 2–7 each varied one parameter

(see Table 1). The first set of experiments tested a range of values for biodiffusion coefficients ($D_{b,max}$) equal to 0, 1, and 25 cm^2 yr^{-1}; for Cases 2, 1, and 3, respectively. The second set varied flood input and considered a very thin (0.38 cm, Case 6), thin (0.75 cm, Case 1), and thicker (1.5 cm, Case 7) initial fluvial deposit. The influence of resuspension intensity was considered, both by varying the bed shear stress to include no (0 Pa, Case 4), moderate (2.7 Pa, Case 1), and intense (6.0 Pa, Case 5) resuspension; and by evaluating the sensitivity of radioisotopic profiles to the specification of the active transport layer thickness, i.e., the depth from which sediment can be recruited for resuspension during a model timestep. To prevent the active transport layer from being overly large for Cases 1–7, it was limited to a maximum of 0.5 cm below the sediment bed surface. Case 8 did not limit the active transport layer thickness, but implemented the commonly-used stress-dependent formulation (see [32,39]), via which the active layer thickness reached 1.8 cm.

To analyze the radioisotope behavior, model output was characterized in terms of the calculated penetration depth, radioisotopic inventory, detection timescale, and surface activity; we define those terms here. Surface activity (dpm g^{-1}) represented the average activity in the top 1 cm of the seabed. The radioisotopic inventories (dpm cm^{-2}) represented the depth integrals in the bed per cross-sectional area. Penetration depths (cm) of ^{7}Be and ^{234}Th have been used to infer the thicknesses of flood and storm deposits, and for each model run were characterized by the maximum depth below the sediment surface for which the ^{7}Be and ^{234}Th activities exceeded an assumed detection limit of 0.1 dpm g^{-1}. To explore how biodiffusion, resuspension intensity, and flood deposit thickness influenced the likelihood of detection using ^{7}Be or ^{234}Th, we evaluated the detection timescale, calculated as the length of time for which surface activity exceeded 0.1 dpm g^{-1}. The detection timescales of fluvial deposits were calculated as time elapsed since the flood event (i.e., in this case, the first day of the model run) based on detectability of ^{7}Be. For storm reworking, the detection timescale of ^{234}Th was calculated relative to the end of the last resuspension event (Day 125, except for the no resuspension Case 4). We define the thickness of the physically reworked material (cm) as the sum of the thicknesses of the resuspended material and the active transport layer; because this is the thickness of the sediment bed impacted during a storm event by erosion, redeposition, and armoring.

Table 1. Parameters for each model run. Bold print marks the parameters that differ for Cases 2–8.

Case	$D_{b,max}$ (cm^2 yr^{-1})	Bed Stress (Pa)	Flood Layer (cm)	Active Layer (cm)
1	1	2.7	0.75	0.5
2	**0**	2.7	0.75	0.5
3	**25**	2.7	0.75	0.5
4	1	**0**	0.75	0.5
5	1	**6**	0.75	0.5
6	1	2.7	**0.38**	0.5
7	1	2.7	**1.51**	0.5
8	1	2.7	0.75	**1.8**

3. Results

The ^{7}Be and ^{234}Th activity profiles changed in response to episodic deposition and resuspension, and persistent biodiffusion and decay (Figure 3). The initial, 0.75 cm-thick, fluvial deposit contained uniformly high ^{7}Be and ^{234}Th activity (Figure 3a). During erosional episodes, activity profiles in the bed changed as sediment that carried radioisotopes was resuspended (Figures 2 and 3). Upon redeposition, profiles for both radioisotopes showed a surface layer that had uniform activities overlaying sediment whose activities decayed with depth (Figure 3c). Biodiffusion mixed both radioisotopes into the bed throughout the run, which acted to reduce radioisotope activities in the surface layer. As expected, bed inventories of ^{7}Be and ^{234}Th become different during episodes of resuspension, as ^{234}Th was adsorbed from seawater onto the fine and medium sediment with each storm (Figure 3c,d). In contrast, storm resuspension had no net effect on ^{7}Be bed inventory so that, over time, ^{7}Be inventories decreased via decay, and surface activities were diluted via biodiffusion. Late in the model, after Day 130,

inventories decreased due to the decay of ^{7}Be and ^{234}Th, and surface tracer activities were reduced via biodiffusion (Figure 2d,e).

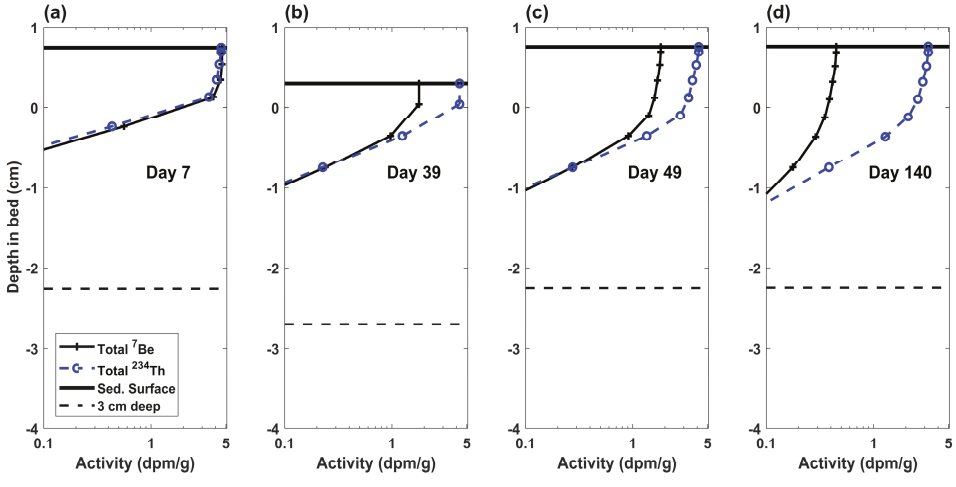

Figure 3. Vertical profiles of seabed radioisotope activities at four instances for Case 1. (**a**) Day 7 after initial deposition, (**b**) Day 39 at peak of a resuspension event, (**c**) Day 49 after redeposition, and (**d**) Day 140 during the extended quiescent period. Solid black lines represent bed surface and thick dashed lines represent three centimeters deep in the bed. The bed height prior to initial deposition was defined as $z_{bed} = 0$.

3.1. Sensitivity to Biodiffusivity

Results from model runs that used different biodiffusion coefficients (Cases 1, 2, and 3; Table 1) illustrate the influence of biodiffusion intensity on radioisotope bed profiles. Figure 4a–f shows ^{7}Be and ^{234}Th profiles for these runs after the third and seventh resuspension events (Days 49 and 140, respectively). With increasing biodiffusion intensity, surficial sediments that carry high radioisotope activities were mixed into the seabed at faster rates, increasing the penetration depths for both ^{234}Th and ^{7}Be, and correspondingly decreasing surface activities. However, ^{234}Th surface activities decreased less than ^{7}Be because resuspended sediment adsorbed new ^{234}Th from seawater, elevating bed inventories of ^{234}Th as biodiffusion intensity increased. The ^{234}Th and ^{7}Be detection timescales of flood and storm beds decreased with increasing intensity of biodiffusion (Table 2). As $D_{b,max}$ increased, each radioisotope was mixed more rapidly into the bed, diluting surface activities by vertical mixing, so that surface activities fell below the detection limit more quickly.

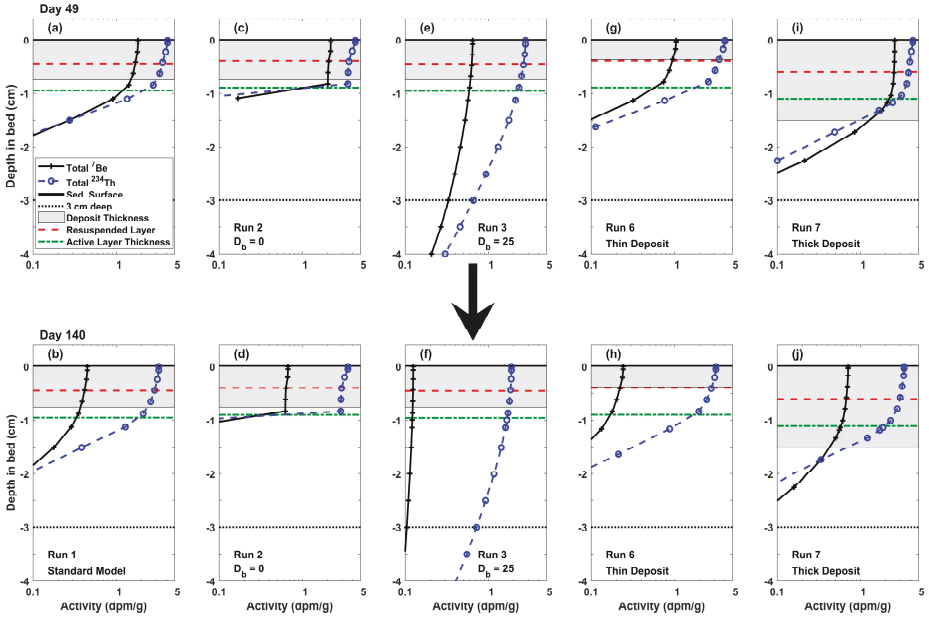

Figure 4. Radioisotope profiles calculated that (**a**,**b**) used $D_{b,max}$ = 1 cm^2 yr^{-1} and had a flood deposit 0.75 cm thick (Case 1), (**c**,**d**) neglected biodiffusion (Case 2), (**e**,**f**) used $D_{b,max}$ = 25 cm^2 yr^{-1} (Case 3), (**g**,**h**) had a flood deposit 0.38 cm thick (Case 4), and (**i**,**j**) had a flood deposit 1.51 cm thick (Case 5). Top row shows results on Day 49 while bottom row shows Day 140. Horizontal lines are as described in Figure 3. The gray box represents the extent of the initial flood deposit, red line denotes depth of resuspended layer, green line denotes the maximum penetration of the active layer when sediment was resuspended. The bed height after initial deposition is defined as z_{bed} = 0.

Table 2. Surface activities, bed inventories, penetration depths, and detection timescales after deposition (detection limit = 0.1 dpm g^{-1}) for ^{7}Be and ^{234}Th for all cases. Days 49 and 140 represent times when no sediment was resuspended, but cover a range of time since initial deposition of ^{7}Be.

	Day	Standard	Biodiffusion		Resuspension		Thickness		Active
		Case 1	Case 2	Case 3	Case 4	Case 5	Case 6	Case 7	Case 8
^{7}Be Surf. Activity (dpm g^{-1})	49	1.62	1.97	0.63	1.7	1.56	0.85	2.53	0.79
	140	0.4	0.61	0.12	0.43	0.39	0.21	0.68	0.22
^{7}Be Bed Inventory (dpm cm^{-2})	49	1.07	1.07	1.07	1.07	1.07	0.53	2.13	1.07
	140	0.33	0.33	0.33	0.33	0.33	0.16	0.66	0.33
^{7}Be Penetration Depth (cm)	49	1.88	1.26	4.94	1.8	1.91	1.55	2.57	3.2
	140	1.88	1.07	3.44	1.77	1.91	1.39	2.56	2.97
^{7}Be TD (months)		8.0	9.6	5.2	8.2	8	6.6	9.4	6.8
^{234}Th Surf. Activity (dpm g^{-1})	49	3.41	3.51	2.59	0.82	3.56	3.04	3.85	3.7
	140	2.72	2.87	1.82	0.05	2.86	2.52	3	2.96
^{234}Th Bed Inventory (dpm cm^{-2})	49	2.07	1.87	3.19	0.51	2.27	1.8	2.75	4.58
	140	1.75	1.52	2.74	0.04	1.95	1.58	2.1	3.73
^{234}Th Penetration Depth (cm)	49	1.86	1.09	5.03	1.48	1.93	1.69	2.25	3.42
	140	1.97	1.09	5.7	0	2.11	1.96	2.21	3.49
^{234}Th TD (months)		4.2	4.6	3.2	4.1	4.3	4.1	4.3	4.4

3.2. Sensitivity to Fluvial Deposit Thickness

Cases 6 and 7 had initial fluvial deposit thicknesses of 0.38 and 1.5 cm, one-half and double the deposit thickness of Case 1, respectively. Because the fluvial deposit provided the initial source of radioisotopes to the seabed, the deposit thickness directly influenced penetration depth and bed inventory for both radioisotopes early in the model run (Figure 4a,g,i; Table 2). Physical mixing was especially important for Case 6, for which the thickness of the resuspended layer exceeded that of the initial fluvial deposit.

The ^{7}Be surface activity remained higher over time for the thicker deposits than for the thinner deposit, but the differences did not scale linearly with deposit thickness due to physical and biological mixing (Figure 4; Table 2). Doubling the fluvial deposit thickness increased the ^{7}Be surface activity by 56% and the ^{7}Be penetration depth by 37% on day 49 of the model runs (Table 2). The initial fluvial thickness played an even smaller role in the detection timescale, with thicker deposits remaining detectable for only slightly longer than calculated for the thinner deposits; doubling the flood thickness increased the detection timescale for ^{7}Be by roughly 18% (Table 2).

The relative thicknesses of the physically reworked layer compared with the initial flood deposit affected the response of the ^{234}Th activities. Cases 1 and 6 had similar ^{234}Th penetration depths (Figure 4a,b,g,h; Table 2) because they were set by the thickness of the physically reworked layers. The fact that the initial fluvial deposit thickness for Case 7 exceeded that of the resuspended layer directly affected the penetration depth (Figure 4a,i; Table 2). There was feedback between fluvial deposit thickness and mass of sediment resuspended, because the fluvial layer only contained fine and medium sediment. A thicker fluvial layer therefore supplied more fine and medium sediment near the surface, allowing more mobile sediment to be eroded and become tagged with fresh ^{234}Th in the water column. This increased the ^{234}Th inventories and penetration depths after resuspension events (Table 2).

3.3. Sensitivity to Resuspension Intensity

Cases 4 and 5 explored how the seabed profiles of ^{7}Be and ^{234}Th responded to changes in resuspension intensity by varying the magnitude of the maximum bed shear stress, τ_b. The cases featuring zero (Case 4), medium (Case 1), and high resuspension intensity (Case 5) yielded erosion depths of 0, 0.46, and 0.56 cm, respectively (Figure 5). For the cases that included resuspension, the thickness of the fluvial deposit (0.75 cm) exceeded the peak erosion depths. Bed inventories of ^{234}Th increased with resuspension intensity; energetic events suspended more sediment which then scavenged ^{234}Th from the water column (Table 2). The case with no resuspension therefore had much lower ^{234}Th surface activity and bed inventory than the other cases (Figure 5c,d). In contrast, resuspension did not affect ^{7}Be bed inventories, as the model assumed that ^{7}Be was only supplied in the initial flood deposit. Via physical mixing, erosion and redeposition cycles increased penetration depths for both radioisotopes. During periods of erosion, the active transport layers shifted deeper into the seabed, mixing radioisotope-tagged surficial sediments with underlying lower-activity sediment. This decreased surface activities and detection time-scales with increasing resuspension intensity for ^{7}Be, because it was not replenished during storms.

Case 8 evaluated the role of the active layer thickness on resuspension intensity and its impact on modeled radioisotope profiles. While other cases limited the active transport layer thickness to a maximum of 0.5 cm, Case 8 used a widely accepted formulation (i.e., [39]) for it that reached 1.8 cm during the storm. Therefore, though bed stresses were identical, the amount of suspended sediment and the eroded depth was almost doubled in Case 8 compared to Case 1. The active transport layer thickness also greatly influenced the modeled radioisotope signatures (Figure 5a,b,g,h). While total ^{7}Be bed inventory was insensitive to the active transport layer thickness, the increased erosion and concurrent mixing of the surficial few centimeters of the bed effectively diluted the surface activity for ^{7}Be and increased the penetration depth (Figure 5a,b,g,h). In contrast, the surface activity of ^{234}Th was insensitive to the increased active transport layer thickness, (Table 2, Figure 5a,b,g,h), but the resultant

higher resuspension depths nearly doubled the ^{234}Th inventory and the penetration depths for Case 8 relative to Case 1 (Table 2, Figure 5a,b,g,h).

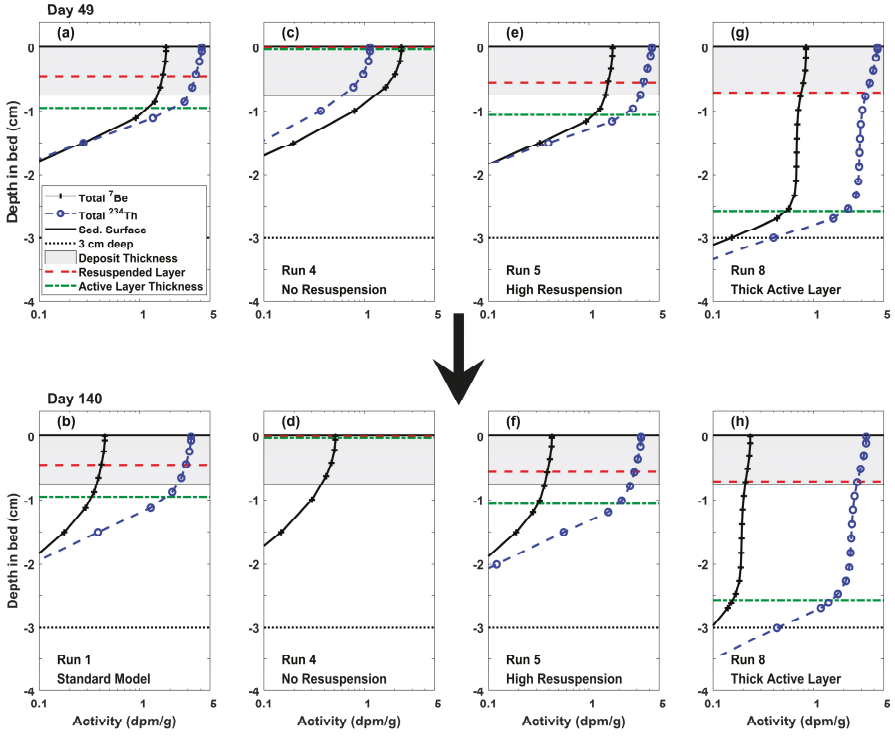

Figure 5. Radioisotope profiles that had (**a**,**b**) resuspension depth of 0.46 cm (Case 1), (**c**,**d**) no resuspension (Case 4), (**e**,**f**) resuspension depth of 0.56 cm (Case 6), and (**g**,**h**) a thick active layer (Case 8). Top row shows results on day 49; while bottom row shows day 140. Horizontal lines as described in Figure 3. Gray boxes represent the initial extents of the flood deposit, red lines denote depth of resuspended layer, green lines denote depth of maximum active layers. The bed height after deposition was defined as $z_{bed} = 0$. Note that day 140 for Run 4 (**d**) has zero ^{234}Th, which decayed below the detection limit by this time.

4. Discussion

4.1. Synthesis of Sensitivity Tests

The results summarized in Table 2 demonstrate that variable bioturbation rates, resuspension intensity, initial flood deposit thickness, and active layer thickness affected modeled radioisotope profiles, inventories, penetration depths, and detection time scales to varying degrees. The biodiffusion sensitivity tests (Cases 2 and 3) generated results that deviated most from Case 1. Note that these biodiffusion rates spanned a larger range than considered in the other sensitivity trials, but this reflects the significant uncertainty in characterizing biodiffusion coefficients (see [46]). In Case 3, enhanced bioturbation increased the ^{234}Th and ^{7}Be penetration depths, reduced surface activities, and caused the shortest detection timescales for any of the model runs (Table 2, Figures 4 and 5). Case 2 neglected biodiffusion and produced the thinnest penetration depth and longest detection time scale of the cases considered (Table 2). Varying the initial fluvial layer thickness appreciably affected the ^{7}Be results, especially ^{7}Be bed inventory, more so than ^{234}Th. Results from the cases that investigated resuspension intensity and active layer thickness suggested that increasing resuspension,

in the presence of bioturbation, worked to dissipate the terrestrial ^{7}Be signal, while enhancing the oceanic ^{234}Th signal.

The reactive tracer model responded reasonably to a range of dissipative and intensifying conditions for two radioisotopes that are indicative of terrestrial and oceanic sources. Analysis of the idealized test case results produced radioisotope profiles and metrics similar to those observed on continental shelf environments (e.g., [5,9,17]), and consistent with patterns noted in field observations. For example, bioturbative processes are known to mix radioisotopes into the seabed, increasing penetration depths and reducing detection time scales [16,17,23,25]. Similar to the results that varied fluvial layer thickness (Cases 6 and 7; Figure 4; Table 2), bed inventories of ^{234}Th and ^{7}Be have been observed to correlate positively with initial flood layer thickness [5]. Model experiments also provided scenarios wherein shorter-lived ^{234}Th was observed at greater depth than the longer-lived ^{7}Be (Cases 1, 3, 6, 8) as observed in the Adriatic Sea [9].

4.2. Limitations of Model as Implemented Here

This model marks a first step in integrating sediment transport process models [32] with the radioisotopic tracers that have been increasingly used as indicators of sediment transport processes (e.g., [3,5–7,9,13]). This section reviews some of the assumptions that were made in developing this model and discusses their implications.

The model discussed herein used a relatively simple approach to represent behavior of radioisotopes, but integrated them into an established sediment transport model. In particular, the model employed a simple conceptual model for the sources of the radioisotopes, and for their interactions with sediment that would be appropriate for river-dominated areas where these radioisotopes have been used to infer source and transport processes. To represent an initial flood source for sediment, the only source of ^{7}Be was assumed to be sediment suspended at the start of the model run, which had a prescribed activity of associated ^{7}Be. While it is known that activities of fluvially discharged ^{7}Be vary in time [9], our idealized scenario represented only an initial flood pulse so that temporal variation in ^{7}Be was not an issue for the runs presented. Additionally, our conceptual model neglected other sources of ^{7}Be; for example, direct precipitation has been noted as a source of ^{7}Be on non-river influenced continental shelves [49]. Similarly, the conceptual model simplified the processes that influence ^{234}Th activities in coastal environments. The model also assumed that all suspended sediment carried a constant, pre-set activity of ^{234}Th. This was equivalent to assuming that sorption of ^{234}Th to sediment grains occurred instantaneously upon suspension in the model water column, and that there was no variation in background ^{234}Th concentrations. In actuality, the association of ^{234}Th with suspended sediment grains may take days to equilibrate, dependent on suspended sediment concentrations [3,19,43], and ^{234}Th concentrations are known to vary with salinity within estuaries and on river-influenced shelves [1]. Additionally, the model assumed that the activities of the radioisotopes on the muddy sediment did not vary with grain size or water column properties.

The sediment transport model also included some simplifications. For example, the resuspension of muddy sediment is subjected to cohesive processes such as bed consolidation and flocculation. The version of the CSTMS used here [32] neglected these processes, so that the sediment classes had pre-set, constant values to represent erodibility and settling velocity. For application to reworking of muddy flood deposits, future studies might consider using the radioisotopic reactive tracer module presented here with the version of the CSTMS that also accounts for flocculation and bed consolidation [38].

Bedload was not directly represented in our model, though the CSTMS provides bedload formulations that can be applied to the upper-most sediment bed layer, i.e., the active transport layer [32]. We did not use the bedload transport formulations, however. Because our idealized one-dimensional (vertical) model assumes uniform horizontal sediment fluxes, there would be no net erosion or deposition from bedload. One conceptualization of the active transport layer, however, is as a bedload layer from which sediment can be suspended [40]. As bedload intensifies, the active layer thickens, which in our model acted to mix and dilute the radioisotope tracer concentrations in the

upper sediment bed. The sensitivity of surface activity and penetration depth to the formulation of the active transport layer (Cases 1 and 8) illustrates this.

4.3. Future Applications

As discussed in the previous section, our idealized model used a relatively simple representation of radioisotopes and neglected some sediment transport processes. Though this model did not represent the full complexities of actual radioisotope source terms, or particle–radioisotope interactions, the model itself could provide a venue for future studies that consider the impact of these complexities on sediment bed geochronological tracer profiles. Additionally, by developing our coupled reactive tracer–sediment transport model within a community modeling framework, this paves the way for future studies to consider the potential impacts of other sediment transport processes or radioisotopic chemistry on the geochronological record.

In addition to idealized studies such as reported here, the geochronological model should provide useful insight if applied to realistic field settings. For example, we have used a similar one-dimensional (vertical) version of the model to represent a site offshore of the Mississippi subaqueous delta [50]. This model was implemented to replicate observed radioisotopic profiles [6]. The model-produced radioisotopic profiles were then used within various analytical models from the literature to derive deposition rate, etc., from the simulated profiles; which were then compared to the actual model deposition rates. Results showed that the analytical model estimates can be unreliable if assumptions regarding the biodiffusion rate and radioisotope activity of freshly deposited sediment are incorrect [50].

It would be useful to add the capability of our sediment transport geochronological model to a full three-dimensional model, such as that developed for the Waipaoa River Shelf, NZ [51], or a northern Gulf of Mexico continental shelf model [48,52]. Both of these efforts attempted to use radioisotopic data for comparison to model estimates of sediment deposition; but this exercise presented challenges that may be abated by direct inclusion of the radioisotopes within the transport equations. Accounting for geochronology within realistic domain models could facilitate model validation by enabling direct comparison between the modeled and measured quantities, i.e., profiles of ^{234}Th and ^{7}Be. Within a joint field and modeling study, this capability could enable careful model–data comparisons that could yield insight into the specification of some model parameters that have been difficult to constrain, such as the active transport layer thickness.

5. Conclusions

A sediment transport model has been modified to account for reactive terms and represent transformations of particulate tracers in the water column and seabed. The model was applied to calculate sediment bed profiles of short half-life radioisotopes ^{7}Be and ^{234}Th that have been used to interpret deposits of river derived sediment and marine sediment resuspension, respectively. Examples were provided in an idealized one-dimensional (vertical) model that represented sediment suspension and the seabed, and that evaluated the response of radioisotope profiles to variations in riverine sediment input, storm intensity, and biodiffusive mixing coefficient. Radioisotopic values such as surface activity, inventory, and penetration depth were analyzed from model results and compared to the sediment input and reworking represented in the model. The intensity of biodiffusion affected the persistence of detectable fluvial event beds. Using a biodiffusion coefficient of 25 cm^2 yr^{-1}, the fluvial event bed would be obscured within days or weeks. Both resuspension and biodiffusion increased the seabed inventory of ^{234}Th. Biodiffusion diluted the surface layer by mixing sediment enriched with ^{234}Th (and ^{7}Be) with underlying material. When surficial sediment underwent cycles of resuspension and redeposition, however, it became enriched in ^{234}Th and thereby increased the total bed inventory upon redeposition.

Author Contributions: Conceptualization, J.J.B., C.K.H., C.R.S.; Methodology, J.J.B., C.K.H.; Software, J.J.B., C.K.H., C.R.S.; Validation, J.J.B., C.K.H., T.A.K.; Formal Analysis, J.J.B., T.A.K.; Investigation, J.J.B., T.A.K.;

Resources C.K.H.; Data Curation, J.J.B., C.K.H.; Writing-Original Draft Preparation, J.J.B., C.K.H.; Writing-Review & Editing, J.J.B., C.K.H., T.A.K., C.R.S.; Visualization, J.J.B.; Supervision, C.K.H.; Project Administration, C.K.H.; Funding Acquisition, C.K.H.

Funding: The Bureau of Ocean Energy Management (BOEM) provided funding for Birchler, Harris, and Kniskern. During his M.S. program Birchler received additional funds from VIMS' Office of Academic Studies. This work was partially supported by the U.S. Geological Survey, Coastal and Marine Geology Program.

Acknowledgments: Use of firm and product names is for descriptive purposes only and does not imply endorsement by the U.S. Government. The authors are thankful for input and support from G. Auad (BOEM). The authors appreciate input from VIMS' faculty members of Birchler's M.S. committee, namely C. Friedrichs, S. Kuehl, and L. Schaffner. The authors also appreciate input from an anonymous reviewer of an earlier version of this manuscript, two anonymous reviewers of this journal, and input from R.C. Mickey and J. Moriarty (USGS). We feel that their input helped to improve this submission.

Conflicts of Interest: The authors declare no conflict of interest.

References

1. Waples, J.T.; Benitez-Nelson, C.; Savoye, N.; Rutgers van der Loeff, M.; Baskaran, M.; Gustafsson, O. An introduction to the application and future use of ^{234}Th in aquatic systems. *Mar. Chem.* **2006**, *100*, 166–189. [CrossRef]
2. Dibb, J.E.; Rice, D.L. Geochemistry of beryllium-7 in Chesapeake Bay. *Estuar. Coast. Shelf Sci.* **1989**, *28*, 379–394. [CrossRef]
3. Feng, H.; Cochran, J.K.; Hirschberg, D.J. ^{234}Th and ^{7}Be as tracers for the transport and dynamics of suspended particles in a partially mixed estuary. *Geochim. Cosmochim. Acta* **1999**, *63*, 2487–2505. [CrossRef]
4. Kniskern, T.A.; Kuehl, S.A. Spatial and temporal variability of seabed disturbance in the York River subestuary. *Estuar. Coast. Shelf Sci.* **2003**, *58*, 37–55. [CrossRef]
5. Sommerfield, C.K.; Nittrouer, C.A.; Alexander, C.R. ^{7}Be as a tracer of flood sedimentation on the northern California continental margin. *Cont. Shelf Res.* **1999**, *19*, 225–361. [CrossRef]
6. Corbett, D.R.; McKee, B.A.; Duncan, D. An evaluation of mobile mud dynamics in the Mississippi River deltaic region. *Mar. Geol.* **2004**, *209*, 91–112. [CrossRef]
7. Kniskern, T.A.; Mitra, S.; Orpin, A.R.; Harris, C.K.; Walsh, J.P.; Corbett, D.R. Characterization of a flood-associated deposit on the Waipaoa River shelf using radioisotopes and terrigenous organic matter abundance and composition. *Cont. Shelf Res.* **2014**, *86*, 66–84. [CrossRef]
8. Baskaran, M.; Santschi, P.H. The role of particles and colloids in the transport of radionuclides in coastal environments of Texas. *Mar. Chem.* **1993**, *43*, 95–114. [CrossRef]
9. Palinkas, C.M.; Nittrouer, C.A.; Wheatcroft, R.A.; Langone, L. The use of ^{7}Be to identify event and seasonal sedimentation near the Po River delta, Adriatic Sea. *Mar. Geol.* **2005**, *222–223*, 95–112. [CrossRef]
10. Mullenbach, B.L.; Nittrouer, C.A. Rapid deposition of fluvial sediment in the Eel Canyon, northern California. *Cont. Shelf Res.* **2000**, *20*, 2191–2212. [CrossRef]
11. Corbett, D.R.; Dail, M.; McKee, B.A. High-frequency time-series of the dynamic sedimentation processes on the western shelf of the Mississippi River Delta. *Cont. Shelf Res.* **2007**, *27*, 1600–1615. [CrossRef]
12. Boudreau, B.P. Is burial velocity a master parameter for bioturbation? *Geochim. Cosmochim. Acta* **1994**, *58*, 1243–1249. [CrossRef]
13. McKee, B.A.; DeMaster, D.J.; Nittrouer, C.A. The use of ^{234}Th/^{238}U disequilibrium to examine the fate of particle-reactive species on the Yangtze continental shelf. *Earth Planet. Sci. Lett.* **1984**, *68*, 431–442. [CrossRef]
14. Smoak, J.M.; DeMaster, D.J.; Kuehl, S.A.; Pope, R.H.; McKee, B.A. The behavior of particle-reactive tracers in a high turbidity environment: ^{234}Th and ^{210}Pb on the Amazon continental shelf. *Geochim. Cosmochim. Acta* **1996**, *60*, 2123–2137. [CrossRef]
15. Aller, R.C.; Benninger, L.K.; Cochran, J.K. Tracking particle-associated processes in nearshore environments by use of ^{234}Th/^{238}U disequilibrium. *Earth Planet. Sci. Lett.* **1980**, *47*, 161–175. [CrossRef]
16. Wheatcroft, R.A. Time-series measurements of macrobenthos abundance and sediment bioturbation intensity on a flood-dominated shelf. *Prog. Oceanogr.* **2006**, *71*, 88–122. [CrossRef]
17. Wheatcroft, R.A.; Drake, D.E. Post-depositional alteration and preservation of sedimentary event layers on continental margins, I. The role of episodic sedimentation. *Mar. Geol.* **2003**, *199*, 123–137. [CrossRef]

18. Dibb, J.E. Atmospheric deposition of beryllium-7 in the Chesapeake Bay region. *J. Geophys. Res.* **1989**, *94*, 2261–2265. [CrossRef]
19. Aller, R.C.; Cochran, J.K. $^{234}Th/^{238}U$ Disequilibrium in near-shore sediment: Particle reworking and diagenetic time scales. *Earth Planet. Sci. Lett.* **1976**, *29*, 37–50. [CrossRef]
20. McKee, B.A.; Nittrouer, C.A.; DeMaster, D.J. Concepts of sediment deposition and accumulation applied to the continental shelf near the mouth of the Yangtze River. *Geology* **1983**, *11*, 631–633. [CrossRef]
21. Wheatcroft, R.A. Preservation potential of sedimentary event layers. *Geology* **1990**, *18*, 843–845. [CrossRef]
22. Wheatcroft, R.A.; Wiberg, P.L.; Alexander, C.R.; Bentley, S.J.; Drake, D.E.; Harris, C.K.; Ogston, A.S. Post-depositional alteration and preservation of sedimentary strata. In *Continental-Margin Sedimentation: From Sediment Transport to Sequence Stratigraphy*; International Association of Sedimentologists Special Publication no. 37; Nittrouer, C.A., Austin, J.A., Field, M.E., Kravitz, J.H., Syvitski, J.P.M., Wiberg, P.L., Eds.; Blackwell Publishing: Malden, MA, USA, 2007; pp. 101–155, ISBN 9781405169349.
23. Nittrouer, C.A.; DeMaster, D.J.; McKee, B.A.; Cutshall, N.H.; Larson, I.L. The effect of sediment mixing on Pb-210 accumulation rates for the Washington continental shelf. *Mar. Geol.* **1984**, *54*, 201–221. [CrossRef]
24. Bentley, S.J.; Sheremet, A.; Jaeger, J.M. Event sedimentation, bioturbation, and preserved sedimentary fabric: Field and model comparisons in three contrasting marine settings. *Cont. Shelf Res.* **2006**, *26*, 2108–2124. [CrossRef]
25. Nittrouer, C.A.; Sternberg, R.W. The formation of sedimentary strata in an allochthonous shelf environment: The Washington continental shelf. *Mar. Geol.* **1981**, *42*, 201–232. [CrossRef]
26. Sadler, P.M. The influence of hiatuses on sediment accumulation rates. *GeoRes. Forum* **1999**, *5*, 15–40.
27. Bentley, S.J.; Sheremet, A. New model for the emplacement, bioturbation and preservation of fine-scaled sedimentary strata. *Geology* **2003**, *31*, 725–728. [CrossRef]
28. Ma, Y.; Friedrichs, C.T.; Harris, C.K.; Wright, L.D. Deposition by seasonal wave- and current-supported sediment gravity flows interacting with spatially varying bathymetry: Waiapu shelf, New Zealand. *Mar. Geol.* **2010**, *275*, 199–211. [CrossRef]
29. Kniskern, T.A.; Kuehl, S.A.; Harris, C.K.; Carter, L. Sediment accumulation patterns and fine-scale strata formation on the Waiapu River shelf, New Zealand. *Mar. Geol.* **2010**, *270*, 188–201. [CrossRef]
30. Lesser, G.R.; Roelvink, J.A.; van Kester, J.A.T.M.; Stelling, G.S. Development and validation of a three-dimensional morphological model. *Coast. Eng.* **2004**, *51*, 883–915. [CrossRef]
31. Neumeier, U.; Ferrarin, C.; Amos, C.L.; Umgiesser, G.; Li, M.Z. Sedtrans05: An improved sediment-transport model for continental shelves and coastal waters with a new algorithm for cohesive sediments. *Comput. Geosci.* **2008**, *34*, 1223–1242. [CrossRef]
32. Warner, J.C.; Sherwood, C.R.; Signell, R.P.; Harris, C.K.; Arango, H.G. Development of a three-dimensional, regional, coupled wave, current, and sediment-transport model. *Comput. Geosci.* **2008**, *34*, 1284–1306. [CrossRef]
33. Moriarty, J.M.; Harris, C.K.; Hadfield, M.G. A hydrodynamic and sediment transport model for the Waipaoa Shelf, New Zealand: Sensitivity of fluxes to spatially-varying erodibility and model nesting. *J. Mar. Sci. Eng.* **2014**, *2*, 336–369. [CrossRef]
34. Palinkas, C.M.; Halka, J.P.; Li, M.; Sanford, L.P.; Cheng, P. Sediment deposition from tropical storms in the upper Chesapeake Bay: Field observations and model simulations. *Cont. Shelf Res.* **2014**, *86*, 6–16. [CrossRef]
35. Haidvogel, D.B.; Arango, H.; Budgell, W.P.; Cornuelle, B.D.; Curchitser, E.; Di Lorenzo, E.; Fennel, K.; Geyer, W.R.; Hermann, A.J.; Lanerolle, L.; et al. Ocean forecasting in terrain-following coordinates: Formulation and skill assessment of the regional ocean modeling system. *J. Comput. Phys.* **2008**, *227*, 3595–3624. [CrossRef]
36. Shchepetkin, A.F.; McWilliams, J.C. The regional oceanic modeling system (ROMS): A split-explicit, free-surface, topography-following-coordinate oceanic model. *Ocean Model.* **2005**, *9*, 347–404. [CrossRef]
37. Fennel, K.; Wilkin, J.; Previdi, M.; Najjar, R. Denitrification effects on air-sea CO_2 flux in the coastal ocean: Simulations for the northwest North Atlantic. *Geophys. Res. Lett.* **2008**, *35*, L24608. [CrossRef]
38. Sherwood, C.R.; Aretxabaleta, A.L.; Harris, C.K.; Rinehimer, J.P.; Verney, R.; Ferré, B. Cohesive and mixed sediment in the Regional Ocean Modeling System (ROMS v3.6) implemented in the Coupled Ocean–Atmosphere–Wave–Sediment Transport Modeling System (COAWST r1234). *Geosci. Model Dev.* **2018**, *11*, 1849–1871. [CrossRef]

39. Harris, C.K.; Wiberg, P.L. Approaches to quantifying long-term continental shelf sediment transport with an example from the northern California STRESS mid-shelf site. *Cont. Shelf Res.* **1997**, *17*, 1389–1418. [CrossRef]
40. Wiberg, P.L.; Drake, D.E.; Cacchione, D.A. Sediment resuspension and bed armoring during high bottom stress events on the northern California inner continental shelf: Measurements and predictions. *Cont. Shelf Res.* **1994**, *14*, 1191–1219. [CrossRef]
41. Moriarty, J.M.; Harris, C.K.; Fennel, K.; Friedrichs, M.A.; Xu, K.; Rabouille, C. The roles of resuspension, diffusion and biogeochemical processes on oxygen dynamics offshore of the Rhône River, France: A numerical modeling study. *Biogeosciences* **2017**, *14*, 1919–1946. [CrossRef]
42. Moriarty, J.M.; Harris, C.K.; Friedrichs, M.A.M.; Fennel, K.; Xu, K. Impact of seabed resuspension on oxygen and nitrogen dynamics in the northern Gulf of Mexico: A numerical modeling study. *J. Geophys. Res. Oceans* **2018**, *123*, 1–27. [CrossRef]
43. Santschi, P.H.; Li, Y.-H.; Bell, J.J. Natural radionuclides in Narragansett Bay. *Earth Planet. Sci. Lett.* **1979**, *47*, 201–213. [CrossRef]
44. Baskaran, M.; Ravichandran, M.; Bianchi, T.S. Cycling of ^{7}Be and ^{210}Pb in a high DOC, shallow, turbid estuary of south-east Texas. *Estuar. Coast. Shelf Sci.* **1997**, *45*, 165–176. [CrossRef]
45. Carslaw, H.S.; Jaeger, J.C. *Conduction of Heat in Solids*; Clarendon Press: Oxford, UK, 1959; ISBN 9780198533689.
46. Boudreau, B.P. *Diagenetic Models and Their Interpretation*; Springer: Berlin, Germany, 1997; ISBN 9783642643996.
47. Birchler, J.J.; Harris, C.K.; Kniskern, T.A. *A Model Archive for Sediment Transport Model Including Short-Lived Radioisotopes: Model Description and Idealized Test Cases*; Virginia Institute of Marine Science, College of William and Mary: Gloucester Point, VA, USA, 2018.
48. Xu, K.; Harris, C.K.; Hetland, R.D.; Kaihatu, J.M. Dispersal of Mississippi and Atchafalaya sediment on the Texas-Louisiana shelf: Model estimates for the year 1993. *Cont. Shelf Res.* **2011**, *31*, 1558–1575. [CrossRef]
49. Benitez-Nelson, C.R.; Buesseler, K.O.; Crossin, G. Upper ocean carbon export, horizontal transport, and vertical eddy diffusivity in the southwestern Gulf of Maine. *Cont. Shelf Res.* **2000**, *20*, 707–736. [CrossRef]
50. Birchler, J.J.; Harris, C.K.; Kniskern, T.A.; Sherwood, C.R. Numerical model of geochronological tracers for deposition and reworking applied to the Mississippi subaqueous delta. *J. Coast. Res. Spec. Issue 85 Proc. 5th Int. Coast. Symp.* **2018**, 456–460. [CrossRef]
51. Moriarty, J.M.; Harris, C.K.; Hadfield, M.G. Event-to-seasonal sediment dispersal on the Waipaoa River Shelf, New Zealand: A numerical modeling study. *Cont. Shelf Res.* **2015**, *110*, 108–123. [CrossRef]
52. Xu, K.; Mickey, R.C.; Chen, Q.J.; Harris, C.K.; Hetland, R.; Hu, K.; Wang, J. Shelf sediment transport during Hurricanes Katrina and Rita. *Comput. Geosci.* **2016**, *90*, 24–39. [CrossRef]

Journal of
Marine Science and Engineering

MDPI

Article

Detailed Hydrodynamic Feasibility Assessment for Leque Island and Zis a Ba Restoration Projects

Adi Nugraha * and Tarang Khangaonkar

Pacific Northwest National Laboratory, Marine Sciences Division, 1100 Dexter Avenue North, Suite 400, Seattle, WA 98109, USA; tarang.khangaonkar@pnnl.gov

* Correspondence: adi.nugraha@pnnl.gov; Tel.: +1-206-528-3413

Received: 29 September 2018; Accepted: 14 November 2018; Published: 16 November 2018

Abstract: Numerous restoration projects are underway in Puget Sound, Washington, USA with the goal of re-establishing intertidal wetlands that were historically lost due to dike construction for flood protection and agricultural development. One such effort is the restoration effort within the Stillaguamish Delta, benefitting from the cumulative effects from the Leque Island and zis a ba restoration projects. The preferred restoration design calls for the removal of perimeter dikes at the two sites and the creation of tidal channels to facilitate the drainage of tidal flows. A 3-D high-resolution unstructured-grid coastal ocean model based on FVCOM was developed to evaluate the hydrodynamic response of the estuary to restoration alternatives. A series of hydrodynamic modeling simulations were then performed to quantify the hydrodynamic response of the nearshore restoration project, such as periodic inundation, suitable currents, and desired habitat/salinity levels. Sediment impacts were also examined, including the potential for excessive erosion or sedimentation requiring maintenance. Simulation results indicate that the preferred alternative scenario provides the desired estuarine response, which is consistent with the planned design. A decrease in velocities and bed shear in the main river channels was noted for the restored condition associated with the increased inundation of tidal flat area and reduced tidal flows through the main channels. High bed shear near the restored tidal channel entrances indicates that the inlets may evolve in size until equilibrium is established.

Keywords: hydrodynamics; feasibility assessments; nearshore restoration; FVCOM; Puget Sound; Salish Sea

1. Introduction

Puget Sound is a complex system of estuaries, basins, deltas, and habitats located at the northwestern coast of the USA. It houses large populations of birds, marine mammals, and fish. Puget Sound supports a massive community of hunters, fishermen and nature enthusiasts, etc. Over the last 150 years, economic development in Puget Sound has resulted in the alteration of habitat-sustaining processes and significant losses of wildlife habitat and fishes. A series of engineering activities such as the construction of dikes for irrigation practices that took place over a period of approximately 100 years has been recognized as one of the major causes of those habitat changes and losses [1]. In addition, the condition of these historic perimeter dikes in many Puget Sound estuaries has deteriorated and has become a concern from a maintenance, environmental issues and economic perspective. A potential long-term solution to the flooding, environmental and dike maintenance issues, while also providing ecological benefits of restored tidal marsh habitat with the goal of recovering the salmon fishery in Puget Sound, is nearshore restoration through dike removal or breaching. This has been actively evaluated by Washington State Department of Fish and Wildlife (WDFW), the U.S. Army Corp of Engineers (USACE), and the National Oceanic and Atmospheric Administration (NOAA) together with sovereign Indian nations [2,3]. This is also the case at "Leque Island" and "zis a ba" sites close to the mouth of Stillaguamish River estuary, where restoration actions have been proposed, and is the subject of this assessment.

Eight restoration scenarios including simultaneous restoration actions at the Leque-adjacent zis a ba site have been evaluated by Ducks Unlimited Inc. in collaboration with WDFW and the Stillaguamish Tribe. These scenarios included existing dike removal, the removal of damaged and repaired dike sections to create breaches, lowering the dike and the construction of new setback dikes. With the help of a detailed 3-D hydrodynamic model of the Stillaguamish estuary, we examined the effects of the proposed restoration actions on physical oceanographic parameters such as water surface elevations, salinity, currents, and bed shear stress relative to existing conditions. Numerous modeling studies based on the 3-D hydrodynamic model have been conducted in the past to improve the ecosystem and water quality due to anthropogenic causes such as excessive nutrient loading [4,5] and engineering activities [6–8] in the Puget Sound region.

We also examined the response of the proposed restoration scenarios to high-flow conditions critical for assessing erosion impacts and long-duration runs using a year-long record from 2003, when the highest number of flood flow events in recent years occurred. Based on the results, the indications were that proposed changes for most scenarios would provide an estuarine response consistent with the planned design [9].

In this effort, we updated the model with improved bathymetry using new LIDAR data collected by the Stillaguamish Tribe and the U.S. Geological Survey (USGS). The configuration of the preferred restoration designs at the Leque Island and zis a ba sites were updated from the conceptual levels to design and pre-construction level detail, and the updated information was incorporated into the modeling framework through further grid refinement. The model was then applied with a focus on site-specific questions related to impacts of the selected alternatives on nearby infrastructure such as dikes, outfalls, and pipelines with respect to inundation, erosion, and sedimentation. The results were examined relative to the baseline at specified locations of interest.

2. Materials and Methods

2.1. Study Area

Leque Island and zis a ba are former tidal marshlands that are located close to the mouth of the Old Stillaguamish River Channel (OSRC) in the Stillaguamish River Delta. The study sites are between Skagit Bay and Port Susan Bay (Figure 1a). The OSRC splits into two distributary channels, West Pass and South Pass, along the eastern shoreline of Leque Island. On the northeast side of Leque Island, the main connection between Skagit Bay and Port Susan Bay is West Pass of the Stillaguamish River. West Pass flows north of Leque Island into Skagit Bay. South Pass flows along the southeast shoreline of Leque Island into Port Susan Bay. The 36-ha zis a ba site is located northeast of Leque Island, separated by South Pass. The Old Stillaguamish River mainstream flows around the east and north sides of zis a ba, separating zis a ba and the City of Stanwood to the north. South Pass separates zis a ba from Leque Island to the west.

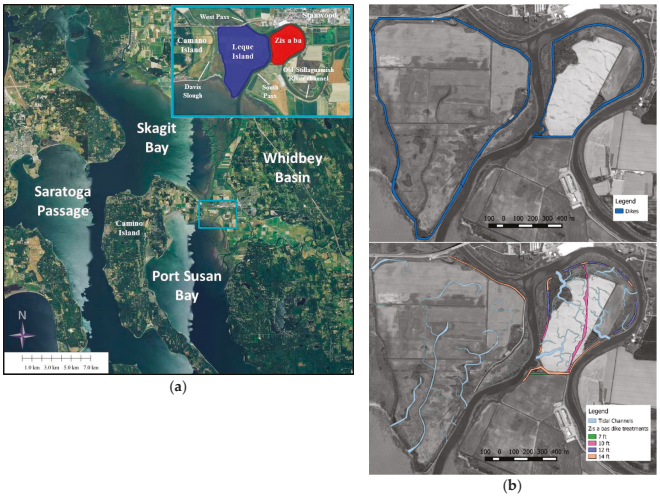

(a) (b)

Figure 1. (**a**) Location of the Leque Island and zis a ba sites in Whidbey Basin. (**b**) Schematic representation of (**top**) the baseline scenario and (**bottom**) the preferred restoration alternative scenario.

2.2. Hydrodynamics of Port Susan Bay and Skagit Bay

The model was constructed using the unstructured grid Finite Volume Community Ocean Model (FVCOM) version 2.7 framework [10]. The approach was to use the FVCOM hydrodynamic model of Port Susan Bay and Skagit Bay [9], suitably updated with recent bathymetry information provided by the Stillaguamish Tribe and USGS, to first simulate existing (pre-restoration) conditions to serve as the baseline for comparison with the preferred restoration conditions. The preferred restoration condition consists of the modified bathymetry and topography of the study area.

In particular, perimeter dikes at the Leque Island and zis a ba sites would be removed or breached to allow the restoration of tidal processes and periodic inundation and dewatering during ebb and flood. To facilitate the drainage of the site during ebb, tidal channels were incorporated per designs developed by Hood [11] from an allometric analysis of tidal channel planform relative to marsh areas coupled with LIDAR data, and the number, location and size (i.e., width and length) of tidal channels for Leque Island were computed. At the zis a ba site, in addition to tidal drainage channels, the placement of a berm in the middle of the site was proposed, resulting in a division of the site into two sub-basins. The berm placement was driven by the need to protect an underground wastewater outfall line. Figure 1b is a schematic representation of the dike and tidal channel configuration for (top) the baseline scenario corresponding to the existing pre-restoration condition and (bottom) the preferred restoration alternative scenario corresponding to post restoration condition as evaluated in this manuscript.

The baseline scenario refers to the existing conditions, maintaining the current river system by permanently repairing failed dikes on Leque Island. The preferred restoration alternative scenario includes the full restoration of Leque Island, eliminating all dikes on the southern side of the island, and retaining a spur dike along the northeastern border of the island as described in Table 1 below.

Table 1. Descriptions of the model scenarios at the Leque Island and zis a ba sites.

Scenario	Leque Island	zis a ba
Baseline	Existing conditions	Existing conditions
Preferred alternative: full restoration at Leque Island and zis a ba sites	Partial removal of existing dike (retaining northeastern spur dike), creation of tidal channels, filling existing ditch and borrow area	Partial removal of existing dike, lowering the perimeter dike elevation, creation of tidal channels, construction of a berm, filling existing ditch and borrow area

2.3. Hydrodynamic Model Setup and Validation

2.3.1. Model Setup, Bathymetry Update and Grid Refinement

Bathymetry was created from different data sources. The main source of bathymetry and topography in the intertidal regions was LIDAR data obtained from the Puget Sound LIDAR Consortium. That bathymetry was then updated using new LIDAR data obtained by The Nature Conservancy (TNC) in 2012. The Snohomish County Surface Water Management Division provided channel cross-section data for Hatt Slough and the OSRC including the West Pass and South Pass reaches. We further updated the bathymetry using the most recent LIDAR data from detailed surveys conducted near the zis a ba project site by the Stillaguamish Tribe. Finally, bathymetry was linearly interpolated into the grid. In the vertical direction, a vertical sigma coordinate system was used using five uniformly distributed vertical layers.

The grid includes Skagit Bay, Port Susan Bay, and Swinomish Channel. In this study, two different grids were generated: (1) the baseline grid and (2) the preferred alternative grid. For the baseline, the grid remained coarse for the inner part of Leque Island and zis a ba sites, but was refined along West Pass, South Pass, and the lower Stillaguamish River (Figure 2a). The inner part is defined as the area of the Leque Island interior to the dikes that is not under tidal inundation. This refinement effort was aimed at understanding in detail the erosion and deposition areas along the Stillaguamish River channels outside of the proposed restoration sites under existing conditions. The baseline grid consists of 35,630 elements and 19,380 nodes in the horizontal plane. This grid was used for validation simulations and for generating baseline conditions for comparison with the preferred alternative simulations.

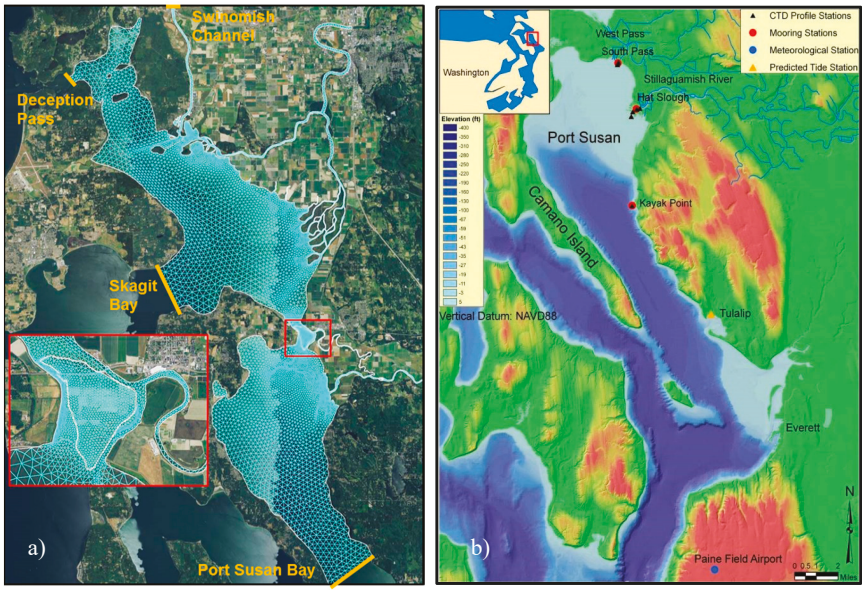

Figure 2. (**a**) Baseline model grid of the Skagit and Stillaguamish River estuaries including Skagit Bay, Port Susan Bay, and the Leque Island and zis a ba. The inset shows detail the Leque Island and zis a ba project sites. (**b**) Oceanographic observation stations at Port Susan Bay, October 2005.

2.3.2. Boundary Conditions

We specified tidal elevation at four open boundaries: (1) the mouth of Skagit Bay; (2) Deception Pass; (3) Swinomish Channel; and (4) the mouth of Port Susan Bay using the X-TIDE program for the period from 10 to 26 October 2005.

We specified salinity as a constant value of 30 ppt along the Port Susan, Yokeko Point, and Padilla Bay boundaries. This boundary value is based on field data collected at Kayak Point Station. Salinity was set to 25 ppt at the Skagit Bay boundary, based on available Skagit Bay data from previous studies. At all boundaries, we set the temperature to 14 °C. The temperature effect on density-induced currents was not considered in the simulation. Field data indicated that temperature variations are not significant (<3 °C) compared to salinity variation (<20 ppt) during the time of simulation.

We obtained wind data from NOAA's National Weather Service site at the Everett/Paine Field Station, which is approximately 30 miles south of the study area. The dominant wind direction is toward the north with wind speed average ≈ 3.4 m/s during the period of interest. Wind force was applied uniformly to the entire model domain and applied at the water-surface as wind stress.

The inflows to the Stillaguamish River system include the Stillaguamish River and the Skagit River. For this study, the total Stillaguamish River flow into Port Susan Bay was estimated by summing the flows from the North and South Forks of the Stillaguamish River. Flow data were obtained from USGS gauge 12167000 near Arlington, Washington and Washington State Department of Ecology gauge 05A105 at RM 33.4 on the South Fork Stillaguamish. The period from 10 to 26 October 2005 during which field data were collected in Port Susan Bay, was selected for the simulation. The average river flow during the period of interest was 69.57 m^3/s.

Skagit River flows were obtained from the USGS gauge 12200500 at Mount Vernon, Washington. The Skagit River influences the project site and Port Susan Bay through estuarine flow that occurs from Skagit Bay to Port Susan through the West Pass of the Old Stillaguamish River. The average river flow during the period from 10 to 26 October 2005 was 349.17 m^3/s, with a high-flow event (about 651 m^3/s as a daily average) that was observed on 18 October 2005.

2.4. Model Validation Results

We conducted this validation effort to ensure that model performance was within a reasonable level of accuracy. The model validation includes a comparison of predicted water surface elevation, salinity, and velocity time series results with observed data. Oceanographic data collected by TNC from 10 to 26 October 2005 were used for model validation. These data were collected as part of the hydrodynamic and ecological assessment for the Port Susan Bay restoration project near the mouth of the Stillaguamish River [12].

Mooring station locations are shown in Figure 2b. Two mooring stations were deployed in the main channels of South Pass and Hatt Slough near the mouth of the Stillaguamish River. The South Pass station was equipped with a current meter and conductivity–temperature–depth (CTD) instrument for continuous tidal elevations, salinity and temperature measurements. Hatt Slough Station was equipped with an acoustic Doppler current profiler (ADCP) for continuous current measurements and a CTD for continuous tidal elevations, salinity, and temperature measurements.

Two CTDs were deployed at the Kayak Point Station. Instantaneous salinity and temperature profiles were also sampled at the South Pass, Hat Sough, and Kayak Point stations during the deployment and retrieval of the instruments.

Predicted water surface elevations are in good agreement with the observed monitoring data at the Kayak Point, Hatt Slough, and South Pass Stations (Figure 3a). The spring-neap tidal cycle and the diurnal variation were well reproduced in the model. Predicted high and low tidal phases also were matched well with observed data. The predicted tidal range at the Kayak Point station ranges from −1 to 3 m as also observed in the Puget Sound coastal region. Weaker tidal elevations were found at South Pass and Hatt Slough. The tidal ranges at South Pass and Hatt Slough were in the range of 3 m and 2 m, respectively, due to the effects of shallow water depths and river backwater. During the high-flow event from 17 to 21 October 2005, tidal elevations at Hatt Slough and South Pass were further elevated because of the river backwater effect.

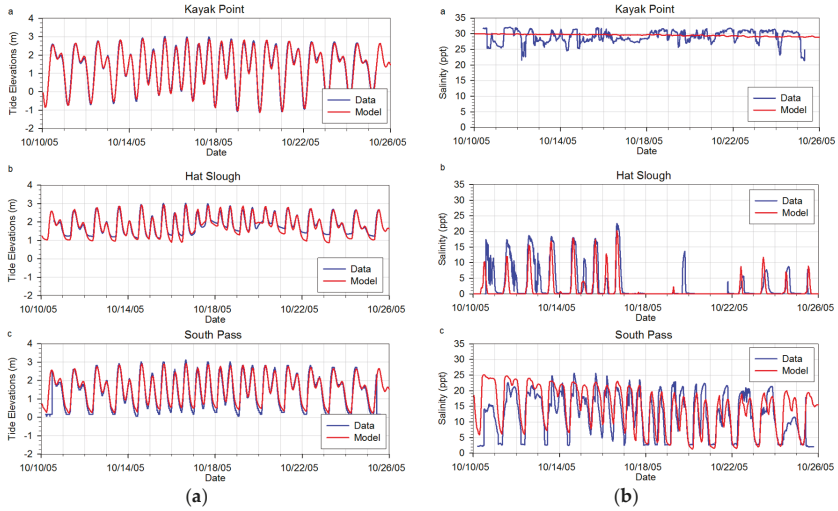

(**a**) (**b**)

Figure 3. Comparison of predicted and measured (**a**) water surface elevations and (**b**) salinity at the Kayak Point, Hatt Slough, and South Pass stations, respectively.

Table 2 provides validation error statistics comparing measured water surface elevation data to simulated results. Error statistics include the root mean square error (RMSE), mean error (ME), and mean error relative (RME) [6]. The overall root mean square error (RMSE) relative to tidal range is <10% with a negative bias of 4 cm and average RMSE of 24 cm.

Table 2. Model error statistics for water surface elevation, salinity, and velocity.

Station	ME (m)	RMSE (m)	RME (%)
Tide: water surface elevation (m)			
Kayak Point	−0.05	0.26	6.33
Hatt Slough	−0.07	0.23	11.92
South Pass	0.00	0.24	7.27
Salinity (ppt)			
Kayak Point	0.48	1.51	1.83
Hatt Slough	−1.62	2.20	4.46
South Pass	−2.81	4.38	5.71
Velocity (m/s)			
Hatt Slough (u)	−0.07	0.08	0.11
South Pass (u)	0.01	0.13	0.18
Mean	−0.03	0.11	0.14
Hatt Slough (v)	−0.04	0.19	0.24
South Pass (v)	0.01	0.03	0.04
Mean	−0.01	0.11	0.14

The predicted salinity time series were compared with field data. Figure 3b shows the comparison of the predicted and observed salinity time series at the Kayak Point, Hatt Slough, and South Pass stations. Predicted salinities matched reasonably well with the observed data, except at the Kayak Point station. Little variation is detected for predicted salinity at Kayak Point because salinity variations there were mainly controlled by the open-boundary condition. At the open boundary, the salinity was specified as constant at 30 ppt. Salinity at the Hatt Slough Stations showed strong tidal fluctuations, varying from 0 ppt during low tide to 20–25 ppt during high tide in a full tidal cycle. Sharp salinity intrusion was

observed during high tide at the Hatt Slough Station. Some discrepancies between observed data and modeled salinity were detected at the Hatt Slough and South Pass Stations. We believe the source of this error is the lack of information on fresh-water river flow distribution between Hatt Slough and the OSRC.

Validation error statistics comparing observed data to simulated results for salinity were computed (Table 2). The overall RMSE is 4 ppt with a bias of −1.3 ppt and a mean absolute salinity error of 2.7 ppt.

Predicted velocities were compared to field-observed data at South Pass and Hatt Slough. We decomposed the predicted velocities into north and south components for a direct comparison to the observed data. Predicted velocities generally matched well with the observed data at both the South Pass and Hatt Slough stations (Figure 4). Predicted velocities at the South Pass station were dominated by the north component, whereas velocities at the Hatt Slough station were dominated by the east component.

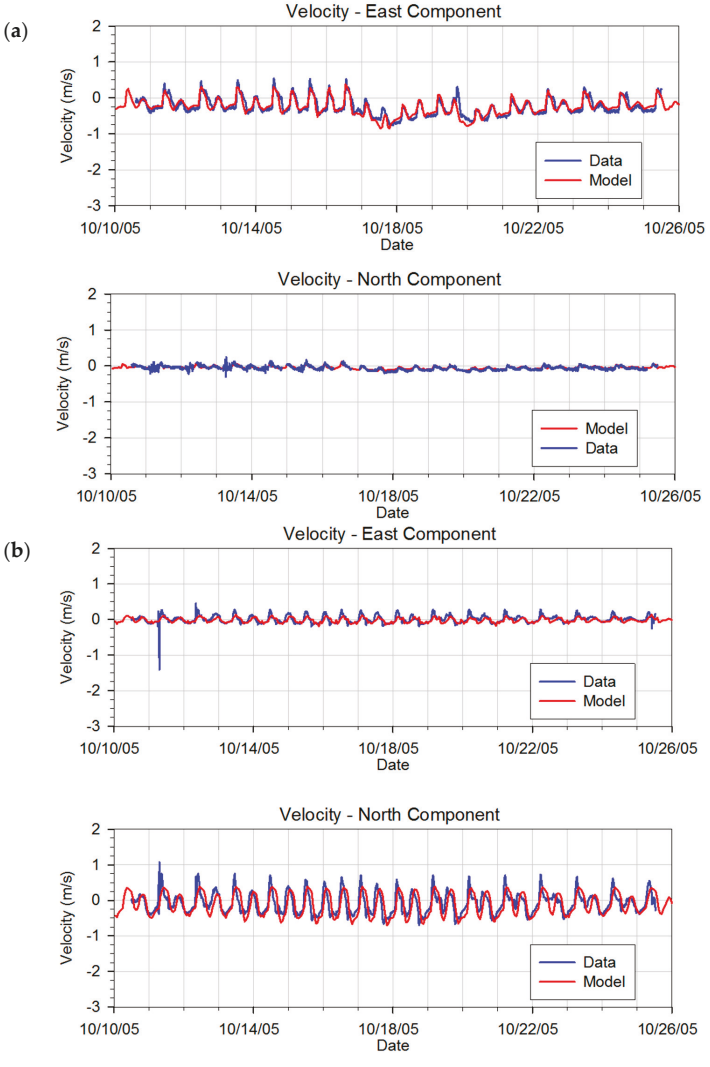

Figure 4. Comparison of predicted and measured velocity components at the Hatt Slough (**a**) and South Pass (**b**) stations, respectively. Data is from mid-depth of the water column.

Error statistics comparing measured versus simulated velocity are also provided in Table 2. The comparison was done for a mid-depth layer at both sites. Model predictions match the field data well at a reasonable level of accuracy. Overall, the RMSE in the north and south directions is less than 14 cm/s, and the mean absolute error is 7 cm/s, except at the Hatt Slough station. This represents <10% error relative to the range of current magnitudes in the Stillaguamish River estuary.

2.5. Simulation of the Preferred Restoration Alternative Scenario at Leque Island and Zis a Ba

We selected conditions experienced during field data collection in October 2005 that were used previously in model calibration to serve as the typical conditions. Flooding and inundation (i.e., restoration area, duration, and frequency), salinity variations, and potential for erosion were the parameters of interest. In addition, high-river-flow conditions representing maximum potential for sediment erosion, deposition, and geomorphological changes were also developed. During extreme fluvial events, major geomorphologic changes such as river channel erosion and the enlargement of steep, incised channels often occur. This scenario was evaluated using bank-full, channel-forming flow and used in combination with the October 2005 tidal conditions. The baseline results were regenerated first followed by the preferred restoration results at Leque Island and zis a ba sites for the two estuarine flow conditions.

2.5.1. Preferred Restoration Alternative Scenario Setup

At the Leque Island site, selected alternative restoration action includes the creation of a network of tidal channels and the removal of the majority of the existing dike footprint to restore tidal processes to the entire property. However, a spur dike, which is a linear section of dike adjacent to the West Pass and South Pass bifurcation of the OSRC, is retained. Skagit River System Cooperative has provided predictions and recommendations for the location, number and size (i.e., length) of tidal channels based on allometric analysis of the tidal channel planform relative to marsh area. These proposed tidal channels will allow the effective exchange of water, fish, and nutrients between the marsh and Port Susan Bay [11].

Figure 5 shows grid details corresponding to the preferred alternative at the Leque Island site. The perimeter dike has been lowered to grade and tidal channels have been incorporated. The design widths of the tidal channels vary between 5 m and 20 m and the depths vary between 1 m and 2 m. To avoid high computational costs and model stability, we limited model cells to as small as 2.5 m to allow 5-m wide channels to be represented. The number of cells gradually increases with distance as the channel widths increase towards the channel mouths.

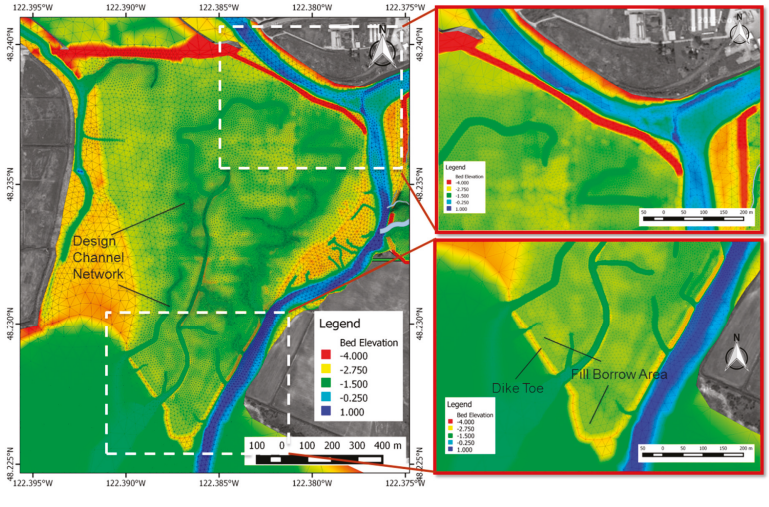

Figure 5. Preferred alternative grid for the Leque Island site.

Figure 6 shows a model grid detail corresponding to the preferred alternative at the zis a ba site. Unlike the Leque Island site, the perimeter dike was lowered to a specified elevation and breached at a number of locations. The preferred alternative design includes sustaining a partial section of dike adjacent to the southwest bank of the OSRC. Also, as shown in Figure 6, the design includes a north-south oriented berm that divides the site into two drainage basins. More details on the zis a ba restoration design can be found in the zis a ba restoration project design [13]. The design widths of tidal channels vary between 2 m and 26 m and depths vary between 0.5 m at the mouth of the channels and approximately −2 m at the upstream end of the channels.

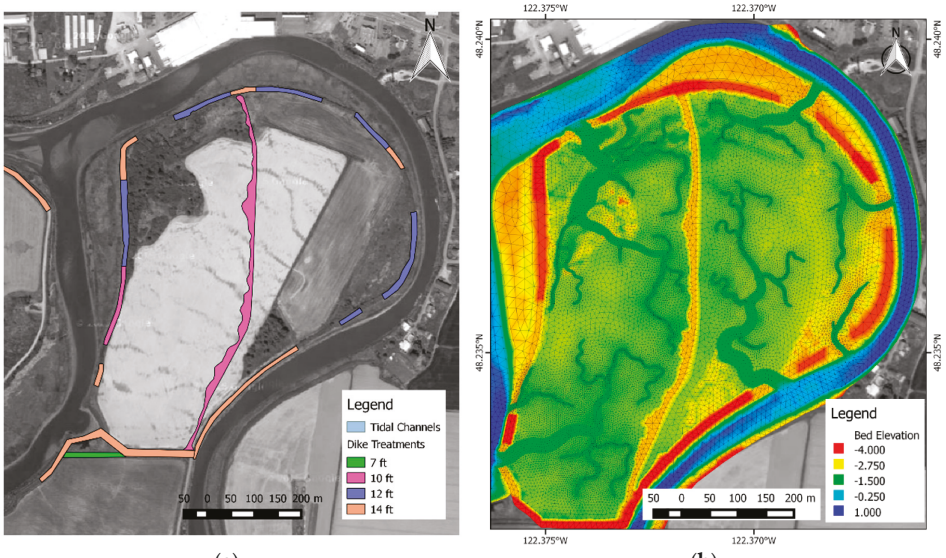

Figure 6. Preferred alternative design (**a**) and grid (**b**) for the zis a ba site.

The model input, parameters and settings were the same as used in the validation and baseline scenario simulation. On the Pacific Northwest National Laboratory (PNNL) high performance cluster using 384 processors, simulations of selected alternative scenarios took about a day of computer time to simulate two-week periods.

2.5.2. Typical Estuarine Conditions of October 2005

The baseline (existing conditions) and the preferred alternatives at the Leque Island and zis a ba sites were both simulated using the same model inputs (i.e., model parameters and forcing) corresponding to typical conditions. We conducted simulations for 2-week periods within the range of 5–26 October 2005, a window selected to represent the typical estuarine conditions.

The results for each scenario are presented as horizontal plots of surface velocity vector distributions overlaid with salinity contours at peak ebb and flood tides. This allows the salinity values to be examined at the two extremes during flood and slack tide, from which areal extents of the tidal exposure may be assessed. We present the contour plots of maximum bed shear stress during a 2-week simulation period, which allows the visual assessment of areas most likely to experience the highest bed shear stresses and potential for sediment erosion. The difference plots of maximum bed shear stress also are presented so that differences between the baseline and preferred alternative scenarios can be examined.

Finally, the time series of water surface elevation (m), salinity (ppt), velocity magnitude (m/s), and bed shear at 11 stations were plotted over a period of 16 days. Time series plots for the preferred restoration alternative scenario were provided with baseline results for relative comparison and evaluated with reference to the desired characteristics for a tidal restoration project. Figure 7 shows the locations of the 11 stations where time series plots of water surface elevation, salinity, bottom velocity, and bed shear stress were generated over the complete 2-week simulation. The model's bottom velocity was obtained from velocity information at the lowermost layer of the model sigma-layers (i.e., 10th layer). Bed shear stress was internally computed in the model using the formula $\tau_b = \rho\, C_d |u^*|$, where ρ is sea water density, C_d is the drag coefficient, and $|u^*|$ is the critical bed shear velocity.

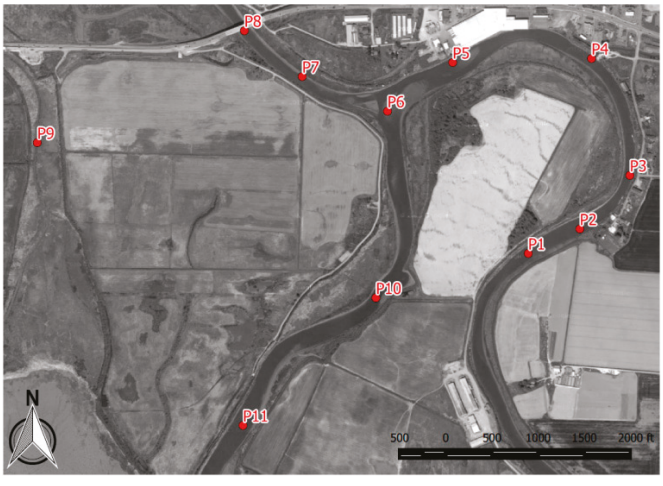

Figure 7. Eleven station locations on the Leque Island and the zis a ba sites.

Guidance from the Skagit River System Cooperative [14] provides information about the desired water characteristics after restoration; those characteristics are a depth range between 20 cm and 38 cm and a salinity range between 5 ppt and 15 ppt, which can support fish habitat.

We examined bed shear stress as the best indicator of expected sediment transport given site-specific variability in bed characteristics and critical shear stress properties controlling erosion potential. We presented bed shear stress in Pascals (Pa). An approximate correlation between the size of sediment particles and critical shear stress for erosion are provided in [15]. Assuming non-cohesive sediments, particles erode and re-suspend when bed shear stress exceeds the limit of critical shear stress values. Silt has maximum critical stress for erosion 0.11 Pa, whereas sand has maximum critical stress for erosion 1.26 Pa.

2.5.3. Simulation of Stillaguamish River High-Flow Conditions

The performance of the proposed restoration actions during high-river-flow conditions was evaluated primarily to assess potential erosion and deposition concerns. The high flow was defined as the bank-full flow condition of 750.62 m^3/s. This flow was determined through sensitivity tests reported in Whiting and Khangaonkar [6]. The sensitivity test was conducted by increasing daily average flow values in increments of 566 m^3/s of the 16-day period in October 2005. Locations along both the Old Stillaguamish River and Hatt Slough were selected to identify where overtopping seemed most likely to happen. The final flow of 750.62 m^3/s was selected as the design high-flow value that the river system could sustain before overtopping occurred.

3. Results & Discussion

3.1. Baseline Scenario

The baseline scenario represents the conditions of the system as it exists today subject to tidal and stream flow forcing. Figure 8a shows a close-up of the baseline scenario grid covering Leque Island and zis a ba surrounded by the perimeter dike.

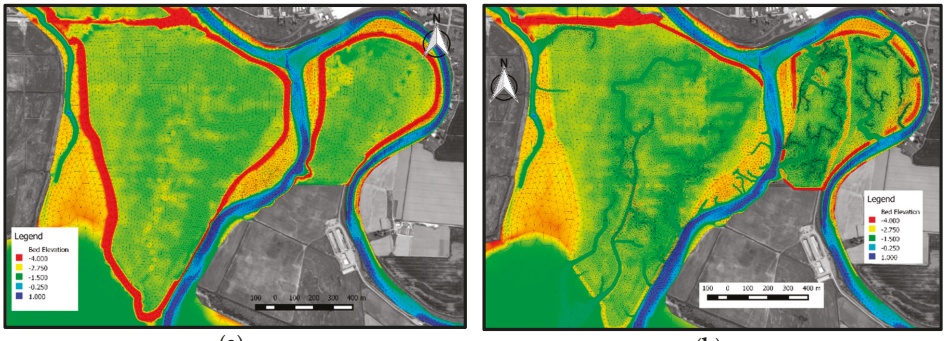

Figure 8. (**a**) Baseline scenario grid overlaying the bed elevation map. (**b**) Preferred restoration alternative scenario grid overlaying the bed elevation map.

3.1.1. Typical Estuarine Flow Conditions

Predicted horizontal salinity and velocity distributions in the surface layer corresponding to high tide and low tide on 24 October 2005 for typical estuarine and high-flow conditions are presented. The mouth of the Old Stillaguamish River is strongly influenced by tides. This strong tidal effect is seen clearly in salinity plots that show upstream propagation up the Lower Old Stillaguamish River during incoming flood tide. Tidal exchange between Skagit Bay and Port Susan Bay occurs through the West Pass and South Pass channels. Figure 9 shows inundation and salinity contour plots at high (bottom) and low tides (top), respectively. The intertidal flats in Port Susan and Skagit Bay are fully inundated, reaching elevations above the toes of the perimeter dikes during high tide, and exposed during the ebb tide. The perimeter dike prevents the inundation of the Leque Island and zis a ba restoration areas. The improvement of model bed elevation by increasing grid resolution along the main river channel increased the simulated resolution of the wetting and drying intertidal regions during the ebb and flood periods.

Fresh water from the OSRC appears to exit into Port Susan mostly through South Pass. During low tide following ebb, the salinity difference between West Pass and South Pass can be as high as 6 ppt (Figure 9: top). The salinity levels and intrusion upriver near the project sites at Leque and zis a ba on the OSRC were sensitive to the fraction of the fresh water split between the Old Stillaguamish River and Hatt Slough. Salinity levels at Davis Slough remain relatively high throughout the tidal cycles as they are controlled primarily by Skagit Bay salinities.

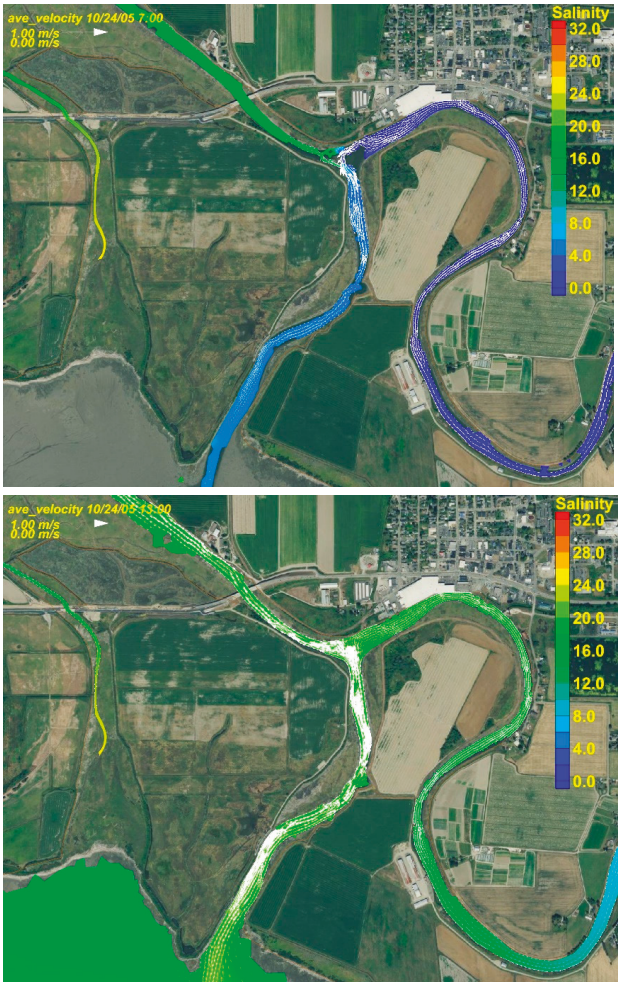

Figure 9. Horizontal distribution of salinity at low tide (07:00: **a**) and high tide (13:00: **b**) for the baseline scenario on 24 October 2005.

3.1.2. High-Flow Conditions

In these high-flow conditions, we focus mainly on examining and identifying regions of high bed shear stress with potential for erosion. Figure 10 shows the maximum and average of bed shear stress for the baseline scenario at high-flow condition (750.62 m^3/s) over a 2-week simulation period. As expected, South Pass experiences high bed shear stress as it acts as the main tidal channel connecting Port Susan and Skagit Bay and provides exchange flow associated with the OSRC. From the plan view of the mean bed shear stress, higher bed shear stresses (>5 Pa) are mostly predicted in South Pass and West Pass reaches immediately downstream of the OSRC channel split at Leque Island.

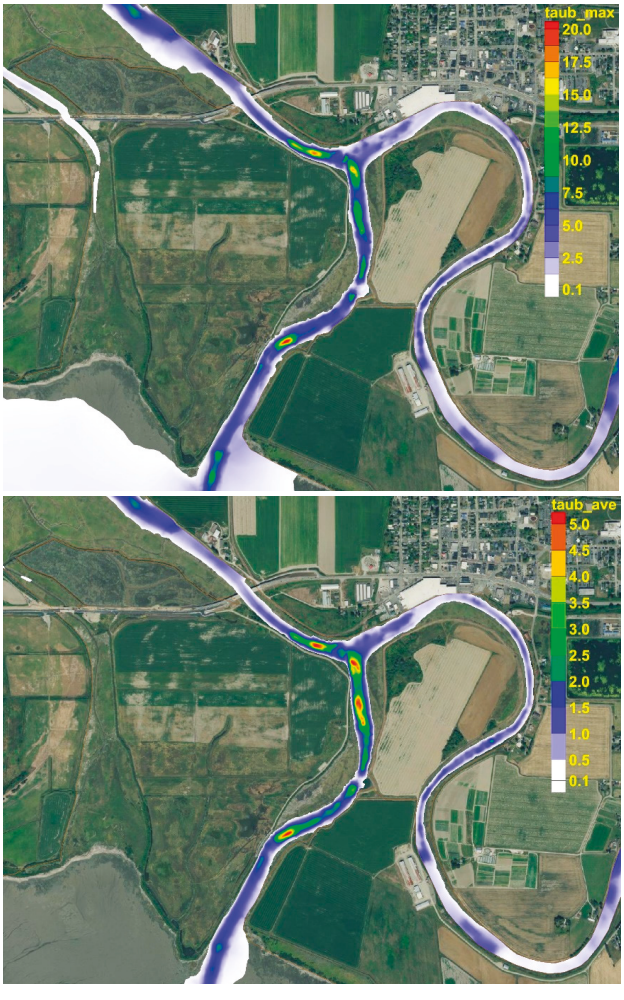

Figure 10. Horizontal distribution of maximum (**a**) and mean bed shear stress in Pa (**b**) for the baseline scenario for the high-flow (bank-full) condition at 750.62 m^3/s.

3.2. Preferred Restoration Alternative Scenario

Figure 8b shows the grid for the preferred restoration alternative scenario, which involves the partial removal of the perimeter dikes and the creation of a network of tidal channels on both the Leque Island and the zis a ba sites.

3.2.1. Typical Estuarine Conditions

To facilitate a quantitative comparison of the preferred alternative scenarios and the baseline scenario, we selected 3 out of 11 stations in the main river channels near the Leque Island and zis a ba sites. Station P1 was selected at the lower OSRC near zis a ba. Station P7, located near the 532 Bridge, was selected to represent West Pass, at which point the water flux is mainly controlled by Skagit Bay. We selected Station P10 to represent South Pass (see Figure 7 for locations of stations P1, P7, and P10.)

The preferred restoration alternative does not cause any significant changes in water elevations at the West Pass and the lower OSRC stations. The mean water surface elevation for the preferred restoration alternative scenario is ≈0.01 m lower relative to the baseline scenario.

However, the results show that the restoration action would alter the predicted salinity at West Pass, South Pass, and the OSRC stations. Salinity is mainly controlled by tidal mixing and upstream fresh-water discharge from the Stillaguamish River. As shown in Figure 11, there is a notable decrease in salinity levels in South Pass (P10), and the influence extends all the way north into West Pass (P7) during high tide. The plot shows that salinity in the preferred alternative scenario can be up to 2 ppt lower than the baseline scenario in West Pass, South Pass, and the lower OSRC stations. The results indicate that the proposed restoration will result in a small decrease in the amount of seawater intrusion into the OSRC, West Pass and South Pass channels.

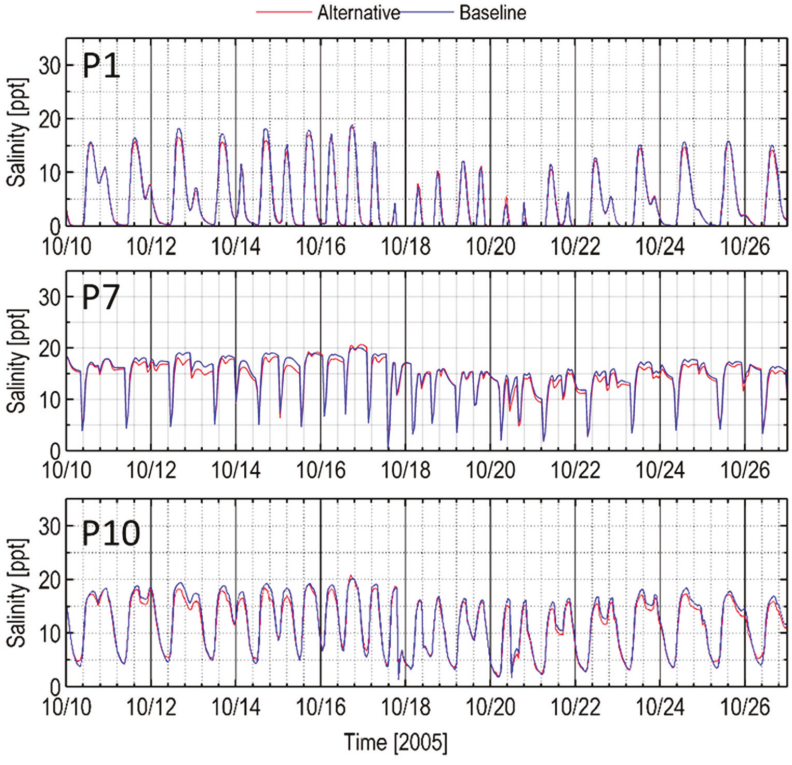

Figure 11. Preferred vs. baseline scenarios: time series of Salinity at Station P1, P7, and P10 for typical estuarine conditions (October 2005).

The inundation areas at high and low tides at Leque Island and zis a ba are shown in Figure 12. During high tide, Leque Island is nearly fully inundated (Figure 12b). The tidal channels connecting Leque Island with South Pass and Port Susan bring seawater into the Leque Island site. The tidal channel at the northwest side connecting Davis Slough and Leque Island also contributes to the inundation. During low tide, southern tidal channels at Port Susan and South Pass become primary drainage channels, allowing water to be transported back to Port Susan (Figure 12a). It appears that the restoration area does not drain fully during low tide. Pockets of seawater are shown to remain in the Leque Island. This is due to the fact that the model does not account for the percolation of wetted areas and cannot resolve fine

scale undulations of bathymetry and the associated drainage. It should be noted that the areas that do not drain are isolated low areas, which will be inundated during the next high tide.

The outflow of freshwater from OSRC primarily occurs through the South Pass during ebb which also carries the majority of net outflow to Port Susan Bay and remains relatively unchanged in the preferred restoration alternative scenario. In the existing as well as in the restored condition, a relatively small outflow of brackish water to Skagit Bay also occurs through West Pass during the flood period.

The predicted horizontal distribution of salinity for the preferred restoration alternative scenario over the restored area is also shown in Figure 12. The seawater enters Leque Island site primarily from the tidal channels at Port Susan Bay and South Pass (Figure 12b). On the zis a ba site, brackish water (≈14 ppt) inundation occurs through the west side of the island and the presence of the berm separates the east side of zis a ba. Inundation of the east side of the zis a ba site occurs with brackish water of lower salinity (≈4 ppt) from the Old Stillaguamish River main stem through channels excavated as part of the restoration design.

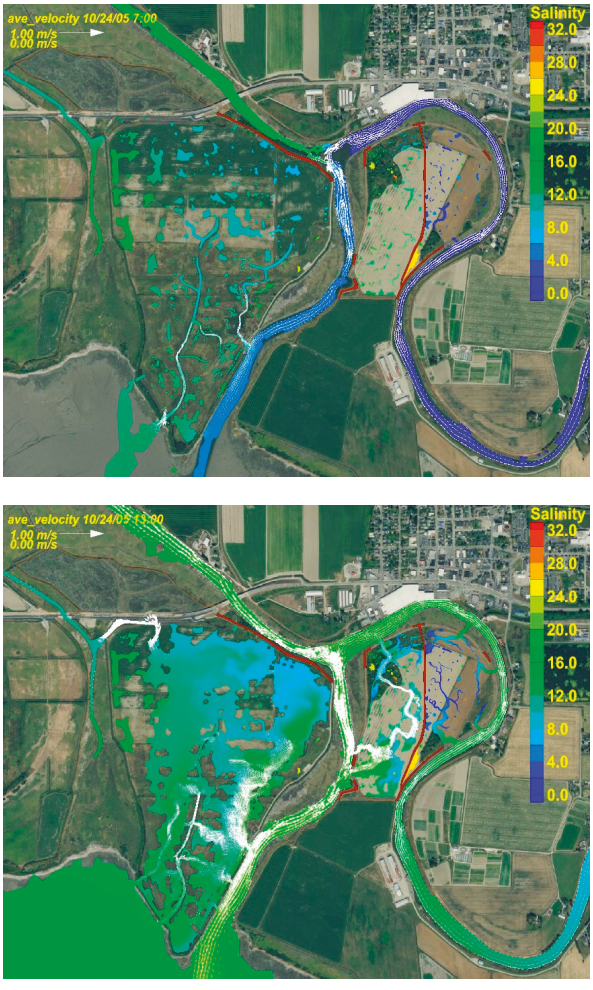

Figure 12. Horizontal distribution of salinity at low tide (07:00: **a**) and high tide (13:00: **b**) for the preferred restoration alternative scenario on 24 October 2005.

Figure 13 is a difference-plot showing the change in predicted salinity between the baseline scenario and the preferred restoration alternative conditions at high and low tides. During low tide following ebb, salinity concentrations are lower (≈−0.5 ppt) in West Pass relative to the baseline, as also shown in the P7 station time series plot (Figure 11), but are relatively unaffected in South Pass or OSRC. A similar reduction in salinity is noted in all three channels during high tide following flood, indicating an overall reduction in the intrusion of saline water from Port Susan. It is noted that this comparison only represents the spring high/low tide condition and that pockets of higher (≈+0.5 ppt) salinity water may be trapped and intrude upstream during other periods in the tidal cycle as seen in the high tide panel at the upstream end of OSRC.

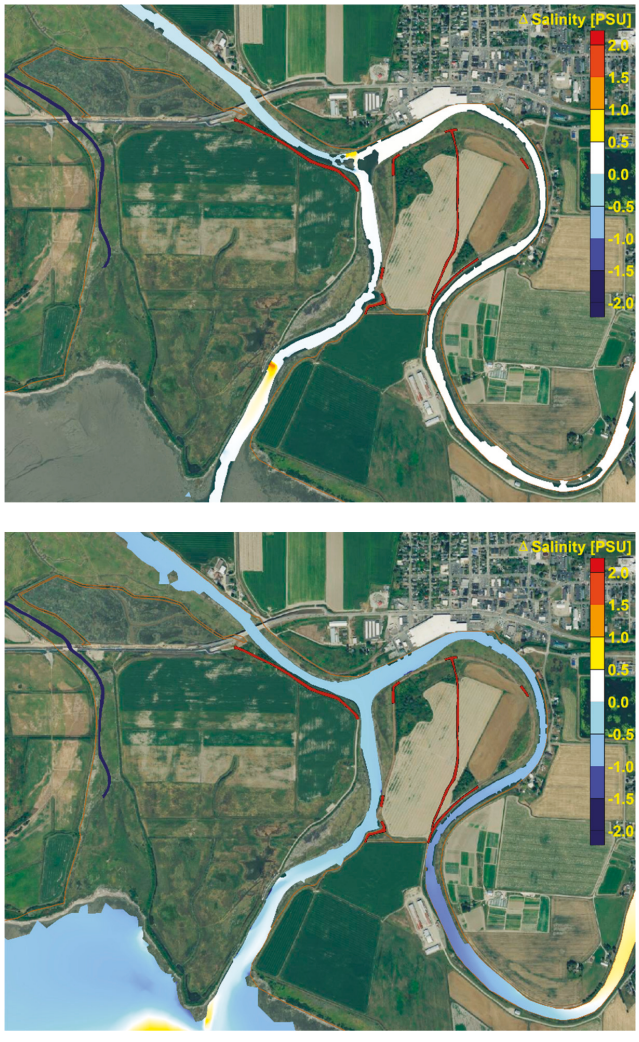

Figure 13. Salinity difference contours of the preferred restoration alternative scenario relative to the baseline at low tide (07:00: **a**) and high tide (13:00: **b**) on 24 October 2005.

The comparison of results indicate that the proposed restoration action will not result in significant changes in velocities at P1, P7, and P10 stations (figure not shown). At P1 and P7, the differences are

negligible; however, in South Pass, an increase in peak velocity is noticeable during flood as well as ebb. An increase in peak velocity of up to 0.09 m/s during spring tide is predicted in South Pass for the preferred restoration alternative scenario.

Figure 14 presents the time series of bed shear stress at the representative stations. Mean bed shear stress at West Pass is predicted to be lower by 0.01 Pa relative to the baseline scenario. Mean bed shear stress at South Pass is predicted to increase by 0.04 Pa, with a peak increase of 0.8 Pa during spring tide. These results indicate that, while West Pass is predicted to experience a slightly lower bed shear stress under the preferred restoration alternative scenario, South Pass will likely experience higher bed shear stress.

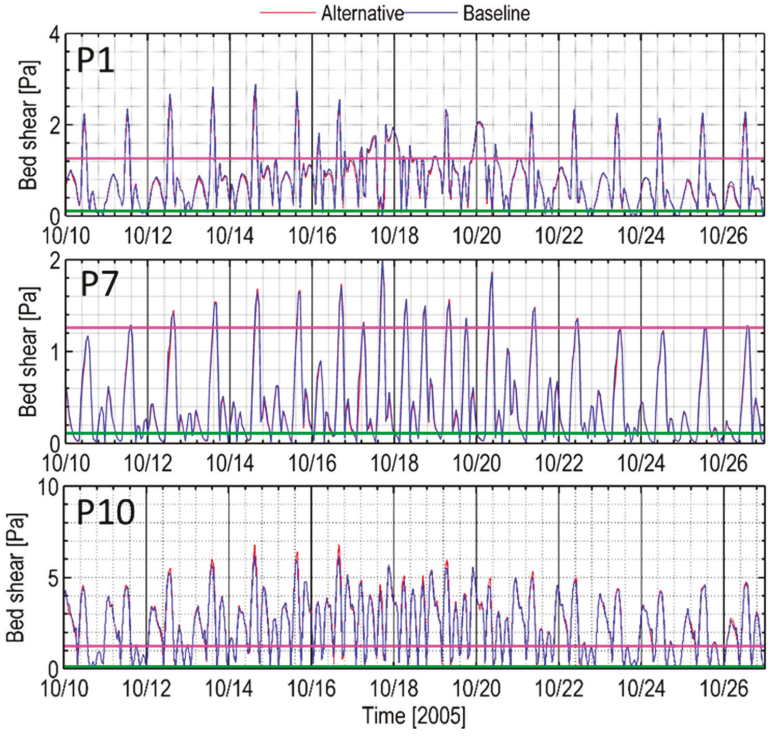

Figure 14. Preferred vs. baseline scenarios: time series of bed shear stress at stations P1, P7, and P10 for typical estuarine conditions (October 2005). Critical bed shear for erosion of sand (0.11 Pa) and gravel (1.26 Pa) are marked as green and pink lines.

3.2.2. High-Flow Conditions

The focus of the high-flow simulation was to evaluate the impact of the proposed restoration action on bed shear stress during channel-forming flow conditions. An examination of the time series of water elevations at the Old Stillaguamish River (P1), West Pass (P7), and South Pass (P3) shows that water surface levels are not significantly different in the preferred restoration alternative scenario relative to those in the baseline scenario. This implies that the storage volume offered by the restored marshes is not significant with respect to the flood reduction benefit that is often associated with restoration actions in flood plains.

An examination of the time series results of predicted velocity magnitudes at Station P1 (ORSC), P7 (West Pass), and P10 (Port Susan) for the preferred restoration alternative scenario shows that the velocity magnitudes under high flows are relatively unchanged compared to the baseline scenario.

Figure 15 shows that velocity magnitudes in West Pass and the lower OSRC in particular remained relatively unchanged under the preferred restoration alternative scenario relative to the baseline scenario. In South Pass, velocity magnitudes were predicted to be higher relative to the baseline scenario during peak flood period by ≈0.12 m/s and relatively little change is seen during ebb when peak velocities are nearly twice as high as those during the flood.

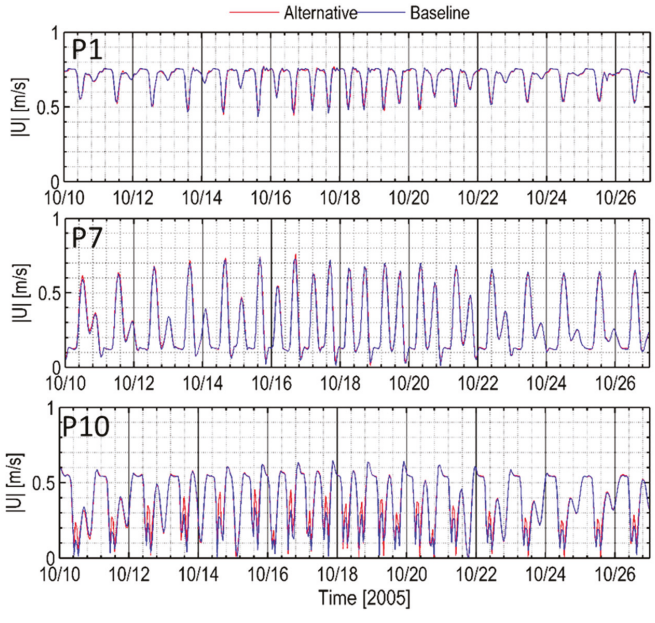

Figure 15. Preferred vs. baseline scenarios: time series of velocity magnitude at Stations P1, P7, and P10 for bank-full conditions at 750.62 m^3/s river flow (tides and wind corresponding to October 2005).

The time series of predicted bed shear stress at the same representative locations during high river flow are shown in Figure 16 for the baseline and preferred alternative scenarios. During the high-flow condition, under the preferred restoration alternative scenario, bed shear stress changes in West Pass and Old Stillaguamish River are relatively small with an average increase of 0.01 Pa. A higher bed shear stress increase of 1.5 Pa is predicted at South Pass station P10 relative to the baseline scenario during the flood period, but relatively little change is predicted during peak ebb, during which peak bed shear stress values reach as high as 7 Pa. These magnitudes, which were above the critical bed shear stress for sand and higher grain sizes in the baseline, were a little higher during the flood tidal period. This could result in an increased upstream movement of sediment during the flood tide.

Figure 17 shows the horizontal distribution of maximum and mean bed shear stress for high-flow (bank-full) conditions at 750.62 m^3/s. The simulated mean bed shear stress result shows that from Twin City Foods downstream to the river channel breach, bed shear stresses higher than 4.5 Pa are noted. This result indicates that the predicted bed shear stress is likely higher in the entire OSRC around zis a ba. The tidal channels over the restoration sites at Leque Island and zis a ba are predicted to experience bed shear stresses in the 1.5 Pa to 2.0 Pa range, which are lower than those predicted in the main river channels. However, bed shear stresses in the tidal channels are also above the critical bed shear stress for sand and gravel during high-flow conditions.

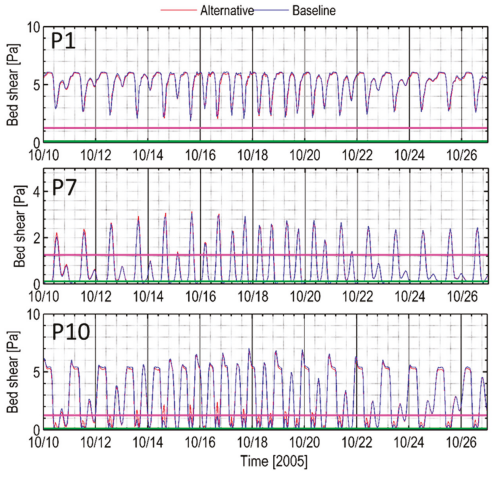

Figure 16. Preferred vs. baseline scenarios: time series of bed shear stress at Stations P1, P7, and P10 for bank-full conditions at 750.62 m^3/s river flow (tides and wind corresponding to October 2005). Critical bed shear for the erosion of sand (0.11 Pa) and gravel (1.26 Pa) is marked as green and pink lines.

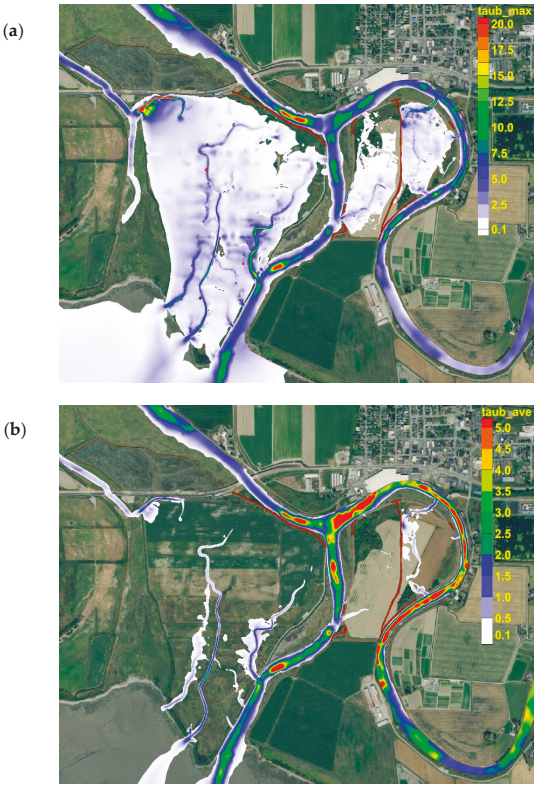

Figure 17. Horizontal distribution of maximum (**a**) and mean bed shear stress (**b**) for the preferred restoration alternative scenario for high-flow (bank-full) conditions at 750.62 m^3/s.

Figure 18 shows a mean bed shear stress difference plot for the preferred restoration alternative scenario and the baseline scenario. An increase in bed shear stress is predicted at most locations in West Pass and South Pass. A decrease in bed shear stress is noted in the OSRC section just east of zis a ba and between the mouths of the tidal channel from zis a ba. This decrease in bed shear is associated with a reduction in river channel flow due to the fraction that is diverted over the east zis a ba site. The presence of tidal channels could alter the bed shear stress in the West Pass and South Pass channels. An increase of up to 0.3 Pa of bed shear stress relative to the baseline can occur in West Pass and South Pass channels at these locations. This increase is small relative to the typical magnitude of bed shear stress, which is significantly higher than that needed for the movement of silt and sand and will not result in a significant increase in scour or channel widening.

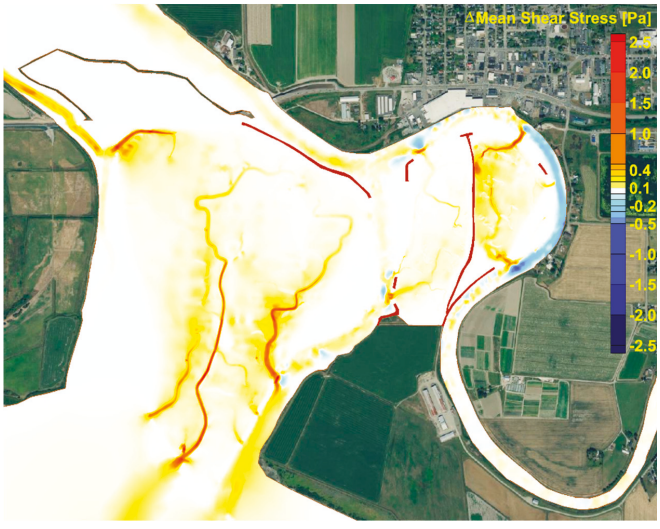

Figure 18. Mean difference bed shear stress contours of the preferred restoration alternative scenario relative to the baseline scenario at the high-flow (bank-full) condition at 750.62 m^3/s.

Bed shear stress distributions in West Pass during high flow conditions are higher under the preferred restoration alternative scenario relative to the baseline scenario, which is opposite to the predictions for typical estuarine flow conditions. Unlike high-flow conditions, the creation of tidal channels and storage across eastern zis a ba leads to a slight increase in bed shear stress along the eastern bend of Old Stillaguamish River around zis a ba. Very little change is predicted in the bed shear stress upstream of the Twin Foods facility. Bed shear stresses at the Leque Island and zis a ba restoration sites are predicted to be highest near the mouth of the tidal channels. The entrance to the tidal channels will likely evolve until an equilibrium cross section is reached.

To facilitate quantitative comparison of scenarios, cumulative frequency statistics were generated for bed shear stress at the selected 11 stations.

Table 3 provides the percentage of the time that bed shear stresses exceed 0.11 Pa (i.e., sand erosion) at the 11 time series stations at the high-flow (bank-full) Condition. An examination of the time series of bed shear stress at stations in the Old Stillaguamish River (P1, P2, P4, P5, and P6) shows that bed shear stresses are not significantly different in the preferred restoration alternative scenario relative to those in the baseline scenario. Bed shear at these locations will be greater than 0.11 Pa (sand erosion) 100% of the time. Stations P10 and P11 (South Pass) experience bed shear stress exceeding 0.11 Pa roughly 80–90% of the time, which is lower compared to the Lower Old Stillaguamish River. The percentage of time that the bed shear stress exceeds 0.11 Pa are $\approx$ 60–80% at Stations P7 and P8 located in West

Pass. Overall, the results indicate that the preferred restoration alternative scenario would increase the percentage of time for bed shear stress to exceed 0.11 Pa at West Pass and South Pass, while the Lower Old Stillaguamish River would experience the same condition in the percentage of time bed shear stress that exceeds 0.11 Pa. In summary, the increases in bed shear will ensure that sediment deposition is not predicted to be a problem; yet, the increases are small enough for increased scour also not to be likely, other than that predicted at the mouths of the tidal drainage channels at restoration sites.

Table 3. Bed shear stress response for all scenarios.

Location	Percentage of Time of Bottom Shear Stress [%]	
	Alternative	Baseline
	>0.11 Pa (Sand)	>0.11 Pa (Sand)
P1	100	100
P2	100	100
P3	100	100
P4	100	100
P5	100	100
P6	100	100
P7	66.91	63.91
P8	75.27	75.25
P9	4.89	1.95
P10	90.77	89.48
P11	85.68	79.15

4. Conclusions

A three-dimensional hydrodynamic model of Port Susan Bay, Skagit Bay, and the interconnecting region including the restoration sites at Leque Island and zis a ba region was developed to generate detailed quantitative oceanographic information for the preferred restoration alternative scenario as part of the restoration feasibility assessment. The effects of restoration involving combinations of creating tidal channels and the removal of sections of dikes from the Leque Island and zis a ba sites were evaluated and compared with baseline (i.e., existing) conditions. A series of hydrodynamic modeling simulations including a typical condition of October 2005 and a high-flow condition representing bank-full conditions were performed for both scenarios, and a set of parameters (i.e., water elevation, salinity, and bed shear stress) was evaluated to quantify the hydrodynamic response of the near-shore restoration project.

The model was first applied to existing conditions prior to restoration, representing the baseline scenario. The baseline simulation successfully reproduced coastal hydrodynamics in the intertidal region of interest in Port Susan Bay near the mouth of the Stillaguamish River, which is tidally dominated with large variations in water-surface levels (≈3 m range) and salinity (0 to 25 ppt). The baseline simulation also showed that the model results, especially water levels in the Stillaguamish River distributaries entering Port Susan Bay (Hatt Slough and OSRC), are sensitive to the respective distributary channel characteristics over the tidal flats in Port Susan Bay. The salinity levels and intrusion upriver near the project sites at Leque Island and zis a ba on the OSRC were also sensitive to the fraction of the fresh water split between Old Stillaguamish River and Hatt Slough.

Following validation, the model was applied to test the response of the preferred restoration alternative scenario at Leque Island and zis a ba for typical estuarine flow conditions and high-flow (bank-full) conditions. An examination of the simulation results for the typical estuarine flow conditions of October 2005 shows that the preferred restoration alternative scenario at Leque Island and zis a ba results in an immediate desired tidal response and the restoration of estuarine functions over the Leque Island and zis a ba project site, which were previously diked off and shielded from tidal exposure. In addition, the results show clearly that proposed actions will likely not cause a significant change in the hydrodynamic behavior of the estuary.

Simulations with the preferred restoration alternative also showed a small lowering in water-surface levels (≈0.01 m lower relative to the baseline scenario) in West Pass, South Pass, and OSRC stations. This result indicates that there is a small decrease in the pressure gradient relative to baseline conditions as the tidal prism is now distributed over the restored area. Under the preferred restoration alternative scenario, there are notable changes to salinity relative to the baseline scenario. The results indicate that proposed restoration will likely decrease the amount of seawater intrusion into the OSRC, West Pass and South Pass channels. As a result, predicted salinities in the preferred alternative scenario are ≈0.5 ppt lower than the baseline scenario in West Pass, South Pass, and the lower OSRC stations.

An examination of tidally averaged velocities and flows shows that the outflow of freshwater from OSRC primarily occurs through the South Pass during ebb, which also carries the majority of net outflow to Port Susan Bay and remains relatively unchanged in the preferred restoration alternative scenario. Results indicate that proposed restoration action will not result in significant changes in velocities at most locations. At the Leque Island and zis a ba restoration sites, bed shear stress is predicted to be highest near the entrances of the tidal channel that drain the sites. It is expected that the mouths of these tidal channel entrances will likely evolve until an equilibrium cross-section is reached.

The potential for erosion and flooding-related damage was examined using the bank-full river flow condition for the baseline and preferred alternative scenario. The results reflect the fact that the locations of the Leque Island and zis a ba restoration sites are near the river mouth. These sites are primarily dominated by the influence of tidal exchange flow and not significantly affected by changes in river flow. During high-flow (bank-full) conditions, the Leque Island and zis a ba sites also experienced increases in velocity magnitudes and bed shear stresses relative to typical flow conditions, especially in the main river channels. However, results for the preferred restoration alternative scenario show that the velocity magnitudes under high flows are relatively unchanged compared to the baseline scenario. In South Pass, velocity magnitudes were predicted to be higher relative to the baseline scenario during peak flood period by ≈0.12 m/s and relatively little change is seen during ebb when peak velocities are nearly twice as high as those during the flood. During the high-flow condition, under the preferred restoration alternative scenario, bed shear stresses in West Pass and South Pass are slightly higher.

Overall, simulation results indicate that the preferred restoration alternative scenario provides an estuarine response consistent with the planned design. The preferred restoration actions would result in relatively minor changes in water surface elevations and salinity in the OSRC surrounding the restoration sites. Because of changes in the tidal prism from increased storage and drainage from the restoration sites, minor changes in velocity magnitude and associated bed shear stresses are predicted. At most locations in the surrounding river channels, under typical flow conditions, there is a small reduction in bed shear stress and a small increase in bed shear stress near the mouths of tidal drainage channels from the restoration sites. These changes in bed shear are negligible relative to the typical magnitude of bed shear stress under baseline conditions, which is significantly higher than that needed for the movement of silt and sand. The overall conclusion based on the results is that tidal estuarine functions will be successfully restored at the Leque Island and zis a ba sites through the proposed actions and should lead to an increase in available tidal marsh area in the system. Also, the impacts on existing circulation and estuarine characteristics would be relatively small.

Author Contributions: Conceptualization, A.N. and T.K.; methodology, A.N. and T.K.; model development and validation, A.N.; formal analysis, A.N. and T.K.; writing—original draft preparation, A.N. and T.K.; writing—review & editing, A.N. and T.K.; project administration, T.K.

Funding: This research was funded by Ducks Unlimited, Inc. through CWFO Agreement No 69998 under contract DE-AC05-76RL01830.

Acknowledgments: The authors would like to thank The Nature Conservancy, Cardno, and Snohomish County for providing LIDAR survey, bathymetric survey, and oceanographic monitoring data for use in model development and validation. We also would like to thank; Jonathan Whiting of Pacific Northwest National Laboratory for providing information on bathymetry data and previous phase model assessment result. Steve Liske of Duck Unlimited Inc. who provided the designs for the Leque Island and zis a ba restoration project, background

information, historic monitoring data; and Loren Brokaw of Washington State Department of Fish and Wildlife who provided direction and guidance for the assessment and helped facilitate numerous technical discussions and stakeholder meetings.

Conflicts of Interest: The authors declare no conflict of interest.

References

1. Liu, J.G.; Dietz, T.; Carpenter, S.R.; Alberti, M.; Folke, C.; Moran, E.; Pell, A.N.; Deadman, P.; Kratz, T.; Lubchenco, J.; et al. Complexity of coupled human and natural systems. *Science* **2007**, *317*, 1513–1516. [CrossRef] [PubMed]
2. Battin, J.; Wiley, M.W.; Ruckelshaus, M.H.; Palmer, R.N.; Korb, E.; Bartz, K.K.; Imaki, H. Projected impacts of climate change on salmon habitat restoration. *Proc. Natl. Acad. Sci. USA* **2007**, *104*, 6720–6725. [CrossRef] [PubMed]
3. Scholz, N.L.; Myers, M.S.; McCarthy, S.G.; Labenia, J.S.; McIntyre, J.K.; Ylitalo, G.M.; Rhodes, L.D.; Laetz, C.A.; Stehr, C.M.; French, B.L.; et al. Recurrent die-offs of adult coho salmon returning to spawn in Puget Sound lowland urban streams. *PLoS ONE* **2011**, *6*, e28013. [CrossRef] [PubMed]
4. Khangaonkar, T.; Sackmann, B.; Long, W.; Mohamedali, T.; Roberts, M. Simulation of annual biogeochemical cycles of nutrient balance, phytoplankton bloom(s), and DO in Puget Sound using an unstructured grid model. *Ocean Dyn.* **2012**, *62*, 1353. [CrossRef]
5. Khangaonkar, T.; Nugraha, A.; Xu, W.W.; Long, W.; Bianucci, L.; Ahmed, A.; Mohamedali, T.; Pelletier, G. Analysis of hypoxia and sensitivity to nutrient pollution in Salish Sea. *J. Geophys. Res. Ocean.* **2018**, *123*, 4735–4761. [CrossRef]
6. Khangaonkar, T.; Nugraha, A.; Hinton, S.; Michalsen, D.; Brown, S. Sediment transport into the Swinomish Navigation Channel, Puget Sound—Habitat restoration versus navigation maintenance needs. *J. Mar. Sci. Eng.* **2017**, *5*, 19. [CrossRef]
7. Khangaonkar, T.; Nugraha, A.; Wang, T.P. Hydrodynamic zone of influence due to a floating structure in a Fjordal Estuary—Hood Canal Bridge Impact Assessment. *J. Mar. Sci. Eng.* **2018**, *6*, 119. [CrossRef]
8. Yang, Z.; Wang, T.; Cline, D.; Williams, B. Hydrodynamic modeling analysis to support nearshore restoration projects in a changing climate. *J. Mar. Sci. Eng.* **2014**, *2*, 18–32. [CrossRef]
9. Whiting, J.; Khangaonkar, T. *Hydrodynamic Modeling Analysis for Leque Island and zis a ba Restoration Feasibility Study*; Technical Report for United States Department of Energy, Document Number PNNL-24023; Pacific Northwest National Laboratory: Seattle, WA, USA, January 2015.
10. Chen, C.; Liu, H.; Beardsley, R.C. An unstructured, finite-volume, three-dimensional, primitive equation ocean model: Application to coastal ocean and estuaries. *J. Atmos. Ocean. Technol.* **2003**, *20*, 159–186. [CrossRef]
11. Hood, W.G. *Conceptual Tidal Channel Design for the Leque Island Restoration Site*; Technical Report; Skagit River System Cooperative: La Conner, WA, USA, June 2015.
12. Yang, Z.Q.; Khangaonkar, T.; Lee, C. *Hydrodynamic Modeling Analysis for Leque Island Restoration Feasibility Study*; Technical Report for Ducks Unlimited, Inc., Document Number PNWD-3813; Pacific Northwest National Laboratory: Seattle, WA, USA, January 2007.
13. Stillaguamish Tribe of Indians. *Zis a ba Restoration Project Design*; Technical Report 42445008; Cardno: Snohomish County, WA, USA, May 2016.
14. Hood, W.G.; Skagit River System Cooperative, La Conner, WA, USA; Khangaonkar, T.; Pacific Northwest National Laboratory, Seattle, WA, USA. Personal communication, 2014.
15. Julien, P.Y. *Erosion and Sedimentation*; Cambridge University Press: Cambridge, UK, 1998.

Journal of
Marine Science and Engineering

MDPI

Article

A Sensitivity Analysis of the Wind Forcing Effect on the Accuracy of Large-Wave Hindcasting

Taiping Wang, Zhaoqing Yang *, Wei-Cheng Wu and Molly Grear

Pacific Northwest National Laboratory, 1100 Dexter Avenue North, Suite 500, Seattle, WA 98109, USA; taiping.wang@pnnl.gov (T.W.); wei-cheng.wu@pnnl.gov (W.-C.W.); molly.grear@pnnl.gov (M.G.)
* Correspondence: zhaoqing.yang@pnnl.gov; Tel.: +1-206-528-3057

Received: 29 September 2018; Accepted: 5 November 2018; Published: 14 November 2018

Abstract: Deployment of wave energy converters (WECs) relies on consistent and accurate wave resource characterization, which is typically achieved through numerical modeling using deterministic wave models. The accurate predictions of large-wave events are critical to the success of wave resource characterization because of the risk on WEC installation, maintenance, and damage caused by extreme sea states. Because wind forcing is the primary driver of wave models, the quality of wind data plays an important role in the accuracy of wave predictions. This study evaluates the sensitivity of large-wave prediction to different wind-forcing products, and identifies a feasible approach to improve wave model results through improved wind forcing. Using a multi-level nested-grid modeling approach, we perform a series of sensitivity tests at four representative National Data Buoy Center buoy locations on the U.S. East and West Coasts. The selected wind-forcing products include the Climate Forecast System Reanalysis global wind product and North American Regional Reanalysis regional wind product as well as the observed wind at the buoys. Sensitivity test results indicate a consistent improvement in model predictions for the large-wave events (e.g., >90th percentile of significant wave height) at all buoys when observed-wind data were used to drive the wave model simulations.

Keywords: wave energy; wind forcing; large-wave hindcast; multi-level nested-grid modeling; CFSR; NARR; WaveWatch III; SWAN

1. Introduction

The accuracy of wave models in simulating wave climates is critical to the success of wave energy development, especially in nearshore regions where wave energy development is most likely to occur. As recommended by the International Electrotechnical Commission Technical Specifications (IEC TS) [1], the development of wave energy projects relies on consistent and accurate wave resource characterization, which is typically achieved through high-resolution wave modeling at the project sites. One gap in this modeling effort is the accurate prediction of large-wave events, e.g., the waves that account for the 90th percentile of the significant wave height and are usually produced by storms, such as tropical and extratropical cyclones.

In many wave modeling studies, large waves have been consistently underpredicted compared to measurements at buoys, especially under extreme weather conditions, such as hurricanes and typhoons [2,3]. For instance, Pan et al. [3] evaluated the performance of an operational wind wave forecasting system in Taiwan, and found the averaged peak wave heights were underestimated during typhoon events. By using multiple wind inputs to model a cyclone event, a regional wave model used near Newport, Oregon underestimated the large waves for all simulations [4]. A global wave model using the Climate Forecast System Reanalysis (CFSR) global wind product for the long-term wave hindcast also produced the largest errors during winter months and large-wave events [5]. In our earlier studies [6,7], we successfully applied two third-generation spectral wave

models, WaveWatch III (WWIII) [8,9] and the Unstructured version of Simulate Wave Near Shore (UnSWAN) [10], to simulate wave climates on the U.S. West Coast based on the National Oceanic and Atmospheric Administration's (NOAA's) National Centers for Environmental Protection (NCEP) global CFSR wind product [11]. Overall, the model-data comparisons showed satisfactory model performance with correlation coefficients (R) greater than 0.9 for both the omnidirectional power and significant wave height at nearly all validation National Data Buoy Center (NDBC) buoys. However, the results also indicated that, especially for the nearshore buoys, both models tend to underpredict the significant wave height and wave power during large-wave events [6,7].

As pointed out by other similar studies, the underestimation of large waves could be partially constrained by the accuracy of wind forcing during the storm events, especially of those operational global wind-model products [2–4,12]. A quick comparison of the CFSR wind with observed wind at NDBC buoys also confirmed that the discrepancy in wave predictions appears to be consistent with that in the wind forcing. Figure 1 shows the comparisons between CFSR wind and observed buoy wind at two buoys in the northeast Pacific Ocean—an offshore buoy, NDBC 46002 (~270 nautical miles offshore), and a nearshore buoy, NDBC 46026 (18 nautical miles from San Francisco, CA, USA). The comparisons indicate that the CFSR wind product generally performs much better in the open ocean than in the nearshore regions. At the nearshore Buoy 46026, the CFSR wind product substantially underestimates high wind (i.e., wind speed greater than 5 m/s).

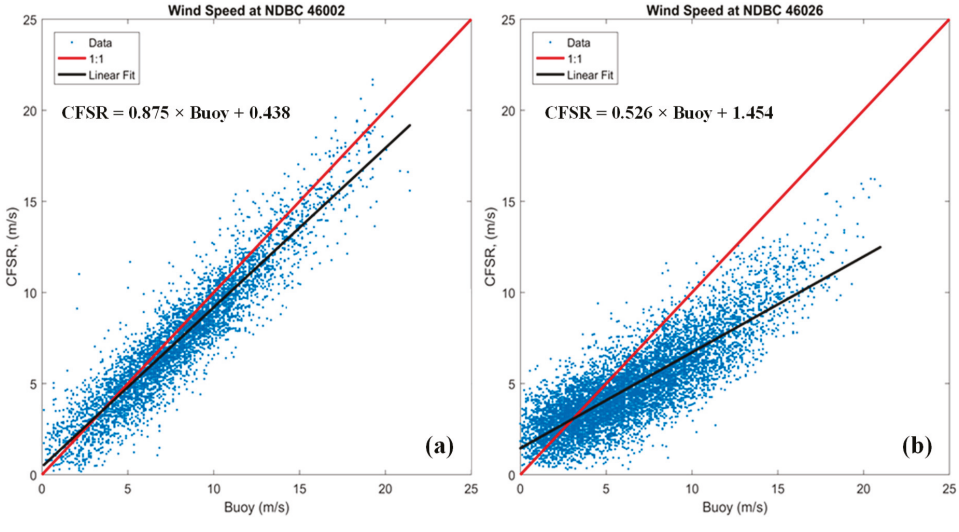

Figure 1. Scatterplot comparisons of CFSR wind speed and observed wind speed at NDBC Buoys 46002 (**a**) and 46026 (**b**) in the northeast Pacific Ocean.

Because wind forcing is the primary driver for wave models, its quality plays a critical role in determining the accuracy of wave predictions. Thus, it is necessary to investigate whether wave model results can be improved by using more accurate wind-forcing products, such as observed wind. This paper presents a study to evaluate the sensitivity of wave models to different wind-forcing products and to identify a feasible approach for improving wave model results through improved wind forcing, with a special focus on large-wave predictions. Improving large-wave prediction not only provides important siting information for WEC development, but also reduces associated maritime risk, such as damage to coastal zones and coastal infrastructure.

2. Methods

2.1. Selection of Study Sites

To conduct the wind-sensitivity tests, we selected four representative NDBC buoys as the study sites and reviewed available wind-model products. A number of NDBC buoys in U.S. West and East Coasts were evaluated, and four representative buoys were finally selected based on the combination of the following criteria:

- Availability of high-quality wave data for wave model validation and wind data for evaluation of the quality of the modeled wind products;
- high wave energy resource and proximity to shore; and
- representativeness of regional distribution.

In general, the number of NDBC buoys that have high-quality, concurrent wave and wind observations is limited. We reviewed all nearshore NDBC buoys on the U.S. West and East Coasts and selected four study sites based on the criteria listed above. Of the four sites, two are located on the West Coast and two on the East Coast (Figure 2). Specifically:

1. NDBC 46050, Stonewall Bank, Oregon, USA. This site was selected because of its high wave resource potential and high-quality wave and wind data, as well as its intermediate water depth and proximity to shore (20 nautical miles from Newport, OR, USA). It is also adjacent to the North Energy Test Site, managed by the Pacific Marine Energy Center, and has been studied extensively [6,13–16].
2. NBDC 46026, San Francisco, California, USA. This site was selected to represent the wind and wave characteristics of the California coast. NDBC 46026 is located 18 nautical miles from San Francisco and has long-term wind and wave records dating back to 1982. Unlike the narrow continental shelf off the Oregon and northern California coasts, the continental shelf off San Francisco Bay is relatively broad and NDBC 46026 is at a shallow-water depth of 53 m. This study site will provide insight into the effect of wind forcing on shallow-water wave modeling on the West Coast.
3. NDBC 44013, Boston, Massachusetts, USA. Although wave resources on the East Coast are smaller than those on the West Coast, the New England region still has a significant amount of wave energy, according to the Electric Power Research Institute, Inc. (Palo Alto, CA, USA) [17]. Based on a recent analysis by the National Renewable Energy Laboratory (NREL) [18], the Massachusetts coast is among the highest-ranked sites in terms of wave resources and market potential. Therefore, the Boston Harbor and coast were selected for their relatively high wave resource as being representative of the New England region. NDBC 44013 is located 16 nautical miles offshore at a water depth of 64.5 m. It also has good quality, long-term observed wave and wind data dating back to 1984.
4. NDBC 41025, Diamond Shoals, NC, USA. North Carolina's coast is the only region identified as a high-resource and -market potential site south of the New England coast in NREL's study [18]. NDBC 41025 is located near the edge of the continental shelf break and the Hatteras Canyon. It is located at a water depth of 68.3 m and about 16 nautical miles from Cape Hatteras. The North Carolina coast is also regularly subjected to the threat of tropical cyclones. Therefore, this study site will provide important information regarding the effect of extreme wind events on the accuracy of model simulations for large waves.

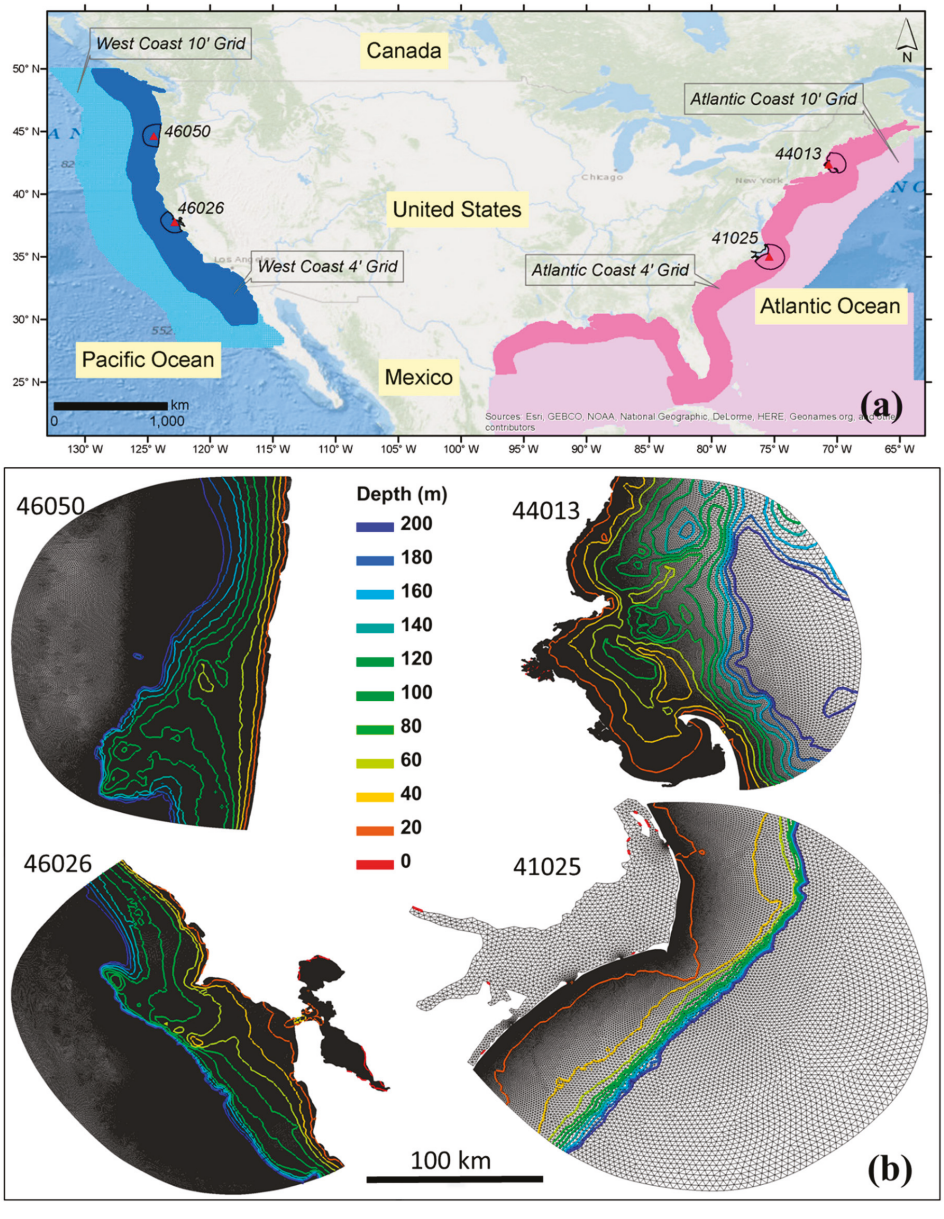

Figure 2. (**a**) Locations of the four selected NDBC buoys (triangles) and the corresponding UnSWAN local domain boundaries. The NOAA's 10-arc minute and 4-arc minute WWIII domain coverages for the U.S. West Coast and Atlantic Coast are also indicated in the figure. (**b**) The four UnSWAN model grids with depth contours.

2.2. Review of Wind Products

Many community atmospheric modeling products are publicly available for use to drive ocean circulation and surface wave models. Among them, the following six global and regional atmospheric products are the most common ones currently being used by the ocean modeling community (Table 1):

- NOAA NCEP's CFSR. Since 2011, the CFSR was upgraded to CFS Version 2 (CFSv2);
- NOAA NCEP's Global Forecast System (GFS);
- European Centre for Medium-Range Weather Forecasts (ECMWF);
- Japan Meteorological Agency's Japanese ReAnalysis (JRA);
- NCEP's North American Regional Reanalysis (NARR); and
- NCEP's North American Mesoscale Forecast System (NAM).

Table 1. Evaluated wind-model products.

Product Name		Spatial Coverage	Spatial Resolution	Temporal Range	Temporal Resolution
CFSR	CFSR	Global	0.5 degree	1979–2010	Hourly
	CFSv2	Global	0.5 degree	2011–present	Hourly
ECMWF	ERA-Interim	Global	0.703 degree	1979–present	3-hourly
	ERA-20C	Global	1.125 degree	1900–2010	3-hourly
GFS		Global	0.5 degree	2007–2014	3-hourly
		Global	0.25 degree	2015–present	3-hourly
JRA		Global	0.562 degree	1957–2016	3-hourly
NARR		North America	32.463 km	1979–present	3-hourly
NAM		North America	12.19 km	2004–present	6-hourly

The spatial and temporal coverages and resolutions of these six wind products are listed in Table 1. Due to time and resource constraints, a subset of wind products was further selected to drive wave simulations for the wind-sensitivity analysis after a comparative review of their performance against the observed wind and their temporal and spatial resolutions. Figure 3 shows the performance statistics of wind speed for the full year of 2016. As indicated by the negative bias at nearly all buoys, most wind-model products tend to underpredict wind speed in comparison to buoy observations. Overall, the performance statistics for all four global products are comparable. For the two regional products, NAM performs better than NARR, especially when judged by the correlation coefficient (R) and root mean square error (RMSE) parameters. The comparisons also indicate that all model products perform the worst at NDBC 46026, the shallow-water buoy off the coast of San Francisco Bay.

Because CFSR/CFSv2 wind has a much higher temporal resolution (hourly) than the other three global products (three-hourly) and has been widely used for wave energy resource modeling on the U.S. coasts, we decided to use the global wind product from CFSR/CFSv2 for wind-sensitivity analysis. Due to time and resource constraints, other global wind products (ECMWF, JRA, and GFS) were not considered in this study. For the regional wind product, because the six-hourly resolution of NAM is far below the IEC TS criterion for temporal resolution, we chose to use NARR for this study.

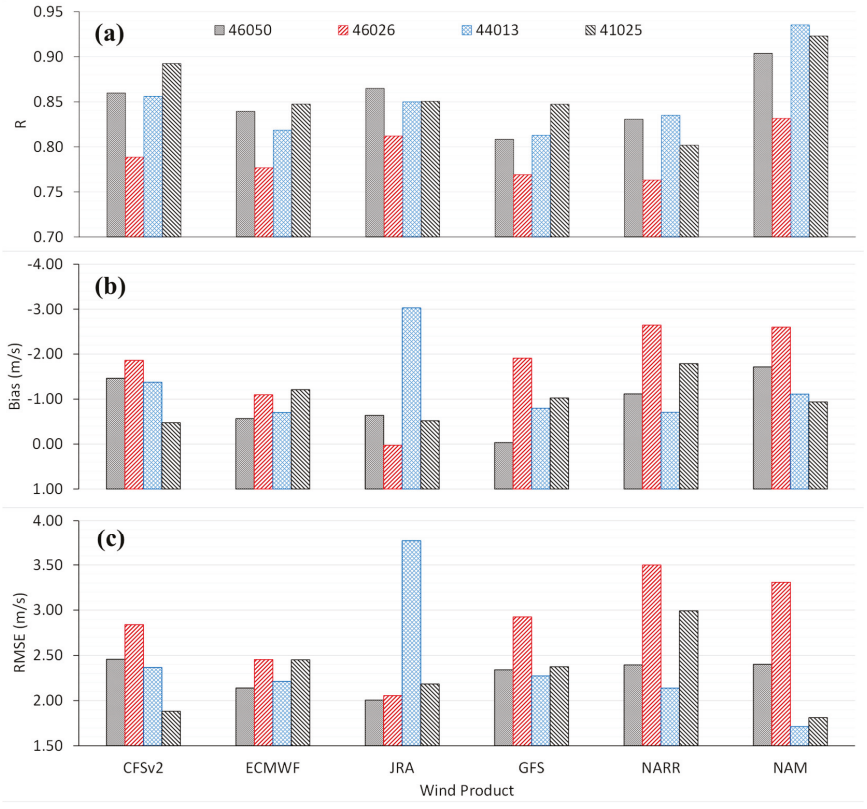

Figure 3. Performance statistics of three representative parameters ((**a**)—R; (**b**)—bias; and (**c**)—RMSE for all six wind products evaluated in this study. The correlation coefficient, R, is calculated at the significance level of $\alpha = 0.05$ throughout this study.

2.3. Model Configuration

Following the path of previous wave modeling work [6,7], we employed a similar multi-level nested-grid modeling approach in this study. This approach combines the strength of the WWIII and UnSWAN models in simulating waves in open oceans with structured grids and those in nearshore regions with flexible, unstructured grids. WWIII and SWAN are among the most widely used third-generation, phase-averaging spectral wave models. WWIII has been maintained and used by NOAA's NCEP for operational ocean wave forecasts from global to regional scales [9]. SWAN is developed at Delft University of Technology, and computes random, short-crested, wind-generated waves in coastal regions and inland waters [10]. The unstructured version of SWAN is especially suitable for simulating waves in nearshore regions with complex geometry. Specifically, we generated fine-resolution (from ~100 m to several kilometers) UnSWAN model grids around the four NDBC buoys (Figure 2) to serve as the local-level model domains. The model grid bathymetry was interpolated from NOAA's three arc-second Coastal Relief Model and available high-resolution (1/3 arc-second) tsunami bathymetry data sets. In addition, the three nested structured-grid WWIII model domains provided wave open boundaries for the UnSWAN domains. The WWIII model configuration was based on NOAA/NCEP's multi-resolution, nested WWIII model package [8], which includes a global model domain of 30′ resolution and two finer levels (10′ and 4′) of nesting domains for the U.S. West and East

Coasts (Figure 2). Hourly spectral output from the 4-arc minute WWIII model domains provided the open boundary forcing at each open boundary node of the UnSWAN domains.

The model configuration for UnSWAN simulations was specified in the same way as that specified by Wu et al. [7]; i.e., the model uses 24 direction bins and 29 spectral frequency bins with a logarithmic increment factor of 1.1 covering the frequency range from 0.035 Hz to 0.505 Hz. This spectral resolution meets the minimum requirements specified by the IEC TS; i.e., a minimum of 25 frequency components and 24 to 48 directional components, and a frequency range covering at least 0.04 to 0.5 Hz. The WWIII model was configured in a way similar to that described by Chawla et al. [8], except that the ST2 source term package was replaced with the ST4 source term package, and the spectral resolution was changed to 29 bins, matching those used by the UnSWAN model. The ST4 physics package consists of new parameterizations for swell, wave breaking, and short-wave dissipations of wind-generated waves, which are consistent under a wide range of conditions and at scales from the global ocean to coastal regions [19]. The previous study demonstrated that the ST4 package consistently produced more accurate model results for unidirectional power density and significant wave height parameters [6]. The model versions used in this study are v41.20 for UnSWAN and v5.08 for WWIII.

2.4. Model Simulations

Five sensitivity runs (Table 2) were conducted, including the baseline-condition simulations for the WWIII and UnSWAN models (Runs 1 and 2, respectively), in which both models were forced by the CFSR wind. The configuration of the baseline condition was also consistent with that in the previous studies [6,7]. Because the primary focus of this study was to evaluate whether better wind forcing, especially with the most accurate observational wind data at the buoys, can improve wave results, a sensitivity run (Run 4) with observed wind forcing was conducted for all UnSWAN domains. Meanwhile, a sensitivity run (Run 3) without wind was conducted to examine the effect of wind forcing on wave simulations at the local-level UnSWAN domains. Lastly, to evaluate whether the regional wind product with a finer spatial resolution could improve wave model results, we conducted a sensitivity run (Run 5) by replacing CFSR wind with NARR wind for the 4′ WWIII model domains using the nested-grid WWIII model. To be consistent with previous studies [6,7], we decided to use the same calendar year of 2009 as the simulation period in this study.

Table 2. Designed model runs.

Run#	Model Runs	Model Grids	Wind Forcing
1	Baseline WWIII	WWIII Domains	CFSR
2	Baseline UnSWAN	UnSWAN Domains	CFSR
3	UnSWAN without Wind	UnSWAN Domains	Zero
4	UnSWAN with Observed Wind	UnSWAN Domains	Observed
5	WWIII with NARR	WWIII Domains	CFSR + NARR

A number of statistics parameters (e.g., R, RMSE) have been widely used for assessing numerical model performance [6,7,15,16] and quantifying the discrepancies between model predictions and observations. These metrics represent an average estimate of the difference between predicted values and measured ones over a defined period of simulation. In this study, we calculated the same metrics for all model simulations by primarily focusing on significant wave height—the most representative parameter indicating the performance of wave models. The performance metrics include the aforementioned R, bias, RMSE, percentage error (PE), scatter index (SI), and percentage bias. The equations are provided in the Appendix A at the end of this paper.

3. Results and Discussion

3.1. Baseline Condition with CFSR Wind

The model results for each sensitivity simulation were analyzed and compared to buoy observations. Figure 4 shows the time series comparisons between model predictions and field observations of significant wave height at all four buoys. The performance metrics are presented in Table 3. Overall, both WWIII and UnSWAN predictions compared very well with the data; the predictions had a correlation coefficient greater than 0.9 at most stations. The models were able to capture the seasonal variability and most individual wave events. WWIII appears to perform slightly better than UnSWAN, which is consistent with previous findings [6]. Both WWIII and UnSWAN show a positive bias at most buoys except for NDBC 44013, and UnSWAN predictions are even more positively biased than the WWIII predictions.

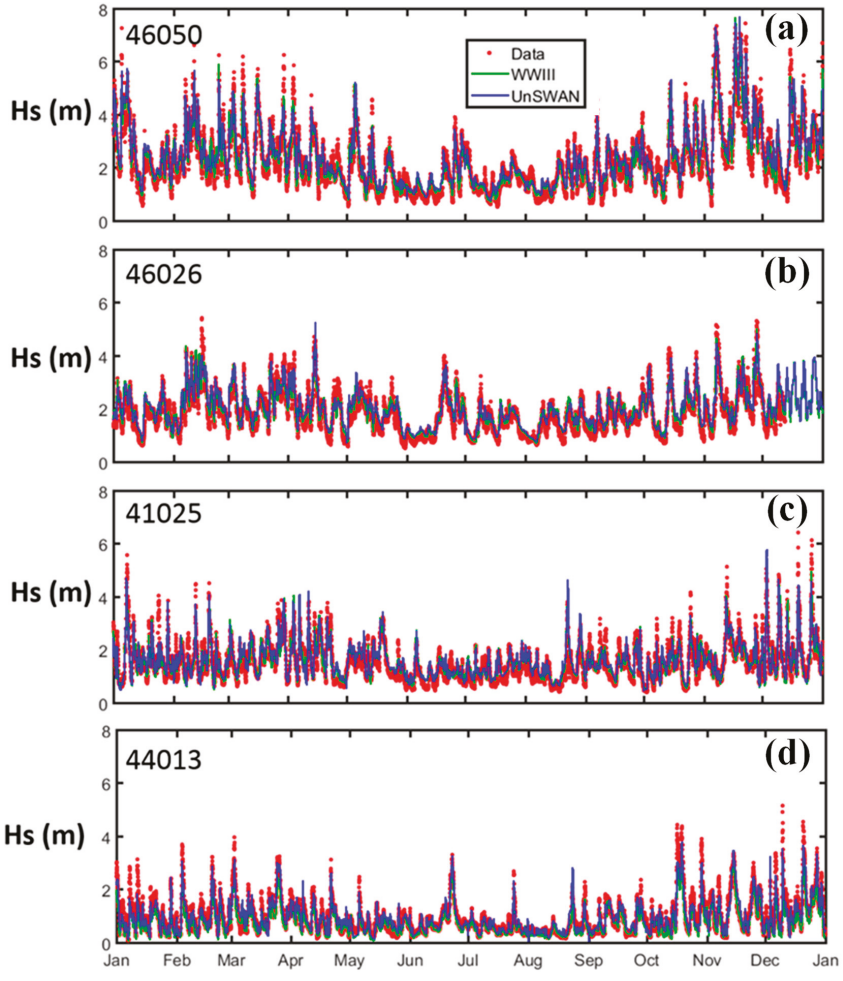

Figure 4. Time series comparisons of significant wave height between model simulations and buoy observations at all four buoys ((**a**)—46050; (**b**)—46026; (**c**)—41025; and (**d**)—44013) for the baseline-condition simulations in 2009.

Table 3. Performance metrics for the WWIII and UnSWAN models.

Model Run	Station	RMSE	PE (%)	SI	Bias	Bias (%)	R
WWIII	46050	0.35	5.48	0.15	0.04	1.63	0.95
	46026	0.30	8.57	0.16	0.09	4.63	0.93
	44013	0.30	−13.55	0.31	−0.17	−17.21	0.94
	41025	0.31	7.34	0.20	0.05	2.95	0.91
UnSWAN	46050	0.43	12.0	0.18	0.17	7.6	0.94
	46026	0.33	12.0	0.16	0.15	8.2	0.93
	44013	0.24	7.0	0.25	0.0	0.1	0.93
	41025	0.35	10.0	0.22	0.08	5.3	0.87

3.2. Simulation without Wind Forcing

To evaluate the wind effect, we analyzed and compared the results of significant wave height for the no-wind sensitivity run with those of the baseline condition. The results (Figure 5) show the one-month time series comparisons in summer and winter, respectively. Obviously, without wind forcing for the UnSWAN domain, the model results became substantially worse compared to those in the baseline condition forced by the CFSR wind. For instance, at Buoy 46026, the major wave events around 20 June 2009 were largely under predicted (Figure 5), suggesting local wind plays an important role in wave generation, and thus must be considered.

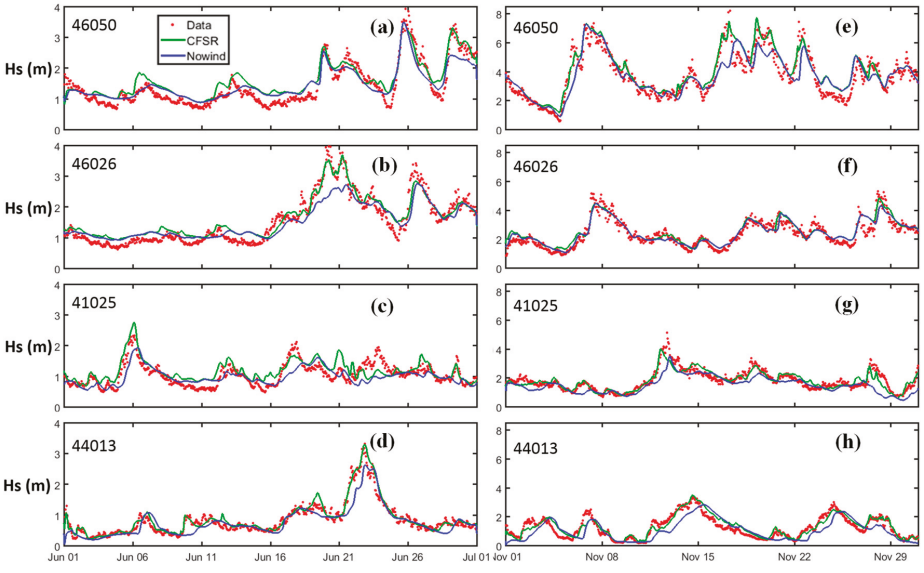

Figure 5. Comparison of significant wave heights between the baseline condition, no-wind condition, and buoy observations for the month of June (**a**–**d**) and November (**e**–**h**) in 2009.

3.3. Simulation with Observed Wind

It is important to see if observed wind forcing can improve UnSWAN model results, especially for the large-wave events. Figure 6a shows the probability distribution comparisons of significant wave height between the baseline condition and the sensitivity run with observed wind. Overall, the results are comparable to those of the baseline condition. The model performance was improved for large waves with buoy-wind, especially at the two nearshore buoys, 46026 and 44013, e.g., significant wave height > 5 m at NDBC 46026 and significant wave height > 3.5 m at NDBC 44013. Figure 6b

shows the bivariate distribution of occurrence as a function of the significant wave height and peak period. Similarly, model performance for predicting the probability of large wave occurrence was noticeably improved at buoy station 46026 and 44013. However, we notice that the bias becomes more positive at all buoys, indicating an increased over-prediction by the model. This is expected because the observed wind speed is generally greater than the CFSR wind speed, based on the initial analysis. The main objective of this study was to examine whether the large-wave events (i.e., >90th percentile of significant wave height in 2009) can be better captured by the model with the observed wind forcing.

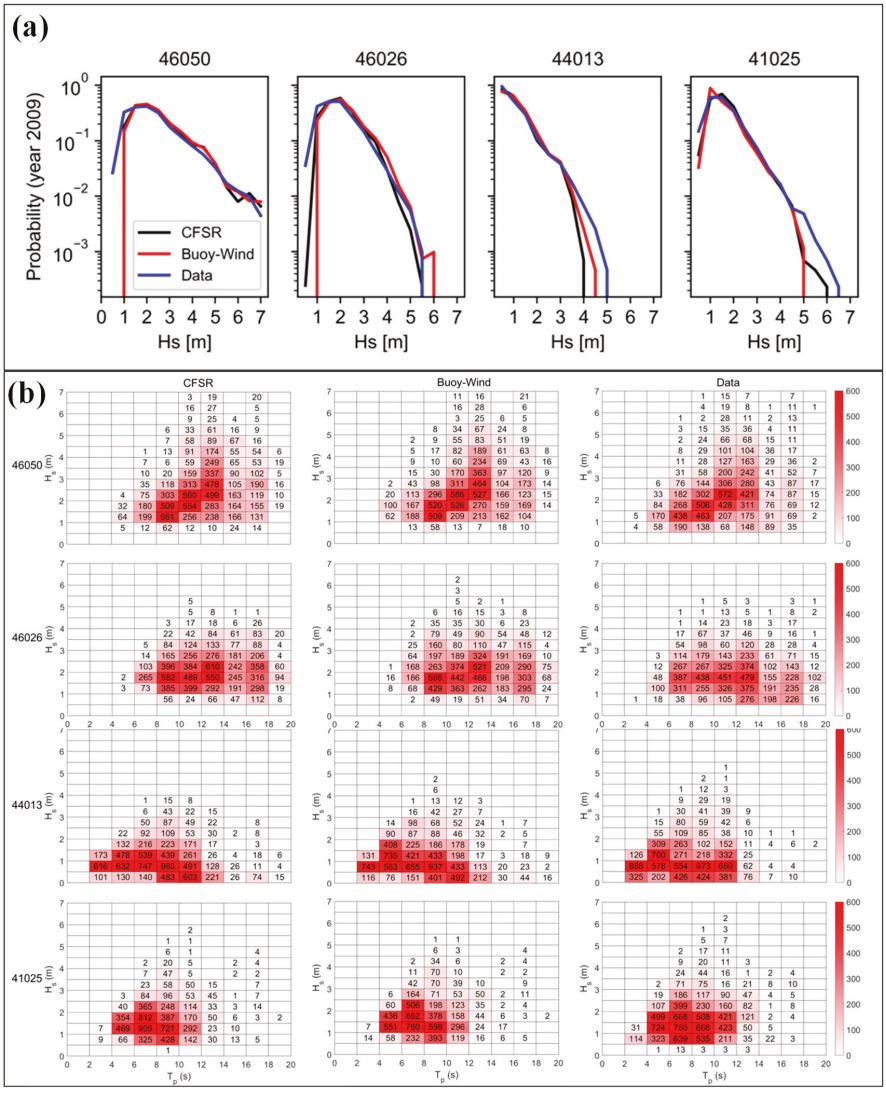

Figure 6. (**a**) Probability distributions of significant wave heights and (**b**) bivariate distribution of occurrence defined by the significant wave height and peak period for the baseline condition, observed-wind condition, and buoy observations in 2009.

Figure 7 shows a zoomed-in view of the time series comparisons for example large-wave events at all four buoys. The performance metrics for large waves only in Year 2009 are also summarized in Table 4. As can be seen in Figure 7, by driving the model simulations with observed wind, there is a better match between model predictions and observations at the peaks. The error statistics for the large waves were overall improved relative to those in the baseline condition forced by CFSR wind, which were under-predicted compared to observed significant wave height, as indicated by the negative bias values. The consistent improvement for nearly all the parameters confirmed that observed wind forcing is very useful in producing more accurate wave results during large-wave events.

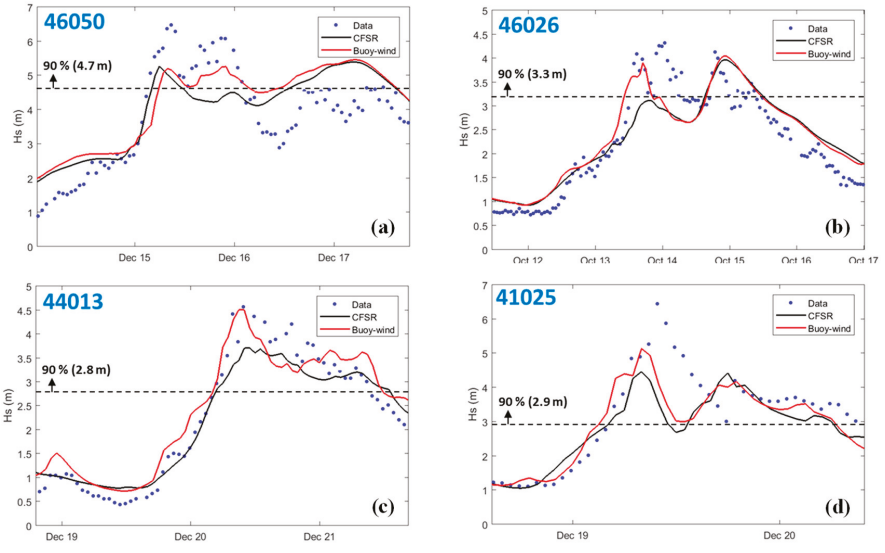

Figure 7. Comparison of significant wave heights between the baseline condition, observed-wind condition, and buoy observations at all four buoys ((**a**)—46050; (**b**)—46026; (**c**)—44013; and (**d**)—41025) for the example large-wave events in 2009.

Table 4. Performance metrics for large (>90th percentile of significant wave height) waves only.

Station	Wind	RMSE	PE (%)	SI	Bias	Bias (%)	R
46050	CFSR	0.81	−5.1	0.15	−0.29	−5.1	0.67
	Observed	0.77	−4.7	0.14	−0.27	−4.8	0.68
46026	CFSR	0.49	−5.2	0.13	−0.22	−5.6	0.57
	Observed	0.48	2.4	0.12	0.08	2.0	0.58
44013	CFSR	0.6	−12.7	0.21	−0.44	−13.3	0.55
	Observed	0.58	−9.6	0.19	−0.34	−10.2	0.47
41025	CFSR	0.83	−9.9	0.25	−0.41	−11.0	0.47
	Observed	0.69	−5.2	0.2	−0.23	−6.4	0.55

3.4. Simulation with NARR Wind

To investigate whether the regional wind product with higher spatial resolution can improve wave predictions, a sensitivity run using the NARR wind product was conducted for the nested WWIII model domains. In this test, the three-hourly NARR wind field was only applied to the WWIII 4′ domains due to its limited spatial coverage. The performance metrics for the yearly simulation results are summarized in Table 5. Compared to the baseline condition using the CFSR wind product, the NARR wind product appeared not to improve model predictions. In contrast, the results for those

relatively large-wave events at all four buoys were even further under predicted, as indicated by the scatterplot comparisons (Figure 8). For instance, for an observed wave height > 5 m at 46050, >3 m at 46026, 44013, and 41025, the underprediction by the NARR wind becomes more apparent compared to that forced by the CFSR wind. This finding also agrees with that in the previous wind analysis that NARR wind shows a greater negative bias than the CFSR wind. This sensitivity test suggests regional wind-model products, such as NARR, do not produce better wave model results than those produced by the CFSR wind product, so they are not recommended for wave resource assessment modeling studies.

Table 5. Performance metrics for WWIII simulations with NARR wind.

Station	Wind	RMSE	PE (%)	SI	Bias	Bias (%)	R
46050	CFSR	0.35	5.48	0.15	0.04	1.63	0.95
	NARR	0.43	1.50	0.19	−0.06	−2.87	0.93
46026	CFSR	0.30	8.57	0.16	0.09	4.63	0.93
	NARR	0.35	4.24	0.19	0.00	0.10	0.89
44013	CFSR	0.30	−13.55	0.31	−0.17	−17.21	0.94
	NARR	0.40	−21.75	0.41	−0.26	−26.08	0.92
41025	CFSR	0.31	7.34	0.20	0.05	2.95	0.91
	NARR	0.37	−1.29	0.23	−0.10	−6.13	0.88

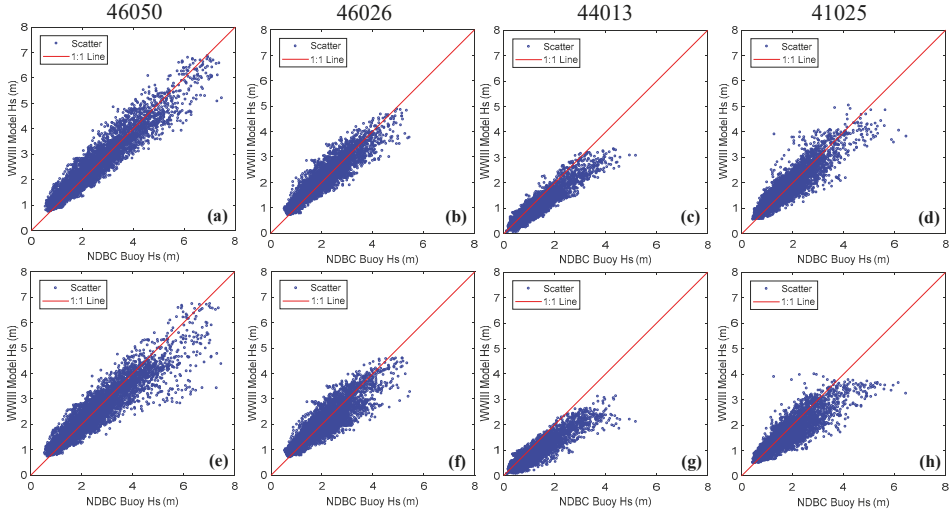

Figure 8. Scatterplot of WWIII-predicted significant wave height vs. buoy observations for the baseline condition with the CFSR wind forcing (**a**–**d**) compared with those for the sensitivity run using the NARR wind forcing (**e**–**h**) at all four buoys.

4. Conclusions

The sensitivity tests confirmed that wind forcing for the local domain is important in producing more accurate wave results and thus cannot be ignored. Although the observed wind forcing did not improve the models' overall performance in predicting significant wave height, it did improve model predictions for large waves, which is crucial for the survival of WECs. This study also suggests that regional weather forecast products, such as NARR, do not necessarily improve wave model performance despite their finer spatial resolutions. On another note, only significant wave height was selected as a representative wave parameter to evaluate the wind forcing effect on large wave

prediction. Although wave height is critical to assess the force and potential damage of large waves on WECs, other parameters, such as the wave period, should be considered to calculate the hydrodynamic force on WECs during extreme weather conditions (e.g., storms) [20,21]. Therefore, future work should include more systematic comparison of additional wave parameters.

Overall, the CFSR wind product is still considered one of the best global wind products for driving wind-wave simulations, as suggested by the 32-year wave hindcasts by NOAA using the CFSR wind [5]. The positive bias values for significant wave height at most stations except Buoy 44013, which is located on the U.S. East Coast, are also consistent with NOAA's findings, which indicated that the positive bias was primarily caused by the inadequate swell dissipation algorithms in WWIII [5]. Because swells are most prominent in the Pacific Ocean, inadequate swell dissipation caused positive bias at the buoys on the U.S. West Coast. Interestingly, the positive bias was further amplified by UnSWAN at all buoys. The exact mechanism by which this amplification occurs warrants further investigation in future studies.

The improvement of large-wave predictions using observed wind suggests that the wind-sea model component is sensitive to wind forcing at local domains. However, the performance for the whole year did not show the same improvement. More research could be conducted on the spectral partition to identify the response of individual spectral components (e.g., swells, wind-sea) to various local wind-forcing products. Lastly, this study applied observed wind at a single buoy location for the entire local domain, which may underestimate the spatial variability of wind forcing across the domain. Better spatial interpolation methods would improve upon the accuracy of these results and should be considered in future studies.

Author Contributions: Conceptualization, Z.Y. and T.W.; Methodology, Z.Y. and T.W.; Validation, T.W. and W.-C.W.; Formal Analysis, Z.Y., T.W. and W.-C.W.; Investigation, Z.Y. and T.W.; Resources, Z.Y.; Data Curation, W.-C.W. and T.W.; Writing-Original Draft Preparation, T.W., Z.Y. and M.G.; Writing-Review & Editing, T.W., Z.Y., W.-C.W. and M.G.; Visualization, T.W. and W.-C.W.; Supervision, Z.Y.; Project Administration, Z.Y.; Funding Acquisition, Z.Y.

Funding: This study was funded by the Water Power Technology Office of the U.S. Department of Energy's Office of Energy Efficiency and Renewable Energy, under Contract DE-AC05-76RL01830 to the Pacific Northwest National Laboratory.

Acknowledgments: The authors would like to thank the technical steering committee, chaired by Bryson Robertson at the West Coast Wave Initiative of the University of Victoria, for their oversight and input to this model study. Gabriel Garcia Medina at Pacific Northwest National Laboratory helped with Figure 6 and is also acknowledged.

Conflicts of Interest: The authors declare no conflict of interest.

Appendix A

The performance metrics are defined as follows:

The root mean square error (RMSE), or root mean square deviation, is defined as:

$$\mathrm{RMSE} = \sqrt{\frac{\sum_{i=1}^{N}(P_i - M_i)^2}{N}}, \tag{A1}$$

where N is the number of observations, M_i is the measured value, and P_i is the predicted value.

The RMSE represents the sample standard deviation of the differences between predicted values and measured values.

The percentage error (PE) is defined as:

$$\mathrm{PE}(\%) = \frac{100}{N}\sum_{i=1}^{N}\left(\frac{P_i - M_i}{M_i}\right) \tag{A2}$$

and is the average PE over the period of comparison.

The scatter index (SI) is the RMSE normalized by the average of all measured values over the value of comparison, where:

$$\mathrm{SI} = \frac{\mathrm{RMSE}}{\overline{M}}, \tag{A3}$$

and where the overbar indicates the mean of the measured values.

Model bias, which represents the average difference between the predicted and measured value, is defined as:

$$\mathrm{Bias} = \frac{1}{N}\sum_{i=1}^{N}(P_i - M_i). \tag{A4}$$

Percentage bias, which is defined as:

$$\mathrm{Bias}(\%) = \frac{\sum_{i=1}^{N} P_i - \sum_{i=1}^{N} M_i}{\sum_{i=1}^{N} M_i} \times 100 \tag{A5}$$

is also commonly used to normalize bias.

The linear correlation coefficient, R, is defined as:

$$\mathrm{R} = \frac{\sum_{i=1}^{N}\left(M_i - \overline{M}\right)\left(P_i - \overline{P}\right)}{\sqrt{\left(\sum_{i=1}^{N}\left(M_i - \overline{M}\right)^2\right)\left(\sum_{i=1}^{N}\left(P_i - \overline{P}\right)^2\right)}} \tag{A6}$$

and is a measure of the strength of the linear relationship between the predicted and measured values. In this study, R was tested at the significance level of 0.05.

References

1. International Electrotechnical Commission. *Marine Energy—Tidal and Other Water Current Converters—Part. 101: Wave Energy Resource Assessment and Characterization*; Report No. IEC TS 62600-101; International Electrotechnical Commission: Geneva, Switzerland, 2015.
2. Bidlot, J.-R.; Holmes, D.J.; Wittmann, P.A.; Lalbeharry, R.; Chen, H.S. Intercomparison of the performance of operational ocean wave forecasting systems with buoy data. *Weather Forecast.* **2002**, *17*, 287–310. [CrossRef]
3. Pan, S.-Q.; Fan, Y.-M.; Chen, J.-M.; Kao, C.-C. Optimization of multi-model ensemble forecasting of typhoon waves. *Water Sci. Eng.* **2016**, *9*, 52–57. [CrossRef]
4. Ellenson, A.; Özkan-Haller, H.T. Predicting large ocean wave events characterized by bimodal energy spectra in the presence of a low-level southerly wind feature. *Weather Forecast.* **2018**, *33*, 479–499. [CrossRef]
5. Chawla, A.; Spindler, D.M.; Tolman, H.L. Validation of a thirty year wave hindcast using the climate forecast system reanalysis winds. *Ocean Model.* **2013**, *70*, 189–206. [CrossRef]
6. Yang, Z.; Neary, V.S.; Wang, T.; Gunawan, B.; Dallman, A.R.; Wu, W.-C. A wave model test bed study for wave energy resource characterization. *Renew. Energy* **2017**, *114*, 132–144. [CrossRef]
7. Wu, W.C.; Yang, Z.; Wang, T. Wave Resource Characterization Using an Unstructured Grid Modeling Approach. *Energies* **2018**, *11*, 605. [CrossRef]
8. Chawla, A.; Spindler, D.; Tolman, H. *WAVEWATCH III Hindcasts with Re-Analysis Winds. Initial Report on Model Setup*; NOAA/NWS/NCEP Technical Note 291; NOAA: Silver Spring, MD, USA, 2011; 100p.
9. Tolman, H.; WAVEWATCH III Development Group. *User Manual and System Documentation of WAVEWATCH III Version 4.18*; NOAA/NWS/NCEP Technical Note 316; NOAA: College Park, MD, USA, 2014; 311p.
10. Zijlema, M. Computation of wind-wave spectra in coastal waters with swan on unstructured grids. *Coast. Eng.* **2010**, *57*, 267–277. [CrossRef]
11. Saha, S.; Moorthi, S.; Pan, H.-L.; Wu, X.; Wang, J.; Nadiga, S.; Tripp, P.; Kistler, R.; Woollen, J.; Behringer, D.; et al. The NCEP climate forecast system reanalysis. *Bull. Am. Meteorol. Soc.* **2010**, *91*, 1015–1058. [CrossRef]
12. Cavaleri, L. Wave modeling missing the peaks. *J. Phys. Oceanogr.* **2009**, *39*, 2757–2778. [CrossRef]
13. Lenee-Bluhm, P.; Paasch, R.; Özkan-Haller, H.T. Characterizing the wave energy resource of the US Pacific Northwest. *Renew. Energy* **2011**, *36*, 2106–2119. [CrossRef]

14. Garcá-Medina, G.; Özkan-Haller, H.T.; Ruggiero, P.; Oskamp, J. An inner-shelf wave forecasting system for the US Pacific Northwest. *Weather Forecast.* **2013**, *28*, 681–703. [CrossRef]
15. Garcá-Medina, G.; Özkan-Haller, H.T.; Ruggiero, P. Wave resource assessment in Oregon and southwest Washington, USA. *Renew. Energy* **2014**, *64*, 203–214. [CrossRef]
16. Neary, V.; Yang, Z.; Wang, T.; Gunawan, B.; Dallman, A.R. *Model Test Bed for Evaluating Wave Models and Best Practices for Resource Assessment and Characterization*; Sandia National Lab. (SNL-NM): Albuquerque, NM, USA, 2016.
17. Jacobson, P.; Hagerman, G.; Scott, G. *Mapping and Assessment of the United States Ocean Wave Energy Resource*; Electric Power Research Institute: Palo Alto, CA, USA, 2011.
18. Kilcher, L.; Thresher, R. *Marine Hydrokinetic Energy Site Identification and Ranking Methodology Part I: Wave Energy*; National Renewable Energy Lab (NREL): Golden, CO, USA, 2016.
19. Ardhuin, F.; Rogers, E.; Babanin, A.; Filipot, J.-F.; Magne, R.; Roland, A.; van der Westhuysen, A.; Queffeulou, P.; Lefevre, J.-M.; Aouf, L. Semiempirical dissipation source functions for ocean waves. Part I: Definition, calibration, and validation. *J. Phys. Oceanogr.* **2010**, *40*, 1917–1941. [CrossRef]
20. Alberello, A.; Chabchoub, A.; Gramstad, O.; Toffoli, A. Non-Gaussian properties of second-order wave orbital velocity. *Coast. Eng.* **2016**. [CrossRef]
21. Alberello, A.; Chabchoub, A.; Monty, J.P.; Nelli, F.; Lee, J.H.; Elsnab, J.; Toffoli, A. An experimental comparison of velocities underneath focussed breaking waves. *Ocean Eng.* **2018**, *155*. [CrossRef]

Journal of
Marine Science and Engineering

MDPI

Article

Water Quality Model Calibration via a Full-Factorial Analysis of Algal Growth Kinetic Parameters

James D. Bowen [1,*] and Noyes B. Harrigan [2]

[1] Civil and Environmental Engineering Department, University of North Carolina at Charlotte, Charlotte, NC 28223, USA
[2] WK Dickson & Co., Inc., Charlotte, NC 28205, USA; nharrigan@wkdickson.com
* Correspondence: jdbowen@uncc.edu; Tel.: +1-704-687-1215

Received: 2 October 2018; Accepted: 8 November 2018; Published: 12 November 2018

Abstract: The two-dimensional, laterally-averaged mechanistic eutrophication model CE-QUAL-W2 version 3.72 was used to predict chlorophyll-a concentrations across two different time periods in the Neuse River Estuary, North Carolina. Chlorophyll calibration was performed for two time periods simultaneously by performing a full-factorial experiment that tested seven algal kinetic growth parameters over three levels for a single algal group. A cluster of up to six computers each running between two and ten instances of the program was used to complete and manage the data for 2187 runs for each period. Six numeric criteria were used to determine which runs performed acceptably, yielding a group of 27 cases that met all of the criteria. Calibration performance of the set of cases outperformed a previously calibrated model using three algal groups that met only four of the six selection criteria. Calibration performed this way allowed for a more rational specification of model calibration performance and provided uncertainty estimates of model predictions, albeit at the cost of a considerable increase in computational requirements that necessitated the use of a computer cluster.

Keywords: water quality; model calibration; estuary; eutrophication; CE-QUAL-W2; phytoplankton; algal growth kinetics

1. Introduction

Algal blooms have plagued the Neuse River Estuary (NRE) for decades [1,2] and multiple models have been employed to study eutrophication in the estuary [3–5]. Despite the development of a water quality model-based total maximum daily load (TMDL) analysis and regulations to reduce total nitrogen (N) loading to the estuary by 30% from the 1995 baseline year, algal blooms still occur throughout the estuary [6]. The fraction of water samples that exceed the chlorophyll-a criteria of 40 μg/L has decreased in some, and increased in other parts of the estuary [7].

The timing, extent, and magnitude of the blooms appears to be affected by hydrologic variability affecting water residence time and nutrient supply, as well as seasonal variations in temperature and light [6,8]. In addition, although inorganic N loading to the estuary has been reduced by 15–25% since the 1990s, this reduction has been offset by an increase in organic N loading of approximately 15% and an increase in N loading from the Trent River tributary of approximately 30% [7].

These changes and the continued presence of blooms and water quality criteria violations point to the need to better understand trends in water quality in the Neuse Estuary that have been observed since the model-based TMDL was performed more than ten years ago. In that previous work, algal species with similar growth characteristics were grouped together to form three functional phytoplankton groups (i.e., diatoms + dinoflagellates, chlorophytes + cryptophytes, and cyanobacteria). Water quality calibration was achieved on a constituent-by-constituent basis, adjusting relevant

kinetic parameters by trial and error to provide the best agreement between predicted and observed concentrations [9], as based upon multiple calibration criteria.

This article reexamines the procedure used to calibrate the algal constituents in a process-based multi-dimensional water quality model of the Neuse River Estuary that has been further developed to simulate a second, more recent multi-year period. A mechanistic, two-dimensional, laterally-averaged model (CE-QUAL-W2) was used to simulate water quality dynamics in the estuary. Multi-dimensional mechanistic eutrophication models such as CE-QUAL-W2 typically have more than twenty water quality constituents and upwards of one hundred kinetic parameters that must each be calibrated. The algal constituents pose a particular problem for calibration because of the need to specify how algal growth rate simultaneously depends upon light intensity, temperature, and the concentrations of multiple nutrients. Specifying these growth rate relationships typically requires specification of ten to twenty parameters per algal constituent. Traditionally, calibration of parameters in a water quality model has been done via a trial and error approach that seeks to minimize the difference between observations of a water quality constituent and corresponding model predictions of that constituent in the water body [10–12].

Several innovative calibration approaches have recently been developed for mechanistic water quality models. Huang and Liu utilized a hybrid genetic algorithm parameter search method together with a neural network based approximation of the input–output relationships of the mechanistic model to calibrate twenty-nine parameters of a CE-QUAL-W2 based lake water quality model [13]. A particle swarm automatic calibration method was used as part of a multi-objective calibration of a CE-QUAL hydrodynamic and temperature model for a reservoir. Ten parameters were calibrated automatically by optimizing a goodness-of-fit based objective function for temperature and water surface elevation [14,15]. While most researchers have based eutrophication model calibration on algal biomass (i.e., chlorophyll-a concentrations), some have based their calibration on comparisons of model predicted and observed algal productivity and photosynthesis-irradiance (P-I) curves [16]. In this case, researchers found significant differences in model predicted algal productivity using their approach as compared to a corresponding model calibrated using the traditional biomass-based approach. Arhonditsis et al. developed a statistically based Bayesian calibration methodology to determine parameter values and their uncertainty for a six-parameter water quality model [17] of a coastal embayment in Greece. In related work, the Bayesian calibration methodology has been employed for a mesotrophic lake in Washington State, USA [18].

In this study, a rigorous investigation of the algal parameter space was undertaken by a full-factorial design testing seven algal parameters at three different levels for a single algal group, with the objective of finding the optimum combination of parameters to characterize phytoplankton growth in the estuary. Of particular interest was how this automated calibration approach using a single algal constituent would compare with respect to calibration performance to an earlier Neuse River Estuary model that used three algal constituents calibrated using the traditional trial and error approach [9]. A secondary objective of the work was to develop a multi-objective calibration utilizing numeric criteria that reflected the intended use of the model for environmental management purposes. We sought to demonstrate a paradigm shift in how mechanistic models are calibrated. Instead of a single "optimal" parameter set, we systematically searched the parameter space for many parameter sets that meet our criteria for the necessary calibration performance. This work was part of a larger, comprehensive project whose goal was to determine the effect of inorganic versus organic nitrogen loading reduction on phytoplankton growth and biomass, and the fate of anthropogenic nutrient loading to the estuary [19]. The two-dimensional, laterally-averaged mechanistic eutrophication model CE-QUAL-W2 version 3.72 [20] was used to predict chlorophyll-a concentrations across two different periods—a previously modeled period and a more recent one. To make the large number of runs needed to independently vary the parameters, a program was written that would allow multiple computers to work in parallel to perform many model runs and individually report their progress to a cloud-based file that was used so that all model runs were completed by the computer cluster.

2. Materials and Methods

2.1. Model Set-Up

CE-QUAL-W2 (Portland State University, Portland, OR, USA) is a two-dimensional (longitudinal and vertical) hydrodynamic and water quality model. The model assumes lateral (bank to bank) homogeneity, and is therefore best suited for long and narrow bodies. It has been applied to rivers, lakes, reservoirs, estuaries, and combinations of waterbodies [20]. For this study, version 3.72 was obtained from the developers as FORTRAN source code and was compiled to create executables that could be run on Windows, OS-X, and LINUX workstations.

In addition to its hydrodynamics aspects, Version 3.72 allows the user to track 28 water-quality variables, 14 of which were used in this model (Table 1), and 60 derived variables. The W2 computational grid used here consisted of 151 segments divided into 11 branches with five tributaries of branch 1, the main branch (Figure 1). In the z-grid vertical layering scheme, each segment consisted of up to eighteen 0.5–2.0 m thick active vertical layers, depending on the local water depth. Model input and calibration data were based upon a long-term dataset provided by the University of North Carolina Institute of Marine Sciences (IMS) and the North Carolina Department of Environmental Quality (NCDEQ). Eleven mid-river water quality sampling stations (i.e., IMS Neuse River Estuary Modeling and Monitoring Project (MODMON) stations 0-180) are sampled and analyzed for a broad array of water quality constituents on a bi-weekly basis [21,22]. The two modeling periods (1998–2000 and 2006–2008) were chosen on the basis of data availability, the presence of events that could provide insight into eutrophication dynamics in the estuary (e.g., flow extremes and large algal blooms), and the composition of nitrogen loading. In both cases, initial conditions were handled by starting the model from constant values and allowing at least six months for it to "spin up" to stable conditions. Flows, temperatures, and constituent inflow concentrations were specified for each branch and tributary within the modeled area. The amount, temperature, and nitrogen concentration of precipitation in addition to other meteorological variables (i.e., air temperature, dewpoint temperature, wind speed, wind direction, and cloud cover) were also specified. Elevation head, temperature, and constituent concentrations were provided at the downstream boundary of the branch 1 (i.e., segment 77) near the mouth of the NRE at Pamlico Sound. All components were assumed to vary linearly in time between monitoring events, and vertical profiles of temperature and constituent concentrations were created through interpolation of near-surface and near-bottom data.

Table 1. Neuse Estuary Eutrophication Model (NEEM) water quality constituents.

No.	Constituent	Unit
1	Salinity (TDS)	g/L
2	Tracer	mg/L
3	Inorganic Suspended Solids (ISS) = Salinity (TDS)	mg/L
4	Orthophosphate (PO_4^{3-})	mg/L
5	Ammonium (NH_4^+)	mg/L
6	Nitrate-Nitrite (NO_3^- + NO_2^-)	mg/L
7	Dissolved Silica	mg/L
8	Labile Dissolved Organic Matter (L-DOM)	mg/L
9	Refractory Dissolved Organic Matter (R-DOM)	mg/L
10	Labile Particulate Organic Matter (L-POM)	mg/L
11	Refractory Particulate Organic Matter (R-POM)	mg/L
12	Biological Oxygen Demand (BOD)	mg/L
13	Algal Group	mg/L
14	Dissolved Oxygen	mg/L

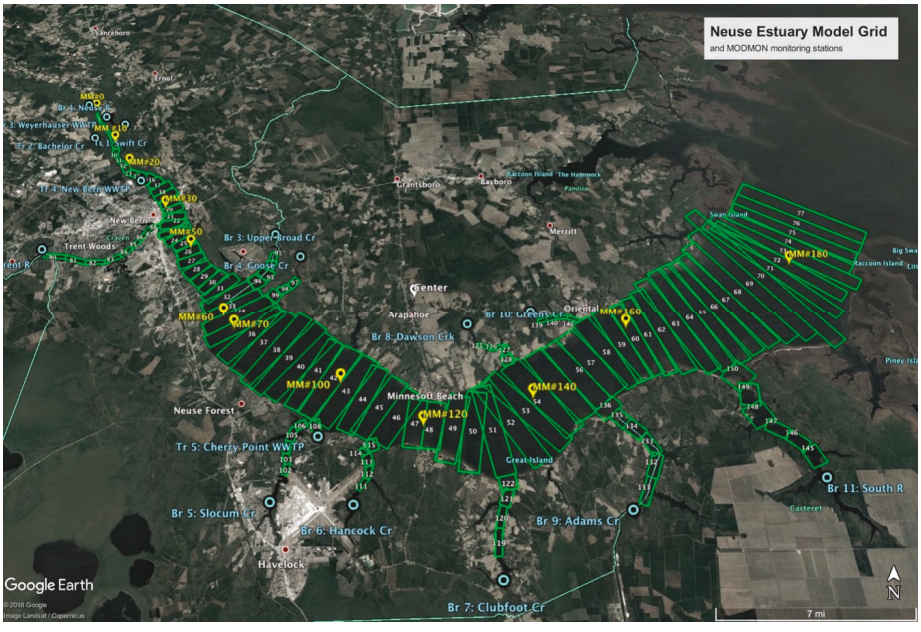

Figure 1. W2 model grid and IMS ModMon monitoring stations.

Hydrodynamic and conservative transport model calibration were performed by comparing model predictions of water temperature and salinity to observed data. Incident short-wave solar radiation, bottom roughness, bottom elevation, wind-sheltering, vertical mixing, and downstream boundary salinity were varied to produce the best agreement between model predictions and observed values at twelve Neuse River Estuary Modeling and Monitoring Project (ModMon) stations for both the bottom and surface layers.

In previous modeling work on the Neuse, water quality calibration was achieved on a constituent by constituent basis, adjusting relevant kinetic parameters to provide the best agreement between predicted and observed concentrations of orthophosphate, ammonium, nitrate-nitrite, and dissolved oxygen [9]. The initial phase of water quality calibration in this investigation began with a similar approach, varying the parameters governing zero-order sediment oxygen demand (SOD), water-column denitrification rate, light extinction coefficients, and phosphorous partitioning until satisfactory preliminary results were obtained. The results were considered preliminary because concentrations of these constituents can both influence and be influenced by algal growth in the estuary, and the calibration of chlorophyll-a (chl-a) was saved for last.

When a similar trial-and-error approach was attempted for the factors controlling algal growth, the performance of the model in predicting chlorophyll-a concentrations was less than satisfactory. Despite having comparable R^2 to earlier work and low mean error, the model's predicted cumulative distribution function (CDF) showed significant deviation from the observed CDF at higher chlorophyll-a values. As a result, exceedance probabilities (i.e., the frequency of chl-a > 40 ug/L) were underestimated, and response to nitrogen-load reduction was minimal. Since the prediction of algal blooms was integral to the goals of the larger study, it was decided that a full-factorial analysis of algal growth parameters was warranted.

2.2. Algal Growth Parameters

W2v3.72's algal rate equation (Equation (1)) is a function of six processes, but only five were modeled here (i.e., loss due to feeding by zooplankton was not used, since zooplankton concentration was not modeled).

$$algal\ flux = growth - respiration - excretion - mortality - settling - net\ loss\ to\ grazing \quad (1)$$

The rate of each process is the product of a maximum first order rate constant (i.e., maximum algal growth, A; respiration, AR; excretion, AE; mortality rate, AM; and settling rate, AS), a multiplier for the limiting growth factor, and multipliers for the effect of temperature. Nutrient growth-limiting factors are calculated using a Monod formulation dependent upon nutrient concentration and a half-saturation constant (phosphorus, AHSP; nitrogen, AHSN; and silica, AHSSI), while the growth limiting factor for light is a function of the available light and light saturation intensity at maximum photosynthetic rate, ASAT [23].

AG, AHSP, AHSN, and ASAT were varied over three levels (Table 2) independently, while the four parameters affecting algal sink (AR, AE, AM, and AS) were varied over three levels, but not independently of each other. The three levels were chosen so that the parameter varied by a factor of ten over the levels with the middle level representing that used in the previous version of the Neuse Estuary Eutrophication model (NEEM).

Table 2. Algal growth parameters and levels tested via full-factorial design.

Parameter	W2 Designation	Unit	Low Value	Middle Value	High Value
Maximum algal growth rate	AG	d^{-1}	0.553	1.75	5.53
Maximum algal respiration rate	AR	d^{-1}	0.0116	0.0367	0.116
Maximum algal excretion rate	AE	d^{-1}	0.00949	0.0300	0.0949
Maximum algal mortality rate	AM	d^{-1}	0.00528	0.0167	0.0528
Algal settling rate	AS	$m\ d^{-1}$	0.0136	0.0430	0.136
Algal half-saturation for phosphorus-limited growth	AHSP	$g\ m^{-3}$	0.00219	0.00693	0.0219
Algal half-saturation for nitrogen-limited growth	AHSN	$g\ m^{-3}$	0.0164	0.0520	0.164
Algal half-saturation for silica-limited growth	AHSSI	$g\ m^{-3}$	0.0001	0.0001	0.0001
Light saturation intensity at maximum photosynthetic rate	ASAT	$W\ m^{-2}$	39.53	125.0	395.3
Width of rate-multiplier function	AT4−AT1	°C	14	24	34
Midpoint of rate-multiplier function	(AT1+AT4)/2	°C	17	21	25

The multipliers for the effect of temperature are determined from the rising and falling limb of a rate multiplier curve [24] modeled by specifying four temperatures (AT1-AT4) and the fraction of the maximum rate at each temperature (AK1-AK4). Varying all eight of these parameters would result in a prohibitively large number of permutations, so only two aspects of the temperature relative growth rate function (i.e., the "width" of the curve and the location of its midpoint) were varied over three levels. Values were chosen to give a narrow, medium, and wide range of the function as well as to provide a low, middle, and high midpoint of the function (Figure 2). The fraction of the maximum rate (AK1–AK4) was not varied, so that all cases had the same shape for the relative growth rate vs. temperature function, as shown in Figure 2.

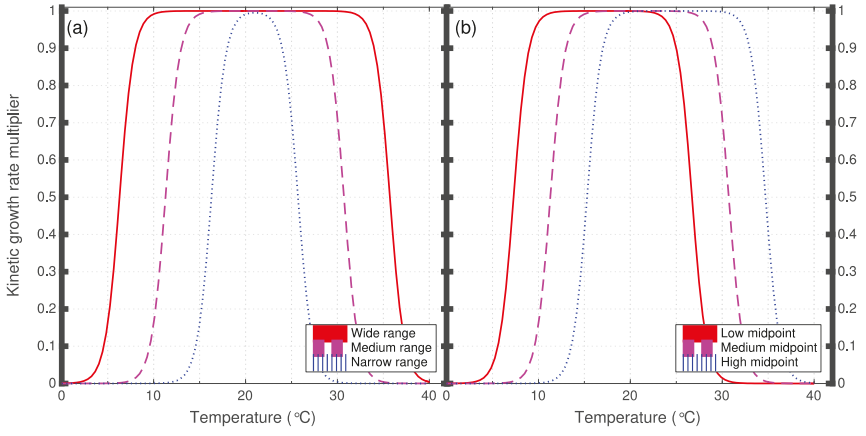

Figure 2. Example kinetic growth rate multiplier curves for tested algal growth temperature levels. Panel (**a**) shows the effect of varying the width of the function while maintaining a constant temperature optimum. Panel (**b**) shows the effect of varying the temperature optimum while maintaining the width of the function.

2.3. Run Management

A MATLAB script was written that would allow multiple computers to work in parallel (Figure 3). When the program is run, the individual computer in the cluster generates a list of runs needed to be performed and compares it to a centrally-stored file containing a log of runs completed. The computer identifies the next run to be made, generates a control file that corresponds to the values of the algal parameters for that run, and then performs the run. Each computer will continue to make runs (at different processing speeds) until all are completed. The cluster of up to six computers each running between two and ten instances of the program took approximately 1300 hours of computational time to complete all 2187 runs for both periods. A statistics script was then used to read the time series output files of the model for each run and report calibration performance and other relevant data to a central file.

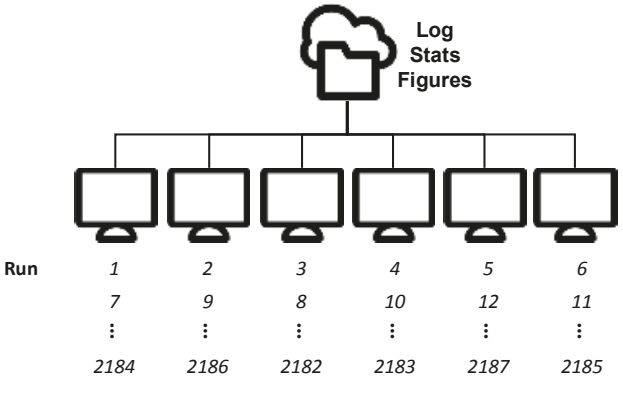

Figure 3. Conceptual representation of the computer cluster used to perform parallel runs.

3. Results

The results were evaluated by analyzing each run's combined calibration performance over the 1998–2000 and 2006–2008 periods. Six calibration performance criteria were utilized that captured

bottom and surface chlorophyll-a predictions at all ModMon stations (Table 3). Normalized mean error and coefficient of determination were used to assess agreement between model-predicted and observed chlorophyll-a. However, it was found that a run could have comparatively good values on these statistics, yet still fail to match the observed cumulative distribution function (CDF) adequately, especially at higher chlorophyll concentrations. Thus, CDF error, log CDF error, and exceedance probability were added to assess these "fit" characteristics. CDF error was defined as the total area between the predicted and observed cumulative distribution function curves (in units of μg/L chlorophyll-a). Log CDF error was defined the same way but was computed on the log-transformed chlorophyll-a data, and then transformed back into standard chlorophyll units.

Table 3. Performance criteria for selection of algal growth parameter runs.

Criteria	Constituent	Variable	Condition	# Meeting Criteria (Out of 2187 Trials)
1	CHLA	Abs normalized mean error	<13%	450
2	CHLA	Nash–Sutcliffe model efficiency	>46%	339
3	CHLA	40 μg/L exceedance probability	>3.1%	542
4	CHLA	Average CDF error	<4.70 μg/L	417
5	CHLA	Average log CDF error	<0.13 μg/L	406
6	DIN	$\frac{1}{2}$ saturation exceedance probability	<72%	894
			# Meeting ALL criteria =	27/2187 = 1.2%

Exceedance probability was defined as the probability of the model-predicted chlorophyll-a exceeding 40 μg/L. This statistic was calculated to assess how well the model matched observed frequency of chlorophyll-a concentrations that are above North Carolina's water quality criteria. Finally, dissolved inorganic nitrogen (DIN) exceedance probability was defined as the probability of the total DIN concentration (i.e., ammonia + nitrate + nitrite) exceeding the half-saturation constant for nitrogen-limited growth (AHSN). This last criterion was added to prioritize runs where algal growth was sensitive to nitrogen concentrations in the estuary.

In this study, it was not our intention to seek an "optimal" parameter set, and in fact, no single model performed significantly better with respect to our six calibration criteria. Instead, it was found that the vast majority of runs fared relatively poorly on one or more of the calibration criteria. Histograms of each calibration criterion were created (Figure 4) to assess the performance distribution for each criterion across the full set of cases. For each criterion, the initial threshold performance was set based upon judgement as to the necessary performance of the model. Minor changes in the threshold performance for individual criterion were also set iteratively so that degree of selectivity was roughly similar between criteria. The performance criteria were also adjusted slightly to give a reasonable number of cases that met all six performance criteria. Only the cases that met all six calibration criteria were considered suitable parameter sets, conditional upon their performance on the other hydrodynamic and water quality criteria. Once specified, these same model calibration criteria were used to test the previously calibrated Neuse River Estuary model that used three algal subgroups and the prior set of algal kinetic and temperature parameters. The model was run for both periods (1998–2000, 2006–2008) and the overall calibration performance assessed. This case met only four of the six calibration criteria, failing to meet the conditions for chlorophyll and DIN exceedance probability.

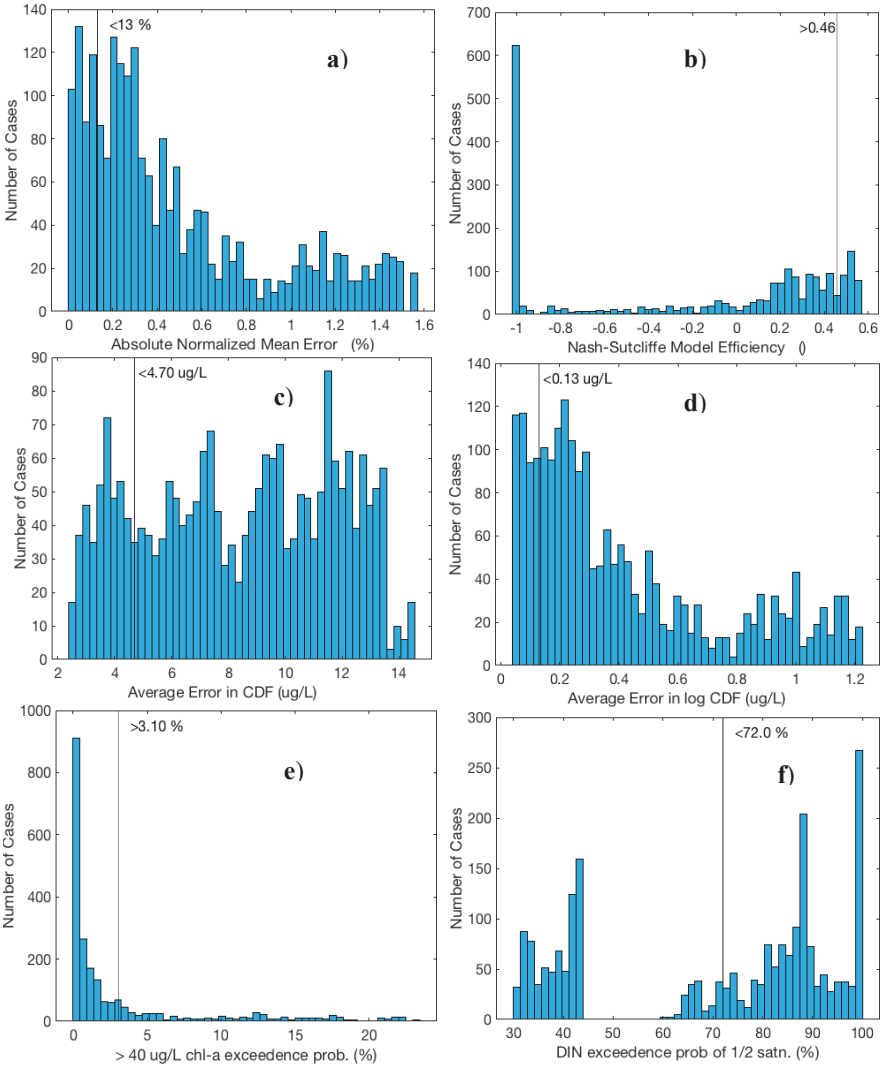

Figure 4. Histograms of calibration performance for the six criteria used to select model parameter sets (#1-5 used chl-a concentrations, #6 used DIN concentrations). The six criteria were: (**a**) absolute value of normalized mean model error (%); (**b**) Nash–Sutcliffe model efficiency; (**c**) average CDF error; (**d**) average log-transformed CDF error; (**e**) percentage of chl-a predictions above 40 ug/L; and (**f**) percentage of DIN concentrations above N $\frac{1}{2}$ saturation constant for growth.

The mean and standard deviation of the fit statistics (normalized mean error, normalized mean absolute error, normalized root mean squared error, and coefficient of determination) across the 27 cases give an indication of how well the cases performed and how much variation exists between cases (Table 4). No case performed so poorly on these constituents as to justify its removal from the pool of cases.

Table 4. Mean and standard deviation of calibration performance statistics across 27 runs.

Constituent	ME (%)	MAE (%)	RMSE (%)	Nash–Sutcliffe Model Efficiency (%)	# obs.
Temperature	0.71 ± 0 (0%)	5.59 ± 0 (0%)	7.58 ± 0 (0%)	96.0 ± 0 (0%)	3252
Salinity	10.4 ± 0 (0%)	249 ± 0 (0%)	37.1 ± 0 (0%)	85.1 ± 0 (0%)	3252
Ext. coefficient	1.29 ± 0 (0%)	20.8 ± 0 (0%)	27.1 ± 0 (0%)	46.2 ± 0 (0%)	1540
Nitrate	1.90 ± 0.1 (27%)	224 ± 1 (1%)	33.7 ± 0.4 (1%)	83.0 ± 0.4 (0.4%)	1956
Ammonia	−15.3 ± 2.8 (19%)	66.0 ± 1 (2%)	127 ± 0.9 (0.7%)	−13.1 ± 1.6 (12%)	3175
Phosphate	0.92 ± 2 (220%)	55.0 ± 2.4 (4.4%)	100 ± 4.0 (4%)	12.4 ± 6.8 (55%)	3005
Dissolved O_2	−5.50 ± 0.60 (11%)	20.4 ± 0.03 (0.14%)	29.7 ± 0.07 (0.25%)	51.1 ± 0.20 (0.5%)	3252
Chlorophyll-a	11.6 ± 0.80 (7%)	35.8 ± 0.60 (1.7%)	47.4 ± 0.80 (1.6%)	49.3 ± 1.6 (3.2%)	3182

As expected, varying algal growth parameters had no effect on temperature, salinity, or extinction coefficients, resulting in no variation among the 27 selected cases. The other five constituents were sensitive to algal growth parameters, with orthophosphate performance showing the highest degree of variation between runs.

Scatter plots (Figures 5 and 6), cumulative frequency distributions (Figure 7), and time histories (Figures 8–11) of model predicted versus observed values were constructed for both periods using the best performing run for each constituent. Time histories are shown here for a representative station in the upper estuary station (ModMon 30) and a station in the middle estuary (ModMon 100) for one of the twenty-seven runs that met all six calibration performance criteria. For the cumulative frequency distributions (CDFs), the data for both periods were combined into one plot, since CDF error was used as a selection criterion.

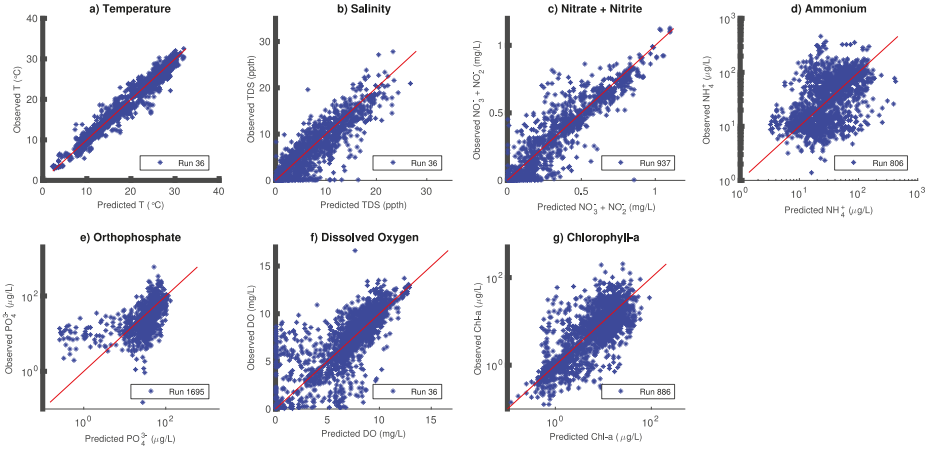

Figure 5. Predicted versus observed scatter plots for hydrodynamic and water quality parameters for 1998–2000. The predicted = observed line is shown in red. Panels show (**a**) temperature, (**b**) salinity, (**c**) nitrate + nitrite, (**d**) ammonium, (**e**) orthophosphate, (**f**) dissolved oxygen, and (**g**) chlorophyll-a.

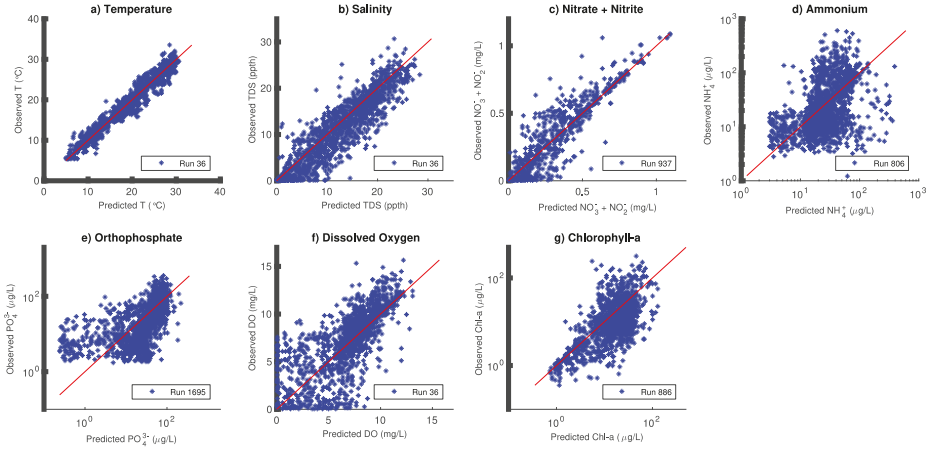

Figure 6. Predicted versus observed scatter plots for hydrodynamic and water quality parameters for 2006–2008. The predicted = observed line is shown in red. Panels show (**a**) temperature, (**b**) salinity, (**c**) nitrate + nitrite, (**d**) ammonium, (**e**) orthophosphate, (**f**) dissolved oxygen, and (**g**) chlorophyll-a.

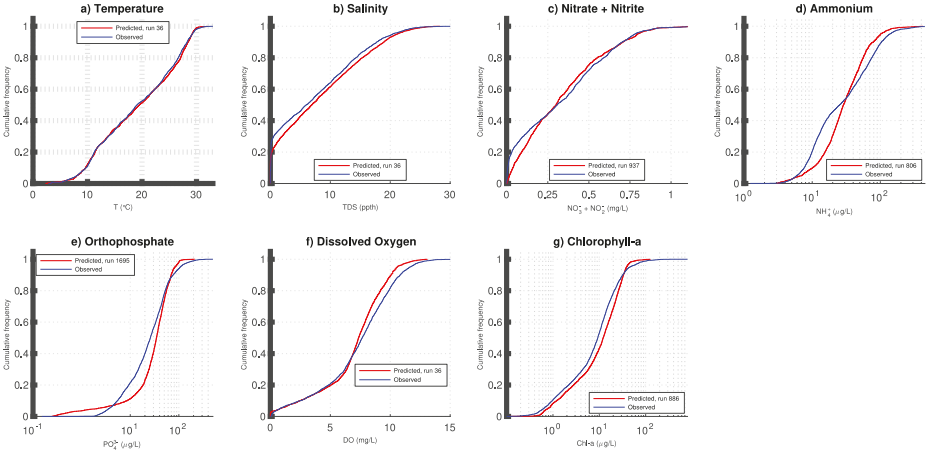

Figure 7. Cumulative frequency distributions for hydrodynamic and water quality variables for 1998–2000 and 2006–2008 combined. Panels show (**a**) temperature, (**b**) salinity, (**c**) nitrate + nitrite, (**d**) ammonium, (**e**) orthophosphate, (**f**) dissolved oxygen, and (**g**) chlorophyll-a.

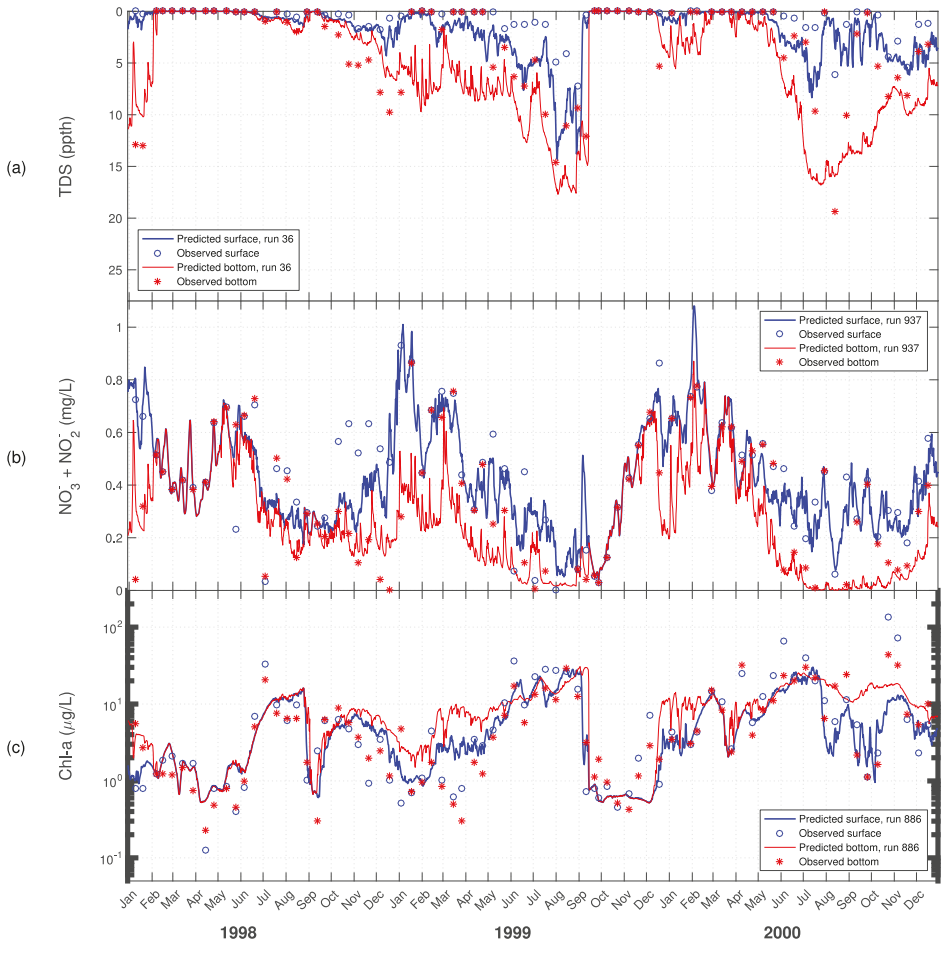

Figure 8. Time series for predicted versus observed values of: (**a**) salinity; (**b**) nitrate + nitrite; and (**c**) chlorophyll-a at ModMon 30 for 1998–2000.

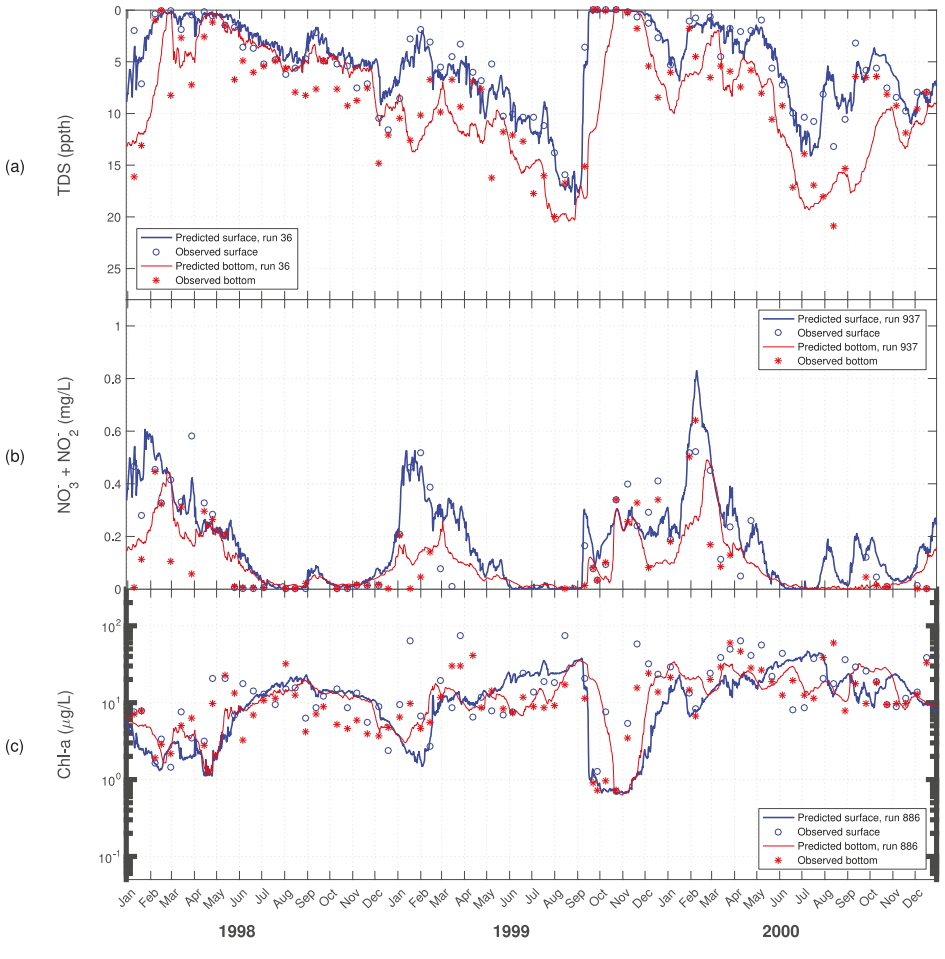

Figure 9. Time series for predicted versus observed values of: (**a**) salinity; (**b**) nitrate + nitrite; and (**c**) chlorophyll-a at ModMon 100 for 1998–2000.

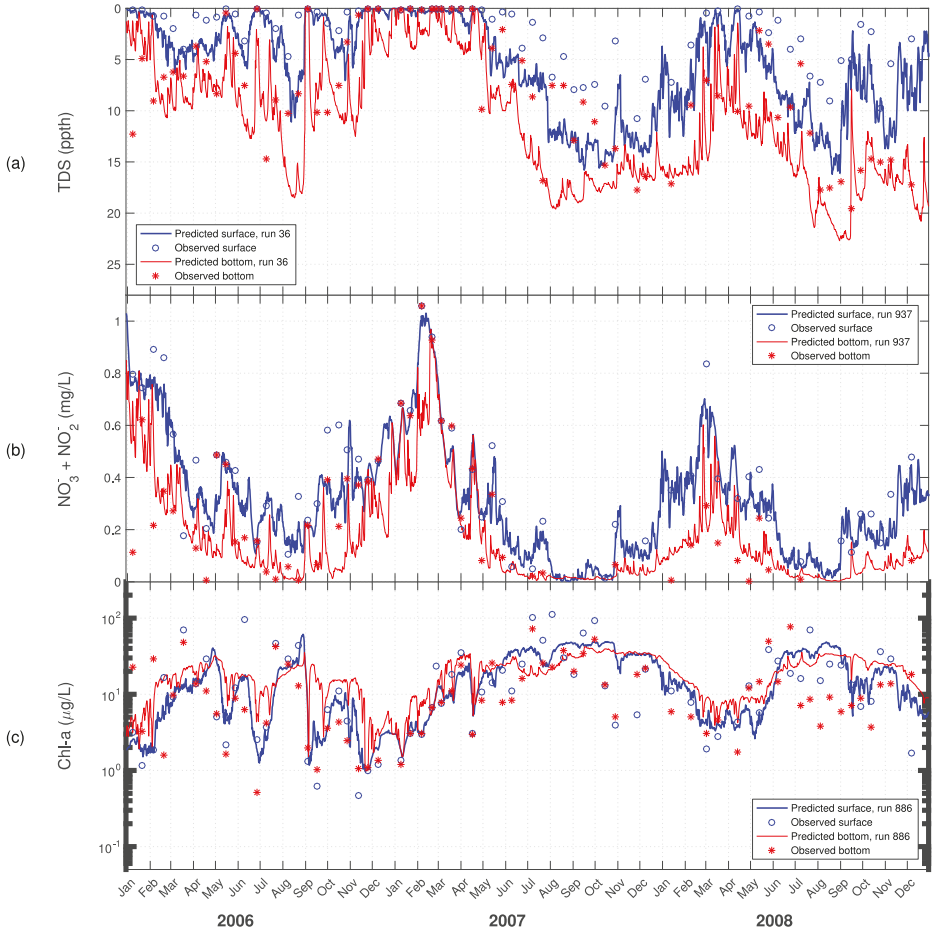

Figure 10. Time series for predicted versus observed values of: (**a**) salinity; (**b**) nitrate + nitrite; and (**c**) chlorophyll-a at ModMon 30 for 2006–2008.

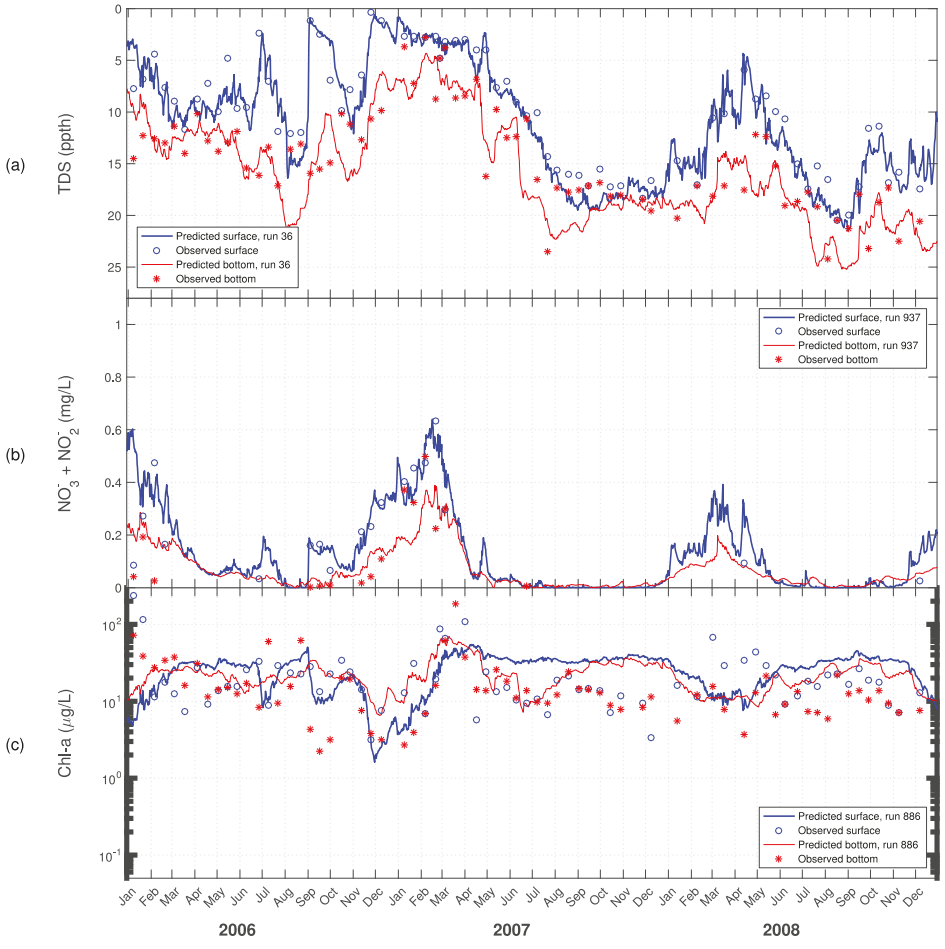

Figure 11. Time series for predicted versus observed values of: (**a**) salinity; (**b**) nitrate + nitrite; and (**c**) chlorophyll-a at ModMon 100 for 2006–2008.

Comparisons of model predicted and observed time series of temperature, salinity, and nitrate + nitrite showed high correlation, followed by chlorophyll-a and dissolved oxygen, with orthophosphate and ammonium showing the lowest correlation between the two datasets (Figures 5 and 6).

4. Discussion

The full-factorial analysis calibration method used was found to be practical in this instance only by considering a limited number of kinetic parameters for a single algal group and by utilizing the collective computational power of a computer cluster. Even with the cluster, running all 2187 cases for two separate periods took nearly a week and approximately 1300 hours of total computational time. Only seven adjustable parameters were utilized, yet the previous Neuse Estuary Eutrophication Model used three algal groups with 17 adjustable algal kinetic parameters for each group. A full factorial analysis done in the same fashion with $51 = 3 \times 17$ algal parameters would have required testing 2.1×10^{24} cases. Even limiting the growth rate specification of each algal group to only seven parameters as was done here would have required $3^{(3 \times 7)} = 1.5 \times 10^{10}$ cases. We found that there are still some significant drawbacks to conducting calibration in the manner done here. There are, however,

some advantages that were realized with the method. First, the simultaneous consideration of multiple criteria necessitated an intentional consideration of the necessary performance of the calibrated model. In doing this, we decided that it was reasonable to consider more than the typical set of model "fit" criteria such as the mean error and the Nash–Sutcliffe model efficiency [25,26]. We added criteria that considered how well the model would simulate the observed distribution of chl-a values, and the frequency of chl-a values above the current numeric water quality criteria. These sorts of criteria will likely be important should the model eventually be used as a regulatory tool. Another advantage of this method is that it provides an estimate of model uncertainty. Degree of model fit is given not as a single set of numbers but as a range over the 27 cases (Table 4). Understanding how planned nutrient reduction scenarios might affect algal growth is integral to the management of eutrophication in the Neuse Estuary. Such scenario testing with the model would also include a range of values, and would provide model users an estimate of the reliability of model predictions. Thus, the outputs of the method described here more closely align with the way similar models have been used for nutrient-management in the estuary. Finally, the full-factorial calibration method, using a single algal group outperformed the previous model that used three algal groups. Using the full-factorial approach, we found 27 cases that met all six calibration criteria, yet the previous model, which had but a single set of parameters, met only four of the six calibration criteria.

With regard to calibration performance of our set of 27 acceptable model parameter sets, we found that model predictions of chlorophyll-a correlated moderately well (Table 4) with those observed at ModMon stations (mean Nash–Sutcliffe Model Efficiency = 49.3%) but were slightly higher on average than the corresponding observed data (ME = 11.6%). Variation in mean error between the 27 selected runs was minimal, with no case having lower than a 10% mean error or explaining greater than 52% of the variation in the observed data. There was considerable difference in the performance of the model between the two periods, as 1998–2000 had both a considerably better mean error (6.0% vs. 15.9%) and a higher model efficiency (57% vs. 27%). The previously calibrated Neuse Estuary Eutrophication Model (NEEM) had a lower mean error (−0.17%) for the 1998–2000 period but accounted for less of the observed variation in the data as compared with the updated NEEM (36.5% vs. >52%).

The chl-a observed data from 1998–2000 and 2006–2008 show a seasonal pattern where maximum values are reached during the summer months (Figures 8c, 9c, 10c and 11c). This pattern is interrupted by periods where high flow events wash algae out of the upper and middle estuary sections, causing chlorophyll-a to drop sharply (e.g., April 1998, September 1998, January 1999, September–November 1999, July 2006, September 2006, and December 2006). With the exception of April 1998, this pattern is captured reasonably well by the model at ModMon 30 for both periods. As noted previously, the model responds more slowly than the observed data after the major storms of Hurricanes Floyd and Irene during September and November of 1999 (Figure 8c). Observed chlorophyll-a concentrations begin trending upward immediately after the November storm, but the model takes unit mid-December to respond similarly. In addition, the model has some difficulty in capturing the pattern in observed chlorophyll-a concentrations registered during the six summers modeled plus November 2000 and March 2006. This behavior is also evident in the cumulative distribution frequency diagram where the model generally overpredicts chlorophylls lower than 40 μg/L, but underpredicts the ones above (Figure 7g).

As shown in the time history plots of model predicted vs. observed chlorophyll-a concentrations, similar behavior is seen for ModMon 100 with the exception of the last half of the 2006–2008 period (Figure 11c). Aside from the small dip in the spring of 2008 in response to a series of small storms, the model's predictions of chlorophyll-a are almost totally unresponsive. The observed low in December 2007 succeeded by a high the following March are absent from the model's predictions.

Another difference of note is the way stratification is predicted by the model. During period of stratification, the observed chlorophylls almost always exceed those of the bottom at that time and place. This is as expected, since the availability of light, and, thus, algal growth should be greatest in the surface layers. However, when the model predicts stratification, it often predicts higher chlorophylls

at the bottom. This behavior is more prominent at ModMon 30 (Figures 8 and 10) than at ModMon 100 (Figures 9 and 11).

The model in this investigation used a simple linear regression to vary the extinction coefficient with salinity, since salinity is closely associated with the clarity and color of water in the estuary. However, salinity only accounts for 44% of the variation in the extinction coefficient. Since previous research has demonstrated that light availability affects phytoplankton productivity in the NRE [27], it is necessary in future versions of the NEEM to be able to predict extinction coefficients with greater reliability.

Elevation data came from many different locations, times, agencies, and methods. In addition, no elevation data were available for 1 January 2000–31 May 2002 and after 1 January 2009. A more frequent, accurate, and complete source of elevation data is needed to predict tidal flows into and out of the estuary.

All flows in the eleven branches and three non-WWTP tributaries were scaled from the Neuse and Trent Rivers using the ratios of drainage areas. Thus, the assumption was made that the drainage areas have the same runoff coefficients. In the future, it may be possible to capture both the spatially and temporally varying runoff characteristics of the drainage areas with a GIS-based tool. This information can then be used to more accurately predict the flows in the non-gauged branches and tributaries.

The simple treatment of sediment employed in this model uses a combination of a constant zero-order SOD and a temperature-dependent, first-order SOD. Furthermore, denitrification was modeled as solely a water-column process, and as such was not DO-dependent. The model does not calculate sediment to water column nutrient fluxes based on organic matter delivery to the sediments. The previous version of the Neuse River Estuary featured a custom sediment diagenesis subroutine and may explain why it was better able to predict ammonia, orthophosphate, and dissolved oxygen. We are currently working to assess whether the updated sediment model of the latest version of CE-QUAL-W2 (Version 4) can better simulate sediment/water-column fluxes, nutrients and dissolved oxygen in this system.

5. Summary

Chlorophyll calibration was performed for both time periods simultaneously by performing a full-factorial experiment consisting of testing seven algal kinetic growth parameters over three levels. Six criteria were used to determine which runs performed acceptably. As a result, the mean and standard deviation of the 27 cases that met all of the criteria were used in all subsequent analyses. The set of algal kinetic parameters used in the previous W2 study of the Neuse River Estuary [9] did not meet all six criteria.

Although average chlorophyll performance for the new model period (2006–2008) was relatively weak, performance for the earlier time period improved considerably over previous work [4,9,28]. Compared to the most recent W2 effort, the average calibration performance for both periods combined decreased significantly for ammonia, decreased slightly for phosphate and dissolved oxygen and increased for nitrate + nitrite. The results of the work suggest that improvements in the model should focus on improving the downstream boundary specification, specification of non-point source nutrient loads from the most downstream part of the watershed, and improving the sediment diagenesis sub-model.

Author Contributions: Conceptualization, J.B.; Methodology, J.B.; Software, J.B. and N.H.; Validation, J.B. and N.H.; Formal Analysis, N.H.; Investigation, J.B and N.H.; Resources, J.B.; Data Curation, J.B. and N.H.; Writing-Original Draft Preparation, N.H.; Writing-Review & Editing, J.B. and N.H.; Visualization, J.B. and N.H.; Supervision, J.B.; Project Administration, J.B.; Funding Acquisition, J.B.

Funding: This research was funded by the North Carolina Water Resources Research Institute grant number 2016-0454-01, and by the U.S. Geological Survey grant number 2016-1887-01.

Conflicts of Interest: The authors declare no conflict of interest. The funders had no role in the design of the study; in the collection, analyses, or interpretation of data; in the writing of the manuscript, and in the decision to publish the results.

References

1. Paerl, H.W. Nuisance phytoplankton blooms in coastal, estuarine, and inland waters. *Limnol. Oceanogr.* **1988**, *33*, 823–847. [CrossRef]
2. Pinckney, J.L.; Millie, D.F.; Vinyard, B.T.; Paerl, H. Environmental controls of phytoplankton bloom dynamics in the Neuse River Estuary, North Carolina, USA. *Can. J. Fish. Aquat.Sci.* **1997**, *54*, 2491–2501. [CrossRef]
3. Stow, C.A.; Roessler, C.; Borsuk, M.E.; Bowen, J.D.; Reckhow, K.H. Comparison of estuarine water quality models for total maximum daily load development in Neuse River Estuary. *J. Water Resour. Plan. Manag.* **2003**, *129*, 307–314. [CrossRef]
4. Bowen, J.D.; Hieronymus, J.W. A CE-QUAL-W2 model of Neuse Estuary for total maximum daily load development. *J. Water Resour. Plan. Manag.* **2003**, *129*, 283–294. [CrossRef]
5. Bowen, J.D.; Hieronymus, J. *Neuse River Estuary Modeling and Monitoring Project Stage 1: Predictions and Uncertainty Analysis of Response to Nutrient Loading Using a Mechanistic Eutrophication Model*; Report No. 325 for Water Resources Research; Institute of the University of North Carolina: Raleigh, NC, USA, October 2000.
6. Paerl, H.W.; Hall, N.S.; Peierls, B.L.; Rossignol, K.L.; Joyner, A.R. Hydrologic variability and its control of phytoplankton community structure and function in two shallow, coastal, lagoonal ecosystems: the Neuse and New River Estuaries, North Carolina, USA. *Estuaries Coasts* **2014**, *37*, 31–45. [CrossRef]
7. Lebo, M.E.; Paerl, H.W.; Peierls, B.L. Evaluation of progress in achieving TMDL mandated nitrogen reductions in the Neuse River Basin, North Carolina. *Environ. Manag.* **2012**, *49*, 253–266. [CrossRef] [PubMed]
8. Paerl, H.W.; Valdes, L.M.; Piehler, M.F.; Stow, C.A. Assessing the effects of nutrient management in an estuary experiencing climatic change: The Neuse River Estuary, North Carolina. *Environ. Manag.* **2006**, *37*, 422–436. [CrossRef] [PubMed]
9. Hieronymus, J.; Bowen, J.D. *Calibration and Verification of a Two-dimensional Laterally Averaged Mechanistic Model of the Neuse River Estuary*; Report No. 343c for Water Resources Research; Institute of the University of North Carolina: Raleigh, NC, USA, July 2004.
10. Liu, W.C.; Chen, W.B.; Kimura, N. Impact of phosphorus load reduction on water quality in a stratified reservoir-eutrophication modeling study. *Environ. Monit. Assess.* **2009**, *159*, 393–406. [CrossRef] [PubMed]
11. Etemad-Shahidi, A.; Afshar, A.; Alikia, H.; Moshfeghi, H. Total dissolved solid modeling; Karkheh reservoir case example. *Int. J. Environ. Res.* **2009**, *3*, 671–680.
12. Gelda, R.K.; Effler, S.W. Testing and application of a two-dimensional hydrothermal model for a water supply reservoir: Implications of sedimentation. *J. Environ. Eng. Sci.* **2007**, *6*, 73–84. [CrossRef]
13. Huang, Y.; Liu, L. Multiobjective water quality model calibration using a hybrid genetic algorithm and neural network–based approach. *J. Environ. Eng.* **2010**, *136*, 1020–1031. [CrossRef]
14. Afshar, A.; Kazemi, H.; Saadatpour, M. Particle swarm optimization for automatic calibration of large scale water quality model (CE-QUAL-W2): Application to Karkheh Reservoir, Iran. *Water Resour. Manag.* **2011**, *25*, 2613–2632. [CrossRef]
15. Afshar, A.; Shojaei, N.; Sagharjooghifarahani, M. Multiobjective calibration of reservoir water quality modeling using multiobjective particle swarm optimization (MOPSO). *Water Resour. Manag.* **2013**, *27*, 1931–1947. [CrossRef]
16. Grangere, K.; Lefebvre, S.; Ménesguen, A.; Jouenne, F. On the interest of using field primary production data to calibrate phytoplankton rate processes in ecosystem models. *Estuar. Coast. Shelf Sci.* **2009**, *81*, 169–178. [CrossRef]
17. Arhonditsis, G.B.; Papantou, D.; Zhang, W.T.; Perhar, G.; Massos, E.; Shi, M. Bayesian calibration of mechanistic aquatic biogeochemical models and benefits for environmental management. *J. Mar. Syst.* **2008**, *73*, 8–30. [CrossRef]
18. Arhonditsis, G.B.; Qian, S.S.; Stow, C.A.; Lamon, E.C.; Reckhow, K.H. Eutrophication risk assessment using Bayesian calibration of process-based models: Application to a mesotrophic lake. *Ecol. Model.* **2007**, *208*, 215–229. [CrossRef]
19. Bowen, J.; Harrigan, N.B. *Comparing the Impact of Organic Versus Inorganic Nitrogen Loading to the Neuse River Estuary With a Mechanistic Eutrophication Model*; Report No. 470 for Water Resources Research; Institute of the University of North Carolina: Raleigh, NC, USA, September 2017.

20. Cole, T.M.; Wells, S.A. *CE-QUAL-W2: A Two-Dimensional, Laterally Averaged, Hydrodynamic and Water Quality Model, Version 3.72 User Manual*; Technical Report; Department of Civil and Environmental Engineering, Portland State University: Portland, OR, USA, 2015.
21. Paerl, H.W.; Rossignol, K.L.; Hall, S.N.; Peierls, B.L.; Wetz, M.S. Phytoplankton community indicators of short-and long-term ecological change in the anthropogenically and climatically impacted Neuse River Estuary, North Carolina, USA. *Estuaries Coasts* **2010**, *33*, 485–497. [CrossRef]
22. Paerl, H.W.; Valdes, L.M.; Peierls, B.L.; Adolf, J.E.; Harding, L.J.W. Anthropogenic and climatic influences on the eutrophication of large estuarine ecosystems. *Limnol. Oceanogr.* **2006**, *51*, 448–462. [CrossRef]
23. Steele, J.H. Environmental control of photosynthesis in the sea. *Limnol. Oceanogr.* **1962**, *7*, 137–150. [CrossRef]
24. Thornton, K.W.; Lessem, A.S. A temperature algorithm for modifying biological rates. *Trans. Am. Fish. Soc.* **1978**, *107*, 284–287. [CrossRef]
25. McCuen, R.H.; Knight, Z.; Cutter, A.G. Evaluation of the Nash–Sutcliffe efficiency index. *J. Hydrol. Eng.* **2006**, *11*, 597–602. [CrossRef]
26. Krause, P.; Boyle, D.; Bäse, F. Comparison of different efficiency criteria for hydrological model assessment. *Adv. Geosci.* **2005**, *5*, 89–97. [CrossRef]
27. Boyer, J.N.; Christian, R.R.; Stanley, D.W. Patterns of phytoplankton primary productivity in the Neuse River estuary, North Carolina, USA. *Mar. Ecol. Prog. Ser.* **1993**, *97*, 287–297. [CrossRef]
28. Wool, T.A.; Davie, S.R.; Rodriguez, H.N. Development of three-dimensional hydrodynamic and water quality models to support total maximum daily load decision process for the Neuse River Estuary, North Carolina. *J. Water Resour. Plan. Manag.* **2003**, *129*, 295–306. [CrossRef]

Journal of
Marine Science and Engineering

MDPI

Article

Model Development and Hindcast Simulations of NOAA's Integrated Northern Gulf of Mexico Operational Forecast System

Zizang Yang [1,*], Lianyuan Zheng [2], Phillip Richardson [1], Edward Myers [1] and Aijun Zhang [2]

[1] NOAA/National Ocean Service/Coast Survey Development Laboratory, 1315 East-West Highway, Silver Spring, MD 20910, USA; phil.richardson@noaa.gov (P.R.); edward.myers@noaa.gov (E.M.)

[2] NOAA/National Ocean Service/Center for Operational Oceanographic Products and Services, 1305 East-West Highway, Silver Spring, MD 20910, USA; lianyuan.zheng@noaa.gov (L.Z.); aijun.zhang@noaa.gov (A.Z.)

* Correspondence: zizang.yang@noaa.gov; Tel.: +1-240-847-8255

Received: 2 October 2018; Accepted: 6 November 2018; Published: 12 November 2018

Abstract: NOAA's National Ocean Service is upgrading three existing northern Gulf of Mexico (GOM) operational nowcast/forecast systems (OFS) by integrating them into one single system (INGOFS) and developing additional domain coverage to encompass the lower Mississippi River, Lake Pontchartrain, Texas coastal embayments, and Mexican coastal waters. The system will produce real-time nowcast and short-range forecast guidance for water levels, 3-dimensional currents, water temperature, and salinity. INGOFS will be implemented using the Finite Volume Community Ocean Model (FVCOM). This paper describes the model configuration and results from a one-year (2 August 2016–1 August 2017) hindcast simulation. The model grid is composed of about 300,000 nodes and 600,000 elements, and has a spatial resolution ranging from 45 m near the coast to around 10 km on the open ocean boundary. It uses the FVCOM wetting and drying feature, the quadratic bottom friction scheme, and the two-equation model of the Mellor-Yamada Level 2.5 turbulence closure scheme. The hindcast results of water levels, surface temperatures, and salinity were verified by comparing the model time series with in situ observations. The root-mean-squared errors are about 0.08 m for water levels, about 1.1 °C for temperatures, and about 3.7 psu for salinity. The hindcast configuration will be further tested in a nowcast/forecast environment for a one-year period. The upgraded system is anticipated to be in operational production in mid-2020.

Keywords: Gulf of Mexico; operational nowcast and forecast system; Finite Volume Community Ocean Model; water level; temperature; salinity

1. Introduction

Coastal waters of the northern Gulf of Mexico (NGOM) encompass broad coastal regions spanning from the coast of Mexico in the west to the U.S. Gulf Coast in the northwest, north, and northeast (Figure 1). The hydrodynamic states in the region are governed by fresh water inflows from river discharge, off shelf dynamics, wind forcing and heat flux across the air-sea interface, and tidal fields [1–6]. The coastal circulation field is characterized by the combined seasonal buoyancy-driven coastal currents and by intrusions onto the shelf of the Loop Currents. Cross-shelf exchanges via mixing are driven by episodic wind events and by intrusions onto the shelf of the Loop Currents. River runoff onto the shelf is highly variable. Both the Atchafalaya River and the Mississippi River flow onto the Louisiana shelf, with a combined annual average discharge of over 14,000 m^3/s [7]. The major portion of this runoff flows westward onto the west Louisiana shelf and the remaining portion flow eastward onto the Louisiana-Mississippi-Alabama shelf. Both flows introduce buoyancy forcing, and largely define the baseline alongshore coastal currents in the NGOM region.

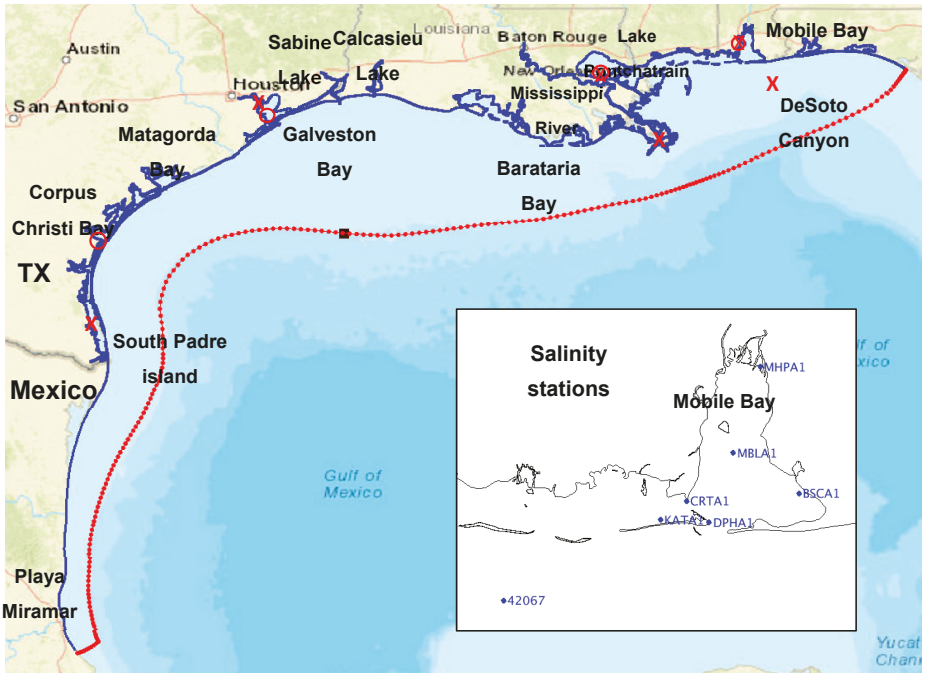

Figure 1. Map of northern Gulf of Mexico. Blue and red lines combine to delineate the INGOFS model grid boundary. The red line represents the model's open ocean boundary. Marked are the water level (WL) (o) and the sea-surface temperature (SST) stations (x) (Section 4). The inset displays the salinity stations (Section 4). From west to east are shown the WL stations 8735391, 8761927, 8771013, and 8775792; and the SST stations 42012, MCGA1, NWCL1, PILL1, MGPT2, and PMNT2.

The eastern and western NGOM, divided by the Mississippi River delta, demonstrate distinctive circulation features [7,8]. A large, semi-permanent, cyclonic surface gyre exists in the eastern NGOM [5,9,10]. This gyre branches into two flows: a northward flow following the western rim of the De Soto Canyon, and a southeastward flow along the Florida Shelf break. Both the weather band (2–10 days) wind-driven currents and sea level fluctuations are strong in the winter when the eastern shelf is influenced by a series of cold fronts from the north. The Loop Currents extrude water onto the shelf in the DeSoto Canyon (Figure 1) and thus, directly modulate the local density and circulation fields.

Circulation in the western NGOM is influenced largely by river discharge induced buoyancy forcing and by the regional wind field [11–13]. The combined effect of the buoyancy flux and the easterly wind stress produces a yearly mean westward coastal circulation along the Louisiana–Texas coast. The flow field is highly modulated by wind field fluctuations. Over the inner shelf, currents are predominantly modulated by winds in the weather band, while the outer shelf currents are driven primarily by mesoscale activity [14,15]. Using the Regional Ocean Modeling System (ROMS), Zhang et al. [13] studied the effects of wind forcing on the dynamics of buoyancy circulation over the Louisiana–Texas shelf. They identified that in the winter and fall, under the impact of the prevailing down coast wind, most of the interior water was dominated by a geostrophic balance in the cross-shore momentum budget. In the spring and summer, the Ekman flow, driven by strong onshore wind, played a major role in modulating the circulation fields.

Tides in the NGOM region are modest [4], with either diurnal or mixed characteristics. The mean tidal amplitude ranges from several centimeters to less than 0.5 m. The strongest tidal currents are

usually less than 15 cm/s. Using both mathematical analysis and one-dimensional water column numerical simulation, Burchard and Hetland [16] quantified the impact of tidal straining on the estuarine circulations. They found that without wind forcing and river inflows, tidal straining is responsible for about two-thirds of the estuarine circulation, while gravitational circulation is responsible for the remaining one-third.

The Gulf Coast is an area of active economic and recreational activities. The hydrographic and hydrodynamic states demonstrate significant impacts on the local ecosystem and daily human life. Operational hydrodynamic forecasting is of vital importance in support of harmful algal bloom (HAB) forecasts, marine navigation, emergency response, and the environmental management communities.

The National Oceanic and Atmospheric Administration (NOAA) currently has three operational oceanographic nowcast/forecast systems (OFS) for the NGOM region. These three OFS are the Northern Gulf of Mexico OFS (NGOFS), the nested northwest Gulf of Mexico OFS (NWGOFS), and the nested northeast OFS (NEGOFS) (https://tidesandcurrents.noaa.gov/ofs/ngofs/ngofs.html). The systems all use the Finite Volume Community Ocean Model (FVCOM) [17] as the core hydrodynamic model. They each produce eight-hour nowcasts and up to 48-hour forecast guidance of water levels, three-dimensional (3-D) currents, temperatures, and salinity fields. The three systems differ in their domain coverage, model grid resolution, and in their methods of applying open ocean boundary forcing [18,19].

Figure 2a depicts the domain of each system. Table 1 lists the size and spatial resolution of each model grid. The NGOFS domain spans the northern Gulf of Mexico coastal shelf from South Padre Island, Texas in the west to west of Panama City, Florida in the east. It lacks coverage of many alongshore estuaries and embayments and does not resolve fine coastline features. NWGOFS and NEGOFS were developed to partially resolve the NGOFS' limitations. Both NWGOFS and NEGOFS have higher spatial resolutions than NGOFS. NWGOFS covers Lake Charles, Sabine-Neches, Galveston, and Matagorda Bay, whereas NEGOFS covers Mobile Bay, Pascagoula, and the Gulfport area.

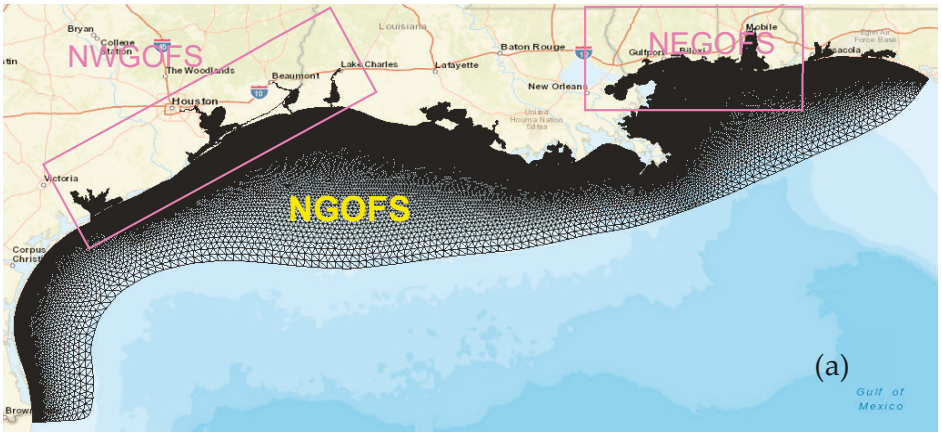

Figure 2. *Cont.*

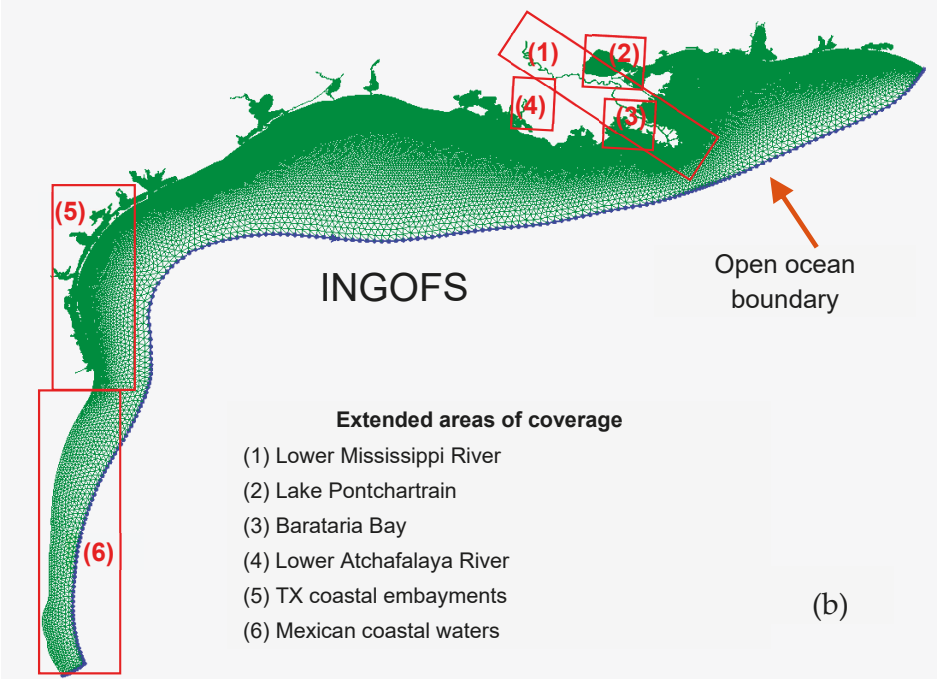

Figure 2. Model grids. (**a**) Combined grids of three existing OFS, and (**b**) the INGOFS grid.

Table 1. Dimension and resolution of NGOFS, NWGOFS, NEGOFS, and INGOFS model grids.

Model	Number of Nodes	Number of Elements	Element Size (min, max)
NGOFS	90,267	174,474	(150 m–11 km)
NWGOFS	85,707	160,444	(60 m–3.5 km)
NEGOFS	68,455	131,008	(45 m–2.2 km)
INGOFS	303,714	569,405	(45 m–11 km)

Figure 3 shows the diagram to illustrate the conceptual structure, forcing data inputs, system operations, analysis, and the archive of model outputs. The Center for Operational Oceanographic Products and Services (CO-OPS) implemented the OFS on the Weather and Climate Operational Supercomputing System (WCOSS), which is operated by the National Centers for Environmental Prediction (NCEP), Central Operations (NCO), of NOAA. The system runs make use of NCEP's North American Mesoscale (NAM) outputs for the atmospheric forcing, and the U.S. Geological Survey (USGS) river discharge for the river forcing. The water levels, currents, water salinity, and water temperatures used by NGOFS for open boundary conditions (OBC) are generated from NCEP's Global Real-Time Ocean Forecast System (G-RTOFS). The NEGOFS/NWGOFS OBC are taken from the NGOFS outputs via a one-way nesting approach [19]. The native formats of the forcing files are different from those required by FVCOM. The OFS (NGOFS, NEGOFS, and NWGOFS) use the Coastal Ocean Modeling Framework (COMF) [20] software package to transform the data sets into Network Common Data Form (NetCDF) files with data structures that conform to FVCOM requirements. Using the Continuous Operational Real-Time Monitoring System (CORMS) (https://tidesandcurrents.noaa.gov/corms.html), CO-OPS and NCO team up to monitor and log the system operations on a 24 × 7 basis.

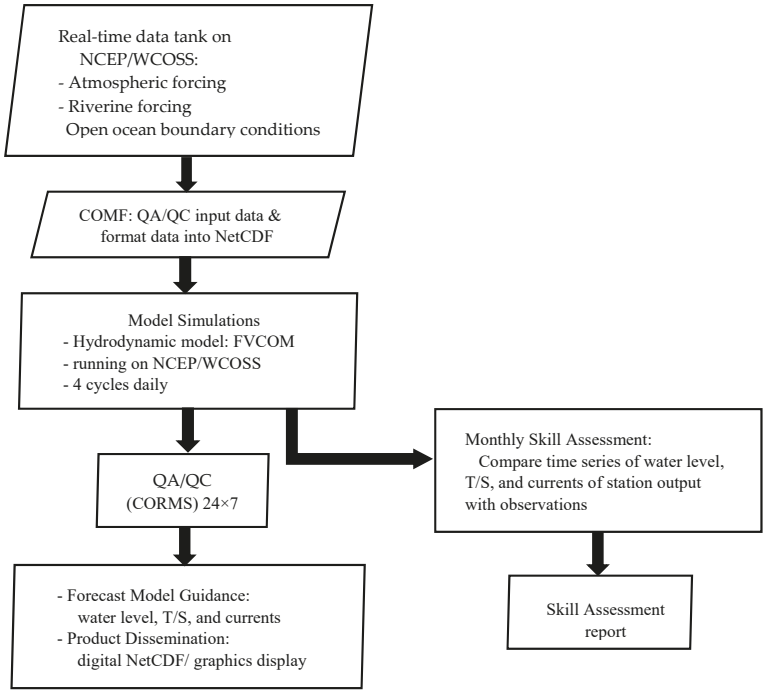

Figure 3. Conceptual structure and the operational and data analysis procedures of the NGOM operational forecast systems.

Three OFS produce six hours of nowcast, and up to 48 hours of forecast guidance, for water levels and three-dimensional currents, water temperatures, and salinity four times a day at 0300, 0900, 1500 and 2100 UTC. Both the hourly field and the 6-minute station (at locations with available observed data) NetCDF outputs are archived and disseminated at the Linux data tank (https://opendap.co-ops.nos.noaa.gov/netcdf/) of the National Ocean Service (NOS). In addition, COMF generates time series plots of station outputs (24-hour nowcast and 48-hour forecast), which include water levels, currents, temperatures, salinity, and surface winds. These outputs are depicted in both contour and vector map plots. Additional graphics include the animation of water levels, currents, temperatures, salinity, and surface winds. The graphics are published through the NOS operational forecast system (OFS) webpage at (https://tidesandcurrents.noaa.gov/ofs/ngofs/ngofs.html). To ensure a high level of model skill, CO-OPS validates the model performance each month by comparing the time series of station outputs with observed data using the NOS skill assessment software [21], which generates model skill reports.

In recent years, the Gulf Coast user community has proposed a growing need for forecast guidance in the NGOFS areas not covered by the three existing OFS. A short list of these areas include the lower Mississippi River course, Lake Pontchartrain, various Texas coastal embayments, Mexican coastal waters, etc. (Figure 1). From an operational point of view, it is more efficient to operate and maintain one combined system, rather than three separate systems. To fulfill user needs and to foster the system's operational efficacy, NOAA decided to combine the three existing OFS into one integrated system. The domain of this new system includes the combined domains of the three existing OFS, as well as the previously unresolved coastal embayments and river courses. Tentatively, it is named the Integrated Northern Gulf of Mexico OFS (INGOFS). Like NGOFS, INGOFS will use FVCOM as its core hydrodynamic model. It is designed to produce a real-time nowcast, and up to 48 hours of

forecast guidance for water levels, 3-D currents, water temperatures, and salinity. It is planned to begin operations in mid-2020.

This article describes technical details of the INGOFS development and model configuration, as well as the setup and verification of a one-year (2 August 2016–1 August 2017) simulation. Since the model run was for a historical period, it will be referred to as hindcast in the following. This section introduces background information including the initiative for the system development. Section 2 describes the model hindcast simulation setup. Section 3 describes the observational data used to verify the hindcast results. Section 4 presents the model results. Section 5 discusses the domain-averaged model skill of the water surface temperatures and water levels, and the impact of initial salinity conditions on the model performance. Section 6 states the summary and future plans.

2. Methods

INGOFS uses the Finite Volume Community Ocean Model (FVCOM) [17] as its core hydrodynamic model. FVCOM is an unstructured grid, finite-volume, three-dimensional, primitive equation ocean circulation model. It uses triangular grids to map the model domain in the horizontal and a terrain-following σ-coordinate in the vertical. The unstructured grid enables an accurate coastal geometric fit. FVCOM is a prognostic model; it is composed of internal and external modes which are computed separately using two split steps. The model uses a second-order finite-volume method to solve the equations of motion by the flux calculation in the integral form of primitive equations. The approach provides an ideal representation of momentum, mass, salt, and heat conservation.

The turbulence parameterization employs the modified Mellor and Yamada level-2.5 turbulence closure model [22] for vertical mixing. The Smagorinsky formulation [23] is used for horizontal mixing. FVCOM was successfully applied to studies of the deep ocean [24], the continental shelf [25], and estuaries [26,27]. A detailed description of FVCOM is available at http://fvcom.smast.umassd.edu/FVCOM/index.html.

The INGOFS domain encompasses broad NGOM coastal waters spanning from the coast of Mexico near (97.6° W, 21.8° N) in southwest, across the U.S. Gulf Coast in the northwest, north, and northeast, and all the way to the west of Panama City in the east (Figures 1 and 2). The domain's open ocean boundary approximates the 300-m isobaths, except near the Mississippi River mouth, where the model boundary extends further outward beyond the shelf break to a depth as great as 1700 m. Except for the portion of the grid in Mexican coastal waters, the INGOFS grid shares the same open ocean boundary as that of NGOFS.

In addition to encompassing the combined NGOFS, NWGOFS, and NEGOFS domains, the INGOFS domain also covers the Lower Mississippi River course, Lake Pontchartrain, Barataria Bay, the lower Atchafalaya River, Texas coastal inlets, and a portion of the Mexican coastal waters (Figures 1 and 2). From the perspective of grid generation, the INGOFS grid is composed of two parts: the combined NGOFS and NWGOFS/NEGOFS grid, and the newly generated grids for extended coverage. The former includes Lake Charles, Sabine-Neches, Galveston Bay, Matagorda Bay, Mobile Bay, Pascagoula, and Gulfport. Figure 2a,b shows the combined NGOFS, NWGOFS/NEGOFS grid and the INGOFS grid, respectively. Figure 4a,b displays close up views of the grids covering the Texas coastal embayments and the lower Mississippi River and adjacent waters, respectively. The INGOFS grid is composed of 303,714 nodes and 569,405 elements. For comparison with the existing OFS grids, Table 1 lists the dimensions and spatial resolution of both the existing OFS and the INGOFS grids.

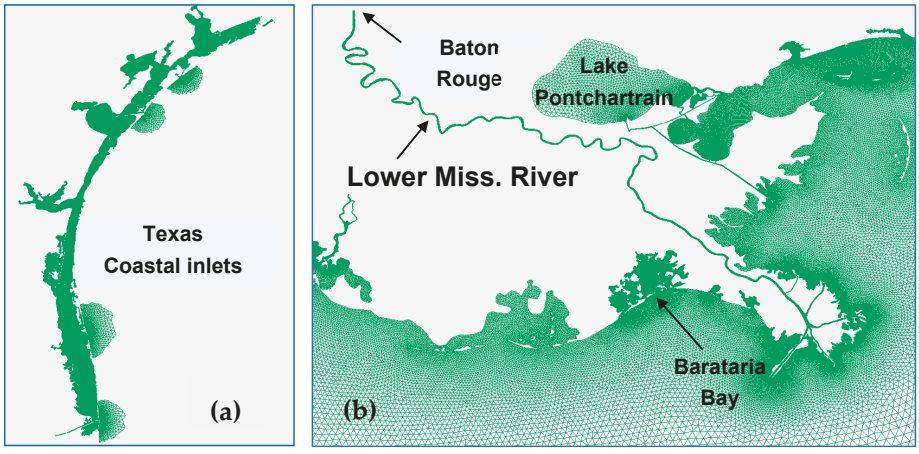

Figure 4. Close up view of the INGOFS model grid in two regions, (**a**) Texas coastal embayments, and (**b**) the lower Mississippi River course, Barataria Bay, and Lake Pontchartrain.

The INGOFS bathymetry was populated using NGOFS, NWGOFS/NEGOFS grid bathymetry, the Vertical Datum (VDatum) (https://vdatum.noaa.gov/welcome.html) model grid bathymetry [28], the NOAA Sounding and Electronic Chart (ENC) bathymetry, and the ADCIRC model grid bathymetry in the Western North Atlantic, Caribbean and Gulf of Mexico ADCIRC Tidal Database (EC2015) [29]. Depending on sources of the INGOFS grid generation and geographical locations, bathymetry was populated in three ways. For any portion of the grid which originated from any of the three existing OFS, the bathymetry remained to be the same as the bathymetry in the source grid. For the remaining portion of the grid in U.S. coastal waters, the bathymetry was populated by linearly interpolating the combined VDatum model grid for the Mississippi River and the New Orleans region [28], as well as the ENC and sounding bathymetry. Bathymetry of the grid covering Mexican waters was populated by linearly interpolating the EC2015 ADCIRC grid bathymetry. Figure 5 displays the color-coded bathymetry.

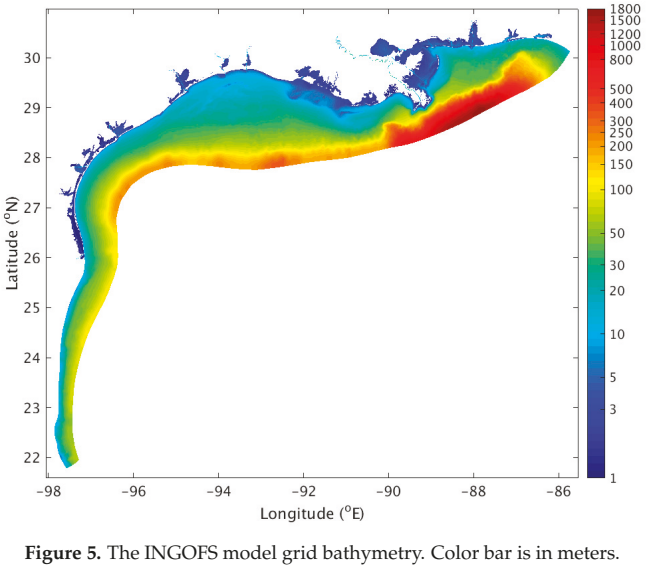

Figure 5. The INGOFS model grid bathymetry. Color bar is in meters.

Using the above model grid and bathymetry configuration, we conducted a one-year (2 August 2016–1 August 2017) hindcast simulation. The simulation was driven with the complete suite of model forcing data including open ocean boundary forcing of the combined tidal and subtidal water levels and currents. Additional model forcing included 3-dimensional temperatures (T) and salinity (S), river flows, and sea-surface meteorological forcing. The tidal water level harmonics were interpolated using the EC2015 tidal database [29]. Considering the relative importance of various tidal constituents in the model domain, we chose eight major tidal constituents, namely, luni-solar (K_1), principal lunar (O_1), principal solar (P_1), elliptical lunar (Q_1), principal lunar (M_2), principal solar (S_2), elliptical lunar (N_2), and luni-solar (K_2) to reconstruct the tidal forcing data.

The non-tidal open ocean conditions used the nowcast results from the Global Real-Time Ocean Forecast System (G-RTOFS) [30,31]. G-RTOFS is run by the National Centers for Environmental Prediction (NCEP) of NOAA. G-RTOFS makes use of the Naval Oceanographic Office's configuration of the 1/12-degree eddy resolving global Hybrid Coordinates Ocean Model (HYCOM) as its core hydrodynamic model. The HYCOM model has horizontal dimensions of 4500 by 3298 and 32 hybrid layers (isopycnals in the deep, isolevel in the mixed layer, and sigma in shallow) in the vertical. The system assimilates in situ profiles of temperature and salinity from a variety of sources, and also assimilates remotely sensed sea-surface temperature (SST), sea-surface height (SSH), and sea-ice concentrations. It runs once a day and produces nowcast and forecast guidance for sea surface values of SSH, SST, and sea-surface salinity (SSS) at three-hour intervals. In addition, it produces full volume parameters (3-dimensional temperature, salinity, currents, and mixed layer depths) at six-hour intervals. The nowcast outputs of three-hourly water levels and six-hourly 3-D currents, temperatures (T) and salinity (S), and non-tidal forcing were spatially interpolated onto the model grid's open ocean boundaries and temporally interpolated throughout the INGOFS hindcast period.

The river forcing used discharge from 29 rivers along the INGOFS land boundary. Table 2 lists the USGS station identifications (IDs) and station names. Some big rivers, with wide cross sections, were resolved through multiple grid nodes. In such cases, river discharge was evenly distributed across the nodes. Discharge from the 29 rivers is distributed over 63 model nodes. Figure 6 shows the river node locations.

Table 2. USGS river station IDs and names.

No.	IDs	Station Names	No.	IDs	Station Names
1	2365500	Chocta Whatchee River at Caryville, FL	16	8015500	Calcasieu River Near Kinder, LA
2	2368000	Yellow River at Milligan, FL	17	8030500	Sabine Rv Nr Ruliff, TX
3	2375500	Escambia River Near Century, FL	18	8041780	Neches Rv Saltwater Barrier at Beaumont, TX
4	2376500	Perdido River at Barrineau Park, FL	19	8066500	Trinity Rv at Romayor, TX
5	2470629	Mobile River Near Landon, MS	20	8069000	Cypress Ck Nr Westfield, TX
6	2471019	Tensaw River Near Mount Vernon, AL	21	8075000	Brays Bayou at Houston, TX
7	2479000	Pascagoula River at Merrill, MS	22	8075400	Sims Bayou at Hiram Clarke St, Houston, TX
8	2479560	Escatawpa River Near Agricola, MS	23	8076000	Greens Bayou Nr Houston, TX
9	2481510	Wolf Rv Nr Landon, MS	24	8116650	Brazos Rv Nr Rosharon, TX
10	2489500	Pearl River Near Bogalusa, LA	25	8162500	Colorado Rv Nr Bay City, TX
11	2492000	Bogue Chitto River Near Bush, LA	26	8164000	Lavaca Rv Nr Edna, TX
12	7374000	Mississippi River at Baton Rouge, LA	27	8164800	Placedo Ck Nr Placedo, TX
13	7375500	Tangipahoa River at Robert, LA	28	8188800	Guadalupe Rv Nr Tivoli, TX
14	7381600	Lower atchafalaya River at Morgan City, LA	29	8211200	Nueces Rv at Bluntzer, TX
15	8012000	Nezpique Near Basile, LA			

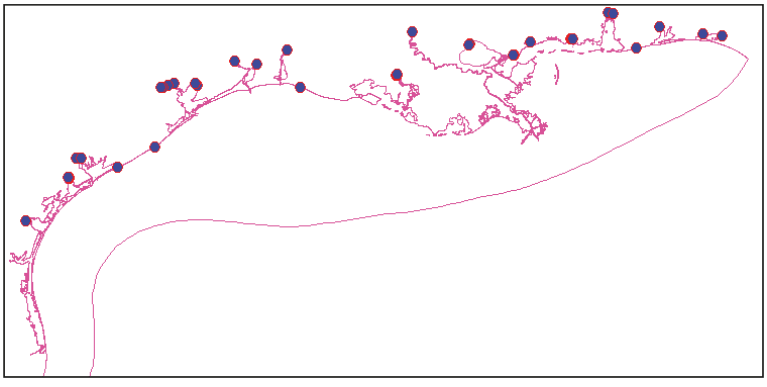

Figure 6. River forcing locations on the INGOFS grid. Discharges of the 18 rivers total are distributed across 63 grid nodes.

The river flow data were from the U.S. Geological Survey (USGS) river discharge observations [32]. It is noted that not all USGS river discharge measurements were accompanied by simultaneous water temperature measurements. For the stations without temperature data, the temperature measurements from nearby Center for Operational Oceanographic Products and Services (CO-OPS) stations were used. The salinity was specified to be zero for all 29 rivers.

The hindcast made use of the 6-km resolution forecast guidance from the NOAA National Centers for Environmental Prediction's (NCEP's) North American Mesoscale Forecast Modeling System (NAM) for surface forcing. The INGOFS hindcast was forced with 10-m wind velocity to compute the surface wind stress, and with 2-m surface air temperature and relative humidity. Additional forcing included the total shortwave radiation, downward longwave radiation, the FVCOM bulk formulation to calculate the air-sea momentum, and the Coupled Ocean–Atmosphere Response Experiment (COARE) algorithm [33] to compute heat flux across the air-sea interface.

The hindcast simulation ran from 2 August 2016 to 1 August 2017. It started from a still water state with the water temperature and salinity fields initialized with combined NGOFS, NWGOFS/NEGOFS outputs. The model was configured in 20 sigma layers. It used the FVCOM wetting and drying feature, the quadratic bottom friction scheme, and the two-equation model of the Mellor-Yamada Level 2.5 turbulence closure scheme. The internal model time step was 9 s and the external to internal time step split ratio was equal to 3.

3. Observational Data

The observational data used to verify the model results included water level time series from the National Ocean Service (NOS) CO-OPS water level stations. Temperature data (T) and salinity data (S) from CO-OPS meteorological observation stations, and temperature data from National Data Buoy Center (NDBC) buoys were also included. The water level data were downloaded via the CO-OPS online archive [34]. Table A1 lists the station IDs, names, and station location information.

The T and S data collected from either the CO-OPS or NDBC buoys were downloaded through the NDBC online archive [35]. The observation depths ranged between 0.5 m and 3 m beneath the sea surface.

Please note that every CO-OPS station possesses dual station IDs—one in the CO-OPS naming convention and one in the NDBC naming convention. To be clear, the stations are hereafter referred to only by their NDBC IDs. Tables 3 and A2 show the station IDs, names, and geographical information for temperature and salinity, respectively.

Table 3. Station meta data of surface salinity observations.

No.	IDs	Station Names	Longitude (°E)	Latitude (°N)
1	42067	USM3M02	−88.649	30.043
2	BSCA1	Bon Secour, AL	−87.829	30.329
3	CRTA1	Cedar Point, AL	−88.14	30.308
4	PHA1	Dauphin Island, AL	−88.078	30.251
5	KATA1	Katrina Cut, Al	−88.213	30.258
6	BLA1	Middle Bay Lighthouse, AL	−88.011	30.437
7	HPA1	Meaher Park, AL	−87.936	30.667

4. Results of Hindcast Simulations

Following an initial 6-day ramping up of both water level and velocity forcing on the open ocean boundary, the hindcast model run (Section 2) continued for another 9 days to ensure that an equilibrium state was reached. The time series of water levels, temperatures and salinity were recorded at 6-minute intervals from the 15th day to the end of the hindcast simulation. We then verified the model results by comparing the model time series outputs with the observed time series (Section 3). We calculated root-mean-square errors (RMSE) of water levels, sea-surface temperatures (SST), and salinity (SSS).

4.1. Water Level

Figure 7a–d shows both the model (red lines) and the observed (blue lines) total water level times series at stations 8735391, 8761927, 8771013, and 8775792. The station sites span from the Texas coastal inlets in the western model domain to Galveston Bay, Texas, Lake Pontchartrain, and Mobile Bay in the eastern domain. They were selected to roughly represent the model performance in various areas across the Gulf Coast domain. For clarity of display, only two months (1 September through 1 November 2016) of the entire 1-year comparison are displayed. The model and data exhibit favorable agreement in both tidal and subtidal frequencies. The RMSE at the four stations were 7.9 cm, 8.1 cm, 8.5 cm, and 7.6 cm, respectively.

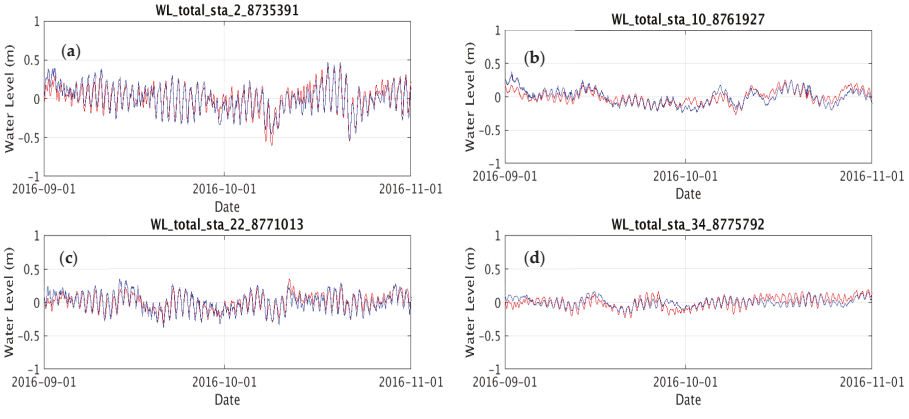

Figure 7. Comparison of model (red lines) and observed (blue lines) water levels at CO-OPS water level stations (**a**) 8735391, (**b**) 8761927, (**c**) 8771013, and (**d**) 8775792. See the station locations in Figure 1.

To investigate the model performance on the subtidal water levels, total water level time series were low-pass filtered with a 30-day Fourier Transform low-pass filter. Figure 8a–d shows the model and observed subtidal time series between August 15, 2016 and August 1, 2017 at the same four stations as shown in Figure 7. The hindcast simulation successfully reproduced the observations in both time and magnitude during both eventful and uneventful periods. For instance, it accurately reproduced the water level setup in mid-June 2017 at stations 8735391 and 8761927 (Figures 7 and 8) and setdown

near the end of January 2017 at station 8771013. During quiescent periods such as September through November 2017, the model results also demonstrate favorable agreement with observations at all four stations. The model RMSEs at the four stations were 6.8 cm, 7.7 cm, 6.9 cm, and 7.2 cm, respectively.

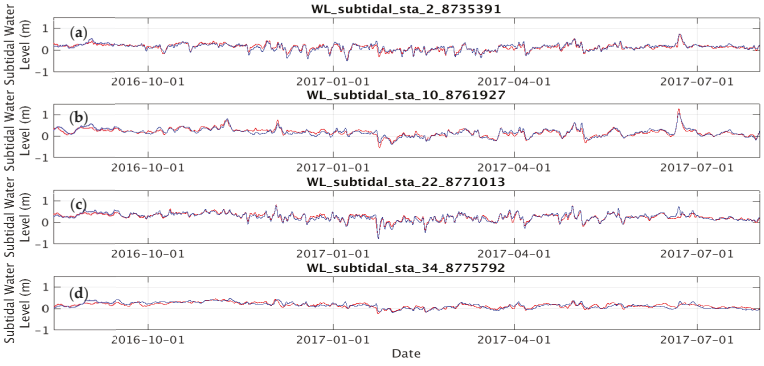

Figure 8. Comparison of model (red lines) and observed (blue lines) water levels at CO-OPS water level stations (**a**) 8735391, (**b**) 8761927, (**c**) 8771013, and (**d**) 8775792. See the station locations in Figure 1.

Figure 9a,b illustrates the RMSE maps of the total and subtidal model water levels at 55 CO-OPS water level stations (Table A1). In general, RMSE is evenly distributed across the model domain, except for stations 8760721 and 8761955 along the lower Mississippi River. Comparing the model-data water level time series in addition to the Mississippi River discharge measured at USGS station 07374000 (Baton Rouge, LA) (Table 2), it has been identified that the larger RMSE can be attributed to the water level setup from a large river discharge event which occurred between May and June of 2017. The river discharge during this period reached a magnitude as large as about 36,400 m^3/s as compared with an average value of about one-third of that value during the remaining time of the hindcast period. Not including the two Mississippi River stations, the average total water level RMSE equals about 8.6 cm with a standard deviation (SD) of 1.8 cm, and the average subtidal RMSE equals about 7.4 cm with a SD of 1.7 cm.

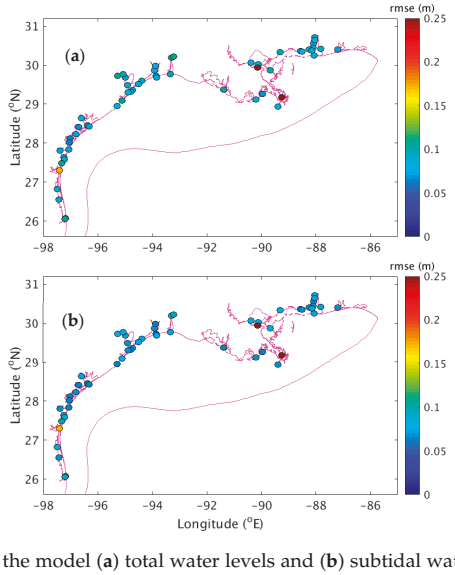

Figure 9. The RMSE of the model (**a**) total water levels and (**b**) subtidal water levels at 55 CO-OPS stations (Section 4.1).

The monthly mean RMSE and absolute values of the model-data differences (|bias|) of the modeled total water levels at each station were averaged over the 53 stations out of the total 55 stations (Table A1). The two Mississippi River stations, 8760721 and 8761955, were deemed to be outliers, and hence, were excluded. Figure 10a,b shows the RMSE and |bias|, respectively. The RMSE ranges between 0.06 cm and 0.11 cm and the |bias| ranged between 0.01 m and 0.06 m. Nether of the two properties exhibited significant seasonal variability.

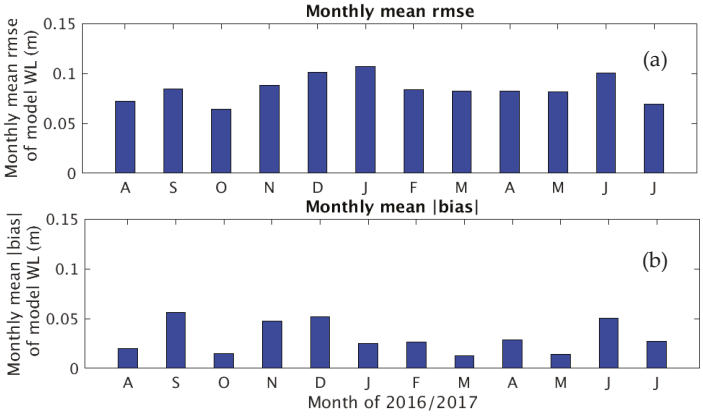

Figure 10. Monthly means of (**a**) the root-mean-square errors (RMSE) and (**b**) absolute model-data differences (|bias|) of the hindcast total water level.

Figure 11 illustrates the pattern match between the model results and the observations in a Taylor Diagram [36]. In general, a Taylor Diagram provides a graphical framework that allows a suite of modeled variables to be compared with observed data. The model-data correlation coefficient (COR) and the standard deviation (SD) of both the modeled and observed data from each station were calculated using the time series data described in the above. The magnitude of both the SD and the RMSE vary across the range of stations. To eliminate the factor of station variability, the normalized SD (nSD) and the normalized RMSE (nRMSE) were calculated by dividing the model SD and RMSE by the SD of the observed data. The nRMSE measures the ratio of the model RMSE to the SD of the observed data. When shown in the Taylor Diagram, modeled patterns that agree well with observations will lie nearest to the line of nSD equal to 1 [37].

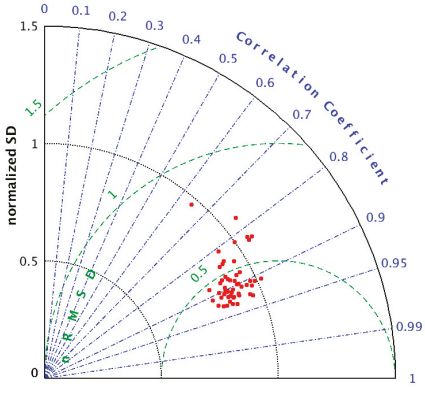

Figure 11. The Taylor Diagram of water level. Shown on the plot are the model-data correlation coefficient, normalized SD and normalized RMSE (nRMSE).

Shown in Figure 11 are the model-data COR, the nSD, and the nRMSE. The majority of data points lie close to the line of nSD equal to 1. This indicates that most of the stations demonstrate a rather favorable pattern match between the model results and the observations. The model results and observed data are highly correlated; the averaged COR equals to 0.91. With the exception of one outlier station (ID 8776139) with a COR equal to 0.49, the COR ranges from 0.76 to 0.94 with an average of 0.88; the nSD ranges between 0.79 and 1.07 with an average of 0.91; and the nRMSE ranges between 0.36 and 0.99 with an average equal to 0.45.

4.2. Sea-Surface Temperature (SST)

Figure 12 illustrates the monthly model mean and observed mean SST at stations 42012, MCGA1, NWCL1, PILL1, MGPT2, and PMNT2, respectively. From top to bottom, the stations are located in the open coastal area southeast of Mobile Bay, Lake Pontchartrain, the lower Mississippi River, Galveston Bay, and the Texas coastal embayments. They were chosen to investigate model performance in both the offshore and in embayment areas. In the figure, the left panel illustrates monthly average SST of model (red bars) and observations (blue bars), as well as the standard deviation of each data set. The right panel illustrates the corresponding monthly averaged model bias in terms of model-data difference for each month.

In general, the hindcast simulation successfully captured seasonal cycles in SST and demonstrated favorable agreement with observations. Both model and observed SST demonstrate significant seasonal variability, with SST ranging from about 9 °C in the winter season to about 32 °C in the summer season. The model bias ranges between −1.8 °C and 1.7 °C. In the summer season, the model over predicted SST, whereas in the winter season it over predicted SST at the open coastal station (42012) and at the lower Mississippi River station (PILL1) and underpredicted SST at the other embayment stations.

Figure 13 displays the color-coded RMSE at 52 stations (Table A2). The RMSE ranges from 0.6 °C to around 2.1 °C. In general, the model demonstrates better skills, with RMSE less than 0.8 °C, in the offshore areas as opposed to nearshore embayments. Compared with the relatively deeper offshore areas, the embayments usually experience far more sophisticated ambient conditions, such as large river discharge and significant diurnal cycles in the surface forcing. Therefore, it is far more challenging to accurately reproduce the SST field in coastal embayments than in offshore areas.

Figure 14a,b shows the RMSE and the absolute average of the model-data differences, respectively. The RMSE ranged between 0.7 °C and 1.5 °C, and the bias ranged between −0.3 °C and 0.2 °C. The maximum RMSE appeared between December 2016 and January 2017. This indicates that the model was least satisfactory in reproducing the winter season SST. In general, the bias was positive between August and December, 2016 and negative between January and July, 2017. The SST was slightly overpredicted during the former period and underpredicted during the latter.

Figure 15 shows the Taylor Diagram to illustrate the model-data COR, the normalized standard deviation (nSD), and the normalized RMSE (nRMSE). The three parameters were calculated using the same method as described for water levels in Section 4.1. The majority of data points lie close to the line of nSD equal 1. This indicates that most of the stations demonstrate rather favorable pattern match between the model results and the observations. The model results and observed data are highly correlated; the averaged COR equals to 0.95. With the exception of one station (ID 42067) with a COR equal to 0.77, the COR ranges between 0.93 and 1.0 with an average of 0.98; nSD ranges between 0.81 and 1.24 with an average of 0.99; nRMSE ranges between 0.17 and 0.27 with an average equal to 0.21.

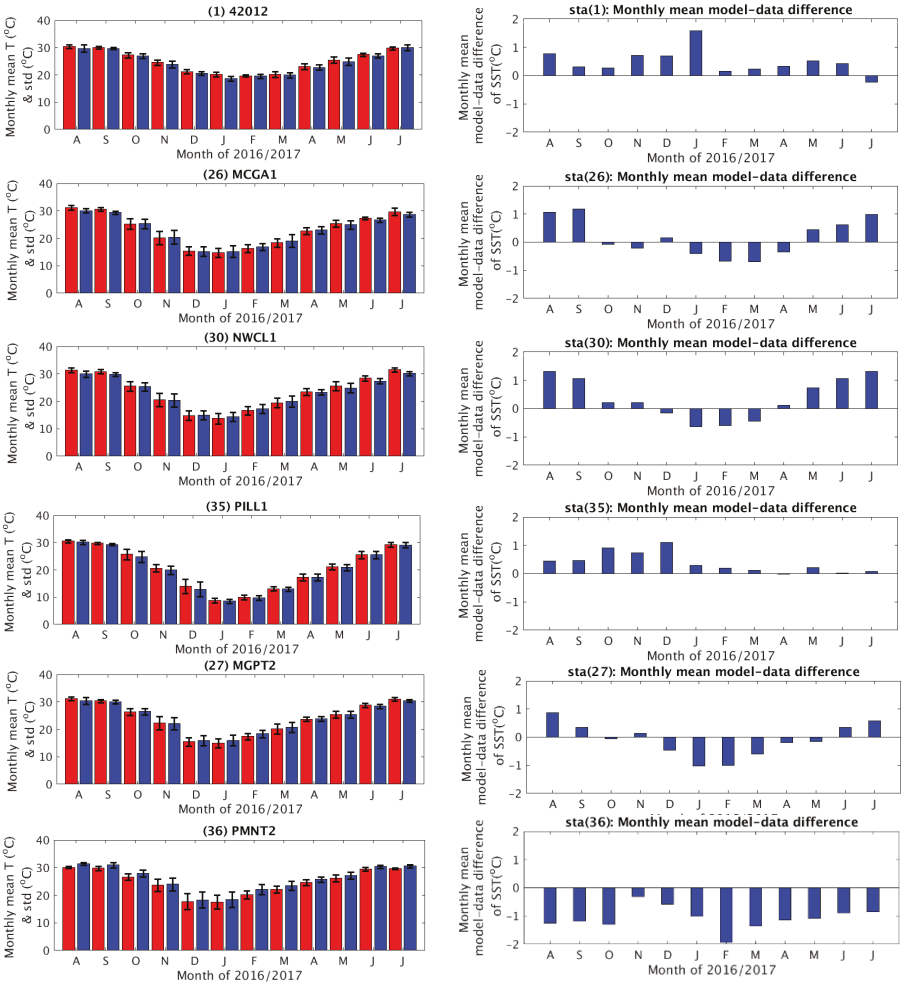

Figure 12. Left panel—Comparison of monthly model output mean SST (red bars), and monthly observed mean SST (blue bars), and the standard deviation of each data set. Right panel—monthly mean model bias. The station IDs are shown in the title of each plot. See the station locations in Figure 1.

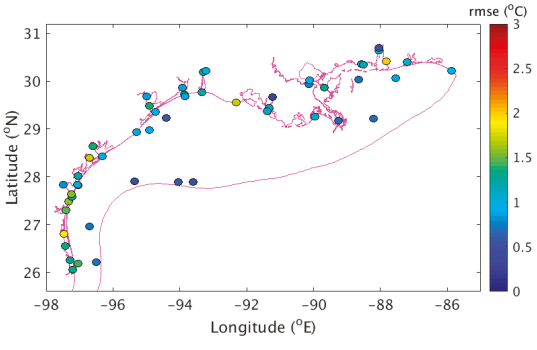

Figure 13. Color-coded RMSE of the modeled SST at 52 stations (Table A2).

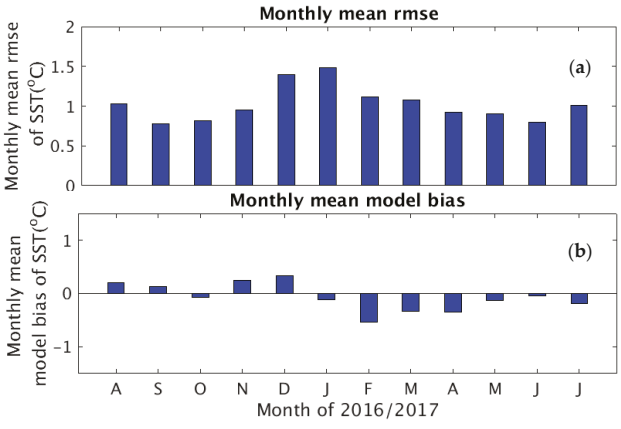

Figure 14. Monthly mean (**a**) RMSE and (**b**) the absolute model-date differences of the hindcast SST.

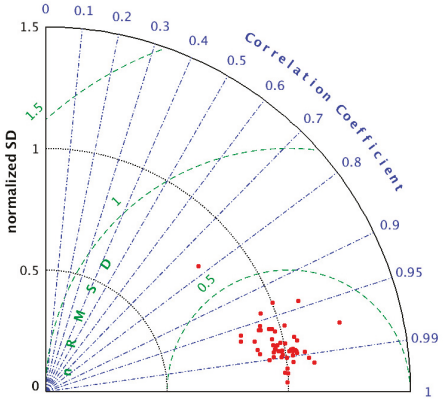

Figure 15. The Taylor Diagram of the sea-surface temperature. Shown on the plot are the model-data correlation coefficient, normalized SD (nSD) and normalized RMSE (nRMSE).

4.3. Sea-Surface Salinity (SSS)

During the hindcast period, salinity observations were available at seven stations (Table 3). All seven stations are situated either inside or close to Mobile Bay that represents a rather small area of the entire INGOFS domain. Station 42067 is situated offshore, southwest of the MB. Stations BSCA1, CRTA1, DPHA1, and KATA1 are located in the lower MB, while stations MBLA1 and MHPA1 are located in the mid- and upper MB, respectively.

The malfunction of salinity sensors by bio-fouling is very common in coastal areas of the northern gulf of Mexico [18]. Many observed data were easily deemed to be false measurements due to the malfunction of salinity sensors. Figure 16a,b showed the SSS time series at stations CRTA1 and DPHA1, respectively. To point out a few problematic data points, SSS exhibited a nearly 10 psu change within a one-hour period in 14 March 2017 or a nearly 20 psu daily change in 10 April 2017.

Considering the geographical limitation of the station locations and the data quality of observations, it is noted that the hereafter presented model-data comparison results were far from being representative from the perspective of obtaining an objective assessment of the model skill assessment for the entire domain.

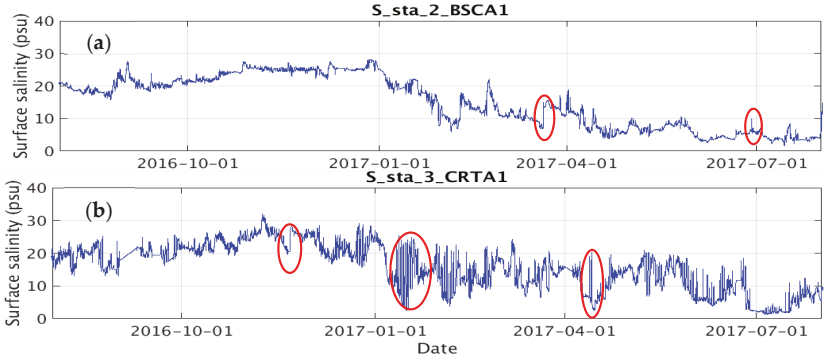

Figure 16. The observed surface salinity time series at stations (**a**) BSCA1 and (**b**) CRTA1. Red ellipses marked occurrences the sensor false measurements.

Figure 17 illustrates the comparison of monthly mean SSS between the modeled and observed SSS at the seven stations. The inset of Figure 1 shows the station locations. The left panel shows the model (red bars) and observed (blue bars) monthly means, as well as the standard deviation of each data set. The modeled and observed SSS exhibited similar seasonal variability. In general, SSS gradually increased from summer of 2016 and peaked at nearly 32 psu in the winter of 2016. As the time gradually approached the summer of 2017, SSS dropped to 5–13 psu in the mid-bay area (station MBLA1) and even reached nearly zero psu at the upper bay station MHPA1. The monthly averaged model bias ranged from −6 psu to 6 psu. The yearly mean model RMSE at each station was, respectively, 2.6, 3.7, 3.8, 5.4, 4.9, 3.0, and 2.7 psu.

The right panel shows the monthly mean absolute model-data differences. The model skill was least satisfactory in the winter season of the year. The model bias ranged from about 2 psu in February 2017 to 2.1 psu in January 2017, with a yearly average of 0.7 psu. The model overpredicted SSS between February and April of 2017 and overpredicted SSS in the remaining hindcast period.

It is noted that the initial salinity condition of the hindcast runs was populated with the combined NGOFS and NWGOFS/NEGOFS outputs (Section 1). In addition, we tested running hindcast simulations using the initial conditions populated with the G-RTOFS salinity field. The G-RTOFS domain did not cover small coastal embayments such as Mobile Bay, etc. Hence, the INGOFS salinity field in the area was extrapolated from nearby G-RTOFS offshore model grid points outside of the embayments. This naturally caused the INGOFS initial salinity fields in the embayments to be much more saline than observations and may produce a large model-data discrepancy.

We compared the modeled time series from the two different initial conditions with observations at six stations (Table 3). Figure 18a–d shows the surface-salinity fields at the upper bay station MHPA1, at mid-bay stations MBLA1 and BSCA1, and at the offshore station 42067. They represent the upper, mid-bay, lower, and offshore stations, respectively. It was found that the impact of initial conditions may persist as long as two and a half months (until mid-October 2016) in the upper and lower bay region, nearly three months (until the beginning of November 2016) at the upper-bay station, and about one and a half months at the offshore station. After the initial one to two months, the two salinity time series gradually converge, and the impact of the initial condition difference becomes insignificant.

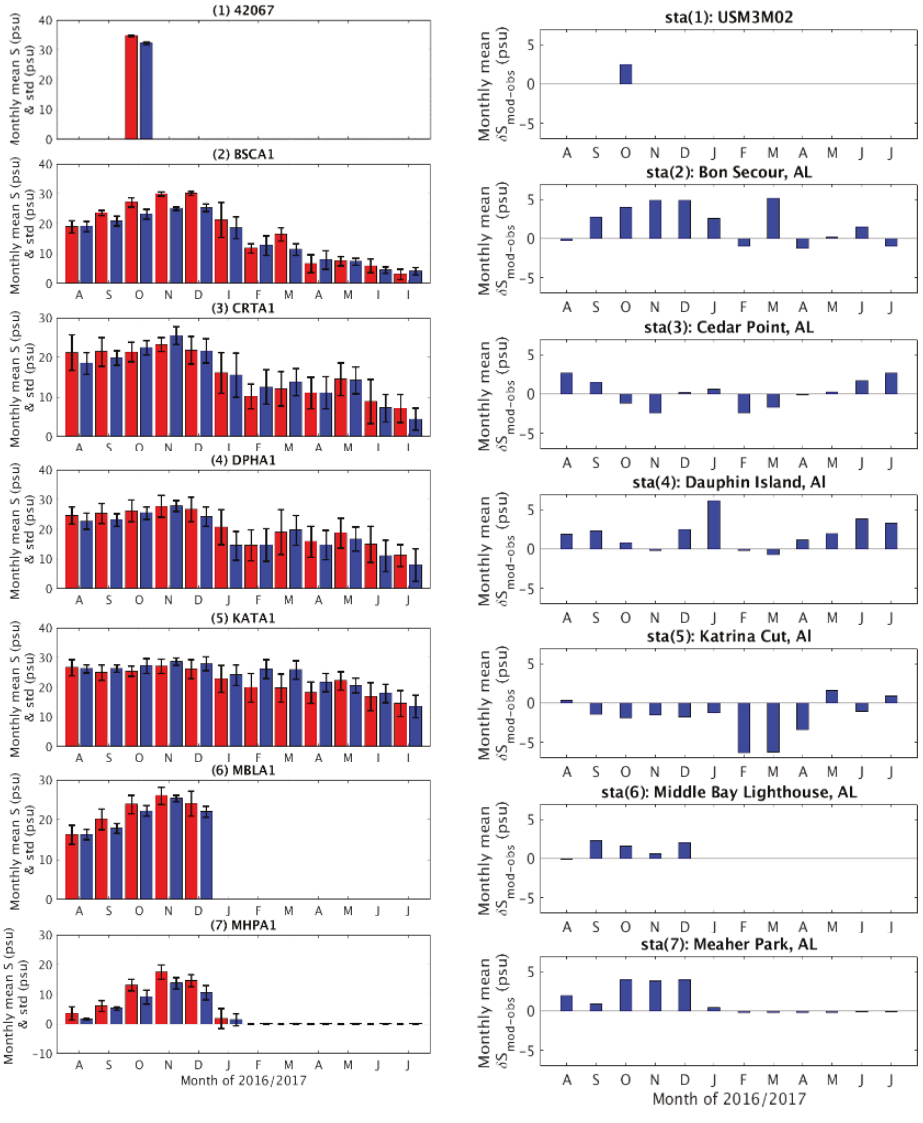

Figure 17. Comparison of monthly mean SSS between the hindcast results and observation, (left panel) monthly mean SSS of model (red bars), observations (blue bars), and the standard deviation of each data set and (right panel) monthly mean model bias. The station IDs are shown in the title of each plot. See the station locations in Figure 1.

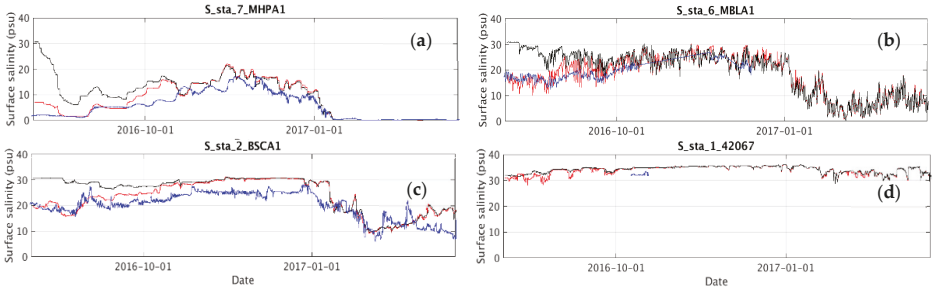

Figure 18. Comparison of the observed (blue lines) and the hindcast (black and red lines) salinity time series at stations (**a**) MHPA1, (**b**) MBLA1 and (**c**) BSCA1, and (**d**) 42067. The two model time series correspond to initial salinity conditions populated with G-RTOFS (black lines) and NGOFS (red lines), respectively.

5. Discussion

5.1. Comparison of Model Skills with Other OFS

This section compares the model performance of water levels (WL) and sea-surface temperatures (SST) between the INGOFS and the NGOFS/NWGOFS/NEGOFS (hereafter referred to as NGOFS for simplicity of description). Figure 19a shows the comparison of the water level RMSE in a scatter plot, while Figure 19b shows the map of the RMSE differences between INGOFS and NGOFS at 28 stations. Similarly, Figure 20a,b shows the SST comparison between INGOFS and NGOFS at 26 stations. The RMSE of INGOFS was calculated based on the hindcast results described in Section 4. The RMSE of NGOFS was taken from previous publications on the NGOFS development and model skill [18,19]. It was calculated based on hindcast simulations from different time periods from those of the INGOFS; however, since the results were objective and representative of NGOFS model skill, it is valid to compare the two RMSE data sets. Interested readers are recommended to reference the above publications for technical details. To conduct the comparison, we identified the stations used in both the INGOFS and NGOFS skill evaluations and compared the RMSE between INGOFS and NGOFS. There are no salinity stations shared between INGOFS and NGOFS and hence, comparison of salinity is omitted in the present discussion.

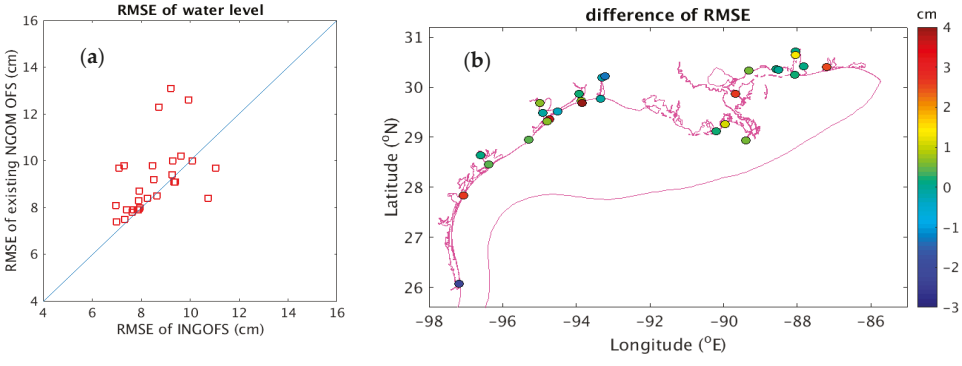

Figure 19. Comparison of the water level skill between the INGOFS and the NGOFS, (**a**) scatter plot of RMSE and (**b**) the RMSE difference between INGOFS and NGOFS.

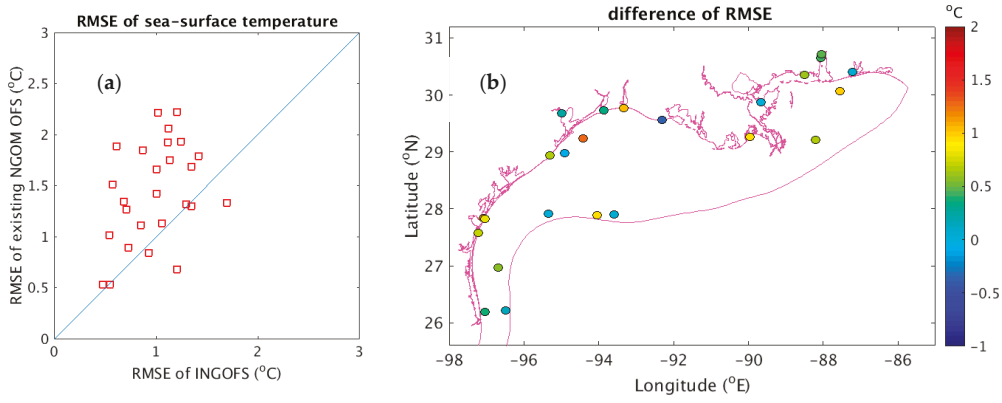

Figure 20. Comparison of the SST skill between the INGOFS and the NGOFS, (**a**) scatter plot of RMSE and (**b**) the RMSE difference between INGOFS and NGOFS.

INGOFS demonstrates slightly better model skill than does NGOFS for both water levels and sea-surface temperatures (Figures 19 and 20). For water levels, INGOFS exhibits slightly smaller RMSE than NGOFS. The INGOFS RMSE ranges between 7.0 cm and 11.0 cm, whereas the NGOFS RMSE ranges between 7.4 cm and 13.1 cm. The RMSE difference between INGOFS and NGOFS ranges from −3.9 cm to 2.3 cm, and the average of the differences over all 28 stations is about −0.6 cm. For SST, the RMSE of INGOFS ranges between 0.5 °C and 1.7 °C, while the RMSE of NGOFS ranges between 0.5 °C and 2.2 °C. The RMSE difference between the two ranges from −0.5 °C to 1.3 °C, and the average of the differences over all 26 stations is 0.4 °C.

5.2. Limitation of the RMSE Analysis

The RMSE has its limitation as a statistical parameter in terms of objectively representing the model errors. It is based on averaged squared differences and hence tends to be insensitive to lower magnitude events and biased towards higher magnitude events [38–40]. However, the present discussions of the INGOFS performance (Section 4) are focused on using the RMSE. Hence, the model skill results are not entirely comprehensive. Statistical indices to differentiate low, medium, and high data values may assess the model performance more effectively [38–40]. This method will be applied in future assessments of the INGOFS performance and is expected to give a more comprehensive and objective depiction of the model skill.

In the following, we show results from a preliminary investigation on the distribution of the RMSE values. We calculate occurrence frequency (F) and cumulative frequency (CF) of various RMSE values over the entire time series (Section 4). To estimate F and CF, the absolute value of each point in the model-data difference time series was calculated for all stations (Tables A1 and A2). We then blended the data points into one data set and sorted the data into multiple bins according to their magnitudes and estimated the frequency and cumulative frequency of the data occurrence in each bin. The RMSE of the data points in each bin was then estimated. Figure 21a,b displays F and CF of the RMSE for water level and SST, respectively. In each plot, the abscissa corresponds to the central value of each RMSE bin, whereas the bar charts (blue) and the curve (orange) represent F and CF, respectively. The bin width is 0.02 m for water levels and 0.1 °C for the SST. Both water levels and SST demonstrate similar characteristics for F and CF. Both F and CF decrease drastically in a monotonic manner with the increasing RMSE. This indicates that greater model RMSEs account for a much smaller portion of the total occurrence than the smaller values. For water levels, the RMSE values less than 0.15 m accounts for over 80% of the total occurrence. For SST, the RMSE values less than 2 °C accounts for about 90% of the total occurrence.

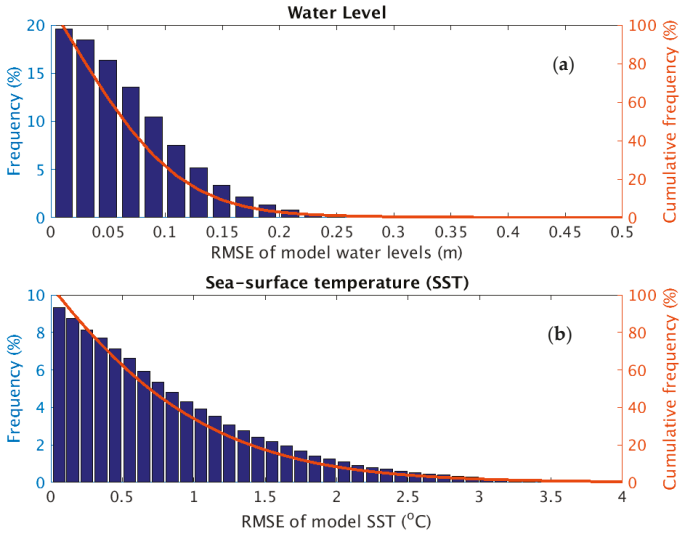

Figure 21. Frequency and cumulative frequency of the model RMSE for (**a**) the water levels and (**b**) the sea-surface temperatures.

6. Summary and Conclusions

NOAA's National Ocean Service (NOS) is upgrading the northern Gulf of Mexico (GOM) operational nowcast/forecast system (NGOFS) by integrating the three existing operational systems, NGOFS, NEGOFS, and NWGOFS, into a single system. The new system will have extended domain coverage to encompass the lower Mississippi River, Lake Pontchartrain, Texas coastal embayments, and the coast of Mexico. It is aimed to produce real-time nowcasts and short-range forecast guidance for water levels, 3-dimensional currents, water temperatures, and salinity over the continental shelf in the northern Gulf region, the adjacent coastal estuaries, and the lower Mississippi River. Upon completion, the system will support marine navigation, emergency response, environmental management, and harmful algal bloom (HAB) forecasts. This paper described the hydrodynamic model development, configuration and verification of a one-year hindcast simulation (August 2016–July 2017).

The upgraded NGOFS will be implemented using the Finite Volume Community Ocean Model (FVCOM). The system domain includes the northern GOM continental shelf from north of Cabo Rojo, Mexico in the southwest all the way to Panama City, FL in the northeast. The model grid is composed of about 300,000 nodes, 600,000 elements, and has a spatial resolution ranging from 45 m near the coast to around 10 km on the open ocean boundary.

The hindcast forcing data included atmospheric forecast guidance from the NOAA/NWS North American Mesoscale (NAM) numerical weather prediction modeling system, river discharge observations from U.S. Geological Survey gauges, and open ocean boundary conditions derived from the NWS Global Real-Time Operational Forecast System (G-RTOFS) and the ADCIRC EC2015 tidal database. The hindcast performance of water levels, temperatures, and salinity were verified by comparing the modeled and observed time series. The RMSE was 7.4 cm for water level, 1.1 °C for water surface temperatures, and 3.7 psu for surface salinity. The relatively large RMSE for salinity was partially attributed to quality issues of the observational data due to the sensor malfunction. In addition, the model-data comparison for salinity was limited to seven stations in Mobile Bay and adjacent waters. Hence the results were far less satisfactory to represent the model skill throughout the entire system domain.

For next steps, the development team will conduct systematic skill assessment on the hindcast results of water level, currents, temperatures and salinity using the standard NOS skill assessment

software [21]. Leading up to the completion of the model development, the upgraded NGOFS will be further tested in a nowcast/forecast environment for about a one-year period. It is anticipated to be in operational production on NWS's NCEP Weather and Climate Operational Supercomputing System (WCOSS) in mid-2020.

Author Contributions: All the authors contributed to the system development. Z.Y. and Lianyuan conducted the hindcast simulation and the model result verification.

Acknowledgments: Changsheng Chen and Jianhua Qi at the University of Massachusetts provided valuable comments on the system development and hands-on help on the hindcast FVCOM model configurations. Two anonymous reviewers provided insightful comments and suggestions that substantially improved this paper. The authors would like to express our sincere gratitude to their help.

Conflicts of Interest: The authors declare no conflicts of interest.

Appendix A

Table A1. Station meta data of water level observations.

No.	IDs	Station Names	Longitude (°E)	Latitude (°N)
1	8735180	Dauphin Island	−88.075	30.25
2	8735391	Dog River Bridge	−88.088	30.5652
3	8735523	East Fowl River, Hwy 193 Bridge	−88.1139	30.4437
4	8741533	Pascagoula NOAA Lab, MS	−88.5667	30.3583
5	8747437	St. Louis Bayentrance	−89.3258	30.3264
6	8760721	Pilot Town	−89.2583	29.1783
7	8760922	Pilots Station E, SW Pass, LA	−89.4067	28.9317
8	8761305	Shell Beach, Lake Borgne	−89.6732	29.8681
9	8761724	East Point, Grand Isle	−89.9567	29.2633
10	8761927	New Canal USCG station, Lake Pontchartrain	−90.1134	30.0272
11	8762483	I-10 Bonnet Carre Floodway, TX	−90.39	30.0683
12	8764314	Eugene Island, North of Atchafalaya Bay	−91.3839	29.3675
13	8767961	Bulk Terminal	−93.3007	30.1903
14	8768094	Calcasieu Pass	−93.3429	29.7682
15	8770475	Port Arthur	−93.93	29.8667
16	8770570	Sabine Pass	−93.8701	29.7284
17	8770613	Morgans Point, Barbours Cut	−94.985	29.6817
18	8770808	High Island, ICWW	−94.3903	29.5947
19	8770822	Texas Point, Sabine Pass	−93.8418	29.6893
20	8770971	Rollover Pass	−94.5133	29.515
21	8771013	Eagle Point	−94.9183	29.48
22	8771341	Galveston Bay Entrance, TX	−94.7248	29.3573
23	8771450	GALVESTON, Galveston Channel	−94.7933	29.31
24	8771486	Galveston Railroad Bridge, TX	−94.8967	29.3017
25	8771972	San Luis Pass	−95.1133	29.095
26	8773259	Port Lavaca, TX	−96.6094	28.6403
27	8773701	Port O'Connor, Matagorda Bay	−96.3883	28.4517
28	8773767	Maragorda Bay Entrance Channel, TX	−96.3283	28.4267
29	8774513	Copano Bay, TX, TCOON	−97.0217	28.1183
30	8774770	Rockport, TX	−97.0467	28.0217
31	8775237	Port Aransas, TX	−97.0733	27.8383
32	8775296	USS Lexington, TX	−97.39	27.8117
33	8775792	Packery Channel	−97.2367	27.6333
34	8775870	Corpus Christi	−97.2167	27.58
35	8776139	S. BirdIsland, TX	−97.3217	27.48
36	8776604	Baffin Bay, TX	−97.405	27.295
37	8777812	Rincon Del San Jose, TX	−97.4917	26.825
38	8779748	South Padre Island, TX	−97.1767	26.0767
39	8779770	Port Isabel	−97.215	26.06
40	8778490	Port Mans Field, TX	−97.4217	26.555
41	8774230	Aransas Wildlife Refuge	−96.795	28.2283
42	8773037	Seadrift TCOON, TX	−96.7117	28.4083
43	8772447	USCG Freeport, TX	−95.3017	28.9433
44	8770777	Manchester, Houston Ship Channel	−95.2658	29.7263
45	8770733	Lynchburg Landing, San Jacinto River	−95.0783	29.765
46	8770520	Rainbow Bridge	−93.8817	29.98
47	8767816	Lake Charles	−93.2217	30.2236
48	8762075	Port Fourchon	−90.1993	29.1142
49	8741041	Dock E, Port of Pascagoula	−88.5054	30.3477
50	8739803	Bayou LaBatre Bridge	−88.2477	30.4057
51	8738043	West Fowl River, Hwy 188 bridge	−88.1586	30.3766
52	8737048	MOBILE, Mobile River, State Dock	−88.0433	30.7083
53	8736897	Coast Guard Sector Mobile	−88.0583	30.6483
54	8732828	Weeks Bay, AL	−87.825	30.4167
55	8729840	Pensacola	−87.2111	30.4044

Table A2. Station meta data of water surface temperature observations.

No.	IDs	Station Names	Longitude (°E)	Latitude (°N)	Model-Data Difference (°C)
1	42012	44 NM SE of Mobile, Al	−87.555	30.065	0.48
2	42019	60 nm South of Freeport, TX	−95.353	27.913	−0.23
3	42020	60 nm SSE of Corpus Christi, TX	−96.694	26.968	−0.01
4	42035	22 nm East of Galveston, TX	−94.413	29.232	0.17
5	42040	64 NM South of Dauphin Island, Al	−88.207	29.212	−0.21
6	42043	GA-252 TABS B	−94.919	28.982	0.51
7	42044	PS-1126 TABS J	−97.051	26.191	0.77
8	42045	PI-745 TABS K	−96.5	26.217	−0.08
9	42046	HI-A595 TABS N	−94.037	27.89	−0.27
10	42047	HI-A389 TABS V	−93.597	27.897	−0.04
11	42067	USM3M02	−88.649	30.043	0.62
12	AMRL1	LAWMA, Amerada Pass, LA	−91.338	29.45	0.08
13	BABT2	Baffin Bay, TX	−97.405	27.297	−0.57
14	BKTL1	Lake Charles Bulk Terminal, LA	−93.296	30.194	0.07
15	CAPL1	Calcasieu, La	−93.343	29.768	0.52
16	CARL1	Carrollton, LA	−90.135	29.933	0.52
17	EINL1	North of Eugene Island, LA	−91.384	29.373	0.12
18	EPTT2	Eagle Point, TX	−94.917	29.481	−0.77
19	FCGT2	USCG Freeport, TX	−95.303	28.943	−0.04
20	FRWL1	Fresh Water Canal Locks, La	−92.305	29.555	−0.11
21	GISL1	Grand Isle, LA	−89.958	29.265	−0.42
22	GNJT2	Galveston Bay Entrance (North Jetty), TX	−94.725	29.357	0.22
23	IRDT2	South Bird Island, TX	−97.322	27.48	−0.58
24	LCLL1	Lake Charles, La	−93.222	30.223	0.41
25	MBET2	Matagorda Bay Entrance Channel, TX	−96.327	28.422	0.39
26	MCGA1	Coast Guard Sector Mobile, AL	−88.058	30.649	0.17
27	MGPT2	Morgans Point, TX	−94.985	29.682	−0.09
28	MQTT2	Bob Hall Pier, Corpus Christi, Tx	−97.217	27.58	−0.08
29	NUET2	Nueces Bay, TX	−97.486	27.832	−0.37
30	NWCL1	New Canal Station, LA	−90.113	30.027	0.34
31	OBLA1	Mobile State Docks, AL	−88.04	30.705	0.11
32	PACT2	Packery Channel, TX	−97.237	27.634	−0.34
33	PCBF1	Panama City Beach, FL	−85.88	30.213	0.36
34	PCLF1	Pensacola, FL	−87.212	30.403	0.38
35	PILL1	Pilottown, LA	−89.259	29.179	0.38
36	PMNT2	Port Mansfield, TX	−97.424	26.559	−1.06
37	PNLM6	Pascagoula NOAA Lab, MS	−88.567	30.358	0.53
38	PORT2	Port Arthur, TX	−93.93	29.867	0.48
39	PTAT2	Port Aransas, TX	−97.05	27.828	−0.23
40	PTIT2	Port Isabelle, TX	−97.215	26.06	−0.01
41	RCPT2	Rockport, TX	−97.048	28.024	0.17
42	RLIT2	Realitos Peninsula, TX	−97.285	26.262	−0.21
43	RSJT2	Rincon del San Jose, TX	−97.471	26.801	0.51
44	RTAT2	Port Aransas, TX	−97.073	27.84	0.77
45	SBPT2	Sabine Pass North, TX	−93.87	29.73	−0.08
46	SDRT2	Seadrift, TX	−96.712	28.407	−0.27
47	SHBL1	Shell Beach, LA	−89.673	29.868	−0.04
48	TESL1	Tesoro Marine Terminal, Berwick, Atchafalaya River, LA	−91.237	29.668	0.62
49	TXPT2	Texas Point, Sabine Pass, TX	−93.842	29.689	0.08
50	ULAM6	Dock East Port of Pascagoula, MS	−88.505	30.348	−0.57
51	VCAT2	Port Lavaca, TX	−96.595	28.64	0.07
52	WBYA1	Weeks Bay, Mobile Bay, AL	−87.825	30.417	0.52

References

1. Etter, P.C.; Ulm, W.F.; Cochrane, J.D. The relationship of the wind stress to heat flux divergence of Texas-Louisiana shelf waters. *Cont. Shelf Res.* **1986**, *4*, 547–552. [CrossRef]
2. Morey, S.; Zavala-Hidalgo, J.; O'Brien, J.J. The seasonal variability of continental shelf circulation in the Northern and Western Gulf of Mexico from a high-resolution numerical model. In *Circulation in the Gulf of Mexico: Observations and Models*; Sturges, M., Lugo-Fernandez, A., Eds.; American Geophysical Union: Washington, DC, USA, 2005; pp. 203–218.
3. Sturges, W.; Lugo-Fernandez, A. *Circulation in the Gulf of Mexico: Observations and Models*; American Geophysical Union: Washington, DC, USA, 2005.

4. Westerink, J.J.; Muccino, J.C.; Luettich, R.A. Resolution requirements for a tidal model of the Western North Atlantic and Gulf of Mexico. In *Computational Methods in Water Resources IX, Volume 2: Mathematical Modeling in Water Resources*; Russell, T.F., Ewing, R.E., Brebbia, C.A., Gray, W.G., Pinder, G.F., Eds.; Computational Mechanics Publications: Southampton, UK, 1992; pp. 669–674.
5. Longley, W.L. *Freshwater inflows to Texas Bays and Estuaries, Ecological Relationships and Methods for Determination of Needs*; Texas Water Development Board and Texas Parks and Wildlife Department: Austin, TX, USA, 1994; p. 386.
6. Hofmann, E.E.; Worley, S.J. An investigation of the circulation of the Gulf of Mexico. *J. Geophys. Res.* **1986**, *91*, 14221–14236. [CrossRef]
7. Dinnel, S.P.; Wiseman, W.J. Freshwater on the west Louisiana and Texas shelf. *Cont. Shelf Res.* **1986**, *6*, 765–784. [CrossRef]
8. Dzwonkowski, B.; Park, K. Subtidal circulation on the Alabama shelf during the Deepwater Horizon oil spill. *J. Geophys. Res.* **2012**, *117*, C03027. [CrossRef]
9. Elliott, B.A. Anticyclonic rings in the Gulf of Mexico. *J. Phys. Oceanogr.* **1982**, *12*, 1292–1309. [CrossRef]
10. Kelly, F.J. Physical oceanography/water mass characterization. In *Mississippi-Alabama Continental Shelf Ecosystem Study: Data Summary and Synthesis. Volume II: Technical Narrative*; Brooks, J.M., Giammona, C.P., Eds.; U.S. Dept. of the Interior, Minerals Mgmt. Service, Gulf of Mexico OCS Region: New Orleans, LA, USA, 1991.
11. Zhang, Z.; Hetland, R.D. A numerical study on convergence of alongshore flows over the Texas-Louisiana shelf. *J. Geophys. Res.* **2012**, *117*, C11010. [CrossRef]
12. Zhang, X.; Marta-Almeida, M.; Hetland, R.D. A high-resolution pre-operational forecast model of circulation on the Texas-Louisiana continental shelf and slope. *J. Oper. Oceanogr.* **2012**, *5*, 1–16. [CrossRef]
13. Zhang, Z.; Hetland, R.; Zhang, X. Wind-modulated buoyancy circulation over the Texas-Louisiana shelf. *J. Geophys. Res. Oceans* **2014**, *119*, 5705–5723. [CrossRef]
14. Wiseman, W.J.; Rabalais, N.N.; Turner, R.E.; Dinnel, S.P.; MacNaughton, A. Seasonal and interannual variability within the Louisiana coastal current: Stratification and hypoxia. *J. Mar. Syst.* **1997**, *12*, 237–248. [CrossRef]
15. DiMarco, S.F.; Howard, M.K.; Reid, R.O. Seasonal variation of wind-driven diurnal current cycling on the Texas-Louisiana Continental Shelf. *Geophys. Res. Lett.* **2000**, *27*, 1017–1020. [CrossRef]
16. Burchard, H.; Hetland, R. Quantifying the Contributions of Tidal Straining and Gravitational Circulation to Residual Circulation in Periodically Stratified Tidal Estuaries. *J. Phys. Oceanogr.* **2010**, *40*, 1243–1262. [CrossRef]
17. Chen, C.; Liu, H.; Beardsley, R. An unstructured grid, finite-volume, three dimensional primitive equations ocean model: Application to coastal ocean and estuaries. *J. Atmos. Oceanic Technol.* **2003**, *20*, 159–186. [CrossRef]
18. Wei, E.; Yang, Z.; Chen, Y.; Kelley, J.W.; Zhang, A. *The Northern Gulf of Mexico Operational Forecast System (NGOFS): Model Development and Skill Assessment*; NOAA Technical Report NOS CS33; NOAA: Silver Spring, MD, USA, 2014.
19. Wei, E.; Zhang, A.; Yang, Z.; Chen, Y.; Kelley, G.W.; Aikman, F.; Cao, D. NOAA's Nested Northern Gulf of Mexico operational forecast systems development. *J. Mar. Sci. Eng.* **2014**, *2*, 1–17. [CrossRef]
20. Zhang, A.; Yang, Z. *High Performance Computer Coastal Ocean Modeling Framework for the NOS Costal Operational Forecast System*; NOAA Technical Report NOS CO-OPS 069; U.S. Department of Commerce: Silver Spring, MD, USA, 2014. Available online: https://tidesandcurrents.noaa.gov/publications/NOAA_Technical_Report_NOS_COOPS_069.pdf (accessed on 1 June 2018).
21. Zhang, A.; Hess, K.W.; Wei, E.; Myers, E. *Implementation of Model Skill Assessment Software for Water Level and Current*; NOAA Technical Report NOS CS 24; U.S. Department of Commerce, National Oceanic and Atmospheric Administration: Silver Spring, MD, USA, 2006.
22. Mellor, G.L.; Yamada, T. Development of a turbulence closure model for geophysical fluid problems. *Rev. Geophys.* **1982**, *20*, 851–875. [CrossRef]
23. Smagorinsky, J. General circulation experiments with the primitive equations I. the basic experiment. *Mon. Weather Rev.* **1963**, *91*, 99–164. [CrossRef]
24. Chen, C.; Gao, G.; Zhang, Y.; Beardsley, R.C.; Lai, Z.; Qi, J.; Lin, H. Circulation in the Arctic Ocean: Results from a high-resolution coupled ice-sea nested Global-FVCOM and Arctic-FVCOM system. *Prog. Oceanogr.* **2015**, *141*, 60–80. [CrossRef]

25. Zheng, L.; Weisberg, R.H. Modeling the West Florida coastal ocean by downscaling from the deep ocean, across the continental shelf and into the estuaries. *Ocean Modell.* **2012**, *48*, 10–29. [CrossRef]
26. Zhao, L.; Chen, C.; Cowles, G. Tidal flushing and eddy formation in Mount Hope Bay and Narragansett Bay: An application of FVCOM. *J. Geophys. Res.* **2006**, *111*, C10015. [CrossRef]
27. Zheng, L.Y.; Weisberg, R.H. Rookery Bay and Naples Bay circulation simulations: applications to tides and fresh water inflow regulation. *Ecol. Model.* **2010**, *221*, 986–996. [CrossRef]
28. Yang, Z.; Myers, E.; White, S. *VDatum for Eastern Louisiana and Mississippi Coastal Waters: Tidal Datums, Marine Grids, and Sea Surface Topography*; NOAA Technical Memorandum NOS CS 19; U.S. Department of Commerce: Silver Spring, MD, USA, 2010. Available online: https://vdatum.noaa.gov/download/publications/CS_19_FY09_26_Zizang_VDatum_NewOrleans_techMemor.pdf (accessed on 16 June 2018).
29. Szpilka, C.; Dresback, K.; Kolar, R.; Feyen, J.; Wang, J. Improvements for the Western North Atlantic, Caribbean and Gulf of Mexico ADCIRC tidal database (EC2015). *J. Mar. Sci. Eng.* **2016**, *4*, 72. [CrossRef]
30. Mehra, A.; Rivin, I.; Garraffo, Z.; Rajan, B. Upgrade of the Operational Global Real Time Ocean Forecast System. Available online: https://www.wcrp-climate.org/WGNE/BlueBook/2015/individual-articles/08_Mehra_Avichal_etal_RTOFS_Upgrade.pdf (accessed on 29 October 2016).
31. Garaffo, Z.D.; Kim, H.C.; Mehra, A.; Spindler, T.; Rivin, I.; Tolman, H.L. Modeling of 137Cs as a tracer in a regional model for the Western Pacific, after the Fukushina-Daiichi Nuclear power plant accident of March 2011. *Weather Forecast.* **2016**, *21*, 553–579. [CrossRef]
32. U.S. Geological Survey (USGS). USGS Water Data for the Nation. Available online: http://waterdata.usgs.gov/nwis/ (accessed on 15 October 2013).
33. Cowles, G.W.; Lentz, S.J.; Chen, C.; Xu, Q.; Beardsley, R.C. Comparison of observed and model-computed low frequency circulation and hydrography on the New England Shelf. *J. Geophys. Res.* **2008**, *113*, C09015. [CrossRef]
34. Center for Operational Oceanographic Products and Services (CO-OP). Water Levels—Station Selection. Available online: http://tidesandcurrents.noaa.gov/stations.html?type=Water+Levels (accessed on 18 March 2018).
35. National Data Buoy Center (NDBC). Archive of Historical Ocean Data. Available online: http://www.ndbc.noaa.gov/data/historical/ocean/ (accessed on 18 March 2018).
36. Taylor, K.E. Summarizing multiple aspects of model performance in a single diagram. *J. Geophys. Res.* **2001**, *106*, 7183–7192. [CrossRef]
37. National Center for Atmospheric Research Staff (Ed.) The Climate Data Guide: Taylor Diagrams. Available online: https://climatedataguide.ucar.edu/climate-data-tools-and-analysis/taylor-diagrams (accessed on 18 October 2018).
38. Dawson, C.W.; Wilby, R.L. Hydrological modelling using artificial neural networks. *Prog. Phys. Geogr.* **2001**, *25*, 80–108. [CrossRef]
39. Dawson, C.W.; Abrahart, R.J.; See, L.M. HydroTest: A web-based toolbox of evaluation metrics for the standardized assessment of hydrological forecasts. *Environ. Mode. Softw.* **2007**, *22*, 1034–1052. [CrossRef]
40. Jain, A.; Srinivasulu, S. Development of effective and efficient rainfall-runoff models using integration of deterministic, real-coded genetic algorithms and artificial neural network techniques. *Water Resour. Res.* **2004**, *40*. [CrossRef]

Journal of
Marine Science and Engineering

MDPI

Article

Improvements for the Eastern North Pacific ADCIRC Tidal Database (ENPAC15)

Christine Szpilka [1,*], Kendra Dresback [1], Randall Kolar [1] and T. Christopher Massey [2]

[1] School of Civil Engineering and Environmental Science, University of Oklahoma, 202 W. Boyd Room 334, Norman, OK 73019, USA; dresback@ou.edu (K.D.); kolar@ou.edu (R.K.)
[2] US Army Corps of Engineers, Eng. Research & Development Center, Coastal & Hydraulics Lab, 3909 Halls Ferry Road, Vicksburg, MS 39180, USA; Chris.Massey@usace.army.mil
* Correspondence: cmszpilka@ou.edu; Tel.: +1-405-325-5911

Received: 3 October 2018; Accepted: 2 November 2018; Published: 7 November 2018

Abstract: This research details the development and validation of the updated Eastern North Pacific (ENPAC) constituent tidal database, referred to as ENPAC15. The database was last updated in 2003 and was developed using the two-dimensional, depth integrated form of the ADvanced CIRCulation coastal hydrodynamic model, ADCIRC. Regional databases, such as ENPAC15, are capable of providing higher resolution near the coast, allowing users to more accurately define tidal forcing for smaller sub-regions. This study follows the same methodology as the EC2015 updates for the eastern coast of the United States and six main areas of improvement in the modeling configurations are examined: (1) placement of the open ocean boundary; (2) higher coastal resolution; (3) updated global bathymetry; (4) updated boundary forcing using two global tidal databases; (5) updated bottom friction formulations; and (6) improved model physics by incorporating the advective terms in ADCIRC. The skill of the improved database is compared to that of its predecessor and is calculated using harmonic data from three sources. Overall, the ENPAC15 database significantly (52% globally) reduces errors in the ENPAC03 database and improves the quality of tidal constituents available for sub-regional models in the ENPAC region.

Keywords: tidal constituent database; ADvanced CIRCulation model (ADCIRC); Eastern North Pacific Ocean (ENPAC); coastal ocean modeling

1. Introduction

Accurate predictions of the ocean's tides are necessary for many coastal engineering applications. The propagation of tides into localized coastal areas is highly dependent upon the shape and bathymetric profile of the estuary itself and its inlets, as well as proper assignment of tidal boundary conditions outside the estuary. Thus, even with a highly resolved and accurate model domain, localized simulation results are only as good as the boundary conditions that are applied.

Coastal ocean models often utilize tidal databases in order to specify the tidal boundary conditions in small-scale regional studies, such as those undertaken for storm surge inundation [1–3]; sediment transport [4–6]; sea level rise [7–10]; real-time surge forecast systems [11–14]; passive transport of oil spills [15]; passive fish and larval transport, as well as coupled ecological behavior [16–18]; coupled hydrodynamic-marsh interactions with biological feedback [19] and combined hydrologic and hydrodynamic processes [13,20]. For reliable modeling of these complex physical processes, it is necessary to have accurate representation of the tidal boundary forcing. When no other source is available, this forcing must be taken from global databases, which are highly accurate in the deep ocean but often lack the resolution to resolve the more complex interactions over the shelf and in shallower coastal regions [21]. More recently, the Oregon State University Tidal Inversion Software (OTIS) has added smaller regional scale products for many coastal regions; however, these are still provided on relatively coarse grids (1/30° to 1/60°) and until recently only included the primary diurnal and

semi-diurnal constituents [22]. Therefore, it is necessary to create regional tidal databases with higher resolution that can better represent the near-shore environment. Often, these high-resolution products are created for specific marine environments, for example: east Florida [23], Western North Atlantic Ocean [24–26], Eastern North Pacific Ocean [27] and Western Europe [28].

This study is concerned with the tidal response for the Pacific Ocean along the western coast of North America. This region falls within what has been called either the Northeast Pacific Region or the Eastern North Pacific (ENPAC) region, which encompasses all marine and coastal waters from the Bering Strait to the north along the west coast of North America to the Baja Peninsula and along the west coast of Mexico to the border with Guatemala [29]. Historically, three tidal databases utilizing the ADvanced CIRCulation (ADCIRC) hydrodynamic model have been developed for this region [27]; each of these databases developed the tidal profile within the domain by forcing the open ocean with global tidal data. Figure 1 presents these historical database domains, as well as the current database, (only open ocean boundaries shown) within the geographical ENPAC region. Note that, although these databases do not encompass the entire geographic region, it is convenient to use the ENPAC abbreviation.

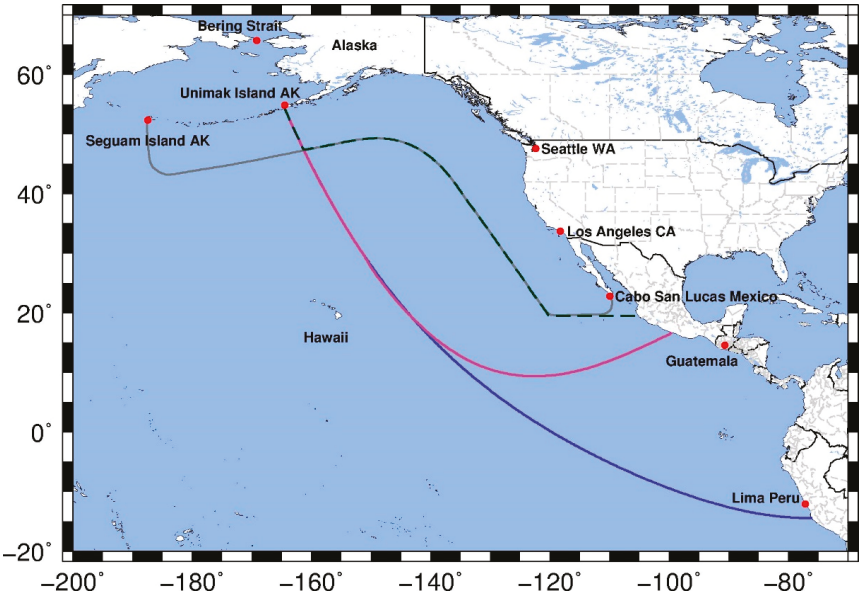

Figure 1. Location of current and historical tidal databases within the Eastern North Pacific region: ENPAC1994 (blue), ENPAC02 (magenta), ENPAC03 (dashed dark green) and ENPAC15 (gray).

The tidal database for the Eastern North PACific region was originally developed in 1994 (called ENPAC1994); it utilized an unstructured grid and resolution varied from about 15 km along the coast to 60 km in the open ocean. Bathymetric information was obtained from the 1988 version of the Earth Topography 5-arc-minute grid (ETOPO-5) [30]. However, the results from this tidal database did not provide good agreement with the field data, and, in some areas, did not provide any improvement over the global ocean tidal models [27].

The first update was not undertaken for nearly ten years; ENPAC02 included increased grid resolution, a reduction of the overall domain and updated bathymetric profiles. Bathymetry was defined from the available National Ocean Service (NOS) soundings database and the 1998 version of the ETOPO-2 product [31] where soundings were not available. The domain extent was reduced to avoid the cluster of tidal amphidromes off the South American coast. The final ENPAC02 model had

grid resolutions ranging from about 8 km along the coast to 60 km in the deep ocean. The combination of improved bathymetry, increased coastal resolution and reduction in the domain extent improved the results with the ENPAC02 database; however, major problems persisted with the amplitude and phase of the semi-diurnal constituents [27].

In 2003, further changes were made to the domain extent, primarily moving the boundary closer to shore; the area eliminated was a portion of the deep ocean waters where the amphidromes associated with the semi-diurnal constituents resided. Additionally, the entire coastline was resolved, even further resulting in an average coastal resolution of 1 km. These modifications to the model domain led to increased accuracy in the tidal results, particularly the semi-diurnal constituents, and the database was released as ENPAC03; it provided elevation harmonics for the eight major tidal constituents and three nonlinear constituents (K_1, O_1, P_1, Q_1, M_2, S_2, N_2, K_2, M_4, M_6, steady) at any location within the domain [27].

The latest version presented herein, ENPAC15, has significantly enhanced coastal resolution with a minimum element size of 20 m along small channels and man-made barriers and an average element size of 65 km at the open boundary. Typical resolution along the mainland United States coastline is 200–400 m; at this time, the Alaskan coastline has not been updated and resolutions in that area range from 2 to 5 km. The ENPAC15 database provides the amplitude and phase for the 37 standard NOS tidal constituents [32] for both elevation and velocity. The model domain features of the various ENPAC tidal databases are provided in Table 1.

Table 1. Summary of grid features for Eastern North Pacific domain ADCIRC tidal databases.

Database Name	Num. of Mesh Nodes	Num. of Mesh Elements	Avg. Coastal Resolution (km)	Min. Coastal Resolution (m)	Avg./Max Deep Ocean Resolution (km)
ENPAC1994	27,494	52,444	15–20	7900	58/90
ENPAC02	290,715	567,145	8 (15–20) [1]	3200	60/96
ENPAC03	272,913	531,680	1–2 (5) [2]	755	35/53
ENPAC15	553,802	1,038,443	0.2–0.4	28	65/85

[1] The coastline was only resolved from Vancouver Island to California, the remainder of mesh is same as ENPAC1994.
[2] The coastline was more finely resolved from Vancouver Island to Mexico, while the Alaskan coast remained coarser but was refined.

With each successive update, the ENPAC databases have gained accuracy in the internal tidal signals. However, the previous database (ENPAC03) still has significant errors (13% amplitude and 13° phase globally), particularly in the region near Vancouver Island where the interior passages have not been resolved (average errors of 22% amplitude and 25° phase). Furthermore, data availability and technological advancements in the past 10 years provide even greater levels of model sophistication and domain complexity. The overarching objective of this study is to reduce the global and regional errors of the ADCIRC tidal database in the ENPAC region. We realize this objective by incorporating six improvements into the latest generation tidal database: new open ocean boundary location, updated coastal resolution, updated bathymetry, boundary forcing using the latest global tidal databases, comparison of the bottom friction parameterization and inclusion of the advective terms within ADCIRC.

In the following sections, these improvements and the resulting error reductions are presented. The development of the ENPAC15 tidal constituent database and validation methods are summarized in Section 2; skill assessment for global, regional and site-specific locations are provided in Section 3 and a discussion of the results and limitations of the database are provided in Section 4. In the interest of brevity, the skill assessment only covers the eight primary constituents: M_2, S_2, N_2, K_2, O_1, K_1, P_1 and Q_1.

2. Materials and Methods

The methodology of this study closely follows that used for the development of the *EC2015* tidal database for the eastern coast of the United States [26]; therefore, the entire outline and much of the text

provided in Section 2.1, Section 2.2, and Section 2.3 is similar to that of our previous study (in order that this paper is complete enough to stand alone for those readers who are not familiar with that study). While the methodology is similar, it is not the same, due to peculiarities of local regions, so readers are cautioned not to skip these sections entirely. In particular, the subsections within Section 2.2 are region specific to ENPAC and are important for thorough understanding of this current study, as are the discussion of the validation data and methods in Section 2.3.

2.1. ADCIRC Computational Model

2.1.1. General Model Details

The enhancements to this database employ the ADCIRC regional hydrodynamic model. ADCIRC utilizes the full nonlinear shallow water equations, using the traditional hydrostatic pressure and Boussinesq approximations. The depth-averaged generalized wave continuity equation (GWCE) is used to solve for the free surface elevations, while the non-conservative form of the momentum equation is used for the velocity components. There have been many papers written about the development and usage of the ADCIRC computational model, but basic details for the equations of ADCIRC can be found in [33–35].

One of the advances within ADCIRC since the West Coast database was last updated in 2003 is the addition of Manning's n to represent bottom friction. Users can now specify specific quadratic friction coefficients, Chezy friction coefficients or Manning's n values throughout the domain. For the Manning's implementation, the n values are converted to an equivalent quadratic friction coefficient within ADCIRC (for each node and at every time step) before the bottom stress is calculated [36]. Note that the computed quadratic friction coefficient can also be limited on the lower end by specifying the minimum *CF* value; otherwise, the values can become quite small as the depth becomes large.

2.1.2. Model Input Parameters

Unless otherwise noted in the appropriate methods and results' subsections, all the ADCIRC model runs used the parameters in the following descriptions. To capture the long-period nonlinear tides, the ENPAC15 tidal database was developed from a 410-day simulation. The model was run from a cold state (zero elevation potential and velocity) and a ramp was applied to both the boundary forcing and the tidal potential forcing functions for the first 25 days. Then, the model was run for another 20 days before the internal ADCIRC harmonic analysis was started for the final 365 days of the simulation (a one-minute interval is used for the internal harmonic decomposition). Tidal potential forcing was applied to the interior of the domain for the eight primary constituents (O_1, K_1, Q_1, P_1, M_2, N_2, S_2 and K_2). In addition to these, the open ocean boundary was also forced with two long-period constituents (Mm and Mf). Tidal boundary forcing was extracted from the OTIS TPXO8-atlas global tidal database [37].

A time-step of 1.0 sec and the default time weighting factors (0.35, 0.30 and 0.35) were used. The lateral eddy viscosity coefficient was set equal to 5.0 m^2/sec. With the exception of the various bottom-friction comparison runs, a nonlinear quadratic bottom-friction scheme with a constant value of 0.0025 was used. Specific friction settings for the Manning's n formulation and the variable *CF* runs are detailed in Section 2.2.5 below. The traditional spatially variable but temporally constant GWCE weighting parameter was used ($\tau_0 = -1$). Finally, variable Coriolis forces were enabled and the nonlinear finite amplitude option was utilized with wetting and drying enabled.

2.2. Improvements for the ADCIRC Tidal Database

Since the development of the ENPAC03 tidal database, many advances have occurred in global tidal databases, available coastal data, options within ADCIRC itself and general computing capability, thus allowing for the inclusion of additional coastal inland areas. For this current ENPAC tidal database, six areas of improvement were examined:

1. Assess the location of the open ocean boundary.
2. Improve the coastal resolution using the National Oceanic and Atmospheric Administration (NOAA) Vertical Datum Transformation (VDatum) product grids.
3. Update the deep-water bathymetry.
4. Use the latest global tidal database products for forcing on the open ocean boundary.
5. Compare three bottom friction schemes for improved accuracy.
6. Improve the model physics by enabling the advective terms within ADCIRC.

In the following subsections, the methods used for each of these areas are detailed. Actual improvements realized in the harmonic constituent accuracy will be presented in the results section.

2.2.1. Open Ocean Boundary Placement

While the removal of the amphidromic points from within the model domain significantly improved the results of the ENPAC03 database relative to the original 1994 database, the original intent of the ENPAC15 model was to include the Hawaiian Islands in the model domain. The operational mesh used by the Extratropical Surge and Tide Operational Forecast System for the Pacific Ocean (ESTOFS-Pacific), which was put into operation in June of 2014, was a good candidate for such an attempt [38]. Figure 2 shows the ESTOFS-Pacific model domain, along with the location of nearby amphidromic points and the various ENPAC domains.

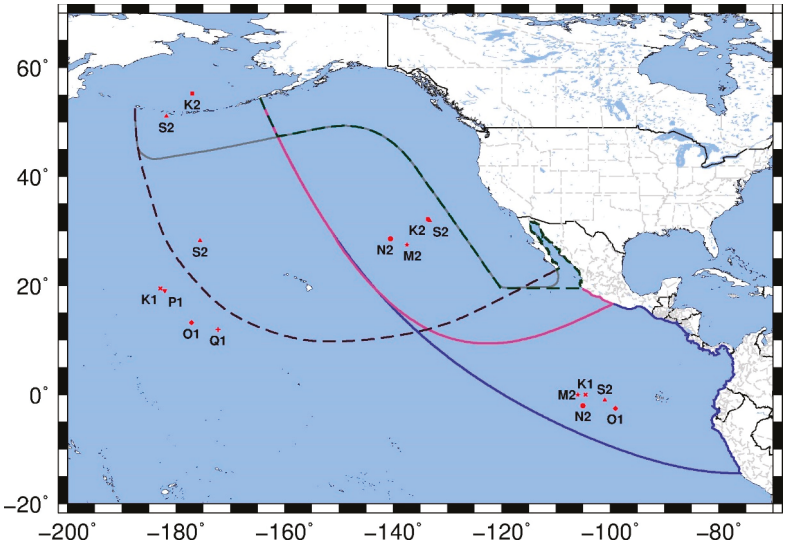

Figure 2. Location of amphidromic points relative to the ESTOFS-Pacific (dashed purple), ENPAC1994 (blue), ENPAC02 (magenta), ENPAC03 (dashed dark green) and ENPAC15 (gray) model domains.

During the development of the ESTOFS-Pacific model, it was determined that the semi-diurnal constituents were underestimated along the coast, particularly along Alaska. In order to mitigate that this in the operational framework, a 20% increase of the semi-diurnal amplitudes along the open-ocean boundary had to be implemented [38]. While this fix was workable in the operational system (where the extended domain is necessary) and the amplitude errors at the Hawaiian Island stations were within acceptable bounds, it was determined that the over estimation at these island stations would not be acceptable in a tidal database. Furthermore, past experience with ENPAC1994 and ENPAC03 clearly indicate that the presence of the amphidromic points for the semidiurnal constituents within the

domain degrades the harmonic results for the same constituents. Therefore, the coast-hugging paradigm of the earlier databases, which avoids these amphidromes, was continued for this version of the database, with the understanding that the Hawaiian Islands can be modeled with boundary conditions extracted from global tidal databases.

Further tests on the ENPAC03 model domain revealed that the presence of the shelf break across the open ocean boundary to the west prevented stable runs when ADCIRC's advective terms were enabled for use (this was confirmed upon examination of the ENPAC03 report as well [27]). Experience gained while updating the Western North Atlantic ADCIRC tidal constituent database revealed that the advective terms played an important role in reducing errors in the shallow near-shore regions [26]. In order to avoid the S2 amphidrome off the Aleutian Islands, an attempt was made to extend the ENPAC03 domain just west of the shelf near longitude -180°. Unfortunately, this was unsuccessful and the model was still unstable at the north-west extents of the open ocean boundary when the advective terms were utilized. Therefore, it was decided to extend the north-west boundary all the way out to the ESTOFS-Pacific extents, as that domain was stable when the advective terms were implemented. Although this incorporates one amphidrome within the domain, accuracy within that region of the model domain is already compromised by the treatment of the Aleutian Island chain as a closed mainland boundary—thus neglecting the interaction with the Bering Sea. Therefore, further inaccuracy in that immediate area was tolerable, with the caveat that the tidal database should not be used to extract boundary conditions for any points west of longitude -164.5° (Unimak Island, AK) where the previous ENPAC03 model domain ended.

Furthermore, the Baja Peninsula was also trimmed from the ENPAC03 model to remove any shelf issues on the south-east extents of the open boundary. The final open ocean boundary was chosen to curve smoothly from about Cabo San Lucas, Baja California Sur, Mexico to Seguam Island, Aleutians West, Alaska and hug the coast in a similar manner to the ENPAC03 model. Figure 2 above also shows the extents of the various ENPAC tidal database domains in relation to the ESTOFS-Pacific domain, as well as the approximate locations of nearby amphidromic points. Note that the ESTOFS-Pacific mesh was trimmed to the ENPAC15 ocean boundary for initial testing of the boundary location before the coastal resolution was increased; this mesh is referred to as ESTOFS-trim.

2.2.2. Increased Coastal Resolution

With each update to the ENPAC tidal database, as data and computational resources were more readily available, more resolution has been added to the coastline. As shown above in Table 1, the latest version has about twice the number of nodes when compared to the ENPAC03 mesh.

Over the past 20 years, NOAA has undertaken an ambitious study of the United States coastline to create a tool for transformation between different vertical datums. The VDatum (Vertical Datum Transformation) tool provides a single source for accurately and easily transforming geospatial data among different tidal, orthometric and ellipsoidal vertical datums along the Unites States coast. It allows the user to combine data from different horizontal and vertical reference systems into a common system in order to create integrated digital elevation models. The interested reader is referred to the VDatum website for more general information about the VDatum tool and for regional publications [39].

In order to create accurate tidal datum fields for the coastal regions, a series of highly resolved coastal grids were developed (or are being developed) for all United States waters. At the time of this study, the two most recent VDatum models available in the ENPAC15 model domain were the Pacific Northwest and Southern California domains, which together encompass the U.S. west coast from Southern California to Washington. The domain for southeast Alaska was being developed concurrently with the ENPAC15 database and was not yet available to update the SE Alaskan coast. Individual reports [40,41] for each of the VDatum domains are available on the VDatum website.

It is important to note that the high-resolution meshes created for the VDatum project are in a Model Zero (MZ) vertical datum. The interested reader is referred to the VDatum Standard Operating Procedure manual [42], but the basic idea is that small corrections are added/subtracted from the

original charted bathymetry in an iterative manner until the simulation converges to a solution. The converged solution is verified against harmonic constituent data available within the region. This was necessary because the original bathymetric sources were all in different tidal datums and no tool existed to transform them into a unified vertical datum. The resulting vertical datum of the high resolution coastline is MZ. Although, model zero is not necessarily the same as mean sea level (MSL) due to nonlinear dynamic effects, for our purposes, we have to assume that the VDatum coastline is approximately relative to MSL.

Additionally, it was desired to include the passages and channels north of Vancouver Island to better capture the hydrodynamics of the Salish Sea up through Johnstone Strait and Queen Charlotte Strait into Queen Charlotte Sound. This area has been extensively studied by the Institute of Ocean Sciences, Fisheries and Oceans Canada (IOS-FOC), who provided us with several unstructured mesh models, of which we decided to incorporate two: the Vancouver Island and Discovery Passage regions [43,44]. These meshes were used to guide our model development for that area, which could not be as detailed. Additionally, the unstructured meshes that had been modeled within a finite volume framework by IOS-FOC would not remain stable in the ADCIRC finite element framework.

As a first step, the Vancouver Island model was used as input to generate a localized truncation error analysis with complex derivatives (LTEA + CD) representation of the greater Vancouver Island region [45,46]. Then, bathymetric detail was updated where possible with the finer scale Discovery Passage model. Finally, extremely shallow regions were either removed by hand or artificially deepened. In general, the representation of that region was cut to the 3 m depth contour, unless that would eliminate important channels. If smaller channels that were important for hydraulic connectivity would be removed in this process, their minimum depth was set to 3.0 m and they were allowed to remain. As such, it is not expected that the results in the Canadian waters would be as accurate as those in the U.S. waters. However, as will be seen in the discussion of the ENPAC15 model results, the incorporation of these channels is important for accuracy in the Puget Sound region. The bathymetric profiles from the IOS-FOC models were in MSL.

Figure 3 shows the extents of the two VDatum and IOS-FOC nearshore domains superimposed on the ENPAC15 model domain, shown to clearly illustrate the regions where coastal resolution was updated. Note that the Discovery Passage region is only a very small part of the larger Vancouver Island domain so the details are not visible at this scale. Instead, a black box is shown around the region of the Vancouver Island model where the bathymetry was replaced with the highly resolved Discovery Passage model. Also note that, in the Kitimat region, the smaller inland channels, visible in the red boundary of Figure 3 near -127.5° longitude 52.5° latitude, were not included in the final ENPAC15 domain, as we are not interested in producing tidal data in that region of the Canadian waters and we had to minimize computational requirements.

Notice that there are several areas of overlap between these regional subdomains. For the overlap in the Pacific Northwest and Southern California VDatum domains, the individual grids were carefully pieced together in such a way as to preserve the source grid with the highest coastal resolution. For the offshore regions within these overlaps, a transitional mesh was created at an appropriate distance from the shoreline that smoothly blended the triangulations of the two VDatum meshes. Finally, the bathymetry from the highest resolution source was reapplied onto the new triangulation.

A slightly different approach was taken within the Salish Sea. A transect was chosen across the Strait of Juan de Fuca at about longitude -124.0°. This location was chosen because the resolution of the Pacific Northwest VDatum mesh and the LTEA + CD representation of the Vancouver Island model from IOS-FOC was nearly the same at this location, providing a smooth transition from one model to the other. Additionally, a gentle curve just outside Queen Charlotte Strait to the southern coast of Vancouver Island was chosen as the extent at the other end of the northern Vancouver Island passages. This curve was chosen to encompass the shallow shelf off the northwestern tip of the island that was better represented within the IOS model and to ensure a smooth transition into the boundary of the Pacific NW model. Within the curved region and through the Salish Sea up to the transect

across the Strait of Juan de Fuca, shown in Figure 3 by the thick blue lines, the model was taken from IOS-FOC sources. Everything outside of this region, including the triangulation for the southern coast of Vancouver Island, was taken from the Pacific Northwest VDatum mesh. However, the bathymetric representation for the southern coast of Vancouver Island was smoother in the IOS-FOC model, so the bathymetry for this immediate region was interpolated from the IOS-FOC model instead. The Puget Sound region was carefully compared to the VDatum model and it was determined that the resolution and bathymetry were essentially equivalent, with the exception of the occasional outliers in bathymetry that can sometimes occur during the model zero iterations of the VDatum process. Therefore, for ease of transition, the Puget Sound region was taken from the IOS-FOC model. Due to the ready availability of NOS data on the internet, the bathymetry sources was more than likely the same for both grids. The boundary was then smoothly transitioned into the Pacific Northwest VDatum model, in a similar manner to the process described earlier for the VDatum overlap region.

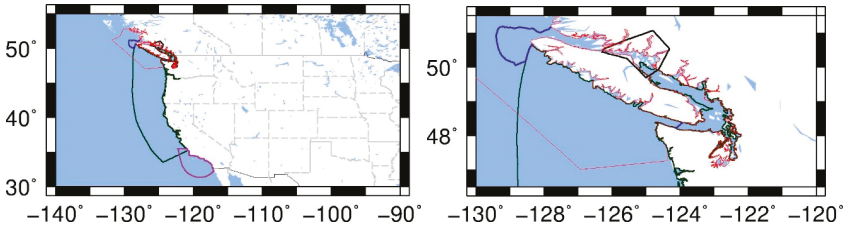

Figure 3. Location of available models for coastal refinement (extents only); global view (left panel) and zoom of Vancouver Island region (right panel): Southern California VDatum (purple), Pacific Northwest VDatum (dark green), Vancouver Island (red), Discovery Passage model (thick black), and location for merging Vancouver boundaries (thick blue).

A comparison of the Vancouver Island and Washington coast region in the ENPAC15 model and the previous ENPAC03 model is shown in Figure 4. Notice in particular that the passages north of the island have been added and in general that the newest model includes more inland channels, rivers and islands, as well as a more detailed shoreline in general. Also note that the region of larger elements south of Vancouver Island is a manifestation of the LTEA + CD process, which minimizes the number of elements in deeper regions.

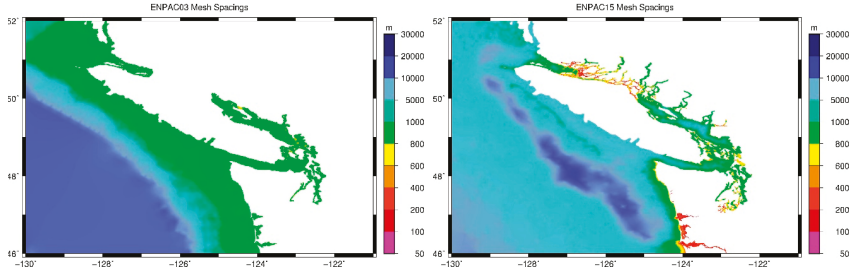

Figure 4. Comparison of coastal resolution in the ENPAC03 (left panel) and ENPAC15 (right panel) models for the Vancouver Island and Washington coast regions.

2.2.3. Updated Global Bathymetry

The final step of mesh development was to blend the highly resolved coastline into the global ocean described in Section 2.2.1 and update the deep-water bathymetry of the ENPAC03 model. The ESTOFS-Pacific model includes the most recent bathymetric profiles available from the National Ocean Service NOS/OCS hydrographic database maintained at the National Geophysical Data Center [47].

Additionally, the ESTOFS-Pacific model utilized the University of California-San Diego/Scripps' global 1-minute bathy/topo dataset [48] outside of the NOS survey areas. Therefore, it was decided that the most straightforward way to update the bathymetry in regions that were not included in VDatum grids or IOS-FOC grids was to trim the ESTOFS-Pacific mesh down to the ocean boundary selected for ENPAC15. This intermediate mesh was also used for some quick comparison tests because it was not as finely resolved along the coast; it will be referred to as ESTOFS-trim. Finally, the improved coastline from VDatum and IOS-FOC sources was merged into the ESTOFS-trim domain by removing all deep water from the merged coastal regions and creating a smooth mesh out to the boundary nodes; then, the ESTOFS-trim bathymetry was interpolated back onto the regions of the mesh that did not come from the high-resolution coastal domains. The resulting ENPAC15 model bathymetry, shown in Figure 5, is referenced to MSL.

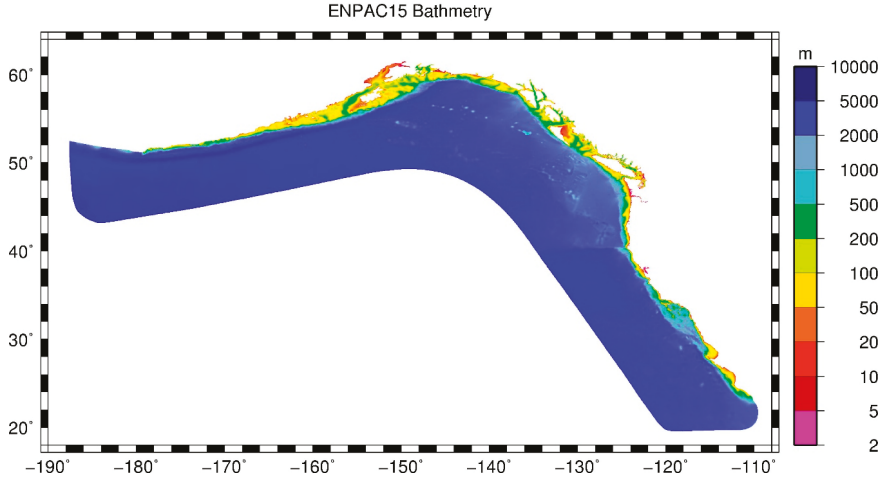

Figure 5. Bathymetry contours for ENPAC15 model.

2.2.4. Updated Open Ocean Forcing

Once an updated physical model had been developed for the entire ENPAC region, it was necessary to extract tidal forcing information from available global tidal models at the open-ocean boundary. Since the last version of the West Coast ADCIRC tidal database in 2003, significant improvements have been made in the global tidal modeling community as well. Herein, we compare two global models: the Oregon State University Tidal Inversion Prediction (sometimes called the OTIS or OSU TPXO system) and the French Tidal Group Finite Element Solution database (often simply called FES). Both of these use data assimilation methods for satellite altimeter data, such as Topex/Poseidon, in the development of their global database.

The FES model utilizes a global unstructured grid to model the tidal barotropic equations in a spectral configuration and then employs data assimilation from long-term satellite altimetry data to correct the tidal signals [49]. FES products are provided on a 1/16 degree resolution for 32 tidal constituents over the global ocean. The most recent version is FES2012, which is distributed by Aviso (Ramonville St. Agne, France) [50].

The OSU TPXO system follows the same general solution techniques with a least square best fit of the Laplace tidal equations and along track averaged data from Topex/Poseidon and Jason satellite altimetry [37,51,52]. The latest TPXO8-Atlas product provides 13 tidal constituents and utilizes a global structured grid with a resolution of 1/6 degree to model the global ocean with local patches of high resolution that use local refinement of 1/30 degree around many of the global coasts.

After extracting boundary information from the FES 2012 and TPXO8-Atlas databases, a visual comparison was made of the amplitude and phase information that would be used as input into the ADCIRC model; ten constituents are used to force the model (diurnal—O_1 K_1 P_1 Q_1; semi-diurnal—M_2 S_2 N_2 K_2; and long term—Mf Mm). In general, there were very few observable differences between these two models but those that did exist were typically concentrated near the coast, which may be due to the difference in near-shore resolution between the two global models. For the semi-diurnal constituents, the amplitude differences were focused near the southern boundary at Cabo San Lucas, Mexico (refer to Figure 1 or Figure 2 for geographic locations within the ENPAC domain); while the K_2 constituent also showed variation in phase along the northern boundary near Seguam Island, Alaska. Similarly, the P_1 and Q_1 constituents showed minor amplitude differences near both coastal boundaries and the other diurnal constituents were in good agreement for amplitude; while, for phase, the O_1 constituent was consistently 11–17 degrees higher along the entire ocean boundary for the TPXO8 database but was similar for the other three diurnal constituents. Finally, for the long-term constituents, both showed minor differences in amplitude and phase all along the boundary but were in fairly good agreement considering the small amplitudes (on the order of 10^{-3} to 10^{-2} m). A more quantitative comparison was made by calculating the maximum absolute difference in amplitude and phase over all 211 open ocean boundary nodes; these results are given in Table 2. Note that there was a single outlier in the S2 constituent phase for the forcing values extracted from the FES12 database; this outlier was removed before calculating the maximum absolute differences. These observations alone were not enough information to determine if one global model was better; actual ADCIRC harmonic differences due to the boundary forcing are examined in the results section.

Table 2. Maximum absolute differences in tidal harmonics for the ten forcing constituents used along the entire ENPAC15 boundary for the TPXO8-Atlas and FES2012 global tidal database products.

Harmonic	**O_1**	**K_1**	**P_1**	**Q_1**	**Mf**	**Mm**
Amplitude (cm)	0.77	1.04	1.58	1.30	0.09	0.09
Phase (degrees)	17.06	1.55	6.70	9.17	6.88	18.32
Harmonic	**M_2**	**N_2**	**S_2**	**K_2**	-	-
Amplitude (cm)	1.56	0.84	0.41	0.69	-	-
Phase (degrees)	2.05	9.21	2.82	22.39	-	-

2.2.5. Bottom Friction Assignment

In this study, three variations of the quadratic friction formulation were compared for the ENPAC15 database: a constant CF version and two variable friction formulations. For the first variable formulation, a combination of the CF values that had been developed for each of the VDatum regions was used, while the second scheme utilized the USGS Woods Hole Coastal and Marine Science Center's usSEABED [53] database of core samples to assign appropriate regional Manning's n friction values.

Of the two VDatum grids that fall within the ENPAC15 model domain, only the Pacific Northwest grid had a variable quadratic bottom friction scheme. Additionally, no bottom friction information was provided for the IOS-FOC domains in Canadian waters. Therefore, the values from the one available region were simply mapped onto the corresponding region of the ENPAC15 domain. Then, the default value from that domain (CF = 0.00375) was applied as the default for the entire ENPAC15 domain as well.

The usSEABED database contains three files for each region: "EXT—numeric data extracted from lab-based investigations, PRS—numeric data parsed from word-based data and CLC—numeric data calculated from the application of models or empirical relationship files" [53]. Each of these datasets describes the data in different ways and has its own limitations; however, they can be combined to create a more extensive coverage of the seafloor characteristics. The database only covers the United States mainland coast and data was available only from about 117.00 W 32.24 N (north of the border with Mexico) to 122.57 W 48.78 N (near the SE end of the Strait of Georgia). Within this region,

a multi-step process was utilized: (1) the three datasets were compared to make sure that they were in general agreement; (2) outliers from the comparison stage were removed; (3) duplicate points were preferentially taken from the EXT dataset; (4) the edited files were then combined into a single data source; (5) the combined file was then assessed and filtered one more time to remove large outliers that affected a wide region due to the sparsity of the data; and (6) finally any points that fell outside of the 1000 m bathymetry contour were removed. This final dataset was then interpolated onto the ENPAC15 model domain within the applicable region only.

The remainder of the domain was assigned shelf-wide values based on anecdotal evidence since no data was available and a depth-interpolation method similar to that used for the EC2015 database was used [26]. Namely, each larger coastal area was assigned a descriptive designation with an associated range of Manning's n values based upon typical values from literature. After a region was classified by bed type, depth-dependent interpolation was used to assign Manning's n values over each section of the coastal shelf. For water depths between 0 m and 5 m, the maximum value was assigned; for depths between 5 m and 200 m, values were linearly interpolated from the maximum at 5 m depth to the minimum value at 200 m depth; for depths between 200 m and 1000 m, the minimum manning value was assigned; finally, for depths greater than 1000 m the post-Ike "deep ocean" value of 0.012 was assigned. Table 3 provides the rough geographical regions that were used in this process, as well as the assigned min/max Manning's n values.

Table 3. Geographic regions used for Manning's n assignment.

Geographic Region	Bed Description	Minimum n Value	Maximum n Value
Baja California	Sandy/gravel	0.022	0.025
U.S. Mainland	assigned from usSEABED data		
S. Vancouver Island	Sandy/gravel	0.022	0.025
N. Vancouver Island	Gravel/rough rock	0.025	0.050
Alaska/ BC	Gravel/cobble	0.025	0.030

2.2.6. Inclusion of ADCIRC Nonlinear Advective Terms

The final effort to improve the physics was to include the nonlinear advective terms in the ADCIRC modeling setup; the interested reader is referred to [54] for details about the development of these terms and equations. In practice, these terms enter in by activating two flags in the ADCIRC input control file. In all previous versions of the ENPAC tidal database, the westernmost edge of the open ocean boundary over the shelf break near Unimak Island, Alaska caused instabilities when the advective terms were activated. Therefore, it was not possible to include advection and compare how the tidal response varied due to these terms. With the new extended open ocean boundary, it is possible for the model to remain stable with these terms activated.

2.2.7. Summary of Tidal Database Improvements

Six different areas of improvement have been presented for the ENPAC15 tidal database. When possible, each model improvement was isolated to determine the accuracy improvement due solely to that component of the project. However, the updated global bathymetry and open-ocean boundary location were combined in the intermediate ESTOFS-trim modeling domain and were not studied individually (recall that the ESTOFS-trim model is a reduction of the ESTOFS-Pacific operational model trimmed down to the ENPAC15 ocean boundary). A summary of the simulations that were completed for this study, including the run designation, description, model domain, advection terms, bottom friction scheme and open ocean boundary forcing are provided in Table 4. For the boundary forcing, the textual label before the dash indicates which global tidal database was used while the number after the dash indicates how many constituents were used. In all subsequent sections, the results will be referred to by the run designation given in this table.

Table 4. Summary of ADCIRC model parameters for the model simulations completed in this study.

Run Designation	Description	Grid	Advection	Friction	Boundary Forcing [1]
ENPAC03	ENPAC03 extract	ENPAC03	Off	0.0025	TPXO6-8
ENPAC03R	ENPAC03 rerun	ENPAC03	Off	0.0025	TPXO8-10
ESTOFS-trim1	TPXO 8.0 forcing	ESTOFS-trim	Off	0.0025	TPXO8-10
ESTOFS-trim2	Advection on	ESTOFS-trim	On	0.0025	TPXO8-10
ESTOFS-trim6	FES 2012 forcing	ESTOFS-trim	Off	0.0025	FES12-10
ENPAC15-CF	Constant friction	ENPAC15	Off	0.0025	TPXO8-10
ENPAC15-Vdat	ENPAC15 release	ENPAC15	Off	VDatum	TPXO8-10
ENPAC15-Mann	Manning's n friction	ENPAC15	Off	Manning	TPXO8-10

[1] The label before the dash indicates which global tidal database was used, while the number after the dash indicates how many constituents were included.

To confirm that we could expect a fair comparison between all results, the ENPAC03 tidal database was rerun with the same version of ADCIRC (v51.06) used in this study. Error analysis verified that the new version of ADCIRC was recreating the harmonic constituents. In subsequent sections, all reference to ENPAC03 results indicate that constituents were directly extracted from the previous version of the database at the same locations as the recent improvements. Meanwhile, the ENPAC03 model domain was also rerun with the same input parameters as the ESTOFS-trim model, including tidal forcing extracted from the global TPXO8 database at the ENPAC03 boundary. Results from this run are denoted by ENPAC03R and are used to test the effects due solely to the boundary location. Note that these were two separate reruns: one with the same input as the original ENPAC03 tidal database to verify that nothing substantial has changed in the ADCIRC model itself (results are not shown herein), and another to mimic one of the ESTOFS-trim model results for boundary comparison (ENPAC03R).

A series of simulations using the ESTOFS-trim model were conducted to test the overall effect of the various database improvements in a faster computing environment. While many such runs were conducted, only three of these tests are discussed herein for comparison of the individual effects of boundary forcing, advective terms and coastal resolution. Recall that the ESTOFS-trim model includes more coastal features than the ENPAC03 model but is not as highly resolved as ENPAC15. Finally, three bottom friction schemes were explored using the full ENPAC15 model; these are denoted by ENPAC15-CF for constant friction, ENPAC15-Vdat for VDatum friction and ENPAC15-Mann for Manning's n friction.

2.3. Validation of the Improved ADCIRC Tidal Database

Three sources of harmonic constituent data were used to validate the new ENPAC15 tidal database; these sources are discussed in Section 2.3.1. Additionally, the various analysis techniques used to compute model errors are discussed in Section 2.3.2.

2.3.1. Validation Data

The National Oceanic and Atmospheric Administration's Center for Operational Oceanographic Products and Services (CO-OPS) keeps a record of tidal harmonic constituent data at stations throughout the coastal United States [55]. Tidal harmonic data was available at 139 such stations in the ENPAC domain. Further data was obtained for 39 stations within Canadian waters from the Institute of Ocean Sciences, Fisheries and Oceans Canada (IOS-FOC) [56]. Finally, historical data from the International Hydrographic Organization (IHO) was used to provide wider coverage, specifically in the deeper regions [57]. There is a certain degree of uncertainty in the IHO data, as information about the source of the constituents (e.g., length of analysis and data records) is not always available; furthermore, the longitude and latitude coordinates used to locate the stations are only specified to three-decimal digits precision, which is sometimes insufficient to determine the physical location of the data collection. Of the about 4190 IHO stations available worldwide, 141 can be accurately located within the ENPAC15 domain; however, only 80 of those are unique locations not already provided in the other data sources (the 61 duplicates are used to assess the accuracy of the data itself). For skill assessment purposes, a total of 258 stations (139 from CO-OPS, 39 from IOS-FOC and 80 from IHO)

were classified into three regional locations: California/Mexico, Oregon/Washington and British Columbia (Pacific Northwest) and Alaska. The global locations of the 258 available data stations are shown in Figure 6; while zoomed views with station numbers are provided in Appendix A.

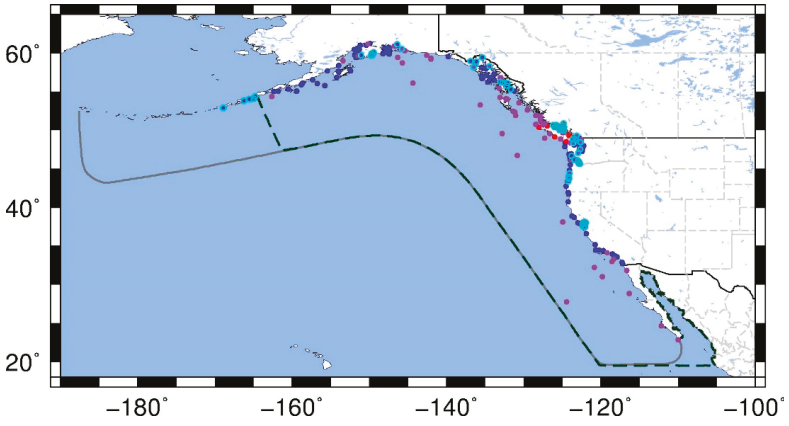

Figure 6. Locations of the 258 available validation stations shown with the ENPAC03 boundary (dashed dark green) and ENPAC15 boundary (gray); stations from three sources: CO-OPS (blue), IOS-FOC (red), and IHO (purple) with dry stations denoted with a cyan circle. Zoomed regional views provided in Appendix A.

Of these 258 stations, only 179 were considered "wet" in the ENPAC03 model—96 are truly within the bounds of the ENPAC03 model and the other 83 are close enough to the boundary to warrant including them (by using nearest element approximations). Stations that were far inland or within small channels that were not physically represented in the older database are not extracted from the ENPAC03 database. For Figure 6 and all the figures in Appendix A, data locations shown with a cyan circle around them are not wet in the ENPAC03 domain and are excluded from any error comparisons that specifically say that only wet stations were used. Appendix B provides a list of the station number, physical location (used for extraction from the ADCIRC databases), station name, assigned region, and the data source for all available stations.

2.3.2. Validation Methods

The same error measures as were used in the EC2015 study are used herein to determine which model best captured the tidal harmonics at the available data stations. For each station, scatter plots of measured and computed amplitude and phase were examined for the eight primary tidal constituents (M_2, S_2, N_2, K_2, O_1, K_1, P_1 and Q_1). Ideally, these plots would have a one-to-one correspondence. Scatter plots including all stations were also made for each of these eight constituents independently and a least-squares linear regression was computed. Additionally, scatter plots comparing the ENPAC03 and ENPAC15 databases for each of these eight constituents were created using 165 of the wet stations in the ENPAC03 database (fourteen of the wet British Columbia stations were neglected because they were located too close to the passages north of Vancouver Island, which were not resolved in the ENPAC03 model).

In addition to the above qualitative measures, three quantitative error measures were calculated to compare the skill of each model. For both the phase and amplitude, the mean absolute error (MAE) was computed as

$$\mathrm{MAE} = \frac{1}{8\,np}\sum_{e=1}^{np}\sum_{k=1}^{8}\left|data_{e,k} - model_{e,k}\right|, \quad (1)$$

where the absolute errors are summed over both the number of constituents (k) and the number of data points for a region (e). To calculate the mean errors for an individual constituent, the second sum would only be computed for $k = 1$ and the 8 is removed from the denominator. In all of the error plots that follow, the first eight points on the left side are for the individual constituents summed for all data stations and the regional error means are shown on the right, separated by a vertical line.

Due to some constituents having very small amplitudes, the mean relative error (MRE) was computed for amplitudes only as

$$\text{MRE} = \frac{1}{8\,np}\sum_{e=1}^{np}\sum_{k=1}^{8}\frac{\left|data_{e,k} - model_{e,k}\right|}{data_{e,k}}, \tag{2}$$

where the same summation rules apply. Note that if the errors are on the same order of magnitude as the data, the relative errors will be close to 100%. Additionally, a composite error, combining the errors in phase and amplitude for each constituent into a single error metric, was computed for each station as

$$A_E = \sqrt{0.5(A_m^2 + A_o^2) - A_m A_o \cos(\pi(h_m - h_o)/180)}, \tag{3}$$

where A_m is the modeled amplitude in meters, A_o is the observed amplitude in meters, h_m is the modeled phase (degrees GMT) and h_o is the observed phase (degrees GMT). As before, the mean root-mean-square error (RMSE) was computed by summing over the number of data points for any region as well as the number of constituents,

$$\textit{Mean}\ \text{RMSE} = \frac{1}{8\,np}\sum_{e=1}^{np}\sum_{k=1}^{8}(A_E)_{e,k}. \tag{4}$$

To compare the skill of the new ENPAC15 database versus the previous ENPAC03 database, harmonic constituents were extracted from the 2003 database at the stations that were within (or close enough to) the bounds of the ENPAC03 model, the wet 2003 stations. Additionally, when comparing the two database versions, only the data stations that were not located within or too close to the inside passages north of Vancouver Island were used for global statistics, even if they were designated as wet (this is due to the fact that, without the passages in the domain, the results for ENPAC03 database at these stations are not valid). Of the 179 stations that were considered wet within the ENPAC03 model, only 165 were used for global statistics; mean errors were then computed for both databases at those 165 locations. However, mean errors were also calculated at all 258 stations for the new ENPAC15 database, as it was not limited by the missing passages. Table 5 provides the total number of stations in each region that were used for statistics for each model. For reference, parenthetical numbers include only the stations that were physically within the lower resolution domains, not the nearest neighbors. Note that station details are also provided for the ESTOFS-trim model; however, in order to be consistent when comparing errors, only the 165 wet (non-passage) ENPAC03 stations are used for computing errors on this model domain.

Table 5. Total number of validation stations available in each region for the most recent models in the ENPAC region.

Model	Global	Alaska	Pacific Northwest	California and Mexico	Deep
ENPAC03	179 (96) [1] / 165 [2]	61 (35)	70 (34)	37 (16)	11
ENPAC15	258	84	116	47	11
ESTOFS-trim	180 (162)	83 (81)	54 (41)	32 (29)	11

[1] Numbers in parentheses indicate how many were within the model domain while the first number includes those stations approximated with nearest neighbors. [2] Fourteen of the wet stations in the Pacific Northwest region were located within the inside passages above Vancouver Island and were not included in the global statistics or the global constituent scatter plots; therefore, there are 165 stations that were used in global statistics/scatters—subsequently indicated by Global (no passage).

3. Results

3.1. Results for the Various Improvements

In this section, some of the model improvements are examined independently to determine how each improvement affects the RMS error. Full error analysis, as described in Section 2.3.2, will be provided in Section 3.2, where the ENPAC03 model is compared to the final release ENPAC15 model. Figure 7 presents the regional mean RMS errors for all eight simulations that were previously presented in Table 4. These mean errors were computed using the 165 wet stations that are common to all model domains (recall that global statistics do not include the 14 stations that are inside the passages around Vancouver Island). Recall also that the ENPAC03R results are from a substantially different simulation than the original extraction from the ENPAC03 database. Differences include: (1) length of simulation (410-day versus 60-day); (2) nodal factors (specific factors for analysis annum 2005 versus default nodal factors); and (3) application of boundary conditions (extracted from the newer TPXO8-Atlas database for 10 constituents versus only the eight primary constituents from the TPXO6 database), such that we would not expect the resulting composite errors to be the same.

While not shown herein, it is of note that the stations located in deeper water and along the Mexican coast do not realize any significant improvements for any of the various models since the modeling domain itself is largely unchanged in this area and the most significant change is related only to the global tidal boundary forcing. Four regions are used for regional error summation: Global (without the passages), Alaska, Pacific Northwest (includes British Columbia, Washington and Oregon) and California/Mexico.

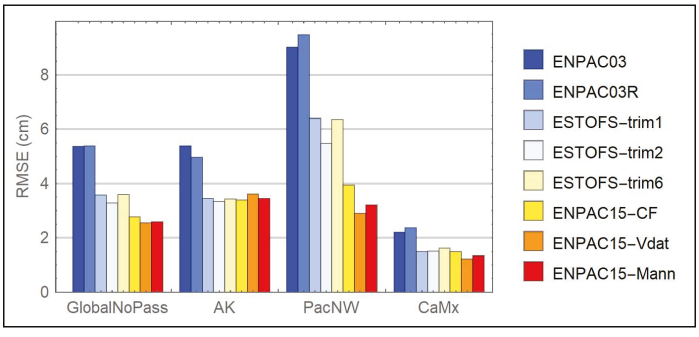

Figure 7. Comparison of regional mean root mean square errors using the 165 wet stations (neglect the stations near inside passages) for all eight study simulations summarized in Table 4.

3.1.1. Comparison of Boundary Placement

As described in Section 2.2.1, the open ocean boundary has been moved further west of the shelf near the Aleutian island chain and continues to hug the coastline to avoid amphidromic points. In order to test how much of an affect the new boundary placement has on the extracted harmonic constituents, the old ENPAC03 model was run with an identical input file as was used for the ESTOFS-trim model: all input parameters are as described in Section 2.1.2.

Concentrating only on the ENPAC03R and ESTOFS-trim1 bars in Figure 7, we note that significant gains in accuracy are realized for all regions, with percent reductions ranging from 30% in Alaska to 37% in California. Unfortunately, it is difficult to determine if this is related solely to the new open boundary location or the change in resolution along the boundary itself for the ESTOFS-trim model domain. Additionally, the deep-water bathymetry was also updated in the ESTOFS-trim model, making it difficult to separate the individual effects of boundary placement, boundary coarseness and deep water bathymetry.

3.1.2. Comparison of Open Ocean Boundary Forcing

As described in Section 2.2.4, two different global tidal databases have been examined as input to the ENPAC15 model: FES12 and TPXO8-Atlas. Looking at the ESTOFS-trim1 and ESTOFS-trim6 bars in Figure 7, we note that the composite errors are similar for all regions; however, the errors from the FES12 boundary conditions are slightly higher, more noticeably in the southern region. These differences are not significant, however, and given the historical application of TPXO products for boundary forcing in the ADCIRC tidal databases and its slightly better performance in this application, it was decided to use the TPXO8-Atlas global products for this latest database update. Meanwhile, examining the ENPAC03 and EPAC03R bars, the inclusion of the two long-term forcing terms (Mm and Mf) and the updated global forcing from TPXO6 to TPXO8 does not appear to significantly affect the results; there are minor changes in the regional mean RMS errors but not globally.

3.1.3. Comparison of Advection

As described in Section 2.2.6, it was desired to include the advective terms within ADCIRC for the latest update. When examining the ESTOFS-trim1 and ESTOFS-trim2 bars, we note that while there is no noticeable difference in the California and Alaska stations, there is a significant improvement (mean RMS error reduction of 0.9 cm or 14%) in the Pacific Northwest stations when the advective terms are utilized, which also improves the global performance. Examination of individual stations in this region indicates typical mean RMS error reductions of 1.5 to 2.0 cm in the inside passages north of Vancouver Island and a maximum reduction of 3.43 cm. This is to be expected since the region north of Vancouver Island has been documented to dissipate a great deal of turbulent and internal tidal energy [43,58], which are not explicitly accounted for in the ADCIRC model. The utilization of the advective terms would allow the model to account for some of this nonlinear dissipation. However, when we turned these terms on with the fully resolved ENPAC15 model domain, instabilities developed in the shallow and narrow passageways north of Vancouver Island. Efforts are ongoing to stabilize this region (through further grid and bathymetry refinement) and allow for incorporation of the advective terms in an updated release, but for now the ENPAC15 tidal database does not include these terms.

3.1.4. Comparison of Increased Coastal Resolution

As described in Section 2.2.3, several refinements were made to the coastal geometry and bathymetry along the North American west coast. Since the operational ESTOFS-Pacific mesh (from which the ESTOFS-trim mesh was cut away) has an even coarser resolution along the coastline than the ENPAC03 model domain, we can compare the ESTOFS-trim1 and ENPAC15-CF bars in Figure 7 to get an idea of what affect this additional resolution has. Recall that we would not expect any improvement in the Alaska region because the coastal resolution was not updated in that area.

Similarly, no improvement is noticed in the mean RMS errors in the California region. However, more significant improvements (38%) are realized in the Pacific Northwest stations, which reduces the global error by 22%. Much of this improvement is likely due to the inclusion of the passages north of Vancouver Island, which were previously absent from all of the ADCIRC tidal databases for the ENPAC region.

3.1.5. Comparison of Bottom Friction Schemes

In this study, three different bottom friction schemes are compared: constant CF = 0.0025, VDatum quadratic friction coefficients and Manning's *n* formulation with *n* values estimated using the USGS usSEABEDS data. Looking at the mean RMS errors for all of the ENPAC15 bars in Figure 7, we note that both of the variable friction options (VDatum and Manning's *n*) provide lower errors than the constant CF version. Furthermore, there is a slight improvement of the VDatum versus Manning's *n* friction schemes. When we recall that the VDatum scheme is essentially constant everywhere except the Columbia River, then it would appear that the slightly higher default value (CF = 0.00375) is responsible for this error reduction rather than the variability of the friction itself. Additionally, we note that the friction schemes tested in this study do not appear to affect the Alaska region much at all, which might be expected since the coastal bathymetry and resolution has not been updated and most of the water is deep enough to make the friction irrelevant.

3.2. Comparison of ENPAC15 and ENPAC03

For this latest ENPAC15 tidal database release, the VDatum friction formulation was used; all other model input parameters are as described in Section 2.1.2. For results and discussion, when we refer to ENPAC03, we have extracted tidal harmonics directly from the previously released database. Scatter plots of computed versus measured amplitudes and phases (and their linear best-fit) for the ENPAC03 and ENPAC15 databases are shown in Figure 8 for the dominant diurnal and semi-diurnal tidal signals: K_1 and M_2. Additionally, Table 6 provides the best fit statistics for all eight primary constituents at the 165 validation stations that are common to both databases (neglecting the inside passage stations). For a perfect fit of the validation data, both the slope and R^2 values would have a value of unity. Notice that the slope is improved for nearly all of the eight constituents, with the exception being O_1 amplitude, Q_1 amplitude and phase, and K_2 amplitude; meanwhile, the R^2 value is closer to unity for all amplitudes and phases, indicating a tighter distribution.

Table 6. Summary of best-fit linear statistics for the 165 common validation stations in the ENPAC03 and ENPAC15 tidal databases.

Tidal		**Harmonic Amplitudes**							
Database		O1	K1	P1	Q1	M2	S2	N2	K2
ENPAC03	Slope	0.982	0.943	0.937	0.967	0.953	0.883	0.931	1.008
	R^2	0.968	0.960	0.976	0.974	0.962	0.955	0.958	0.856
ENPAC15	Slope	1.033	1.027	0.981	0.962	0.968	0.949	0.951	0.975
	R^2	0.996	0.998	0.994	0.989	0.991	0.989	0.988	0.989
Tidal		**Harmonic Phases**							
Database		O1	K1	P1	Q1	M2	S2	N2	K2
ENPAC03	Slope	1.001	0.988	0.980	0.937	0.988	0.960	0.964	0.980
	R^2	0.988	0.994	0.996	0.936	0.982	0.966	0.986	0.970
ENPAC15	Slope	0.996	0.996	0.994	0.923	0.997	0.996	0.995	0.985
	R^2	1.000	1.000	1.000	0.941	0.999	0.999	0.999	0.998

Similarly, if we look at scatter plots of individual stations, we can compare how each of the databases performs for that point. Since there are 258 validation stations, only a few representative stations are provided herein. Figures A6–A14 in Appendix C provide plots for the eighteen stations

that were shown by a black X in Figures A1–A5 in Appendix A; plots are grouped together by sub region: Southern California, San Francisco Bay, Northern California, Washington/Oregon, Puget Sound, British Columbia, Southeast Alaska and Southern Alaska. In order to illustrate the station differences due to the friction formulation, results for both the VDatum and Manning's n friction formulations are shown in these plots, along with the extracted ENPAC03 results. Other than the bottom friction itself, all other ADCIRC parameters are the same for the two newer data sets.

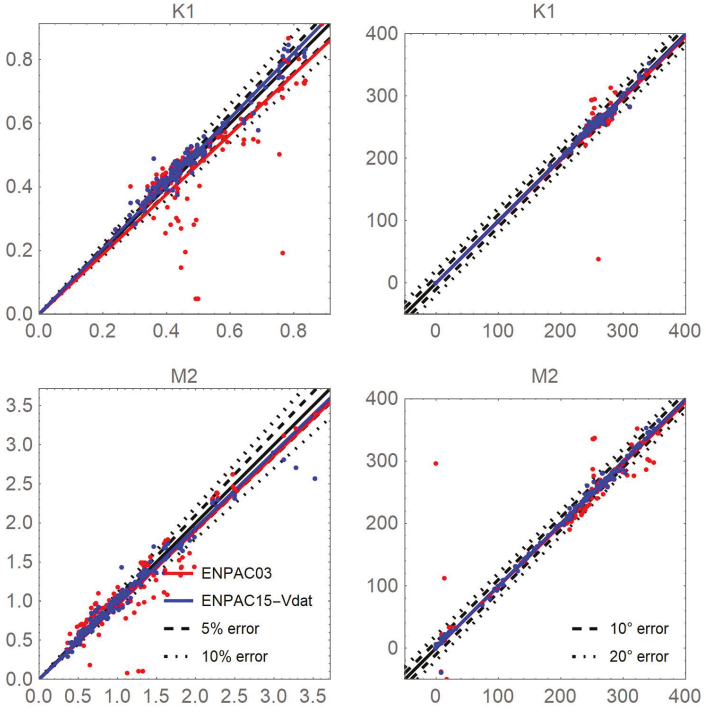

Figure 8. Comparison of scatter plots for the dominant constituents (K_1, M_2) for the ENPAC03 and ENPAC15 tidal databases using the 165 common validation data stations.

We note that very little improvement is seen in the Southern or Northern California stations (Figures A6 and A7), which is expected since the coastline and bathymetry did not change drastically. However, the San Francisco Bay region is more resolved in the newer database, resulting in better amplitude and phase correspondence; note also that the friction formulation makes a significant difference in this shallower water body. Similarly, along the Washington and Oregon coasts, there is marked improvement in the new database due to the inclusion of more coastal features and upper bay water bodies. In the Puget Sound region (Figure A10), we note that the friction formulation plays a more significant role at these shallower stations; and that the phase has been improved but there is still room for improvement in the dominant amplitudes. Notice that the inclusion of the passages north of Vancouver Island has significantly improved the amplitude and phase responses at the stations on either end of the passage (stations 146 and 176), despite them being far removed from the interior passages. Results are not shown within the passages themselves, since the region was not resolved in the ENPAC03 database and no comparison can be made; however, the new database has fairly good agreement throughout this region, although the dominant constituents are overestimated. Additionally, no real improvement is noticed on the southern extents of Vancouver Island since no additional coastal refinement was added. Despite the fact that very little coastal refinement was added

in the Southeast Alaska region, there are significant error reductions at these stations (Figure A12). Meanwhile, the Southern Alaska coast, which had few improvements in coastal resolution but several bathymetry corrections in this latest database, has minor amplitude improvement. Note that the results along the Alaskan coast are largely independent of the friction scheme, except for the shallower areas (station 117 in Figure A13).

A comparison of constituent RMS errors by region are shown in Figure 9, while mean absolute phase errors and mean relative amplitude errors are provided in Table 7. Looking primarily at the 165 validation stations that are common to both databases (blue diamonds for ENPAC03 and red circles for ENPAC15), we can draw several general conclusions.

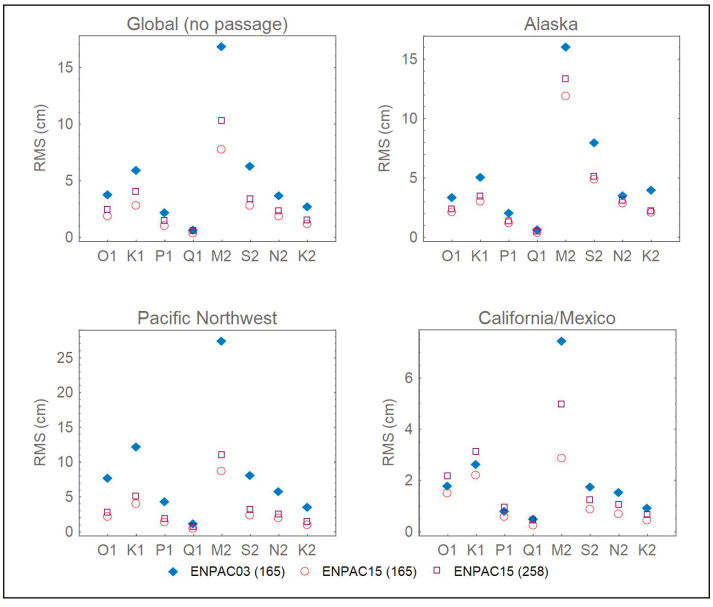

Figure 9. Mean root mean square errors (cm) in harmonic constituents for the ENPAC03 and ENPAC15 ADCIRC tidal databases for each region of the ENPAC model domain (note that the scale is not the same for each region).

- Globally, the greatest improvement in the RMS error is realized for the M_2 constituent (9 cm reduction) and the average reduction is 2.8 cm. Reductions in absolute phase errors range from 4° for the K_1 constituent to 13° for the S_2 constituent, with an average reduction of 8° over all of the constituents. Meanwhile, reductions in mean relative amplitude errors range from 3% for the O_1 constituent to 17% for the K_2 constituent, with an average reduction of 7%. For all error measures, the largest reductions were realized for the semi-diurnal constituents.
- For the Alaskan region, the reductions in RMS errors range from 0.2 cm for the Q_1 constituent to 3.7 cm for M_2, with an average reduction of 1.6 cm. Reduction in absolute phase errors ranged from 1.2° for the M_2 constituent to 6.7° for the K_2 constituent, with an average of 3.5° for all constituents, while the relative amplitude error reductions ranged from about 2% for Q_1 to 20% for K_2, with an average of 6%. In general, the largest amplitude reductions were realized for the semi-diurnal constituents, but the phase errors improved most for the diurnal constituents.
- The greatest improvement was realized in the Pacific Northwest region. Mean RMS error reductions ranged from 0.6 cm for Q_1 to 18.7 cm for M_2, with an average improvement of 6 cm. Meanwhile, the range of mean absolute phase error improvements varies from 8° for K_1 to 37° for K_2, with an average improvement of 21°; and the relative amplitude improvements range

from 7% for P_1 to 29% for K_2, with an average of 13% overall improvement. The semi-diurnal constituents realize the greatest overall improvement in amplitude and phase.

- In the California and Mexico region, moderate improvements are realized; the mean RMS errors improve by 0.2 cm for Q_1 to 4.6 cm for M_2, with an average of 1 cm. Similarly, improvements in the mean absolute phase errors range from 0° for K_1 to 6.2° for K_2, with an average improvement of 2.6°, while improvements in the relative amplitude errors range from 0.6% for O_1 to about 8% for Q_1, with an average improvement of 4% overall. Again, the semi-diurnal constituents realize the greatest overall improvement in amplitude and phase.

Table 7. Comparison of mean relative amplitude (%) and mean absolute phase errors (deg) by region for each of the eight primary harmonic constituents and summed over all 8 constituents for the ENPAC03 (2003) and ENPAC15 (2015) tidal databases: only the 179 wet validation stations are used in the summations.

Mean Relative Amplitude Errors (%)								
	Global (No Passage)		**Alaskan Coast**		**Pacific Northwest**		**California/Mexico**	
	2003	2015	2003	2015	2003	2015	2003	2015
O1	9.68	6.41	8.51	6.55	17.30	5.13	8.60	7.96
K1	10.84	4.93	9.32	4.65	17.10	4.20	9.27	6.94
P1	9.58	5.75	8.44	5.04	14.14	6.77	7.70	5.04
Q1	11.13	7.47	7.56	5.82	18.57	9.27	14.10	6.54
M2	12.49	5.85	10.71	4.73	20.67	10.66	11.07	5.07
S2	16.24	6.93	13.76	6.36	26.54	11.25	11.15	5.62
N2	12.94	6.68	11.37	6.61	21.26	10.45	9.24	5.22
K2	26.10	9.05	26.21	6.44	44.87	15.82	14.00	9.34
All 8	13.64	6.62	11.98	5.78	22.61	9.18	10.61	6.47
Mean Absolute Phase Errors (deg)								
	Global (no Passage)		**Alaskan Coast**		**Pacific Northwest**		**California/Mexico**	
	2003	2015	2003	2015	2003	2015	2003	2015
O1	10.45	3.32	7.91	3.71	21.44	3.85	3.87	2.62
K1	7.13	3.31	7.78	3.85	12.21	4.33	2.30	2.30
P1	9.06	4.05	8.76	5.03	16.77	4.38	3.45	2.78
Q1	13.79	9.36	20.77	16.73	16.22	4.50	4.74	3.46
M2	13.33	3.82	5.90	4.75	29.71	4.16	6.30	2.21
S2	17.00	4.24	8.14	5.46	35.57	4.04	5.69	2.64
N2	13.64	4.60	7.24	5.40	25.62	4.72	7.44	3.21
K2	20.94	8.11	17.97	11.27	44.86	7.95	11.16	4.96
All 8	13.15	5.05	10.54	7.01	25.46	4.74	5.63	3.02

Finally, it is also instructive to see if there are sub-regional patterns in the errors (at the individual water body scale), which can help to guide future efforts at improving the tidal database. Plots of relative amplitude and absolute phase errors for the dominant M_2 constituent at each of the 258 stations are provided for the global domain for the ENPAC15 model in Figure 10 in the text, while zoomed views of the smaller sub-regions are provided in Figures A15–A25 in Appendix D (the same zoom views given in Appendix A). For this study area, the M_2 constituent is dominant for all regions except the inside passages north of Vancouver Island and Puget Sound, where the K_1 constituent is of similar magnitude in some areas. Therefore, error plots for the K_1 constituent are also provided for the Puget Sound sub region (Figure A20) and the Vancouver Island sub region (Figure A22). Points shown in blue are underestimating the amplitudes (or exhibit a phase lag), while points shown in red are overestimating (exhibit a phase lead). The symbol shapes indicate to what degree the model is over/under estimating; we would like to see amplitude errors less than 10% and phase errors less than

20°. Unless specifically noted, all subsequent comments refer to the M_2 constituent. Several general trends can be gleaned from these plots.

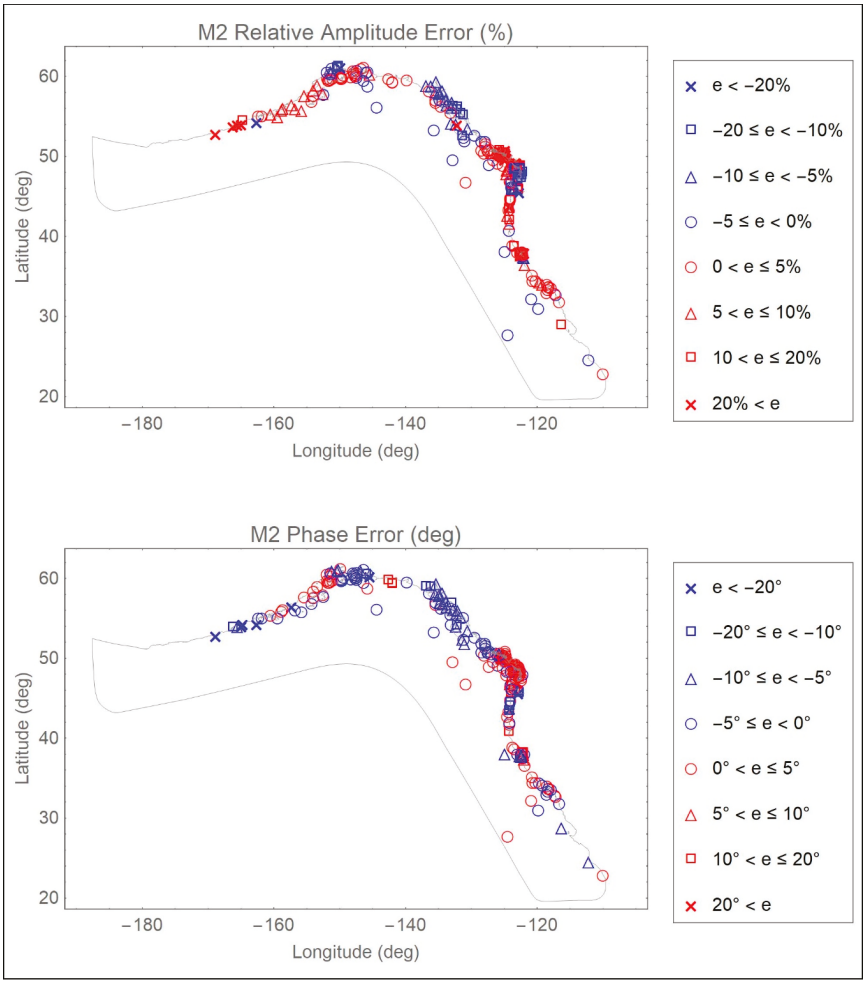

Figure 10. Relative amplitude (%) and absolute phase errors (deg) in the M_2 constituent at each of the 258 global validation stations for the ENPAC15 database. Zoomed views are provided in Appendix D.

- For Southern California, the ENPAC15 database is slightly overestimating the amplitude (generally within 5%) and phases are within ±5° from the data. Meanwhile, in San Francisco Bay, the database is more significantly overestimating the amplitudes, with the exception of the lower bay are where the data is underestimated; and the phases are generally within ±5° to 10°. This indicates the need to verify the bathymetry in this area and try a variable friction representation. Finally, along the Northern California coast, the amplitudes are overestimated by a more significant amount (over 20% for some stations), but the phases are generally within ±5°.
- Along the Oregon and Washington coast, generally, the amplitudes are underestimated and the phases are within ±5°. However, the further upriver stations in the Columbia River have higher errors, which may be indicative of the boundary being placed within the tidally influenced zone

that is not being captured with the boundary condition at the end of the river, as well as the lack of freshwater inflow at the boundary.

- In the Puget Sound region, it is interesting that the M_2 amplitudes are significantly overestimated (greater than 20%) in the channels heading east above Vancouver Island but are underestimated by 5–10% in the lower Puget Sound region; meanwhile, the phases exhibit a lead throughout much of this region (ranging from 5–20°). While the K_1 amplitudes exhibit the same over/under regional trend, they are generally within 5% of the data; however, the phases exhibit a more conservative lag (5–10°) instead of a lead as compared to M_2 constituent. Similarly in the Canadian waters above Vancouver Island, the M_2 constituent is significantly overestimated (greater than 20%) in the interior passages but is more conservatively overestimated (0–10%) as you enter Queen Charlotte Strait to the east, while the interior passages exhibit slight phase leads and the easternmost parts of the channels slight phase lags (±5°). Meanwhile, the K_1 constituent exhibits moderate amplitude overestimation of 0–10% and phase lags of 0–10°. For the region above Vancouver Island, it is important to note that the freshwater riverine flow can be significant in many of these channels, but it is neglected in our model. This neglegance has an impact on the accuracy of the tidal signal as you progress further up the channels.
- Along the southeast coast of Alaska, the amplitudes are underestimated by 5–20% in the interior passages and slightly overestimated (less than 5%) on the exterior coast, while the phases exhibit lags from 5 to 20°. Meanwhile, along the southern Alaskan coast, there is generally very good agreement for both amplitudes and phases (within ±5% or 5°), with the exception of the upper reaches of Cook Inlet, where amplitudes are underestimated up to 20%. Recall that the entire Alaskan coast received only minor bathymetric and coastline alignment updates, so we would not expect significant improvements. As you progress further west along the coast (past about 153° W), the amplitudes are more severely overestimated starting at 5% and going above 20% as you approach the boundary of the model, but the phase remains in good agreement until you pass 162° W. Recall that the coastline past Unimak Island is defined by a mainland boundary condition and does not include the interaction with the Bering Sea through the Aleutian Islands; therefore, we would not expect good agreement past 165° W.

4. Discussion

Table 8 provides a summary of the global RMS errors for the eight primary constituents, as well as the mean regional errors summed over these constituents (graphically presented in Figure 7), for each of the eight model simulations done as part of this study (statistics computed using only the 165 common validation data points). Returning to the six improvements (presented in Section 2.2) that were implemented to meet the objective of reducing the errors realized in the ENPAC03 database, we note the following:

- The placement of the open ocean boundary itself results in significant improvements for all regions (ENPAC03R vs. ESTOFS-trim1): global improvement of 33%. As was seen in previous databases for the ENPAC region, the location of the open ocean boundary can have significant impact on the accuracy of the interior model. However, as the ESTOFS-trim model incorporates newer bathymetry and has different resolution throughout, it is impossible to separate the effects of boundary placement, coarser mesh resolution at the boundary and updated deep water bathymetry when determining the source of these noted improvements.
- The improvements in coastal resolution (ESTOFS-trim1 vs. ENPAC15-CF) result in significant reductions in error for the Pacific Northwest region (38%), but no measurable change in the Alaska and California regions: global reduction of 22%. Recall that the coast of Alaska was not updated, as the VDatum project for that region is still ongoing. Furthermore, examination of individual station scatterplots for the California region indicate that some significant improvements are realized in the San Francisco Bay area but not in the open ocean coastal stations. The Pacific Northwest improvements are most likely attributable to the inclusion of the passages north of Vancouver Island.

- Meanwhile, the updated boundary forcing (ENPAC03 vs. ENPAC03R) slightly increases the mean RMS errors for some constituents (K_1, M_2) while decreasing others (S_2 and K_2). Comparison of the along boundary forcing values applied from the TPXO6 and TPXO8 products indicate only minor changes in amplitudes and no changes in applied phases near the westernmost ocean boundary (near Alaska) and no changes elsewhere. Therefore, the changes between the resulting harmonics are more than likely due to the addition of the long-term constituents in the forcing suite; recall that the ENPAC database was only forced with the diurnal and semi-diurnal constituents. However, there is very little change noted when results are compared for the TPXO8 (ESTOFS-trim1) and FES12 (ESTOFS-trim6) forcing.
- In general, the use of a variable bottom friction scheme (ENPAC15-Mann) results in lower error metrics than when a constant value is used (ENPAC15-CF), for all constituents and regions. However, the same effect can also be attained by using a slightly higher constant value (ENPAC15-Vdat). Therefore, more work needs to be done in determining appropriate variable values and comparing scatterplots by station instead of just regionally, in order to decide which scheme is best. Ideally, each sub region would be carefully calibrated taking into consideration actual bed formations and sea bed materials.
- The inclusion of the advective terms in the governing equations (ESTOFS-trim1 vs. ESTOFS-trim2), most notably, results in improvements in the Pacific Northwest region (14%) and particularly the M_2 and K_1 constituents. This is to be expected as the passages north of Vancouver Island are known to dissipate a great deal of internal energy. Further work must be done to stabilize these passages so that the advective terms can be utilized in the next tidal database release.
- The overall error reductions due to the combined effects of all five improvements (no advection) that were used in the latest database (ENPAC15-VDat vs. ENPAC03) are as follows: the global errors are reduced by 52%; while the regional errors are reduced by 33% in Alaska, 68% in the Pacific Northwest and 45% in California. Users of ENPAC15 can expect greater accuracy in any localized region where they apply boundary conditions, but particularly in the Pacific Northwest.

These results indicate that most of the reduction in harmonic constituent errors are due to the increased coastal resolution and updated bathymetry, as well as the actual placement of the boundary itself. Furthermore, the addition of the advective terms would improve the results in the Pacific Northwest region, if the model was to remain stable. On average, very little overall improvement was realized solely from the bottom friction representation; however, the friction contributes to localized effects on the harmonic accuracy and it is important to have an accurate representation of the bottom friction in the shallower regions. Finally, the updated ocean boundary forcing does not have a large effect on the overall accuracy.

To put these errors in context, the mean RMS error (summed over all eight primary constituents) between the three data sets (CO-OPS, IOS-FOC and IHO) was computed at the 61 stations that were duplicated in any two data sets. The mean error for all 61 stations was 1.1 cm, while the minimum and maximum error over all stations were 0.01 cm and 7.6 cm, respectively. Therefore, on average, one could expect the data itself to be in error by about 1 cm at a given station, which accounts for about 20% of the global RMS errors reported for the ENPAC03 model in Table 8, about 30% of the ESTOFS-trim models and 40% of the error for the ENPAC15 models. The error measures reported throughout the paper include these errors in the data; thus, a significant portion of the reported errors may stem from the uncertainty in the data itself.

Future improvements to the ENPAC tidal database should include updated resolution and bathymetry for the Alaskan coastal waters and could include better bottom friction representations in individual water bodies that have not been optimized (e.g., San Francisco Bay, Puget Sound, the inside passages north of Vancouver Island and in southeast Alaska and Cook Inlet). Additionally, for the database to be valid west of the old ENPAC03 model domain, a more accurate representation of the Aleutian Island chain and the connection to the Bering Sea would be necessary. It could also be

informative to use a mesh with coarser coastal resolution, such as ESTOFS-trim, to further explore the effects of boundary location on the accuracy of the tidal harmonics.

It is important to note that the simulation used to compute the ENPAC15 database does not include all physical processes which can affect the model response including (but not limited to) density driven flows, riverine discharge, sediment transport and resulting bed morphological changes, large-scale oceanic currents or wind and atmospheric pressure driven flows. To minimize the effects of these limitations, it is recommended that users of the ENPAC15 tidal database follow three basic guidelines: (1) choose your regional open ocean boundary location to be well outside of estuaries and bays; (2) make sure that your regional model bathymetry matches the database bathymetry at your boundary and (3) do not extract any data west of the old ENPAC03 model domain (near 160° W) as the Aleutian Island chain is treated as a mainland boundary and results are not accurate past this point. Additionally, while harmonic information is available for 37 constituents, use caution when applying larger suites as only eight have been validated. For the interested reader, further guidelines and limitations are provided in Appendix E. The ENPAC15 tidal database is available on the ADCIRC website [59].

Table 8. Summary of RMS errors (cm) for the 165 common validation stations: global means for the 8 primary constituents and regional means summed over all eight primary harmonic constituents.

Mean Global Constituent RMS Errors (cm)								
Run Designation	**O1**	**K1**	**P1**	**Q1**	**M2**	**S2**	**N2**	**K2**
ENPAC03	3.83	5.98	2.22	0.70	16.90	6.33	3.72	2.75
ENPAC03R	3.77	6.12	2.21	0.65	18.03	5.92	3.85	2.07
ESTOFS-trim1	2.83	4.70	1.53	0.47	11.09	3.77	2.47	1.47
ESTOFS-trim2	2.60	4.27	1.36	0.42	10.29	3.41	2.25	1.43
ESTOFS-trim6	2.99	4.52	1.47	0.59	11.16	3.73	2.50	1.54
ENPAC15-CF	2.26	3.56	1.16	0.41	8.42	2.94	1.89	1.36
ENPAC15-Vdat	1.94	2.87	1.09	0.45	7.80	2.86	1.95	1.24
ENPAC15-Mann	2.16	3.30	1.08	0.41	7.71	2.75	1.79	1.28

Mean Regional RMS Errors (cm)				
Run Designation	**Global**	**Alaska**	**Pacific Northwest**	**California and Mexico**
ENPAC03	5.36	5.39	9.03	2.21
ENPAC03R	5.39	4.97	9.47	2.36
ESTOFS-trim1	3.58	3.46	6.40	1.49
ESTOFS-trim2	3.29	3.34	5.48	1.52
ESTOFS-trim6	3.60	3.43	6.35	1.63
ENPAC15-CF	2.78	3.40	3.94	1.49
ENPAC15-Vdat	2.55	3.62	2.91	1.22
ENPAC15-Mann	2.59	3.45	3.21	1.34

Author Contributions: Conceptualization, R.K. and T.C.M.; Data Curation, C.S.; Formal Analysis, C.S.; Funding Acquisition, T.C.M.; Investigation, C.S.; Methodology, C.S.; Project Administration, R.K.; Resources, R.K. and T.C.M.; Software, C.S. and K.D.; Supervision, K.D. and T.C.M.; Validation, C.S.; Visualization, C.S.; Writing—Original Draft, C.S.; Writing—Review and Editing, C.S., K.D., R.K. and T.C.M.

Funding: This research was funded by the Institute of Water Resources and the Engineer Research and Development Center | U.S. Army Corps of Engineers BAA 12-5008 under contract W912HZ-13-P-0046. Additional resources were provided by the University of Oklahoma. Any opinions, conclusions, or findings are those of the authors and are not necessarily endorsed by the funding agencies.

Acknowledgments: The computing for this project was performed at the OU Supercomputing Center for Education and Research (OSCER) at the University of Oklahoma (OU). The authors would also like to acknowledge Mike Foreman at IOS-FOC for providing model domains and validation data for the areas covering British Columbia, as well as Pete Bacopoulos for creating the LTEA mesh for the Vancouver Island region. Finally, the authors acknowledge the assistance of Jiangtao Xu, Edward Myers and Jesse Feyen (among others) at NOAA for providing a summary of harmonic validation data for all stations currently covered by CO-OPS, VDatum models and input files for the US West Coast, the ESTOFS-Pacific operational mesh for the West Coast of the United States, and for assisting in extracting input data from the FES12 global database. Figures 1–6 were generated using a modified version of FigureGen [14]. The authors also thank the reviewers for providing constructive comments to improve the presentation of the paper.

Conflicts of Interest: The authors declare no conflict of interest. T.M. as a representative of the funding sponsor was involved in designing the study and reviewing the final product. The funders had no role in the collection, analyses, or interpretation of data; in the writing of the manuscript; or in the decision to publish the results.

Appendix A

The locations of the 258 validation stations are plotted with the model domain boundaries shown for the ENPAC03 (green) and ENPAC15 (gray) databases. Each figure in this Appendix zooms into a specific sub-region of the ENPAC domain in order to show the details of the coastline near the stations. Stations indicated with a black X designate those which scatter plots are provided for in Appendix C and the numbers correspond to the list of stations provided in Appendix B. The three data sources are indicated by color as follows: CO-OPS in blue, IOS-FOC in red and IHO in magenta. Furthermore, those stations that are dry in the ENPAC03 database, and will not be used for comparison with other models, are indicated with a cyan circle around the station point.

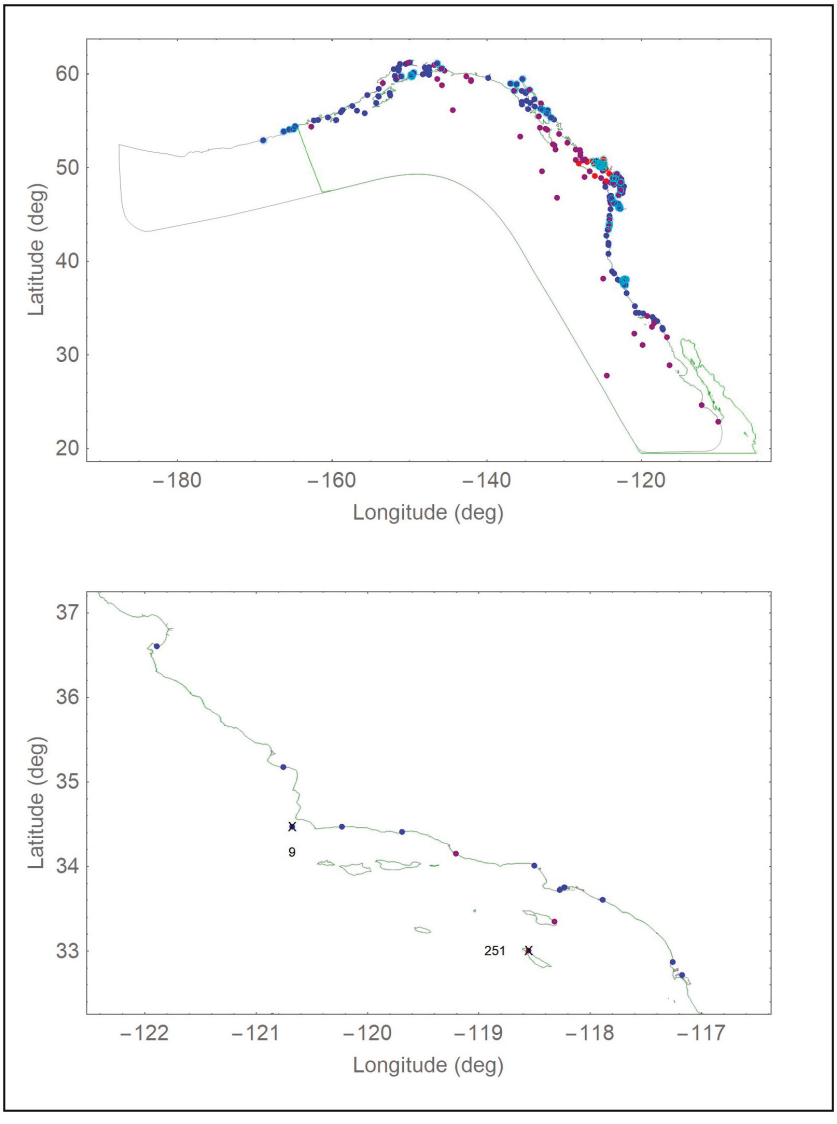

Figure A1. Location of validation stations: global and Southern California.

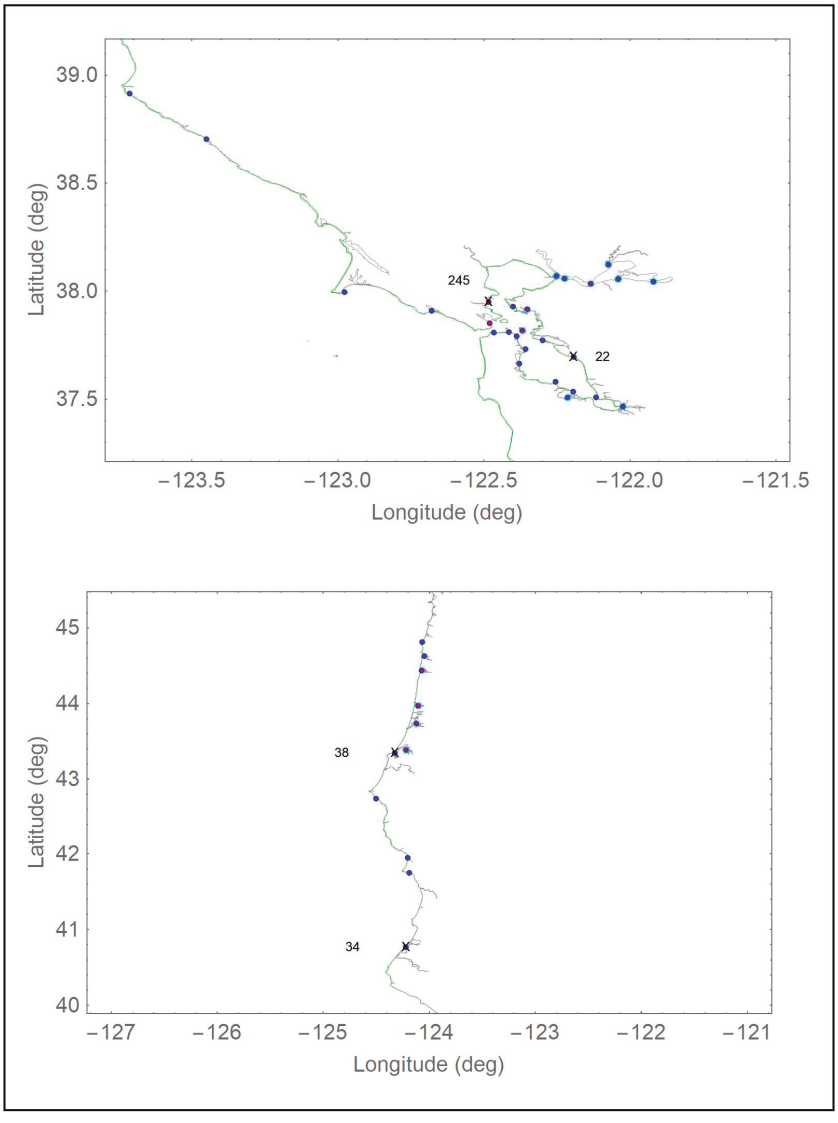

Figure A2. Location of validation stations: San Francisco Bay and Northern California.

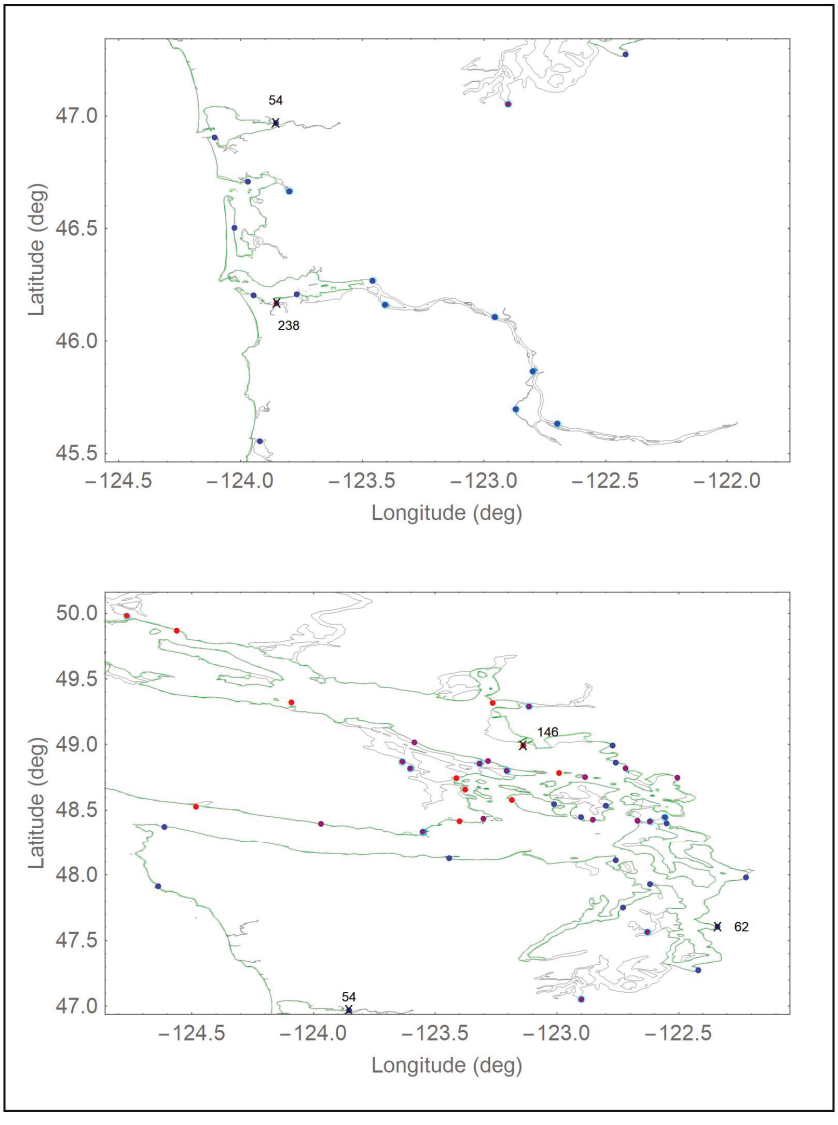

Figure A3. Location of validation stations: Columbia River and Puget Sound.

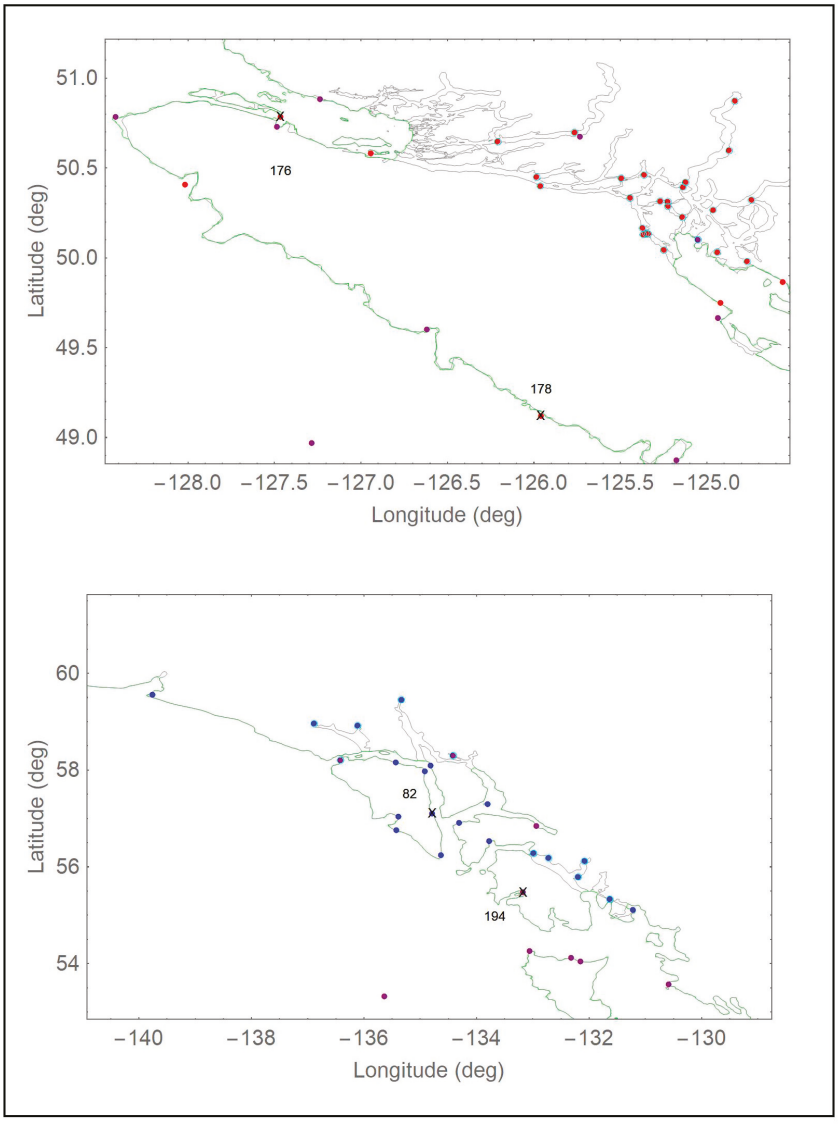

Figure A4. Location of validation stations: British Columbia and Southeast Alaska.

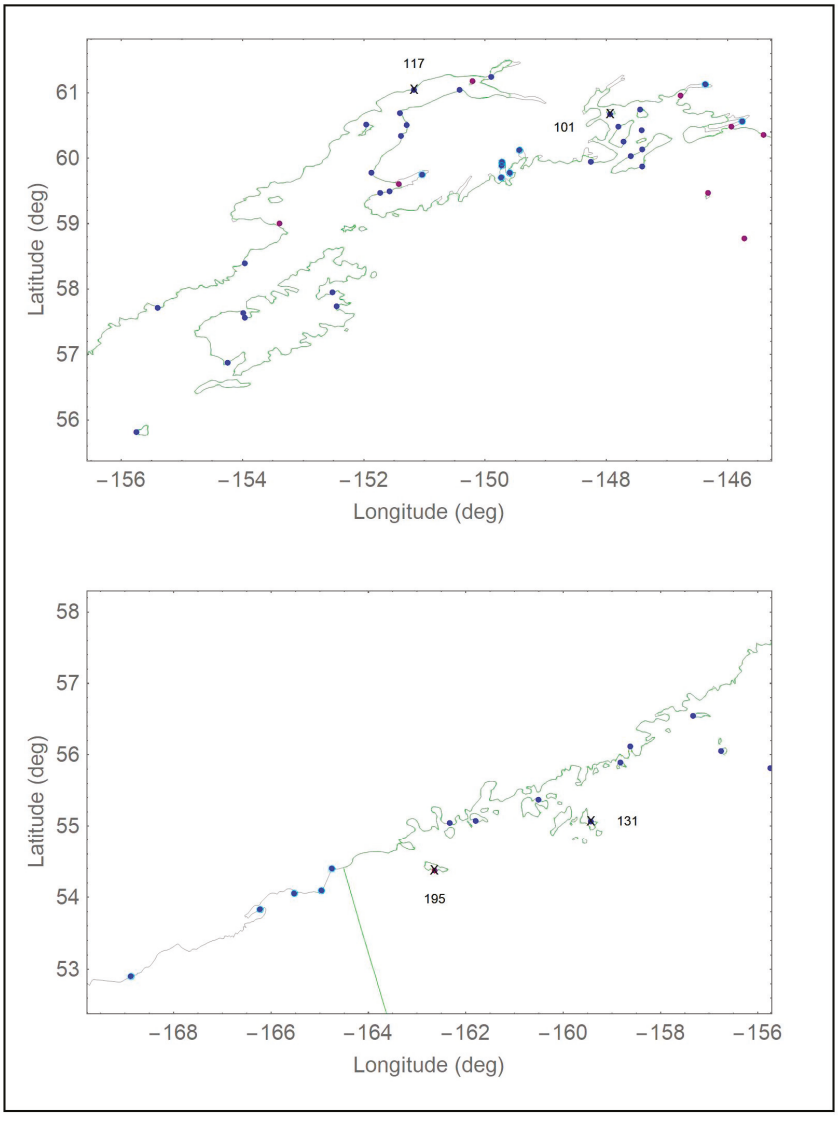

Figure A5. Location of validation stations: South Alaska.

Appendix B

The locations, names and regional classification of all 258 validation stations are given herein. For the first 139 stations, the official CO-OPS station number is provided in the source designation column, while IOS-FOC is used to designate those stations from the Institute of Ocean Sciences—Fisheries and Oceans Canada and IHO to designate the historical stations from the International Hydrographic Organization. Stations marked with a single asterisk are considered wet in the ENPAC03 model even though they are approximated by their nearest neighbor (actual longitude and latitude coordinates were not shifted when extracting from the ENPAC03 database, as the nearest element is most likely where the station would have been manually shifted anyway). Meanwhile, those marked with a double asterisk are not included in

scatter plots or statistical error metrics for the ENPAC03 database since they are well outside the domain of the boundary or are in channels and other features that are not represented in the ENPAC03 model domain. Abbreviations for the region designations are as follows: Alaska—AK, British Columbia—BC, Washington—WA, Oregon—OR, California—CA, Mexico—MX, and deep water—D. Note that for statistics, the British Columbia, Washington and Oregon stations were grouped into a single Pacific Northwest category; however, they are listed separately for interested readers. Similarly, the California and Mexico stations were grouped into a single category for statistical analysis.

Table A1. Location and source information for validation data. For the first 139 stations, the number in the Source column is the CO-OPS station identifier.

Station	Longitude	Latitude	Station Name	Region	Source
1 *	−117.17360	32.71400	San Diego, San Diego Bay	CA	9410170
2	−117.25800	32.86670	La Jolla, Pacific Ocean	CA	9410230
3 *	−117.88300	33.60330	Newport Beach, Newport Bay Ent	CA	9410580
4 *	−118.27200	33.72000	Los Angeles, Outer Harbor	CA	9410660
5 *	−118.22700	33.75170	Long Beach, Terminal Island	CA	9410680
6 *	−118.50000	34.00830	Santa Monica, Pacific Ocean	CA	9410840
7	−119.68501	34.40830	Santa Barbara, Pacific Ocean	CA	9411340
8 *	−120.22831	34.46939	Gaviota State Park, Pacific Ocean	CA	9411399
9	−120.67300	34.46830	Oil Platform Harvest (Topex)	CA	9411406
10 *	−120.76000	35.17670	Port San Luis, San Luis Obispo	CA	9412110
11 *	−121.88800	36.60500	Monterey, Monterey Harbor	CA	9413450
12 *	−122.46500	37.80669	San Francisco, San Francisco Bay	CA	9414290
13 *	−122.41300	37.81000	North Point [Pier 41] S.F.Bay	CA	9414305
14 *	−122.38698	37.79002	Pier 22 1/2, San Francisco Bay	CA	9414317
15	−122.35700	37.73000	Hunters Point, S.F. Bay	CA	9414358
16	−122.37700	37.66500	Oyster Point Marina, S.F. Bay	CA	9414392
17	−122.25300	37.58000	San Mateo Bridge, West Side	CA	9414458
18	−122.19300	37.53330	Redwood Creek, C.M. No. 8,S.F.B	CA	9414501
19	−122.11500	37.50670	Dumbarton Bridge, S. F. Bay	CA	9414509
20 **	−122.21200	37.50670	Redwood City, Wharf 5, S.F. Bay	CA	9414523
21 **	−122.02300	37.46500	Coyote Creek, Alviso Slough	CA	9414575
22 *	−122.19200	37.69500	San Leandro Marina, S.F.Bay	CA	9414688
23	−122.29833	37.77167	Alameda, San Francisco Bay	CA	9414750
24	−122.40000	37.92830	Richmond, Chevron Oil Pier	CA	9414863
25 **	−121.91800	38.04330	Mallard Island, Suisun Bay	CA	9415112
26 **	−122.22300	38.05830	Crockett, Carquinez Strait	CA	9415143
27 **	−122.03950	38.05600	Port Chicago, Suisun Bay	CA	9415144
28 **	−122.25000	38.07000	Mare Is.Naval Shipyard, Carquin	CA	9415218
29 **	−122.07300	38.12323	Suisun Slough Entrance	CA	9415265
30 *	−122.67854	37.90871	Bolinas, Bolinas Lagoon	CA	9414958
31 *	−122.97670	37.99610	Point Reyes, Drakes Bay	CA	9415020
32	−123.44940	38.70329	Green Cove, Pacific Ocean	CA	9416409
33 *	−123.71061	38.91330	Arena Cove, Pacific Ocean	CA	9416841
34 *	−124.21700	40.76670	North Spit, Humboldt Bay	CA	9418767
35	−124.18300	41.74500	Crescent City, Pacific Ocean	CA	9419750
36 *	−124.20092	41.94525	Pyramid Point, Smith River	CA	9419945
37	−124.49828	42.73897	Port Orford, Pacific Ocean	OR	9431647
38 *	−124.32200	43.34500	Charleston, Coos Bay	OR	9432780
39 *	−124.04300	44.62500	South Beach, Yaquina River	OR	9435380
40 *	−124.06300	44.81000	Depoe Bay	OR	9435827
41 *	−123.91894	45.55453	Garibaldi, Tillamook Bay	OR	9437540
42 *	−123.94500	46.20170	Hammond, Columbia River	OR	9439011
43 *	−123.76831	46.20731	Astoria, Tongue Point, Columbia	OR	9439040
44 **	−123.40500	46.16000	Wauna, Columbia River	OR	9439099
45 **	−122.86800	45.69670	Rocky Point, Multnomah Channel	OR	9439189
46 **	−122.79700	45.86500	St. Helens, Columbia River	OR	9439201

Table A1. *Cont.*

Station	Longitude	Latitude	Station Name	Region	Source
47 **	−122.69704	45.63158	Vancouver, Columbia River	WA	9440083
48 **	−122.95420	46.10559	Longview, Columbia River	WA	9440422
49 **	−123.45602	46.26707	Skamokawa, Columbia River	WA	9440569
50	−124.02300	46.50170	Nahcotta, Willapa Bay	WA	9440747
51 **	−123.79800	46.66404	South Bend	WA	9440875
52 *	−123.96692	46.70746	Toke Point, Willapa Bay	WA	9440910
53 *	−124.10508	46.90431	Westport, Grays Harbor	WA	9441102
54 *	−123.85300	46.96830	Aberdeen, Grays Harbor	WA	9441187
55 *	−124.63700	47.91330	La Push, Quillayute River	WA	9442396
56	−124.61170	48.37081	Neah Bay, Strait of Juan De Fuca	WA	9443090
57 *	−123.44000	48.12500	Port Angeles, Juan De Fuca	WA	9444090
58	−122.75800	48.11170	Port Townsend, Admiralty Inlet	WA	9444900
59	−122.61700	47.92670	Foulweather Bluff, Twin Spits	WA	9445016
60 *	−122.72700	47.74830	Bangor	WA	9445133
61 *	−122.41670	47.27120	Tacoma, Commencement Bay	WA	9446484
62 *	−122.33931	47.60264	Seattle, Puget Sound	WA	9447130
63 *	−122.22300	47.98000	Everett	WA	9447659
64	−122.54800	48.40000	Sneeoosh Point, Skagit Bay	WA	9448576
65 **	−122.55500	48.44500	Turner Bay, Similk Bay	WA	9448657
66	−122.75800	48.86330	Cherry Point, Strait of Georgia	WA	9449424
67 *	−122.76900	48.99227	Blaine, Drayton Harbor	WA	9449679
68 *	−123.00980	48.54580	Friday Harbor, San Juan Channel	WA	9449880
69 *	−122.79700	48.53500	Armitage Island	WA	9449932
70 *	−122.90000	48.44670	Richardson, Lopez Island	WA	9449982
71 *	−131.21900	55.10280	Custom House Cove, Mary Island	AK	9450296
72 **	−131.62619	55.33183	Ketchikan, Tongass Narrows	AK	9450460
73 **	−132.19088	55.78828	Magnetic Point, Union Bay	AK	9450753
74 **	−132.07650	56.11512	Thoms Point, Zimovia Strait	AK	9450970
75 **	−132.71750	56.17830	Point Harrington, Clarence Strait	AK	9451005
76 **	−132.98500	56.27670	Bushy Island, Snow Passage	AK	9451074
77	−133.76610	56.52760	Monte Carlo Island	AK	9451247
78	−134.62713	56.23934	Port Alexander, Baranof Island	AK	9451054
79	−135.41829	56.75322	Golf Island, Necker Islands	AK	9451421
80	−134.30400	56.90856	Saginaw Bay, Kuiu Island	AK	9451497
81	−135.38450	57.03000	Sitka, Baronof Island, Sitka Sound	AK	9451600
82	−134.77960	57.09860	Baranof, Warm Spring Bay	AK	9451625
83 *	−133.79700	57.29500	The Brothers, Stephens Passage	AK	9451785
84 **	−134.41200	58.29818	Juneau, Gastineau Channel	AK	9452210
85 *	−134.80600	58.08410	Hawk Inlet Entrance	AK	9452294
86	−134.91580	57.96780	False Bay, Chatham Strait	AK	9452328
87 **	−135.32880	59.44960	Skagway, Taiya Inlet	AK	9452400
88	−135.43190	58.15240	Hoonah	AK	9452438
89 **	−136.10800	58.91330	Muir Inlet, Glacier Bay	AK	9452584
90 **	−136.88110	58.95960	Tarr Inlet	AK	9452749
91 *	−139.74890	59.54850	Yakutat, Yakutat Bay	AK	9453220
92 **	−145.75300	60.55830	Cordova, Orca Inlet, Pr William Sd	AK	9454050
93 **	−146.36200	61.12360	Valdez, Prince William Sound	AK	9454240
94	−147.40050	60.13250	Perch Point, Montague Island	AK	9454561
95 *	−147.39840	59.87220	Wooded Island	AK	9454562
96	−147.41000	60.42500	Seal Island	AK	9454564
97 *	−147.43700	60.73670	Storey Island North Side	AK	9454571
98	−147.59300	60.02800	Montague Island, Ne Bazel Pt	AK	9454616
99 *	−147.70950	60.24760	Snug Harbor, Knight Island	AK	9454662
100 *	−147.79270	60.47560	Herring Point, Knight Island,	AK	9454691
101 *	−147.93200	60.66910	Perry Island (South Bay)	AK	9454721
102 *	−148.24540	59.94370	Point Erlington, Erlington Island	AK	9454814
103 **	−149.42667	60.12000	Seward, Resurrection Bay	AK	9455090
104 **	−149.58630	59.77430	Agnes Cove	AK	9455120

Table A1. *Cont.*

Station	Longitude	Latitude	Station Name	Region	Source
105 **	−149.71340	59.94060	Aialik Bay, North End	AK	9455145
106 **	−149.71800	59.88500	Aialik Sill, Aialik Bay	AK	9455146
107 **	−149.72500	59.70240	Camp Cove, Harris Penninsula	AK	9455151
108 *	−151.71990	59.46400	Seldovia, Cook Inlet	AK	9455500
109	−151.56500	59.49150	Kasitsna Bay, Kachemak Bay	AK	9455517
110 **	−151.03000	59.74400	Bear Cove, Kachemak Bay	AK	9455595
111	−151.86703	59.77197	Anchor Point	AK	9455606
112 *	−151.38240	60.33670	Cape Kasilof, Cook Inlet	AK	9455711
113 *	−151.95200	60.51170	Kaligan Island, Cook Inlet	AK	9455732
114	−151.28470	60.50330	Chinulna Point, Cook Inlet	AK	9455735
115 *	−151.39800	60.68330	Nikiski, Cook Inlet	AK	9455760
116	−150.41300	61.03670	Point Possession (T-39, Opr-469)	AK	9455866
117	−151.16300	61.04331	North Foreland	AK	9455869
118	−149.89180	61.24010	Anchorage, Knik Arm, Cook Inlet	AK	9455920
119 *	−153.95800	58.39170	Nukshak Island, Shelikof Strait	AK	9456717
120 *	−152.51090	57.94530	Ouzinkie	AK	9457287
121 *	−152.43930	57.73170	Kodiak Island, Womens Bay	AK	9457292
122	−153.95800	57.56340	Larsen Bay, Kodiak Island	AK	9457724
123 *	−153.98280	57.63500	Uyak (Cannery Dock), Uyak Bay	AK	9457728
124 *	−154.23530	56.87600	Alitak, Lazy Bay	AK	9457804
125	−155.39300	57.70670	Puale Bay	AK	9458209
126	−155.74000	55.80830	Chirikof Island, Sw Anchorage	AK	9458293
127 *	−156.74550	56.05170	Chowiet Island, Semidi Island	AK	9458519
128	−157.32760	56.54120	West End, Sutwik Island	AK	9458665
129	−158.61160	56.11330	Hump Island, Kuiukta Bay	AK	9458964
130 *	−158.82000	55.89030	Mitrofania Island	AK	9459016
131 *	−159.41870	55.06730	Herendeen Island, Shumagin	AK	9459163
132	−160.50200	55.36600	Sand Point, Popof Island	AK	9459450
133	−161.79200	55.07320	Dolgoi Harbor, Dolgoi Island	AK	9459758
134	−162.32700	55.03890	King Cove, Deer Passage, Pacific	AK	9459881
135 **	−164.74572	54.39364	Scotch Cap, Unimak Island	AK	9462808
136 **	−164.95370	54.09160	Tigalda Bay, Tigalda Island	AK	9462782
137 **	−165.51417	54.05222	Rootok Island, Rootok Strait	AK	9462723
138 **	−166.21625	53.82892	Biorka Village, Beaver Inlet	AK	9462645
139 **	−168.87130	52.90130	Nikolski	AK	9462450
140	−124.48200	48.52500	Port Renfrew	BC	IOS-FOC
141	−123.39900	48.41300	Victoria Harbour	BC	IOS-FOC
142	−123.18300	48.57700	Hanbury Point	BC	IOS-FOC
143	−123.37400	48.65600	Sidney	BC	IOS-FOC
144	−123.41100	48.74400	Fulford Harbour	BC	IOS-FOC
145	−122.98900	48.78200	Patos Island	BC	IOS-FOC
146	−123.13700	48.99100	Tsawwassen	BC	IOS-FOC
147	−123.26300	49.31700	Point Atkinson	BC	IOS-FOC
148	−124.08900	49.31900	Winchelsea Islands	BC	IOS-FOC
149	−124.55960	49.86450	Powell River	BC	IOS-FOC
150	−124.91820	49.74880	Little River	BC	IOS-FOC
151 **	−124.76550	49.97900	Lund	BC	IOS-FOC
152 **	−124.93720	50.02990	Twin Islands	BC	IOS-FOC
153 **	−124.73990	50.32120	Channel Islands	BC	IOS-FOC
154 **	−124.96110	50.26480	Redonda Bay	BC	IOS-FOC
155 **	−125.24650	50.04300	Campbell River	BC	IOS-FOC
156 **	−125.33670	50.13330	Maude Island East	BC	IOS-FOC
157 **	−125.36330	50.12830	Nymphe Cove	BC	IOS-FOC
158 **	−125.34790	50.13540	Seymour Narrows	BC	IOS-FOC
159 **	−125.36870	50.16460	Brown Bay	BC	IOS-FOC
160 **	−125.13930	50.22560	Welsford Island	BC	IOS-FOC
161 **	−125.22280	50.28750	Bodega Anchorage	BC	IOS-FOC
162 **	−125.22410	50.31140	Owen Bay	BC	IOS-FOC

Table A1. *Cont.*

Station	Longitude	Latitude	Station Name	Region	Source
163 **	−125.26810	50.31480	Okis Islands	BC	IOS-FOC
164 **	−125.13620	50.39250	Big Bay	BC	IOS-FOC
165 **	−125.12120	50.42020	Turnback Point	BC	IOS-FOC
166 **	−124.86940	50.59790	Orford Bay	BC	IOS-FOC
167 **	−124.83560	50.87270	Waddington Harbour	BC	IOS-FOC
168 **	−125.44160	50.33280	Chatham Point	BC	IOS-FOC
169 **	−125.36110	50.46090	Shoal Bay	BC	IOS-FOC
170 **	−125.49190	50.44240	Cordero Islands	BC	IOS-FOC
171 **	−125.96010	50.39870	Kelsey Bay	BC	IOS-FOC
172 **	−125.98330	50.45000	Yorke Island	BC	IOS-FOC
173 **	−125.76300	50.69800	Siwash Bay	BC	IOS-FOC
174 **	−126.20700	50.64700	Montagu Point	BC	IOS-FOC
175	−126.94100	50.58100	Alert Bay	BC	IOS-FOC
176	−127.46300	50.78400	Port Hardy	BC	IOS-FOC
177	−128.01400	50.40700	Winter Harbour	BC	IOS-FOC
178	−125.95700	49.11900	Tofino	BC	IOS-FOC
179	−150.20000	61.17500	Fire Island Cook Inlet	AK	IHO
180	−146.76666	60.95000	Rocky Point	AK	IHO
181	−145.93000	60.47600	Cape Whitshed	AK	IHO
182	−145.39999	60.35300	Pete Dahl Slough	AK	IHO
183	−142.56667	59.71667	Iapso #30_2.1.5	AK	IHO
184	−151.41667	59.60000	Homer	AK	IHO
185	−146.31667	59.46667	Middleton Island	AK	IHO
186	−141.98334	59.33333	Iapso #30_2.1.6	AK	IHO
187	−141.98334	59.25000	Iapso #30_2.1.4	AK	IHO
188	−153.38333	59.00000	Shaw Island Cook Inlet	AK	IHO
189	−145.71666	58.76667	Iapso #30_2.1.3	D	IHO
190	−134.41667	58.29900	Juneau	AK	IHO
191	−136.41450	58.20000	Granite Cove	AK	IHO
192	−132.93330	56.83470	Petersburg	AK	IHO
193	−144.36667	56.13334	Surveyor Seamount	D	IHO
194	−133.16700	55.47020	Craig	AK	IHO
195	−162.63333	54.37030	Peterson Bay Sanak Island	AK	IHO
196	−133.05000	54.25450	Langara Island	BC	IHO
197	−132.31667	54.11666	Wiah Point	BC	IHO
198	−132.14999	54.04210	Masset Harbour	BC	IHO
199	−130.57550	53.57020	Griffith Harbour	BC	IHO
200	−135.63333	53.31667	Bowie Seamount	D	IHO
201	−129.48334	52.65000	Mc Kenny Island	BC	IHO
202	−131.35330	52.46650	Section Cove	BC	IHO
203	−131.16667	52.35000	Copper Island	BC	IHO
204	−131.01666	51.93333	Cape St James	BC	IHO
205	−128.43333	51.90000	Gosling Island	BC	IHO
206	−127.89020	51.86666	Namu	BC	IHO
207	−127.82160	51.58850	Addenbroke Island	BC	IHO
208	−127.83334	51.25000	Egg Island	BC	IHO
209	−127.23334	50.88334	Raynor Group	BC	IHO
210	−128.41667	50.78333	Cape Scott	BC	IHO
211	−127.48334	50.72710	Port Hardy	BC	IHO
212	−125.73172	50.67270	Glendale Cove	BC	IHO
213	−125.05000	50.10000	Whaletown Bay	BC	IHO
214	−124.93266	49.66520	Comox	BC	IHO
215	−126.61667	49.60100	Nootka	BC	IHO
216	−132.78334	49.58333	Union Seamount	D	IHO
217	−123.11353	49.28978	Vancouver	BC	IHO
218	−123.58334	49.01667	Porlier Pass	BC	IHO
219	−127.28333	48.96667	Iapso #30_2.1.2	D	IHO
220	−123.28030	48.87370	Georgina Point	BC	IHO

Table A1. *Cont.*

Station	Longitude	Latitude	Station Name	Region	Source
221	−123.63333	48.86907	Crofton	BC	IHO
222	−123.31541	48.85398	Village Bay	BC	IHO
223	−125.17420	48.87250	Bamfield Inlet	BC	IHO
224	−123.60001	48.81667	Maple Bay	BC	IHO
225	−122.71667	48.81667	Ferndale	WA	IHO
226	−123.20420	48.80000	Samuel Islands (S. Shore)	BC	IHO
227	−122.88333	48.75000	Echo Bay	WA	IHO
228	−122.50250	48.74680	Bellingham	WA	IHO
229	−123.30000	48.43333	Oak Bay	BC	IHO
230	−122.85001	48.42765	Aleck Bay	WA	IHO
231	−122.66666	48.41667	Reservation Bay	WA	IHO
232	−122.61540	48.41420	Yokeko Point	WA	IHO
233	−123.96790	48.39380	Point No Point	BC	IHO
234	−123.54885	48.33427	Pedder Bay	BC	IHO
235	−122.62604	47.56237	Bremerton	WA	IHO
236	−122.89850	47.05180	Olympia	WA	IHO
237	−130.81667	46.76667	Iapso #30-2.1.1	D	IHO
238	−123.85001	46.16667	Astoria Youngs Bay	OR	IHO
239	−124.06667	44.43333	Waldport_Alsea Bay	OR	IHO
240	−124.10001	43.96667	Florence	OR	IHO
241	−124.11667	43.73333	Gardiner_Umpqua River	OR	IHO
242	−124.21667	43.38334	Marshfield_Coos Bay	OR	IHO
243	−124.89999	38.15000	Iapso #30-2.1.14	D	IHO
244	−122.13333	38.03333	Benicia	CA	IHO
245	−122.48334	37.95000	Point San Quentin	CA	IHO
246	−122.35001	37.91490	Richmond	CA	IHO
247	−122.47970	37.85000	Sausalito	CA	IHO
248	−122.36667	37.81667	Yerba Buena Island	CA	IHO
249	−119.20200	34.14865	Port Hueneme	CA	IHO
250	−118.31667	33.35000	Avalon_Catalina Island	CA	IHO
251	−118.54814	33.00115	Wilson Cove San Clemente Island	CA	IHO
252	−120.85001	32.23333	Iapso #30-2.1.12	D	IHO
253	−116.63351	31.84948	Ensenada	MX	IHO
254	−119.80000	31.03333	Iapso #30-2.1.11	D	IHO
255	−116.28333	28.86667	Isla Guadalupe	D	IHO
256	−124.43333	27.75000	Iapso #30-2.1.13	D	IHO
257	−112.15340	24.63060	Magdalena Bay	MX	IHO
258	−109.97200	22.84400	Cabo San Lucas	MX	IHO

* All stations denoted by a single asterisk are outside the model domain of the ENPAC03 database but are extracted using the nearest wet neighbor as they are suitably near the coastline. ** All stations denoted by a double asterisk are not extracted from ENPAC03 for data analysis or plotting as they are either well outside the model domain or located in small channels or other features that are not resolved in the ENPAC03 model domain.

Appendix C

Scatter plots for the eighteen stations denoted with a black X in Appendix A are provided herein. Both the ENPAC15 Manning's n and VDatum friction variations are compared to the ENPAC03 model. Note that the different friction formulations generally create more of a difference in the amplitude response than they do in the phase response. Plots are grouped according to region, starting at the southern extent of the domain.

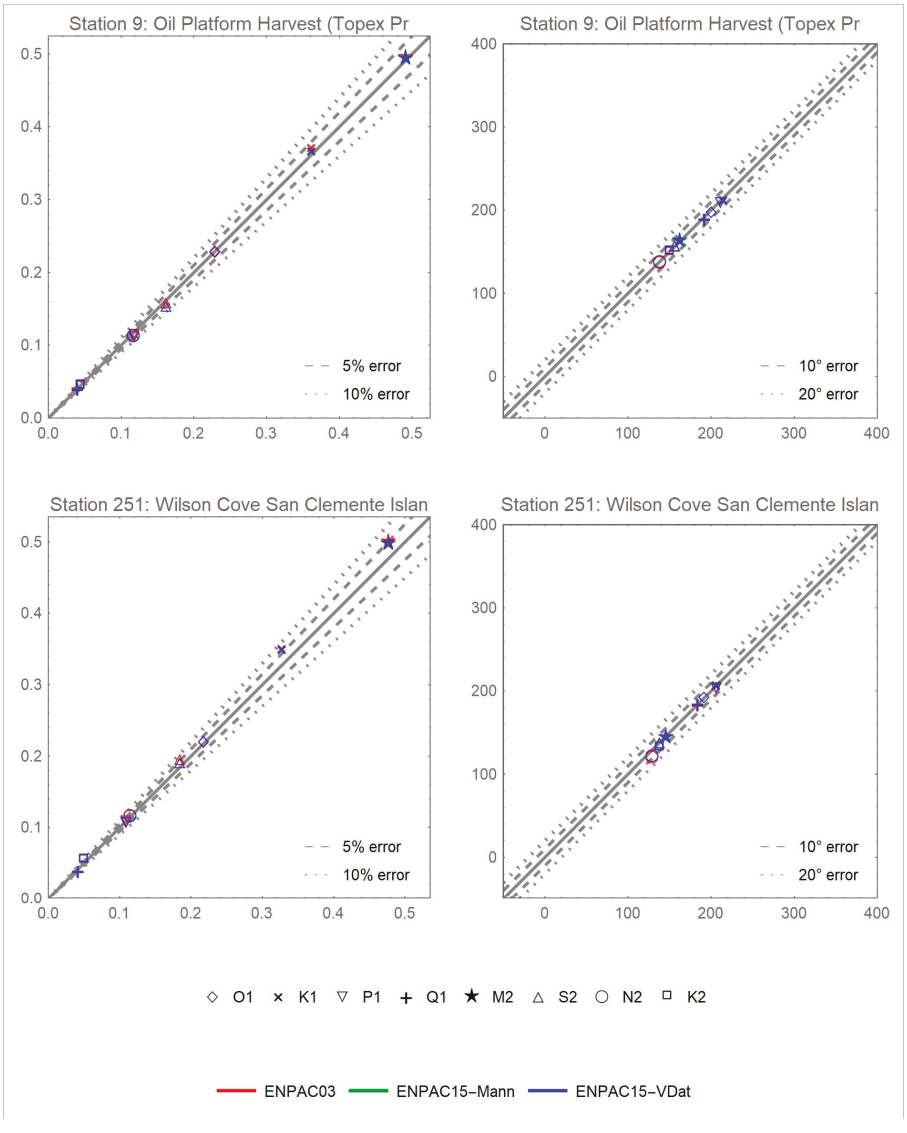

Figure A6. Scatterplots of errors for two Southern California stations, locations shown in Figure A1.

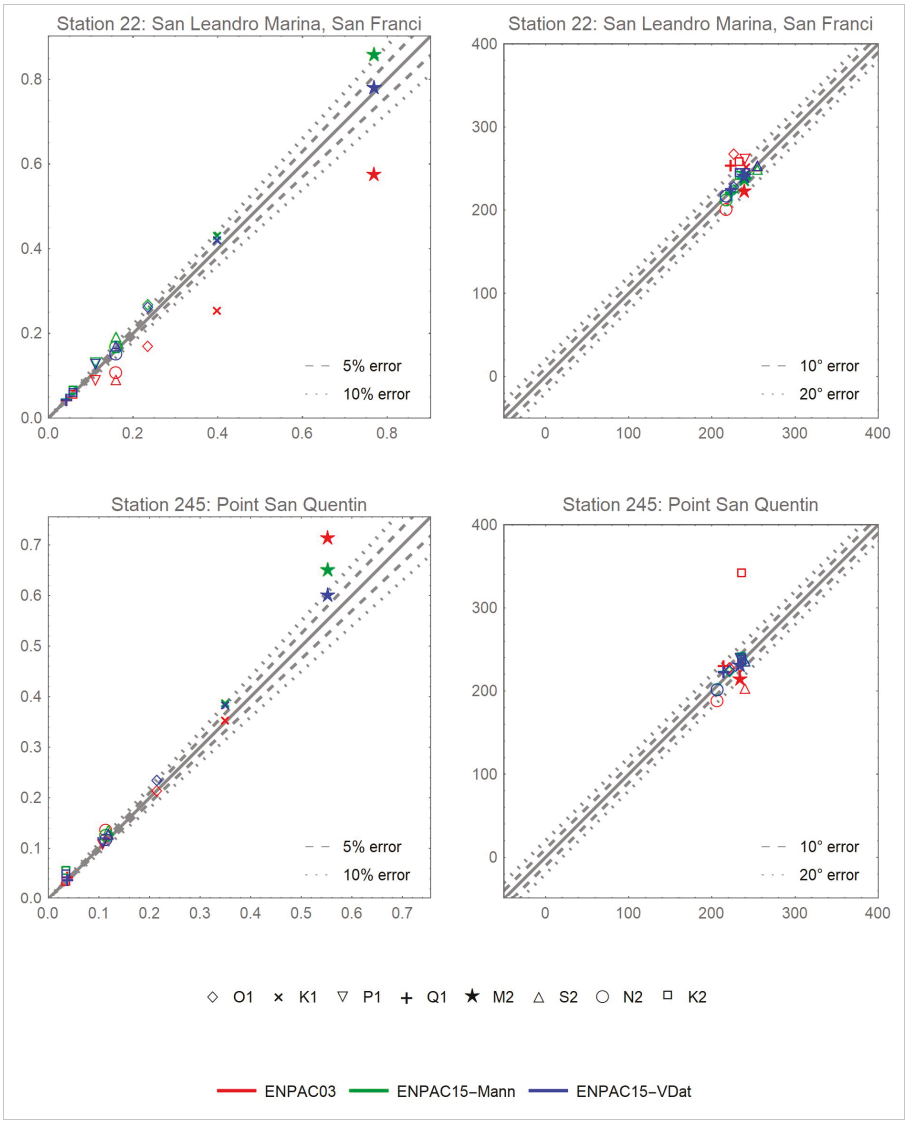

Figure A7. Scatterplots of errors for two San Francisco Bay stations, locations shown in Figure A2.

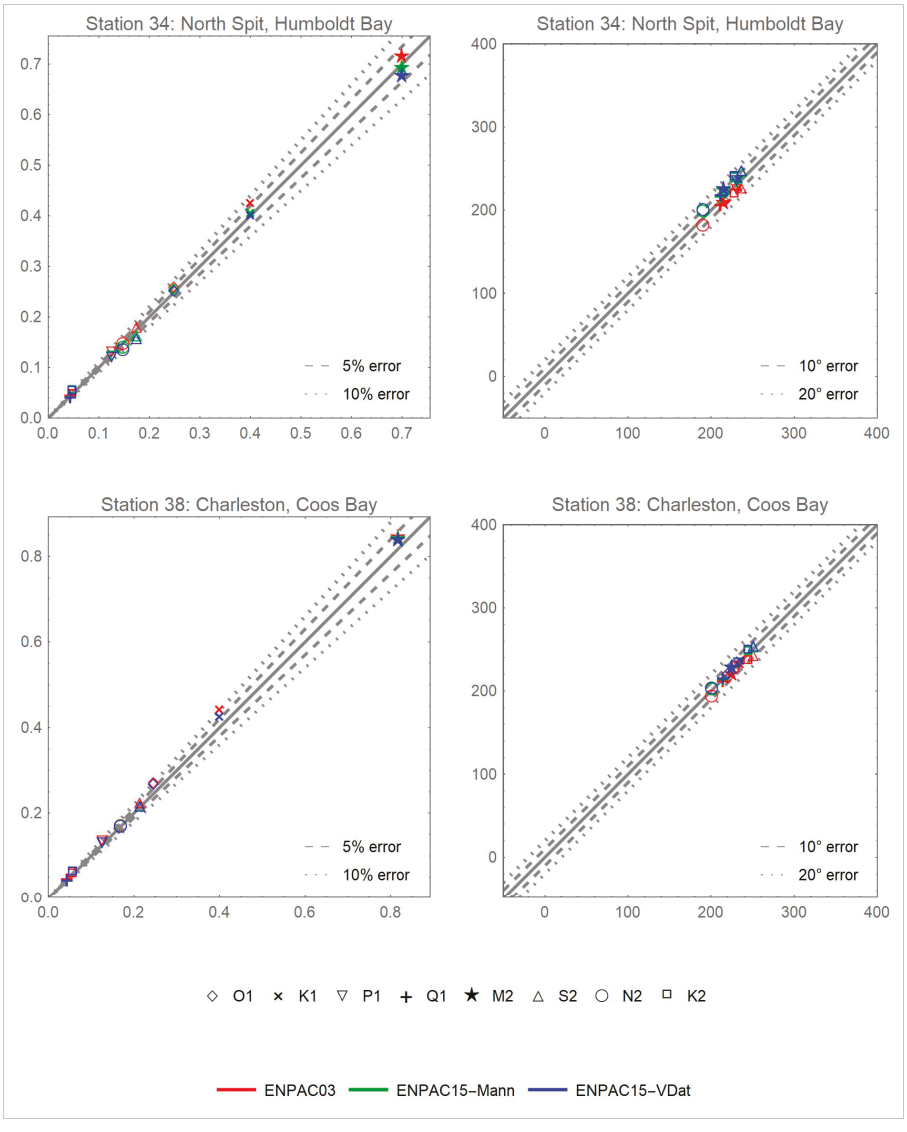

Figure A8. Scatterplots of errors for two Northern California stations, locations shown in Figure A2.

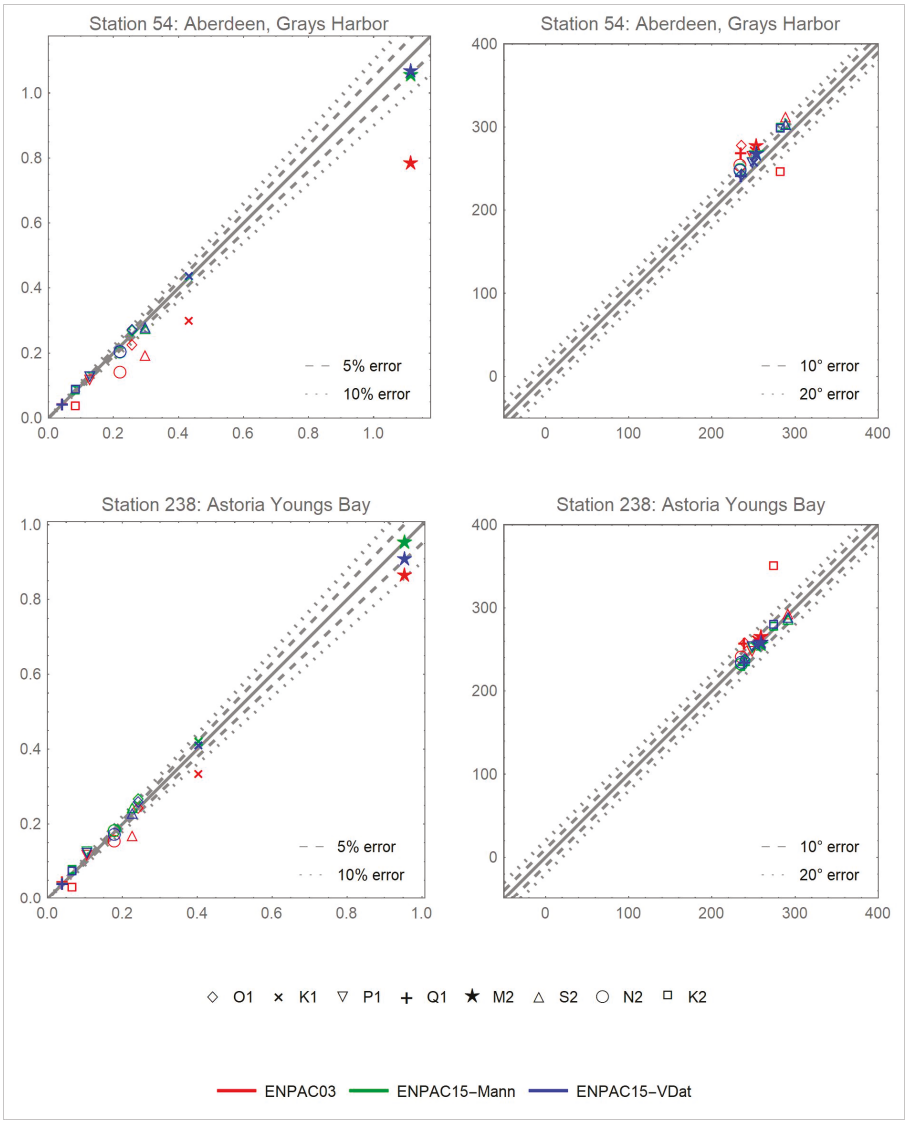

Figure A9. Scatterplots of errors for two Oregon/Washington stations, locations shown in Figure A3.

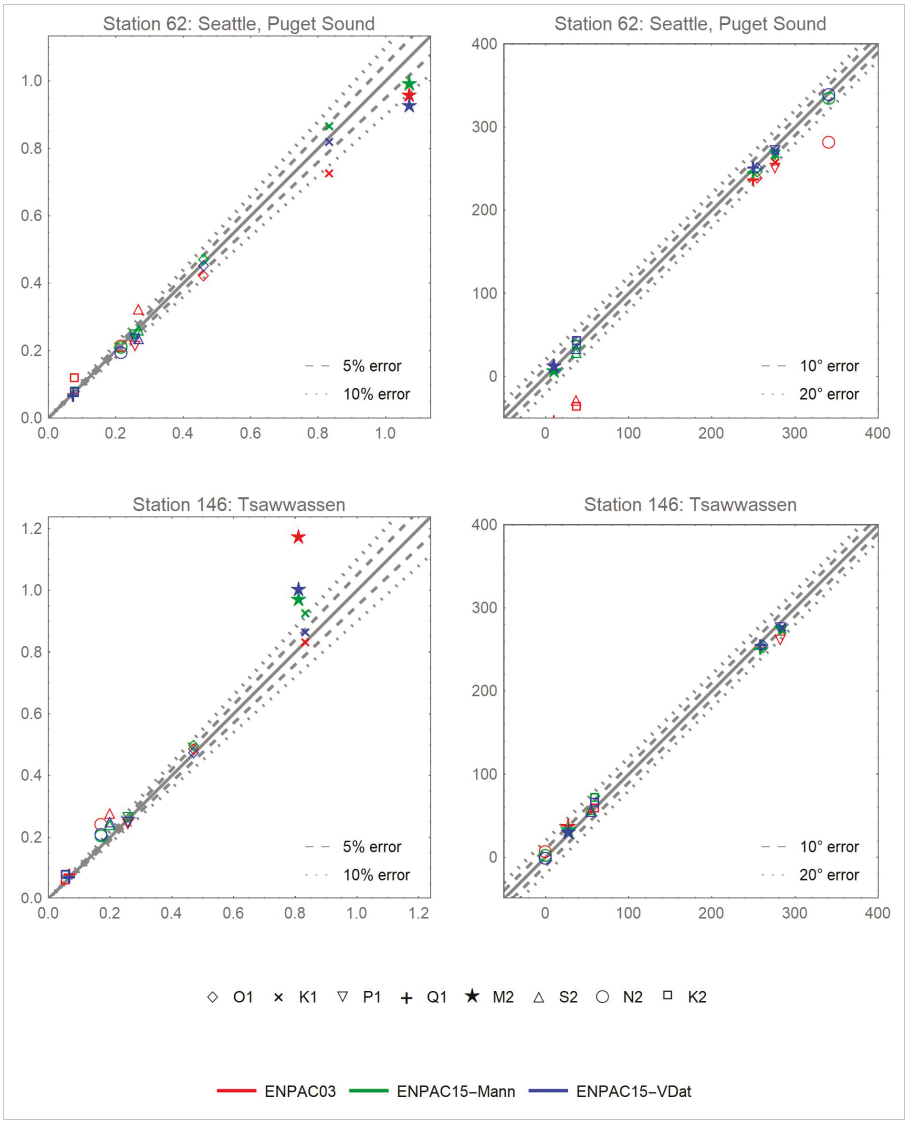

Figure A10. Scatterplots of errors for two Puget Sound stations, locations shown in Figure A3.

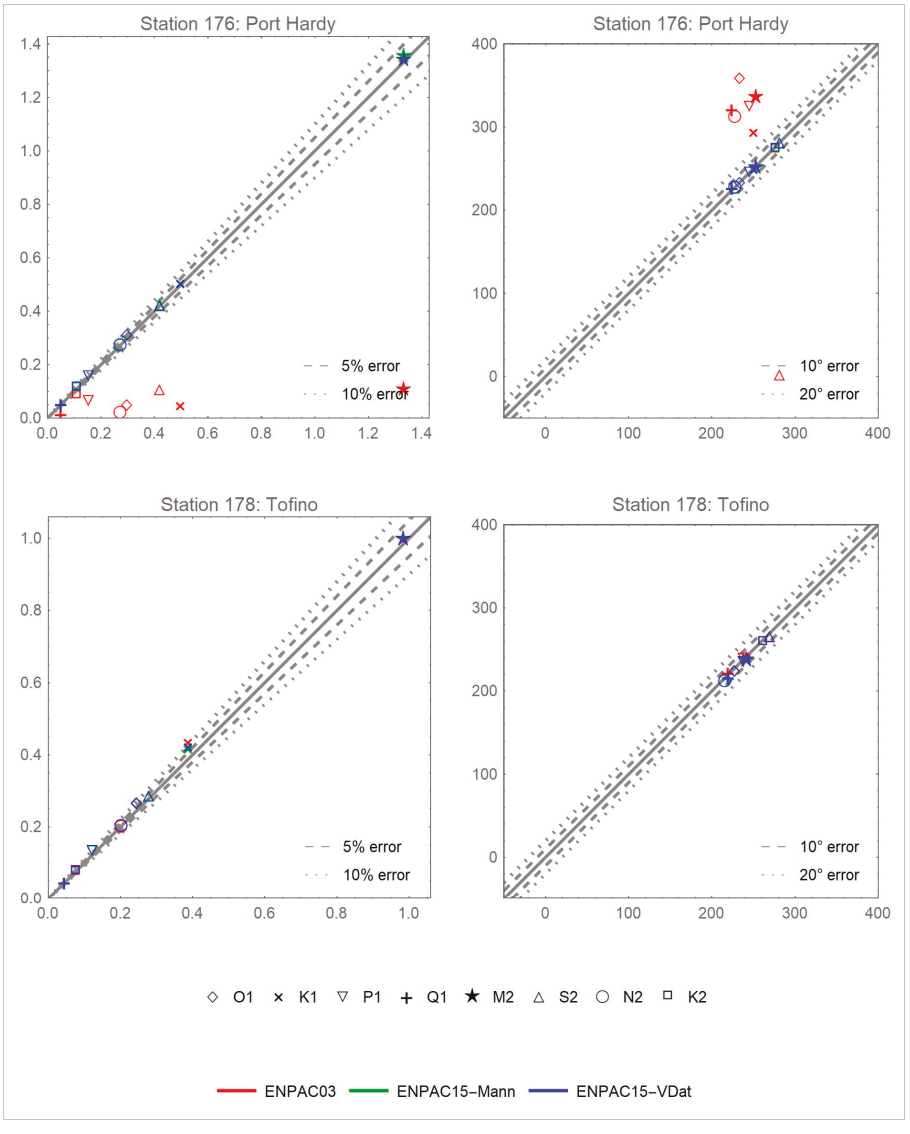

Figure A11. Scatterplots of errors for two British Columbia stations, locations shown in Figure A4.

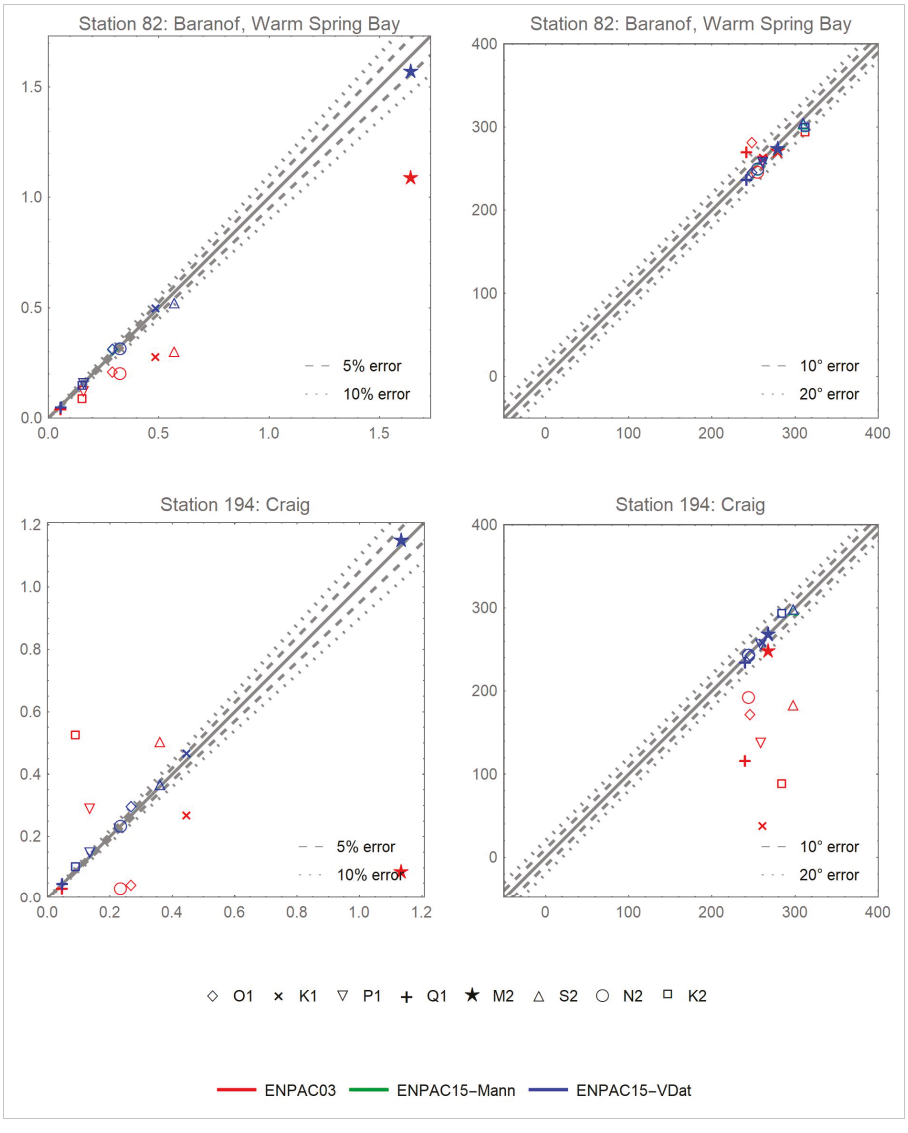

Figure A12. Scatterplots of errors for two Southeast Alaska stations, locations shown in Figure A4.

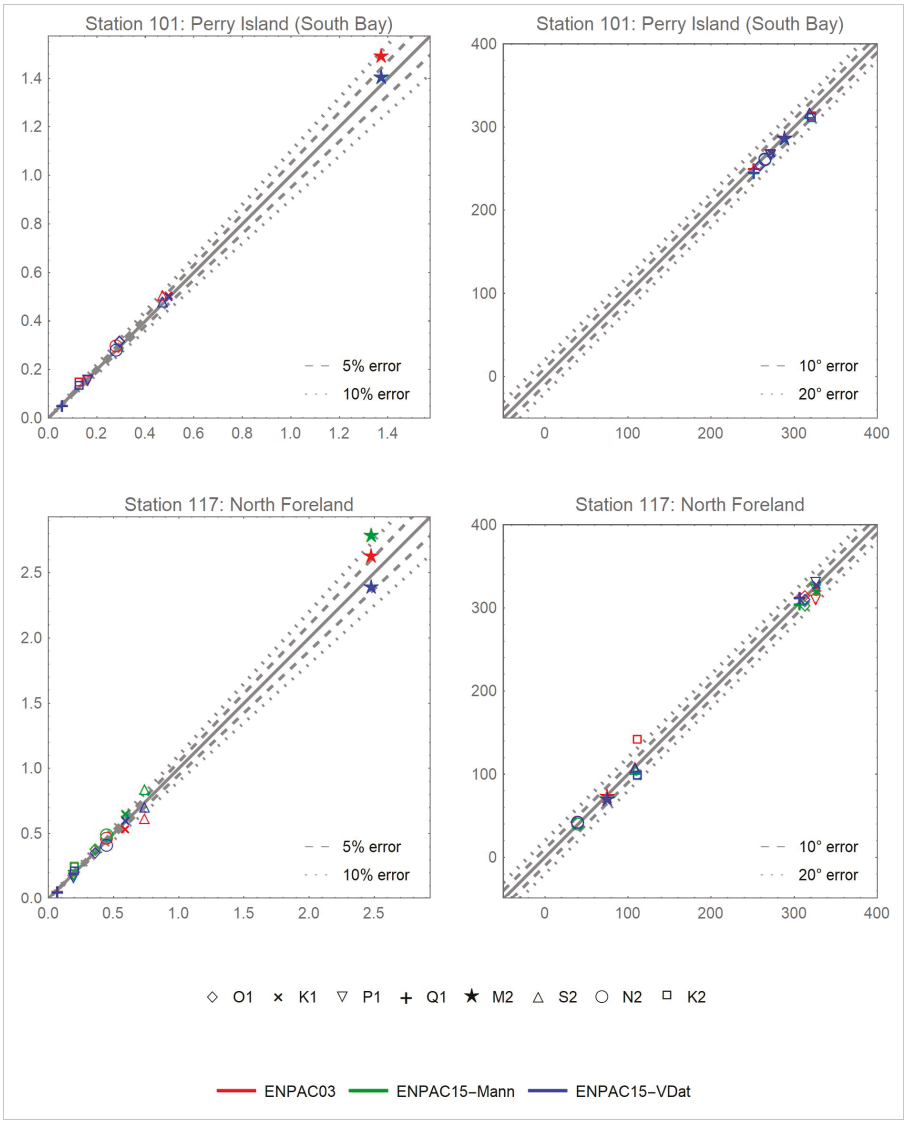

Figure A13. Scatterplots of errors for two Southern Alaska coast stations, locations shown in Figure A5.

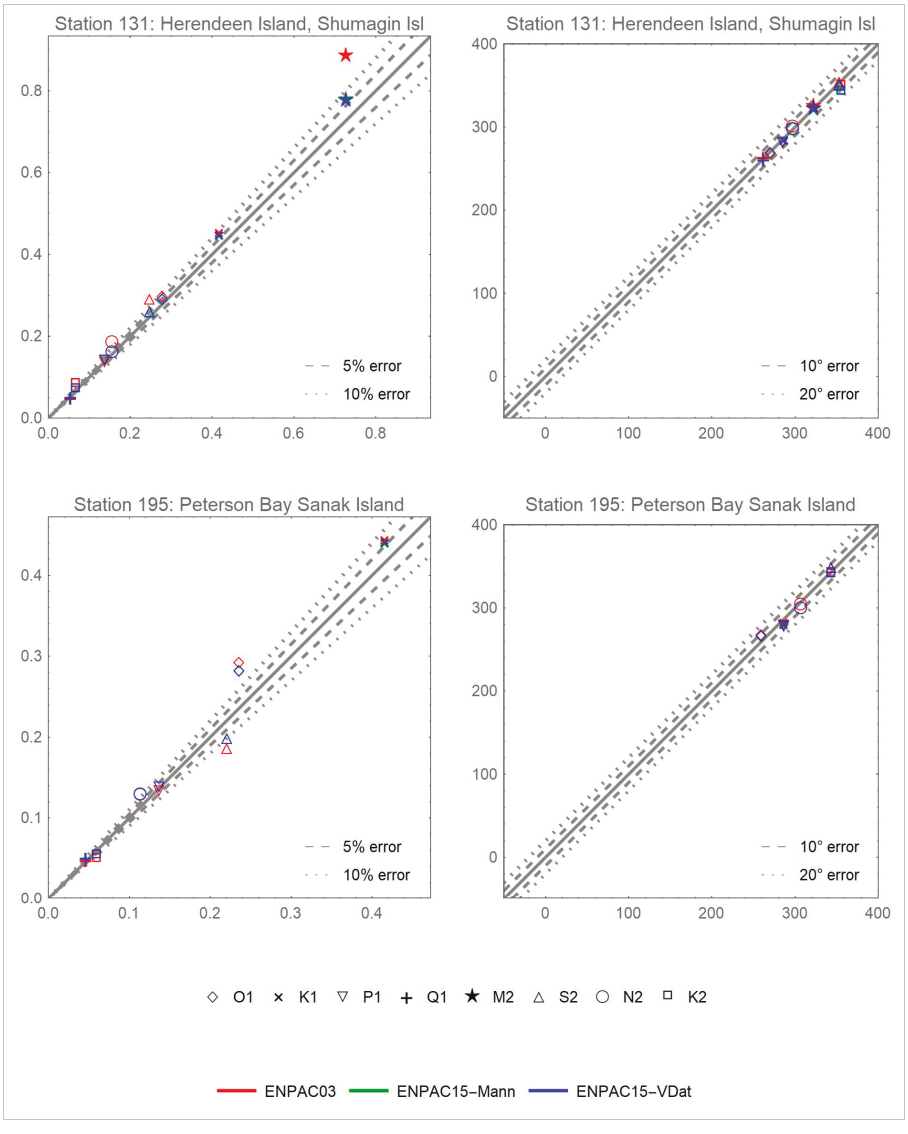

Figure A14. Scatterplots of errors for two Southern Alaska coast stations, locations shown in Figure A5.

Appendix D

The actual geographic distribution of errors for the M_2 and K_1 constituents in the ENPAC15 tidal database are provided at all 258 validation stations in the following seven figures. The dominant M_2 constituent is plotted for all of the same regional views shown in Figures A1–A5; however, the K_1 constituent is only shown for the Vancouver Island area shown in Figure A4. Symbol shapes denote the magnitude of the errors while the colors represent whether the ENPAC15 model is over (red) or underestimating (blue) the amplitudes. Similarly, blue symbols denote locations where the model exhibits a phase lag while red symbols denote a phase lead.

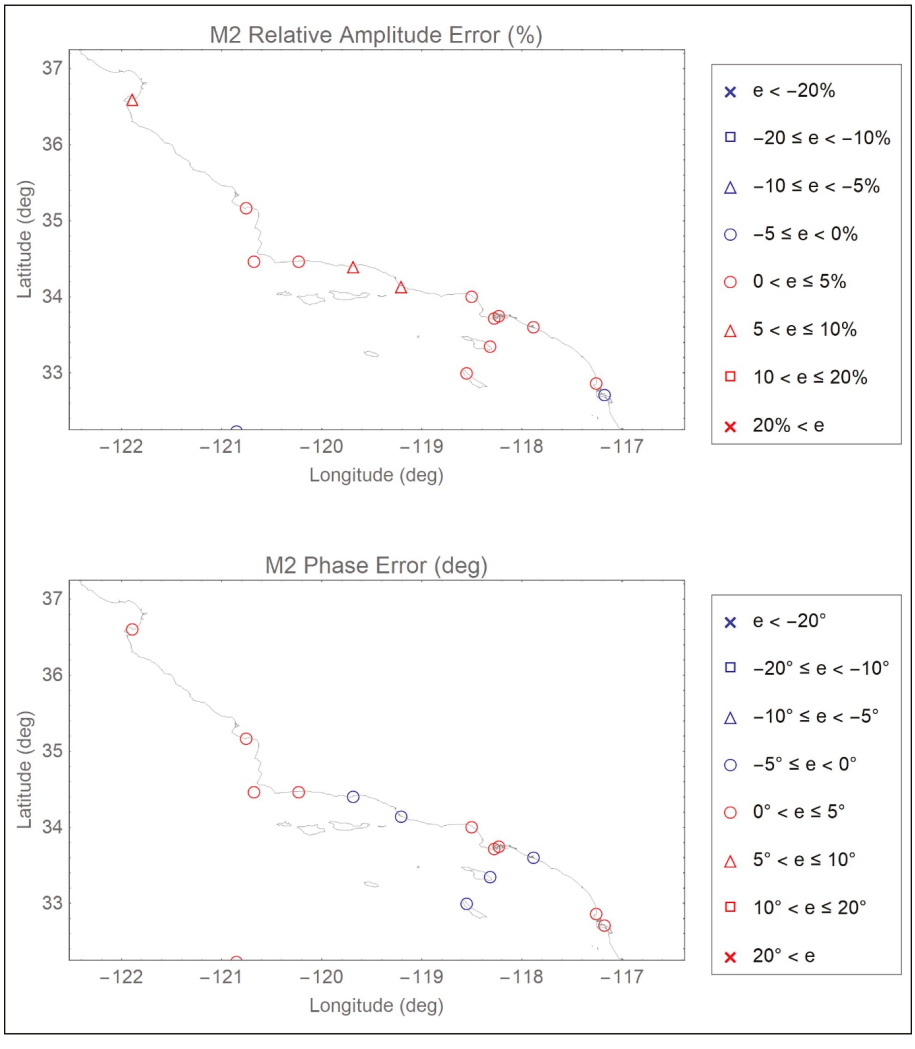

Figure A15. Distribution of ENPAC15 relative amplitude (%) and absolute phase (deg) errors for the M_2 constituent: Southern California coast view.

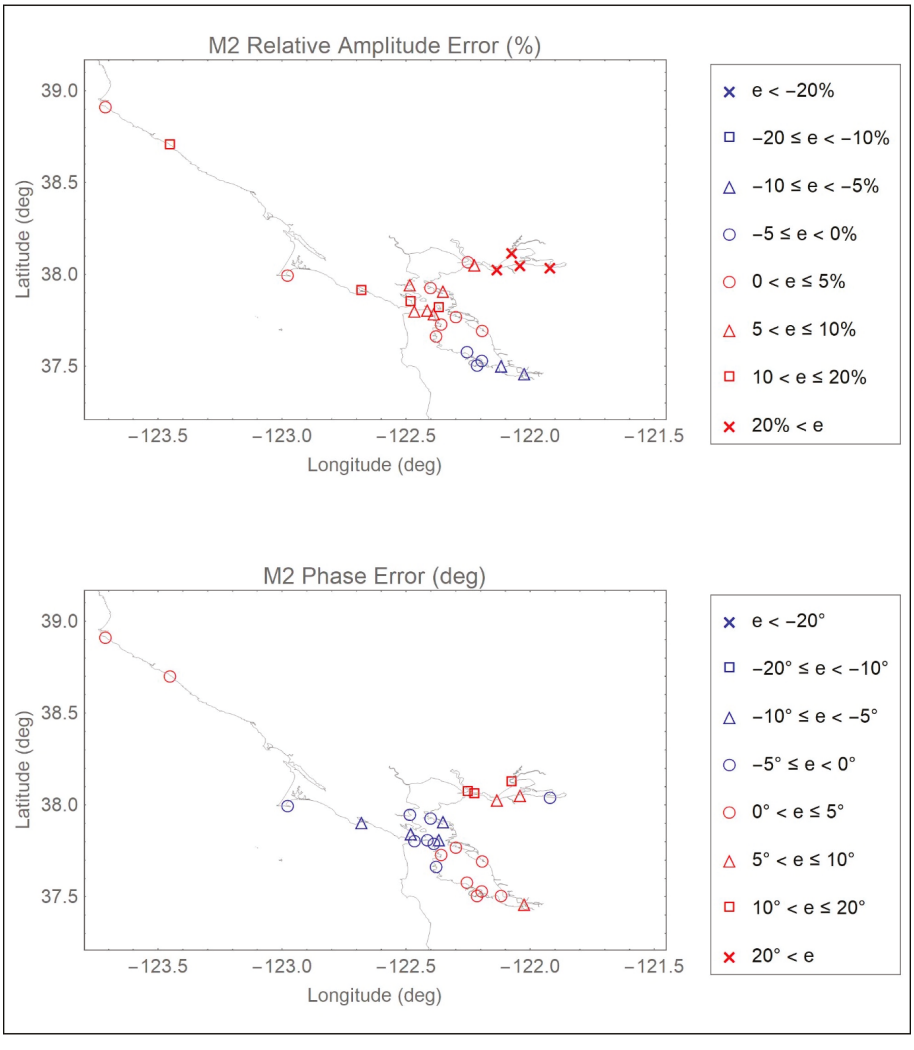

Figure A16. Distribution of ENPAC15 relative amplitude (%) and absolute phase (deg) errors for the M_2 constituent: San Francisco Bay view.

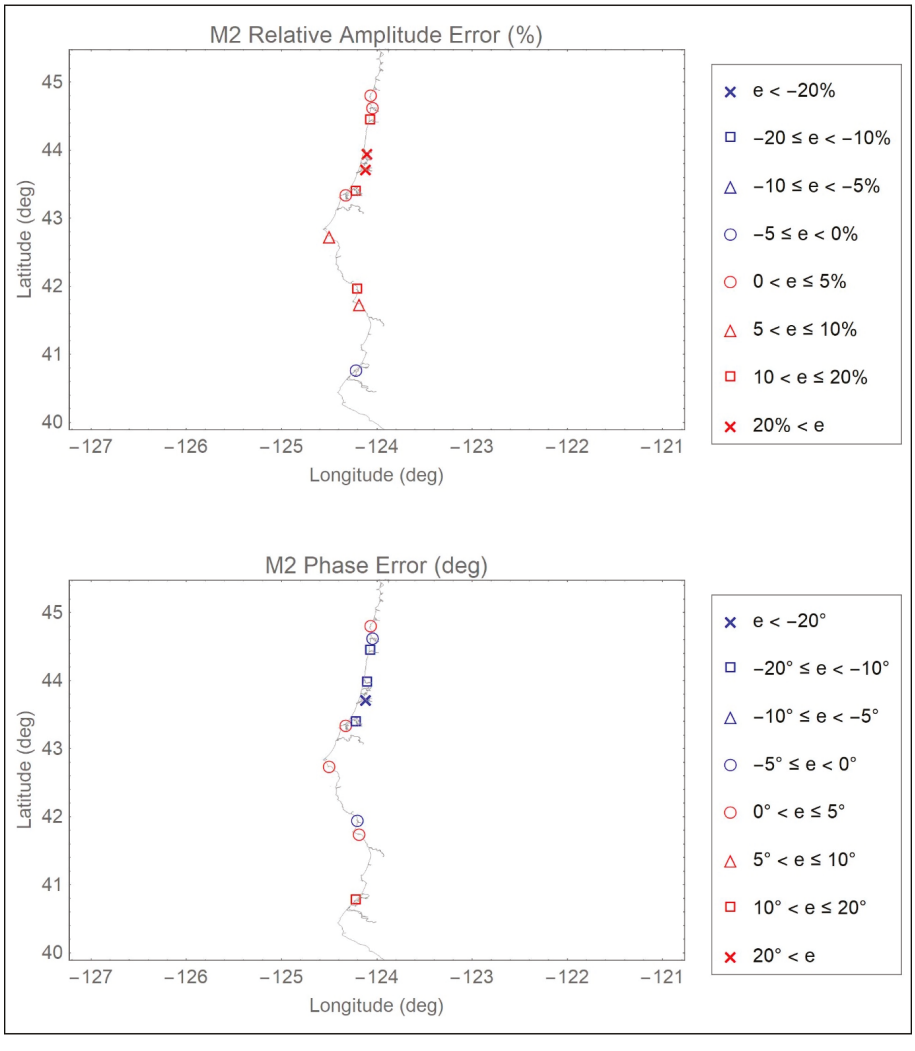

Figure A17. Distribution of ENPAC15 relative amplitude (%) and absolute phase (deg) errors for the M_2 constituent: Northern California coast view.

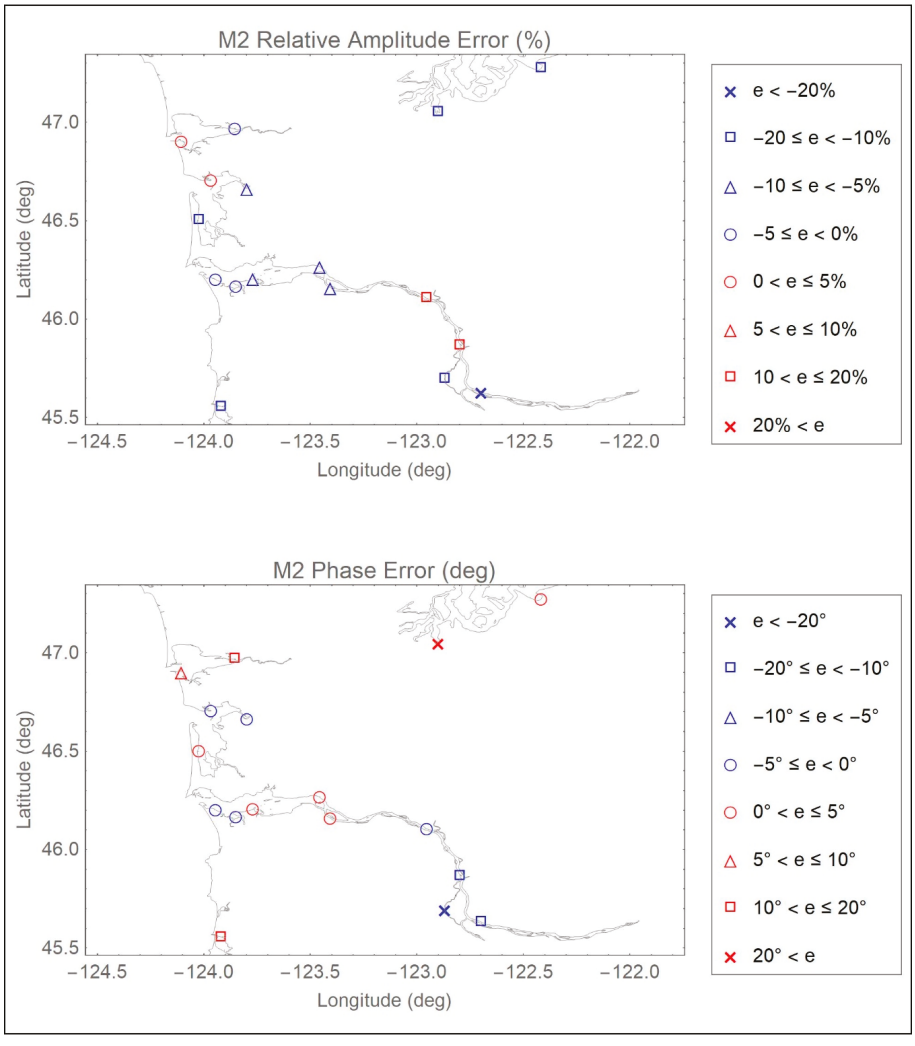

Figure A18. Distribution of ENPAC15 relative amplitude (%) and absolute phase (deg) errors for the M_2 constituent: Oregon and Washington coast view.

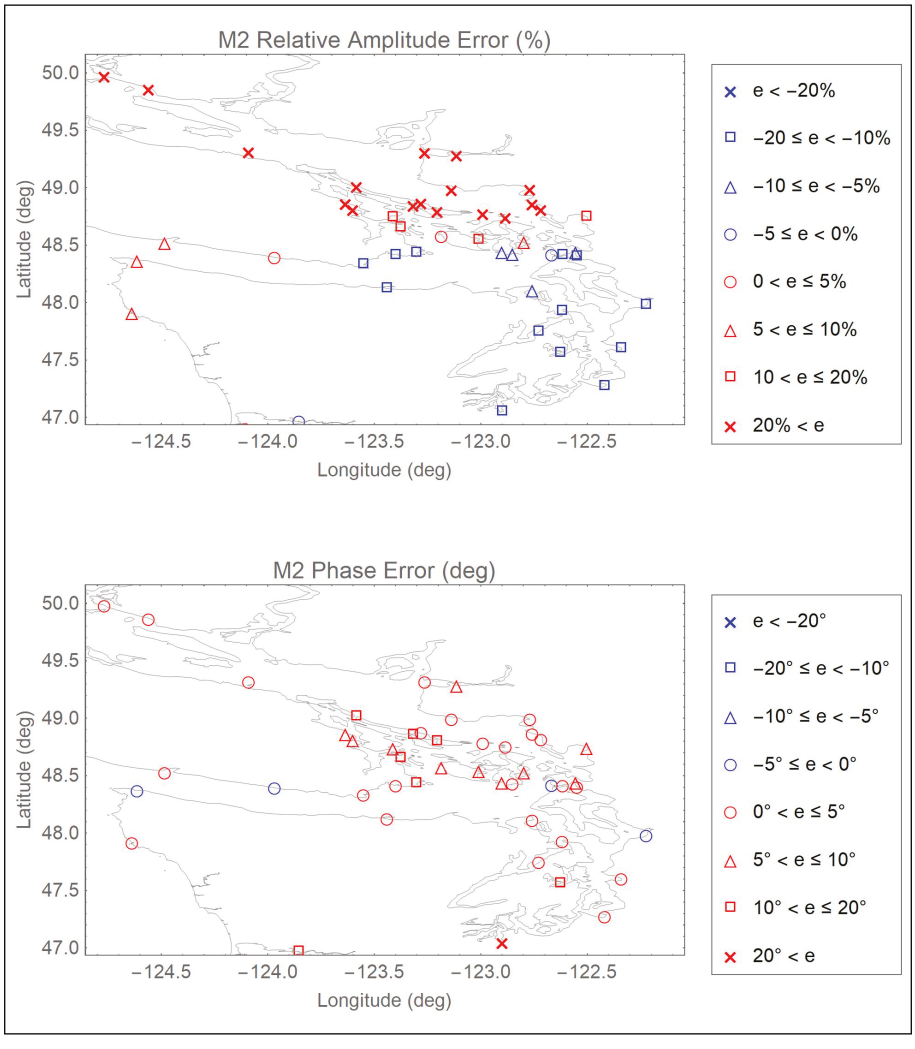

Figure A19. Distribution of ENPAC15 relative amplitude (%) and absolute phase (deg) errors for the M_2 constituent: Puget Sound view.

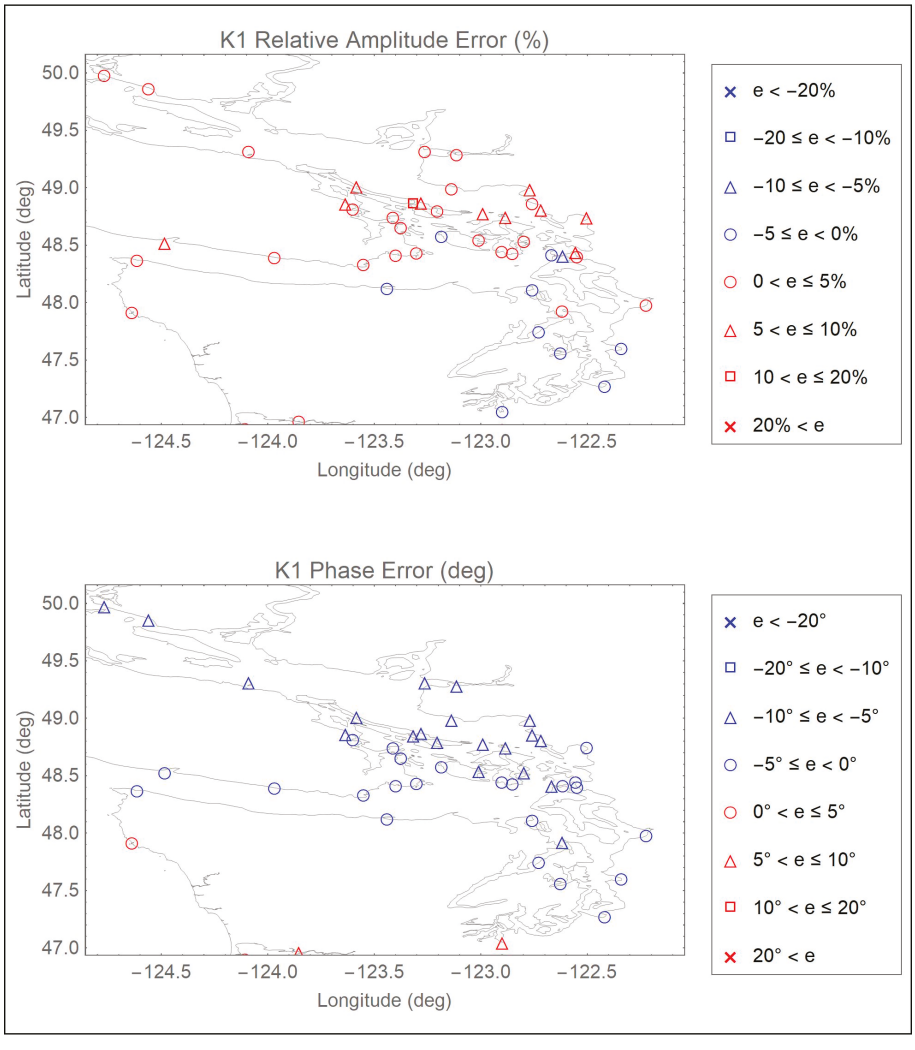

Figure A20. Distribution of ENPAC15 relative amplitude (%) and absolute phase (deg) errors for the K_1 constituent: Puget Sound view.

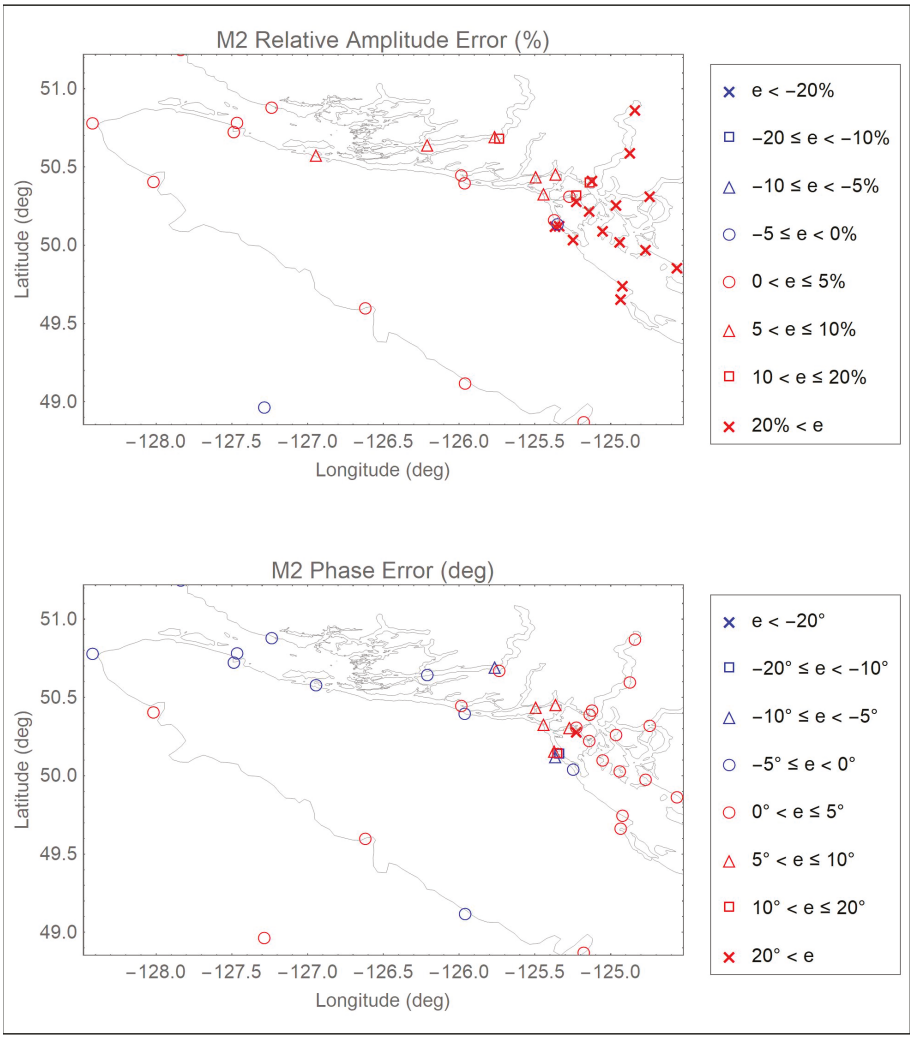

Figure A21. Distribution of ENPAC15 relative amplitude (%) and absolute phase (deg) errors for the M_2 constituent: British Columbia coast view.

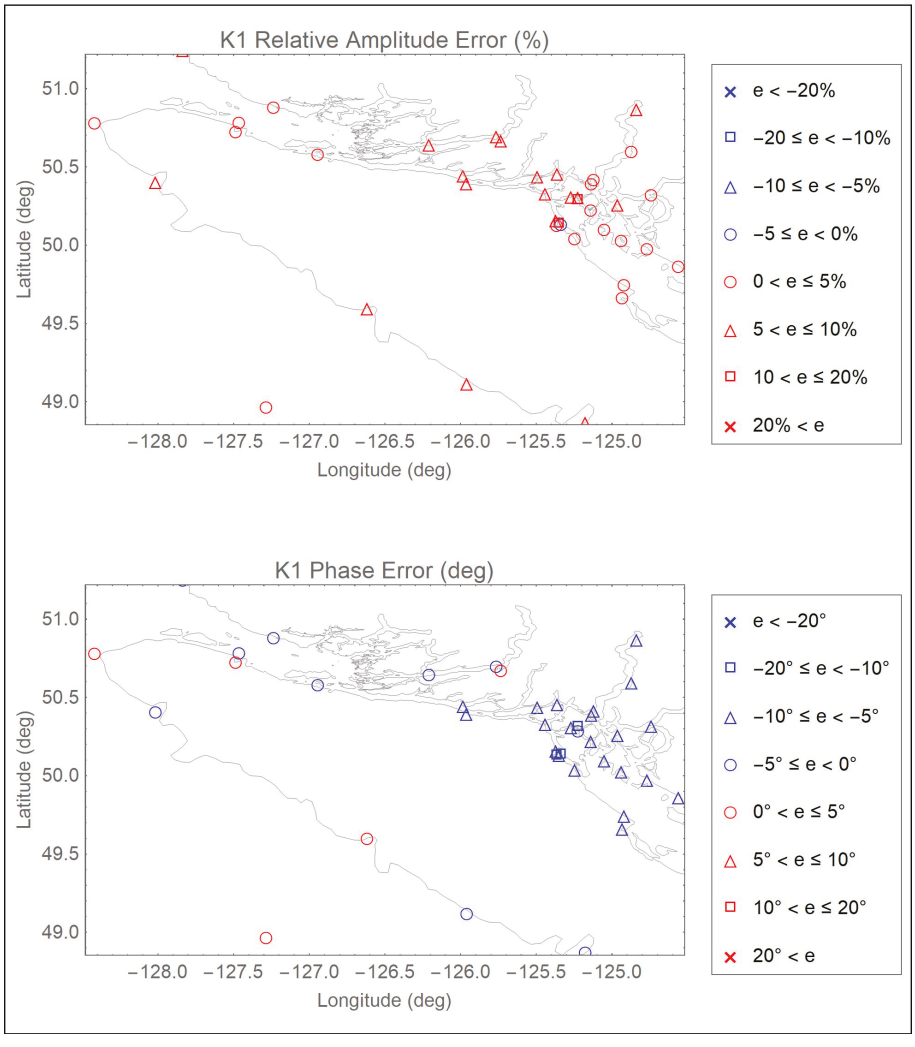

Figure A22. Distribution of ENPAC15 relative amplitude (%) and absolute phase (deg) errors for the K_1 constituent: British Columbia coast view.

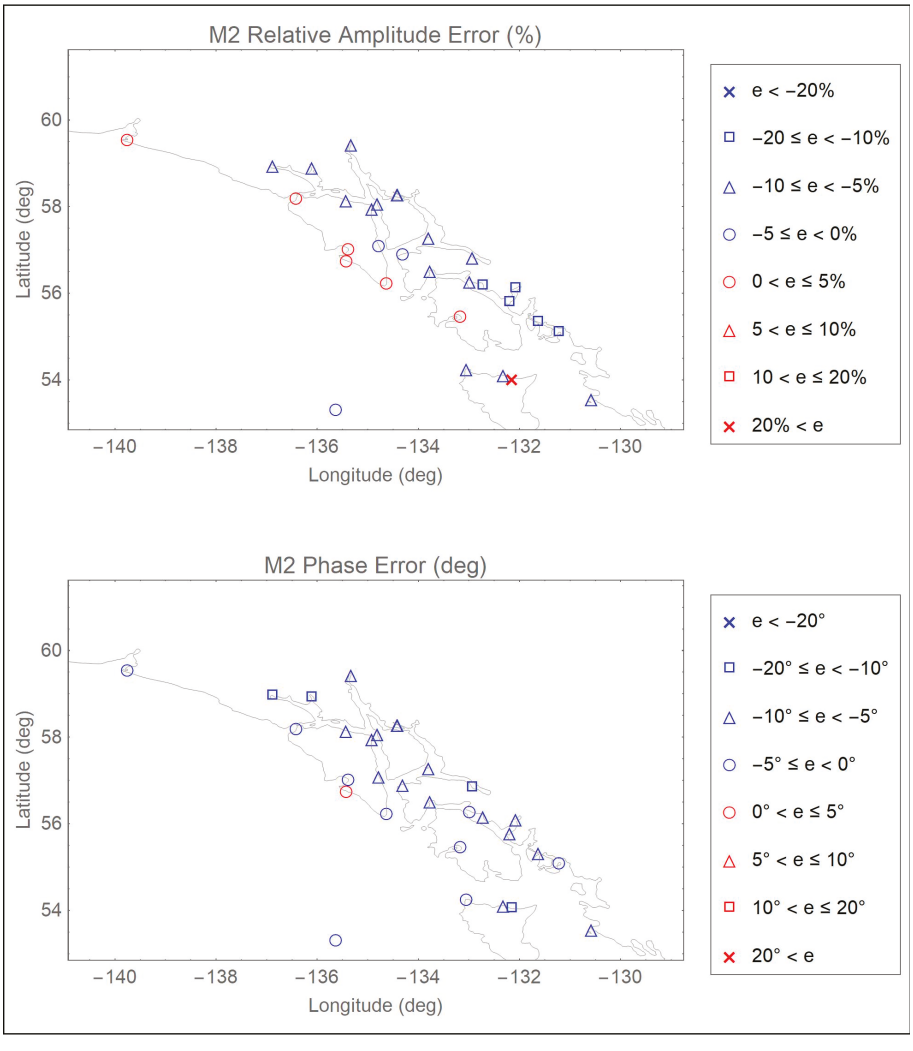

Figure A23. Distribution of ENPAC15 relative amplitude (%) and absolute phase (deg) errors for the M_2 constituent: Southeast Alaska view.

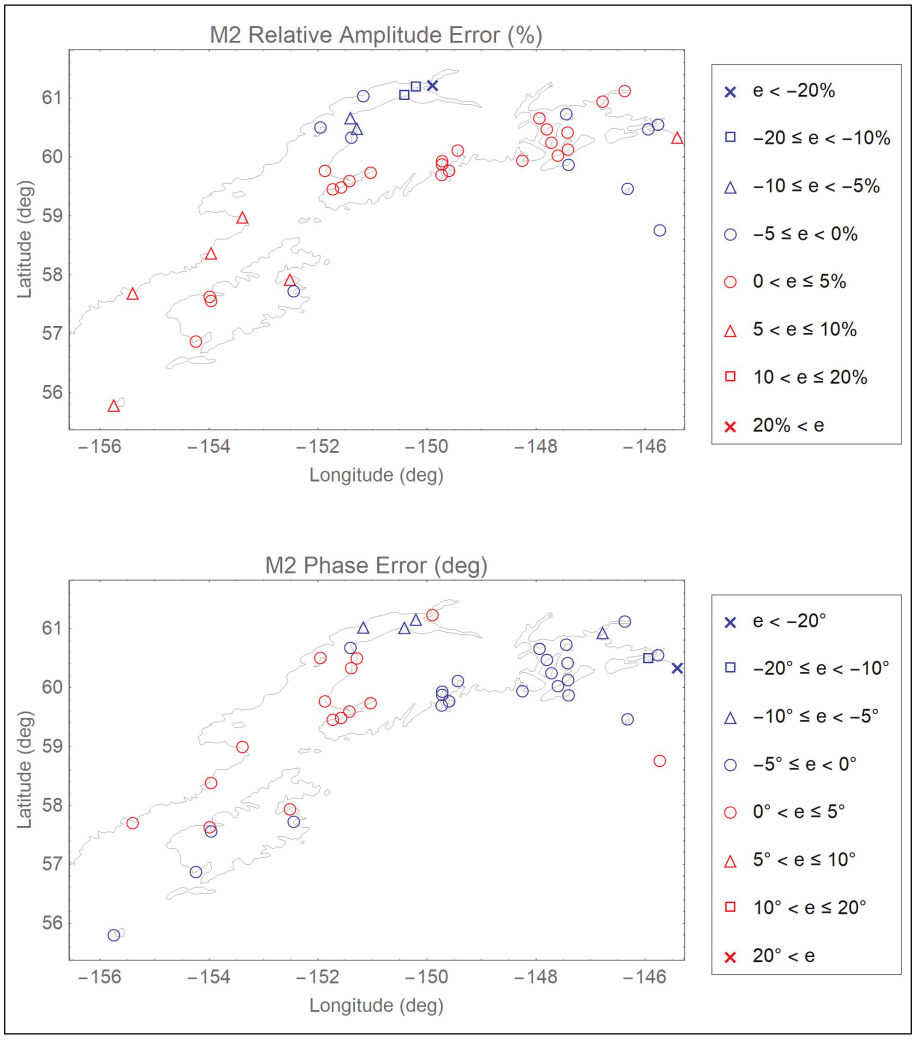

Figure A24. Distribution of ENPAC15 relative amplitude (%) and absolute phase (deg) errors for the M_2 constituent: Southern Alaska coast view one.

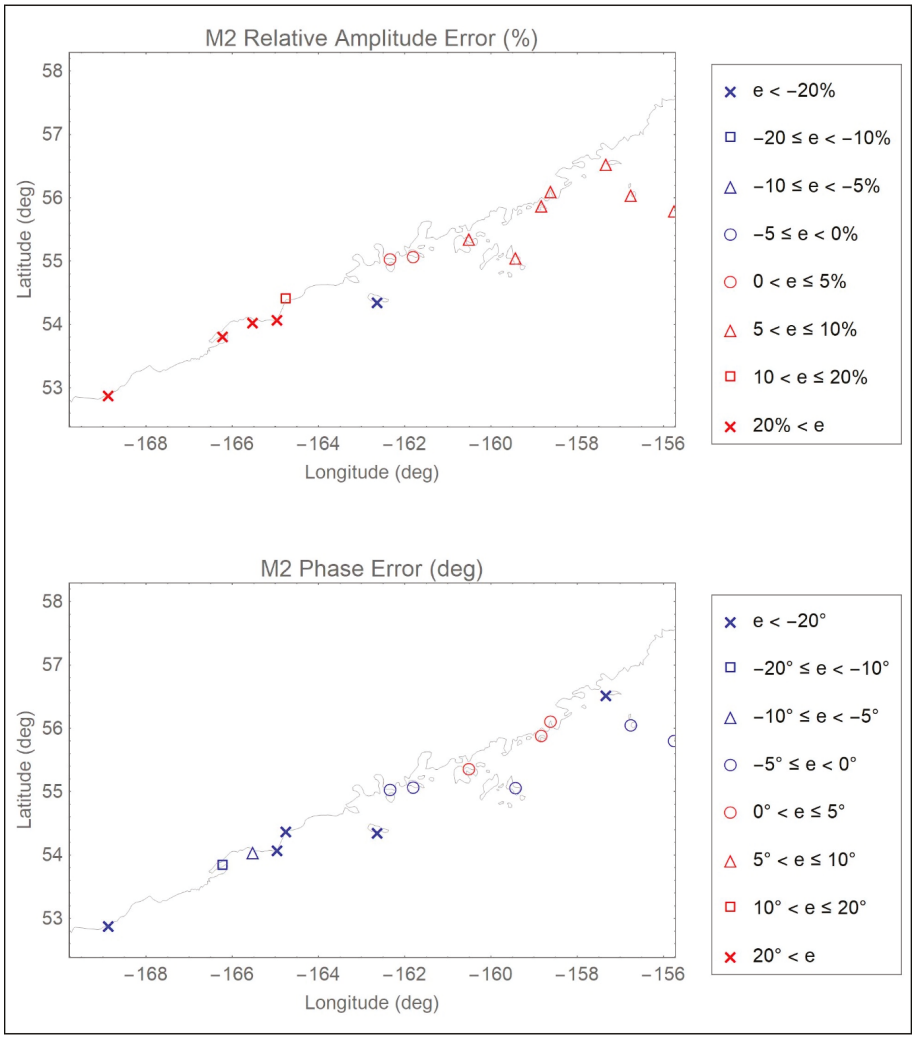

Figure A25. Distribution of ENPAC15 relative amplitude (%) and absolute phase (deg) errors for the M_2 constituent: Southern Alaska coast view two.

Appendix E

Herein, we provide general applicability and usage guidelines for the ENPAC15 tidal database. It is recommended that users read through these sections to understand the limitations of the database before they apply it to their own regions of interest.

Appendix E.1. Applicability Guidelines for the ENPAC15 Tidal Database

The ENPAC15 tidal database provides elevation amplitudes and phases throughout the ENPAC domain for all 37 constituents frequently used by NOS. Although data for all 37 constituents are included in the database, care should be taken when deciding how many of these constituents are important for the user's intended application. Often, accurate results can be obtained when using only the primary astronomic tides, particularly if the boundary of interest is in deeper water, far removed

from the coastline. Furthermore, only the eight primary astronomic constituents (M_2, S_2, N_2, K_2, O_1, K_1, P_1 and Q_1) were validated in this study.

It is important to note that the ENPAC15 database does not include all physical processes which can affect the model response including (but not limited to) density driven flows, riverine discharge, sediment transport and resulting bed morphological changes, large-scale oceanic currents or wind and atmospheric pressure driven flows. Depending upon the magnitude, each of these physical processes can have significant impacts on the accuracy of a given model. The user is cautioned that the database includes only barotropic computations of tidal circulation and does not consider any other physical processes.

Furthermore, how accurately the ENPAC15 grid geometry and bathymetry describe the region of specific interest influences the accuracy and appropriateness of applying database values. Therefore, further caution is recommended when applying the database along the Alaskan coast, as the coastline has not been significantly updated since the 2003 release. Recall that the Aleutian Island chain is approximated as a mainland boundary west of Unimak Island, Alaska, neglecting interaction with the Bering Sea. Therefore, the tidal response of the model west of this point, and, in the immediate area, is not accurate and the database should not be used to extract values in those areas.

Finally, the prevailing hydrodynamics in a specific region will determine how accurately the currents will be predicted. If the surface elevation response and currents are dominated by astronomical tides, then the database will provide an excellent prediction of the response. A good estimate of the accuracy of the ENPAC15 tides can be obtained by examining the regional error estimates given in Tables 7 and 8, or by examining the error plots provided for the dominant constituents in Appendix D; although plots are only provided for the M_2 and K_1 constituents, in general, all four of the semi-diurnal constituents follow the same regional trends, as do the diurnal constituents.

Appendix E.2. Usage Guidelines for the ENPAC15 Tidal Database

The ENPAC15 tidal constituent database can be applied anywhere *east* of Unimak Island, Alaska (160° W) within the defined ENPAC domain—refer to Figure 1. For locations that are tidally dominated and for which the ENPAC15 grid accurately describes both local geometry and bathymetry, the database can be directly applied to extract tidal elevations and currents. Because the thirty-seven constituents are computed at every node and are defined within the framework of a finite element grid, values at any point within the domain can be readily interpolated from the nodal values within which the point lies.

The location of the boundary where values are to be extracted should be placed away from the region of immediate interest and should never be placed within embayments, estuaries, or other small water bodies. In general, it is best to locate the regional boundary in deeper water somewhat removed from the coast whenever possible. Finally, it is recommended that the regional model be developed in such a way that the bathymetry at the regional boundary matches the bathymetry of the database model domain.

The ENPAC15 tidal database is available on the ADCIRC website as two separate compressed files: ENPAC15_elev-only_tidaldatabase.tar, which contains all of the extraction programs, grids, input files and sample notes but only has the fort.53 elevation harmonics; and ENPAC15_tidaldatabase.tar, which has everything given in the previous file with the addition of the fort.54 velocity harmonics [58]. Users will only need to download one of the files depending upon whether they wish to have access to the velocity data as well.

An extraction program, ADCIRC_db_extract_2015.F90, together with the ENPAC15 finite element grid file, wc2015_v1a_chk.grd, and input control files accompany the tidal database. The user must supply an input file that provides the number of extraction points desired followed by the list of coordinates for those points. The extraction program will prompt the user for this input files as well as the name of the grid used to create the database. The program will also prompt the user whether they would like to produce the harmonic constituent output for elevations, velocities or both and then will produce the harmonic extraction output for amplitude and phase at the specified location(s) according to the user's request. Elevation output is stored in elev_hc.out while velocity output is stored in vel_hc.out. Additionally, diagnostic output is written to tides.dia and provides the location

of each extraction point in the global mesh as well as the interpolation weights used to calculate the harmonic constituents. The KDTREE2 search algorithms have been incorporated into the new extraction program to facilitate a speedier search response. Finally, the program takes advantage of dynamic allocation in order to avoid the old hardcoded array limitations found in previous extraction routines. The ADCIRC_db_extract_2015.F90 program will work with any old ADCIRC databases that utilized the individual fort.53 and fort.54 file formats.

In addition to the extraction program, the database files also include another utility for "cutting" a portion of the global database out for visualization. The HarmonicResultScope.f90 program works much the same way as ResultScope.f90, for those who are familiar with that ADCIRC utility program. Additional notes about the usage of each of these programs, as well as sample input and output files for each, are included in the TidalExtract/ directory within the database tar file.

For the interested reader, a time-history of response can be readily Fourier synthesized using the outputs in the elev_hc.out and vel_hc.out files. For example, a time-history of water-surface elevation can be computed as

$$\zeta(x,y,t) = \sum A_i(x,y) f_i(t_0) \cos[\sigma_i(t - t_0) + V_i(t_0) - h_i(x,y)], \quad \text{(A1)}$$

where $A_i(x,y)$ and $h_i(x,y)$ are the amplitude and phase, respectively, at the location (x,y) of interest for constituent i, which are provided by the ENPAC15 tidal database, and the frequency $\sigma_i = 2\pi/T_i$. The frequencies σ_i in rad/sec and periods T_i in hours for each of the 37 constituents included in the database are presented in Table A2. It is important to specify frequencies precisely, at least to eight significant figures. The nodal factor $f_i(t_0)$ and the equilibrium argument, $V_i(t_0)$, relative to reference time t_0 can be computed using program tide_fac.f, which is available as a utility program on the ADCIRC website [60].

Table A2. Frequencies and periods for ENPAC15 harmonic constituents.

Constituent	Frequency (rad/s)	Period (h)
M(2)	0.0001405189	12.42
N(2)	0.0001378797	12.66
S(2)	0.0001454441	12.00
O(1)	0.0000675977	25.82
K(1)	0.0000729212	23.93
K(2)	0.0001458423	11.97
L(2)	0.0001431581	12.19
2N(2)	0.0001352405	12.91
R(2)	0.0001456432	11.98
T(2)	0.0001452450	12.02
Lambda(2)	0.0001428049	12.22
Mu(2)	0.0001355937	12.87
Nu(2)	0.0001382329	12.63
J(1)	0.0000755604	23.10
M(1)	0.0000702820	24.83
OO(1)	0.0000782446	22.31
P(1)	0.0000725229	24.07
Q(1)	0.0000649585	26.87
2Q(1)	0.0000623193	28.01
Rho(1)	0.0000653117	26.72
M(4)	0.0002810378	6.21
M(6)	0.0004215567	4.14
M(8)	0.0005620756	3.11
S(4)	0.0002908882	6.00
S(6)	0.0004363323	4.00
M(3)	0.0002107784	8.28
S(1)	0.0000727221	24.00

Table A2. *Cont.*

Constituent	Frequency (rad/s)	Period (h)
MK(3)	0.0002134401	8.18
2MK(3)	0.0002081166	8.39
MN(4)	0.0002783986	6.27
MS(4)	0.0002859630	6.10
2SM(2)	0.0001503693	11.61
Mf	0.0000053234	327.86
Msf	0.0000049252	354.37
Mm	0.0000026392	661.31
Sa	0.0000001991	8765.82
Ssa	0.0000003982	4382.91

References

1. Dietsche, D.; Hagen, S.C.; Bacopoulos, P. Storm surge simulations for hurricane hugo (1989): On the significance of inundation areas. *J. Waterw. Port Coast. Ocean Eng.* **2007**, *133*, 183–191. [CrossRef]
2. Irish, J.L.; Resio, D.T.; Ratcliff, J.J. The influence of storm size on hurricane surge. *J. Phys. Oceanogr.* **2008**, *38*, 2003–2013. [CrossRef]
3. Kerr, P.C.; Donahue, A.S.; Westerink, J.J.; Luettich, R.A.; Zheng, L.Y.; Weisberg, R.H.; Huang, Y.; Wang, H.V.; Teng, Y.; Forrest, D.R.; et al. U.S. IOOS coastal and ocean modeling testbed: Inter-model evaluation of tides, waves, and hurricane surge in the Gulf of Mexico. *J. Geophys. Res. Ocean* **2013**, *118*, 5129–5172. [CrossRef]
4. Pandoe, W.W.; Edge, B.L. Case study for a cohesive sediment transport model for Matagorda Bay, Texas, with Coupled ADCIRC 2D-Transport and SWAN wave models. *J. Hydraul. Eng.* **2008**, *134*, 303–314. [CrossRef]
5. Grzegorzewski, A.S.; Johnson, B.D.; Wamsley, T.V.; Rosati, J.D. Sediment transport and morphology modeling of Ship Island, Mississippi, USA, during storm events. In Proceedings of the Coastal Dynamics 2013, Arcachon Convention Centre, Arcachon, France, 24–28 June 2013; pp. 1505–1516.
6. Miles, T.; Seroka, G.; Kohut, J.; Schofield, O.; Glenn, S. Glider observations and modeling of sediment transport in Hurricane Sandy. *J. Geophys. Res. Ocean* **2015**, *120*, 1771–1791. [CrossRef]
7. Feyen, J.; Hess, K.; Spargo, E.; Wong, A.; White, S.; Sellars, J.; Gill, S. Development of a continuous bathymetric/topographic unstructured coastal flooding model to study sea level rise in North Carolina. In Proceedings of the Ninth International Conference on Estuarine and Coastal Modeling, Charleston, SC, USA, 3 October 2005; pp. 338–356.
8. Atkinson, J.; McKee Smith, J.; Bender, C. Sea-level rise effects on storm surge and nearshore waves on the Texas coast: Influence of landscape and storm characteristics. *J. Waterw. Port Coast. Ocean Eng.* **2013**, *139*, 98–117. [CrossRef]
9. Bilskie, M.V.; Hagen, S.C.; Medeiros, S.C.; Passeri, D.L. Dynamics of sea level rise and coastal flooding on a changing landscape. *Geophys. Res. Lett.* **2014**, *41*, 927–934. [CrossRef]
10. Cheng, T.K.; Hill, D.F.; Beamer, J.; García-Medina, G. Climate change impacts on wave and surge processes in a Pacific Northwest (USA) estuary. *J. Geophys. Res. Ocean* **2015**, *120*, 182–200. [CrossRef]
11. Mattocks, C.; Forbes, C. A real-time, event-triggered storm surge forecasting system for the state of North Carolina. *Ocean Model.* **2008**, *25*, 95–119. [CrossRef]
12. Fleming, J.G.; Fulcher, C.W.; Luettich, R.A.; Estrade, B.D.; Allen, G.D.; Winer, H.S. A real time storm surge forecasting system using ADCIRC. In Proceedings of the 10th International Conference on Estuarine and Coastal Modeling, Newport, RI, USA, 5–7 November 2008; pp. 893–912.
13. Dresback, K.M.; Fleming, J.G.; Blanton, B.O.; Kaiser, C.; Gourley, J.J.; Tromble, E.M.; Luettich, R.A.; Kolar, R.L.; Hong, Y.; Van Cooten, S.; et al. Skill assessment of a real-time forecast system utilizing a coupled hydrologic and coastal hydrodynamic model during Hurricane Irene (2011). *Cont. Shelf Res.* **2013**, *71*, 78–94. [CrossRef]
14. Dietrich, J.; Dawson, C.; Proft, J.; Howard, M.; Wells, G.; Fleming, J.; Luettich, R.; Westerink, J.; Cobell, Z.; Vitse, M.; et al. Real-time forecasting and visualization of hurricane waves and storm surge using SWAN + ADCIRC and FigureGen. In *Computational Challenges in the Geosciences*; Dawson, C., Gerritsen, M., Eds.; Springer: New York, NY, USA, 2013; Volume 156, pp. 49–70.

15. Dietrich, J.C.; Trahan, C.J.; Howard, M.T.; Fleming, J.G.; Weaver, R.J.; Tanaka, S.; Yu, L.; Luettich, R.A.; Dawson, C.N.; Westerink, J.J.; et al. Surface trajectories of oil transport along the Northern Coastline of the Gulf of Mexico. *Cont. Shelf Res.* **2012**, *41*, 17–47. [CrossRef]
16. Carr, S.; Hench, J.; Luettich, R.; Forward, R.; Tankersley, R. Spatial patterns in the ovigerous Callinectes sapidus spawning migration: Results from a coupled behavioral-physical model. *Mar. Ecol.* **2005**, *294*, 213–226. [CrossRef]
17. Oliveira, A.; Fortunato, A.B.; Pinto, L. Modelling the hydrodynamics and the fate of passive and active organisms in the Guadiana estuary. *Estuar. Coast. Shelf Sci.* **2006**, *70*, 76–84. [CrossRef]
18. Reyns, N.B.; Eggleston, D.B.; Luettich, R.J.A. Secondary dispersal of early juvenile blue crabs within a wind-driven estuary. *Limnol. Oceanogr.* **2006**, *51*, 1982–1995. [CrossRef]
19. Alizad, K.; Hagen, S.C.; Morris, J.T.; Bacopoulos, P.; Bilskie, M.V.; Weishampel, J.F.; Medeiros, S.C. A coupled, two-dimensional hydrodynamic-marsh model with biological feedback. *Ecol. Model.* **2016**, *327*, 29–43. [CrossRef]
20. Tromble, E.; Kolar, R.; Dresback, K.; Luettich, R. River flux boundary considerations in a coupled hydrologic-hydrodynamic modeling system. In Proceedings of the 12th International Conference on Estuarine and Coastal Modeling 2011, St. Augustine, FL, USA, 7–9 November 2011; pp. 510–527.
21. Lyard, F.; Lefevre, F.; Letellier, T.; Francis, O. Modelling the global ocean tides: modern insights from FES2004. *Ocean Dyn.* **2006**, *56*, 394–415. [CrossRef]
22. OTIS Regional Tidal Solutions. Available online: http://volkov.oce.orst.edu/tides/region.html (accessed on 19 September 2018).
23. Parrish, D.M.; Hagen, S.C. A tidal constituent database for the east coast of Florida. In Proceedings of the Fourth International Symposium on Ocean Wave Measurement and Analysis, San Francisco, CA, USA, 2–6 September 2002; pp. 1605–1614.
24. Westerink, J.J.; Luettich, R.A.; Muccino, J.C. Modelling tides in the western North Atlantic using unstructured graded grids. *Tellus* **1994**, *46*, 178–199. [CrossRef]
25. Mukai, A.Y.; Westerink, J.J.; Luettich, R.A.; Mark, D. *Eastcoast 2001: A Tidal Constituent Database for the Western North Atlantic, Gulf of Mexico and Caribbean Sea*; Technical Report for ERDC/CHL TR-02-24; U.S. Army Engineer Research and Development Center, Coastal and Hydraulics Laboratory: Vicksburg, MS, USA, 2002; p. 201. Available online: http://www.unc.edu/ims/adcirc/publications/2002/2002_Mukai01.pdf (accessed on 27 June 2016).
26. Szpilka, C.; Dresback, K.; Kolar, R.; Feyen, J.; Wang, J. Improvements for the western north Atlantic, Caribbean and Gulf of Mexico ADCIRC tidal database (EC2015). *J. Mar. Sci. Eng.* **2016**, *4*, 72. [CrossRef]
27. Spargo, E.; Westerink, J.; Luettich, R., Jr.; Mark, D. *ENPAC 2003: A Tidal Constituent Database for Eastern North Pacific Ocean*; Technical Report ERDC/CHL TR-04-12; U.S. Army Engineer Research and Development Center, Coastal and Hydraulics Laboratory: Vicksburg, MS, USA, 2004; Available online: http://www.unc.edu/ims/ccats/tides/ENPAC_2003_report.pdf (accessed on 18 September 2018).
28. Guillou, N.; Neill, S.P.; Robins, P.E. Characterising the tidal stream power resource around France using a high-resolution harmonic database. *Renew. Energy* **2018**, *123*, 706–718. [CrossRef]
29. Kelleher, G.; Bleakley, C.; Wells, S. *A Global Representative System of Marine Protected Areas IV*; The World Bank: Washington, DC, USA, 1995.
30. *ETOPO-5 Bathymetry/Topography Data*; Data Announcement 88-MGG-02, National Geophysical Data Center; National Oceanic and Atmospheric Administration, U.S. Department of Commerce: Boulder, CO, USA, 1988.
31. *GEODAS CD-ROM Hydrographic Survey Data*; Data Announcement 98-MGG-03, National Geophysical Data Center; National Oceanic and Atmospheric Administration, U.S. Department of Commerce: Boulder, CO, USA, 1998.
32. Schureman, P. *Manual of Harmonic Analysis and Prediction of Tides*; Special Publication 98, Coast and Geodetic Survey; U.S. Dept. of Commerce: Washington, DC, USA, 1958; p. 317.
33. Kinnmark, I. *The Shallow Water Wave Equations: Formulation, Analysis and Application*; Lecture Notes in Engineering; Springer: Berlin/Heidelberg, Germany, 1986; Volume 15, ISBN 9783540160311.
34. Luettich, R.A.; Westerink, J.J.; Scheffner, N.W. *ADCIRC: An Advanced Three-Dimensional Circulation Model for Shelves, Coasts, and Estuaries; Report 1: Theory and Methodology of ADCIRC-2DDI and ADCIRC-3DL*; Technical Report CERC-TR-DRP-92-6; U.S. Army Corps of Engineers, U.S. Department of the Army: Washington, DC, USA, 1992.

35. Kolar, R.L.; Gray, W.G.; Westerink, J.J.; Luettich, R.A. Shallow water modeling in spherical coordinates: equation formulation, numerical implementation, and application. *J. Hydraul. Res.* **1994**, *32*, 3–24. [CrossRef]
36. Bunya, S.; Dietrich, J.C.; Westerink, J.J.; Ebersole, B.A.; Smith, J.M.; Atkinson, J.H.; Jensen, R.; Resio, D.T.; Luettich, R.A.; Dawson, C.; et al. A high-resolution coupled riverine flow, tide, wind, wind wave, and storm surge model for Southern Louisiana and Mississippi. Part I: Model Development and Validation. *Mon. Weather Rev.* **2010**, *138*, 345–377. [CrossRef]
37. OSU Tidal Data Inversion. Available online: http://volkov.oce.orst.edu/tides/tpxo8_atlas.html (accessed on 21 July 2018).
38. Xu, J.; Feyen, J. *The Extratropical Surge and Tide Operational Forecast System for the Eastern North Pacific Ocean (ESTOFS-Pacific): Development and Skill Assessment*; NOAA Technical Memorandum NOS CS 36; U.S. Department of Commerce: Silver Spring, MD, USA, 2016. Available online: https://repository.library.noaa.gov/view/noaa/8441 (accessed on 20 September 2018).
39. NOAA/NOS's VDatum 3.6: Vertical Datums Transformation. Available online: http://vdatum.noaa.gov/welcome.html (accessed on 21 July 2016).
40. Myers, E.; Woolard, J.; Yang, Z.; Aikman, F. Development of a vertical datum transformation tool and a bathymetric/topographic digital elevation model for southern California. In Proceedings of the Coastal Society 2008, Redondo Beach, CA, USA, 29 June–2 July 2008.
41. Xu, J.; Myers, E.; White, S. *VDatum for the Coastal Waters of North/Central California, Oregon and Western Washington: Tidal Datums and Sea Surface Topography*; NOAA Technical Memorandum NOS CS 22; U.S. Department of Commerce: Silver Spring, MD, USA, 2010. Available online: https://vdatum.noaa.gov/download/publications/CS_22_FY09_33_Jiangtao_PNW_VDatum_techMemor.pdf (accessed on 19 September 2018).
42. VDatum Manual for Development and Support of NOAA's Vertical Datum Transformation Tool, VDatum. Version 1.01. 2012. Available online: http://www.nauticalcharts.noaa.gov/csdl/publications/Manual_2012.06.26.doc (accessed on 27 June 2016).
43. Foreman, M.G.G.; Sutherland, G.; Cummins, P.F. M2 tidal dissipation around Vancouver Island: an inverse approach. *Cont. Shelf Res.* **2004**, *24*, 2167–2185. [CrossRef]
44. Foreman, M.G.G.; Stucchi, D.J.; Garver, K.A.; Tuele, D.; Isaac, J.; Grime, T.; Guo, M.; Morrison, J. A circulation model for the discovery islands, British Columbia. *Atmosphere-Ocean* **2012**, *50*, 301–316. [CrossRef]
45. Bacopoulos, P.; (University of North Florida, Jacksonville, FL, USA). Personal communication, 2015.
46. Parrish, D.M.; Hagen, S.C. 2D unstructured mesh generation for oceanic and coastal tidal models from a localized truncation error analysis with complex derivatives. *Int. J. Comput. Fluid Dyn.* **2007**, *21*, 277–296. [CrossRef]
47. NOS Hydrographic Survey Data and Products. Available online: https://www.ngdc.noaa.gov/mgg/bathymetry/hydro.html (accessed on 20 September 2018).
48. Smith, W.H.F.; Sandwell, D.T. Global sea floor topography from satellite altimetry and ship depth soundings. *Science* **1997**, *277*, 1956–1962. [CrossRef]
49. Carrère, L.; Lyard, F.; Cancet, M.; Roblou, L.; Guillot, A. FES2012: A new global tidal model taking advantage of nearly 20 years of altimetry measurements. In Proceedings of the Meeting "20 Years of Progress in Radar Altimetry Symposium", Venice, Italy, 24–29 September 2012.
50. Global Tide—FES: Aviso+. Available online: http://www.aviso.altimetry.fr/en/data/products/auxiliary-products/global-tide-fes.html (accessed on 27 June 2016).
51. Egbert, G.D.; Bennett, A.F.; Foreman, M.G.G. TOPEX/POSEIDON tides estimated using a global inverse model. *J. Geophys. Res.* **1994**, *99*, 24821. [CrossRef]
52. Egbert, G.D.; Erofeeva, S.Y. Efficient inverse modeling of Barotropic Ocean tides. *J. Atmos. Ocean. Technol.* **2002**, *19*, 183–204. [CrossRef]
53. USGS Coastal and Marine Geology—usSEABED. Available online: http://walrus.wr.usgs.gov/usseabed/ (accessed on 29 June 2016).
54. Kolar, R.L.; Westerink, J.J.; Cantekin, M.E.; Blain, C.A. Aspects of nonlinear simulations using shallow-water models based on the wave continuity equation. *Comput. Fluids* **1994**, *23*, 523–538. [CrossRef]
55. NOAA Tides and Currents. Available online: http://tidesandcurrents.noaa.gov/ (accessed on 21 July 2018).
56. Foreman, M.G.G.; (Institute of Ocean Sciences—Fisheries and Oceans Canada, Sidney, BC, Canada). Personal communication, 2015.

57. *IHO Tidal Constituent Bank: Station Catalogue*; Department of Fisheries and Oceans: Ottawa, ON, Canada, 1979.
58. Foreman, M.G.G.; Walters, R.A.; Henry, R.F.; Keller, C.P.; Dolling, A.G. A tidal model for eastern Juan de Fuca Strait and the southern Strait of Georgia. *J. Geophys. Res.* **1995**, *100*, 721. [CrossRef]
59. ADCIRC Tidal Database—ADCIRC. Available online: http://adcirc.org/products/adcirc-tidal-databases/ (accessed on 23 September 2018).
60. ADCIRC Utility Programs—ADCIRC. Available online: http://adcirc.org/home/related-software/adcirc-utility-programs/ (accessed on 23 September 2018).

Journal of
Marine Science and Engineering

MDPI

Article

Modelling Behaviour of the Salt Wedge in the Fraser River and Its Relationship with Climate and Man-Made Changes

Albert Tsz Yeung Leung [1,*], Jim Stronach [1] and Jordan Matthieu [2]

[1] Tetra Tech Canada Inc., Water and Marine Engineering Group, 1000-10th Floor 885 Dunsmuir Street, Vancouver, BC V6C 1N5, Canada; Jim.Stronach@tetratech.com
[2] WSP, Coastal, Ports and Maritime Engineering, 1600-René-Lévesque O., 16e étage, Montreal, QC H3H 1P9, Canada; Jordan.Matthieu@wsp.com
* Correspondence: albert.leung@tetratech.com; Tel.: +1-604-644-9376

Received: 20 September 2018; Accepted: 3 November 2018; Published: 6 November 2018

Abstract: Agriculture is an important industry in the Province of British Columbia, especially in the Lower Mainland where fertile land in the Fraser River Delta combined with the enormous water resources of the Fraser River Estuary support extensive commercial agriculture, notably berry farming. However, where freshwater from inland meets saltwater from the Strait of Georgia, natural and man-made changes in conditions such as mean sea level, river discharge, and river geometry in the Fraser River Estuary could disrupt the existing balance and pose potential challenges to maintenance of the health of the farming industry. One of these challenges is the anticipated decrease in availability of sufficient freshwater from the river for irrigation purposes. The main driver for this challenge is climate change, which leads to sea level rise and to reductions in river flow at key times of the year. Dredging the navigational channel to allow bigger and deeper vessels in the river may also affect the availability of fresh water for irrigation. In this study, the salinity in the river was simulated using H3D, a proprietary three-dimensional hydrodynamic numerical model which computes the three components of velocity (u,v,w) in three dimensions (x,y,z) on a curvilinear grid developed specially for Fraser River, as well as scalar fields such as salinity and temperature. The results indicate various levels of impact to the salinity in the river and adaptive measures must be established to maintain the long-term viability of the industry. This study found that sea level rise and changes in river discharge would have a larger impact on the availability of fresh water than would channel deepening at the present sea water level. In a low river discharge regime, the impact from sea level change is more significant than in the high river discharge regime. On the other hand, the influence from changes in river discharge on withdrawal appears to increase when water level is lowered. Dredging the channel to accommodate larger vessels with deeper draft would further affect the salinity and shorten the withdrawal window; the effect of channel deepening becomes more pronounced in the lower flow period.

Keywords: hydrodynamic numerical model; H3D; agriculture; salt wedge; climate change; sea level rise; river discharge; channel deepening

1. Introduction

Many of the largest economies in the world are located near or in a river estuary where saline water from the ocean meets the freshwater draining from inland: The Hudson River in New York, the Mississippi River in New Orleans, the Buffalo Bayou in Houston, the Yellow River in Shanghai, and the Pearl River in Hong Kong, just to name a few. These are not coincident, because an estuary often is of critical commercial value to nearby areas; and altogether, estuaries serve to contribute

not only to human welfare and value to the world's economy, but also provide essential ecosystem services such as food production and recycling of nutrients [1]. Among the many commercial functions it can serve, an estuary can be a conduit for transport of goods and products, and is very often an important water resource for domestic, industrial, and agricultural use. These economic benefits brought forth by an estuary are of course in addition to the environmental benefits resulting from a highly diverse ecosystem that an estuary usually sustains due to its unique hydrodynamic and geomorphologic settings.

The hydrodynamic behavior and salinity of an estuary is sensitive to climate change that could potentially affect sea level and the hydrological characteristics that dictate the amount of watershed runoff. This delicate balance is further complicated by future changes in river management such as channel deepening in order to allow navigation by larger vessels in the estuary. Understanding the complicated interaction between changes in sea level and runoff as well as bathymetry of the river and their impacts on the salinity in the river is therefore essential for developing proper and timely strategies to ensure resiliency of coastal areas against natural and anthropogenic changes in the future.

The hydrodynamics of the Fraser River estuary has been extensively studied in the past: Stronach et al. [2,3], and Halverson and Pawlowicz [4,5] studied and described the river plume dynamics of the Fraser River outflow into the Strait of Georgia. Halverson and Pawlowicz [6], Kostaschuk and Atwood [7], and Ward [8] particularly investigated the river flow and tidal forcing in the Fraser River estuary and their effects on salinity. Yin et al. [9] studied the biological significance of the salt wedge dynamics in the Fraser River estuary. Neilson-Welch and Smith [10] observed and described the effects of the upstream intrusion of saltwater.

There is limited, if any, published literature regarding specifically the effects of sea level rise (SLR) and changes in river discharge and river geometry on salinity distribution in the Fraser River, but similar studies were undertaken in other parts of the world: Krvavica et al. [11] studied the salt wedge in the Rjecina River Estuary in Croatia using a finite volume model; Funahashi et al. [12] developed a numerical model using Delft3DFlow to investigate the response of the salt wedge and salinity distribution in the river to the short-term changes in sea level and river discharge in the Yura Estuary in Japan; and Shaha et al. [13] studied the saltwater intrusion in Sumjin River Estuary in South Korea using the Finite Volume Community Ocean Model (FVCOM) and related intrusion length and river discharge by a power law.

2. Study Site

The Fraser River estuary, located south of Vancouver, is an important part of the economy in the Province of British Columbia (BC), Canada [14]. The Fraser River delta is fertile and, as such, the agricultural industry in the region is thriving, with a noticeable increase in the farmland area in the late 20th and early 21st centuries [15]. There is potential for significant growth in terms of agricultural production, provided that additional water can be withdrawn from the river for irrigation [16]. The low-salinity water withdrawn from the river for irrigation is therefore of critical importance to the continued health of the farmland and its agricultural products.

The Fraser River is connected at its downstream boundary to the Strait of Georgia (SOG), which in turn is connected to the open Pacific Ocean through the connections at Juan de Fuca Strait to the south and Johnstone Strait to the north. Therefore, water level in the SOG and the Fraser River is subject to tidal fluctuations. Figure 1 below illustrates the study location as well as the geographic and hydrographic relations between the Fraser River, the SOG, and the Pacific Ocean.

The tidal range in the Fraser River is variable, depending not only on the tidal fluctuation in the SOG, but also on distance upstream from the river mouth and on river discharge. At the river mouth, the tide is mixed, mainly semi-diurnal, and exhibits a clear alternating neap tide and spring tide pattern. The higher high water level is 2.0 m above mean sea level, which in turn is 3.1 m above chart datum, resulting in a tidal range of 5.1 m. This tidal effect, though diminishing in an upstream direction, can reach as far upstream as Mission, approximately 84 km from the river mouth.

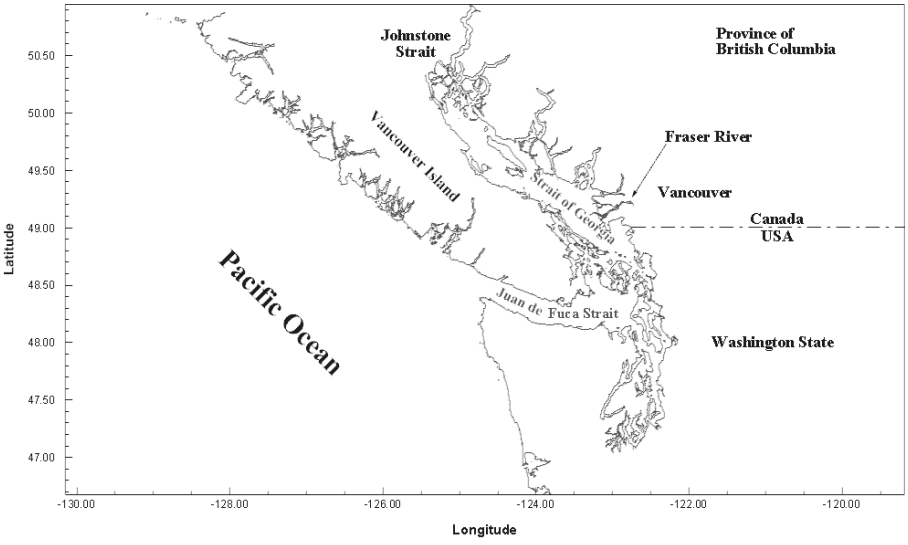

Figure 1. Study location of the Fraser River estuary.

The stratification in the SOG and the Fraser River is due to the presence of saltwater from the Pacific Ocean and freshwater from river runoff. The interaction of the freshwater and saltwater masses in the Fraser River Estuary gives rise to the formation of a salt-wedge, which intrudes from the SOG into the river in an upstream direction. While the salt wedge occupies the part of the water column from the bottom to a certain depth, the fresh river water, upon meeting the salt wedge, travels downstream on top of the salt-wedge. The extent of the intrusion varies depending on the river discharge and water level in the SOG: while the position and salinity of the salt-wedge displays an intra-day pattern in response to the semi-diurnal tidal fluctuation in the Strait, the mean daily position of the salt-wedge moves upstream and downstream in response to the changes in river discharge. The salinity in the river has a strong correlation with the salt-wedge intrusion and thus displays similar fluctuation patterns.

3. Materials and Methods

The core component of the study is the numerical simulation of the salt wedge in the Fraser River, the largest river in BC, which drains into the SOG in the Salish Sea, under a range of climate change, river flow, and river configuration scenarios. A numerical model of the Fraser River, based on the modelling platform H3D developed by Tetra Tech, has been implemented and calibrated for present conditions; however, the fundamental processes: bottom friction, vertical mixing, salt wedge migration under tidal influence, are all intrinsic processes, i.e., their formulation depends only on the specific flow and water level conditions imposed by external influences. In other words, the model is totally objective with respect to evaluating climate change. Thus, the model does not require modification for this work. However, it is important to select and properly quantify climate change scenario inputs for modelling.

3.1. Three-Dimensional Hydrodynamic Numerical Model: H3D

H3D is an implementation of the numerical model developed by Backhaus [17,18], which has had numerous applications to the European continental shelf [19,20], Arctic waters [21,22], and deep estuarine waters [23]. Locally, H3D has been used to model the temperature structure of Okanagan Lake [24], the transport of scalar contaminants in Okanagan Lake [25], sediment movement and

scour/deposition in the Fraser River, circulation and wave propagation in Seymour and Capilano dams, and salinity movement in the lower Fraser River. H3D forms the basis of the model developed by Saucier and co-workers for the Gulf of St. Lawrence [26], and has been applied to the Gulf of Mexico [27].

3.1.1. Theoretical Basis

H3D is a three-dimensional time-stepping numerical model which computes the three components of velocity (u,v,w) on a structured grid in three dimensions (x,y,z), as well as scalar fields such as salinity, temperature, and contaminant concentrations. The model uses the Arakawa C-grid in space [28], and uses a two level semi-implicit scheme in the time domain. The Arakawa C-grid evaluates velocity vector components at the centres of the grid faces (i.e., u-component velocities are evaluated at the centres of the east and west grid faces, v-component velocities on the north and south grid faces, and w-component velocities on the top and bottom grid faces, while scalar quantities are calculated in the grid centres). The size of the model time step varies depending on the horizontal grid size and velocity at each of the grid cells: the model, at each time step and each grid cell, calculates the numerically-stable time step based on the u-, v-, and w-components of the velocity and the x-, y-, and z-dimensions of the grid cell; the model then updates the time step by choosing the largest time step that will satisfy the numerical stability for all grid cells. Details with respect to the derivation of the model are provided in Appendix A.

3.1.2. Grid Geometry

In the horizontal, the grid cells can be either rectilinear or orthogonal curvilinear, depending on the physical characteristics of the water body of interest. Details regarding the horizontal resolution and configuration of the models are described in Section 3.2. In the vertical, the levels near the surface are typically closely spaced to assist with resolving near-surface dynamics. Figure 2 shows a typical grid mesh utilized for the H3D model.

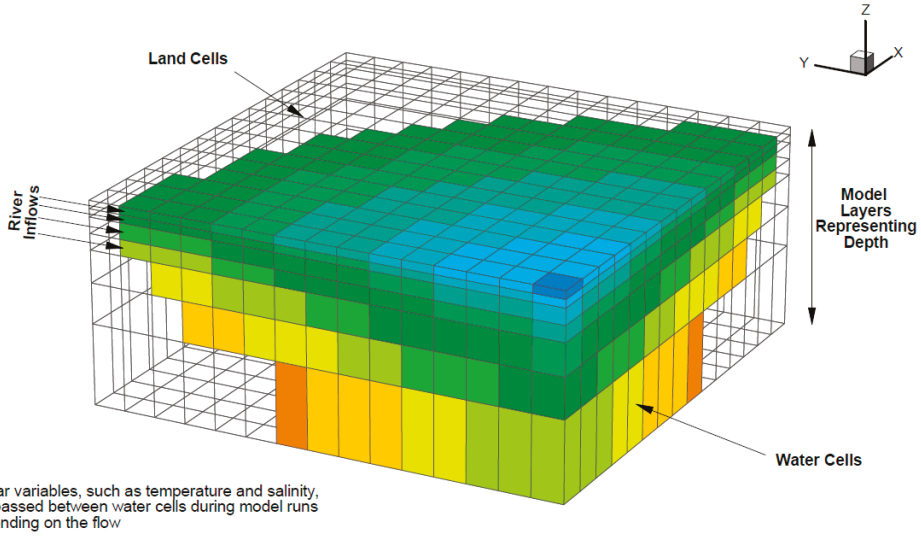

Figure 2. Typical grid mesh used in H3D.

In addition, the model is capable of dealing with relatively large excursions in overall water level as the water level rises and falls in response to varying inflows and outflows, by allowing the number of near-surface layers to change as the water level varies. That is, as water levels rise in a particular

cell, successive layers above the original layer are turned on and become part of the computational mesh. Similarly, as water levels fall, layers are turned off. This procedure has proven to be quite robust, and allows for any reasonable vertical resolution in near-surface waters. When modelling thin river plumes in areas of large tidal range, the variable number of layers approach allows for much better control over vertical resolution than does the σ-coordinate method.

In addition to tides, the model is able to capture the important response, in terms of enhanced currents and vertical mixing, to wind-driven events. This is achieved by applying wind stress to each surface grid point on each time step. Vertical mixing in the model then re-distributes this horizontal momentum throughout the water column. Similarly, heat flux through the water surface is re-distributed by turbulence and currents in temperature simulations.

3.1.3. Turbulent Closure

Turbulence modelling is important in determining the correct distribution of velocity and scalars in the model. The diffusion coefficients for momentum (A_H and A_V) and scalars (N_H and N_V) at each computational cell are dependent on the level of turbulence at that point. H3D uses a shear-dependent turbulence formulation in the horizontal presented by Smagorinsky [29]. The basic form is:

$$A_H = A_{H_0} dx dy \sqrt{\left(\frac{du}{dx}\right)^2 + \left(\frac{dv}{dy}\right)^2 + \frac{1}{2}\left(\frac{\partial v}{\partial x} + \frac{\partial u}{\partial y}\right)^2} \quad (1)$$

where the parameter A_{H0} is a dimensionless tuning variable, and experience has shown it to lie in the range of 0.25 to 0.45 for most water bodies such as rivers, lakes and estuaries.

A shear and stratification dependent formulation, the Level 2 model of Mellor and Yamada [30], is used for the vertical eddy diffusivity. The basic theory for the vertical viscosity formulation is taken from an early paper by Mellor and Durbin [31]. The evaluation of length scale is based on a methodology presented by Mellor and Yamada [30].

For scalars, both horizontal and vertical eddy diffusivity are taken to be similar to their eddy viscosity counterparts, but scaled by a fixed ratio from the eddy viscosity values. Different ratios are used for the horizontal and vertical diffusivities. If data is available for calibration, these ratios can be adjusted based on comparisons between modelled and observed data. Otherwise, standard values based on experience with similar previously modelled water bodies are used. In a recent reservoir simulation with good calibration data, the ratio of vertical eddy diffusivity to vertical eddy viscosity was 0.75 and the ratio between horizontal eddy diffusivity and horizontal eddy viscosity was 1.0.

3.1.4. Scalar Transport

The scalar transport equation implements a form of the flux-corrected algorithm presented by Zalesak [32], in which all fluxes through the sides of each computational cell are first calculated using a second-order method. Although generally more accurate than a first order method, second order flux calculations can sometimes lead to unwanted high frequency oscillations in the numerical solution. To determine if such a situation is developing, the model examines each cell to see if the computed second order flux would cause a local minimum or maximum to develop. If so, then all fluxes into or out of that cell are replaced by first order fluxes, and the calculation is completed. As noted, the method is not a strict implementation of the Zalesak method, but is much faster and achieves very good performance with respect to propagation of a Gaussian distribution through a computational mesh. It does not propagate box-car distributions as well as the full Zalesak method, but achieves realistic simulations of the advection of scalars in lakes, rivers, and estuaries, which is the goal of the model. This scheme as implemented is thus a good tradeoff between precision and execution time, important since in many situations, where more than one scalar is involved, the transport-diffusion algorithm can take up more than half the execution time.

3.1.5. Heat Flux at the Air–Water Interface

The contribution of heat flux to the evolution of the water temperature (T) field is schematized in H3D as:

$$\frac{\partial T}{\partial t} = \frac{\Delta F}{\rho * C_P * h} \tag{2}$$

where ΔF is the net heat flux per unit area retained in a particular layer, ρ is the density of water, C_p is the heat capacity of water, and h is the layer thickness. Heat flux at the air–water interface incorporates the following terms:

- F_{in}: incident short wave radiation. Generally, this is not known from direct observations. Instead, it is estimated from the cloud cover and opacity observations at nearby stations, a theoretical calculation of radiation at the top of the atmosphere based on the geometry of the earth/sun system, and an empirical adjustment based on radiation measurements at Vancouver International Airport for the period 1974–1977. This procedure has worked well for many water bodies, notably Okanagan Lake and the waters of the north coast of British Columbia, in terms of allowing H3D to reproduce the observed temperature distributions in space and time. Values for albedo as a function of solar height are taken from Kondratyev [33].
- F_{back}: net long wave radiation. This is calculated according to Gill [34], involving the usual fourth power dependence on temperature, a factor of 0.985 to allow for the non-black body behaviour of the ocean, a factor depending on vapor pressure to allow for losses due to back radiation from moisture in the air, and a factor representing backscatter from clouds.
- F_L and F_S: Latent heat flux (F_L) is the heat carried away by the process of evaporation of water. Sensible heat flux (F_S) is driven by the air-water temperature difference and is similar to conduction, but assisted by turbulence in the air. Latent and sensible heat fluxes are described by:

$$Q_L = 1.32e^{-2} * L * U_a * (q_{obs} - q_{sat}) * F_l, \text{ and} \tag{3}$$

$$Q_S = 1.46e^{-3} * \rho_{air} * c_p * U_a * (T_{air} - T_{water}) * F_s, \tag{4}$$

  where q_{obs} and q_{sat} are the observed and saturated specific humidities, T_{air} and T_{water} are the air and water temperatures, L is the latent heat of evaporation of water, and C_p is the heat capacity of water, U_a is wind speed, F_l and F_s are latent and sensible factors, which are the scaling factors introduced to account for local factors, and can be adjusted, when needed, to achieve better calibration of the model. Typically, the only adjustment is that sensible factor is doubled when the air temperature is less than the water or ice surface temperature to account for increased turbulence in an unstable air column.

As light passes through the water column it is absorbed and the absorbed energy is a component of the energy balance that drives water temperature. H3D assumes that light attenuation follows an exponential decay law:

$$E(z) = E(z_0) * e^{-k*(z-z_0)}, \tag{5}$$

where $E(z)$ is the insolation at a distance, z, below the water surface, and $E(z_0)$ is the incident insolation at the water surface. The model computes the energy at the top and bottom of each layer and the difference is applied to the general heat equation in that layer. The extinction coefficient (k) is related to the Secchi depth (D_s) by:

$$k = \frac{2.1}{D_s}. \tag{6}$$

Temperature is treated like any other scalar as far as advection and diffusion are concerned.

3.2. Model Implementation

A study of the details of the hydrodynamics of the Fraser River requires model nesting to better resolve small scale processes at and near locations of interest. The model used for this study operates in a triple-nested configuration, shown in Figure 3.

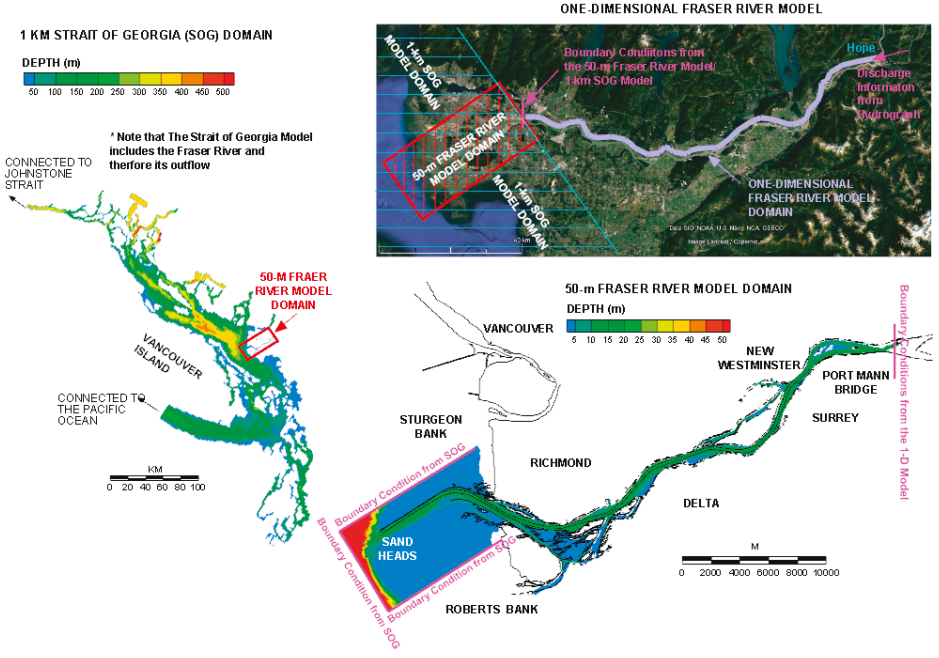

Figure 3. Nesting of the 1-km Strait of Georgia (SOG) model, the 50-m Fraser River model, and the one-dimensional Fraser River model.

The investigation of the behaviour of the salt wedge was undertaken with a nominally 50-m resolution curvilinear model that spans the lower 41 km of the Fraser River, from Sand Heads to the Port Mann Bridge. The model uses 50-m resolution in the along-channel direction, and 20-m in the cross-channel direction. This 50-m resolution model is in turn embedded within a nominally 1-km resolution rectilinear model of the entire SOG. The vertical resolution of the models varies with depth and is 1 m for the top 10 m, 2 m for depth of 10–16 m, 3 m for 16–25 m, 10 m for 25–55 m, 25 m for 55–105 m, 50 m for 105–305 m, and 100 m for 305–505 m. The higher vertical resolution near the top is necessary to resolve the complex hydrodynamic processes and the sharp salinity gradient at the interface of the salt wedge.

Both models simulate tidal, wind-driven, and density-driven currents. Water level, velocity components, and any scalar quantities (i.e., temperature and salinity) output from the coarse grid model are passed on along the boundaries of the fine grid model and used to drive the finer-scale implementation of H3D. The fine-grid implementation provides the details of the effect of small-scale spatial variability in shorelines, depths and structures such as the tunnel cover.

The 1-km SOG model, driven by wind, temperature, and salinity as well as tidal conditions along its open boundaries bordering the northern entrance to the SOG and the western entrances to Juan de Fuca Strait, includes a coarse representation of the Fraser River, extending 41 km upstream from the river mouth at Sand Heads to the Port Mann Bridge. At that location, upstream of all salt wedge penetration, the model is dynamically coupled to a one-dimensional (1-D) model of the Fraser River,

extending to Hope, which is located approximately 130 km upstream from the river mouth and is free of any tidal effects. The model coupling is two-way as the SOG model provides water level to the downstream boundary of the 1-D model, which in turn calculates the flow conditions at that same boundary given the discharge rate at the upstream boundary of the 1-D model at Hope. The initial and boundary conditions for temperature and salinity are provided by Crean and Ages [35], which documented a comprehensive temperature and salinity measurement campaign in the SOG and Juan de Fuca Strait. Tidal conditions are also specified along the open boundaries.

The 50-m lower Fraser River model is driven at its upstream end by flow boundary conditions provided by a separate, dynamically coupled 1-D Fraser River model. At the downstream end, water levels as well as temperature and salinity profiles are obtained from the 1-km SOG model, spatially interpolated from those cells of the 1-km SOG model that correspond to the boundaries of the 50-m Fraser River model.

Table 1 below summarizes the modelling sequence (Seq. #), the initial conditions and boundary conditions utilized for the modelling study:

Table 1. Modelling sequence of the study.

Seq. #	Model	Initial Conditions	Downstream Boundary Conditions	Upstream Boundary Conditions	Dynamic Model Coupling	Objective
1a	1-km SOG	Temperature and salinity profiles	Temperature, salinity and tidal level	Flow conditions provided by the 1-D Fraser River model	1-D Fraser River model for the 1-km SOG model	To provide boundary conditions to the 50-m Fraser River Model
1b	1-D Fraser River-for the 1-km SOG	Water level	Water level from the 1-km SOG model	River hydrograph at Hope	1-km SOG model	To provide upstream boundary conditions to the 1-km SOG model
2a	50-m Fraser River	Temperature and salinity profiles	Temperature, salinity and tidal level provided by the SOG model	Flow conditions provided by the 1-D Fraser River model	1-D Fraser River model for the 50-m Fraser River model	To simulate spatial and temporal salinity distributions in the Fraser River
2b	1-D Fraser River-for the 50-m Fraser River	Water level	Water level from the 1-km SOG model	River hydrograph at Hope	50-m Fraser River model	To provide upstream boundary conditions to the 50-m Fraser River model

3.3. Validation of the Nested Model

The models were initialized on 1 January 2011 and run through the 6-month long harvest season period, between August and December, when the ability to withdraw freshwater from the river is crucial. The year 2011 was chosen for the model validation as this is the year for which bank-to-bank bathymetric survey data collected in the Fraser River estuary is available: the model bathymetry was constructed using this 2011 data set; the Fraser River flow rate in 2011 was used to drive the upstream boundary of the river model, and the tidal conditions in 2011 were specified along the open boundaries in the SOG model. The flow rate at the upstream boundary of the model is the combination of the flow rate at Hope and the estimated runoffs that report to the river downstream of Hope and upstream of the Port Mann Bridge. Figure 4 shows the observed river flow rate at Hope in the year 2011 [36].

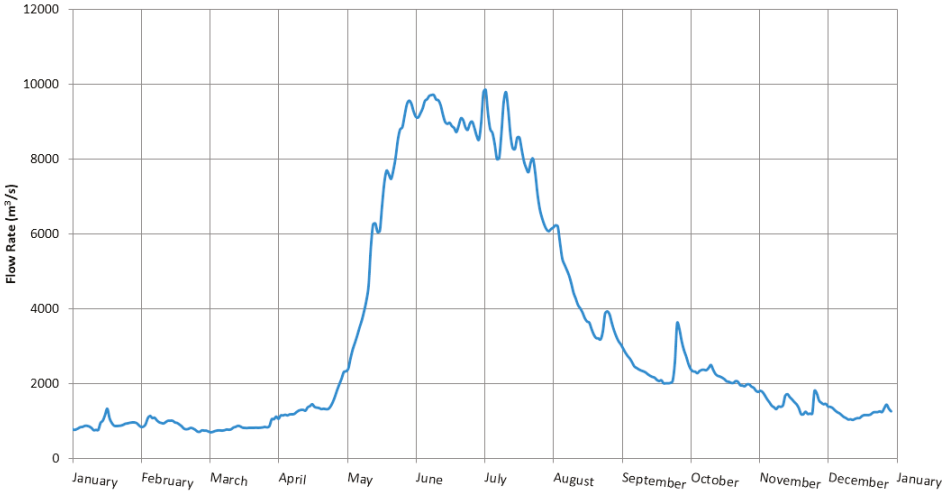

Figure 4. Fraser River flow rate at Hope in 2011.

The model was validated against water levels recorded at New Westminster, which is located 34 km upstream from the river mouth, and against conductivity data collected by a sensor mounted at 2 m depth from a floating platform installed at an irrigation intake near 8081 River Road, Delta, approximately 24 km upstream from the river mouth. Figure 5 shows a comparison of observed and modelled conductivity values at the water intake (location shown in Figure 6) at a depth of 2 m from 3rd to 23rd November 2011, when the leading edge of the salt wedge passed upstream and downstream through the sensor location and the conductivity signal ranged between zero and the maximum value that the sensor could record, 5500 µS/cm. Comparison of the observed and modelled results for months other than November would have been undertaken if not for the lack of reliable, continual conductivity measurement at other locations in the river (identified as data gap in Section 5.4). Also included in the figure are observed and modelled water levels for the same period. Black lines show modelled values and red lines show observed values. Since the conductivity sensor cuts off at 5500 µS/cm, the model results were similarly cut-off to facilitate comparison.

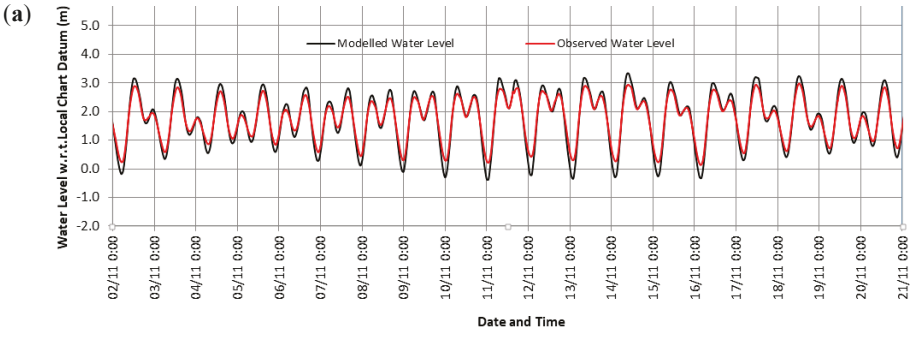

Figure 5. *Cont.*

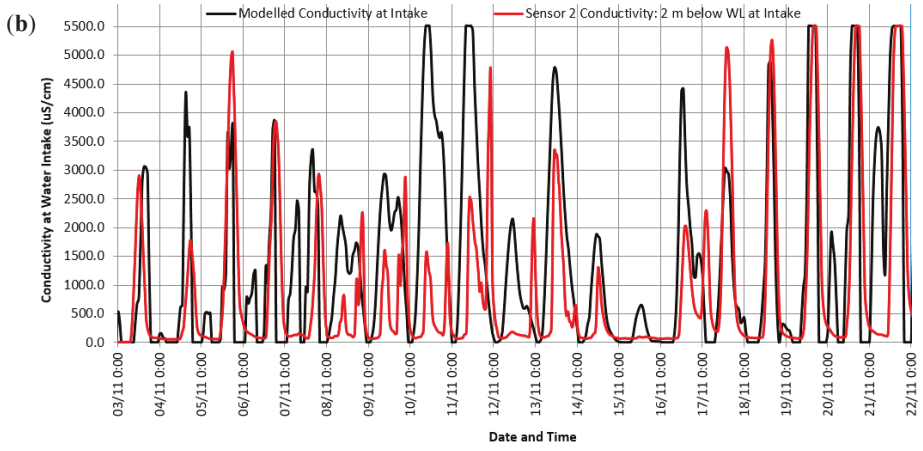

Figure 5. Comparison of observed and modelled results: (**a**) water level and (**b**) conductivity in the Fraser River.

The days on which the observed conductivity is considerably lower than the modelled correspond almost perfectly with the days with rainfall in the catchment downstream of the Harrison River exceeding 15 mm/day: 7, 10–12, 17, 21–22 November. A rainfall of 15 mm/day corresponds, approximately, to an additional flow in the Fraser River of up to 1000 m^3/s, depending on the hydrological processes controlling how this additional water reports to the river. This additional fresh water would undoubtedly lead to significant reduction in conductivity in the river during rainfall events.

Otherwise, the model is, in general, able to re-create the timing and the trend of the conductivity signal, as well as partially the strength of the signal (Correlation Coefficient (R) = 0.53; Root-Mean-Square-Error (RMSE) = 1571 µS/cm or 1.37 ppt), in both the daily time scale and multi-day time scale. However, there are some disagreements in the conductivity values and the exact timing of the fluctuations at the water intake. For example, the model almost always predicts an elevation of conductivity during high tides when river flow is comparatively slower and water level in the river higher (for example, on 7 November); however, the sensor at the intake did not always detect such a conductivity signal.

The complexity in the behaviour of the conductivity signal can be partly understood by considering Figure 6, showing the map of salinity at the 2-m depth, on 11 November 2011, at 7 a.m., where the modelled result appears to deviate the most from the observed value. The vectors indicate the direction and strength of the water movement at the 2-m depth. It can be seen that there is a high degree of spatial variability in the salinity field in the vicinity of the intake. Salinity can vary from 3.5 ppt (4500 µS/cm) to more than 5.0 ppt (6500 µS/cm) near the intake in a matter of metres. Further analysis of model output demonstrates that there are two mechanisms for saline water to intrude onto the relatively shallow shelf on which the intake is located: either a selective withdrawal process, whereby saltier water is drawn up onto the bench from the adjacent deeper water (on both ebb and flood), or a process whereby the toe of the salt wedge rises to the surface upstream of the bench and then falls back partially onto the bench on the ebb tide.

Besides direct comparison of observed and modelled salinity, this model validation can be considered from the perspective of water availability, which describes the onset and offset of salinity intrusion at the water intake and the time window within which river water can be safely withdrawn under the criterion salinity value of 0.35 ppt or conductivity of 400 µS/cm. Figure 7 below compares the observed and modelled number of available hours per running 24 h. The red line represents the observation and the black line represents the model results. Only a short period of record is presented to facilitate visual comparison.

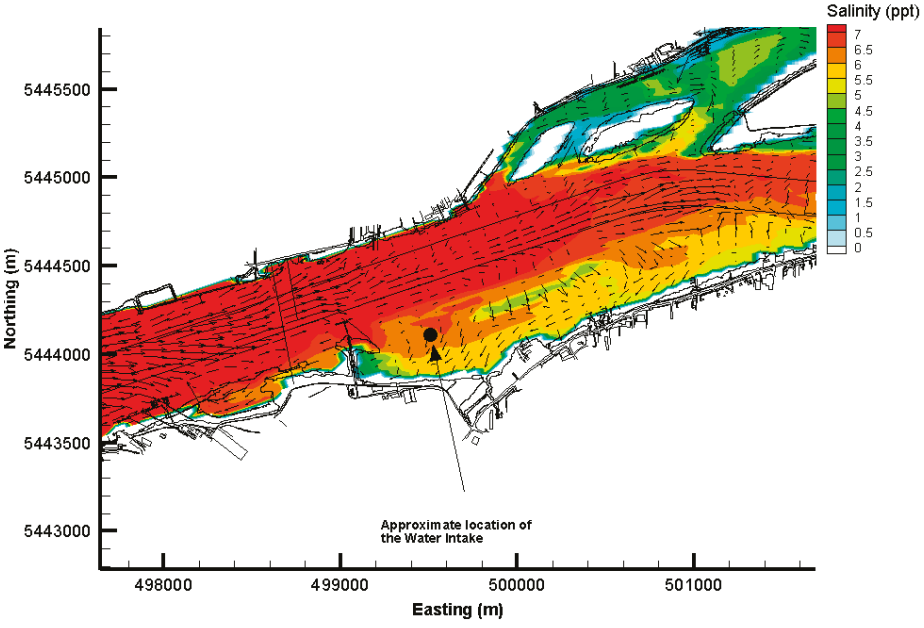

Figure 6. Modelled salinity at 2-m depth in the Fraser River on 11 November 2011 at 7 a.m.

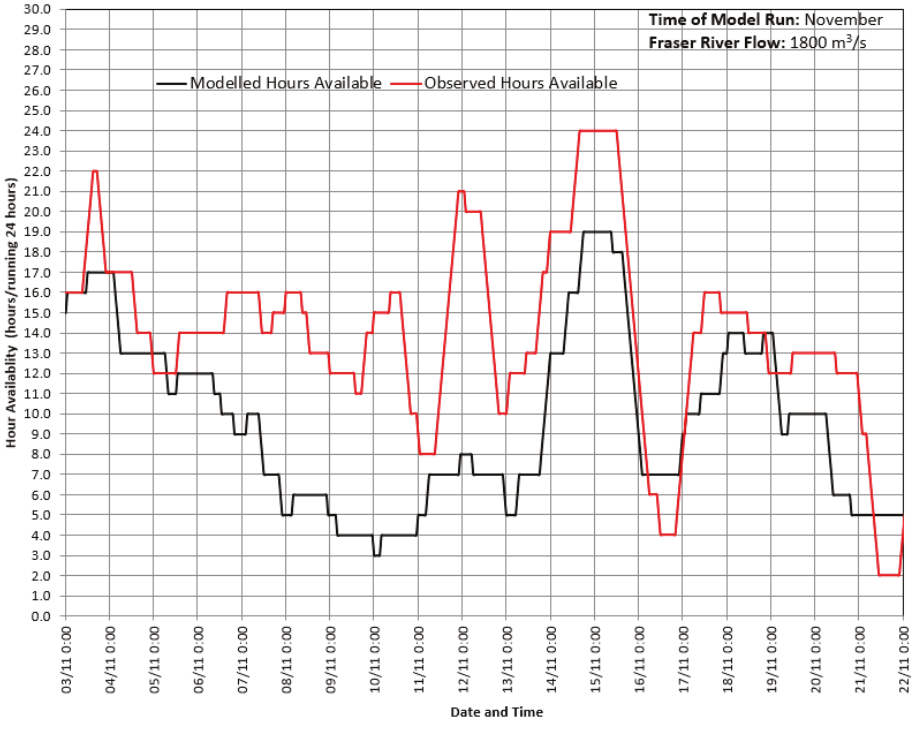

Figure 7. Comparison of observed and modelled available water withdrawal hours in November.

The model, even though more conservative in general, was able to predict the overall trend in availability (R = 0.60; RMSE = 5.9 h). The numerical model predicts that water suitable for irrigation in November is available for 10 h per day whereas observations indicate that suitable water is available, on average, 14 h per day.

3.4. Study Methodology

The effects of changes in environmental (sea level rise and river flow changes as a result of climate change) and anthropogenic (channel deepening) conditions on the behaviour of the salt wedge and salinity distribution in the Fraser River were the main focus of this study. Climate change scenarios were chosen based on the Fraser River flow rate predicted by a Global Climate Model (GCM), selected for its demonstrated ability to closely hindcast the historical flow in the river (Section 3.1), during the irrigation period between August and October. Several sea level rise scenarios were evaluated in this study and ultimately the sea level rises appropriate for the time horizon in year 2050 and year 2100 were used (Section 3.2). Given the projected economic growth of the region, there could be a need to allow deeper draft vessels to navigate the Fraser River to provide sufficient capacity. The dredge depth which allows for most Panamax and derivative vessel classes to navigate in the Fraser River was evaluated in the model study (Section 3.3).

3.4.1. Selecting Climate Scenario and Global Climate Model for Projection of the Fraser River Hydrograph

Three climate scenarios were considered in this study. Denoted A1B, B1, and A2, these scenarios, according to the Fourth Assessment Report (AR4) published by the Intergovernmental Panel on Climate Change (IPCC) in 2007 [37], relate to how different types of societal behaviour lead to different levels of greenhouse gas emissions and subsequent climate change. The emission scenarios based on AR4 were chosen for this study because the projected Fraser River hydrograph derived by the Pacific Climate Institute Consortium, or PCIC, is based on these scenarios. Table 2 summarizes the characteristics of these climate scenarios.

The selection process of a suitable projected Fraser River hydrograph involved evaluation of a set of eight GCMs, driven by the aforementioned three climate scenarios, each representing relatively low, medium, and high atmospheric greenhouse gas concentration increases in the future. These eight GCMs were selected for best matching the downscaled results of these GCMs with the historical data in the 1950–2005 period in western Canada. This method produced an ensemble of all raw projections for temperature and precipitation at a global-scale. The GCMs provided these projections in the form of average temperature and precipitation changes in grid cells, where individual grid cells are approximately 300 km × 300 km (~90,000 sq. km or 9 million hectares) in size. These grid cell values were then statistically downscaled to a watershed-scale resolution of approximately 6 km × 6 km grid cells using a technique called Bias Corrected Spatial Disaggregation before being fed into the Variable Infiltration Capacity (VIC) hydrologic model for estimating streamflow. This approach was discussed in detail in Werner [38] and Schnorbus et al. [39].

An ensemble average was calculated based on the daily flow results derived from these eight different GCMs, each appropriately downscaled to produce Fraser River flows at Hope, and averaged to produce daily flows over an indicated time period. Figure 8 illustrates the ensemble average of the daily Fraser River flow rate under a range of climate change scenarios and different time horizon (present: 2000–2014, short-to mid-term horizon: 2016–2050; long-term horizon: 2051–2098). The data results were published by PCIC [40].

Table 2. Climate scenarios and the associated social, economic, and human theme as presented in AR4.

Climate Scenario	Description	Characteristics
A1B	This scenario is of a more integrated world	• Rapid economic growth • A global population that reaches 9 billion in 2050 and then quickly declines • The quick spread of new and efficient technologies • A convergent world—income and way of life converge between regions. Extensive social and cultural interactions worldwide • Good balance on all different types of energy sources
A2	These scenarios are of a more divided world	• A world of independently operating, self-reliant nations • Continuously increasing population • Regionally oriented economic development
B1	This scenario is of a world more integrated, and more ecologically friendly	• Rapid economic growth as in A1, but with rapid changes towards a service and information economy • Population rising to 9 billion in 2050 and then declining as in A1 • Reductions in material intensity and the introduction of clean and resource efficient technologies. • An emphasis on global solutions to economic, social, and environmental stability

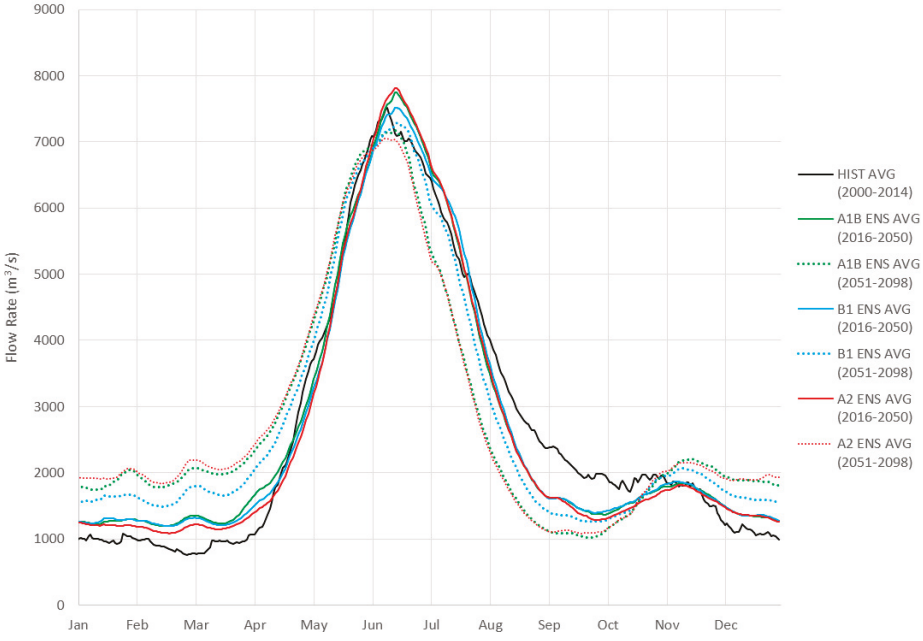

Figure 8. Ensemble historical and modelled daily Fraser River flow rate.

The predicted average flow rate in the irrigation period, under a range of climate change scenarios in 2050 (ranging between 1142 m^3/s and 2352 m^3/s) and 2098 (ranging between 730 m^3/s and 1540 m^3/s), is less than the existing rate (ranging between 1204 m^3/s and 3025 m^3/s).

The climate scenario, A1B, was eventually chosen for the projected Fraser River flow in this modelling study, not only because it represents a scenario which reflects the likely evolution of human society in the next century, but also it projects a lower river discharge and likely higher salinity during the irrigation period. As the original objective of this study was to assist engineers and planners to establish appropriate adaptive measures to maximize freshwater withdrawal for irrigation, the model results based on the A1B scenario would provide the relevant parties conservative estimates

of the withdrawal window such that sufficient resources can be planned and assigned to mitigate the potential impact.

With regard to selecting between the various GCMs, Figure 9 below shows the comparison of the Fraser River hydrograph at Hope between the observed and modelled values derived from the 8 GCM models for calendar years from 1998 to 2004. The level of agreement and disagreement varies both between models, and from month to month and year to year.

This figure indicates that the HADCM (HADley Centre Coupled Model), MIROC (Model for Interdisciplinary Research on Climate), and CSIRO (Commonwealth Scientific and Industrial Research Organization) models simulated the historical Fraser River flow rate closest to the observed flow rate during the irrigation period between September and December. After comparing the Root-Mean-Squared-Error (RMSE) of these models for this critical irrigation period (HADCM: RMSE = 716 m^3/s; MIROC: RMSE = 694 m^3/s; CSIRO: RMSE = 721 m^3/s; all other models: RMSE > 730 m^3/s), the MIROC model was ultimately chosen for provision of the Fraser River hydrographs as input to the hydrodynamic model for simulation in the near to mid-term future (year 2050) and long-term future (year 2100) because MIROC best matches the observed river discharge rate during the irrigation period.

The Fraser River flow that drives the upstream boundary of the river model has been derived by determining the ensemble envelope for the river hydrographs at Hope based on the MIROC model, from which 'dry', 'normal', and 'wet' flow years appropriate for the timeframe of interest were determined. The number of annual hydrographs chosen for formation of the ensemble for each of three time frames (present, 2050 and 2100) was limited to the ten (10) closest years to the time frame of interest, except for the 'present' time frame for which the ten most recent, observed annual hydrograph were used. The 10-year time window size was chosen such that the timeframe is relevant to the reference points in the timeline (e.g., 2050 and 2100). If a longer time window is chosen, the variability within the window will inevitably include the trend from the long-term climate change, not just the result from natural variability. Table 3 describes the hydrographs chosen for the analysis.

Table 3. Fraser River hydrograph chosen for the ensemble analysis.

Timeframe	Year of Chosen Hydrographs for Ensemble Analysis	Type of Data
Present (2014)	2005–2014	Observed
2050	2045–2055	Predicted based on MIROC
2100	2089–2098 [1]	Predicted based on MIROC

[1] 2098 is the end of the river flow prediction based on MIROC published by PCIC as at the time of the study.

Figure 10 summarizes these hydrograph ensembles and properties for present conditions, and conditions in 2050 and 2100. The darker gray areas represent daily flow values between the 90th and 10th percentile, and the lighter gray bands indicate the minimum and maximum flows. The red, green and blue lines represent respectively the dry, normal, and wet years selected for simulation. The normal, dry, and wet years are defined here respectively as the median, driest, and wettest of all the hydrographs in a certain timeframe based on total discharge volume in summer and fall. Note that daily flow in a dry year may exceed the corresponding daily flow in a wet year for short periods, which better reflects the temporal variability of the system: not every day in a dry year is 'dry'. This characteristic illustrates the considerable variability at all time-scales in the Fraser River flow.

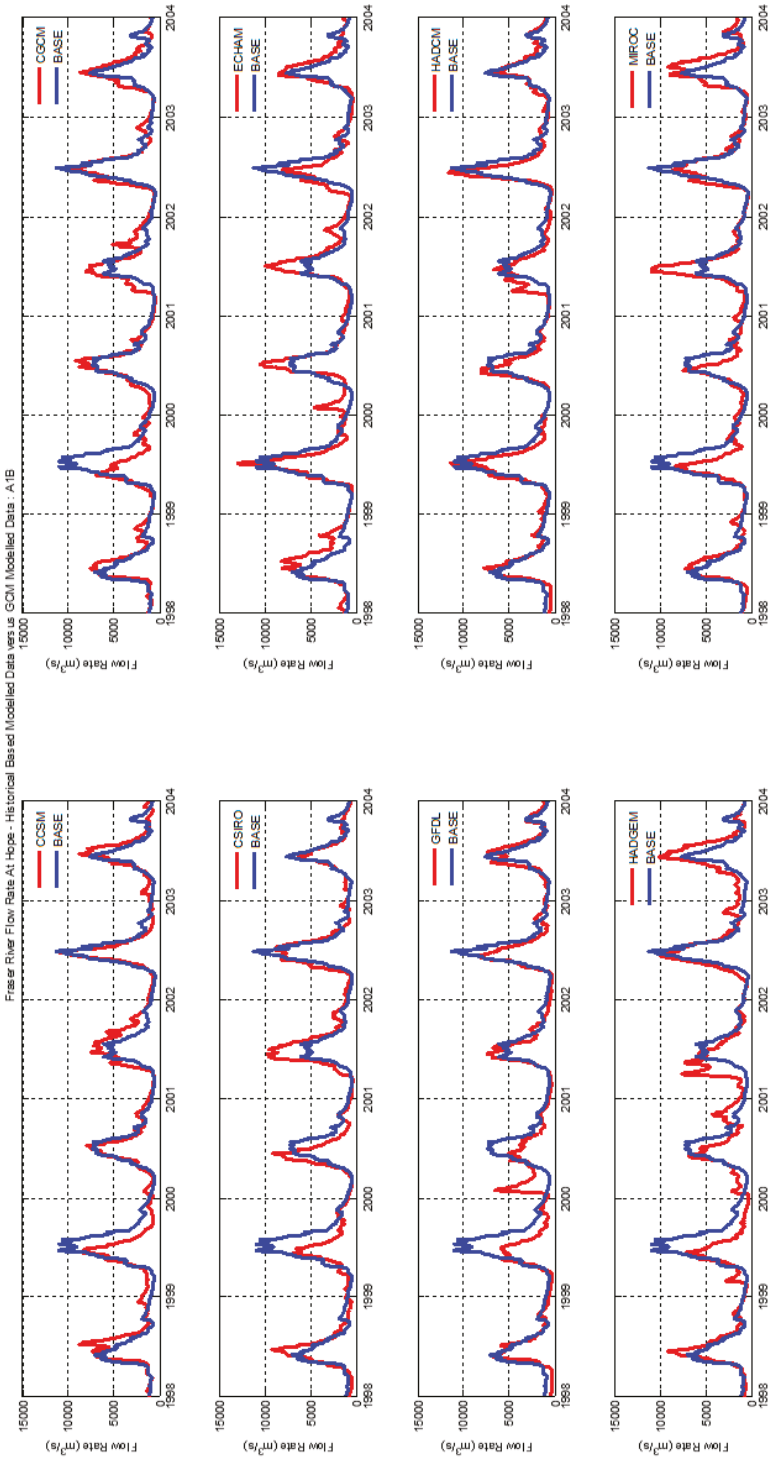

Figure 9. Comparison of observed and modelled Fraser River flow rate for years 1998–2004.

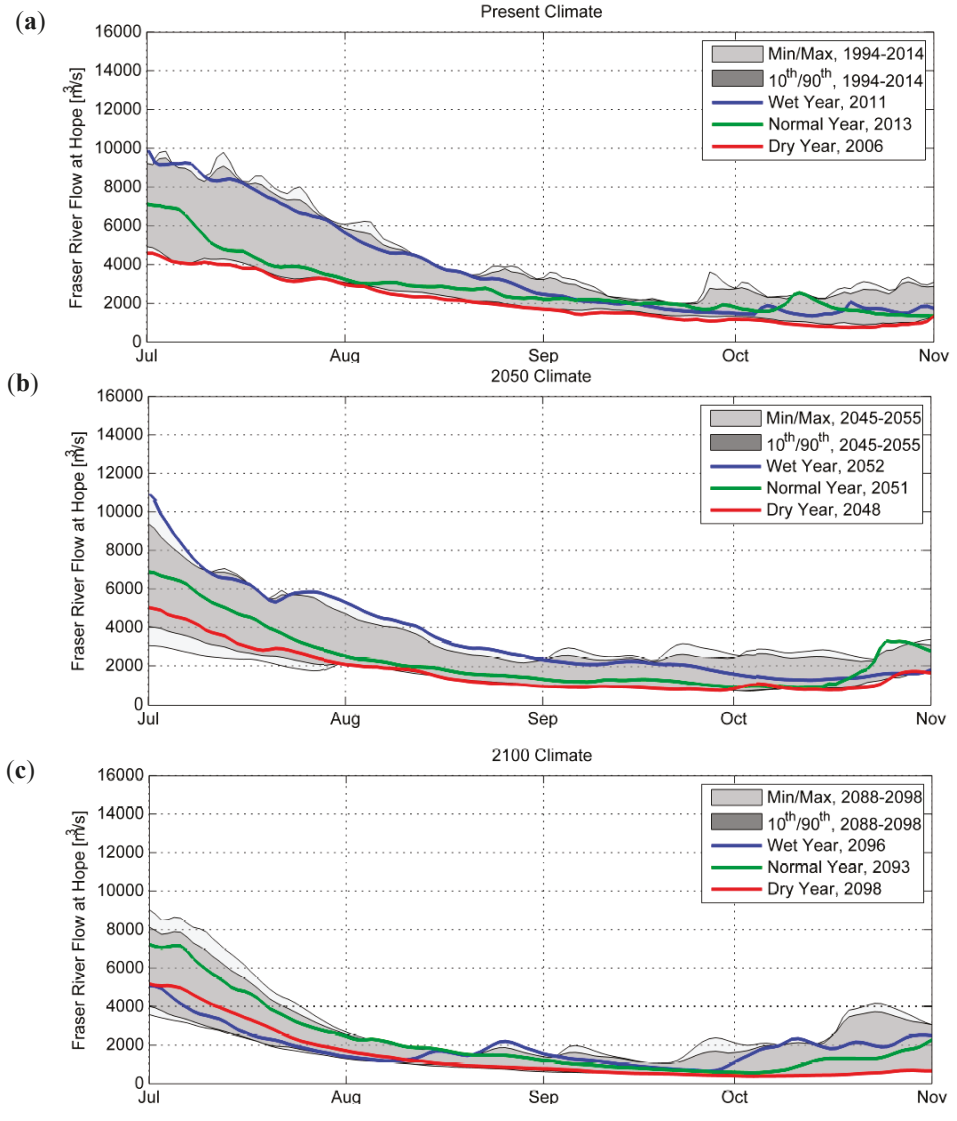

Figure 10. Statistical comparison of selected hydrographs for various timeframes: (**a**) present timeframe; (**b**) year 2050 timeframe; (**c**) year 2100 timeframe.

3.4.2. Selecting Sea Level Rise Scenarios

The change in sea level is not uniform in all parts of the ocean. Past documents and reports published by the IPCC addressed mostly sea level rise on a global scale without giving significant consideration to local effects. The relationship between global and regional mean sea level rise is not simple, owing to the complex relationship between differences in air temperature change and the resulting differential thermal expansion, feedback mechanisms involving local meteorology and wind patterns and changes in tidal hydrodynamics in coastal areas as a result of changes in water depth and circulation.

As stated by the Sea Dike Guidelines [41], the effective sea level rise of 0.5–1.0 m between 2050 and 2100 and 2.0 m between 2100 and 2200 will occur along the BC coast. Given the uncertainty in the predictions and the future evolution of the climate, the upper bound value was a prudent choice for the worst-case scenario for sea level rise. Thus, this study used a sea level rise of 1.0 m for 2050 and 2.0 m for 2100.

Along the open boundaries of the coarse resolution SOG model, the mean sea level was adjusted upward by 1.0 m for SLR of 1.0 m and by 2.0 m for SLR of 2.0 m. All other tidal constituents along the open boundaries of the 1-km SOG model were assumed the same as in the case for SLR of 0.0 m.

3.4.3. Selecting River Dredge Depth Scenarios

Vancouver serves as a gateway to Asia and the rest of North America for sea-going vessels. Previous increases in shipping demand had led to deepening of the river channel. If the shipping demand continues to increase, then there may be a need to deepen the navigation channel. Such deepening would of course be subject to stringent environmental review, because of the potential damage to the ecologically-significant wetlands along the shores of the Fraser River, particularly well-known bird and fish habitats.

Two river dredge depth scenarios were investigated for their effects on the salinity in the river: 11.5 m and 20.0 m below geodetic datum. The current dredge practice of the river bottom, nominally 11.5 m, allows vessels as large as the third-generation Panamax vessels to navigate the river channel; the hypothetical new dredge practice of 20.0-m draft would upgrade to fully allow the fourth-generation Panamax (Post-Panamax, drafting 11–13 m) vessels, the fifth-generation Panamax (Post-Panamax-Plus, drafting 13–14.5 m), and the New-Panamax (drafting 15.2 m) vessels to travel in the river safely.

4. Results

The principal issue of concern is the extent of upstream salt wedge movement and the corresponding effects on near-surface salinities. The study will mainly focus on the salinity at the three candidate sites for future additional intake installations near the existing water intake, which is located approximately 24 km upstream from the river mouth. Figure 11 shows the location of the three sites (Site 1, Site 2, and Site 3). The red lines demarcate the upstream distance along the river from the mouth.

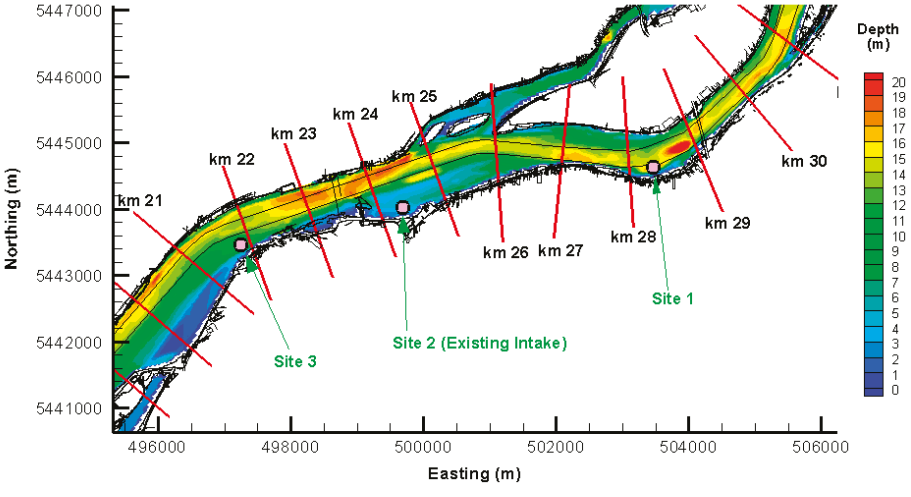

Figure 11. Location of candidate sites for additional water intake installation.

4.1. Difference in Salinity at Different Locations Along the River

Figure 12 shows modelled time-series of salinity at the intake depth at the three sites in a normal year with no sea level rise, over a brief period in September. The green line represents Site 1, the red line represents Site 2, and the blue line represents Site 3 (see Figure 11 for site locations). Figure 12a shows a period in which the salinity progressively increases in the downstream direction from Site 1 to Site 2 and then to Site 3; whereas Figure 12b illustrates the salinity at the three sites for one of the time periods during which the surface water at Site 1 (green line) is saltier than Site 2 (red line). The salinity clearly exhibits a semi-diurnal pattern as a result of the tidal fluctuation; however, the salinity fluctuation decreases gradually in the upstream direction as the tidal fluctuation diminishes. For example, the tidal range (the elevation difference between higher high and lower low water levels) for large tide at Site 1, Site 2 and Site 3 is approximately 3.7 m, versus 4.6 m at Sand Heads, which is located at the mouth of the Fraser River. A similar trend is exhibited in other parts of the irrigation period, but only a short period in September is shown in Figure 12 to emphasize the trend.

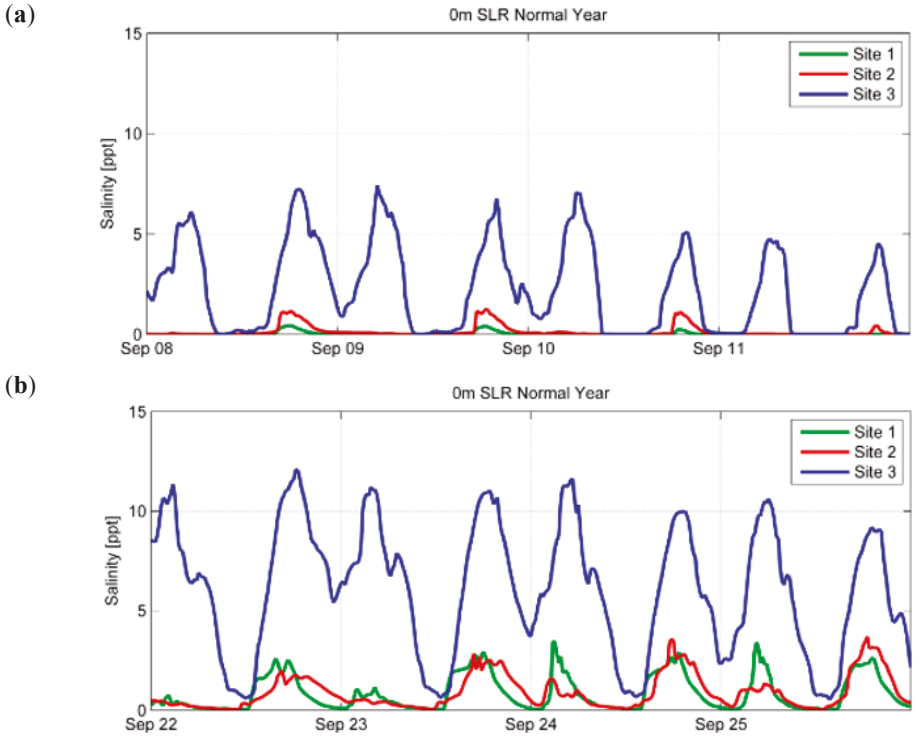

Figure 12. Modelled surface salinity at site 1, site 2, and site 3 in September: (**a**) 8–11 September; (**b**) 22–25 September.

One intriguing aspect of these model results is that salinity is occasionally lower at Site 2 than at Site 1 as indicated in the Figure 12b, even though Site 1 is approximately 4 km upstream of Site 2. This might be caused by the complex processes that govern the hydrodynamics in the shallow area at Site 2, which was demonstrated by the surface salinity contour plot in Figure 6. The figure shows the presence of high salinity waters in the midst of fresher waters, probably due to a combination of local processes of selective withdrawal and upwelling in the river.

Salinity monitoring data collected at Site 1 and Site 2 supports the occurrence of this phenomenon in that surface water at Site 1 is occasionally saltier than Site 2. This complexity renders the salinity in the area difficult to predict, thereby posing challenges to the planning process.

4.2. Effects of Sea Level Rise and River Flow

4.2.1. Time Horizon: Present

Figure 13 shows the trend in surface salinity at Site 2 during the irrigation period from August to October in a normal flow year with 0-m SLR, which represents the present case. The mean monthly flow rate during the period decreases from 3200 m^3/s on 1st August to 2150 m^3/s on 1st September, to 1950 m^3/s on 1st October, and finally to 1600 m^3/s on 31st October (Figure 10). The irrigation threshold of 0.34 ppt is shown in Figure 13 as a black line, the modelled salinity as a green line.

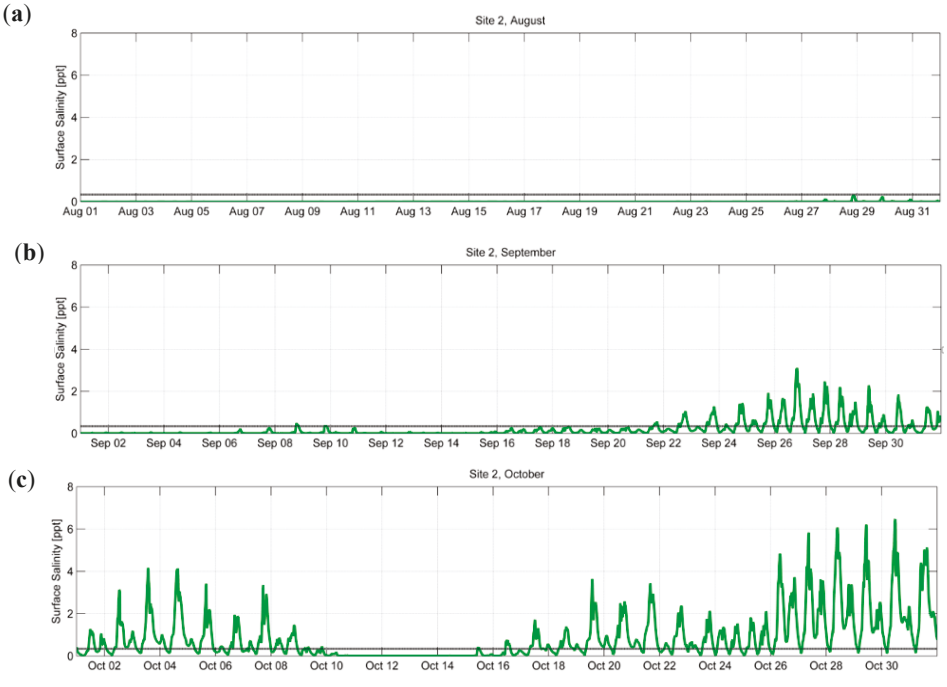

Figure 13. Surface salinity at site 2 between August and October in normal flow year and with 0-m SLR: (**a**) August; (**b**) September; (**c**) October.

The salinity trend shown in Figure 13 is the combined results of (1) the semi-diurnal tidal cycles in the SOG; (2) the alternation of neap tide, when the tidal forcing from the SOG is lower, and spring tide, when the tidal forcing is stronger; as well as (3) the change in river discharge over the period. The semi-diurnal tidal cycles explain the intra-day trend in salinity; the neap and springs tide cycles have led to alternation of high and low salinity in a weekly scale; and the decrease in river discharge between August and October has led to a general rise in the surface salinity at Site 2 and reduction of water availability for irrigation.

In August, the impact of the three aforementioned factors on surface salinity and, hence, water availability is minimal as salinity remains below the criterion value because the river discharge remains sufficiently high to position the salt wedge well downstream of the intake. However, in September, as the river discharge continues to trend downward, the salinity signal appears and becomes more

pronounced with time, indicating the upstream advance and near-by presence of the salt wedge; the water availability for irrigation remains near 100% at the beginning of the month, but the withdrawal window gradually shrinks with increasing surface salinity in the latter parts of the month. In October, the salinity signal continues to grow stronger and the availability window for water withdrawal expectedly becomes even narrower and very limited, entering into the drier part of the Fraser River hydrograph.

It is important to note that the river flow did not decrease at a constant, fixed rate over the time period. A short-term increase in flow rate often occurs due to passage of weather systems or occurrence of rain-on-snow events, especially in the fall season. For example, a likely rain-on-snow event, a typical occurrence in the fall season, might have caused a temporary increase in the river flow rate in early-to-mid October (the green line in Figure 10a). This spike in the flow rate directly led to a decrease in salinity in the river as shown in Figure 13c.

4.2.2. Time Horizon: Year 2050 and Year 2100

Figures 14–16 respectively illustrate the time series of salinity at Site 1, Site 2, and Site 3, for the 15-day period between 20th August and 3rd September, for all three time horizons (green line for the present time with 0-m SLR; black line for the year 2050 case with 1-m SLR, and red line for the year 2100 case with 2-m SLR; the irrigation threshold of 0.34 ppt for salinity is shown with a thin black line). The river flow type (dry, normal, and wet) corresponds to the time horizon of interest (Figure 10). The difference in salinity indicated in these figures is the result of the combined effects from SLR and changes in the Fraser River hydrograph.

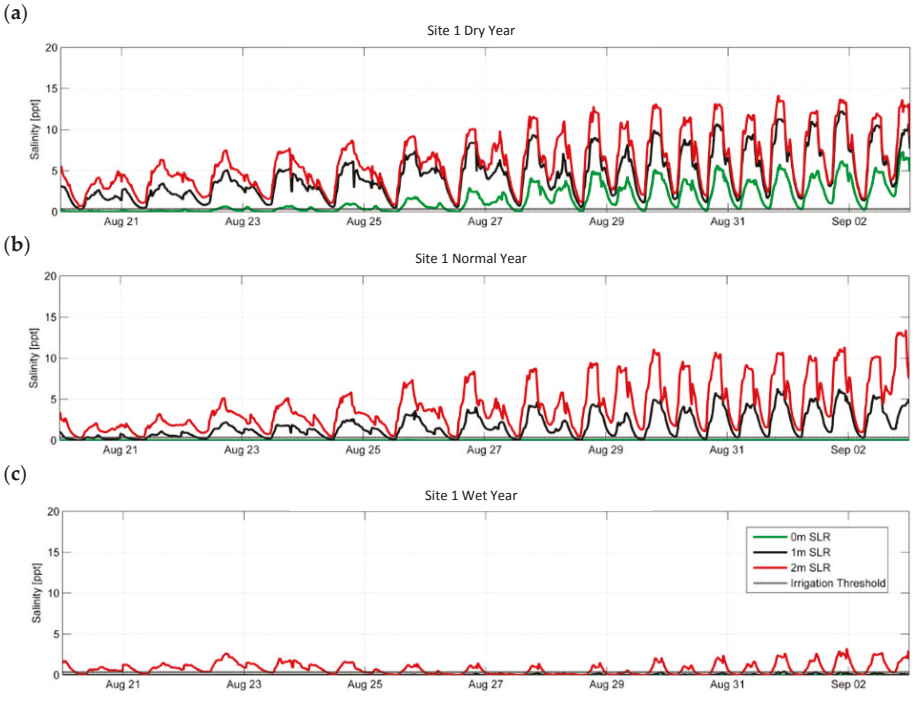

Figure 14. Surface salinity at site 1 in August with 0–2 m SLR: (**a**) dry year; (**b**) normal year; (**c**) wet year.

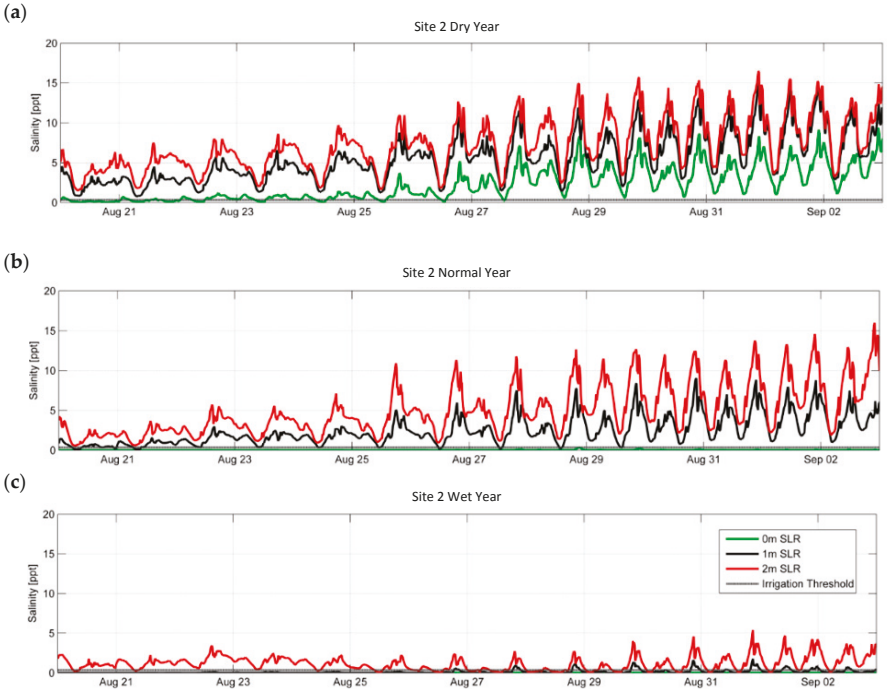

Figure 15. Surface salinity at site 2 in August with 0–2 m SLR: (**a**) dry year; (**b**) normal year; (**c**) wet year.

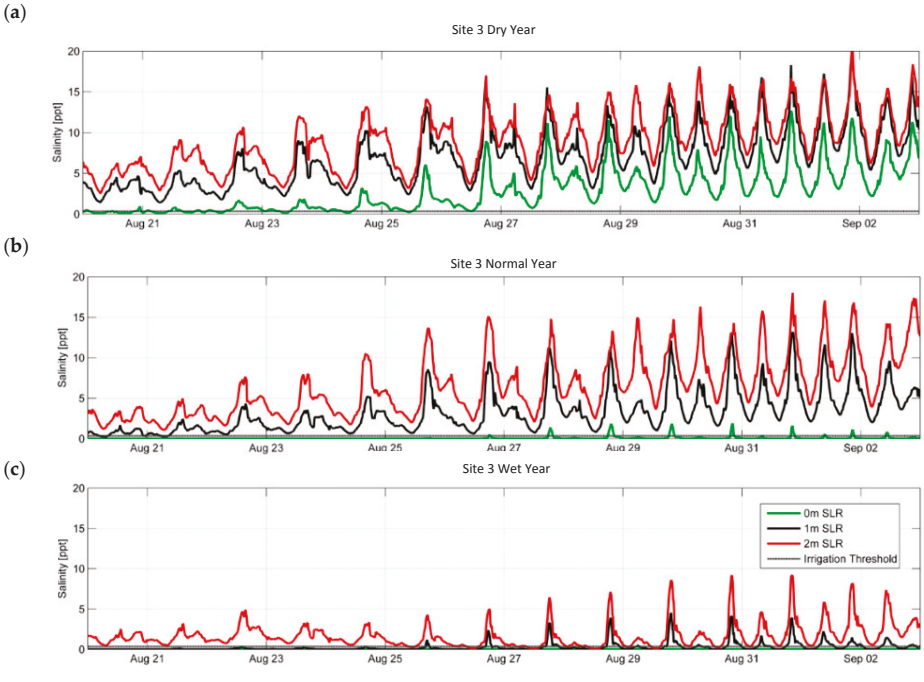

Figure 16. Surface salinity at site 3 in August with 0–2 m SLR. (**a**) dry year; (**b**) normal year; (**c**) wet year.

These figures clearly show an increase in surface salinity at all three sites as a result of sea level rise. For the normal year and wet year cases, especially, an otherwise 100% withdrawal window for the 0-m SLR case could be reduced significantly and, on some days, that window could dwindle to 0% (Site 2 on 31 August—normal flow year, for example) with 1-m SLR and 2-m SLR. This is illustrated by the surface salinity with 1-m SLR remaining continuously above the salinity threshold, whereas the surface salinity for the 0-m SLR case remains below the threshold.

4.3. Effects of Channel Deepening

Figure 17 shows the time series of salinity at Site 2 in a normal flow year and 0-m SLR and with dredging depths that accommodate vessels with 11.5-m draft (green line) and 20-m draft (blue line) for the months of August, September, and October. The irrigation threshold for salinity of 0.34 ppt is again shown in the figure as a thin black line.

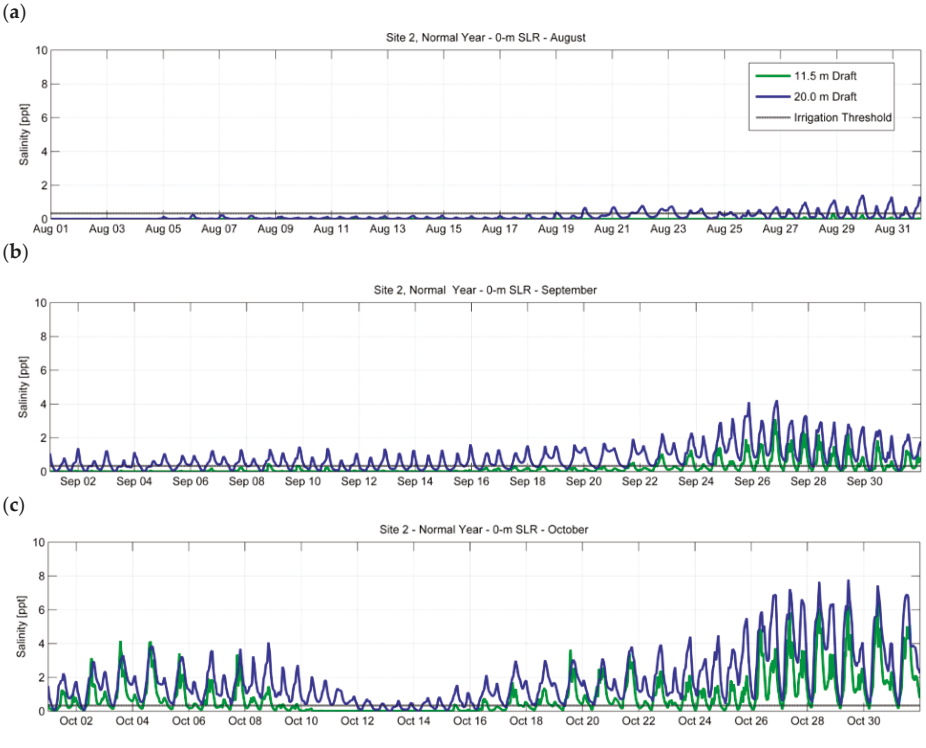

Figure 17. Time series salinity at site 2 with river channel depth capable of accommodating vessels drafting 11.5 m and 20.0 m with 0-m SLR during irrigation period. (**a**) August; (**b**) September; (**c**) October.

Not surprisingly, salinity increases as the channel is deepened, leading to much more frequent exceedances of the salinity threshold and a shorter time window for water withdrawal. The increase in water depth would likely result in a combination of reduced bottom friction acting on the salt wedge and increase in hydrostatic pressure force that drives the salt wedge upstream, thereby allowing the salt wedge to migrate further upstream.

5. Discussion

5.1. Effect of Sea Level Rise and River Flow

Table 4 below summarizes the effects of sea level rise (0-m SLR, 1-m SLR, and 2-m SLR) and river flow (dry, normal, and wet flow years) on water availability (time duration during which salinity is 0.34 ppt) for the existing case, the year 2050 case and the year 2100 case, respectively, for the same time period in August as presented in Figures 12–14. Note the hours of availability presented in Table 4 are the average time duration per day for water withdrawal during the 15-day period plotted in the above figures.

Table 4. Modelled time duration (no. of hours) below salinity criterion of 0.34 ppt at site 1, site 2, and site 3 with various sea level rises and types of flow year.

	Site 1 (h)			Site 2 (h)			Site 3 (h)		
Sea Level Rise	**Dry**	**Normal**	**Wet**	**Dry**	**Normal**	**Wet**	**Dry**	**Normal**	**Wet**
0 m	7.9	24.0	24.0	3.6	23.9	24.0	3.1	23.0	24.0
1 m	0.0	3.8	23.6	0.0	0.8	21.2	0.0	0.4	18.1
2 m	0.0	0.1	8.3	0.0	0.0	3.9	0.0	0.0	1.7

As expected, the model results show that Site 1 will provide a wider withdrawal window than Site 2, which in turn has a wider widow than Site 3. At all three sites, the window becomes narrower with an increase in sea level and with a decrease in river flow. In a lower river discharge regime, the impact of sea level rise appears to be more significant than it does in the high river discharge regime. On the other hand, the influence of river discharge on withdrawal window decreases when the sea level is higher than it does when the sea level is lower.

It is difficult to draw definitive conclusions regarding which factor (sea level rise or river flow) dominates the salt wedge dynamics from this set of model results because, as presented in Section 3.4.1 and in Figure 10, each of the sea level rise cases incorporates different flow rates associated with the projected normal year, dry year, and wet year as predicted by MIROC for its own time horizon (present, year 2050 and year 2100); simply speaking, these model runs have two varying factors, the flow rate and sea level, and it is not immediately obvious which factor is more important in governing the salinity in the river. Investigation on the dominance of these factors has not been undertaken but can be achieved by isolating these two variables in the model and keeping one factor constant and the other variable. However, it might be difficult to consider one factor without changing the other, considering that the projected sea level rise and change in the Fraser River hydrograph are likely both results of climate change.

5.2. Effect of Channel Deepening

Table 5 below summarizes the availability for water withdrawal at Site 1 and Site 2, for the existing and a deepened channel for the 0-m SLR scenarios.

Table 5. Time duration below salinity criterion of 0.34 ppt at site 1 and site 2 with 0-m SLR with river channel accommodating vessels with 11.5-m and 20.0-m drafts.

	Site 1		Site 2	
Month	**11.5-m Draft (h/Day)**	**20.0-m Draft (h/Day)**	**11.5-m Draft (h/Day)**	**20.0-m Draft (h/Day)**
August	24.0	19.8	23.9	15.0
September	22.0	6.1	16.9	1.1
October	15.0	2.3	9.9	0.5

Site 1 and Site 2 both display a reduction in the withdrawal window as a result of channel deepening from 11.5 m to 20.0 m, especially in the latter parts of the irrigation period in October when the flow is lower compared to the earlier parts in August. It appears that channel deepening would not affect the withdrawal availability as much as sea level rise and change in river discharge would: the withdrawal availability with deeper channel remains substantial at both sites in August with 0-m SLR. However, as the flow rate continues to decrease with time between August and October, the influence from channel deepening appears to increase as the nearly completely open withdrawal window would close significantly.

5.3. Comparison with Past Studies

Based on their model results, Krvavica et al. [11] similarly concluded that sea-level and river discharge are the dominant factors controlling salt-wedge intrusion and the relative influence from sea level rise and channeling deepening increases when the river discharge is lower. However, the study by Krvavica et al. concerned the Rječina River that drains into the Adriatic Sea with small tidal range (<1 m) and concluded that the tidal dynamics of that river is not sufficient to cause significant mixing between the freshwater and saltwater masses in the estuary. Shaha et al. [13] found that, during the wet season when river discharge in the Sumjin River is relatively high, sea level plays a less dominant role in determining the salt wedge intrusion.

5.4. Future Studies and Research

There is a significant data gap that needs to be filled in order to fully understand the salt wedge dynamics and behaviour in response to both short-term and long-term changes in climate and river geometry. There is currently a lack of continual, long-term observations of salinity and temperature profiles at multiple locations along the river. When this data gap is addressed, one can delineate the behavior of the salt wedge in the Fraser River and its relationship with changes in environmental (climate change) and man-made forcing. The observations will provide scientists and engineers the necessary data to undertake a more comprehensive modelling study. The results from such a study will assist planners and stakeholders to plot an appropriate, adaptive course of action in a timely fashion to ensure a sustainable future for industries that rely on water drawn from the river and to maintain and enhance the current ecosystem.

Future research should also pursue the relative influence of channel deepening and sea level rise in the Fraser River on salinity distributions and withdrawal windows, which was not undertaken in this study.

Additionally, a Fraser River model with a higher resolution would have resolved better the finer-scale hydrodynamic processes and features that could potentially have immense effects on the salinity distribution and therefore the withdrawal availability for irrigation and other activities.

Finally, development of a local hydrological model that provides a relationship between precipitation and runoff to the Fraser River along the section between Hope and the upstream boundary of the 50-m Fraser River model would have significantly improved the quality of the hydrodynamic model.

6. Conclusions

From this modelling study, some conclusions can be drawn regarding the evolution of salinity in the Fraser River resulting from environmental changes (sea level rise and change in river flow) and direct man-made changes (channel deepening). The following summarizes these conclusions.

- Site 1, located 4 km upstream of Site 2, has consistently shown to have a significantly wider window for water availability in all cases and for all criteria compared to Site 2, the present intake location. This indicates that salinity generally decreases in the upstream direction. However, complex hydrodynamic processes would lead to exceptions to the trend.

- The temporal projection of the withdrawal window is that, even in a wet flow year, the sea level rise of 1 m and 2 m will lead to a large reduction (minimum 85% reduction) in and, in some scenarios, complete elimination of water availability.
- This study found that sea level rise and changes in river discharge appear to have a larger impact on the withdrawal availability than does channel deepening. In a low river discharge regime, the impact from sea level change is more significant than it is in the high river discharge regime. On the other hand, the influence of changes in river discharge on withdrawal availability decreases when the sea level is higher than it does when the sea level is lower. It is difficult, however, to draw definitive conclusions regarding which factor (sea level rise or river flow) dominates the salt wedge dynamics from this set of model results because, as presented in Section 3.4.1 and in Figure 10, each of the sea level rise cases incorporates different flow rates associated with the projected normal year, dry year, and wet year as predicted by MIROC for its own time horizon (present, year 2050 and year 2100); simply speaking, these model runs have two varying factors, the flow rate and sea level, and it is not immediately obvious which factor is more important in governing the salinity in the river. However, it is difficult to consider one factor without another, considering that the sea level rise and change in the Fraser River hydrograph are both results of climate change.
- Dredging the channel to accommodate vessels with a 20 m draft will affect the salinity at the intake and will shorten the withdrawal window. The effect of channel deepening becomes more pronounced in the low flow period. However, the degree of impact from dredging on the salt wedge and on withdrawal availability under other different circumstances (i.e., different sea level rise and different dredge depths) have not been investigated.

Author Contributions: Conceptualization, A.T.Y.L., J.S. and J.M.; Methodology, A.T.Y.L. and J.S.; Software, J.S.; Validation, A.T.Y.L. and J.S.; Formal Analysis, A.L and J.M.; Investigation, A.T.Y.L. and J.M.; Resources, J.S.; Visualization, A.T.Y.L. and J.M.; Writing-Original Draft Preparation, A.T.Y.L. and J.S.; Writing-Review & Editing, A.T.Y.L. and J.S.; Supervision, J.S.; A.T.Y.L. and J.M. contributed to the scenarios selection and ensemble analysis; A.T.Y.L., J.S. and J.M. contributed to the modelling, and A.T.Y.L. and J.S. conceived and wrote the paper.

Funding: This study was funded in part by the Corporation of Delta and in part by the Governments of Canada and British Columbia through the Investment Agriculture Foundation of BC under Growing Forward 2, a federal-provincial-territorial initiative. The program was delivered by the BC Agriculture & Food Climate Action Initiative.

Acknowledgments: In addition to the agencies who contributed financially to this project as stated above, the authors would like to acknowledge Delta Farmers Institute, Corporation of Delta and BC Ministry of Agriculture for their role in the project.

Conflicts of Interest: The authors declare no conflict of interest.

Appendix A. Theoretical Basis of H3D

H3D bears many similarities to the Princeton Ocean Model (POM) [42] in terms of the equations it solves, but differs in how the time-domain aspects are implemented. H3D uses a semi-implicit scheme, allowing relatively large time steps, and does not separately solve the internal and external models as POM does. It also uses a considerably simpler turbulence scheme in the vertical. These considerations combined allow H3D to execute complex problems relatively quickly.

The Equations (A1)–(A11) to be solved are detailed below. The explanation of the symbols that are used in these equations is either provided in the text in this appendix or in Appendix B:

Mass Conservation:

$$\frac{\partial u}{\partial x} + \frac{\partial v}{\partial y} + \frac{\partial w}{\partial z} = 0, \tag{A1}$$

At the end of each time step equation, (1) is used to diagnostically determine the vertical component of velocity (w) once the two horizontal components of velocity (u and v) have been calculated by the model.

X-directed momentum:

$$\begin{array}{l}\frac{\partial u}{\partial t}+u\frac{\partial u}{\partial x}+v\frac{\partial u}{\partial y}+w\frac{\partial u}{\partial z}+g\frac{\partial \eta}{\partial x}+\\ \frac{1}{\rho o}\frac{\partial}{\partial x}\int_{z}^{\eta}(\rho w-\rho o)gdz-fv-\frac{\partial}{\partial x}AH\frac{\partial u}{\partial x}-\frac{\partial}{\partial y}AH\frac{\partial u}{\partial y}-\frac{\partial}{\partial z}AV\frac{\partial u}{\partial z}=0\end{array} \tag{A2}$$

Y-directed momentum:

$$\begin{array}{l}\frac{\partial v}{\partial t}+u\frac{\partial v}{\partial x}+v\frac{\partial v}{\partial y}+w\frac{\partial v}{\partial z}+g\frac{\partial \eta}{\partial y}+\\ \frac{1}{\rho o}\frac{\partial}{\partial y}\int_{z}^{\eta}(\rho w-\rho o)gdz+fu-\frac{\partial}{\partial x}A_H\frac{\partial v}{\partial x}-\frac{\partial}{\partial y}A_H\frac{\partial v}{\partial y}-\frac{\partial}{\partial z}A_V\frac{\partial v}{\partial z}=0\end{array} \tag{A3}$$

Water surface elevation determined from the vertically-integrated continuity equation:

$$\frac{\partial \eta}{\partial t}=-\frac{\partial}{\partial x}\int_{-H}^{\eta}udz-\frac{\partial}{\partial y}\int_{-H}^{\eta}vdz \tag{A4}$$

The effect of wind forcing introduced by means of the surface wind-stress boundary condition:

$$\left(A_V\frac{\partial u}{\partial z},A_V\frac{\partial v}{\partial z}\right)_{z=\eta}=\frac{\rho a}{\rho w}C_{D,air}\vec{U}_{wind}\left|\vec{U}_{wind}\right| \tag{A5}$$

The effect of bottom friction introduced by the bottom boundary condition:

$$\left(A_V\frac{\partial u}{\partial z},A_V\frac{\partial v}{\partial z}\right)_{z=-H}=K_{bottom}\vec{U}_{bottom}\left|\vec{U}_{bottom}\right| \tag{A6}$$

The bottom friction coefficient is usually understood to apply to currents at an elevation of one metre above the bottom. The bottom-most vector in H3D will, in general, be at a different elevation, i.e., at the midpoint of the lowest computational cell. H3D uses the 'law of the wall' to estimate the flow velocity at one metre above the bottom from the modelled near-bottom velocity.

The evolution of scalars, such as salinity, temperature, or suspended sediment, is given by the scalar transport/diffusion equation:

$$\frac{\partial S}{\partial t}+u\frac{\partial S}{\partial x}+v\frac{\partial S}{\partial y}+w\frac{\partial S}{\partial z}-\frac{\partial}{\partial x}N_H\frac{\partial S}{\partial x}-\frac{\partial}{\partial y}N_H\frac{\partial S}{\partial y}-\frac{\partial}{\partial z}N_V\frac{\partial S}{\partial z}=Q \tag{A7}$$

The above Equations (A1)–(A7) are formally integrated over the small volumes defined by the computational grid, and a set of algebraic equations results, for which an appropriate time-stepping methodology must be found. Backhaus [18,19] presents such a procedure, referred to as a semi-implicit method. The spatially-discretized version of the continuity equation is written as:

$$\eta^{(1)}=\eta^{(0)}-\alpha\frac{\Delta t}{\Delta l}(\delta_x U^{(1)}+\delta_y V^{(1)})-(1-\alpha)\frac{\Delta t}{\Delta l}(\delta_x U^{(0)}+\delta_y V^{(0)}), \tag{A8}$$

where superscript (0) and (1) refer to the present and the advanced time, δ_x and δ_y are spatial differencing operators, and U and V are vertically integrated velocities. The factor α represents an implicit weighting, which must be greater than 0.5 for numerical stability. $U^{(0)}$ and $V^{(0)}$ are known at the start of each computational cycle. $U^{(1)}$, and similarly $V^{(1)}$, can be expressed as:

$$U^{(1)}=U^{(0)}-g\alpha\Delta t\eta_x^{(1)}-g(1-\alpha)\Delta t\eta_x^{(0)}+\Delta tX^{(0)}, \tag{A9}$$

where $X^{(0)}$ symbolically represents all other terms in the equation of motion for the u- or v-component, which are evaluated at time level (0): Coriolis force, internal pressure gradients, non-linear terms, and top and bottom stresses. When these expressions are substituted into the continuity Equation (A4),

after some further manipulations, there results an elliptic equation for $\delta_{i,k}$, the change in water level over one time step at grid cell *i,k* (respectively the y and x directions):

$$\delta_{i,k} - (ce\delta_{i,k+1} + cw\delta_{i,k-1} + cn\delta_{i-1,k} + cs\delta_{i+1,k}) = Z_{i,k}, \quad \text{(A10)}$$

where *ce*, *cw*, *cn*, and *cs* are coefficients depending on local depths and the weighting factor (α), and $Z_{i,k}$ represents the sum of the divergence formed from velocities at time level (0) plus a weighted sum of adjacent water levels at time level (0). Once Equation (A10) is solved for $\delta_{i,k}$, the water level can be updated:

$$\eta_{i,k}{}^{(1)} = \eta_{i,k}{}^{(0)} + \delta_{i,k}, \quad \text{(A11)}$$

and Equation (A9) can be completed. At the end of each time step, volume conservation is used to diagnostically compute the vertical velocity *w(j,i,k)* from the two horizontal components *u* and *v*.

Appendix B. Notations

This appendix explains the symbols used in Equations (A1)–(A11) that were not explained explicitly in Appendix A.

u(x,y,z,t): component of velocity in the *x* direction
v(x,y,z,t): component of velocity in the *y* direction
w(x,y,z,t): component of velocity in the *z* direction
S(x,y,z,t): scalar concentration
Q(x,y,z,t): source term for each scalar species
f: Coriolis parameter, determined by the earth's rotation and the local latitude
$A_H(\partial u/\partial x, \partial u/\partial y, \partial v/\partial x, \partial v/\partial y)$: horizontal eddy viscosity
$A_V(\partial u/\partial z, \partial v/\partial z, \partial \rho_{water}/\partial z)$: vertical eddy viscosity
N_H: horizontal eddy diffusivity
$N_V(\partial u/\partial z, \partial v/\partial z, \partial \rho_{water}/\partial z)$: vertical eddy diffusivity
$C_{D,air}$: drag coefficient at the air-water interface
K_{bottom}: drag coefficient at the water/sea bottom interface
ρ_a: density of air
$\rho_w(x,y,z,t)$: density of water
ρ_o: reference density of water
$\eta(x,y,t)$: water surface elevation
H(x,y): local depth of water.

References

1. Costanza, R.; D'Arge, R.; De Groot, R.; Farber, S.; Grasso, M.; Hannon, B.; Limburg, K.; Naeem, S.; O'Neill, R.V.; Paruelo, J.; et al. The value of the world's ecosystem services and natural capital. *Nature* **1997**, *387*, 253–260. [CrossRef]
2. Stronach, J.A. Observational and Modelling Studies of the Fraser River Plume. Ph.D. Thesis, The University of British Columbia, Vancouver, BC, Canada, 1978.
3. Stronach, J.A. The Fraser River plume, Strait of Georgia. *Ocean Manag.* **1981**, *6*, 201–221. [CrossRef]
4. Halverson, M.; Pawlowicz, R. Tide, wind, and river forcing of the surface currents in the Fraser River plume. *Atmos. Ocean* **2016**, *54*, 131–152. [CrossRef]
5. Halverson, M.; Pawlowicz, R. Entrainment and flushing time in the Fraser River estuary and plume from a steady state salt balance analysis. *J. Geophys. Res.-Atmos.* **2011**, *116*. [CrossRef]
6. Halverson, M.; Pawlowicz, R. Estuarine forcing of a river plume by river flow and tides. *J. Geophys. Res.-Atmos.* **2008**, *113*. [CrossRef]
7. Kostaschuk, R.; Atwood, L.A. River discharge and tidal controls on salt-wedge position and implications for channel shoaling: Fraser River, British Columbia. *Can. J. Civ. Eng.* **2011**, *17*, 452–459. [CrossRef]

8. Ward, P.R.B. Seasonal salinity changes in the Fraser River estuary. *Can. J. Civ. Eng.* **2011**, *3*, 342–348. [CrossRef]
9. Yin, K.D.; Harrison, P.J.; Pond, S.; Beamish, R.J. Entrainment of nitrate in the Fraser River estuary and its biological implications. III. Effects of winds. *Estuar. Coast. Shelf Sci.* **1995**, *40*, 545–558. [CrossRef]
10. Neilson-Welch, L.; Smith, L. Saline water intrusion adjacent to the Fraser River, Richmond, British Columbia. *Can. Geotech. J.* **2011**, *38*, 67–82. [CrossRef]
11. Krvavica, N.; Travaš, V.; Ožanić, N. Salt-Wedge Response to Variable River Flow and Sea-Level Rise in the Microtidal Rječina River Estuary, Croatia. *J. Coast. Res.* **2017**, *33*, 802–814. [CrossRef]
12. Funahashi, T.; Kasai, A.; Ueno, M.; Yamashita, Y. Effects of short time variation in the river discharge on the salt wedge intrusion in the Yura Estuary, Japan. *J. Water Resour. Prot.* **2013**, *5*, 343–348. [CrossRef]
13. Shaha, D.C.; Cho, Y.K.; Kim, T.W. Effects of river discharge and tide driven variation on saltwater intrusion in Sumjin River Estuary: An application of finite-volume coastal ocean model. *J. Coast. Res.* **2013**, *29*, 460–470. [CrossRef]
14. Richmond Chamber of Commerce. *The Economic Importance of the Lower Fraser River*; Richmond Chamber of Commerce: Richmond, BC, Canada, 2014.
15. Crawford, E.; MacNair, E. *Fraser Valley & Metro Vancouver Snapshot Report, B.C. Agriculture Climate Change Adaptation Risk + Opportunity Assessment Series*; The British Columbia Agriculture & Food Climate Action Initiative: Victoria, BC, Canada, 2012.
16. Van der Gulik, T.; Neilsen, D.; Fretwell, R.; Tam, S. *Agricultural Water Demand Model—Report for Metro Vancouver*; Metro Vancouver: Vancouver, BC, Canada, 2014.
17. Backhaus, J.O. A semi-implicit scheme for the shallow water equations for applications to shelf sea modelling. *Cont. Shelf Res.* **1983**, *2*, 243–254. [CrossRef]
18. Backhaus, J.O. A three-dimensional model for the simulation of shelf-sea dynamics. *Deutsche Hydro. Z.* **1985**, *38*, 165–187. [CrossRef]
19. Duwe, K.C.; Hewer, R.R.; Backhaus, J.O. Results of a semi-implicit two-step method for the simulation of markedly non-linear flow in coastal seas. *Cont. Shelf Res.* **1983**, *2*, 255–274. [CrossRef]
20. Backhaus, J.O.; Meir-Reimer, E. On seasonal circulation patterns in the North Sea. In *North Sea Dynamics*; Sundermann, J., Lenz, W., Eds.; Springer: Heidelberg, Germany, 1983; pp. 63–84. ISBN 978-3-642-68840-9.
21. Kampf, J.; Backhaus, J.O. Ice-ocean interactions during shallow convection under conditions of steady winds: Three-dimensional numerical studies. *Deep-Sea Res. Part II* **1999**, *46*, 1335–1355. [CrossRef]
22. Backhaus, J.O.; Kampf, J. Simulation of sub-mesoscale oceanic convection and ice-ocean interactions in the Greenland Sea. *Deep-Sea Res. Part II* **1999**, *46*, 1427–1455. [CrossRef]
23. Stronach, J.A.; Backhaus, J.O.; Murty, T.S. An update on the numerical simulation of oceanographic processes in the waters between Vancouver Island and the mainland: The G8 model. *Oceanogr. Mar. Biol.* **1999**, *31*, 1–86.
24. Stronach, J.A.; Mulligan, R.P.; Soderholm, H.; Draho, R.; Degen, D. Okanagan lake limnology: Helping to improve water quality and safety. In *Innovation*; Association of Professional Engineers and Geoscientists of British Columbia: Vancouver, BC, Canada, 2002.
25. Wang, E.; Stronach, J.A. Summerland water intake feasibility study. In Proceedings of the Canadian Water Resources Association BC Branch Conference, Kelowna, BC, Canada, 23–25 February 2005.
26. Saucier, F.J.; Roy, F.; Gilbert, D.; Pellerin, P.; Ritchie, H. The formation of water masses and sea ice in the Gulf of St. Lawrence. *J. Geophys. Res.* **2003**, *108*, 3269–3289. [CrossRef]
27. Rego, J.L.; Meselhe, E.; Stronach, J.A.; Habib, E. Numerical modelling of the Mississippi-Atchafalaya rivers' sediment transport and fate: Considerations for diversion scenarios. *J. Coast. Res.* **2010**, *26*, 212–229. [CrossRef]
28. Arakawa, A.; Lamb, V.R. Computational design of the basic dynamical processes of the UCLA general circulation model. *Methods Comput. Phys.* **1977**, *17*, 173–263.
29. Smagorinsky, J. General circulation experiment with the primitive equations: I. the basic experiment. *Mon. Weather Rev.* **1963**, *91*, 99–164. [CrossRef]
30. Mellor, G.L.; Yamada, T. Development of a turbulent closure model for geophysical fluid problems. *Rev. Geophys.* **1982**, *20*, 851–875. [CrossRef]
31. Mellor, G.L.; Durbin, P.A. The structure and dynamics of the ocean surface mixed layer. *J. Phys. Oceanogr.* **1975**, *5*, 718–728. [CrossRef]

32. Zalesak, S.T. Fully multidimensional flux-corrected transport algorithms for fluids. *J. Comput. Phys.* **1979**, *31*, 335–362. [CrossRef]
33. Kondratyev, K.Y. *Radiation Processes in the Atmosphere*; No. 309; World Meteorological Organization, The University of California: San Diego, CA, USA, 1972.
34. Gill, A.E. *Atmosphere-Ocean Dynamics*; Academic Press: London, UK, 1982.
35. Crean, P.B.; Ages, A.B. *Oceanographic Records from Twelve Cruises in the Strait of Georgia and Juan de Fuca Strait, 1968*; Department of Energy, Mines and Recources, Marine Research Sciences Branch: Ottawa, ON, Canada, 1971.
36. Water Survey of Canada. Available online: https://www.canada.ca/en/environment-climate-change/services/water-overview/quantity/monitoring/survey.html (accessed on 15 February 2016).
37. The Intergovernmental Panel on Climate Change. *Climate Change 2007: The Fourth Assessment Report*; Cambridge University Press: New York, NY, USA, 2007.
38. Werner, A.T. *BCSD Downscaled Transient Climate Projections for Eight Select GCMs over British Columbia, Canada*; Pacific Climate Impacts Consortium, University of Victoria: Victoria, BC, Canada, 2011.
39. Schnorbus, M.A.; Bennett, K.E.; Werner, A.T.; Berland, A.J. *Hydrologic Impacts of Climate Change in the Peace, Campbell and Columbia Watersheds, British Columbia, Canada*; Pacific Climate Impacts Consortium, University of Victoria: Victoria, BC, Canada, 2011.
40. Pacific Climate Impact Consortium. Available online: https://www.pacificclimate.org (accessed on 1 February 2016).
41. Ausenco Sandwell. *Sea Dike Guidelines*; BC Ministry of Environment: Victoria, BC, Canada, 2011; pp. 4–5.
42. Blumberg, A.F.; Mellor, G.L. A description of a three-dimensional coastal circulation model. In *Three-Dimensional Coastal Ocean Models*; Heaps, N.S., Ed.; American Geophysical Union: Washington, DC, USA, 1987; pp. 1–16.

Journal of
Marine Science and Engineering

MDPI

Article

Ice Forecasting in the Next-Generation Great Lakes Operational Forecast System (GLOFS)

Eric J. Anderson [1,*], Ayumi Fujisaki-Manome [2,3], James Kessler [3], Gregory A. Lang [1], Philip Y. Chu [1], John G.W. Kelley [4], Yi Chen [4] and Jia Wang [1]

1 Great Lakes Environmental Research Laboratory, Office of Oceanic and Atmospheric Research, National Oceanic and Atmospheric Administration, Ann Arbor, MI 48108, USA; gregory.lang@noaa.gov (G.A.L.); philip.chu@noaa.gov (P.Y.C.); jia.wang@noaa.gov (J.W.)
2 Department of Climate and Space Sciences and Engineering, University of Michigan, Ann Arbor, MI 48104, USA; ayumif@umich.edu
3 Cooperative Institute for Great Lakes Research, University of Michigan, Ann Arbor, MI 48108, USA; jamkessl@umich.edu
4 Coast Survey Development Laboratory, Office of Coast Survey, National Ocean Service, National Oceanic and Atmospheric Administration, Silver Spring, MD 20910, USA; john.kelley@noaa.gov (J.G.W.K.); yi.chen@noaa.gov (Y.C.)
* Correspondence: eric.j.anderson@noaa.gov; Tel.: +1-734-741-2293

Received: 27 September 2018; Accepted: 18 October 2018; Published: 21 October 2018

Abstract: Ice Cover in the Great Lakes has significant impacts on regional weather, economy, lake ecology, and human safety. However, forecast guidance for the lakes is largely focused on the ice-free season and associated state variables (currents, water temperatures, etc.) A coupled lake-ice model is proposed with potential to provide valuable information to stakeholders and society at large about the current and near-future state of Great Lakes Ice. The model is run for three of the five Great Lakes for prior years and the modeled ice cover is compared to observations via several skill metrics. Model hindcasts of ice conditions reveal reasonable simulation of year-to-year variability of ice extent, ice season duration, and spatial distribution, though some years appear to be prone to higher error. This modeling framework will serve as the basis for NOAA's next-generation Great Lakes Operational Forecast System (GLOFS); a set of 3-D lake circulation forecast modeling systems which provides forecast guidance out to 120 h.

Keywords: ice modeling; operational forecast; FVCOM; CICE; hydrodynamic modeling; Great Lakes

1. Introduction

Ice formation in the Great Lakes occurs each year during the winter season, where typical ice onset occurs in early December and ice-off dates come in late spring (April or May; [1–3]). However, there is a high degree of interannual and inter-lake variability in ice cover driven by atmospheric conditions and lake characteristics, with the maximum extent of ice occurring near late January or early February ([4,5] Table 1). Only under rare occasions do the lakes experience complete or nearly complete freeze-over due to their depth and large thermal heat capacity, with Lake Erie being the exception, experiencing annual maximum ice cover near 82% [1–3]. As such, ice first forms near the shorelines and in protected or shallow bays, followed by progressive growth toward the offshore. Though observations are sparse in space and time, ice thickness shows a high degree of variability, ranging from a few centimeters to over a meter [6–8].

Table 1. Average annual maximum ice cover for the period 1973–2018.

Lake Observations	Superior	Michigan	Huron	Erie	Ontario	Basin
Average Max. ice cover (%)	60.91	39.64	64.60	82.19	29.77	54.28

Ice cover plays a major role in winter lake processes. Presence of ice cover inhibits latent and sensible heat fluxes from the lake to the atmosphere which impact lake surface temperatures, water levels, and hydrometeorological events [9–11]. Ice cover also alters air-water momentum transfer, which influences currents and waves. Ecological impacts can be observed due to ice conditions, where for example, the timing of spring phytoplankton blooms are impacted by water temperatures and ice-off timing [12]. Additionally, ice formation has a direct influence on search and rescue operations, spill response efforts, and commercial navigation.

The Great Lakes (Figure 1) are home to a $77 billion commercial shipping industry and several major ports serving the United States and Canada as well as global trade [13]. With the greatest concentration and thickness of ice focused at the coastline and bays, as well as ice jams in the connecting channels, shipping ports are often inaccessible to most vessels, and thus the shipping season is largely restricted to the ice-free period in the lakes (April–December) or when aid can be provided by US and Canadian ice-cutting vessels. However, for the vessels that continue to operate during ice-covered periods, accurate information on ice extent, concentration, and thickness is crucial to ensure safe navigation. Currently, the only available information on ice conditions comes from the US and Canadian Ice Centers, which coordinate to produce a daily Great Lakes Ice Analysis product. These ice charts are based on remotely sensed data from satellites or flyovers and provide an estimate of ice concentration and distribution based on observed data, which could be hours or days old. However, due to the dynamic nature of ice in the Great Lakes, the ice field can vary dramatically over several hours or a few days due to wind conditions or changes in air temperature [8]. Therefore, observed ice conditions may not be sufficient to provide decision makers with the information necessary to operate safely or effectively over the course of a few days. Yet, currently there exists no operational forecast guidance for ice concentration in the Great Lakes.

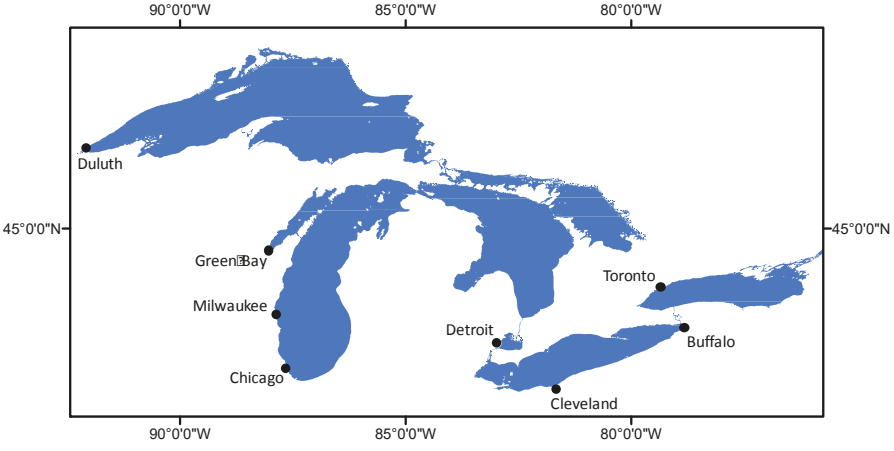

Figure 1. The Great Lakes domain, including Lakes Erie, Michigan, and Huron.

In the US, marine forecast guidance in the Great Lakes for currents, water temperatures, and water level fluctuations, is provided by the National Oceanic and Atmospheric Administration's (NOAA) Great Lakes Operational Forecast System (GLOFS; [14–16]). GLOFS is a set of three-dimensional hydrodynamic computer models that covers each of the Great Lakes and has been operated by

the National Ocean Service (NOS) since 2005. Real-time nowcast and forecast predictions of lake conditions from GLOFS provide decision support guidance for commercial navigation, search and rescue operations, recreational use, spill response, drinking water safety, and lake management. The first generation of GLOFS was developed as a result of the collaboration between the NOAA Great Lakes Environmental Research Laboratory (GLERL) and Ohio State University (OSU), in which the hydrodynamic models were developed using a version of the Princeton Ocean Model (POM; [17]) adapted for the Great Lakes [18]. Although the first implementation of GLOFS did not include ice products, recent work has shown that coupling an ice model to Great Lakes POM models can provide accurate predictions of winter lake conditions [5].

An upgrade to GLOFS is underway to make several model improvements including an increase in model spatial resolution in important regions, expansion of modeling domains, tracking of hydrologic water level changes, and providing support for the development of ecological forecast products in the Great Lakes. This next-generation GLOFS is being developed using the Finite Volume Community Ocean Model (FVCOM, [19]), which includes an internally coupled unstructured grid version of the Los Alamos Sea Ice model (CICE, [20]). Recent work in two-way coupling between the lakes and a regional climate model has demonstrated the capability of CICE in the Great Lakes using evaluation of lake-averaged ice and temperature conditions [21]. However, this effort has not yet been extended and tested in an operational framework, in which a thorough spatio-temporal analysis of ice concentration has been carried out. Therefore, the goal of this study is to implement FVCOM-CICE into the next-generation GLOFS and assess the model's ability to resolve the spatial-temporal distribution of ice concentration in order to meet stakeholder requirements.

2. Methods

2.1. Hydrodynamic Modeling

The next-generation GLOFS is based on FVCOM [19], a three-dimensional, unstructured, free-surface, primitive equation, sigma-coordinate oceanographic model that solves the integral form of the governing equations. FVCOM has been applied in several studies of the coastal ocean, including successful application to operational forecasting in the Great Lakes [22–27]. In this work, the existing FVCOM-based GLOFS models for Lake Erie, Huron, and Michigan will be used to assess performance of the hydrodynamic model in regard to winter conditions and ice formation using CICE. These implementations of FVCOM are based on the Lake Erie Operational Forecast System (LEOFS, [14]) and the Lake Michigan-Huron Operational Forecast System (LMHOFS, [25]), which combines Lakes Michigan and Huron into a single model since they form a single hydrologic system. Horizontal grid resolution in each model ranges from roughly 200 m near the shoreline to 2500 m offshore, with 21 vertical sigma layers evenly distributed throughout the water column. As a result, the LEOFS model contains roughly 12,000 triangular elements, and the LMHOFS model is significantly larger with roughly 170,000 elements. Horizontal and vertical diffusion are handled by the Smagorinsky parameterization [28] and Mellor-Yamada level-2.5 turbulence closure scheme [29], respectively. The air-water drag coefficient is calculated as a function of wind speed [30]. Latent and sensible heat fluxes are calculated from the Coupled Ocean-Atmosphere Response Experiment (COARE, [31–33]) algorithm for LMHOFS and from the SOLAR algorithm for LEOFS [34]. In both cases, the SOLAR algorithm is used to precompute the shortwave and longwave radiation, based on prescribed cloud cover and satellite-derived surface water temperatures. Modeled depths are taken from 3 arc-second bathymetry data from the NOAA National Centers for Environmental Information (NCEI).

Simulations without the ice model will be also conducted to be compared with simulations with the ice model in order to assess the impact of including the ice model on modeled water temperatures. In the non-ice simulations, no ice forms even when the surface water is super-cooled. The water

temperature in the model is floored at −2.0 °C to avoid continual artificial cooling due to the water surface continuously exposed to the cold air above.

2.2. Ice Modeling

An unstructured grid version of the Los Alamos Sea Ice model (CICE; [20,35]) has been included and coupled within FVCOM. The CICE model includes components for ice thermodynamics and ice dynamics, using elastic-viscous-plastic rheology for internal stress [36], and produces two-dimensional fields of ice concentration, thickness, and velocity. A multi-category ice thickness distribution (ITD) model is employed in CICE to resolve mechanical deformation as well as growth and decay [37]. For the Lake Erie and Lake Michigan-Huron models, five categories of ice thickness are defined (5, 25, 65, 125, and 205 cm). The ice surface albedo depends on surface temperature and thickness of ice, as well as the visible and infrared spectral bands of the incoming solar radiation [38]. At ice-covered cells, the net momentum transfer is calculated as a weighted average of the air-water and ice-water stresses by areal fraction of ice. The air-ice drag coefficient C_{D_ai} is a function of wind speed U, given as $C_{D\_ai} = (1.43 + 0.052U) \times 10^{-3}$ and the ice-water drag coefficient is 5.5×10^{-3} [39]. Similarly, the net heat transfer is calculated as a weighted average of the air-water and ice-water heat fluxes. The ice-water heat fluxes are calculated based on the bulk transfer formula [40].

2.3. Simulation Period

Two periods of simulation with three overlapping years are covered in this study. In the Lake Erie simulation, the model was run for the years 2005–2017 using a continuous run (hotstarted) from 1 January 2005. Initial conditions at the start of 2005 were provided by a spin-up simulation in 2004, in which conditions on 1 January, 2004 were coldstarted with a uniform temperature of 4 °C, zero currents, and uniform lake level. Due to computational expense, the Lake Michigan-Huron model (LMHOFS) was simulated for the years 2015–2017, with a spin-up year in 2014. On 1 January 2014, the LMHOFS model was initialized with satellite-derived surface water temperatures from the Great Lakes Surface Environmental Analysis (GLSEA) [41] for the top 50 m with a uniform 4 °C temperature at depths below 50 m. Similar to the Lake Erie case, the spin-up year was coldstarted with zero currents and a uniform (resting) lake level. For both the Lake Erie and Lake Michigan-Huron models, simulations are carried out with and without the ice model.

For the years 2005–2014, hourly atmospheric forcing conditions are provided from the Great Lakes Coastal Forecasting System (GLCFS; [18]), in which observations from coastal and offshore meteorological stations are corrected for over-water conditions and interpolated, along with available in-lake buoys, to the model grid [42]. This method of interpolated forcing conditions has been the operational source of meteorological forcing for the GLOFS since its implementation. However, starting in 2015, model output is available from the High-Resolution Rapid Refresh (HRRR), a 3-km data-assimilated implementation of the Weather Research and Forecasting (WRF) model [43]. In the upgrade of GLOFS, atmospheric forcing conditions are now being provided by the HRRR in operations, and thus for the simulations presented here for the period 2015–2017, both models are driven by HRRR model output. Although not as pertinent to this analysis, lateral boundary conditions are provided for inflows and outflows to the lakes, details of which can be found in previous work [14,25].

2.4. Model Validation

To evaluate modeled ice concentration and spatial distribution, Great Lakes ice concentration data is obtained from the US National Ice Center (NIC; [44]). Through a bi-national coordinated effort between the US NIC and Canadian Ice Center, routine gridded ice analysis products are produced from available data sources including Radarsat-2, Envisat, AVHRR, Geostationary Operational and Environmental Satellites (GOES), and Moderate Resolution Imaging Spectroradiometer (MODIS). Spatial resolution of the ice charts, hereafter referred to as NIC, is 2.55 km in 2005, and 1.8 km from 2006–2017. The resulting NIC data set defines ice concentration values from 0 to 100% on 10% increments.

Assessment of model skill in simulating ice concentration is evaluated using root mean squared error (RMSE, Equation 1) between the model and observed value

$$\mathrm{RMSE} = \sqrt{\frac{\sum_{t=1}^{T} \left(i_{t_m} - i_{t_o}\right)^2}{T}} \tag{1}$$

where i_{tm} is modeled ice at time t, i_{to} is observed ice from the NIC, and T is the total number of records. RMSEs are calculated to assess skill in three categories: (1) lake-wide ice extent expressed as a fraction, (2) spatially computed RMSE of ice concentration in each model grid cell, and (3) spatially computed RMSE of binary ice cover in each model grid cell (presence/absence of ice). To perform the spatial skill assessment (categories 2 and 3), the model output is interpolated onto the NIC grid and the RMSEs between corresponding cells are computed. Since the NIC data is given in 10% increments, for category 3, the modeled binary ice cover is defined as 1 when ice concentration in a cell exceeds 10%, which is the threshold for ice presence in the NIC, and 0 otherwise. These RMSE values are tabulated and plotted as time series. Additionally, to identify and address trends in ice model performance, the spatial concentration RMSEs are evaluated as a function of time of year, observed ice concentration, and modeled ice thickness. Based on category 1, modeled ice on/off dates are plotted in order to evaluate the timing and length of the ice season for each lake. Based on categories 2 and 3, the spatial distribution of error is averaged through time and plotted on a map to identify any regions with consistently high/low error. In addition to ice assessment, observed surface water temperatures from the GLSEA are compared to modeled (with and without including the ice model) lake-wide average surface temperatures for the ice season (December through April).

3. Results

The Lake Erie and Lake Michigan-Huron models are simulated for the years 2005–2017 and 2015–2017, respectively, with and without the ice model enabled. In regard to the ice simulations (averaged over the 2015–2017 period), the spatial pattern of ice cover is reasonably simulated in comparison with the NIC analyses (Figure 2), as represented by the development of nearshore ice in freezing period, high ice cover and offshore open water region in the mid-season, and decay from the south in the melting period.

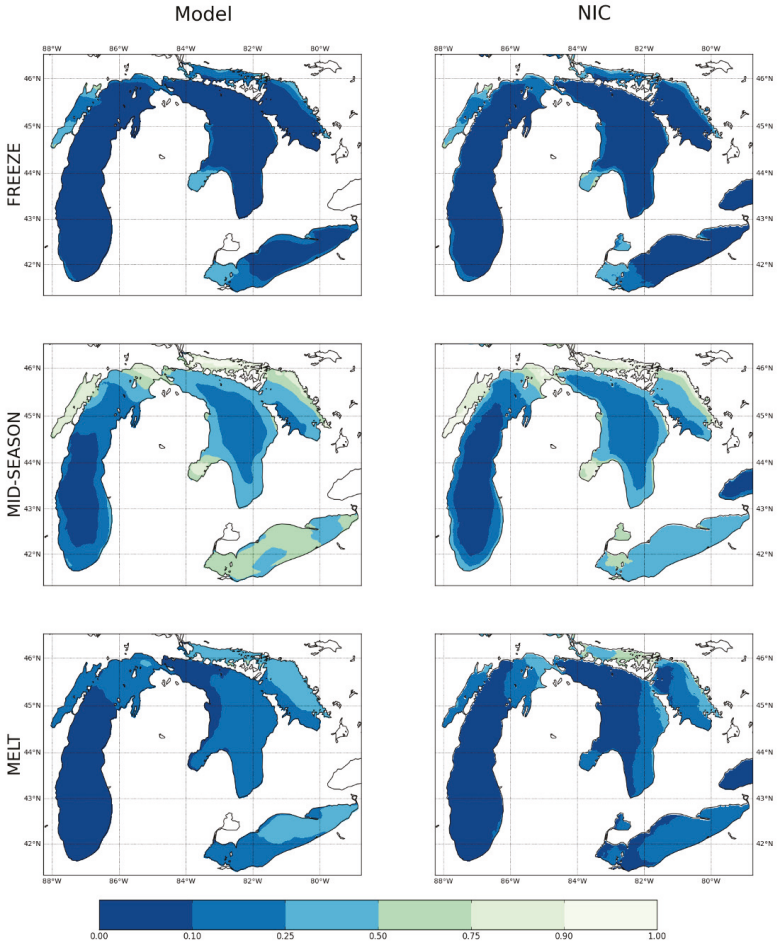

Figure 2. Spatial pattern of ice concentration (0–1) for freezing (1 December–15 January), mid-season (16 January–15 March), and melting (15 March–1 May) seasons. Averaging is performed for each season from 2015–2017. Left column shows the model results from LEOFS and LMHOFS, and right column shows the NIC analysis.

3.1. Erie Ice Skill Statistics

For Lake Erie, the simulation period covers low-, intermediate-, and high-ice years, revealing model performance under a wide array of conditions (Figure 3). In a majority of years, the model successfully follows the lake-wide ice extent as produced by the NIC each year, capturing the initial formation of ice, annual maximum ice, and the ice-off timing, with a few exceptions. The largest divergence between the modeled lake extent and that reported by the NIC occurs during a late-March pulse in 2006 and again in 2017, where the model significantly overpredicts late season ice. In years 2005, 2007, and 2008, and to a lesser extent in 2001, the model also shows a tendency to melt more rapidly in the spring than the NIC. However, in each of these cases, both the model and the NIC showed a decreasing trend in lake-ice leading to the ice-off date. During extreme high- or low-ice years, the model also performs well, where RMSE in the low-ice year of 2012 is 0.01 (Table 2), and in the high-ice years of 2014 and 2015, RMSEs are 0.07 and 0.08, respectively (Table 2).

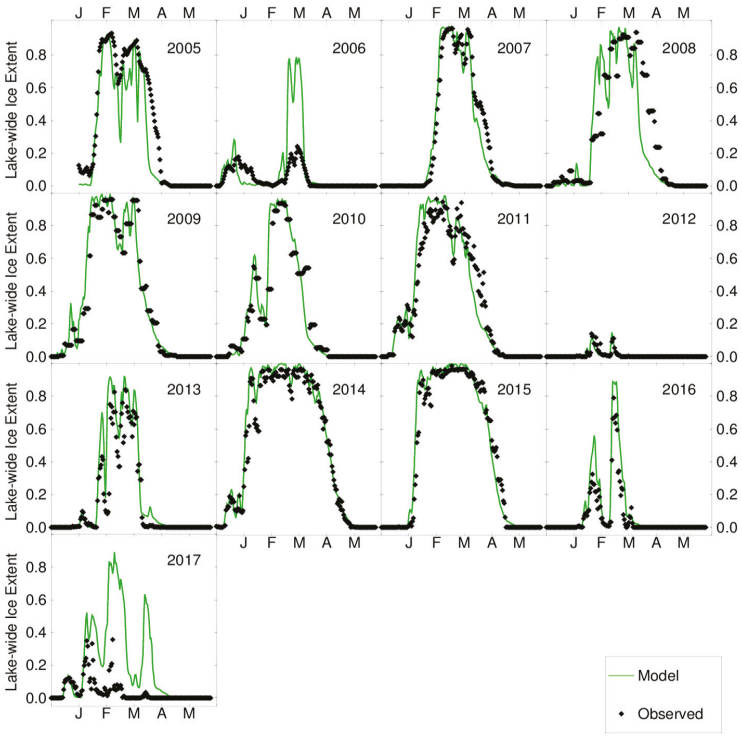

Figure 3. Simulated lake-wide average ice extent for Lake Erie (**green line**) and the ice extent from the NIC (**black dots**).

Table 2. Seasonal mean RMSEs [0–1] of simulated lake-wide ice area, ice concentration at pixels, and binary ice cover at pixels. The lake-wide RMSEs are normalized by an area of each lake. The seasonal means are calculated from 1 December in the previous year to 31 May.

Year	**Erie**			**Michigan**			**Huron**		
	lake wide	spatial		lake wide	spatial		lake wide	spatial	
		concentration	binary		concentration	binary		concentration	binary
2005	0.17 [1]	0.21 [1]	0.25 [1]						
2006	0.17	0.15	0.24						
2007	0.08	0.13	0.17						
2008	0.19	0.22	0.26						
2009	0.10	0.18	0.25						
2010	0.12	0.19	0.26						
2011	0.11	0.21	0.25						
2012	0.01	0.03	0.06						
2013	0.13	0.16	0.23						
2014	0.07	0.18	0.23						
2015	0.08	0.15	0.18	0.09 [1]	0.20 [1]	0.31 [1]	0.13 [1]	0.26 [1]	0.34 [1]
2016	0.09	0.10	0.17	0.01	0.07	0.11	0.03	0.12	0.18
2017	0.28	0.26	0.38	0.04	0.10	0.15	0.05	0.14	0.21
mean	0.12	0.17	0.23	0.05	0.12	0.19	0.07	0.17	0.24

[1] Averaging period for the initial year (2005 for LEOFS and 2015 for LMHOFS) is from 1 January to 31 May.

The overall lake-wide extent RMSE for Lake Erie is 0.12 (Table 2); however most of the error, or difference between the model and the NIC, is found during the periods of rapid ice formation and ice melting, resulting in an "M-shape" in the time series of RMSE (Figure 4). The overall RMSE is higher for spatial concentration (0.17) and higher still for spatial binary (0.23), though the trends between all three RMSE's are fairly consistent through time (Figure 4). In a few cases, e.g., April–May 2014, the lake-wide error is very low compared to the spatial errors. This indicates that although the model reproduced realistic lake-wide ice extent, the distribution of ice did not agree well with observations, which further motivates the need for spatial skill analyses.

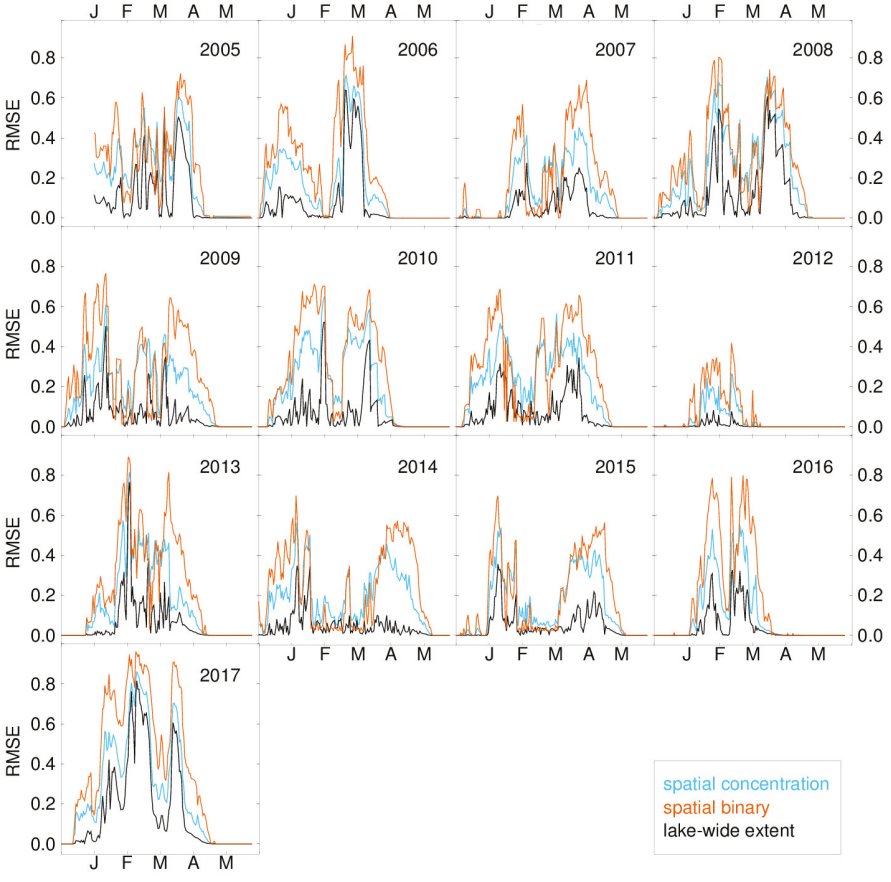

Figure 4. Time series of ice simulation errors between the Lake Erie model and the NIC based on the three methods: Pixel-to-pixel RMSE based on ice concentration (**cyan**), pixel-to-pixel RMSE based on binary ice cover (**orange**), and lake-wide absolute error (**black**). Please note that lake-wide absolute error shows only the magnitude of error (i.e., does not show the sign of model bias).

When evaluating spatial concentration RMSE as a function of month (Figure 5a), interestingly, the M-shape pattern that exists in Figure 4 disappears. This is likely because the timing of maximum ice cover shifts from year to year. Thus, in the long-term mean, such patterns are smoothed out, and the larger RMSEs occur during the peak ice months, January through March. In Figure 5b, the model shows the lowest median RMSE for the 0–5% category, indicating that the model performs relatively well over open water or regions with low ice concentration. The data frequency is the highest for

0–5% ice concentration and much lower in the other categories, showing a slight increase toward the higher ice concentration categories. Such distribution is well captured by the model. When RMSEs are evaluated as a function of modeled ice thickness (Figure 5c), the median RMSE is slightly higher at the thinnest ice thickness range (0–5 cm), and then fairly comparable across the other ice thickness categories. The data frequency shows that the modeled ice thickness is the most common for the 35–65 cm range, and least common for ice thicker than 135 cm. Due to the limited availability of observational ice thickness data, no validation is possible at the time of this writing.

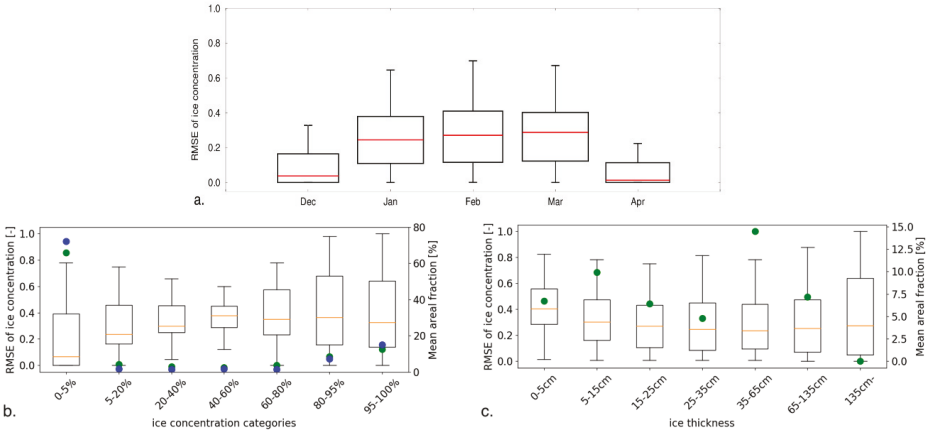

Figure 5. Ranges of spatial concentration RMSE as functions of (**a**) months, (**b**) observed ice concentration, and (**c**) modeled ice thickness for the LEOFS 2005-2017 simulation results. A box extends from the lower and upper 25% of the RMSEs. A horizontal line within each box denotes the median value. The whiskers show the range of RMSE, extending from the box toward farthest data points within the interquartile range (i.e., length of the box) from the upper and lower bounds of the box. In (**b**,**c**), solid circles show mean areal fractions for observation (blue) and model (green), representing data frequency for each category. For (**c**), open water cells are excluded.

3.2. Michigan-Huron Ice Skill Statistics

For the Lake Michigan-Huron model, the results are similar to those seen for Lake Erie, even with a shorter simulation period. However, unlike Lake Erie, ice formation is primarily constrained to the shallow bays and coastal areas during freezing, peak ice, and melting periods (Figure 2). Time series of ice extent shows a reasonable agreement between simulated and NIC peak ice for all three years (Figure 6). In the heavy-ice year of 2015, the peak ice in Lake Michigan is slightly overpredicted; however, ice melting is captured, resulting in a mean RMSE of 0.09 (Table 2). In Lake Huron, the opposite is true, where peak ice matches well with NIC, but the model experiences a slower decline in ice melting, contrary to the melting trend in Lake Erie, and results in a slightly higher RMSE (0.13, Table 2). In 2016 and 2017, both intermediate- to low-ice years, simulated lake-wide ice extent follows the NIC more closely with the exception of the very end of the 2017 season. Unlike the Lake Erie results, the error time series in Figure 7 does not show the M-shape pattern except for Lake Huron in 2015. This is likely because ice cover is not restricted by the coastlines for Michigan and Huron, except for under conditions with unusually high ice cover (e.g., Huron in 2015).

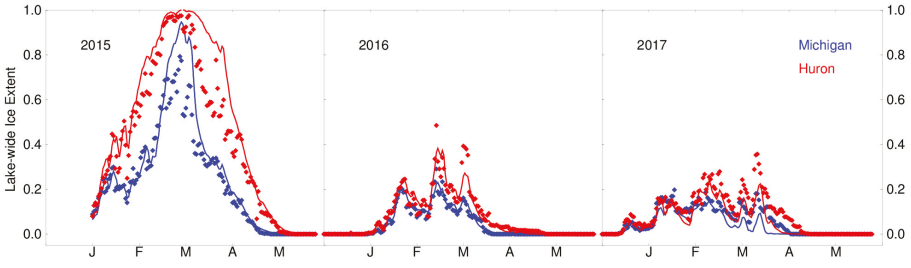

Figure 6. Lake-wide average ice extent for Lake Michigan (**blue**) and Lake Huron (**red**). The model ice extent (solid lines) is compared to the NIC (diamonds).

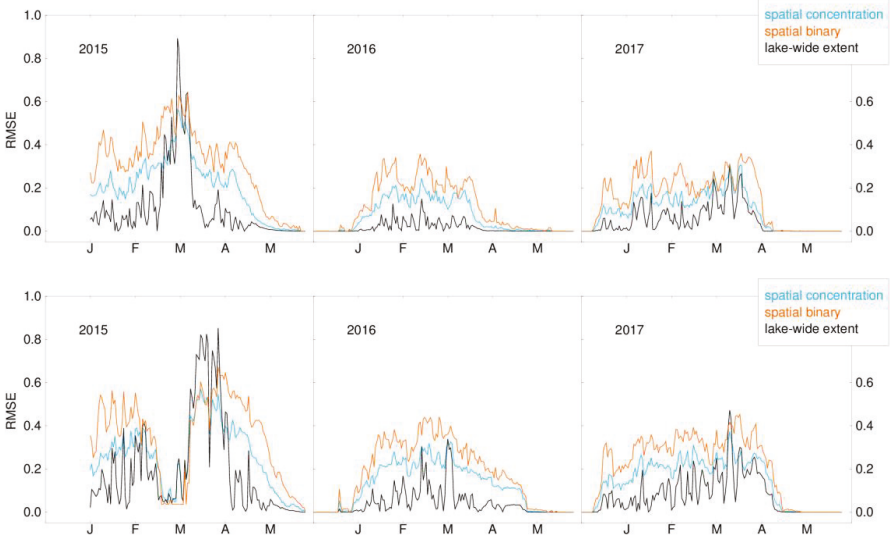

Figure 7. Time series of ice simulation errors between the Lake Michigan-Huron model and the NIC based on the three methods for (**top**) Lake Michigan and (**bottom**) Lake Huron: Pixel-to-pixel RMSE based on ice concentration (cyan), pixel-to-pixel RMSE based on binary ice cover (orange), and lake-wide absolute error (black). Please note that lake-wide absolute error shows only the magnitude of error (i.e., does not show the sign of model bias).

Overall lake-wide RMSE between the model and NIC are 0.05 for Lake Michigan and 0.07 for Lake Huron, respectively. Similar to Erie, the spatial RMSE is higher for concentration, 0.12 and 0.17 for Michigan and Huron, and higher still for binary with 0.19 and 0.24. The RMSE trends as functions of time, thickness and concentration for Lakes Michigan and Huron (Figures 8 and 9) are also similar to that of Erie. Again, the lowest median RMSE occurs at 0–5% ice concentration, and the median RMSE's are largest for the thinnest ice (0–5 cm).

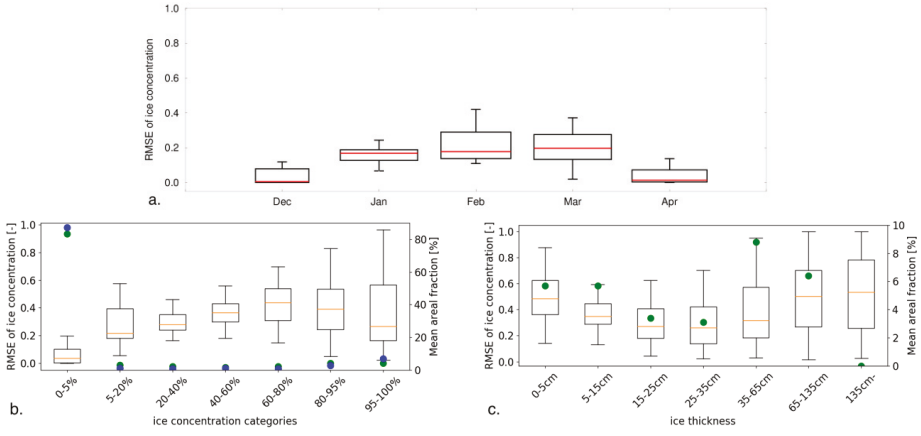

Figure 8. Ranges of spatial concentration RMSE as functions of month (**a**), ice concentration (**b**) and ice thickness (**c**) for Lake Michigan from the LMHOFS 2015–2017 simulation results. See the caption of Figure 5 for the explanation of the box, whiskers, and solid circles. For (**c**), open water cells are excluded.

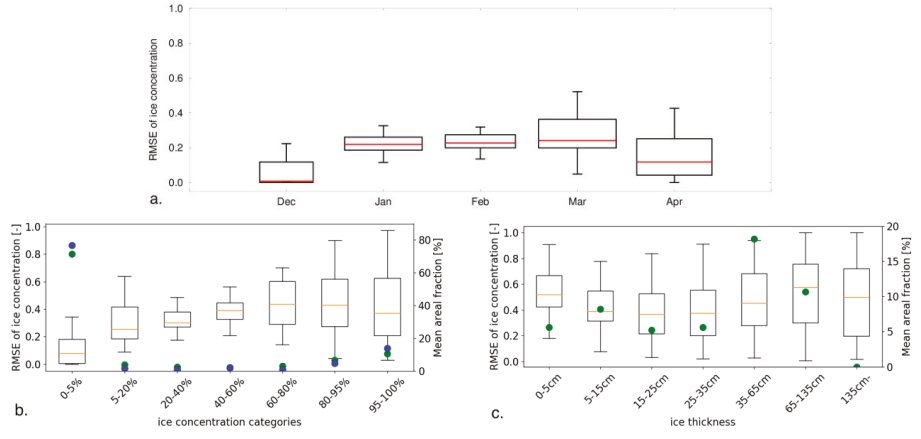

Figure 9. Ranges of spatial concentration RMSE as functions of month (**a**), ice concentration (**b**) and ice thickness (**c**) for Lake Huron from the LMHOFS 2015–2017 simulation results. See the caption of Figure 5 for the explanation of the box, whiskers, and solid circles. For (**c**), open water cells are excluded.

3.3. Ice Duration and Spatial Maps

Based on the lake-wide extent analyzed above, ice on and off dates by the models are compared with the NIC in all simulations years (Figure 10, Table 3). For Erie, 10 of the 13 simulated years show very good agreement with observed ice onset (within 5 days), and 5 of 13 years show extremely good agreement (within 1 day). Erie ice-off dates show a similar trend (9/13 are within 1 week and 5/13 are within 1 day). However, 2005 and 2017 show notably low skill for Erie. In 2017, the ice-on date by the Lake Erie model matched the NIC within one day but the ice-off date was 46 days later than the NIC. The Lake Michigan and Huron model performs well in producing accurate ice-on dates (Lake Michigan: all within 3 days, Lake Huron: all within 1 day), but show varied results in producing ice-off dates. Please note that in 2017, Michigan and Huron's modeled ice season ended much too soon, despite the opposite being true for Erie.

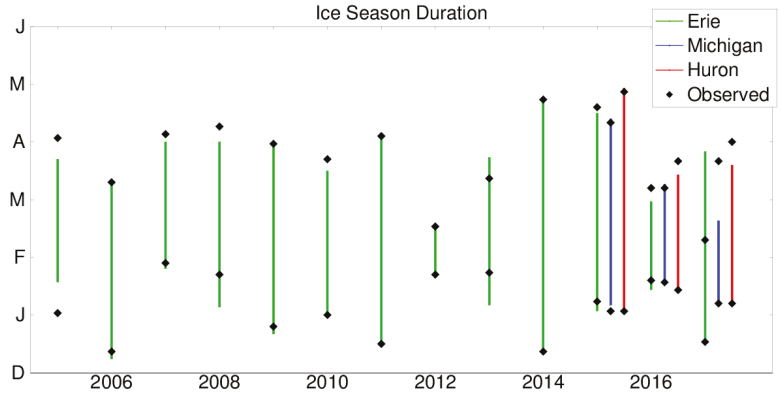

Figure 10. Modeled vs observed ice season duration for all simulated years. The duration is defined as the period of time between ice onset (first day lake-wide extent exceeds 10%) and ice-off (last day extent exceeds 10%). The y-axis shows the length and timing of the ice season by month.

Table 3. Ice season length (in days) as defined in Figure 10.

Year	Erie		Michigan		Huron	
	NIC	Model	NIC	Model	NIC	Model
2005	91	64				
2006	88	92				
2007	67	66				
2008	77	86				
2009	95	100				
2010	81	76				
2011	108	107				
2012	25	24				
2013	49	77				
2014	131	131				
2015	101	103	98	97	114	115
2016	48	46	49	50	67	59
2017	53	98	74	42	84	71

Extending the analysis of spatial ice extent, time-averaged spatial error maps are shown in Figure 11 for concentration RMSE. Lakes Michigan and Huron tend to show higher error in the shallow, protected coastal regions and less error offshore. This is likely an artifact of the ice formation pattern discussed earlier, as ice rarely extends to the offshore and thus error is inherently lower (see Figure 2). Erie's spatial error, which is averaged over a much greater simulation period, is nearly homogeneous. The two regions with increased error are the southern portion of the western basin and the southern portion of the eastern basin, likely related to difficulties in simulating ice-initiation and ice-melting in those regions, respectively. Unlike in Lakes Michigan and Huron, the frequent offshore ice formation in Lake Erie, or absence of open-water conditions, does not produce a similar low-error region in the offshore.

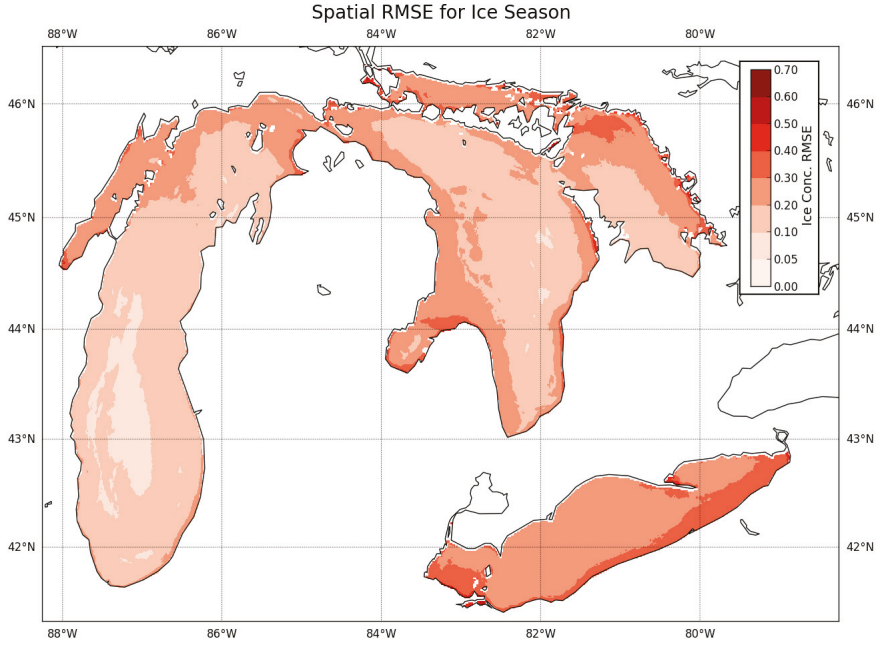

Figure 11. Spatial distribution of ice concentration RMSE averaged throughout the entire ice season for all simulated years.

3.4. Water Temperatures

Finally, in terms of the impact on water temperatures, the inclusion of the ice model improves the winter water surface temperatures by eliminating a cold-water bias present in the non-ice simulations (Table 4, Figure 11). This can most likely be attributed to the presence of artificially cooled water in the non-ice simulation, where water temperatures can drop below freezing. Accordingly, the difference between the with and without ice model simulations is evident during the months of January, February, and March (Figure 12). Slight differences between the two simulations are found in April, especially for Lake Erie, which may be improvements made with the ice model simulations where spring warm-up in surface water temperature is realistically delayed by remnant of ice cover later in spring. The RMSE between the model water temperature and GLSEA improves by 0.43 °C for Lake Erie and by 0.21 and 0.26 °C for Michigan and Huron, respectively, when the ice model is activated (Table 4).

Table 4. Surface water temperature RMSE (°C) between model simulations and observed temperatures from satellite-derived lake surface temperature from the GLSEA during winter months (1 December–30 April).

Satellite-Derived Temperature	FVCOM-CICE	FVCOM (No-Ice)
Lake Erie GLSEA	0.69	1.12
Lake Michigan GLSEA	0.66	0.87
Lake Huron GLSEA	0.68	0.94

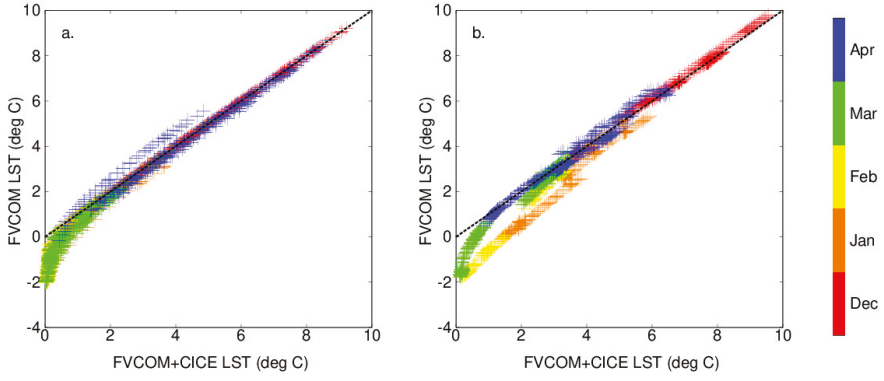

Figure 12. Lake surface temperature (LST) for Lake Erie (**left**) and Lake Michigan-Huron (**right**) for simulations of FVCOM with and without CICE during the winter months.

4. Discussion

Ice conditions in the Great Lakes result from dynamic processes that yield significant spatio-temporal variability, and most often resemble a continual marginal ice zone that is in constant flux due to atmospheric conditions such as wind speed and direction and air temperature. As such, having updated and accurate information on ice conditions is crucial to safe commercial navigation and United States Coast Guard (USCG) operations. Historically, operational models of the Great Lakes have not included ice conditions as part of the available forecast guidance, and thus decision makers are limited to recent observational-based products such as ice charts produced by the National Ice Center (NIC). In the work presented here, the Los Alamos Sea Ice model (CICE) has been included as part of the next-generational GLOFS and a skill assessment is carried out for Lakes Erie, Michigan, and Huron in regard to modeled ice cover as compared to the NIC.

In general, the FVCOM-CICE model captures the dynamic nature of Great Lakes ice conditions in low-, intermediate-, and high-ice years. The three periods early season freezing or ice formation, mid-season peak ice, and late-season ice melting are reproduced in both Erie and Michigan-Huron. The M-shape of RMSE timeseries indicates relatively high errors in the freezing and melting periods while errors are reduced in the peak period, when model simulations benefit from spatial restrictions by the coastlines. This is evident for Erie in nearly all simulation years and for Huron in 2015. The RMSE timeseries are amplified when spatial distributions of ice are taken into account, indicating limitation of evaluations based on the lake-wide values. The RMSE values for spatial binary ice cover are almost always larger than the corresponding RMSEs for spatial ice concentration. This is rather an artifact of the error calculation with binary ice cover: For example, if modeled ice concentration is 9% at a cell where the NIC has 10%, the differences are only 1% for actual ice concentration but 100% when treated as binary ice cover.

Ultimately, model success must be evaluated based on user requirements for ice concentration accuracy. Interaction with key stakeholders, such as commercial ship captains and the USCG, suggested that although there may be a wide range of requirements depending on conditions or the specific stakeholder, areas of common interest were ice formation and ice-off dates, as well as open versus ice-covered areas. With respect to these measures, the dates of predicted ice initiation and termination were often within 4 days of the NIC (more than half of the Lake Erie simulation years and all of the Lakes Michigan and Huron simulation years). Similarly, the model performed well in predicting areas of open water, often found in Lakes Michigan and Huron, illustrated by the lowest errors found at ice concentration from 0 to 5%. At ice concentrations above 5%, RMSEs were nearly uniform and ranged from 20–40%. In addition, the data frequency is higher at high ice concentrations (>80%), but relatively insignificant at medium ice concentrations (5–80%). These results suggest that stakeholders may find

confidence in the model's ability to predict the binary presence of ice, and thus enable them to plan a shipping route to avoid ice fields. However, if user requirements are established that specifies criteria based on ice concentrations, and/or ice thickness, beyond the presence/absence of ice, more work will be required to evaluate model performance under these guidelines.

Previous work has shown that the next-generation GLOFS, which is based on FVCOM, has performed well for water temperatures in the non-ice period, as well as for currents and water level fluctuations [14,25]. As illustrated, using a coupled FVCOM-CICE model produces an immediate improvement to winter water temperatures, where the ability to form ice when freezing temperatures are reached prevents the unrealistically low water temperatures produced in the existing operational models. This result, in itself, marks an important improvement during the winter season, where often forecast guidance has been limited by unrealistic physical treatment of the lakes (i.e., artificially cooled water).

Discrepancies between modeled and NIC ice concentration may be due to a multitude of reasons. In terms of ice dynamics, some processes that are potentially important for nearshore ice physics are currently not taken into account, such as land-fast ice and ice-wave interaction. Land-fast ice may provide a stable ice zone along the shore resistant to wind disturbance. Surface waves may break ice cover into smaller pieces that are more sensitive to heat fluxes from air and water due to increased contact surface. In terms of ice thermodynamics, inclusion of realistic snow cover on top of the ice would be an important step to the future improvement as it influences calculations of ice albedo and thermal conductivity of the snow/ice medium. Another possible cause for discrepancy could be related to the uncertainty in the meteorological forcing. Previous work has shown that as much as 70% of ice cover variability in the Great Lakes can be explained by surface air temperature alone [45]. As such, the model will show significant sensitivity to the surface air temperature prescribed in the meteorological forcing.

Overall, the addition of an ice model to the existing operational hydrodynamic models can make significant improvements to forecast guidance and support stakeholder needs in navigation, hydropower, recreation, and spill response, as well as enables lake coupling with climate forecast models. As such, this work serves as the precursor to the upgrade of the Great Lakes Operational Forecast System (GLOFS) and to the first-ever operational ice forecast guidance in the Great Lakes within NOAA. As user requirements become better defined, additional skill assessment can guide avenues for model improvement and refinement.

Author Contributions: The paper was conceived of and written by E.A., A.F., and J.K. E.A., A.F., and J.K. carried out the model simulations and post-processing of results. The upgrade of GLOFS was conceived of and is being carried out by E.A., P.C., J.G.W.K., and G.L. The CICE model was adapted to the Great Lakes by A.F. and J.W. Model skill assessment was conceived of by J.G.W.K., Y.C., A.F., and E.A., and carried out by A.F. and J.K.

Funding: This research was carried out with support of the National Oceanic and Atmospheric Administration (NOAA) Great Lakes Environmental Research Laboratory (GLERL) and National Ocean Service (NOS), and the NOAA Research Acceleration Transition Program (RTAP).

Acknowledgments: The authors would like to acknowledge Changshen Chen from the University of Massachusetts Dartmouth for model support, as well as the United States Coast Guard (USCG) and representatives from the Great Lakes shipping community for support and engagement in defining user requirements. This is GLERL contribution number 1899.

Conflicts of Interest: The authors declare no conflicts of interest.

References

1. Assel, R.; Cronk, K.; Norton, D. Recent trends in Laurentian Great Lakes ice cover. *Clim. Chang.* **2003**, *57*, 185–204. [CrossRef]
2. Assel, R.A. *A Computerized Ice Concentration Data Base for the Great Lakes*; NOAA GLERL: Ann Arbor, MI, USA, 1983.

3. Wang, J.; Kessler, J.; Hang, F.; Hu, H.; Clites, A.; Chu, P. *Great Lakes Ice Climatology Update of Winters 2012–2017: Seasonal Cycle, Interannual Variability, Decadal Variability, and Trend for the Period*; NOAA GLERL: Ann Arbor, MI, USA, 2017; pp. 1–14.
4. Wang, J.; Bai, X.; Hu, H.; Clites, A.; Colton, M.; Lofgren, B. Temporal and spatial variability of Great Lakes ice cover, 1973–2010. *J. Clim.* **2012**, *25*, 1318–1329. [CrossRef]
5. Wang, J.; Hu, H.; Schwab, D.; Leshkevich, G.; Beletsky, D.; Hawley, N.; Clites, A. Development of the Great Lakes Ice-circulation Model (GLIM): Application to Lake Erie in 2003–2004. *J. Gt. Lakes Res.* **2010**, *36*, 425–436. [CrossRef]
6. Rondy, D.R. *Great Lakes Ice Cover, Great Lakes Basin Framework Study*; Appendix 4; Great Lakes Basin Commission: Ann Arbor, MI, USA, 1976.
7. Bolsenga, S.J. A Review of Great Lakes Ice Research. *J. Gt. Lakes Res.* **1992**, *18*, 169–189. [CrossRef]
8. Hawley, N.; Beletsky, D.; Wang, J. Ice thickness measurements in Lake Erie during the winter of 2010–2011. *J. Gt. Lakes Res.* **2018**, *44*, 388–397. [CrossRef]
9. Wright, D.M.; Posselt, D.J.; Steiner, A.L. Sensitivity of Lake-Effect Snowfall to Lake Ice Cover and Temperature in the Great Lakes Region. *Mon. Weather Rev.* **2013**, *141*, 670. [CrossRef]
10. Assel, R.A.; Quinn, F.H.; Sellinger, C.E. Hydroclimatic Factors of the Recent Record Drop in Laurentian Great Lakes Water Levels. *BAMS* **2004**, 1144–1148. [CrossRef]
11. Xiao, C.; Lofgren, B.M.; Wang, J. WRF-Based assessment of the Great Lakes' impact on cold season synoptic cyclones. *Atmos. Res.* **2018**, *214*, 189–203. [CrossRef]
12. Vanderploeg, H.A.; Bolsenga, S.J.; Fahnenstiel, G.L.; Liebeg, J.R.; Gradner, W. Plankton ecology in an ice covered bay of Lake Michigan: Utilization of a winter phytoplankton bloom by reproducing copepods. *Hydrobiologia* **1992**, *243–244*, 175–183. [CrossRef]
13. Martin Associates. *Lawrence Region Economic Impacts of Maritime Shipping in the Great Lakes-St.Lawrence Region*; US Department of Transportation: Washington, DC, USA, 2018 July.
14. Kelley, J.G.W.; Chen, Y.; Anderson, E.J.; Lang, G.A.; Xu, J. *Upgrade of NOS Lake Erie Operational Forecast System (LEOFS) to FVCOM: Model Development and Hindcast Skill Assessment*; NOS CS 40, NOAA; NOAA Technical Memorandum: Silver Spring, MD, USA, 2018.
15. Kelley, J.G.W.; Chu, P.; Zhang, A.; Lang, G.A.; Schwab, D.J. *Skill Assessment of NOS Lake Michigan Operational Forecast System (LMOFS)*; NOS CS 8, NOAA; NOAA Technical Memorandum: Silver Spring, MD, USA, 2007.
16. Kelley, J.G.W.; Zhang, A.; Chu, P.; Lang, G.A. *Skill Assessment of NOS Lake Huron Operational Forecast System (LHOFS)*; NOS CS 23, NOAA; NOAA Technical Memorandum: Silver Spring, MD, USA, 2010.
17. Mellor, G.L. Users Guide for Ocean Model. *Ocean Model.* **2004**, *8544*, 0710.
18. Schwab, D.J.; Bedford, K.W. Initial Implementation of the Great Lakes Forecasting System: A Real-Time System for Predicting Lake Circulation and Thermal Structure. *Water Qual. Res. J.* **1994**, *29*, 203–220. [CrossRef]
19. Chen, C.; Beardsley, R.C.; Cowles, G. An unstructured grid, finite volume coastal ocean model (FVCOM) system. *Oceanography* **2006**, *19*, 78–89. [CrossRef]
20. Hunke, E.C.; Lipscomb, W.H.; Turner, A.K.; Jeffery, N.; Elliott, S. *CICE: The Los Alamos Sea Ice Model Documentation and Software User's Manual LA-CC-06-012*; Los Alamos National Laboratory: Santa Fe, NM, USA, 2015; Volume 115.
21. Xue, P.; Pal, J.S.; Ye, X.; Lenters, J.D.; Huang, C.; Chu, P.Y. Improving the simulation of large lakes in regional climate modeling: Two-way lake-atmosphere coupling with a 3D hydrodynamic model of the great lakes. *J. Clim.* **2017**, *30*, 1605–1627. [CrossRef]
22. Anderson, E.J.; Schwab, D.J.; Lang, G.A. Real-Time Hydraulic and Hydrodynamic Model of the St. Clair River, Lake St. Clair, Detroit River System. *J. Hydraul. Eng.* **2010**, *136*, 507–518. [CrossRef]
23. Anderson, E.J.; Bechle, A.J.; Wu, C.H.; Schwab, D.J.; Mann, G.E.; Lombardy, K.A. Reconstruction of a meteotsunami in Lake Erie on 27 May 2012; Roles of atmospheric conditions on hydrodynamic response in enclosed basins. *J. Geophys. Res.* **2015**, *120*, 1–16. [CrossRef]
24. Anderson, E.J.; Schwab, D.J. Meteorological influence on summertime baroclinic exchange in the Straits of Mackinac. *J. Geophys. Res. Oceans* **2017**, *122*. [CrossRef]
25. Anderson, E.J.; Schwab, D.J. Predicting the oscillating bi-directional exchange flow in the Straits of Mackinac. *J. Gt. Lakes Res.* **2013**, *39*, 663–671. [CrossRef]

26. Bai, X.; Wang, J.; Schwab, D.J.; Yang, Y.; Luo, L.; Leshkevich, G.A.; Songzhi, L. Modeling 1993–2008 climatology of seasonal general circulation and thermal structure in the Great Lakes using FVCOM. *Ocean Mod.* **2013**, *64*, 40–63. [CrossRef]
27. Luo, L.; Wang, J.; Schwab, D.J.; Vanderploeg, H.A.; Leshkevich, G.A.; Bai, X.; Hu, H.; Wang, D. Simulating the 1998 spring bloom in Lake Michigan using a coupled physical-biological model. *J. Geophys. Res.* **2012**, *117*, 14. [CrossRef]
28. Smagorinsky, J. General Circulation Experiments with the Primitive Equations. *Mon. Weather Rev.* **1963**, *91*, 99–164. [CrossRef]
29. Mellor, G.L.; Yamada, T. Development of a turbulent closure model for geophysical fluid problems. *Rev. Geophys.* **1982**, *20*, 851–875. [CrossRef]
30. Large, W.G.; Pond, S. Open Ocean momentum flux measurements in moderate to strong winds. *J. Phys. Oceanogr.* **1981**, *11*, 324–336. [CrossRef]
31. Fairall, C.W.; Bradley, E.F.; Rogers, D.P.; Edson, J.B.; Young, G.S. Bulk parameterization of air-sea fluxes for Tropical Ocean-Global Atmosphere Coupled-Ocean Atmosohere Response Experiment. *J. Geophys. Res.* **1996**, *101*, 3747–3764. [CrossRef]
32. Fairall, C.W.; Bradley, E.F.; Godfrey, J.S.; Wick, G.A.; Edson, J.B.; Young, G.S. Cool-skin and warm-layer effects on sea surface temperature. *J. Geophys. Res.* **1996**, *101*, 1295–1308. [CrossRef]
33. Fairall, C.W.; Bradley, E.F.; Hare, J.E.; Grachev, A.A.; Edson, J.B. Bulk parameterization of air-sea fluxes: Updates and verification for the COARE algorithm. *J. Clim.* **2003**, *16*, 571–591. [CrossRef]
34. Liu, P.C.; Schwab, D.J. A comparison of methods for estimating u*, from given uz and air-sea temperature differences. *J. Geophys. Res.* **1987**, *92*, 6488–6494. [CrossRef]
35. Gao, G.; Chen, C.; Qi, J.; Beardsley, R.C. An unstructured-grid, finite-volume sea ice model: Development, validation, and application. *J. Geophys. Res. Oceans* **2011**, *116*, 1–15. [CrossRef]
36. Hunke, E.C.; Dukowicz, J.K. An Elastic–Viscous–Plastic Model for Sea Ice Dynamics. *J. Phys. Oceanogr.* **1997**, *27*, 1849–1867. [CrossRef]
37. Thorndike, A.S.; Rothrock, D.A.; Maykut, G.A.; Colony, R. The Thickness Distribution of Sea Ice. *J. Geophys. Res.* **1975**, *80*, 4501. [CrossRef]
38. Briegleb, B.; Bitz, C.; Hunke, E.; Lipscomb, W.; Schramm, J. *Description of the Community Climate System Model Version 2: Sea Ice Model*; UCAR: Boulder, CO, USA, 2002.
39. Proshutinsky, A.; Steele, M.; Zhang, J.; Holloway, G.; Steiner, N.; Häkkinen, S.; Holland, D.M.; Gerdes, R.; Koeberle, C.; Karcher, M.; et al. The Arctic Ocean Model Intercomparison Project (AOMIP). *EOS Trans. Am. Geophys. Union* **2001**, *82*, 637–644. [CrossRef]
40. Maykut, G.A.; McPhee, M.G. Solar Heating of the Arctic Mixed Layer. *J. Geophys. Res. Oceans* **1995**, *100*, 24691–24703. [CrossRef]
41. Schwab, D.J.; Leshkevich, G.A.; Muhr, G.C. Automated mapping of surface water temperature in the Great Lakes. *J. Gt. Lakes Res.* **1999**, *25*, 468–481. [CrossRef]
42. Beletsky, D.; Schwab, D.J.; Roebber, P.J.; McCormick, M.J.; Miller, G.S.; Saylor, J.H. Modeling wind-driven circulation during the March 1998 sediment resuspension event in Lake Michigan. *J. Geophys. Res. Oceans* **2003**, *108*. [CrossRef]
43. Benjamin, S.G.; Weygandt, S.S.; Brown, J.M.; Hu, M.; Alexander, C.R.; Smirnova, T.G.; Olson, J.B.; James, E.P.; Dowell, D.C.; Grell, G.A.; et al. A North American hourly assimilation and model forecast cycle: The rapid refresh. *Mon. Weather Rev.* **2016**, *144*, 1669–1694. [CrossRef]
44. U.S. National Ice Center: Naval Ice Center. Available online: www.natice.noaa.gov/products/great_lakes.html (accessed on 1 July 2018).
45. Titze, D. Characteristics, Influence, and Sensitivity of Ice Cover in the Great Lakes. Ph.D. Thesis, University of Minnesota, Minneapolis, MN, USA, November 2016.

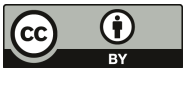

Journal of
Marine Science and Engineering

MDPI

Article

Hydrodynamic Zone of Influence Due to a Floating Structure in a Fjordal Estuary—Hood Canal Bridge Impact Assessment

Tarang Khangaonkar *, Adi Nugraha and Taiping Wang

Pacific Northwest National Laboratory, U.S. Department of Energy, Seattle, WA 98109, USA; adi.nugraha@pnnl.gov (A.N.); taiping.wang@pnnl.gov (T.W.)
* Correspondence: tarang.khangaonkar@pnnl.gov; Tel.: +1-206-528-3053

Received: 17 September 2018; Accepted: 10 October 2018; Published: 15 October 2018

Abstract: Floating structures such as barges and ships affect near-field hydrodynamics and create a zone of influence (ZOI). Extent of the ZOI is of particular interest due to potential obstruction to and impact on out-migrating juvenile fish. Here, we present an assessment of ZOI from Hood Canal (Floating) Bridge, located within the 110-km-long fjord-like Hood Canal sub-basin in the Salish Sea, Washington. A field data collection program allowed near-field validation of a three-dimensional hydrodynamic model of Hood Canal with the floating bridge section embedded. The results confirm that Hood Canal Bridge, with a draft of 4.6 m covering ~85% of the width of Hood Canal, obstructs the brackish outflow surface layer. This induces increased local mixing near the bridge, causes pooling of water (up-current) during ebb and flood, and results in shadow/sheltering of water (down-current). The change in ambient currents, salinity, and temperature is highest at the bridge location and reduces to background levels with distance from the bridge. The ZOI extends ~20 m below the surface and varies from 2–3 km for currents, from 2–4 km for salinity, and from 2–5 km for temperature before the deviations with the bridge drop to <10% relative to simulated background conditions without the bridge present.

Keywords: Hood Canal; floating bridge; Salish Sea; hydrodynamics; Finite-Volume Community Ocean Model (FVCOM); circulation; anthropogenic impact; zone of influence; Salish Sea model

1. Introduction

Hood Canal is a fjordal sub-basin within the Salish Sea region of Pacific Northwest. The Salish Sea is a collective name given to waterbodies that include the Strait of Juan de Fuca, Strait of Georgia, Puget Sound, and all their connecting channels and adjoining waters (see Figure 1). In the spring and summer, many Salish Sea sub-basins regularly experience algae blooms, and some of the sub-basins such as Hood Canal, East Sound, and regions of South Sound show signs of hypoxia [1]. Development of a comprehensive water-quality model of the Salish Sea was initiated in response to the above concerns about management of nutrient pollution and the assimilative capacity of the Salish Sea [2–4]. Of particular interest was the ability to simulate low dissolved oxygen (DO) events in the Salish Sea, including those responsible for fish kills and other chronic impacts in the Hood Canal region. Numerous studies were conducted in the past to determine what contributes to low DO events in Hood Canal, such as natural meteorological and oceanographic conditions, as well as anthropogenic causes, such as excessive nutrient loading [5,6].

The Hood Canal sub-basin includes a unique anthropogenic modification in that it hosts the Hood Canal Bridge (HCB), which is one of 11 floating bridges in use in the world. The geographic location of this 1992-m-long bridge, about 10 km from the mouth of Hood Canal, is indicated in Figure 1. Hood Canal is a 110-km-long narrow fjord-like sub-basin of Puget Sound with an average width of

2.4 km, a mean depth of 51.1 m, and a maximum depth of ~187 m, and it has a sill approximately 10–20 km from the mouth. The floating section of the bridge occupies ~85% of the width of Hood Canal, with a fixed opening at either end for small vessel traffic. The bridge has a design draft of 4.57 m. As part of the Salish Sea model development process, presence of the floating bridge was considered but not included in the model set-up under the assumption that effects of the bridge were likely a local phenomenon and unlikely to have a significant impact on the larger-scale Salish Sea model performance.

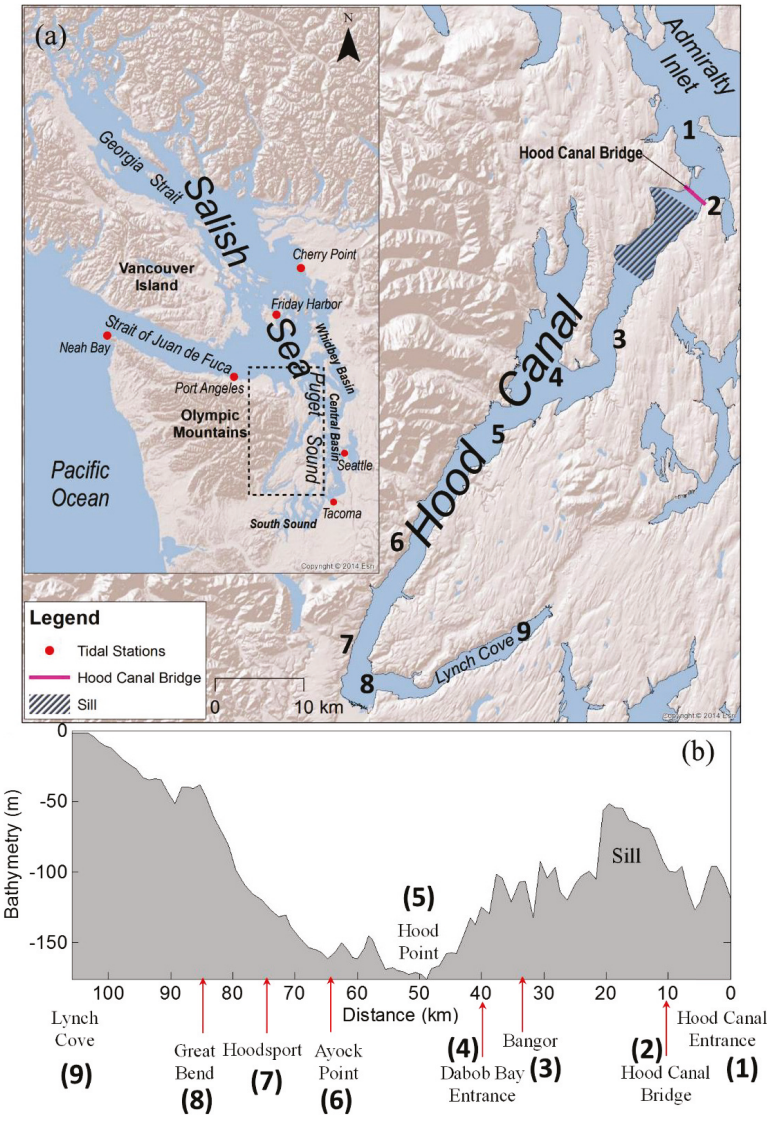

Figure 1. (**a**) Oceanographic regions of Salish Sea including Northwest Straits, Puget Sound, and the inner sub-basins—Hood Canal, Whidbey Basin, and South Sound; (**b**) bathymetric profile of Hood Canal study area.

However, recent research suggests that the bridge may, in fact, alter hydrodynamics and has the potential to increase flushing time in Hood Canal. Circulation here exhibits classic fjord characteristics of a shallow brackish layer at the surface over a deep long and narrow saltwater column that is vulnerable to disruptions due to the presence of floating structures, which could constrict the mixing and transport in the upper layers of the water column [7]. Recent studies also indicate that the bridge is a barrier to fish passage. Slower migration times, higher mortality rates in the vicinity of the bridge relative to other areas on their migration route, and unique behavior and mortality patterns at the bridge suggest the bridge is impeding steelhead migration and increasing predation [8].

In this paper, we present an assessment of the near-field impact of the floating bridge on the tidal hydrodynamics in the Hood Canal fjord environment as a component of the Hood Canal Bridge Environmental Impact Assessment study [9]. In particular, we focus on quantifying the spatial extent of the change in hydrodynamic parameters, such as currents, salinity, and temperature, in the vicinity of the bridge relative to ambient conditions. This near-field region of deviation from ambient background is the zone of influence (ZOI), defined arbitrarily as the distance from the bridge where relative difference induced by the structures reduces to <10% of the maximum deviation. This was accomplished through an application of the Salish Sea model [4] with the HCB embedded in high resolution. We present a summary of field data collected at the bridge, set-up and calibration of the Salish Sea model with a floating bridge module, and application of the model to the development of quantitative estimates of ZOI dimensions. These results inform companion studies addressing the impacts on the swimming behavior and observed mortality of out-migrating juvenile steelhead at HCB. Although this study discusses site-specific efforts, the results and the concern about potential ecological impacts are applicable to all floating bridges worldwide.

2. Materials and Methods

2.1. Oceanographic Data Collection

Oceanographic data collection was planned with two objectives: (1) field confirmation of the hypothesis that the HCB obstructs and alters near-field surface currents; (2) provide near-bridge data for the calibration of hydrodynamic models. Near field, for the purpose of this scope, is defined as the region where the influence of the bridge on current, salinity, and temperature variables is noticeable relative to the ambient (far field). Based on a prior modeling effort [7], the ZOI was expected to vary from as small as one to two bridge widths (18–36 m) normal to the direction of flow, to a much larger region covering several Hood Canal channel widths (2.4–7.2 km), for variables such as currents, temperature, and salinity.

In situ current and conductivity, temperature, and depth (hereafter CTD) measurements were collected over a four-week period, from late April to early June 2017, at three locations near HCB [10]. Figure 2 shows the locations of the stations (a) immediately below the floating bridge span, (b) approximately 500 m upstream (south) of the bridge, and (c) approximately 500 m downstream (north) of the bridge. The bridge-mounted current meter (a) was attached to the floating section of the bridge. Attachment of the acoustic Doppler current profiler (ADCP) to this platform provided a profile of the water currents directly below the bridge. In addition to the ADCP, the bridge-mounted system also included a single-point Aquadopp current meter attached approximately 1 m below the hull of the bridge to collect in situ current data as close to the structure as feasible. The upstream and downstream deployment locations were constrained by the fact that they needed to be bottom-mounted (outside of marine traffic in the surface waters) and away from HCB mooring lines. Also, the maximum water depth at the bridge central span was ~101 m and posed a challenge for the upward-looking ADCP instrument's ability to penetrate the surface layers. They were, therefore, deployed at a depth of approximately 50 m and as far from the shoreline as possible. Continuous CTD measurements were obtained from the bridge and bottom-mounted stations along with CTD casts during deployment and recovery.

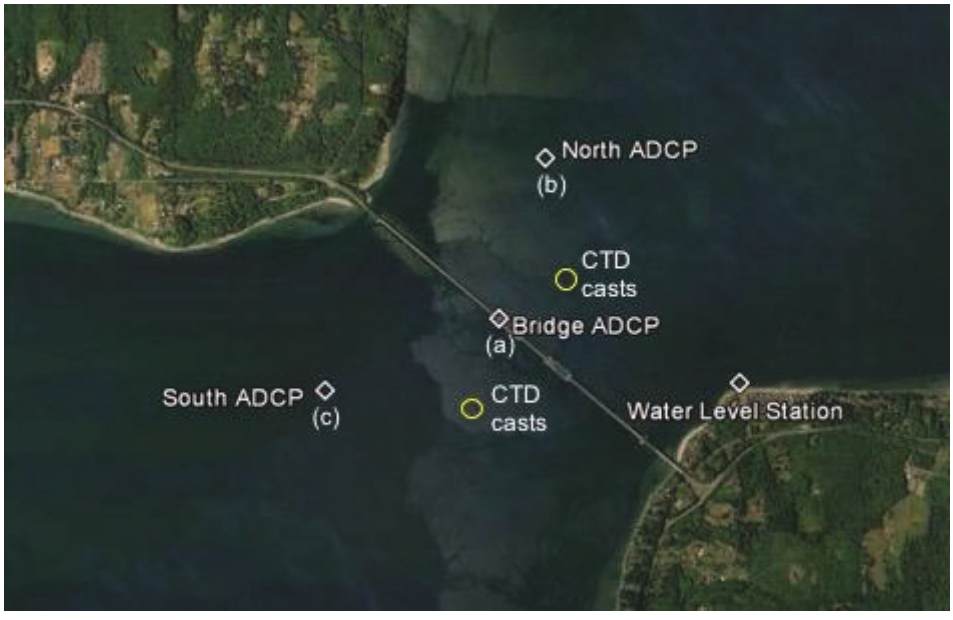

Figure 2. Hood Canal Bridge (HCB) study area showing the floating bridge and the 2017 oceanographic data collection program station locations relative to the bridge.

2.2. The Salish Sea Model Set-Up

The Salish Sea model is an externally coupled hydrodynamic and biogeochemical model developed by the Pacific Northwest National Laboratory in collaboration with Washington State Department of Ecology to support coastal estuarine research, restoration planning, water-quality management, and climate-change response assessments in the region [2–4] The model was constructed using the unstructured grid Finite-Volume Community Ocean Model (FVCOM) [11] version 2.7 framework and integrated-compartment model biogeochemical water-quality kinetics [12,13]. To facilitate enhanced exchange with the Pacific Ocean, the Salish Sea model grid was expanded to include coastal waters around Vancouver Island and the continental shelf from Canada's Queen Charlotte Strait to Oregon's Waldport, south of Yaquina Bay [14]. The model kinetics were also improved through the addition of sediment diagenesis and carbonate chemistry [15], and it is capable of reproducing the observed biogeochemical conditions of the Salish Sea (salinity (S), temperature (T), dissolved oxygen (DO), nitrate, algal biomass, and pH), including near-bed hypoxia in key locations such as the Lynch Cove region of Hood Canal, Penn Cove, and East Sound [4].

Figure 3a shows the Salish Sea model domain and grid with 16,012 nodes and 25,019 triangular elements. The vertical configuration of the model uses 10 sigma-stretched layers distributed using a power law function with an exponent P-Sigma of 1.5, which provides more layer density near the surface. The model was set up for the year 2017 covering the near-field data collection period of April through June. The model is loaded with daily values of freshwater inflow from a total of 23 major gauged rivers, 46 ungauged streams for which flows were estimated through hydrological analysis, and 100 wastewater flows [16]. The model is forced with wind and heat flux at the water surface. Meteorological inputs were obtained from Weather Forecasting Research Model reanalysis data generated by the University of Washington. Tidal forcing at the open boundary was based on tidal constituents (S2, M2, N2, K2, K1, P1, O1, Q1, M4, and M6) derived from the Eastern North Pacific or ENPAC model [17]. Temperature and salinity profiles at the boundary were extracted from World Ocean Atlas 2013 version 2 [18,19] climatological fields of in situ temperature and salinity at a 1° grid

interpolated to the model boundary nodes. Spin up for the hydrodynamic model was conducted through a one-year run initiated from stationary conditions (zero initial velocity and water surface elevation) with uniform T (7 °C) and S (32 practical salinity units (PSU)). The simulation was then repeated using year-end results as the restart initial condition.

As a preliminary step, Salish Sea model validation over the entire domain was first conducted to ensure that modification of the model grid and layering scheme (described in the following section) did not alter the overall model performance. This was done using year-long monitoring data available from a prior year (2014). The error statistics of water-surface elevation, S, and T were computed at nine tide stations and 24 water-quality stations maintained by Washington State Department of Ecology and shown in Figure 3b. Overall calibration results for T and S at all stations were found to be reasonable. Relative water-surface elevation errors were less than 10% at all stations within Puget Sound in United States (US) waters. Domain-wide T root-mean-square error (RMSE) was 0.94 °C with a bias of −0.03 °C. The domain-wide S error was 0.96 PSU with a bias of −0.24 PSU. Model skill scores were also high for T and S with Willmott skill score (WSS) [20] values of 0.96 and 0.80, respectively (see Table 1).

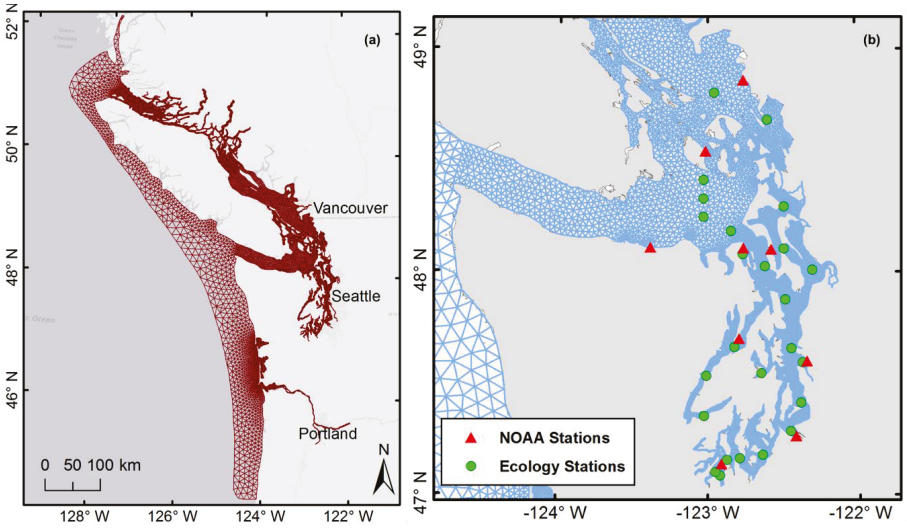

Figure 3. (**a**) Salish Sea model domain and finite-volume grid; (**b**) monthly water-quality monitoring stations from Washington State Department of Ecology.

Table 1. Salish Sea model overall error statistics and skill score for temperature and salinity calibration data for the year 2014 from monthly monitoring profiles.

	Mean Error (Bias)			RMSE			WSS		
	Max	**Min**	**Ave**	**Max**	**Min**	**Ave**	**Max**	**Min**	**Ave**
T (°C)	0.97	−1.77	**−0.03**	2.29	0.40	**0.94**	0.99	0.78	**0.94**
S (PSU)	0.09	−0.93	**−0.24**	2.27	0.39	**0.96**	0.90	0.60	**0.80**

RMSE = root-mean-square error; WSS = Willmott skill score; T = temperature; S = salinity; PSU = practical salinity unit; Max = maximum value of site-specific error statistic among 21 Puget Sound stations; Min = minimum value of site-specific error statistic among 21 Puget Sound stations; Ave = global error statistic considering data and model results from all stations.

2.3. Hood Canal Bridge Module Implementation

The FVCOM framework used in the Salish Sea model is a three-dimensional, free-surface, terrain-following solver for the primitive form of Navier–Stokes equations. The model uses

an unstructured grid in the horizontal dimension and sigma-stretched coordinate system in the vertical dimension. The floating bridge in this framework may be best approximated by a rectangular barge-like pontoon (see Figure 4 for HCB profile and cross-section details). However, representation of the rectilinear shape of the pontoons in this discretized framework requires special attention. While the width and the horizontal dimensions may be represented in a straightforward manner by suitable refinement and arrangement of the triangular elements, representing the uniform draft in a terrain-following sigma coordinate system poses a particular challenge. The dimensions of the bridge were specified as 1992 m long and 18.3 m wide, with a draft of 4.57 m. Figure 5 shows a close-up of the model grid refinement for the HCB region of the domain. The following three techniques were explored:

(a) *Implementation of a velocity block*: This approach is identical to that described by Khangaonkar and Wang (2013) [7] where the impermeable surface block was incorporated into FVCOM with modification of both external and internal modes of the solver. For the baroclinic internal mode, the horizontal velocities at the selected cells and surface layers were always specified as zero such that no horizontal flow was allowed to pass through. During the barotropic external mode calculations, the cross-sectional water column depth at selected cells occupied by the block was adjusted to a new reduced value by subtracting the blocked layer thickness from the total water depth. This modification accommodates the presence of the rigid structure but is an approximation, as non-hydrostatic components of the pressure term, which are likely to be strong in the near field, are neglected. Effects of the bridge on momentum terms are addressed, but are done so as an indirect effect of setting the surface boundary to zero velocity without affecting the pressure term.

(b) *Implementation of momentum sink at the bridge using form drag*: In this approach, the cells occupying the bridge are populated with hypothetical cylinders similar to a densely packed kelp farm. The drag from the cylinders set to sufficiently high value results in blockage of nearly ~95% of surface currents. Although this represents a leaking bridge, the implementation allows effects on continuity, as well as momentum, terms of the governing equations. The implementation of form drag from suspended cylinders in the water column was described by Wang et al. (2013) [21]. This method also requires local modification of the bathymetry to a representative average depth under the bridge for representation of the rectangular shape of the bridge pontoons.

(c) *Free surface pressure modification with a bottom drag*: This method relies on modification of the free surface pressure boundary condition; an increase in pressure equivalent of 4.57 m of head results in a model response of 4.57 m depression of the free surface. This method is an improvement over (a) and (b) in that bathymetry is unaltered. In addition to modifying the free surface, the method also employs drag formulation for the layer immediately under the bridge. This results in flow passing the bridge under modified pressure with suitable reduction in velocity induced by the form drag.

The efficacy of each method was tested by examination of predicted velocity, temperature, and salinity profiles relative to the data collected. Results showed that all methods provided similar performance in terms of near-field impacts to the flow field. For simplicity, the continuity/velocity block method (a) was retained for the remainder of the analysis.

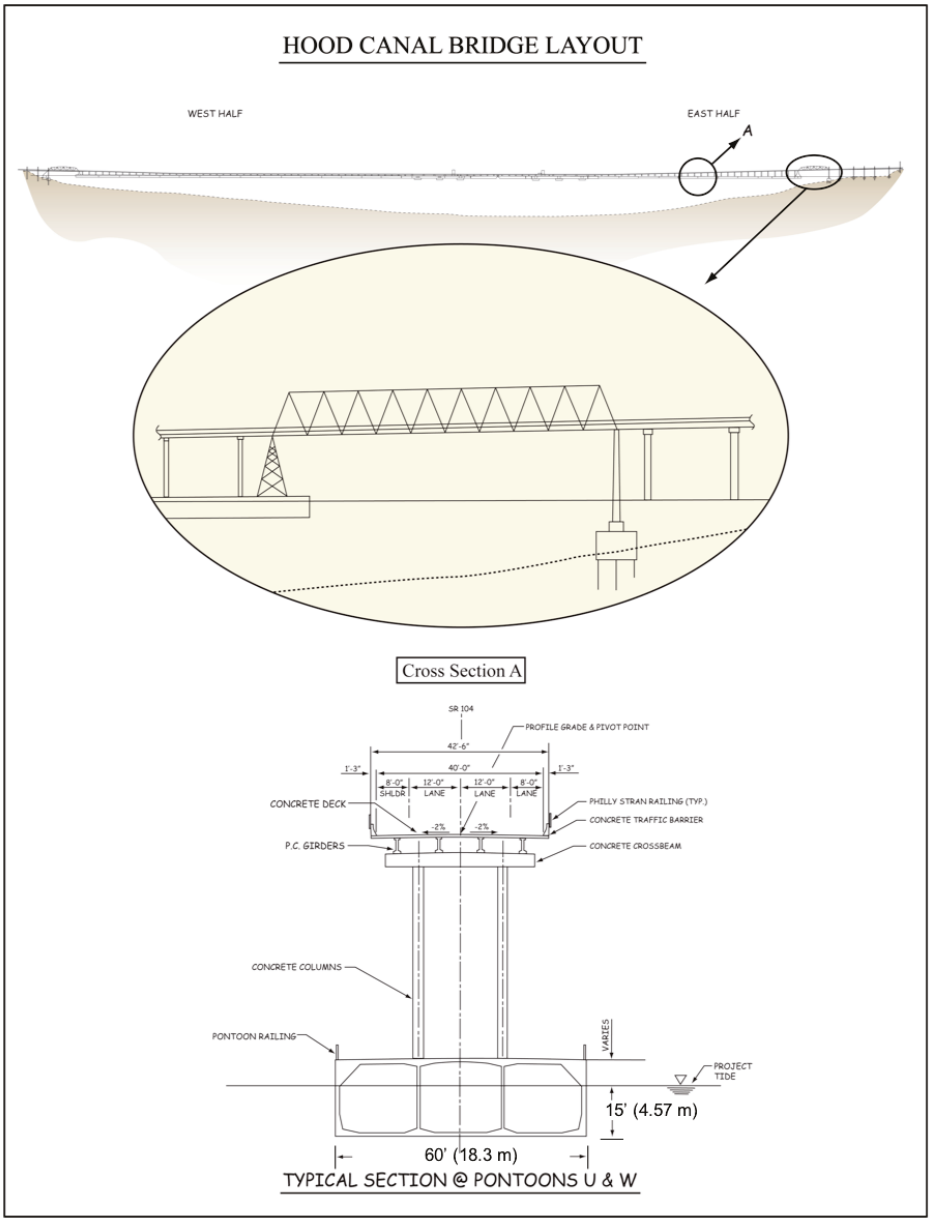

Figure 4. HCB layout with pontoon cross-section and east span details. Detail A is a sectional view across the width of the bridge.

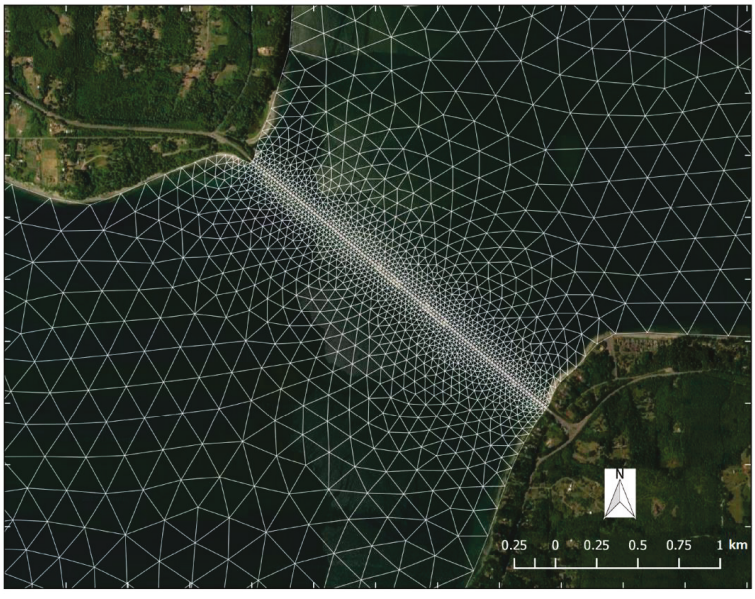

Figure 5. Salish Sea model grid with refinement in the region to facilitate incorporation of the bridge block elements. The grid size is refined such that cell centers are separated by the bridge width distance of 18.3 m. The bridge draft is represented by two layers whose combined thickness is equal to 4.57 m.

2.4. Near-Field Model Validation

The near-field model validation consisted of comparison of predicted water surface elevations, currents, salinity, and temperature results with data measurements during the 2017 field program.

Water surface elevations: Water surface elevation measurements were collected at a station located on the east bank of Hood Canal. Figure 6 shows a comparison of measured data and water surface level simulated by the model. Absolute mean error (AME) or bias at this station was 0.013 m, and RMSE was 0.42 m, which is an error of 8% relative to the tidal range of 5.34 m (Table 2).

Salinity and temperature: In addition to velocity profiles, North ADCP, Bridge ADCP, and South ADCP stations also provided salinity and temperature data. Temperature and salinity data were measured at a depth of 1 m below the bridge hull (5.57 m depth) at the Bridge ADCP station, while at the North ADCP and South ADCP stations, these data were collected at a depth of ~50 m near the seabed. Figure 7 shows the time-series comparison of observed data and simulated salinity and temperature at the three ADCP locations. The salinity variation at the three ADCP stations was successfully reproduced in the model simulations. Predicted temperature variations were also in good agreement with observed data.

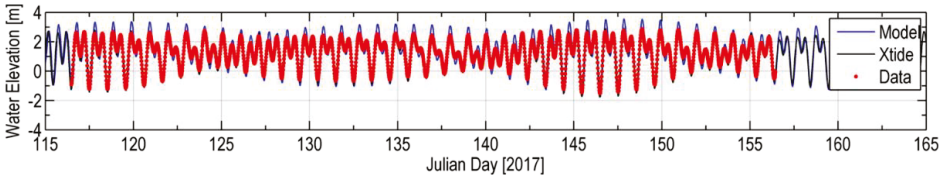

Figure 6. Time series of model result, NOAA harmonic (Xtide) prediction, and observed data for sea-water elevation. Time is shown as Julian days in 2017.

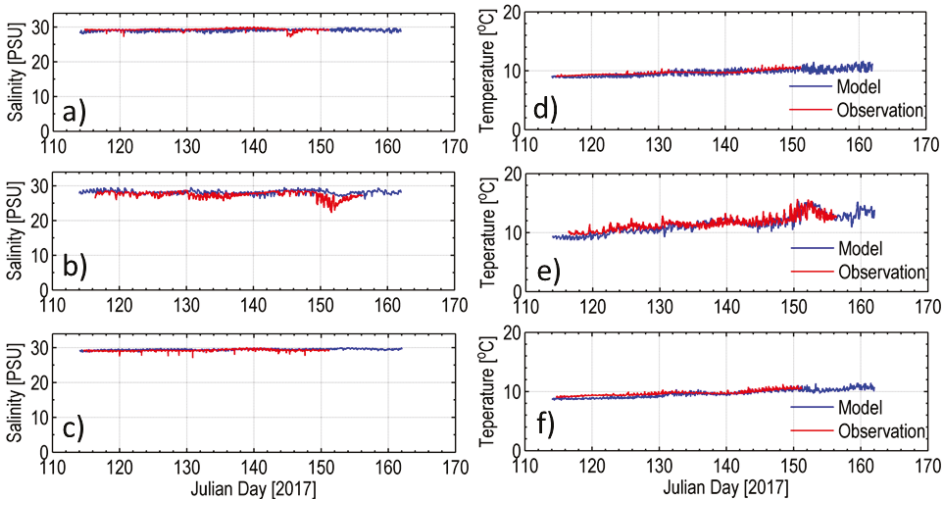

Figure 7. Time series of model results and observed data for salinity (left panel) and temperature (right panel) from 31 May and 1 June 2017. Plots (**a**,**d**) are a comparison for the North acoustic Doppler current profiler (ADCP) station; plots (**b**,**e**) are for the Bridge ADCP station; and plots (**c**,**f**) are for the South ADCP station.

Table 2. Salish Sea model calibration error statistics and skill score for water elevation. AME = absolute mean error.

	AME	RMSE	WSS
Elevation (m)	0.013	0.420	0.960

The error statistics (AME and RMSE) between model predictions and field observations are listed in Table 3. The AME and RMSE for salinity for most stations were less than 1 PSU except for the Bridge ADCP station. The model predicted higher salinity compared to observed data at Julian day 151 when the salinity dropped to 22 PSU. The temperature AME and RMSE were <1 °C for all stations, demonstrating a good match of model predictions with temperature data near the bridge.

Table 3. Salish Sea model validation error statistics and skill score for temperature and salinity at different locations near Hood Canal Bridge (HCB). ADCP = acoustic Doppler current profiler; CTD = conductivity, temperature, and depth.

Station	Temperature			Salinity		
	AME	RMSE	WSS	AME	RMSE	WSS
North ADCP	0.22	0.56	0.74	0.21	0.57	0.30
South ADCP	0.08	0.40	0.85	0.12	0.36	0.41
Bridge ADCP	0.41	0.79	0.90	0.82	1.29	0.47
North CTD	0.47	0.91	0.80	0.33	0.86	0.68
South CTD	0.50	0.80	0.90	0.65	1.03	0.72

A series of CTD casts were also conducted north and south of the bridge. These CTD casts were collected at peak ebb and peak flood, as well as during slack water conditions. The observed salinity and temperature profiles were then compared with simulated temperature and salinity at the same location and time. Figures 8 and 9 show examples of comparisons between observed and simulated salinity and temperature profiles at the north and south CTD cast locations, respectively.

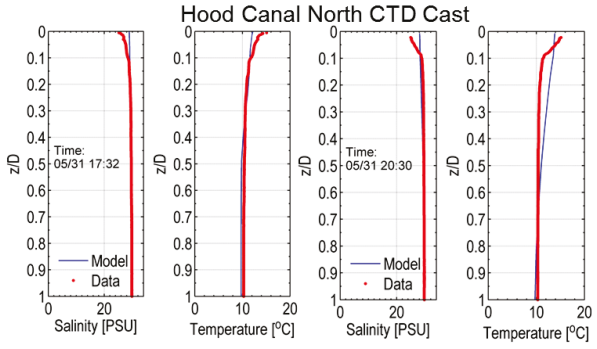

Figure 8. Comparisons of predicted and observed salinities at peak ebb and peak flood north of HCB on 31 May 2017.

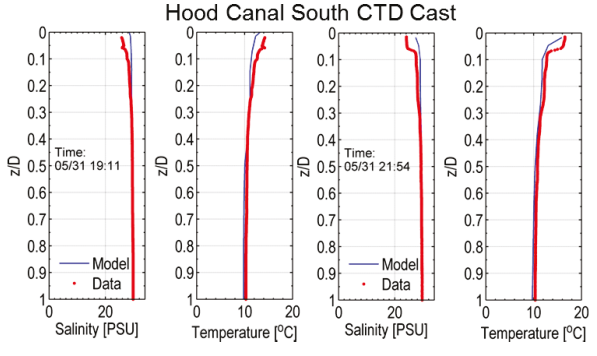

Figure 9. Comparisons of predicted and observed salinities at peak ebb and peak flood south of HCB on 31 May 2017.

The error statistics of temperature and salinity at the north and south CTD locations are also listed in Table 3. For temperature, both locations had AME ~0.5 °C with RMSE <0.8 °C. For salinity, AME and RMSE were 0.65 and 1.03 PSU, respectively. Although overall error statistics for the profiles were acceptable, examination of the results, especially for salinity, shows that the stratification in the upper 10% of the water column in the model is not as strong as in the data. This could be due to the limitation of the model confined to 10 sigma-layers. It could also be associated with near-field mixing induced by the bridge module as incorporated using the cell velocity block option. The results were similar for the three methods used for approximating the bridge block.

Currents: Current predictions at the North ADCP station, the South ADCP station, and the Bridge ADCP station were compared against field observations. The comparisons were selected at depths of 4 m, 9 m, 24 m, 39 m, 54 m, and 69 m. To better illustrate the comparison, velocities were decomposed into longitudinal and transversal components and are provided in Figure 10. The predicted phase of the velocity and the velocity magnitude associated with flooding and ebbing are in good agreement with the field observations. Figure 10 shows a comparison of predicted and observed velocities for different depths at the Bridge ADCP Station. At a depth of 9 m, the ADCP data bin nearest to the surface, the effect of HCB is reflected in both predicted and observed velocities.

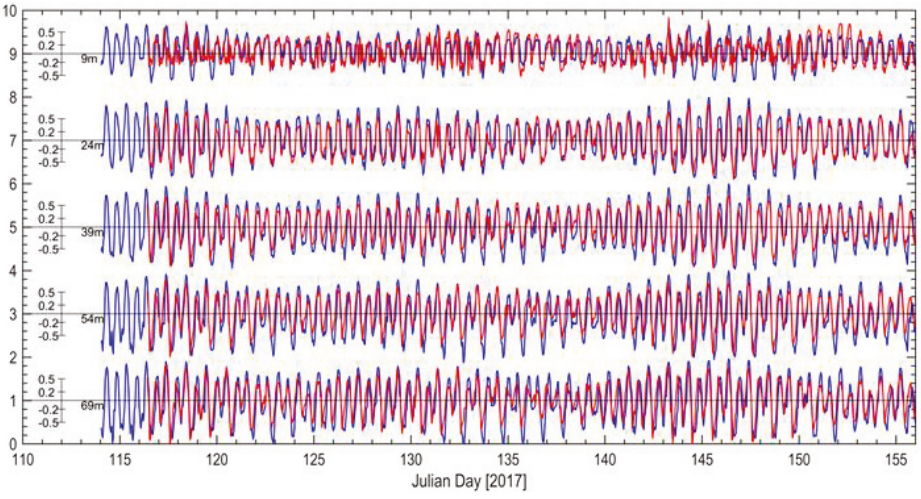

Figure 10. Comparisons of predicted (blue) and observed (red) velocities for different depths at the Bridge ADCP station (example).

In addition to ADCP measurements, in an attempt to get as close to the bridge, pontoon, and hull as possible, a single-point measurement was conducted using an Aquadopp instrument, located 1 m below HCB. Figure 11 shows a comparison between predicted currents and observed data. The model appears to be overestimating the velocity during peak ebb. This region immediately below the bridge is known to generate eddies and shed vortices as the ebbing water is forced under the bridge. The model is unable to resolve these fine-scale eddies, which is one explanation for the error. Due to the fact that the model currently does not include skin friction at the bridge, the slip velocity in the model immediately below the bridge is, therefore, higher than the data.

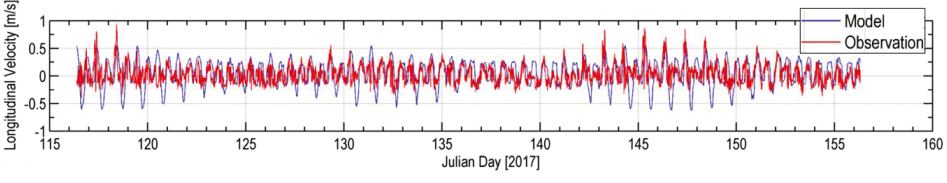

Figure 11. Comparisons of predicted and observed velocities just below HCB.

The corresponding error statistics for current comparisons are summarized in Table 4. All stations had AME <0.03 m/s. The RMSE for all stations was <0.21 m/s, except for the Aquadopp single-point measurement, where a higher RMSE of 0.33 m/s was noted. It is noted that these errors are of magnitude comparable to the sustained swimming velocity of a 120-mm Juvenile Coho Salmon (~0.64 m/s) and the maximum swimming velocity for a 60–63-mm Juvenile Chum Salmon (~0.14 m/s) [22,23]. The WSS for the Aquadropp station was low (0.36) compared to other stations due to the complexity of the measurement. However, the WSS for the North ADCP, the South ADCP, and the Bridge ADCP was >0.89, suggesting that the model calibration results were of sufficient quality for use in ZOI calculations.

Table 4. Salish Sea model calibration error statistics and skill score for velocities.

Station	AME	RMSE	WSS
North ADCP	0.00	0.14	0.94
South ADCP	0.02	0.21	0.89
Bridge ADCP	0.03	0.21	0.92
Aquadopp	0.02	0.33	0.36

To assess the effect of HCB on near-field currents, we examined the data during peak ebb and flood periods for every tidal cycle at the North, South, and Bridge ADCP stations. The expectation was that the effect of the bridge on currents would be at a maximum during peak currents. Figure 12a shows the time series of depth-averaged longitudinal velocity at the bridge. Red triangles and yellow triangles indicate selected peak ebb and flood times, respectively, at which velocity information was extracted in each tidal cycle. The averages of predicted peak velocity profiles during flood and ebb are shown in Figure 12b–g along with measured data.

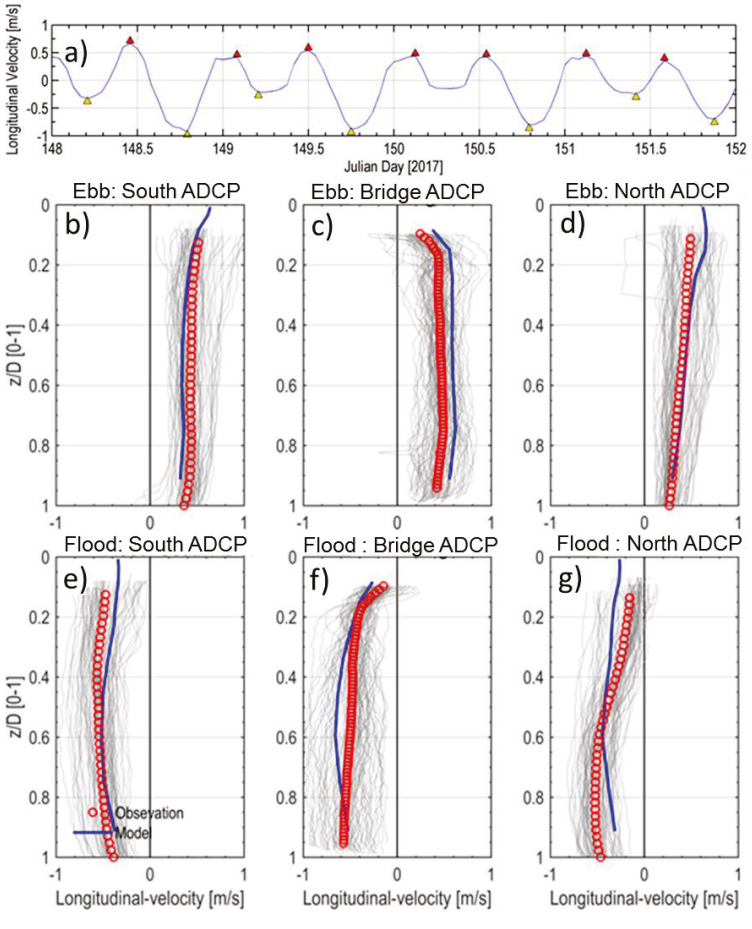

Figure 12. (**a**) Time series of depth-averaged velocity at bridge; (**b**–**g**) comparisons of predicted and observed average velocity profiles at the South, Bridge, and North ADCP stations during maximum flood and ebb tide periods. Gray thin lines represent daily velocity profiles during peak ebb and flood periods.

Positive velocity represents ebb or outflowing current direction due north toward the mouth of Hood Canal. Negative velocity indicates flood tidal currents due south in the opposite direction. Figure 12b–g show that the model is able to match the peak observed average velocity well at all stations during ebb and flood. The velocity reduction due to HCB is reproduced well by the model, as shown in Figure 12c,f. This confirms that the implementation of the bridge module in the Salish Sea model is successful in reproducing the reduction in velocity near the bridge. Small discrepancies were found at all stations that were attributed to approximations associated with smoothing of bathymetry and grid resolution. Similarly, representation of HCB in a sigma-coordinate framework required flattening of the depths immediately below the bridge, resulting in slightly higher velocities in the water column.

3. Results

3.1. Zone of Impact—Surface Layer

To characterize the bridge influence on the near-field environment, two sensitivity test scenario runs were performed. In test 1, the bridge block (1992 m long, 18.3 m wide, and 4.57 m deep) was completely removed, representing the conditions without the bridge. In test 2, the central (movable) span of the bridge with a length of 182 m was left in the open position with the bridge pontoons present in place. The central span is typically opened to allow ship and boat traffic to pass providing a third opening for tidal transport, with the two permanent openings present at the east and west ends of the bridge. To characterize the ZOI, baseline conditions from the summer of 2017 with the bridge in place were compared with the simulated results from the sensitivity tests (1) without the bridge and (2) with the central span open. Comparisons were conducted for predicted currents, salinity, and temperature, and ZOI estimates were obtained through quantifying the difference relative to existing or baseline conditions.

Figure 13 shows contour and velocity vector plots of existing conditions with HCB during ebb and flood. Peak ebb and flood times were selected during a typical spring tide on 27 April 2017, at 10:00 a.m. and 6:00 p.m., respectively, for this examination based on the expectation that maximum impact of the bridge block, reducing the currents to zero, would be strongest during the spring tides and during ebb and flood times. Figure 13a,b are currents with HCB present during the ebb and flood, respectively, for the surface layer. The surface layer occupies the upper 3% of the water column. The ebb currents in the surface layers are stronger than those during the flood. The effect of the HCB structure on currents is noticeable at the bridge where velocity was set to 0 m/s and a shadow of reduced currents exists immediately behind during both ebb and flood.

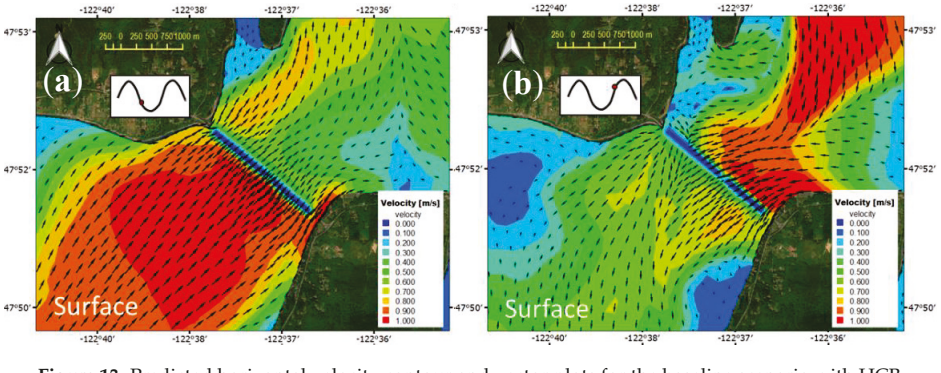

Figure 13. Predicted horizontal velocity contour and vector plots for the baseline scenario with HCB present for (**a**) ebb and (**b**) flood currents in the surface layer. (Typical spring tide on 27 April 2017).

Figure 14 shows the same simulation but without the bridge with a much larger region occupied by currents in the >1 m/s bands.

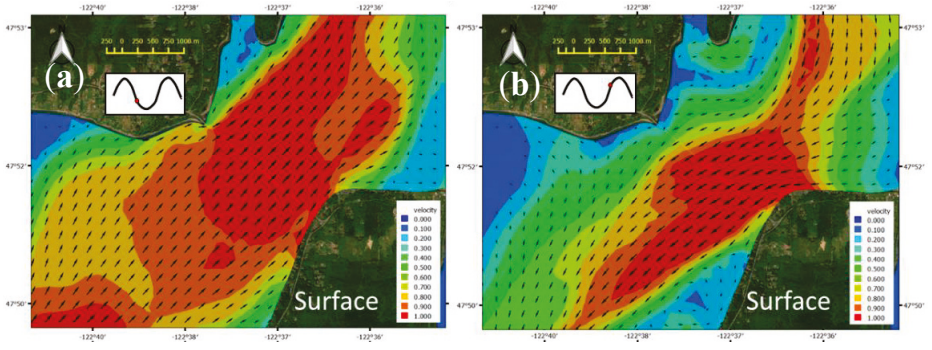

Figure 14. Predicted horizontal velocity contour and vector plots for test 1 scenario without HCB present for (**a**) ebb and (**b**) flood currents in the surface layer. (Typical spring tide on 27 April 2017).

Figure 15 shows surface layer currents with the central span open. The current patterns are similar to those at baseline conditions shown in Figure 13. Relative to the size (length) of the bridge blocking the surface layer, the central span represents an opening of ~9%. The effect of the opening on the currents is most visible in the form of the jet behind the bridge during both ebb and flood.

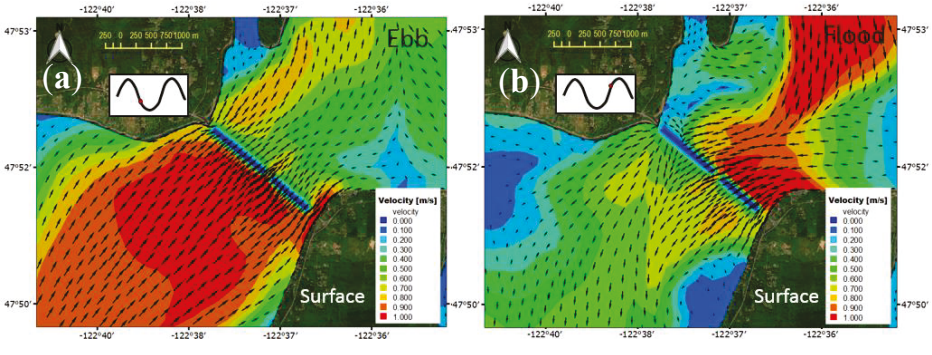

Figure 15. Predicted horizontal velocity contour and vector plots for test 2 scenario with HCB present and middle span open for (**a**) ebb and (**b**) flood currents in the surface layer. (Typical spring tide on 27 April 2017).

The ZOI is best characterized using plots of difference between simulated results from the baseline condition (with the bridge) relative to tests 1 and 2 to provide a direct assessment of the bridge impact. Figure 16a,b show a difference (reduction) in currents during peak ebb and flood with the bridge relative to test 1 without the bridge. Figure 16c,d show a reduction in currents during peak ebb and flood relative to the condition with the bridge draw span open. The effect of the bridge on surface currents is noticeable over a distance of ~1–2 Hood Canal widths in either direction (~2–5 km). Effect of the bridge span opening on currents is limited (~0.25 Hood Canal width, <600 m), but prominent during the ebb tide with stronger surface currents.

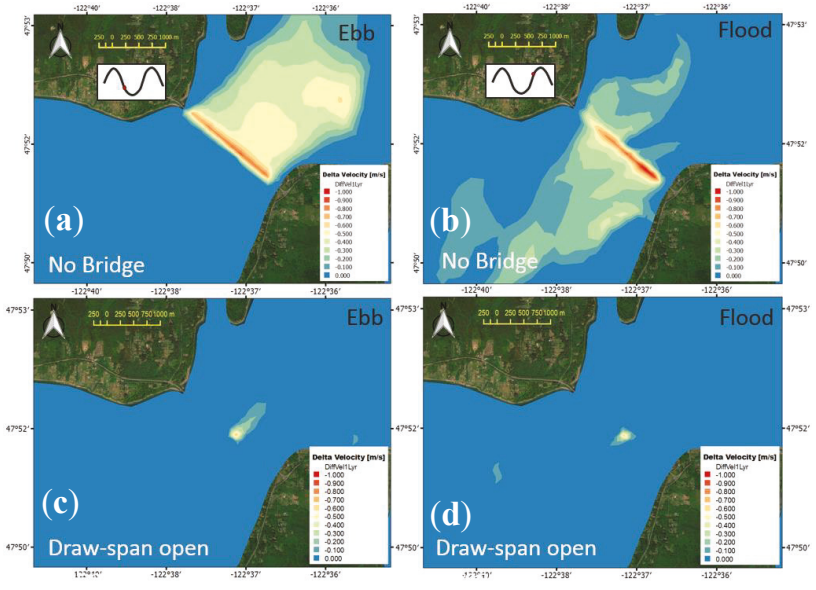

Figure 16. (**a**,**b**) Velocity difference of baseline scenario with HCB relative to test 1 without HCB during peak ebb and flood; (**c**,**d**) velocity difference of baseline scenario with HCB relative to test 2 with draw span open during ebb and flood. (Typical spring tide on 27 April 2017).

These difference plots in the plan view provide a qualitative estimate of the size of the ZOI for currents in the surface layer. The spatial pattern and extents were similar in nature with the influence of HCB most prominently seen behind the bridge during peak ebb and flood conditions. In all cases, the maximum difference of the baseline condition relative to the scenarios was at the bridge itself. In the surface layer, the maximum current difference was −0.88 m/s, the maximum salinity difference was +0.23 PSU, and the maximum temperature difference was −0.49 °C for the selected spring tide on 27 April 2017. The effect of the bridge dissipates with distance from the structure. Unlike velocity, where the effect is directly the result of blocked currents, the influence on salinity and temperature is more complex due to the presence of strong stratification and the increased mixing of surface layers at the bridge. Vertical transects analyzed in the next section provide a better understanding of the influence of the bridge on salinity and temperature.

3.2. Zone of Impact—Vertical Transect

To further quantify the spatial extent of ZOI on current, salinity, and temperature variables in this environment with strong vertical stratification, simulation results were examined along a mid-channel transect across HCB. The assessment was done using two transects: (a) Transect-a, approximately 2.5 km long (length scale of Hood Canal width) across the bridge to provide a detailed characterization of near-field effects; and (b) Transect-b approximately 20 km long (distance from the bridge to the mouth of Hood Canal) to allow examination over larger distances over full tidal excursion (see Figure 17). The results were analyzed as difference plots similar to the plan view maps in the previous section, during the selected typical spring tide of 27 April 2017, at peak ebb (147.42 Julian days (JD), 27 May 2017 10:00 a.m.) and peak flood times (147.75 JD, 27 May 2017 6:00 p.m.).

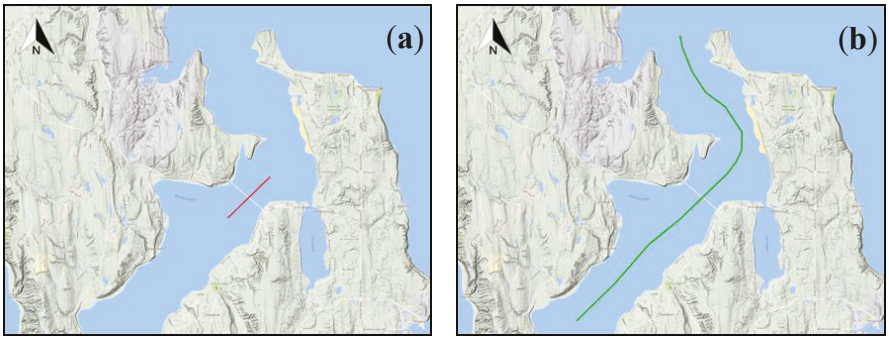

Figure 17. Transects for assessment of zone of influence (ZOI) in a vertical plane: (**a**) short transect for near-field effects; (**b**) longer transect to examine the effects over full tidal excursion.

The near-field effects of HCB on the current, salinity, and temperature in a vertical two-dimensional plane near the ZOI for the example spring tide period are shown in Figures 18–20, respectively, using the shorter Transect-a. The distance between −1.25 km and 0 km represents the section south of the bridge, while that between 0 km and 1.25 km represents the downstream section north of the bridge. As in the surface plan view maps, a reduction in current magnitudes behind the bridge is seen during the flood and ebb. Figure 18a,b show that the currents are reduced behind the bridge relative to the scenario without the bridge. The vertical transect shows that the effect extends beyond the 1.25-km transect length on either side of the bridge and the effect is noticeable mostly in the upper ~10–15 m of the water column. Figure 18c,d show a similar relative difference in currents relative to the scenario with bridge draw span open. The effect is minor with a change of up to 0.3 m/s seen at the draw span opening, extending <500 m from the bridge.

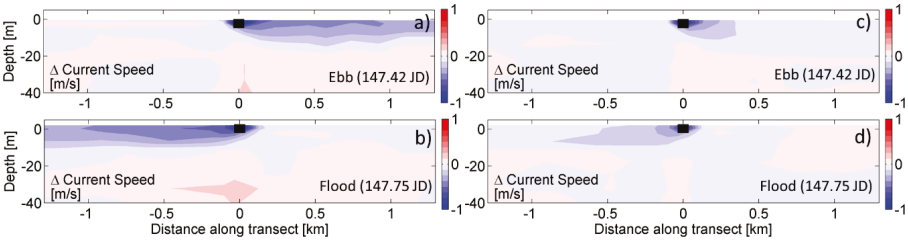

Figure 18. (**a**,**b**) Velocity difference of baseline scenario with HCB relative to test 1 without HCB during peak ebb and flood; (**c**,**d**) velocity difference of baseline scenario with HCB relative to test 2 with draw span open during ebb and flood. (Typical spring tide on 27 April 2017).

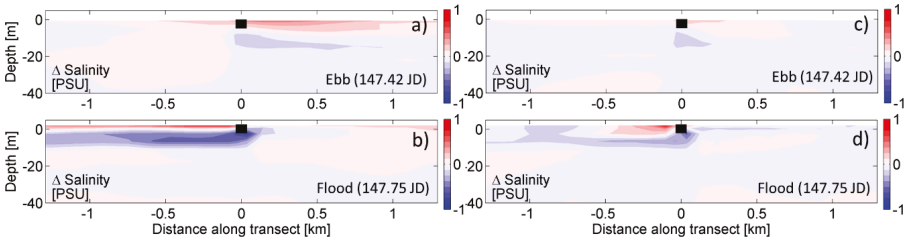

Figure 19. (**a**,**b**) Salinity difference of baseline scenario with HCB relative to test 1 without HCB during peak ebb and flood; (**c**,**d**) velocity difference of baseline scenario with HCB relative to test 2 with draw span open during ebb and flood. (Typical spring tide on 27 April 2017).

Figure 19a,b show the effects of HCB on salinity through difference plots relative to test 1 without the bridge, during ebb and flood, respectively. The surface layer salinity immediately behind the bridge was higher. This was due to the blocking effect of the bridge holding the fresher (lower salinity) water back during flood and ebb. The traversing surface layer was forced to flow under the bridge, resulting in reduced salinity in the deeper layers below the bridge. A similar effect is seen relative to test 2 with the draw span open. Figure 19c,d show a small increase in surface salinity behind the bridge relative to the scenario with the draw span open. Plan view plots are consistent with velocity difference plots in that the effect of test 2 was restricted to a small region near the span opening. Salinity was lower in the layers immediately below the bridge due to fresher water being forced to lower layers by the presence of the bridge relative to the condition with draw span open.

The effect of HCB on temperature is similar to that predicted on salinity. Thermal stratification surface heat flux results in water temperatures in the surface layers being warmer than lower layers. The presence of the bridge holds the surface layers back, resulting in cooler waters immediately behind it relative to test 1 without the bridge during ebb and flood, as shown in Figure 20a,b. The warmer water was forced to traverse underneath the bridge, resulting in warmer waters in the deeper layers behind the bridge. Figure 20c,d show a similar effect but on a smaller scale with a small increase in surface temperature behind the bridge relative to the scenario with the draw span open. Temperatures were higher in the layers immediately below the bridge due to warmer water being forced to lower layers by the presence of the bridge relative to the condition with draw span open.

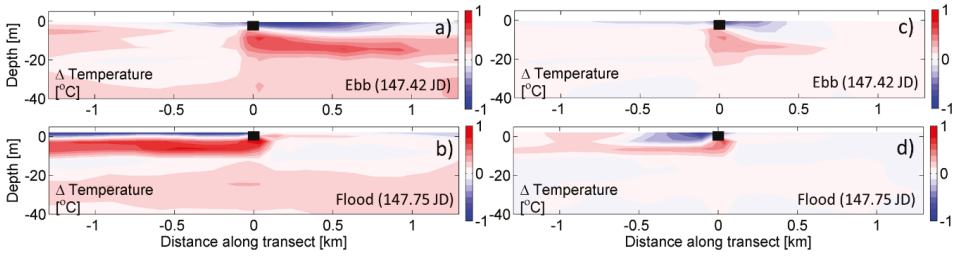

Figure 20. (**a**,**b**) Temperature difference of baseline scenario with HCB relative to test 1 without HCB during peak ebb and flood; (**c**,**d**) velocity difference of baseline scenario with HCB relative to test 2 with draw span open during ebb and flood. (Typical spring tide on 27 April 2017).

4. Discussion

Zone of Influence—Quantitative Assessment

The ZOI extends beyond the Hood Canal width scale of 2.4 km based on the results presented in Section 3. However, to quantify spatial extent, environmentally significant influence must first be defined. Maximum difference induced by HCB relative to test 1 on currents without the bridge occurred at the bridge itself and decayed or dissipated with distance from the bridge. For the purpose of this assessment, we defined ZOI as the distance at which the maximum difference (Δ) dropped to 10% of its value for current and salinity parameters (e.g., if maximum Δ = 1 m/s, then ZOI is where Δ = 0.1 m/s).

We first assessed the horizontal extent of ZOI by examining the changes in surface currents induced by the bridge relative to test 1. With a focus on impacts during peak tidal currents, we averaged multiple (71) peak ebb and peak flood instances over the calibration simulation period (25 April–11 June 2017). We then examined the vertical longitudinal extent of the ZOI by examining the relative difference of the variables for all depth layers along Transect-b over a distance of 20 km. Figure 21 shows the average difference in peak currents due to the presence of HCB relative to test 1 for the 10 model layers. The distance between −10 km and 0 km represents the region south of the bridge, while that between 0 km and 10 km represents the region north of the bridge. Model layers were distributed

using a power law with an exponent of 1.5 such that layers had a higher concentration near the surface. Surface layer 1 occupied 3% of the water column and the bottom layer 10 occupied 15% of the water column. For currents, based on averaging multiple peak ebb and peak flood instances, maximum difference (−0.70 m/s) occurred during the ebb and in the surface layer, extending ~2.02 km north before dropping to −0.07 m/s (10% of the maximum difference). The maximum difference during the flood (−0.57 m/s) also occurred in the surface layer and the influence extended up to 3.43 km. It is interesting to note that, while there was a reduction in surface currents, the model generated a compensating increase in bottom-layer currents during flood, as well as ebb. The zone of influence, therefore, extends over the entire water column. It is important to note that this ZOI for currents is based on average impacts during peak currents. The ZOI spatial extent is smaller at all other times with smaller-magnitude currents.

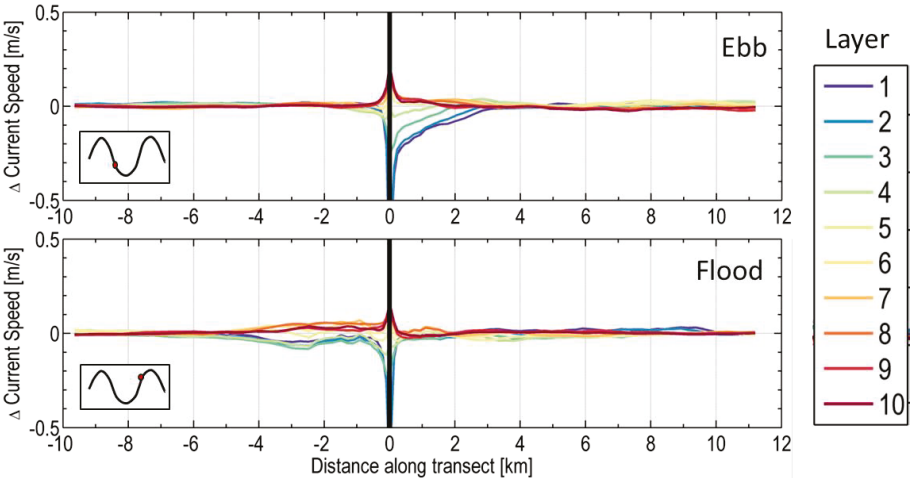

Figure 21. Difference in current magnitudes due to HCB relative to test 1, plotted along Transect-b for all model layers. The (**top**) panel presents peak ebb and the (**bottom**) panel presents peak flood results averaged over the calibration period of 25 April–11 June 2017. (The distance between −10 km and 0 km represents the region south of the bridge, while that between 0 km and 10 km represents the region north of the bridge).

Further examination of the results showed that, unlike velocity, peak instantaneous difference between baseline with bridge and test 1 without the bridge for temperature and salinity did not always occur at the bridge and occurred at various times in the tidal cycle. Peak instantaneous differences that vary in space and time make it difficult to define the ZOI. The approach for temperature and salinity was, therefore, to develop an average ZOI, taking into consideration all time steps.

Figure 22 shows the difference in salinity due to the presence of HCB relative to test 1 computed by averaging the differences over all hourly time steps for each layer. The average salinity difference results show a consistent pattern north and south of the bridge. The peak influence in average salinity occurred at the bridge, and, as described in Section 3, it was controlled by the mixing induced by the structure during ebb and flood. This resulted in an increase in salinity in the upper layers above the bridge draft depth (0–4.57 m) and a corresponding reduction in salinity in the lower layers below the draft from 4.57 m to ~20 m. The near-bed layers were unaffected. Also noticeable is the extent of the effect north of the bridge in the surface where the surface layers show elevated salinity levels ~+0.1 PSU that extend all the way to the mouth of Hood Canal. The effects of bridge-induced mixing resulted in higher salinity concentrations in the surface layers that were transported north in the surface outflow direction. This resulted in persistent and elevated levels of background salinity difference north of the

bridge of 0.06 PSU over 4–10 km. The maximum difference (Δ) in salinity at the bridge was +0.42 PSU that extended 1.96 km to the south before dropping to 10% (0.04 PSU). ZOI determination to the north was complex as background salinity increased past the salinity 10% Δ level. The ZOI to the north was, therefore, provided as a range from 3.80 km where salinity Δ dropped to 10% above the background level of 0.1 PSU to Hood Canal mouth at ~10 km.

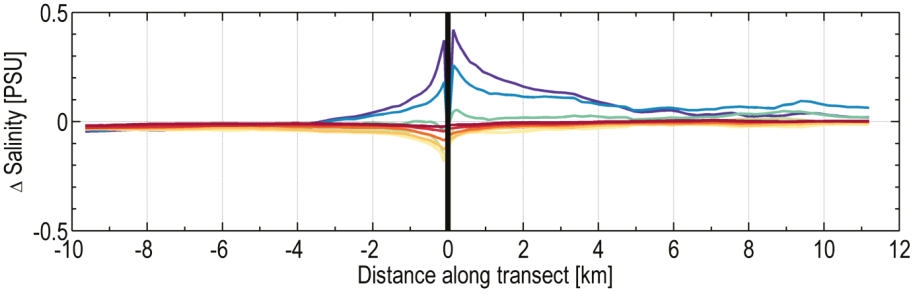

Figure 22. Difference in salinity due to HCB relative to test 1, plotted along Transect-b for all model layers. The plot shows average salinity difference for all hourly time steps over the calibration period of 25 April–11 June 2017. (The distance between −10 km and 0 km represents the region south of the bridge, while that between 0 km and 10 km represents the region north of the bridge).

Figure 23 shows the difference in temperature due to the presence of the bridge relative to test 1 for the 10 model layers. The effect of HCB on temperature, based on averaging the difference for all hourly time steps over the period of 25 April–11 June 2017, was similar to that for salinity. The influence of the bridge on near-field temperature, due to the mixing induced by the bridge, resulted in a decrease in upper layer temperatures and an increase in temperature in lower layers below the draft from 4.57 m to ~20 m. The near-bed layers were unaffected. The effect of the bridge on temperature is noticeable in the downstream region north of the bridge where the surface layers showed a reduction in temperature levels that extended all the way to the mouth of Hood Canal. The maximum average difference (−0.49 °C) in the surface layers, a reduction in surface temperatures, dissipated to 10% ΔT (0.05 °C) ~2.23 km to the south. However, as in the case of salinity, temperature ZOI determination to the north was complex as there was a decrease in background temperature difference of 0.11 °C, over 4–10 km, that exceeded the temperature 10% ΔT level. The ZOI to the north was, therefore, provided as a range from 4.51 km where temperature ΔT dropped to 0.16 °C, 10% Δ above the background level, to Hood Canal mouth at ~10 km. It is noted, however, that the bridge caused an increase in temperatures in the lower layers of up to 0.20 °C.

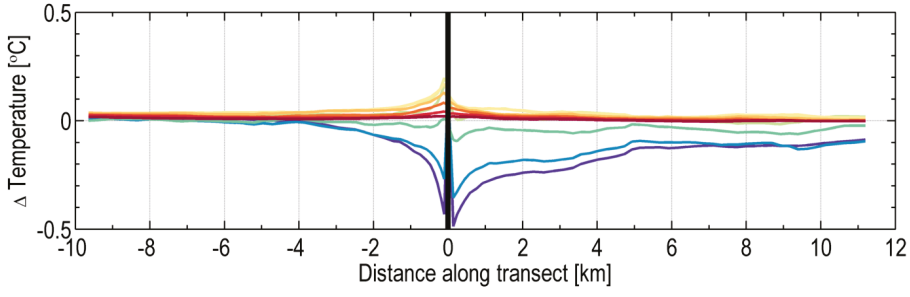

Figure 23. Difference in temperature due to HCB relative to test 1, plotted along Transect-b for all model layers. The plot shows average temperature difference for all hourly time steps over the calibration period of 25 April–11 June 2017. (The distance between −10 km and 0 km represents the region south of the bridge, while that between 0 km and 10 km represents the region north of the bridge).

Table 5 summarizes the ZOI dimensions for the parameters of interest examined using the criterion of a reduction in maximum difference Δ to 10% of its value.

Table 5. Summary of zone of influence (ZOI) characterizing distances over which the difference in predicted maximum difference Δ due to the presence of the bridge relative to the test 1 scenario without the bridge was reduced to 10% of its value. Results in this table are based on an average of all peak ebb and flood instances over the period of 25 April–11 June 2017 for velocity, and an average of all time steps for salinity and temperature.

Variable	Max. (Δ)	South HCB	North HCB
		ZOI (km)	ZOI (km)
Velocity (m/s)	−0.70	2.02	3.43
Salinity (PSU)	0.42	1.96	3.80–10
Temperature (°C)	−0.49	2.23	4.51–10

Although the ZOI calculations and the values presented in Table 5 above used average values of maximum differences, it is noted that instantaneous differences could be as high as 1.22 m/s, 1.66 PSU, and 2.16 °C for velocity, salinity, and temperature, respectively.

5. Conclusions

A combination of oceanographic field data measurements and modeling-based assessment were used to ascertain whether the presence of HCB impacts near-field oceanographic parameters. While some effect was expected simply due to the existence of a large floating object in the path of the tidally influenced fjord-like waterbody of Hood Canal, the extent of influence was not quantified in the past. The results were conclusive in that both field data and model results showed that HCB blocks the movement of surface layer currents over ~85% of the width of Hood Canal. The openings at each end of the bridge (15% of the Hood Canal width) do carry a portion of the tidal flow; however, these openings are in shallow depths and do not fully compensate for the surface layer blockage. As a result, the current profile structure in the water column is altered. The reduction in surface layer currents and tidal flow is compensated by a corresponding increase in bottom-layer currents and flow. The impact is also felt in salinity and temperature magnitudes, particularly in the upper 20 m of the water column.

The ZOI was defined as the distances over which the difference in predicted maximum difference due to the presence of the bridge relative to the conditions without the bridge was reduced to 10% of its value. Based on the simulation conducted using 2017 spring conditions, the ZOI for current extends 3.43 km to the north and 2.02 km to the south of HCB. Maximum current difference based on the average of peak currents was −0.70 m/s at the surface layer. Similarly, the ZOI for salinity extends 3.80 km to the north and 1.96 km to the south, over which salinity deviated from the condition without the bridge. Maximum salinity difference was an increase of 0.42 PSU in the surface layers and an increase of 0.26 PSU in layers immediately below the bridge, based on a temporal average over the duration of the simulation. The ZOI for temperature extends 2.23 km to the south of HCB, over which temperature deviated from the condition without the bridge. Maximum temperature difference at the bridge was a decrease 0.49 °C in the surface layers and a decrease in temperature of 0.36 °C in layers immediately below the bridge, based on a temporal average over the duration of the simulation.

The near-field influence of the bridge on physical parameters of currents, salinity, and temperature as quantified by ZOI extends over 1.96 km to 5.15 km, which is roughly one to two Hood Canal width scales. Our study concludes that the influence on temperature and salinity is restricted to the upper 20 m, but extends through the water depth for current. The influence on temperature and salinity persists beyond the ZOI all the way to the mouth of Hood Canal at the confluence with Admiralty Inlet. The downstream effect is associated with fjord-like estuarine circulation. The brackish outflow in Hood Canal is restricted to surface layers. The presence of the bridge affects this net outflow through

blockage and added turbulence and mixing. The persistent impact is seen in salinity and temperature downstream of the bridge, even after tides are averaged out.

Author Contributions: T.K. led the investigation and was responsible for conceptualization, methodology, and model development and application. T.W. developed the bridge module software. A.N. was responsible for processing and analysis of model results and field data. T.K. and A.N. analyzed the simulation results and developed the methodology for quantifying and summarizing the results.

Funding: This research was managed by Long Live the Kings through grants from the State of Washington. Funding was provided by Washington State with equal in-kind contributions by those participating in the research.

Acknowledgments: This publication is part of the Hood Canal Bridge Ecosystem Impact Assessment: an ecosystem-wide assessment of potential impacts of the Hood Canal Bridge on fish passage and water quality in Hood Canal.

Conflicts of Interest: The authors declare no conflict of interest. The funders had no role in the design of the study; in the collection, analyses, or interpretation of data; in the writing of the manuscript, and in the decision to publish the results.

References

1. Puget Sound Partnership. *2009 State of the Sound Report*; No. PSP09-08; Puget Sound Partnership: Olympia, WA, USA, 2010.
2. Khangaonkar, T.; Yang, Z.; Kim, T.; Roberts, M. Tidally Averaged Circulation in Puget Sound Sub-basins: Comparison of Historical Data, Analytical Model, and Numerical Model. *J. Estuar. Coast. Shelf Sci.* **2011**, *93*, 305–319. [CrossRef]
3. Khangaonkar, T.; Sackmann, B.; Long, W.; Mohamedali, T.; Roberts, M. Simulation of annual biogeochemical cycles of nutrient balance, phytoplankton bloom(s), and DO in Puget Sound using an unstructured grid model. *Ocean Dyn.* **2012**, *62*, 1353–1379. [CrossRef]
4. Khangaonkar, T.; Nugraha, A.; Xu, W.; Long, W.; Bianucci, L.; Ahmed, A.; Mohamedali, T.; Pelletier, G. Analysis of Hypoxia and Sensitivity to Nutrient Pollution in Salish Sea. *J. Geophys. Res. Oceans* **2018**, *123*, 4735–4761. [CrossRef]
5. Newton, J.; Bassin, C.; Devol, A.; Richey, J.; Kawase, M.; Warner, M. Chapter 1: Overview and Results Synthesis. In *Integrated Assessment and Modeling Report*; Hood Canal Dissolved Oxygen Program; University of Washington: Washington, DC, USA, 2011. Available online: http://www.hoodcanal.washington.edu/documents/document.jsp?id=3019 (accessed on 10 December 2018).
6. Cope, B.; Roberts, M. *Review and Synthesis of Available Information to Estimate Human Impacts to Dissolved Oxygen in Hood Canal*; Ecology Publication No. 13-03-016; EPA Publication No. 910-R-13-002; Washington State Department of Ecology and U.S. EPA: Washington, DC, USA, 2013. Available online: https://fortress.wa.gov/ecy/publications/documents/1303016.pdf (accessed on 10 December 2018).
7. Khangaonkar, T.; Wang, T. Potential alteration of fjordal circulation due to a large floating structure—Numerical investigation with application to Hood Canal basin in Puget Sound. *Appl. Ocean Res.* **2013**, *39*, 146–157. [CrossRef]
8. Moore, M.; Berejikian, B.A.; Tezak, E.P. A floating bridge disrupts seaward migration and increases mortality of steelhead smolts in Hood Canal, Washington State. *PLoS ONE* **2013**, *8*, e73427. [CrossRef] [PubMed]
9. Hood Canal Bridge Assessment Team. *Hood Canal Bridge Ecosystem Impact Assessment Plan: Framework and Phase 1 Details*; Long Live the Kings: Seattle, WA, USA, 2016. Available online: https://lltk.org/wp-content/uploads/2016/08/Hood-Canal-Bridge-Impact-Assessment-Plan-FINAL-27September2016.pdf (accessed on 10 December 2018).
10. RPS. *Current Measurements in Hood Canal Data Report*; Maya Whitmont and Kevin Redmond of RPS Group PLC: Seattle, WA, USA, 2017.
11. Chen, C.; Liu, H.; Beardsley, R.C. An unstructured, finite-volume, three-dimensional, primitive equation ocean model: Application Tocoastal Ocean and estuaries. *J. Atmos. Ocean. Technol.* **2003**, *20*, 159–186. [CrossRef]
12. Cerco, C.; Cole, T. *Three-Dimensional Eutrophication Model of Chesapeake Bay*; Tech. Rep. EL-94-4; U.S. Army Corps of Engineers: Vicksburg, MI, USA, 1994.

13. Cerco, C.F.; Cole, T.M. *User's Guide to the CE-QUAL-ICM Three-Dimensional Eutrophication Model*; Release Version 1.0; U.S. Army Corps of Engineers: Washington, DC, USA, 1995; p. 320.
14. Khangaonkar, T.; Long, W.; Xu, W. Assessment of circulation and inter-basin transport in the Salish Sea including Johnstone Strait and Discovery Islands pathways. *Ocean Model.* **2017**, *109*, 11–32. [CrossRef]
15. Bianucci, L.; Long, W.; Khangaonkar, T.; Pelletier, G.; Ahmed, A.; Mohamedali, T.; Roberts, M.; Figueroa-Kaminsky, C. Sensitivity of the regional ocean acidification and the carbonate system in Puget Sound to ocean and freshwater inputs. *Elem. Sci. Anthropocene* **2018**, *6*, 22. [CrossRef]
16. Mohamedali, T.; Roberts, M.; Sackmann, B.S.; Kolosseus, A. *Puget Sound Dissolved Oxygen Model: Nutrient Load Summary for 1999–2008*; Publication No. 11-03-057; Washington State Department of Ecology: Olympia, WA, USA, 2011.
17. Spargo, E.; Westerink, J.; Luettich, R.; Mark, D. Developing a Tidal Constituent Database for the Eastern North Pacific Ocean. In Proceedings of the 8th International Conference on Coastal Modeling, Mexico City, Mexico, 18–24 February 2007.
18. Locarnini, R.A.; Mishonov, A.V.; Antonov, J.I.; Boyer, T.P.; Garcia, H.E.; Baranova, O.K.; Zweng, M.M.; Paver, C.R.; Reagan, J.R.; Johnson, D.R.; et al. *World Ocean Atlas 2013*; Volume 1: Temperature; NOAA Atlas NESDIS 73; Levitus, S., Mishonov, A., Eds.; National Oceanic and Atmospheric Administration: Silver Spring, MD, USA, 2013; p. 40.
19. Zweng, M.M.; Reagan, J.R.; Antonov, J.I.; Locarnini, R.A.; Mishonov, A.V.; Boyer, T.P.; Garcia, H.E.; Baranova, O.K.; Johnson, D.R.; Seidov, D.; et al. *World Ocean Atlas 2013*; Volume 2: Salinity; NOAA Atlas NESDIS 74; Lev-itus, S., Mishonov, A., Eds.; National Oceanic and Atmospheric Administration: Silver Spring, MD, USA, 2013; p. 39.
20. Willmott, C.J. Some comments on the evaluation of model performance. *Bull. Am. Meteorol. Soc.* **1982**, *63*, 1309–1313. [CrossRef]
21. Wang, T.; Khangaonkar, T.; Long, W.; Gill, G. Development of a Kelp-Type Structure Module in a Coastal Ocean Model to Assess the Hydrodynamic Impact of Seawater Uranium Extraction Technology. *J. Mar. Sci. Eng.* **2014**, *2*, 81–92. [CrossRef]
22. Wissmar, R.; Simenstad, C. Energetic Constraints of Juvenile Chum Salmon (*Oncorhynchus keta*) Migrating in Estuaries. *Can. J. Fish. Aquat. Sci.* **1988**, *45*, 1555–1560. [CrossRef]
23. Greene, C.M.; Hall, J.; Small, D.; Smith, P. Effects of Intertidal Water Crossing Structures on Estuarine Fish and Their Habitat: A Literature Review and Synthesis. 2017. Available online: http://www.skagitclimatescience.org/wp-content/uploads/2018/07/Greene-et-al.-2017-review-on-intertidal-water-crossing-structures-and-fish-1.pdf (accessed on 10 December 2018).

Journal of
Marine Science and Engineering

MDPI

Article

Baroclinic Effect on Modeling Deep Flow in Brown Passage, BC, Canada

Yuehua Lin *, David B. Fissel, Todd Mudge and Keath Borg

ASL Environmental Sciences Inc., #1-6703 Rajpur Place, Victoria, BC V8M 1Z5, Canada; dfissel@aslenv.com (D.B.F.); tmudge@aslenv.com (T.M.); kborg@aslenv.com (K.B.)
* Correspondence: alin@aslenv.com; Tel.: +1-250-656-0177 (ext. 146)

Received: 4 August 2018; Accepted: 8 October 2018; Published: 12 October 2018

Abstract: Brown Passage is a deep (up to 200 m) ocean channel connecting the western offshore waters of Hecate Strait and Dixon Entrance on the Pacific continental shelf with the eastern inland waters of Chatham Sound in Northern British Columbia, Canada. A high-resolution 3D finite difference hydrodynamic model, COastal CIRculation and SEDiment transport Model (COCIRM-SED), was developed in 2010 and 2013 to determine the tidal and wind-driven currents of this area. The barotropic model results for ocean currents were found to be in reasonably good agreement with the historical ocean current observations at near-surface and middle depth available for Brown Passage. Operated from October 2014 to April 2015, the first modern oceanographic measurement program in Brown Passage found surprisingly strong near-bottom currents (the 99th percentile current speed reaches 53 cm/s at 196 m). As a result, the COCIRM-SED model was modified and rerun, with the most important change incorporating water density/salinity fields as modeled variables. This change led to considerable improvements in the ability of the model to generate episodes of relatively strong currents in the bottom layers. The bottom intensification in ocean currents in Brown Passage is shown to be due to semi-diurnal internal tides, which were not previously included in the barotropic version of the 3D model. This finding for the near-bottom flow from the qualitative modeling study is important for applications of the potential sediment deposition and resuspension studies.

Keywords: Brown Passage; Chatham Sound; internal tides; circulation; numerical model; stratification; barotropic; baroclinic

1. Introduction

Brown Passage is a deep (up to 200 m below chart datum, i.e., the reference level for depths used on a nautical chart) ocean channel connecting the western offshore waters of Hecate Strait and Dixon Entrance on the Pacific continental shelf with the eastern inland waters of Chatham Sound in Northern British Columbia, Canada (Figure 1). Where Chatham Sound is a semi-enclosed inland sea spanning a total distance of approximately 70 km from south to north and has width of 15–25 km with water depths generally less than 200 m [1]. On its western side, it is separated from the more exposed open waters of Dixon Entrance and Hecate Strait by several island groups separated by channels or passages. Among them the two largest and deepest passages are the eastward extension of Dixon Entrance to the north of Dundas Island; and Brown Passage in central Chatham Sound, which are the most important channels allowing the exchanges of water and wave energy with the larger water bodies to the west.

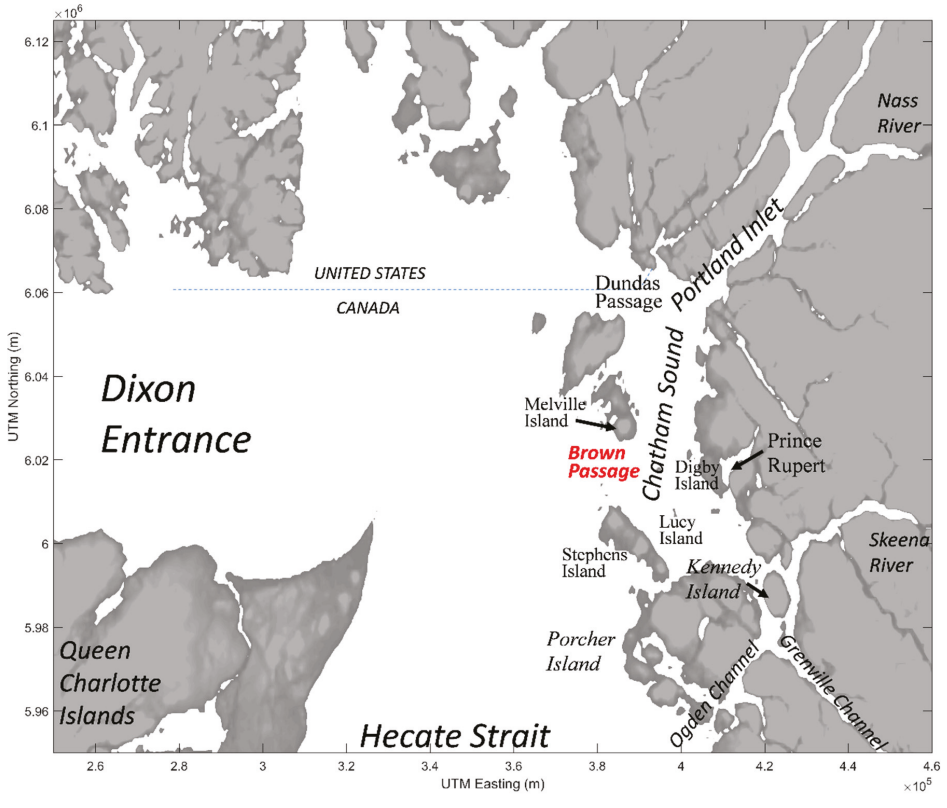

Figure 1. Location of Brown Passage (in red) based on gridded coastline data from gridded bathymetry data (retrieved from the website of the British Oceanographic Data Centre: https://www.gebco.net/data_and_products/gridded_bathymetry_data/).

The ocean currents in Chatham Sound are highly variable due to a combination of forcing by the large mean tidal range within this area, seasonally strong winds, and large peak freshwater discharges from the Skeena and Nass Rivers. Chatham Sound is characterized by lower salinity (~20 Practical Salinity Unit (PSU)) near-surface waters on its eastern side, due to the Skeena River inflow to Southern Chatham Sound [1]. More saline waters present on the western side of the Chatham Sound result from the exchange through Brown Passage and other connecting channels with the higher salinity waters of Hecate Strait and Dixon Entrance.

Oceanographic research of this complex oceanic- and river-dominated inland waterway [2] is being driven by industrial activities related to the expansion of the port of Prince Rupert (Figure 1), along with high levels of marine biological productivity and a very active regional fishery in Chatham Sound [3]. Recent research into this oceanic environment is motivated by studies of the possible use of this area for disposal at sea of dredged sediments arising from expansion of marine terminals in and around the Prince Rupert harbor in Chatham Sound [2]. A better understanding of hydrodynamics throughout the whole water column in Brown Passage is required, for the potential short-term sediment transport and long-term resuspension processes with ocean currents.

The spatial extent of the surface expression of the sediment plume from the Skeena River was derived using historical 30 m resolution LANDSAT imagery (available online from the US Geological Survey). The LANDSAT satellite, LANDSAT-8, which became operational in 2012–2013, has much better radiometric sensitivity (10× Landsat 7) which makes it more useful for water applications

involving subtle signals such as river plumes. One LANDSAT-8 scene, 28 August 2013 (Skeena River discharge of 665 m^3/s) was selected and enhanced, as shown in Figure 2 (Figure 5 in [1]). The more sensitive detection of the LANDSAT-8 satellite image scene reveals that the Skeena River plume is detectable along the eastern half of Chatham Sound into the northern half of Chatham Sound. However, commensurate with the relatively low discharges, the Skeena River plume is confined to the estuarine area with a secondary area of enhanced turbidity levels in the area as far northwest as the Digby Island (Figure 1).

Figure 2. Enhanced Landsat 8 satellite image for (**a**) 28 August 2013 (ebb flow, under 665 m^3/s river discharge from the Skeena River) and (**b**) 5 April 2015 (flood flow, under 200 m^3/s river discharge from the Skeena River).

The pathways of freshwater from the Skeena River are highly dependent on the Skeena River discharge values [4]. Under average discharges, about 70% of the freshwater discharge leaves on the eastern side of central and northern Chatham Sound, where it merges with Nass River freshwater and exits via Dixon Entrance. Only 30% of the freshwater leaves Chatham Sound through the southern and central passages, with half of this being by the way on the west (e.g., Brown Passage, see Figure 3). During late May and early June peak discharges (freshet) of the Skeena and Nass rivers, the freshwater leaves the Sound via all the passages with the greatest flux through Dundas Passage (Figure 1). Nass River discharge also affects Chatham Sound salinity, but its seasonal variability is very similar to Skeena River discharges, except during the fall season, due to a greater effect from precipitation. During freshet, Nass River water extends as far south as Melville Island (Figure 1). Due to the large mean tidal range of Chatham Sound, the salinity, temperature, and freshwater time series at fixed locations were observed to exhibit variability at tidal periods. During periods of unsteady river discharges, large cells of relatively fresh water are discharged into the Sound from the Skeena River; these are gradually dispersed under the influence of the large tides, winds, and the kinetic and potential energy of the freshwater flows themselves.

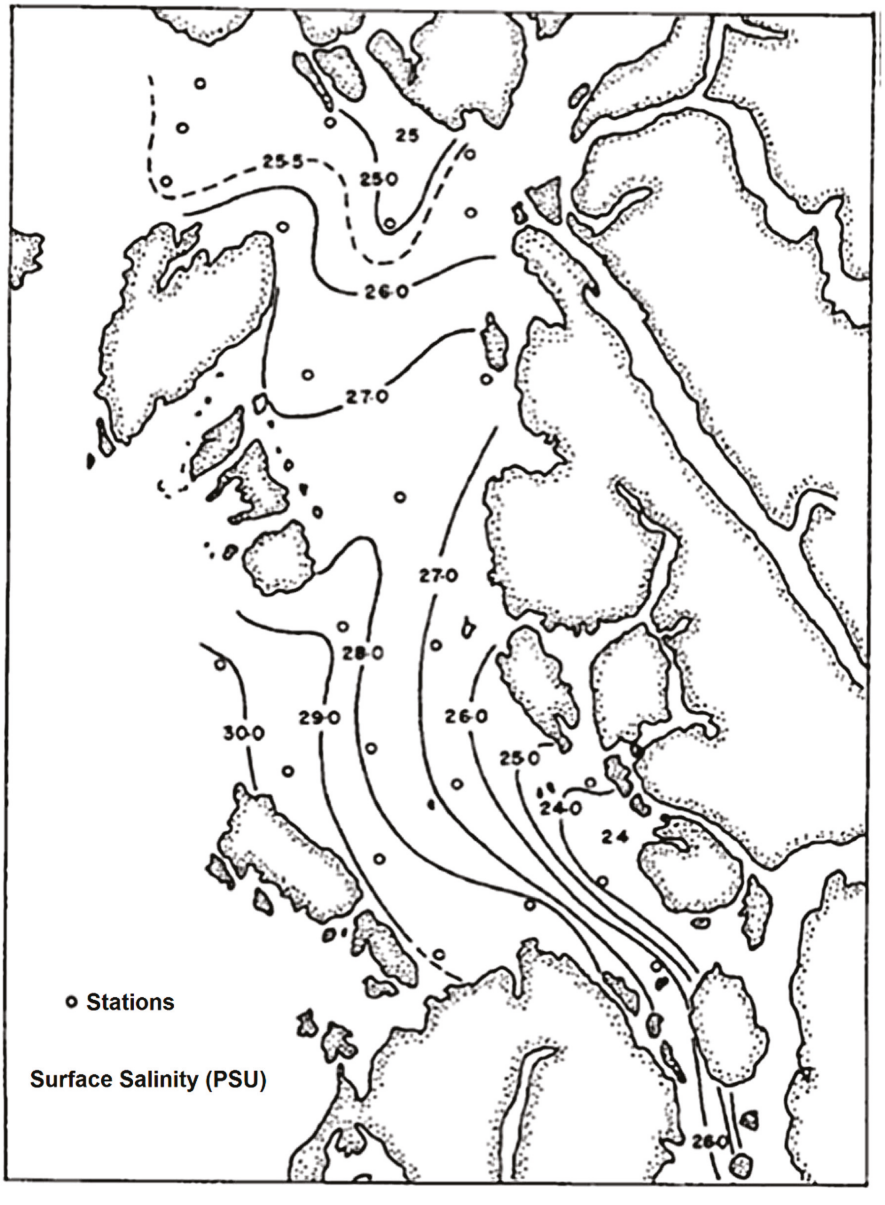

Figure 3. Surface salinity pattern during normal river conditions (under 700–1000 m^3/s river discharge from the Skeena River), 10–19 August 1948 (Figure 6 in [4]).

Historical conductivity temperature depth (CTD) and bottle data extracted from the Department of Fisheries and Oceans (DFO) database (see http://www.pac.dfo-mpo.gc.ca/science/oceans/data-donnees/index-eng.html) for British Columbia (BC) coastal waters (from 183 sites) were examined for Chatham Sound domain by Lin and Fissel (2018) [1]. Each CTD/bottle site provided a vertical profile of the temperature and salinity. During the freshet season of the Skeena River, i.e., June to August (summer), Southern Chatham Sound features lower salinity (as low as 20 PSU) and a wide temperature

range from 6 to 15 °C. During non-freshet seasons (winter: December to February, spring: March to May, and fall: September to November), Southern Chatham Sound has lower salinity (25 PSU) at surface, and temperature ranged only from 7 to 8 °C in winter, 6 to 7 °C in spring, and 8 to 10 °C in fall. Surface salinity is lower than in freshet (summer) season. Water is mainly uniform for both temperature and salinity in Western Chatham Sound, except during summer time (it might be affected by limited data availability as well). However, direct observations for ocean currents in Brown Passage are very rare. Ocean current data were collected in fall 1991 at the DFO ocean current mooring site (CP02) located near the regional ocean disposal site (Figure 4).

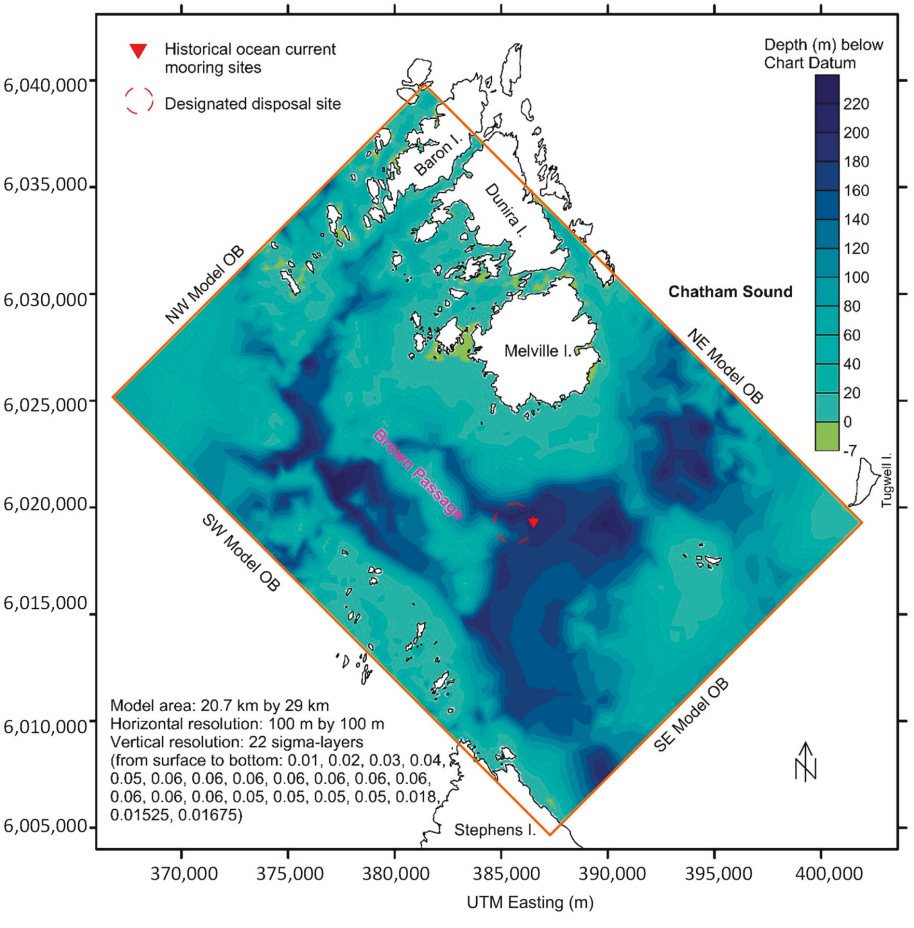

Figure 4. A map of water depths in Brown Passage (meters below chart datum) and the model domain.

The remainder of the paper is arranged as follows. A brief overview of the barotropic modeling is presented in Section 2. The observational data and analysis are presented in Section 3. Section 4 presents the baroclinic modelling and the comparison between model results and observations near the bottom. The final section is a summary and conclusion.

2. Previous Modeling Studies

The circulation of the larger areas of the BC north coast, adjoining Chatham Sound, including Queen Charlotte Sound, Hecate Strait, and Dixon Entrance, has been studied through numerical modeling methods. Hannah et al. (1991) described the wind-driven (no tides), depth-averaged circulation in Queen Charlotte Sound and Hecate Strait [5]. Ballantyne et al. (1996) used a 3D finite element model to compute the buoyancy-driven flows, as well as the barotropic tides of the BC north coast [6]. The tidal currents of the BC north coast have also been modeled by Flather (1987) [7] for the northeast Pacific Ocean; Foreman et al. (1993) [8] for the barotropic tide in the BC north coast; Cummins and Oey (1997) [9] for the barotropic and baroclinic tides of the BC north coast; and Foreman et al. (2000) [10] for assimilating satellite altimeter observations into a barotropic tidal model over the northeast Pacific Ocean. Brown Passage was included in the much larger model BC north coast model domains, but the availability and validity of the model circulation results for Brown Passage were compromised by the poor spatial resolution (e.g., coarser than 1 km in the horizontal).

A much higher spatial resolution 3D finite difference numerical model, COastal CIRculation and SEDiment transport Model (COCIRM-SED; [11–14]), was developed by Jiang and Fissel in 2012 [2]. This model was applied to determine the tidal and wind-driven currents in Brown Passage and used to simulate the transport and deposition of sediments released from disposal at sea activities. COCIRM-SED is a highly integrated model, consisting of five submodules, including circulation, wave, multisize sediment transport, morphodynamics, and water quality. The model can be operated on either an integrated or an individual module basis.

In the barotropic modeling of Brown Passage [2], the COCIRM-SED model was operated over a numerical model domain for the full area of Brown Passage, with a total area of 20.7 km by 29 km (Figure 4). A horizontal grid size resolution of 100 m by 100 m was used for the model area. In the vertical, the model used 22 sigma-layers with higher resolutions realized near the surface and bottom. The depths of model layers are computed as (Sigma-layer thickness) × (Total water depth) = $\Delta\sigma H$. The digital bathymetric data set, in the format of Universal Transverse Mercator (UTM) Easting, UTM Northing, and seabed elevation relative to chart datum, was gridded to provide suitable representation of the water depths in the model. The model was forced by tidal height elevations spanning four open boundaries and by surface winds. The four model open boundaries consist of the four adjoining sides of Brown Passage (Figure 4). The forcing at the four open boundaries are limited to tidal elevations and do not include wind forced flows. Tidal elevations at these four open boundaries were derived from 7 major tidal height constituents (O1, P1, K1, N2, M2, S2, K2) using the DFO standard tidal prediction program [15]. The tidal constituents for the reference Qlawdzeet Anchorage, port of Prince Rupert, and Lawyer Islands, were obtained from Canadian Hydrographic Service of DFO (Table 1). Coriolis force was also activated.

Table 1. Tidal constituents at tide gauge stations used for model open boundary conditions.

Tide Gauge	Qlawdzeet Anchorage (#9315)		Prince Rupert (#9354)		Lawyer Islands (#9312)	
Tidal Constituents	Amplitude (m)	Phase (deg)	Amplitude (m)	Phase (deg)	Amplitude (m)	Phase (deg)
Z0	369.00	0.00	387.09	0.0	387.09	0.00
O1	30.78	129.80	31.25	132.46	31.25	132.44
P1	15.36	136.60	16.06	135.84	16.06	135.82
K1	49.38	139.60	51.44	139.48	51.44	139.46
N2	34.53	14.40	39.52	14.9	39.52	14.87
M2	183.82	34.90	195.65	35.79	195.65	35.76
S2	57.79	56.70	64.45	59.26	64.45	59.23
K2	16.82	48.50	17.38	50.65	17.38	50.62

This model run involved both tidal forcing at the open boundaries and surface wind forcing using measured hourly winds at the Prince Rupert airport weather station for the same period. As shown in Figure 5a, the dominant wind directions in terms of frequency of occurrence and higher wind speeds are from the south to southeast. Wind forcing is applied as a space-uniform but time-varying value on the model grids.

The model was initially tested with a calibration run. Various physical parameters, mainly bottom drag coefficient and horizontal and vertical eddy diffusivity coefficients, as well as major tidal constituent phases, were repetitively adjusted to achieve optimal agreement with the observations and physically reasonable flow patterns in Brown Passage. The Smagorinsky eddy parameterization [16] was used for horizontal diffusivity with coefficient $C = 0.08$. The background vertical diffusion and viscosity were set to 10^{-6} m^2/s with a MY2.5 (Mellor and Yamada) [17] turbulence closure. The bottom roughness parameter was set to 0.001 m with a value of 0.015 for the bottom drag coefficient. Readers are referred to Jiang and Fissel (2011) [2] for more details on the model setup and development.

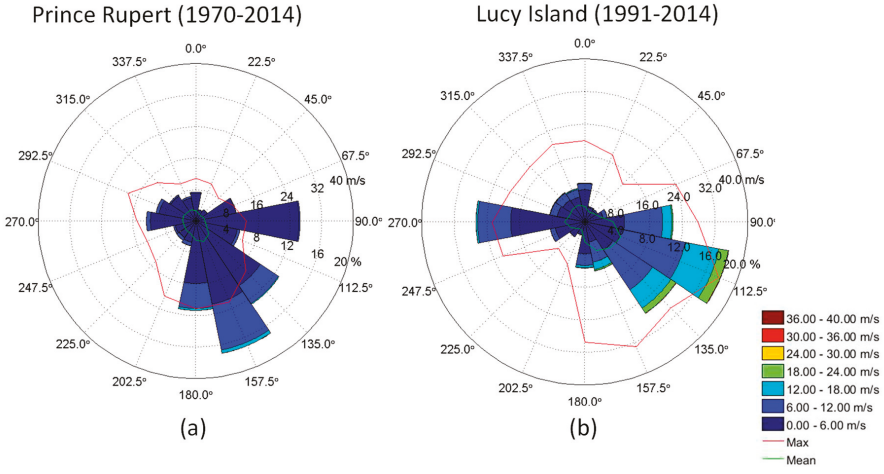

Figure 5. Compass rose plots for wind speed and direction distributions measured at (**a**) Prince Rupert Airport and (**b**) Lucy Island (see Figure 1). The wind datasets were obtained from the Meteorological Service of Canada, Environment and Climate Change Canada.

The model was operated for a 17-day-long fall period (5–22 October 1991) and compared with ocean current data at the DFO current meter mooring site located to the southeast of Melville Island (Figure 4). The model results for ocean currents were found to be in reasonably good agreement with the two sets of ocean current observations at 15 m (Figure 6) and 98 m (Figure 7), notably, the similarity of the large tidal currents of 6–12 September, and the good agreement in the tidal current directions especially at 15 m depth of the model results with the data available for Brown Passage [2]. A statistical analysis of the verification model results shows that the correlation coefficients between modeled and measured current speeds and directions are greater than 0.5 near the surface. Relatively weak correlation with a coefficient at about 0.4 occurs for the verification case at 98 m depth. Readers are referred to Jiang and Fissel (2011) [2] for more details on the model calibration and verification.

Based on the generally favorable model verification results, it was concluded that the circulation module was reasonably well validated and is, thus, suitable for simulating disposal sediment transport and fate in Brown Passage. Based on these results, Brown Passage was thought to be generally well mixed through the middle and lower parts of the water column.

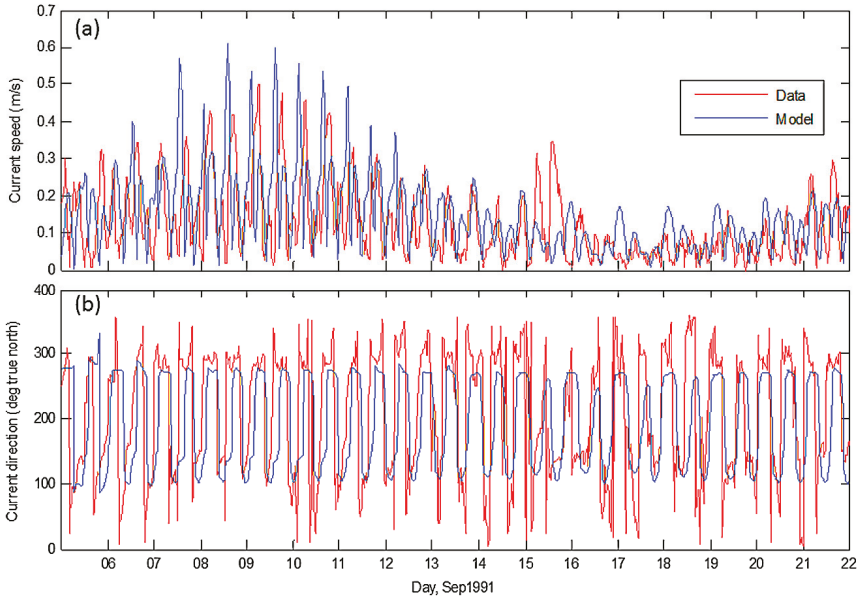

Figure 6. Modeled and measured results of current (**a**) speeds and (**b**) directions located at the historical ocean current mooring site marked in Figure 4 for near-surface ocean currents at 15 m depth. As Figure 4 in [2].

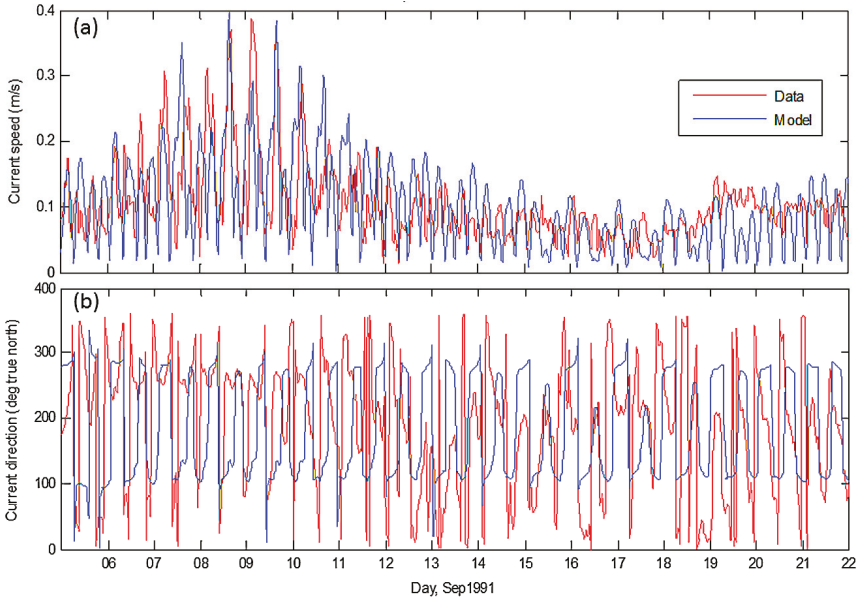

Figure 7. Modeled and measured results of current (**a**) speeds and (**b**) directions located at the historical ocean current mooring site marked in Figure 4 for ocean currents at 98 m depth. As Figure 5 in [2].

3. Near-Bottom Current Measurements in Brown Passage

The first modern oceanographic measurement program for the near-bottom currents in Brown Passage was conducted from mid-October 2014 to April 2015. The measurements were made at a location in approximately 200 m water depth within a previously used ocean disposal site (Figure 8). The mooring configuration was a tautline mooring ASL-DualCage frame supporting an upward-looking acoustic Doppler current profiler (ADCP, 300 kHz) to collect current data through the majority of the water column and a single point current meter (Teledyne doppler volume sampler, DVS) mounted to tandem PORT acoustic releases to measure currents within the bottom 5 m. As well, an RBR XR-420 CTD+Tu instrument was mounted to the DualCage to collect temperature, salinity, and turbidity data (Figure 9). It should be noted that line lengths and heights provided in this image are only approximate. The DVS stopped operating on 9 March 2015, about one month prior to the recovery operations due to an instrument malfunction.

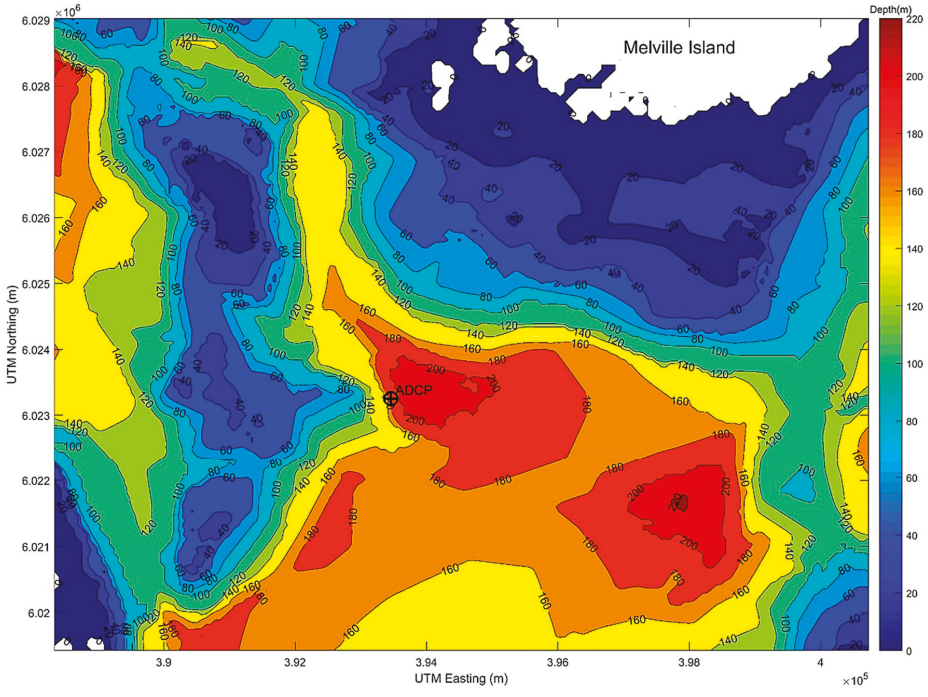

Figure 8. Study area including bathymetry (contours depths below chart datum) and the location of acoustic Doppler current profiler (ADCP) measurements.

Full water column velocities were analyzed at all levels with valid data obtained by the ADCP instrument every 15 min. In addition, currents with 15-min intervals at a single water depth were derived from the DVS (doppler volume sampler) measurements. Plots of speed and direction are shown in Figure 10 for the full water column. The baroclinicity of the flow field was established especially through the directional variability of near-bottom flows, which shows episodes of relatively strong currents in the bottom layers (as red colored bottom areas in Figure 10b) relative to those at mid-depth levels.

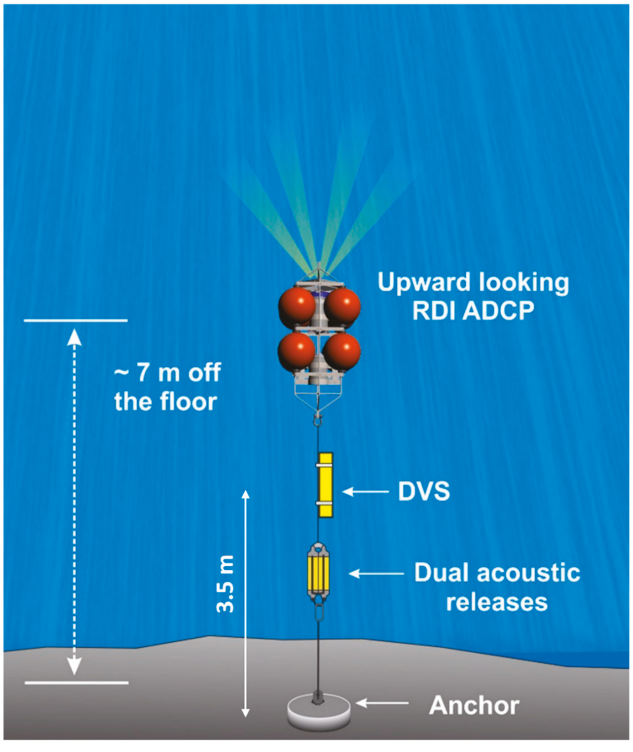

Figure 9. Mooring configuration.

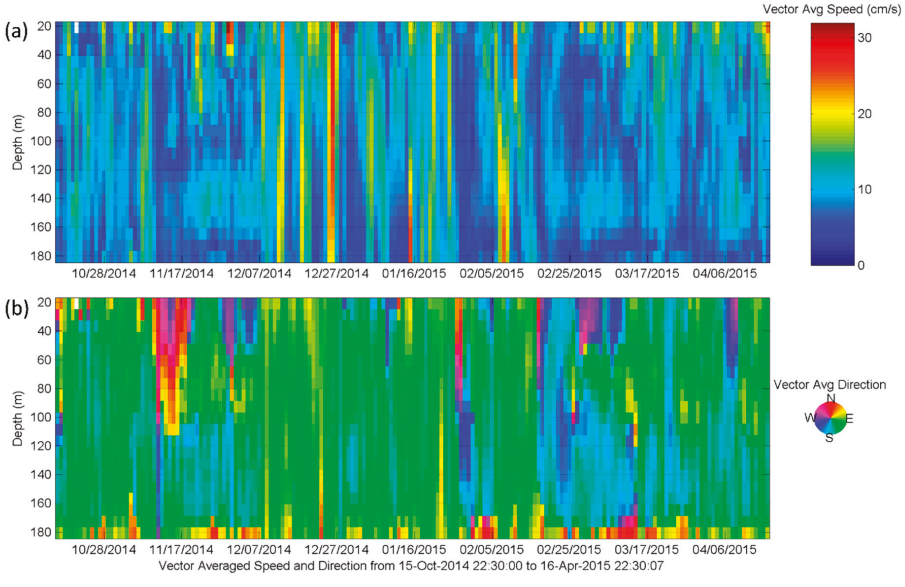

Figure 10. Daily vector average current (**a**) speed and (**b**) direction for the full water column.

The lowest current speeds were observed in the middle of the water column (133 m) rather than near the bottom of the water column, as is more usually the case. The measured current speeds at mid-depth levels are generally consistent with the historical DFO measurements at a nearby location (see Figure 4) at 98 m depth. The 99th percentile current speed from the DFO site was 32 cm/s as compared to a value of 38 cm/s at 98 m measurement depth in the ADCP program.

Larger current speeds occur at near-bottom levels within 25–30 m of the seabed. The 99th percentile current speed is 36 cm/s at 133 m water depth, increasing to 40 cm/s at 181 m depth and 53 cm/s at 196 m water depth, about 3.5 m above the seabed. The cumulative distribution function (CDF) curves for both observed current speed time series at the deepest ADCP measurement level (181 m) and at the DVS measurement level (196 m), shown in Figure 11, reveals that the largest observed current speeds are consistently higher just above the seabed over those observed at 15 m above in the water column. As well as the increased speeds of the currents within 30 m of the seabed, the ship-based temperature and salinity profile measurements revealed higher densities due to increased salinities in this deep boundary layer of the water column.

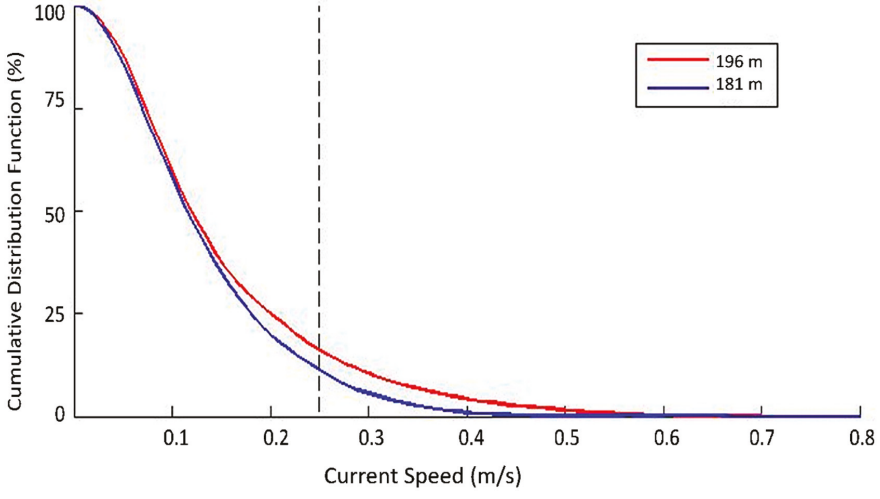

Figure 11. Current speeds at the deepest ADCP measurement level (181 m) and at the DVS measurement level (196 m). The vertical dash line marks 25 cm/s which is associated with 11% cumulative distribution function (CDF) (89th percentile) for 181 m depth and 16% (84th percentile) for 196m depth.

The bottom-mounted CTD-derived time series of temperature and salinity at 7 m off the seabed show large variations of up to 4 °C (temperature) and 1 PSU (salinity) occurring episodically over periods of days to weeks. Three groups of CTD casts were completed during the deployment on 15 October 2014, 27 March 2015, and 18–19 April 2015. There were multiple profiles collected each day with variability in association with different tidal phases. The cast-derived density profiles are shown in Figure 12. In fall 2014, the lower half of the water column is occupied by the more saline deep water than seen in the CTD casts. The potential reason is that higher salinity waters from Hecate Strait moved into Brown Passage from the west during this period. To better examine the water structure and the dynamics of the observed deep flow in Brown Passage, a baroclinic hydrodynamic modeling study was carried out in the next section.

The near-bottom currents are observed at depths of 181 m and 196 m below chart datum, in the measurements of two different instruments, the ADCP and the DVS, so that the baroclinic signals found in these near-bottom currents are not due to the equipment itself.

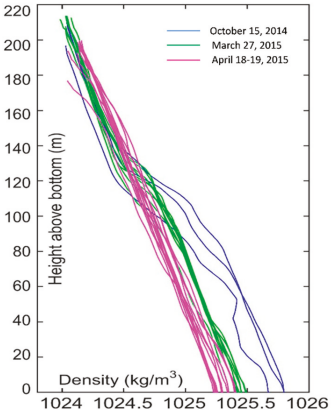

Figure 12. Density profiles as measured by CTD casts during the three periods.

4. Baroclinic Modeling Study for Deep Flow in Brown Passage

4.1. Model Setup

The 3D hydrodynamic model COCIRM-SED used in this study is based on Jiang and Fissel [2] using the same model domain (Figure 4) and resolution in both the horizontal (100 m) and the vertical (22 sigma layers with higher resolutions realized near the surface and bottom). The model was forced at tidal height elevations spanning four open boundaries, and by local surface winds (the remote wind effect is not considered). The surface wind data (applied to model grids at each time step as a uniform value in space) are obtained from the Lucy Island marine weather station (Figure 5b), operated by Environment Canada. Lucy Island winds are more representative of over-water winds for the entire region of study, compared with the overland Prince Rupert Airport winds. However, this would not produce a substantial difference in the deep flow simulation in this study.

In the previous modeling studies, the water column in the Brown Passage was assumed to be well mixed and uniform, essentially barotropic, resulting in minimal flows at the bottom, with current directions as a typical tidal ellipse. In this study, the inputs to the 3D COCIRM-SED model were modified by introducing density stratification due to the vertical changes of salinity (temperature effect is secondary) within the water column. These data were derived from CTD cast data acquired in Brown Passage, as discussed above. The October salinity profiles are selected for initializing the model run (horizontally uniform) and to provide the open boundary conditions from November to December 2014. The selection of the October salinity profiles, rather than March, is to incorporate the higher saline water and associated stronger stratification in the study area.

The following boundary conditions are used. At lateral solid (or closed) boundaries, the normal flow, tangential stress, and normal fluxes of potential temperature and salinity are set to zero (free slip and insulating boundary conditions). Along the model open boundaries, the normal flow, temperature, and salinity fields are adjusted using a method similar to the adaptive open boundary conditions. It first uses an explicit Orlanski radiation condition [18] to determine whether the open boundary is passive (outward propagation) or active (inward propagation). If the open boundary is passive, the model prognostic variables are radiated outward to allow any perturbation generated inside the model domain to propagate outward as freely as possible. If the open boundary is active, the model variables (salinity) at the open boundary are nudged to the CTD profiles (October 2014) at each sigma level with a relaxation time scale of 2 days updated as follows for each time step:

$$S_{t+1}^{i,k} = S_t^{i,k} + \Delta t \epsilon (\hat{S}_t^{i,k} - S_t^{i,k}), \quad (1)$$

where the hat denotes observed salinity, k is the layer number, k is the interface number at open boundaries, and ε is the relaxation time scale. At inner model grid points, relaxation is not to be performed, and the model predicted variables (salinity) are purely prognostic.

It should be noted that although the model can prognostically simulate the dynamics introduced by the water stratification in Brown Passage, the variability of lower frequency (e.g., the seasonal changes) is limited in the model, due to the referential salinity ($\hat{S}_t^{i,k}$) used in Equation 1 being set to be constant (in time) along the open boundaries. In order to reproduce the seasonal variability in the baroclinic fields, variable time series of stratification along the open boundaries needs to be applied; measurements of stratification at the open boundaries is not available, and so cannot be included in this preliminary numerical model study.

4.2. Model Performance

A model run was carried out for Brown Passage and recently acquired ADCP/DVS current data were used for comparison. After a 3-day spin-up period (based on the development of total kinetic energy in the system) starting at rest, the model was integrated from 1 November to 31 December 2014. Model results were saved every 1.5 h for analysis.

Table 2 provides a summary of the modeled and observed ocean current speed statistics from 1 November to 31 December 2014, showing the percentile exceedance levels at 99%, 95%, 75%, 25%, and 5%. The model output agrees closely with the observations up to the 75% percentile. At the 95% percentile speed, the model underestimates the currents at 21 m depth by 0.06 m/s, but the unusually large currents at near-bottom depths of 181 m and 196 m are well modeled, being slightly overestimated by 0.04 m/s or greater. At the 99% percentile speed, the model significantly underestimates the 21 m depth currents by 0.1 m/s but, again, the near-bottom currents at 196 m are within 0.03 m/s of the observed value. This demonstrates the model to be performing satisfactory for the purpose of this study, providing conservative results for the current speed estimates in the deeper portions of the water column.

Table 2. Summary of statistics for the modeled and observed current speeds for the maximum, median, and mean values from 1 November to 31 December 2014, showing the percentile exceedance levels.

Depth (m)	Data	Maximum Speed (m/s)	Median Speed (m/s)	Mean Speed (m/s)	99th Percentile Speed (m/s)	95th Percentile Speed (m/s)	75th Percentile Speed (m/s)	25th Percentile Speed (m/s)	5th Percentile Speed (m/s)	Vector Magnitude (m/s)	Net Direction (°)
21	OBS	0.64	0.19	0.21	0.54	0.42	0.28	0.12	0.06	0.04	122
	MOD	0.52	0.17	0.19	0.44	0.36	0.24	0.12	0.06	0.07	170
77	OBS	0.58	0.13	0.16	0.51	0.35	0.21	0.09	0.03	0.07	119
	MOD	0.43	0.14	0.16	0.39	0.30	0.21	0.10	0.04	0.08	174
133	OBS	0.55	0.13	0.15	0.40	0.32	0.21	0.09	0.03	0.08	141
	MOD	0.50	0.10	0.14	0.42	0.35	0.19	0.07	0.03	0.08	157
181	OBS	0.52	0.12	0.14	0.42	0.33	0.19	0.08	0.03	0.05	83
	MOD	0.55	0.12	0.15	0.48	0.41	0.23	0.07	0.03	0.08	108
196	OBS	0.66	0.12	0.16	0.57	0.42	0.21	0.08	0.03	0.08	44
	MOD	0.63	0.13	0.17	0.54	0.46	0.26	0.07	0.03	0.09	89

First, the modeled and ADCP current results from surface to the middle depth at 21, 77, 133 m are examined (not shown here). Both the model and observed currents exhibited the similar distribution as found by the barotropic run [2] as to the current speeds and directions (see Figures 6 and 7). The currents are typical of tidal channel flows, with flood flow directions ranging from 100 to 150°, and ebb flow directions ranging from 250 to 300°. In the upper layers of the water column, the majority of current speeds are around 0.2 m/s, and there are only a few instances of flows above 0.3 m/s.

In this study, we focus on investigating the strong baroclinic near-bottom flow regime. The hourly modeled current fields were saved and extracted at the depths of 181 m and 196 m for comparison. Time series of model-derived and observed current speeds and directions between 1 November and 31 December 2014 for the depth of 196 m are presented in Figure 13. The baroclinic model results for ocean currents near the seabed were found to be of similar magnitude to the strong observed currents, which is an important improvement from its previous barotropic version [2]. A statistical analysis of the baroclinic model results shows that the correlation coefficients between modeled and measured ADCP/DVS current speeds are somewhat weak (0.23) at 196 m. The weak correlation value is believed to be caused by the absence of variability of low frequency water density and subtidal currents through the open boundaries, which is not included in this qualitative study. For example, for the current speeds from 11 to 22 November, in which the model does not replicate large near-bottom flows while, at other times, these large near-bottom flows are present in the model output.

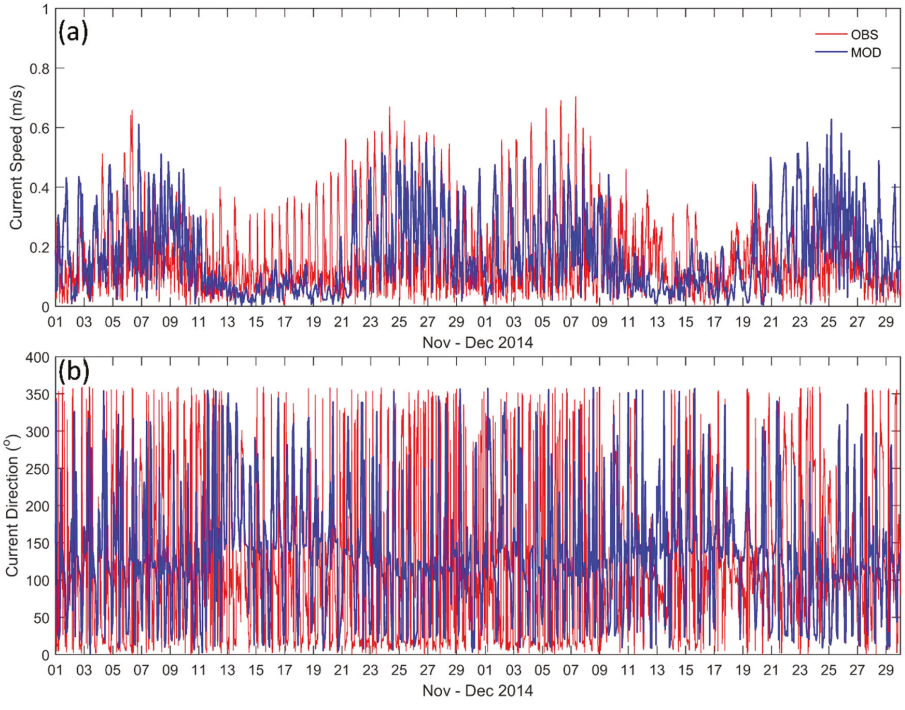

Figure 13. Modeled and measured results located at the ADCP/DVS ocean current mooring site marked in Figure 8 for near-bottom ocean current (**a**) speeds and (**b**) directions at the depth of 196 m.

Figure 14 compares the distribution of model-derived and observed current speeds and directions between 1 November and 31 December 2014 for depths of (a) 181 m and (b) 196 m. Overall, the model results follow the observed values and demonstrated the two modes in the near-bottom flow regime. First, the barotropic mode, which is along the isobath, with an orientation of 120° (flooding) and 300°

(ebbing). In this barotropic mode, near-bottom flood flow can reach 0.5 m/s at 181 m and 196 m, which is stronger than the ebb flow. Second, the newly revealed baroclinic mode is pointing to about 15° (down-slope, see Figure 8) which is associated with the flood flow. The reversed up-slope flow (195°, see Figure 8) is much weaker, which indicates that the baroclinic mode is mainly driven by the flood tides, i.e., the intrusion of deep higher saline water originating to the west of Brown Passage (i.e., Hecate Strait).

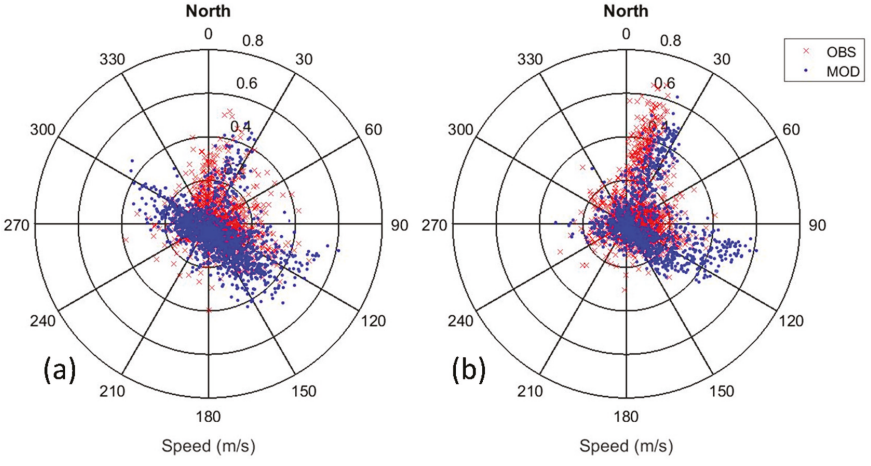

Figure 14. Model results (blue dots) of near-bottom ocean current vectors between 1 November and 31 December 2014, compared with (**a**) ADCP data (red crosses) at 181 m and (**b**) DVS data (red crosses) at 196 m.

Probability density functions of current speeds and directions derived from model results and observations between 1 November and 31 December 2014 were examined in Figure 15. The baroclinic model well reproduced the strong near-bottom speeds, as well as the primary directions. Only slight variations are noted between the modeled and observed near-bottom currents. At the near-bottom depths of 181 and 196 m, the model predicted fewer mid-range currents between 0.1 and 0.2 m/s than in the observed results. The percentage of currents between 0.25 to 0.5 m/s are slightly overestimated (Figure 15a,b). The results for the current direction comparison between observed and modelled values are summarized in Figure 15 as well. The discrepancies in the modelled predictions are also generally small. As shown in Figure 15c,d, the model has slightly less frequent northward (330–360° and 0–30° at 181 m; 300–330° and 0–30° at 196 m) and northeastward near-bottom flows (50–110°), but overestimated the occurrence of southeastward (110–170°) near-bottom flows. The model predicted more northwestward (250–310°) near-bottom flows at the depth of 181 m (more typically tidal with flows in opposite direction) than the observations, which can also be seen in Figure 14a.

Comparisons with observations for the same period show that the model captured both the low frequency and most of the high frequency variability of the current speed very well. For the lower flow levels relevant to the application of modeling sediment transport and fate from disposal at sea, the model has the capacity to generate representative values and distributions of the near-bottom currents for speed and direction.

4.3. Discussion

To demonstrate the effect of the stratification on the deep flow in Brown Passage, a referential barotropic simulation for the exact same period with the baroclinic model have been conducted, by removing the salinity/density field from the modeled variables. The difference of the model-derived near-bottom flow was examined in Figure 16.

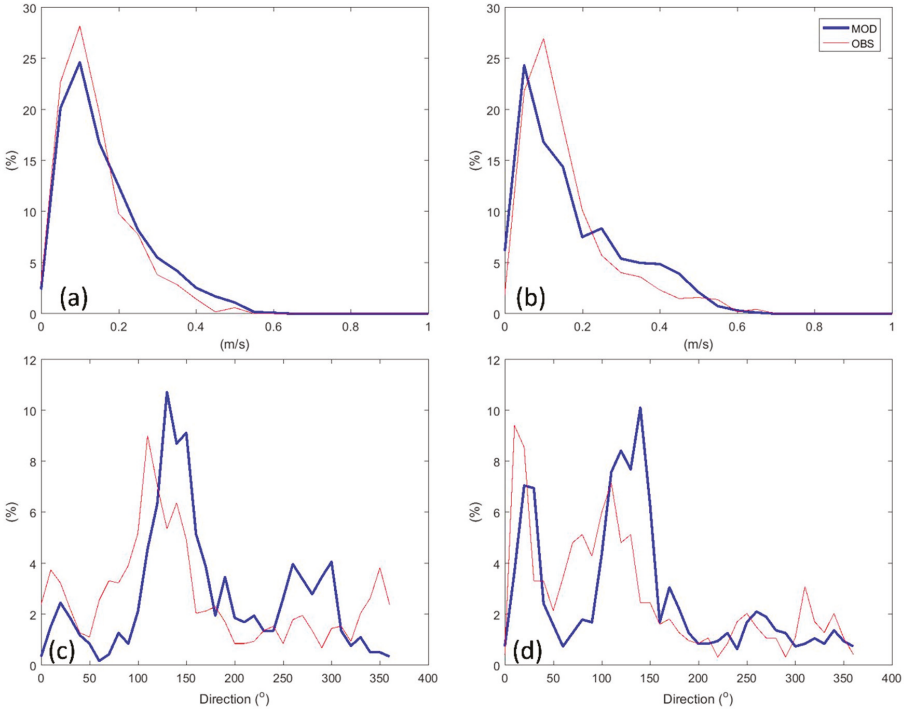

Figure 15. Probability density function of current speeds (**a**,**b**) and directions (**c**,**d**) derived from model results (blue lines) and observations (red lines) between 1 November and 31 December 2014, at (**a**,**c**) 181 m and (**b**,**d**) 196 m.

As shown in Figure 16a, the referential barotropic model demonstrated a typical tidal flow pattern in the near-bottom flow regime, aligned with the direction of the isobath. It did not reproduce the strong northeastward down-slope flow as found in the baroclinic model results (~0.6 m/s). The barotropic flow also exhibited much weaker flooding flow with directions ranging from 90° to 130°. The probability density functions of near-bottom current speeds at 196 m (Figure 16b) indicate that the barotropic model currents has a relatively narrow speed range. The barotropic model underestimated the near-bottom currents with speeds greater than 0.4 m/s or less than 0.1 m/s, compared with the baroclinic model. As to the directional distribution of currents, the barotropic model has less frequent northeastward (0–30°) and southeastward near-bottom flows (100–150°), but overestimated the occurrence of northwestward (310–360°) near-bottom flows (Figure 16c).

Within the two current direction modes of the near-bottom flow as discussed in earlier sections, the strong northward velocity component is found to be the main indicator of the near-bottom baroclinic mode (0–50°). Spectral analysis has been carried out on current speeds from DVS observations and model results from November to December 2014 at the deepest measurement level of 196 m. The power spectral density of the current time series at 196 m has been calculated, and is shown in Figure 17. The model results are comparable to observations. The energy of the baroclinic near-bottom flow is found to be the largest at the semi-diurnal tidal frequency (2 cycles per day) in both model results and observations. Hence, the strong near-bottom flow is believed to be baroclinic semi-diurnal tidal currents (i.e. internal tides).

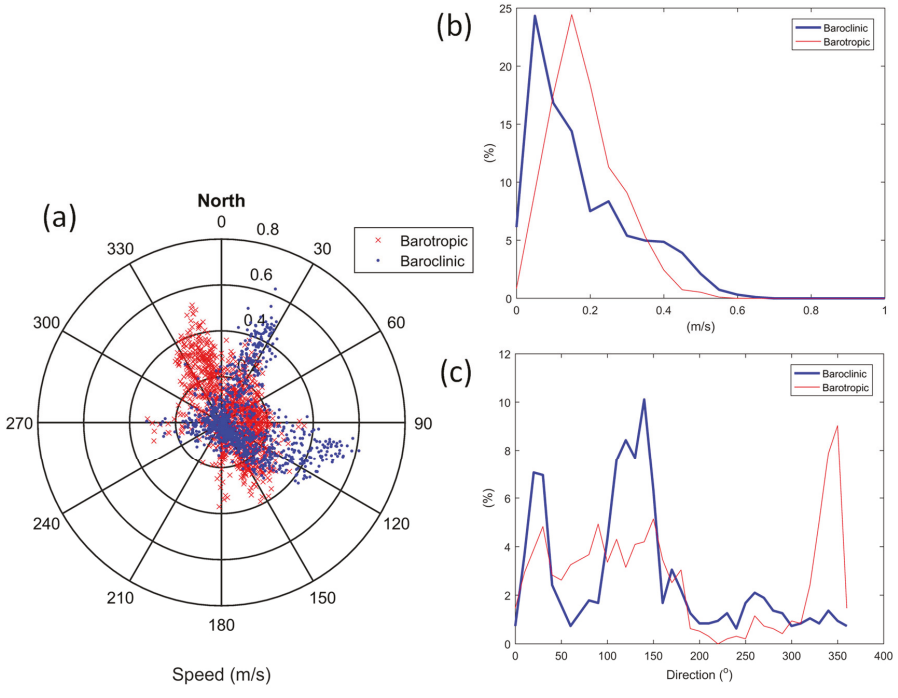

Figure 16. (**a**) Model-derived near-bottom ocean current vectors at 196 m from referential barotropic model results (red crosses), compared with baroclinic model results (blue dots) between 1 November and 31 December 2014. Associated probability density function of current speeds (**b**) and directions (**c**) derived from the barotropic (blue lines) and baroclinic model results (red lines) are also compared.

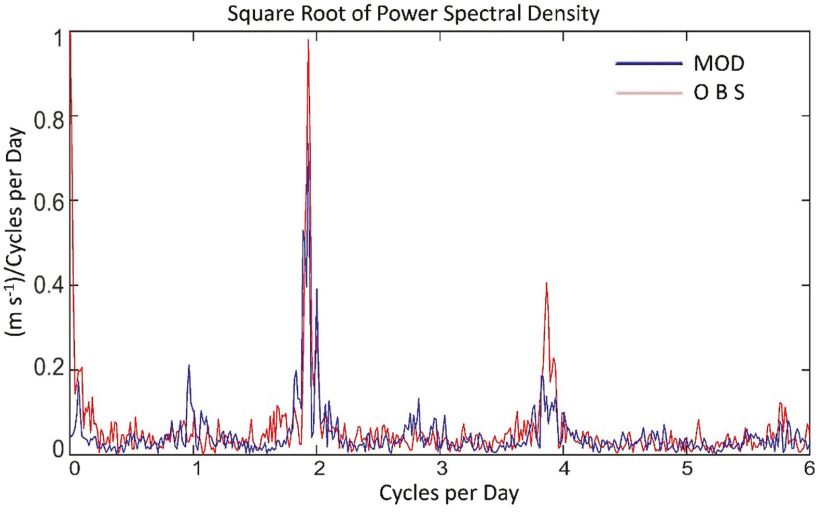

Figure 17. Power spectral density of northward flow component (m/s) of the near-bottom flow at 196 m derived from model results (blue line) and observations.

However, at the very low frequencies of less than 0.2 cycles per day, the model underestimates the power spectrum by comparison with observations, although the total power at these very low frequencies is considerably less than those of the semi-diurnal frequency band. The variability of lower frequency (e.g., the seasonal changes) of the stratification, especially for the higher salinity water intrusion from the west (e.g., Hecate Strait), is not directly represented via the open boundary conditions of this version of the model.

To further investigate the dynamics driving the semi-diurnal tidal currents, time series of density anomalies (time mean removed) measured by the near-bottom CTD unit (Figure 9) during the whole measurement program (later October 2014 to early March 2015) is filtered within the frequency band related to the 9–15 h period (frequency band covering the semi-diurnal variations), as shown in Figure 18. It is clear that there are low frequency variations of bottom density, which is associated with the higher saline water intrusion from Hecate Strait. It is found that the semi-diurnal baroclinic tides, as demonstrated by the large amplitudes of the band filtered density anomalies, is driven by the low frequency high saline water intrusion as seen in the November and December 2014 period.

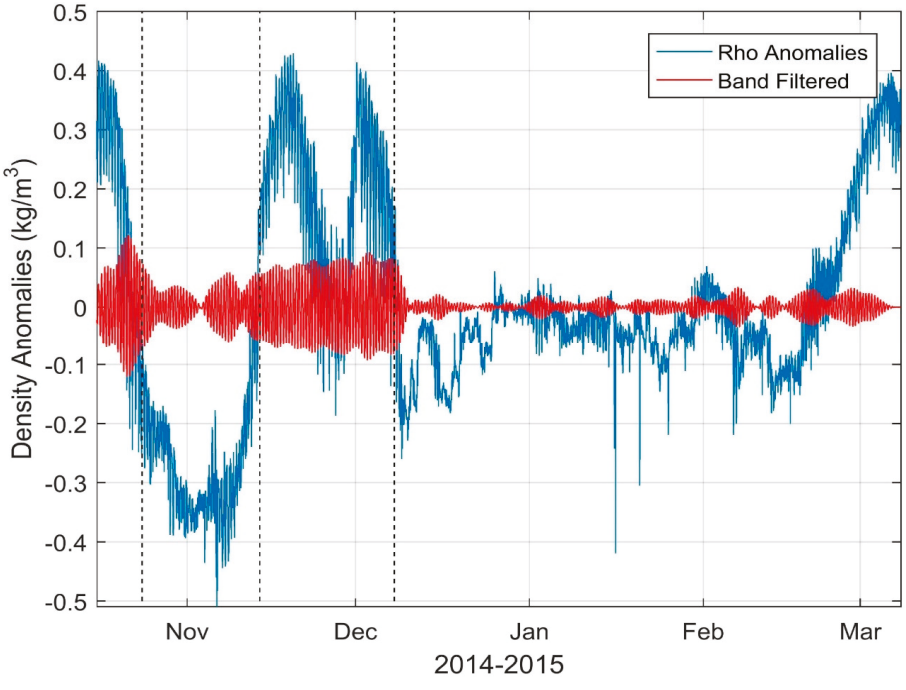

Figure 18. Time series of density (Rho, blue line) anomalies measured by the near-bottom CTD unit. The red line is the band (9–15 h) filtered result.

With the higher salinity and more dense water intrusion in Brown Passage, there is the potential for the semi-diurnal tidal currents to initiate internal waves/tides within the water column along the bottom bathymetry where incident angles or seabed slopes near the critical angle. The Brunt–Väisälä frequency gives an initial insight into the possibility of creating internal waves/tides. The forcing of the barotropic tide is also strong enough in Brown Passage to generate such internal tides so that the M2 tidal constituent can be intensified as shown in both the observed and modeled bottom currents. To better understand the dynamics of the internal tides, additional analysis requiring more extensive observational data sets are required.

5. Summary and Conclusions

Brown Passage is a deep (up to 200 m) ocean channel connecting the western offshore waters of Hecate Strait on the Pacific continental shelf with the eastern inland waters of Chatham Sound in Northern British Columbia, Canada. Recent research into this oceanic environment is motivated by studies of the possible use of this area for disposal at sea of dredged sediments arising from expansion of marine terminals in and around Prince Rupert Harbor in Chatham Sound. The ocean currents in Chatham Sound are highly variable due to a combination of forcing by the large tides within this area, winds, and large freshwater discharges from the Skeena and Nass Rivers. Chatham Sea is characterized by lower salinity near-surface waters on its eastern side due to the Skeena River inflow to Southern Chatham Sound [1]. More saline waters present on the western side of Chatham Sound result from the exchange through Brown Passage and other connecting channels with the higher salinity waters of Hecate Strait. A high-resolution 3D finite difference hydrodynamic model (COCIRM-SED) was developed to determine the tidal and wind-driven currents of this area [2], and then used to simulate the transport and deposition of sediments released from activities involving disposal at sea. The model results for ocean currents were found to be comparable with the two sets of ocean current observations at 15 and 98 m available for Brown Passage, obtained in 1991. Based on these results, Brown Passage was thought to be generally well mixed through the middle and lower parts of the water column.

The first modern oceanographic measurement program carried out to directly determine the near-bottom currents raised questions about the adequacy of the model results for the near-bottom currents in Brown Passage. Using moored bottom instruments operated from October 2014 to April 2015, near-bottom ocean currents at 3.5 m height above seabed were measured, as well as ADCP/DVS-derived current profile data for currents throughout the full water column. CTD profile measurements were also obtained during the deployment and recovery of the bottom-mounted instruments. The measured near-bottom currents were found to be considerably higher than the previous model-derived near-bottom currents. As a result, the COCIRM-SED model was modified and rerun, with the most important change being the use of the observed October 2014 water column density profile in place of the previous barotropic modeling approach. This change led to considerable improvements in the ability of the model to generate episodes of relatively strong currents in the bottom layers, which are shown to be in reasonably good agreement for the near-bottom and deeper ocean currents with the 2014–2015 measurement program, (the 99th percentile current speed can reach 40 cm/s at 181 m depth and 53 cm/s at 196 m water depth).

The inclusion of the resulting density stratification effects to previous oceanographic and sediment transport modeling [2] has improved the ability of the model to generate more realistic near-bottom currents, as shown by the comparison with observed currents at 181 m and 196 m. The power spectral density of the ocean currents has been calculated, and it is found that the energy of the baroclinic near-bottom flow is dominated by the semi-diurnal tidal frequency (2 cycles per day) in both model results and observations. Hence, the strong near-bottom flow is believed to be baroclinic semi-diurnal tidal currents (internal tides). It is suggested that the semi-diurnal baroclinic tides are influenced by the low frequency variations of the higher salinity/density water intrusions from Hecate Strait. The detailed mechanisms for generation of semi-diurnal internal tides within the study area requires additional analysis to identify potential source regions where the bathymetric bottom slope matches the vertical ocean density gradient in the form of the Brunt–Väisälä frequency. This finding is scientifically important to direct further numerical studies on the sediment resuspension from disposal at sea operations [19].

As indicated in Figure 17 (less than 0.2 cycles per day part), it should be noted that although the baroclinic model developed in this study can prognostically simulate the dynamics introduced by the water stratification in Brown Passage, the variability of lower frequency (e.g., the seasonal changes) of the stratification especially for the higher salinity water intrusion from the west (e.g., Hecate Strait) is not directly represented at the open boundary of the model. Beyond this qualitative study, the large-scale intrusions of higher density water entering Brown Passage need to be better represented

in the baroclinic model, especially for the low frequency variations. Future work will require an expanded model domain to cover not only Brown Passage, but also the outer shelf waters of Hecate Strait and Dixon Entrance. A larger model domain would incorporate the low frequency variability of the higher salinity water intrusion into Brown Passage, which could be related to underlying physical mechanisms, such as remote wind fording. An unstructured grid model is proposed for the future numerical modeling study to allow detailed representation of the complex small-scale bathymetric features of Brown Passage while operating with a manageable number of total grid elements over the much expanded model domain, so as to keep the computational requirements for the model to manageable levels.

Author Contributions: The individual contributions of authors to this article consist of: Conceptualization, Y.L. and D.B.F.; Data Collection and its Preliminary Analysis, T.M. and K.B.; Model Development and Validation, Y.L. and D.B.F.; Formal Analysis, Y.L.; Writing—Original Draft Preparation, Y.L.; Writing—Review & Editing, D.B.F.; Project Administration, D.B.F. and T.M.

Funding: The research presented in this article received no external funding. The 2014–2015 oceanographic measurements made in Brown Passage were funded by Pacific North West LNG through a contract between ASL Environmental Sciences Inc. and Stantec Consulting Ltd.

Acknowledgments: The assistance of ASL Environmental Sciences Inc. personnel, James Bartlett, Matthew Stone, Ryan Clouston, and Jeremy Lawrence, who contributed to the collection and preliminary processing of the oceanographic data, is acknowledged. We also acknowledge the contributions of Jianhua Jiang, formerly at ASL and presently at Alberta Energy Regulator (AER) to the early model development.

Conflicts of Interest: The authors declare no conflict of interest.

References

1. Lin, Y.; Fissel, D.B. The ocean circulation of Chatham Sound, British Columbia, Canada: Results from numerical modelling studies using historical datasets. *Atmos. Ocean* **2018**, *56*, 129–191. [CrossRef]
2. Jiang, J.; Fissel, D. Modeling Sediment Disposal in Inshore Waterways of British Columbia, Canada. In Proceedings of the International Conference of Estuarine and Coastal Modeling, St. Augustine, FL, USA, 7–9 November 2011. [CrossRef]
3. Lucas, B.G.; Verrin, S.; Brown, R. (Eds.) *Ecosystem Overview: Pacific North Coast Integrated Management Area (PNCIMA)*; Canadian Technical Report; Appendix A: Geology; Fisheries and Aquatic Sciences: Sidney, BC, Canada, 2007; p. 2667.
4. Trites, R.W. The oceanography of Chatham Sound, British Columbia. *J. Fish Res. Board Can.* **1956**, *13*, 385–434. [CrossRef]
5. Hannah, C.G.; LeBlond, P.H.; Crawford, W.R.; Budgell, W.P. Wind-driven depth-averaged circulation in Queen Charlotte Sound and Hecate Strait. *Atmos. Ocean* **1991**, *29*, 712–736. [CrossRef]
6. Ballantyne, V.A.; Foreman, M.G.G.; Crawford, W.R.; Jacques, R. Three-dimensional model simulations for the north coast of British Columbia. *Cont. Shelf Res.* **1996**, *16*, 1655–1682. [CrossRef]
7. Flather, R.A. A tidal model of the northeast Pacific. *Atmos. Ocean* **1987**, *25*, 22–45. [CrossRef]
8. Foreman, M.G.G.; Henry, R.F.; Walters, R.A.; Ballantyne, V.A. A finite element model for tides and resonance along the north coast of British Columbia. *J. Geophys. Res.* **1993**, *98*, 2509–2531. [CrossRef]
9. Cummins, P.F.; Oey, L.Y. Simulation of barotropic and baroclinic tides off northern British Columbia. *J. Phys. Oceanogr.* **1997**, *27*, 762–781. [CrossRef]
10. Foreman, M.G.G.; Crawford, W.R.; Cherniawsky, J.Y.; Henry, R.F.; Tarbotton, M.R. A high-resolution assimilating tidal model for the northeast Pacific Ocean. *J. Geophys. Res. Ocean.* **2000**, *105*, 28629–28651. [CrossRef]
11. Jiang, J.; Fissel, D.B.; Topham, D. 3D numerical modeling of circulations associated with a submerged buoyant jet in a shallow coastal environment. *Estuar. Coast. Shelf Sci.* **2003**, *58*, 475–486. [CrossRef]
12. Jiang, J.; Fissel, D.B. 3D Hydrodynamic Modeling of Sediment Dynamics on Roberts Bank Fraser River Foreslope, Strait of Georgia, Canada. In Proceedings of the Ninth International Conference on Estuarine and Coastal Modeling, Charleston, SC, USA, 31 October–2 November 2005; pp. 806–823.

13. Jiang, J.; Fissel, D.B.; Borg, K. Sediment plume and dispersion modeling of removal and installation of underwater electrical cables on Roberts Bank, Strait of Georgia, British Columbia, Canada. In Proceedings of the Tenth International Conference on Estuarine and Coastal Modeling, Newport, RI, USA, 5–7 November 2007; pp. 1019–1034.
14. Jiang, J.; Fissel, D.B. Applications of 3D Coastal Circulation Numerical Model in Assessing Potential locations of Installing Underwater Turbines. In Proceedings of the Eleventh International Conference on Estuarine and Coastal Modeling, Seattle, WA, USA, 4–6 November 2009; pp. 478–493.
15. Foreman, M.G.G. Manual for Tidal Heights Analysis and Prediction (Pacific Marine Science Report 77-10), Institute of Ocean Sciences, Patricia Bay. 1977. Available online: http://www.dfo-mpo.gc.ca/Library/54866.pdf (accessed on 10 October 2018).
16. Smagorinsky, J. General circulation experiments with the primitive equations: I. the basic experiment. *Mon. Weather Rev.* **1963**, *91*, 99–164. [CrossRef]
17. Mellor, G.L.; Yamada, T. Development of a turbulence closure model for geographical fluid problems. *Rev. Geophys.* **1982**, *20*, 851–875. [CrossRef]
18. Orlanski, I. A simple boundary condition for unbounded hyperbolic flows. *J. Comput. Phys.* **1976**, *21*, 251–269. [CrossRef]
19. Fissel, D.B.; Lin, Y. Modeling the transport and fate of sediments released from Marine Construction Projects in the coastal waters of British Columbia, Canada. *J. Mar. Sci. Eng.* **2018**, *6*, 103. [CrossRef]

Journal of
Marine Science and Engineering

MDPI

Article

Tidal Datums with Spatially Varying Uncertainty in North-East Gulf of Mexico for VDatum Application

Liujuan Tang [1,2], Edward Myers [1,*], Lei Shi [1], Kurt Hess [1], Alison Carisio [3,4], Michael Michalski [3], Stephen White [5] and Cuong Hoang [1]

1 Coast Survey Development Laboratory, NOAA, Silver Spring, MD 20910, USA; liujuan.tang@noaa.gov (L.T.); l.shi@noaa.gov (L.S.); kurt.hess@noaa.gov (K.H.); cuong.hoang@noaa.gov (C.H.)
2 Earth Resources Technology, Laurel, MD 20707, USA
3 Center for Operational Oceanographic Products and Services, NOAA, Silver Spring, MD 20910, USA; ajhayes1@gmail.com (A.C.); michael.michalski@noaa.gov (M.M.)
4 Lynker Technologies, Boulder, CO 80301, USA
5 National Geodetic Survey, NOAA, Silver Spring, MD 20910, USA; stephen.a.white@noaa.gov
* Correspondence: edward.myers@noaa.gov; Tel.: +1-240-847-8256

Received: 30 July 2018; Accepted: 3 October 2018; Published: 11 October 2018

Abstract: We conducted a VDatum-spatially varying uncertainty study for the North-East Gulf of Mexico. The newly developed tide model incorporated the latest available National Ocean Service (NOS) bathymetry survey data and National Geodetic Survey (NGS) shoreline data, and the datum products reflected the updated tidal datum data from the Center for Operational Oceanographic Products and Services (CO-OPS). A gridding technique based on the wavelength of long waves in the deep ocean was applied to improve model efficiency. In this study, we highlight the creation of the tidal datum products and associated spatially varying uncertainty, which was developed by blending the model results, observations, and measurement errors together using a spatially varying uncertainty method based on a variational approach. The study found that model errors, measurement errors, and lack of observations can contribute to large uncertainty in the tidal datum products. The need for high quality bathymetry data in coastal areas is essential for reducing model error. As for the large uncertainty due to lack of observations or large measurement error, this can be improved by placement of new observations with high precision. Compared to a single uncertainty value, the spatially varying uncertainty provides more accurate representation of the uncertainty for the tidal datum products in VDatum. The uncertainty results will be used to help with decision-making on placement of new tide gauges to further reduce the uncertainty in the VDatum products.

Keywords: tides; tidal datums; VDatum; spatially varying uncertainty (SVU); north-east Gulf of Mexico

1. Introduction

Merging bathymetric and topographic datasets across the land–water interface to create seamless data in the coastal zone is an essential requirement for the protection, management and study of coastal zone processes [1]. The need for accurate data in the coastal zone is increasing and many federal agencies, universities, state and local governments, and other organizations have been collecting high-resolution bathymetry, topography, and shoreline data [2]. Traditionally, data collections by different groups have been operated independently, resulting in data being referenced to different vertical datums. For example, the U.S. Geological Survey (USGS) National Elevation Dataset topographic data are referenced to ellipsoid-based and/or orthometric datums [3], while National Oceanic and Atmospheric Administration (NOAA) National Ocean Service (NOS)'s bathymetry survey

and shoreline data are referenced to tidal datums [4]. A pre-requisite for the integration process is to properly reference all such data to a common vertical datum.

To address this requirement, a number of countries in the world are in the process of developing/updating national vertical transformation projects/tools, such as VDatum in the U.S. [5], Vertical Offshore Reference Frames (VORF) in the U.K. [6], BATHYLLI in France [7], etc. [8] These vertical transformation tools utilize tide stations observations and hydrodynamic modeling to evaluate the difference between tidal datums and the geoid [8].

The VDatum vertical datum transformation software is an outcome of the national VDatum project in the U.S., a joint effort of the tri-office VDatum team of NOAA's Office of Coast Survey (OCS), National Geodetic Survey (NGS), and Center for Operational Oceanographic Products and Services (CO-OPS). The primary purpose is to transform geospatial data vertically between three major classes of vertical datums: tidal, orthometric, and ellipsoid-based datums. At present, VDatum includes 36 different vertical datums. The goal is to have complete coverage of U.S. coastal waters from the landward (i.e., navigable) reaches of estuaries and charted embayments out to 75 nmi offshore [9].

Since its pilot project in Tampa Bay in 2001 [10], VDatum has been created for the continental U.S., Puerto Rico, and the U.S. Virgin Islands. VDatum applications are in development for new areas in Alaska and are also being updated for previous regions to reduce uncertainty. Since the release of VDatum, many applications have benefited from it, including storm surge simulations, tsunami prediction, sea level rise studies [2], ecosystem modeling, and coastal zone management. VDatum also enhances the capabilities of technologies such as kinematic Global Positioning System (K-GPS) for vertical referencing of hydrographic survey depths, use of topographic and bathymetric LiDAR for determining mean lower low water (MLLW) and mean high water (MHW) shorelines, and development of digital elevation models (DEMs).

In this study we focus on tidal datums caused by astronomical tides for VDatum software. VDatum includes a class of seven tidal datums: mean higher high water (MHHW), MHW, mean low water (MLW), MLLW, mean tide level (MTL), diurnal tide level (DTL), and mean sea level (MSL). CO-OPS' coastal water level stations have been providing these tidal datums data, which are derived from time series of water level data at 6 min intervals. For CO-OPS' long term control stations, the full 19 year epoch period are used for the computation of the datums [11]. For example, MSL is computed as the arithmetic mean of hourly water observations over the National Tidal Datum Epoch (NTDE), which presently is the 1983–2001 NTDE. All other shorter period subordinate gauges rely on simultaneous comparisons between their data and the epoch control station. The differences between these two stations are applied to the control station datum to acquire a 19 years' equivalent at the subordinate stations. This helps to mute out the short period meteorological and oceanographic effects which are expected to be experienced by both the control and the subordinate stations.

In general, tidal datum fields vary over horizontal space. Tidal datum data at stations are referenced to measured local water levels and should not be extended into areas having differing oceanographic characteristics. To resolve the spatially varying nature of the tidal datums in between observation locations, hydrodynamic models and spatial interpolation techniques have been employed for each VDatum application that simulate the tidal propagation characteristics in the region of interest. In order to merge all of the individual VDatum applications together to form a continuous national VDatum product, a consistent methodology for computing the tidal datums has been adopted for all region-specific VDatum applications [9]. The approach consists of the following four major steps [2,9]:

(1) First use the bathymetric and coastline data to develop a grid to be used by the hydrodynamic model.
(2) Next calibrate a hydrodynamic model to best simulate the observed tidal datum characteristics for the region.
(3) Then correct the model-data errors using a spatial interpolation technique.
(4) Finally provide the corrected modeled datums (i.e., datum products) on a structured grid of points to be used by the VDatum software.

Following the above methodology, 38 region-specific VDatum applications have been developed for U.S. coastal regions, among which three of them cover the Gulf of Mexico coast [12–14].

For the applications developed prior to 2016, the model-data corrections were made using the Tidal Constituent and Residual Interpolation (TCARI) tool developed by Hess et al. [15,16]. TCARI is a first-order deterministic spatial interpolation tool based on solution of Laplace's equation. The errors between the model results and the CO-OPS station data are interpolated throughout the domain to create an error field for each of the tidal datums. The error field is then used to correct the model results to create a datum field that matches the station data at those locations [17]. The TCARI approach produces a single-value uncertainty estimate in the tidal datums for each model region [18].

To provide a more accurate representation of the uncertainty in each model region, Shi and Myers developed a new statistical interpolation method, namely the spatially varying uncertainty (SVU) method, for VDatum applications in 2016 [19]. It was derived from the variational principle to calculate the corrected tidal datums by blending the model results, observations, and measurement errors together. They show that the new interpolation approach not only reduces the bias and errors, but also produces a spatially varying uncertainty. The uncertainty results can also provide important guidance for decision-making on placement of new tide gauges to further reduce the uncertainty in the VDatum products. This spatially varying uncertainty method has become the new standard for use for developing VDatum applications since then.

Here we apply Shi and Myers' method to study spatially varying uncertainty for the north-east Gulf of Mexico (NEGOF) VDatum region (Figure 1). This is part of an effort to update the three VDatum regions in the Gulf of Mexico in the next few years. The SVU study for the Texas VDatum has been completed nearly at the same time and will be published in a separate paper. The Gulf of Mexico coasts have been impacted frequently and severely by past hurricanes, resulting in changes to the coastline and nearshore bathymetry [20]. This can induce uncertainty in the tidal datums in the area. The SVU helps to identify locations where new gauges would be beneficial in reducing uncertainty in VDatum. Once new data is collected, it will then be merged with the model to do a new VDatum update for this region. The same process will be used as we update other VDatum regions as well.

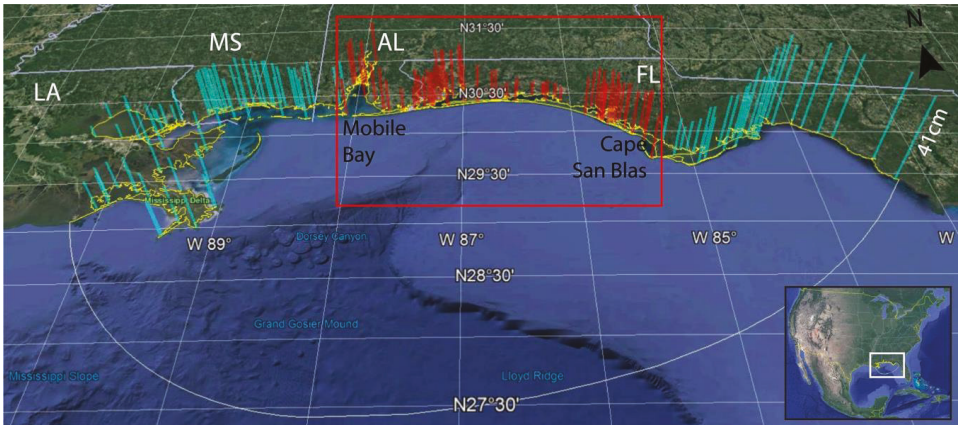

Figure 1. VDatum region (red box) and computational domain for the new tide model for the north-east Gulf of Mexico. Red and cyan bars represent the observed MHW at tide stations within and outside the VDatum region, respectively. As a reference, the first bar from the east represents MHW of 0.41 m. Yellow and white lines are the shoreline and open boundary of the computational domain, respectively. White box indicates the location of NEGOM. Background images are from Google Earth.

The north-east Gulf of Mexico VDatum region is indicated as the red box in Figure 1. It extends from Mobile Bay, Alabama, in the west to Cape San Blas, Florida, in the east. The region is featured

with six bays and relatively flat coastline at the open coast. The bathymetry slope is gentle form shoreline to 40 m water depth and then drops quickly to more than 2000 m deep. The tidal pattern in the region is dominated by diurnal tides [21]. The first version of the tidal model for the region was developed by Dhingra et al. in 2008 [12]. We refer it as the 2008 tidal model in this paper. Since then, new observations on tidal datums and bathymetry survey data have become available. Given the amount of new data, we have redeveloped the tide model to reflect the new information and coverage as best possible.

The rest of this article is organized as follows: Section 2 briefly describes the method; Section 3 presents the data, grid development, and model setup for the new tide model; Section 4 discusses the modeling results, including datum validation, associated spatially varying uncertainty, applications, and lessons learned; summary and conclusion are provided in Section 5.

2. Method

The hydrodynamic model used for this study is the two-dimensional, depth-integrated version of the Advanced Circulation (ADCIRC) model [22,23]. It utilizes the fully non-linear shallow water equations with hydrostatic pressure and Boussinesq approximations. It solves the continuity and the non-conservative momentum equations for free surface elevation and the depth-averaged velocity components. The equations are discretized: horizontally in space using the finite element method with three-node linear triangles; and in time using the finite difference method, the implicit Crank–Nicolson approximation with second order accuracy. The non-linear terms are evaluated explicitly. The ADCIRC code allows a variety of users specified input parameters. Here we used the fully non-linear form of the equations, which includes non-linear bottom friction, finite amplitude, and convection terms. The ADCIRC model has been parallelized using domain decomposition, a conjugate gradient solver, and Message Passing Interface (MPI) based message passing. This parallel version of the code was compiled and run on NOAA's Jet high performance computing system in Boulder, Colorado. The ADCIRC model has been used in previous VDatum areas [12–14], taking advantage of highly flexible, irregularly spaced grids. Numerous studies have shown this model to be robust throughout the Eastern North Atlantic and Gulf of Mexico regions [24,25], and the West Coast [26].

The modeled time series of water surface elevation outputs from the ADCIRC model at each node are then used to tabulate the higher-high, lower-high, higher-low, and lower-low waters, from which tidal datums could be computed. The method for extracting the highs and lows is based on the approach used by CO-OPS [21], which is for analysis of water level measurements at tide stations. The original code is in the C language in the CO-OPS Data Processing and Analysis System (DPAS). The modeled water surface elevation is in general less noisy comparing to the measurements at tide stations. For VDatum, the new Fortran program levels.f (or lv8j.f) was written to duplicate the CO-OPS methodology [9,27]. The program is based on examination of the original C language computer program and related texts, and on discussions with various members of CO-OPS [9]. Seven tidal datums (MHHW, MHW, MSL, MTL, DTL, MLW, and MLLW) are computed based on the highs and lows [21]. The analysis is repeated for time series of water surface elevation at every node in the ADCIRC mesh. We refer to the model datums obtained here as the original model datums (e.g., before correction), to distinguish from the final datum products (after correction with observations). The original model datums are compared to the observations to evaluate the model error.

The next step is to apply the spatially varying method in [19] to the original model datums. The method defines the cost function of the tidal datum field f as:

$$J(f) = \frac{1}{2}(f - f_m)^T P^{-1}(f - f_m) + \frac{1}{2}(f_0 - Hf)^T \left(W^{-\frac{1}{2}}\right)^T R^{-1} W^{-\frac{1}{2}}(f_0 - Hf) \quad (1)$$

where f is a size $(n \times 1)$ vector of the discrete tidal datum product to be determined, f_m is the $n \times 1$ modeled tidal datum field, f_0 is the $m \times 1$ observed tidal datums vector at stations, n is the total node number, m is the total number of tide stations, H is the $m \times n$ interpolation matrix projecting the

modeled field to the observed data locations, P is the $n \times n$ modeled error covariance matrix, R is the $m \times m$ observed error covariance matrix, and W is a $m \times m$ diagonal weight matrix that adjusts how much the final product f deviated from the uncertainty of the observed values at the station locations. Both the observed tidal datums and error standard deviations are provided by CO-OPS [28]. The weight matrix W is used to control how close the analysis field f is to the observations at the station locations. The constraint that the VDatum technical team adopted for statistical interpolation is that the discrepancy between the analysis field and the observations at all tide stations should be equal to or less than 1 cm or the CO-OPS' error value, whichever is less. The weight matrix W will be determined through iteration following this predetermined constraint.

By minimizing the cost function $J(f)$ in Equation (1), we obtain the tidal datum product f:

$$f = \arg\min_{f \in \Re^n} J(f) \tag{2}$$

The uncertainty of f then can be estimated as the posterior error covariance matrix Pa:

$$P_a = Var(f) = (I - GH)P(I - GH)^T + GRG^T \tag{3}$$

where $G = PH^T\left[W^{1/2}R\left(W^{1/2}\right)^T + HPH^T\right]^{-1}$ is the gain matrix and I is the identity matrix [19]. The datum products f and the spatially varying uncertainty Pa computed from Equations (2) and (3) will be used by the VDatum software.

The spatially varying method produces f and Pa on the same triangular grid as the ADCIRC model. Yet the VDatum software requires regularly spaced grids called "marine grids" that contain the datum information at the water nodes and null information at the land nodes [9]. Digitized coastline data are used to determine which points in this marine grid are water and which are land. Points located within water, or within a distance of approximately one-half a marine grid element size of water, are set to water. The f and Pa based on ADCIRC model grid are then populated in to the marine grids.

The final tidal datum products as represented on the VDatum marine grids must be checked in several ways, including (1) a validation test at station locations, (2) a continuity test at common boundaries, (3) an overlapping test, and (4) a polygon test [9]. For the validation test, the marine grid files are checked against observations to confirm that the datums approximately match at the tide stations. The error at each station should be no greater than 1 or 2 cm. When there are adjacent tidal datum grids, there must be a check for continuity of values across the common boundaries (e.g., continuity test). In some regions, the tidal marine grids can actually overlap, resulting in ambiguity in the selection of the correct grid [9]. Therefore, the use of a bounding polygon is necessary. Given a latitude–longitude point in the overlap region, a check is made of whether the point falls within a specific bounding polygon; if so, the marine grid for that region can be used. If not, additional polygons are checked. The overlapping test is to ensure the bounding polygons do not overlap with each other. The polygon test is to check the bounding polygon to ensure it is completely inside the marine grid [9].

Once the tidal datums f and SVU (Pa) in the marine grids pass the above tests, they will be provided to NGS to incorporate into the VDatum software. In the next section, we will show the details in data and grid development.

3. Data and Grid Development

3.1. Study Area and Tidal Datum Data

The VDatum region in this study extends from Mobile Bay, Alabama, in the west to Cape San Blas, Florida, in the east (from -88.0857° E to -85.2811° E). There are 83 NOAA CO-OPS tide stations in the region. Figure 1 shows the station locations and observed MHW datum (the red bars). The height of

each bar represents the MHW at the station. As will be discussed in Section 4, stations in the VDatum region show a three-group pattern, which is correlated to their geographical locations. Group 1 stations are located either on the open coast or in less protected bays. This group has the largest tidal datums in the VDatum region, with MHW around 0.18–0.25 m. Group 2 includes the six stations inside Perdido Bay, with MHW around 0.12 m. The third group has the 8 stations inside the Choctawahatchee Bay, with the smallest MHW around 0.08 m. The tidal pattern in the VDatum region is dominated by diurnal tides.

To reduce the boundary effect, we expanded the model domain boundary away from the center of the VDatum region. The domain was extended approximately 5/6 of the width of the VDatum coverage region both to the east and to the west (Figure 1). This introduced 99 additional NOAA tide stations in the computational domain, which are plotted as the cyan bars in Figure 1. The stations located near the east land boundary in Florida have the largest tidal datum in the domain, with MHW around 0.50 m. The tidal pattern in the area is dominated by mixed tides. The tidal datums at the stations to the west are similar to those of Group 1 in the VDatum region except the four stations located inside Lake Pontchartrain, with smaller MHW values around 0.08 m. The tidal pattern in the area is dominated by diurnal tides.

Altogether there are 182 tide stations in the computational domain. The datum measurement error (root mean square error, or RMSE), are available for 144 stations. The average RMSE is 1.7 cm for the 144 stations, with a 2.9 and 3.4 cm maximum within and outside VDatum region, respectively. RMSE are not available for 38 stations due to insufficient data in CO-OPS' database. Those measurements were mainly from the early 1970s and predated the database (personal communications with CO-OPS' M. Michalski, 2017). For details on how the RMSE for tidal datums were computed for CO-OPS stations, please see [29].

3.2. Shoreline and Bathymetry Data

The MHW coastline was used as the land boundary to create the unstructured grid for the tidal model. It also defines the extent of the VDatum marine grid. The MHW shoreline from NOAA's Continually Updated Shoreline Product (CUSP) data are considered the most recent and accurate shoreline data available [30]. The horizontal datum is the North American Datum of 1983 (NAD83). The data has scales between 1:1000–1:24,000. Individual national shoreline projects and high-resolution LiDAR-derived shoreline were merged to form the framework of the CUSP data [30]. In this study, the MHW shorelines have been updated with all available CUSP data except for the Louisiana coast to the west of the VDatum region, where simplifications are made to the marsh land coast based on the shorelines used by the 2008 VDatum model and the tide model for Eastern Louisiana and Mississippi [13]. For locations where the CUSP data are unavailable, the MHW shoreline from the NGS Vector Shoreline Data [31] are used. Shoreline data were plot over Google Earth Satellite imagery to examine the discrepancy. Corrections were made to certain areas without CUSP data coverage where the shoreline appears to be incomplete or inaccurate. The final coastline used for model development is illustrated as the yellow line in Figure 1.

Table 1 summarizes the bathymetry data used to compile the model grid. Figure 2a shows the spatial extent of major data sources and data priority. In general, the new data sources superseded the old sources when they overlapped. Data are from several primary sources/agencies:

(1) NOAA's NOS bathymetry survey and Electronic Navigational Chars (ENC) data;
(2) National Centers for Environmental Information's (NCEI) Digital Elevation Models (DEMs);
(3) The U.S. Army Corps of Engineers (USACE) survey data;
(4) USGS DEMs.

The NOS sounding data possess the most coverage in the domain. It includes surveys conducted between 1885 and 2016. The datums are referenced to either MLW or MLLW, depending on the years of data collection. Five high-resolution DEMs (1/3 arc sec) from NCEI are available for the region as shown in Figure 2a [32–36]. The Biloxi and Panama City DEMs were developed in 2008, while the Mobile

Bay and New Orleans DEMs were released in 2011. The Southern Louisiana DEM was developed in 2010. These DEMs contain some LiDAR bathymetry and USACE survey data for some of the rivers or intracoastal waterways that are not included in the NOS data. The USGS 10 m Grand Bay DEM based on MLLW developed in 2015 was also used in the study [37]. Data values were converted, when necessary, to the NAD83 horizontal datum and the MSL vertical datum using VDatum software.

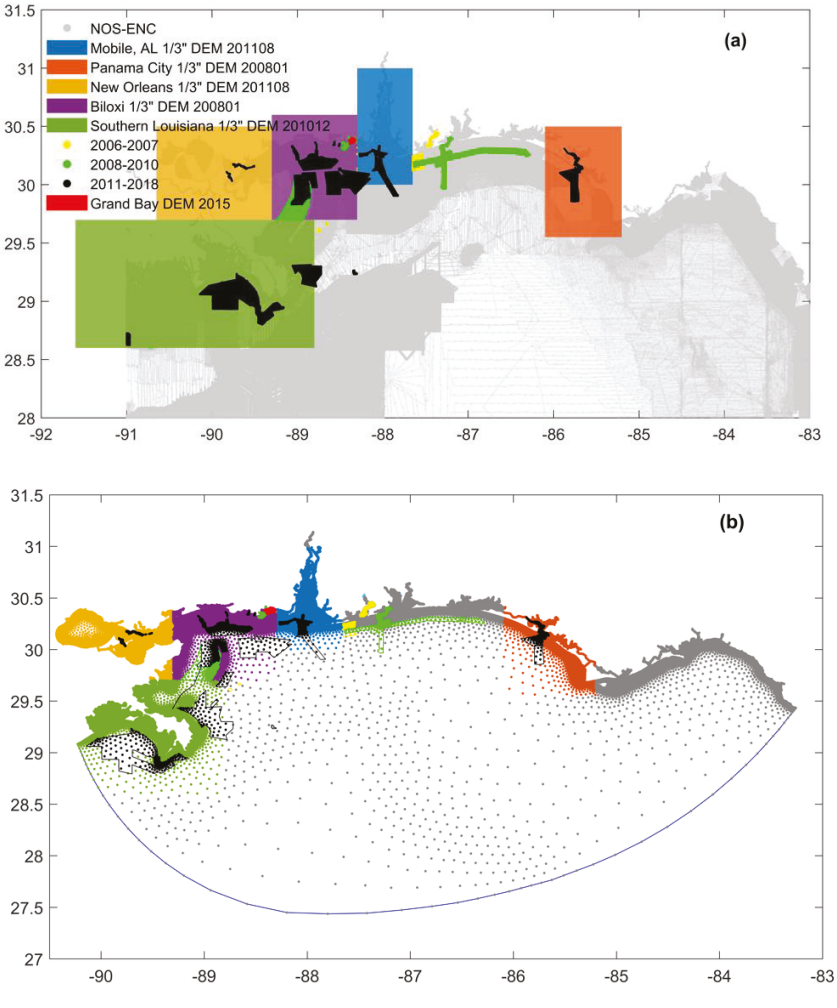

Figure 2. (**a**) Major bathymetry data sources overview. Data priority is based on survey date. The more recent data, the higher data priority. (**b**) Bathymetry data sources at mesh nodes.

3.3. Grid Development

As illustrated in Figure 1, the mesh domain was defined by the coastline (i.e., as the land boundary) and offshore open boundary. The offshore open boundary was extended to locations with depths greater than 3000 m as well as with relatively flat bottom. The VDatum region was centered in the domain. The mainland boundary to the west was similar to the 2008 tidal model while the eastern boundary was extended further east to reduce the boundary effect to the VDatum region.

Table 1. Bathymetry data source overview.

Data Sources	Year	Datum Vertical	Horizontal
NOS Bathymetry Survey	1872–2016	MLLW/MLW	NAD83
ENC	2005	MLLW	NAD83
NCEI Mobile Bay 1/3″ DEM	2011	MHW	NAD83
NCEI New Orleans 1/3″ DEM	2011	MHW	NAD83
NCEI Southern Louisiana 1/3″ DEM	2010	MHW	NAD83
NCEI Biloxi 1/3″ DEM	2008	MHW	WGS84
NCEI Panama City 1/3″ DEM	2008	MHW	WGS84
USGS Grand Bay 10 m DEM	2015	MLLW	NAD83
NCEI Northern Gulf 1″ DEM		MHW	NAD83
USACE Escambia River Survey	2015	MLLW	FL State Plane
[1] Aucilla River Survey	2014	NAVD88	NAD83 903 North
[1] Econfina River Survey	2014	NAVD88	NAD83 903 North
[2] Wakulla River Segment Survey	2015	Unknown	WGS84

[1] Provided by Land & Sea Surveying Concepts, Inc. and Suwannee River District Management District. [2] Data provided by Howard T. Odum Florida Springs Institute [38].

The grid development includes two main processes: (1) mesh generation and (2) water depth interpreting based on data priority. The mesh was generated by using the Surface-water Modeling System (SMS) software [39] with the size function approach. A size function is simply a collection of scatter points (in a scatter data set) that define element resolutions in different portions of the domain. It is an effective approach since it can assign high resolution only to areas that are needed, such as very shallow areas (to better resolve the non-linear wave dynamics), and coastline with high curvatures or areas with sudden changes in depth (to give a better representation of local geometry and bathymetry). We apply different criteria for defining the size function for deep ocean, nearshore, and shoreline respectively.

In the deep ocean, the dynamics of long waves are essentially governed by the shallow water approximations. That is to say, the propagation speed of tides can by approximate by $\sqrt{g\vec{d}}$, where d is the depth of the ocean and g is the acceleration due to gravity. In the study, we used two parameters, wave length (L) and distance to shoreline (D), to control the size function (s). The initial resolution s_0 was set to 10 points per wave length, $s_0 = L/10 = T\sqrt{g\vec{d}}/10$, where T is the wave period. Here we use $T = 3$ h to be on the conservative side, comparing to the typical tidal wave periods of 12 h or longer. Next we adjusted the resolution based on distance to shore based on the ratio of D to a reference distance D_{ref}: $s = s_0\ D/D_{ref}$. In this way, for two points at the same water depth, the one closer to shore has a higher resolution. The reference distance D_{ref} can vary for different ocean depth. We used maximum offshore distances as D_{ref} at various depth contours. Here we give an example on how to generate the size function along the 1000 m depth contour. First we developed a DEM on a rectangular grid based on the bathymetry data. Next we extracted the points along the 1000 m contour line, computed D for all points along the contour, and used $D_{ref} = \max(D)$ at $d = 1000$ m. The process was repeated for different depth contours to obtain the size functions in the deep ocean.

For shallow areas and near the coastline, higher resolutions were assigned manually in SMS. We applied 60 m (or approximately 2-arc-sec) resolution for narrow breakwater entrances, 100–200 m for natural bay entrances as well as along the coastline inside bays within the VDatum region, 400 m for the relatively straight open coastline within or near the VDatum region, and 800 m for coastline areas far away from the VDatum region.

In order to provide good transition from the deep ocean to the coastline, the size function needs to be smoothed so the values (resolutions) do not change too quickly. SMS provides a toolbox to perform the smoothing task. However, some areas still need manually smoothing in addition. Such areas include locations where the open boundary connects to the mainland boundary, and narrow entrances to bays or rivers. Examples in [40] show how smoothing can enhance the poor transition from the open boundary to the mainland boundary and, therefore, improve mesh quality.

Once the model mesh was generated, the next process was to interpolate water depths onto mesh nodes based on data priority. In order to setup priority, the bathymetry data were grouped as shown

in Figure 2a. Each color represents a group of data at a certain priority. The NOS survey data up to 2005 are in gray, representing the based layer of dataset which were also used to develop the 2008 tide model. NOS survey data from 2006 to 2016, which represents the new bathymetry data since the development of the 2008 tide model, were divided into three groups in yellow, green, and black colors in Figure 2a. Each group contains data subsets from different hydrographic surveys. The five filled boxes indicate the coverage of the five NCEI DEMs from 2008–2012. A boundary polygon was then developed for each group or subset. Data priority based on survey date was assigned to each boundary polygon. In general, the more recent data superseded the previous data when they overlapped.

Once boundary polygons and priority are set for all data, the mesh nodes within the boundary polygon of highest priority were then assigned a water depth value using the nearest data point from the dataset. The nearest point selection can avoid using points inside the bay/breakwaters for selecting depth for nodes outside the bay/breakwaters where the boundary polygon is in a complex shape [40]. Figure 2b displays the data sources at the mesh nodes. Figure 3 illustrates the final model grid overlapped on Google Earth. Color indicates water depth. The resolution ranges from 46 km at the open ocean boundary down to 9 m in certain sections of narrow rivers. The grid has 216,155 nodes and 374,318 qelements. Figure 4 shows high resolution applied to the six inlets in the VDatum region. The inlets to Perdido Bay, Choctawahychee Bay, and Panama City have two breakwaters which further narrow the width at the entrance. Those inlets and breakwaters limit the tidal energy that can propagate into the bays.

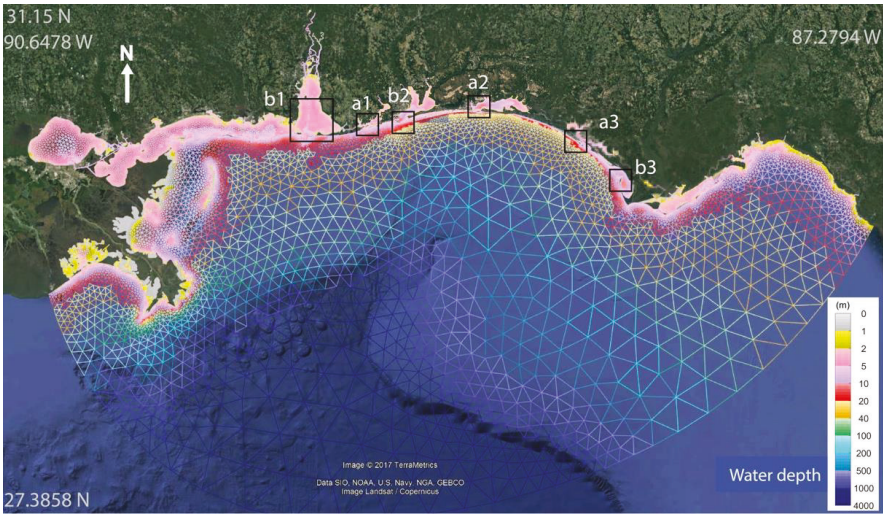

Figure 3. The newly developed tidal model grid for north-east Gulf of Mexico. Colors indicate water depth in meter. See Figure 4 for the close-ups in the boxes. Background image is from Google Earth.

Table 2 summarize the mesh properties. Compared to the 2008 mesh, the new mesh increases 88% and 73% in coverages on shoreline length and computational domain, respectively. However, the total node number increases only by 12%. This is partially due to the 96% decreas in nodes at depths greater than 20 m. Figure 5 compares the mesh and histograms between the 2008 and the new models. The two meshes have similar node distributions spatially (Figure 5 panels a2–a3 and b2–b3). However, the distributions along water depths are quite different (Figure 5 panels a1 and b1). The 2008 mesh has a relatively uniform distribution in shallow water (Figure 5(a1)) while the new mesh increases nodes sharply with decreasing water depths (Figure 5(b1)). So the new mesh represents the shallow bathymetry features more effectively. Note the nodes in deep water account only for 0.8%

of the total nodes (Table 2). That is to say, we put 99.2% of the nodes in shallow water to better resolve the wave dynamics nearshore.

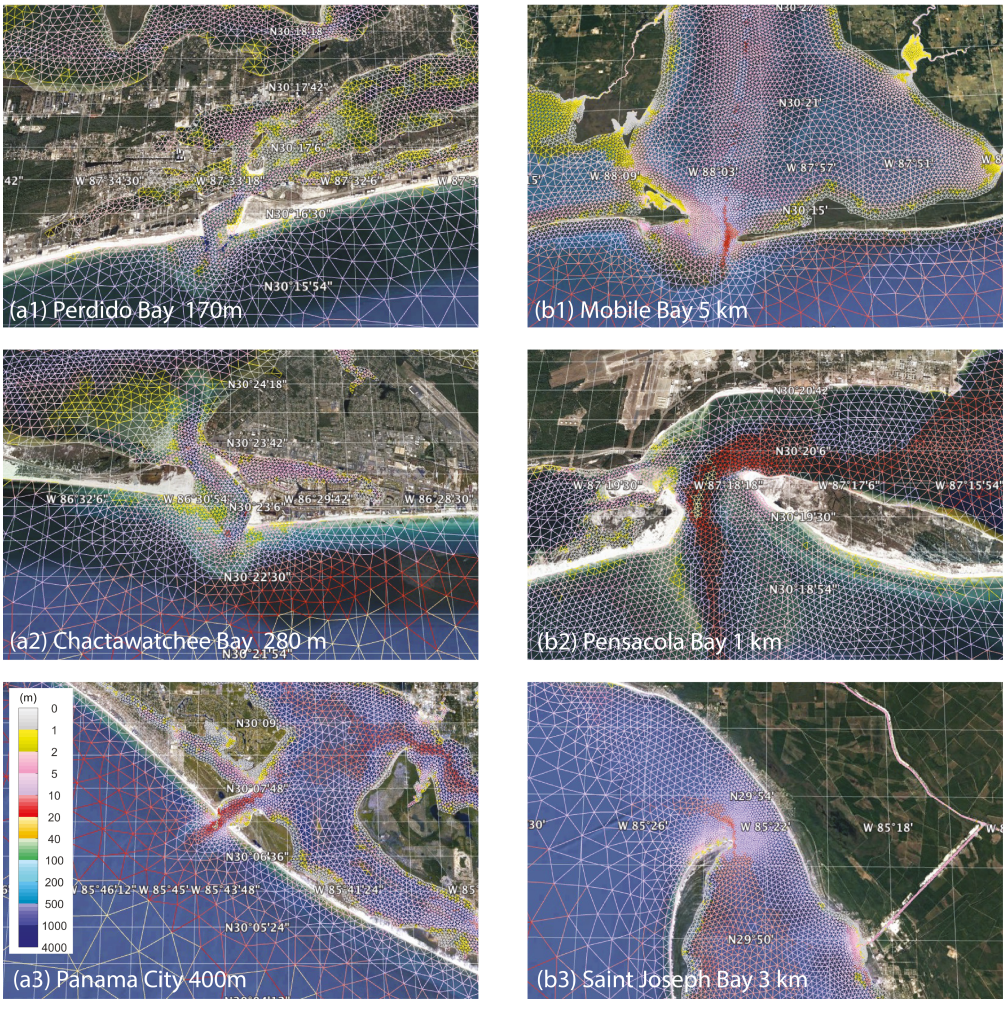

Figure 4. High resolution applied at six inlets to Bays in VDatum region. (**a**) Three narrow inlets with breakwaters. (**b**) Three nature inlets. See Figure 3 for locations.

Table 2. Properties of the 2008 and the newly-developed tide model girds.

Mesh Properties	2008	New Mesh	Increase in %
Shoreline length (km)	3979	7482	88%
Area (km^2)	79,474	137,751	73%
Element number	367,019	374,318	2%
Node number	192,889	216,155	12%
Node number w/depth >20 m (percentage to total nodes)	40,545 (21%)	1777 (0.8%)	−96%
Node number w/depth 10–20 m	28,312	9721	−66%
Node number w/depth <10 m (percentage to total nodes)	124,091 (64%)	205,095 (95%)	65%

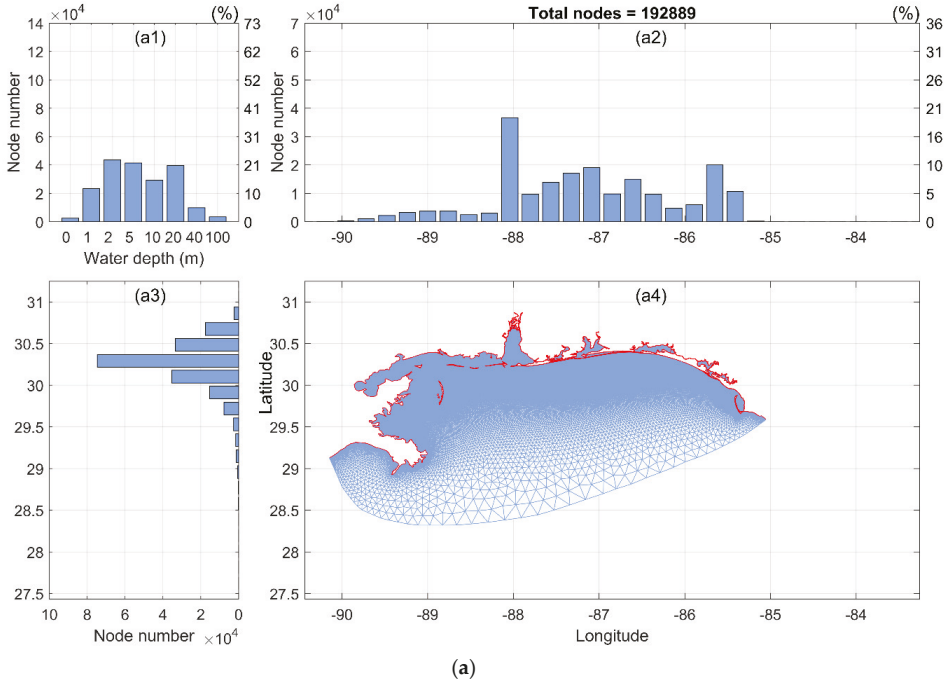

(**a**)

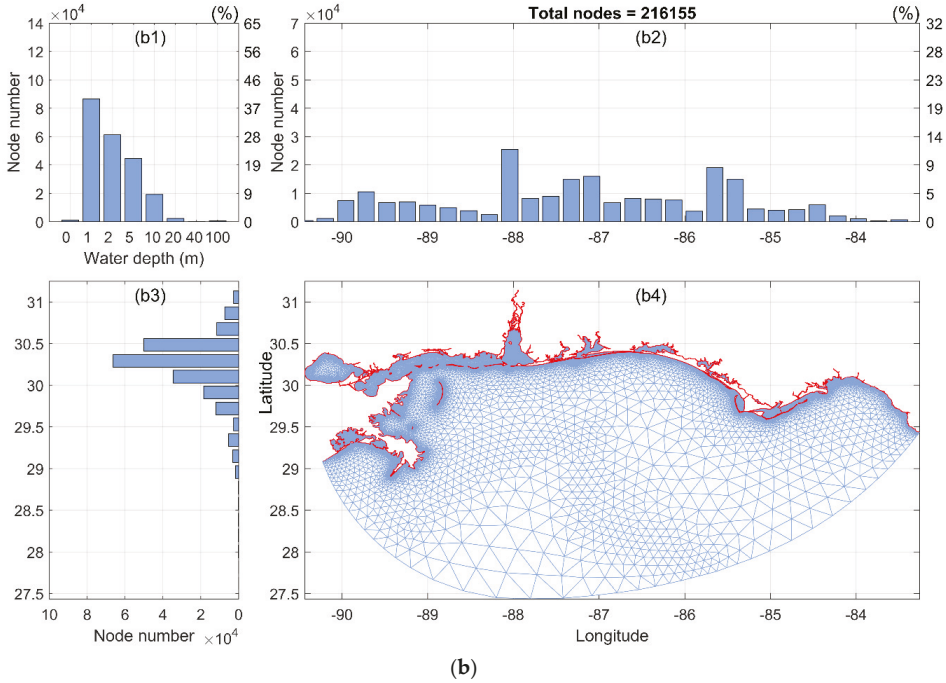

(**b**)

Figure 5. Comparison of the (**a**) 2008 and (**b**) new model meshes. (**1–3**) Histograms of node number versus depth, longitude, and latitude, respectively.

3.4. Model Setup

The ADCIRC model setup includes preparing the open boundary conditions and choosing parameters. The open boundary of the model grid, located in the Gulf of Mexico, was forced with a synthetic tide that was generated using the amplitude and phase of six tidal constituents (K1, O1, Q1, M2, S2, and N2), which were extracted from the East Coast 2015 (or EC2015) tidal constituent database [41]. Similar to [12], the model runs began with a smooth, hyperbolic tangent, time ramp function, which was applied to the boundary forcing tide for the first 5 days. The node factors and equilibrium arguments were set to the values from the middle of 1992, which is in the middle of the 1983–2001 NTDE. A no flow boundary was set for all main land and island boundaries. The lateral eddy viscosity coefficient was set to 5 m^2/s, which was the lowest number tested that did not produce numerical instabilities. The user-specified bottom friction coefficient C_f value was set to a standard value of 0.003 as in [12]. The model was run for 40 days with a 3-s time step. The small time step was due to the Courant number limitation imposed by the small element sizes. The water surface elevation was output at every node in the grid at a 6-min time interval for the last 33 days of the 40-day model run as fort.63.nc, with a file size of 12.8 gigabytes (GB). It takes a total of 3 wall-clock hours to complete the run utilizing 256 processors at NOAA's Research and Development High Performance Computing System's (RDHPCS) Jet system, if we split the huge output file as two. For test runs where only time series at tide stations are needed (e.g., output fort.61.nc of 11.7 megabytes (MB) instead of fort.63.nc), it takes approximately 47 wall-clock minutes for a run. In this way, it not only saves computational resources but also improves the test efficiency.

4. Results and Discussion

4.1. Validation and Error Analyses

In this section, we present the validation and error analyses for the original model results f_m computed from the ADCIRC model. Figure 6a–d compare the modeled datums to observations at tide stations for the four datums, MHHW, MLLW, MHW, and MLW, within and outside VDatum region, respectively. Table 3 summarizes the model errors. Here we use obs_i and $model_i$ for CO-OPS' observations and the modeled datums, respectively. The model error (err_i), percentage error, average error (err_{avg}), and model root mean square error ($rmse$) are calculated as follows:

$$err_i = model_i - obs_i = \frac{1}{Na}\sum_{j=1}^{Na} A_j - obs_i$$

$$\text{percentage } err_i = (model_i - obs_i)/obs_i \times 100$$

$$err_{avg} = \frac{1}{N}\sum_{i=1}^{N}|err_i|$$

$$rmse = \sqrt{\frac{1}{N}\sum_{i=1}^{N} err_i^2}$$

where i is the ith station, A_j is the jth highs or lows from the model time series at the ith station, Na is the total number of A_j from the model time series at the ith station, and N is the number of stations used.

For the 83 tide stations within the VDatum region, the average error is 0.012 m or 7.9% for the four datums (Table 3). This is an improvement in accuracy compared to the 0.018 m (11.0%) average error for the 2008 tide model reported in [12]. As will be discussed in Section 4.3.2, the update in offshore boundary conditions from the EC2015 tidal database [41] contributes to this overall improvement. The greatest improvement is in MLLW: the average error is reduced from 0.022 m (or 12.33%) in [12] to 0.013 m (or 7.2%). Since MLLW is most sensitive to the shallow water depth among the datums, this indicates the new tide model has more accurate representation of shallow water depths in

the coastal area. The results also point to another important conclusion: the gridding technique, i.e., the size function approach based on wave-lengths in the deep ocean enabled effective running of the ADCIRC model.

Table 3. Summary of averaged errors, in meters, for modeled datums at tide stations for the new grid.

Tide Stations	Error	MHHW (m)	MHW (m)	MLW (m)	MLLW (m)	Four Datums (m)
83 stations in VDatum region	avg. error	0.010 6.0%	0.014 9.3%	0.013 8.9%	0.013 7.2%	0.012 7.9%
	RMSE	0.013	0.017	0.017	0.016	0.016
99 stations outside	avg. error	0.028 14.0%	0.020 12.6%	0.020 12.8%	0.032 14.2%	0.025 13.4%
	RMSE	0.035	0.029	0.025	0.038	0.032
All 182 tide stations	avg. error	0.020 10.4%	0.017 11.1%	0.017 11.0%	0.023 11.0%	0.019 10.9%
	RMSE	0.028	0.024	0.022	0.030	0.026

The model errors in the VDatum region are smaller than those outside the region. Figure 7 clearly illustrates this trend. Each bar in Figure 7 represents 2 cm in width along the x axis. In the VDatum region, 95.5% of the modeled datums have error within ± 3 cm, while it is only 65.9% for the outside region. The main purpose of the outside region is to serve as a land boundary condition with relatively coarse resolution. The coarser resolution can contribute to the larger model errors.

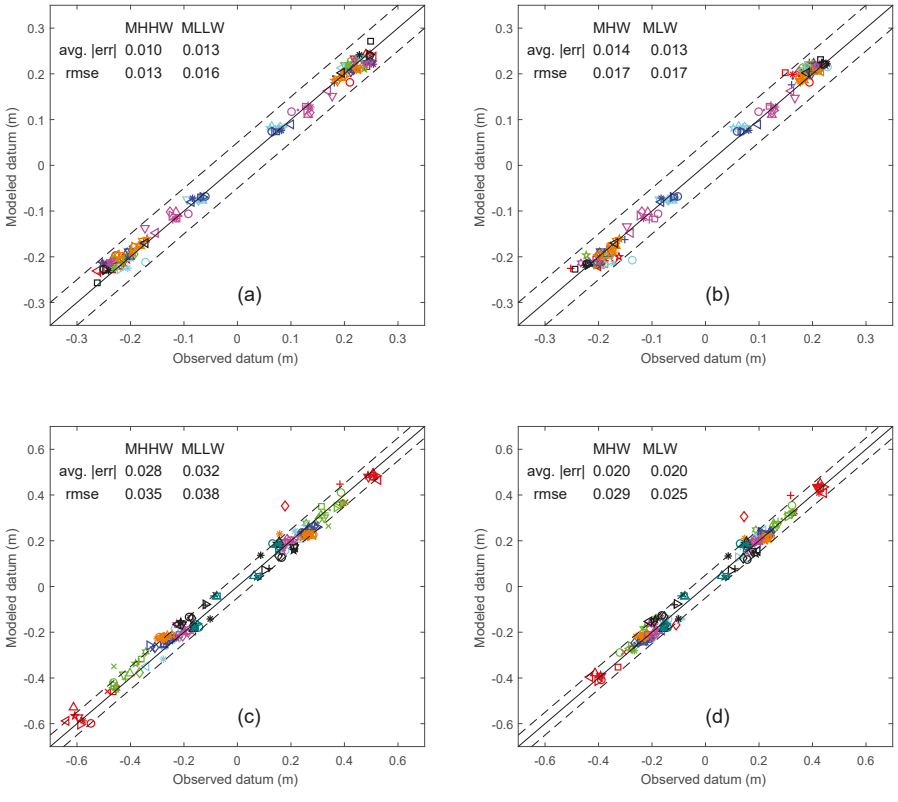

Figure 6. Comparison of the modeled tidal datum and observations for tide stations (**a**,**b**) within and (**c**,**d**) outside the VDatum region. The dashed lines indicate the 5-cm error band.

The maximum model errors in the VDatum region are 0.033, 0.042, 0.054 and 0.073 m for MHHW, MLLW, MHW, and MLW, respectively. Two of them, MHW at station 8728958 and MLW at station

8729169, exceeded the 5-cm error band. These two stations are plotted as the red square and cyan circle respectively in Figure 6b. To explore what factors may correlate to the maximum error, we plot error against the observed differences in datum magnitude, i.e., (1) MHHW-|MLLW| and (2) MHHW-MHW, in Figure 8(1a–d,2a–d), respectively. The result indicates:

(1) The maximum errors for MLW and MHW are relatively independent. That is to say, largest errors in MLW/MLLW do not correspond with largest errors in MHW/MHHW, and vice versa. This indicates different maximum error mechanisms for MLW and MHW.

(2) The maximum errors for MLW and MLLW are highly dependent. Both are from the same station, 8729169 at Shell Point, West Bay, Fla. This indicates a similar maximum error mechanism between MLW and MLLW. This also held for the large MHW and MHHW errors at stations 8728958 and 8728912. Please refer to [40] for station numbering and locations.

(3) The maximum error for MLW/MLLW occurs when the difference in the observed MHHW and |MLLW| is the greatest. Figure 8(1d) indicates there is one such outlier station 8729169. While MHHW-|MLLW| for all other stations are less than 0.027 m, station 8729169 shows a 0.076 m difference, which is more than double of the other stations. As will discussed in Section 4.3, shallow water depth can decrease |MLLW| more effectively than MHHW, due to the greater friction at MLLW. The model and bathymetry data might not well reflect the shallow water depth around station 8729169.

(4) The maximum error for MHW/MHHW occurs when the difference in the observed MHHW and MHW is the largest. Figure 8 panels 2a and 2c indicate two such outlier stations: 8728958 and 8728912. Both are inside the Saint Joseph Bay. Station 8728958 is very close to the entrance of the Bay near the jetty area. We notice there are discrepancies between NOS survey data and the current shoreline. Some survey points with depth fall on to the land area. This indicates the bathymetry data in 1985 for the jetty area might not reflect the current shoreline and depths.

For large model errors at stations outside the VDatum region, we will have a discussion in Section 4.3 as lessons learned.

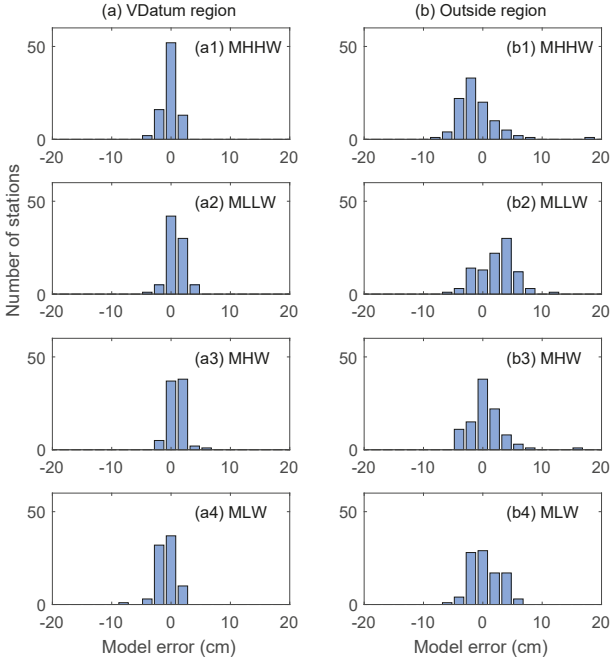

Figure 7. Histograms of model errors for tide stations (**a**) in and (**b**) outside the VDatum region.

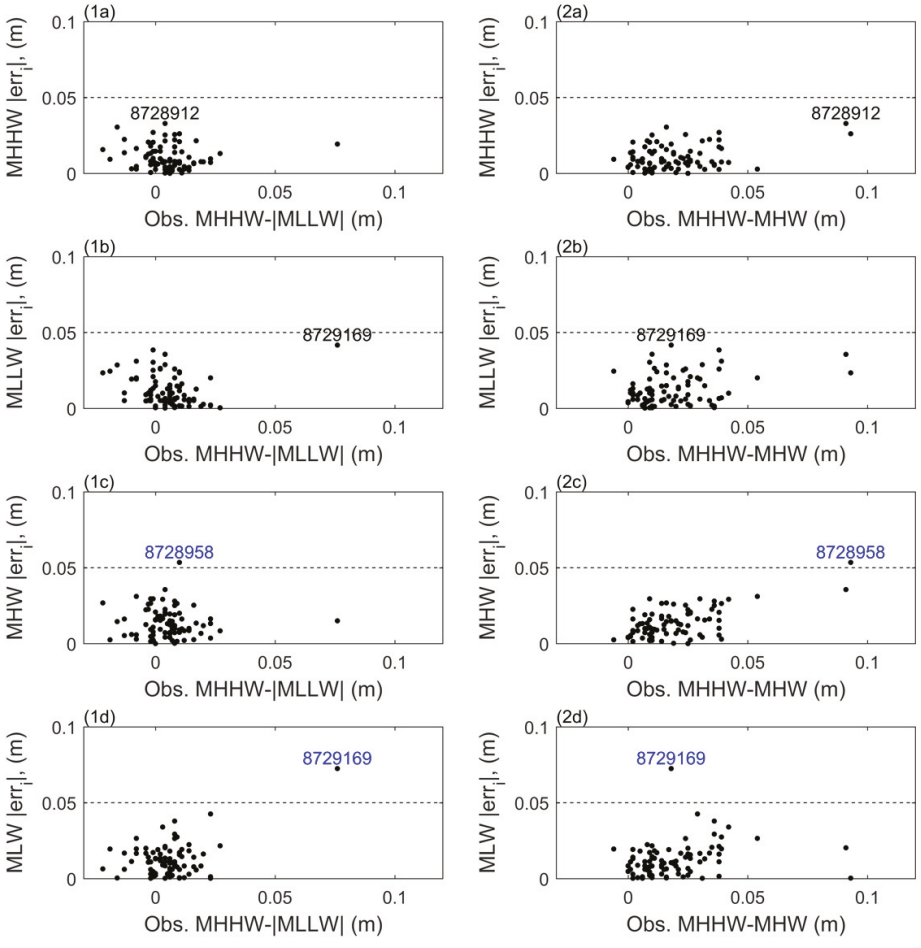

Figure 8. Model errors for (**a**) MHHW, (**b**) MLLW, (**c**) MHW, and (**d**) MLW versus observed differences in magnitude of (**1**) MHHW and MLLW, and (**2**) MHHW and MHW for stations in the VDatum region.

4.2. Datum Products and Spatially Varying Uncertainty

In this section, we present the results after applying the spatially varying uncertainty method. By applying the SVU method to the original model results in Section 4.1, we obtained the datum products f and associated spatially varying uncertainty Pa for the entire model domain as shown in Figure 9a,b, respectively. Rows 1–6 are for the six datum products, MHHW, MHW, MLW, MLLW, MTL, and DTL, respectively. The color map for column a ranges from −0.4 to 0.4 m while color map for column b ranges from 0 to 0.05 m. The final set of tidal datum fields match the observations at stations within a certain limit e.g., 1 cm (at the 182 tide stations in this case). The background model uncertainty had been improved at and around tide stations, and to a lesser extent in the offshore area. The maximum uncertainty is in the middle of the offshore boundary for MHHW (Figure 9(1b)). Two factors contribute to the large uncertainty offshore: (1) the lack of offshore measurements and (2) relatively farther away from tide stations in the computational domain. The uncertainty of MTL and DTL are small due to the small magnitude for these two datums.

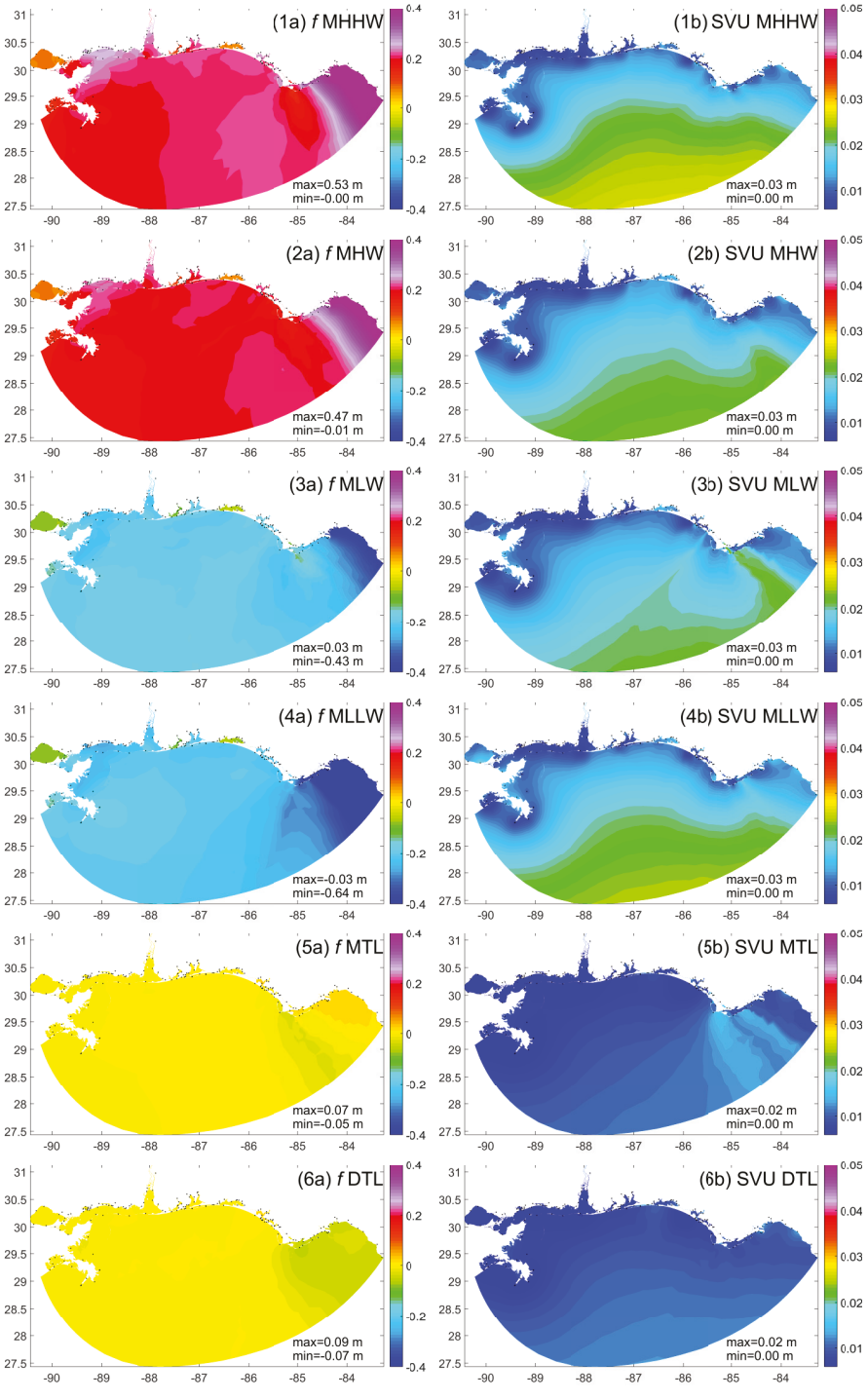

Figure 9. *Cont.*

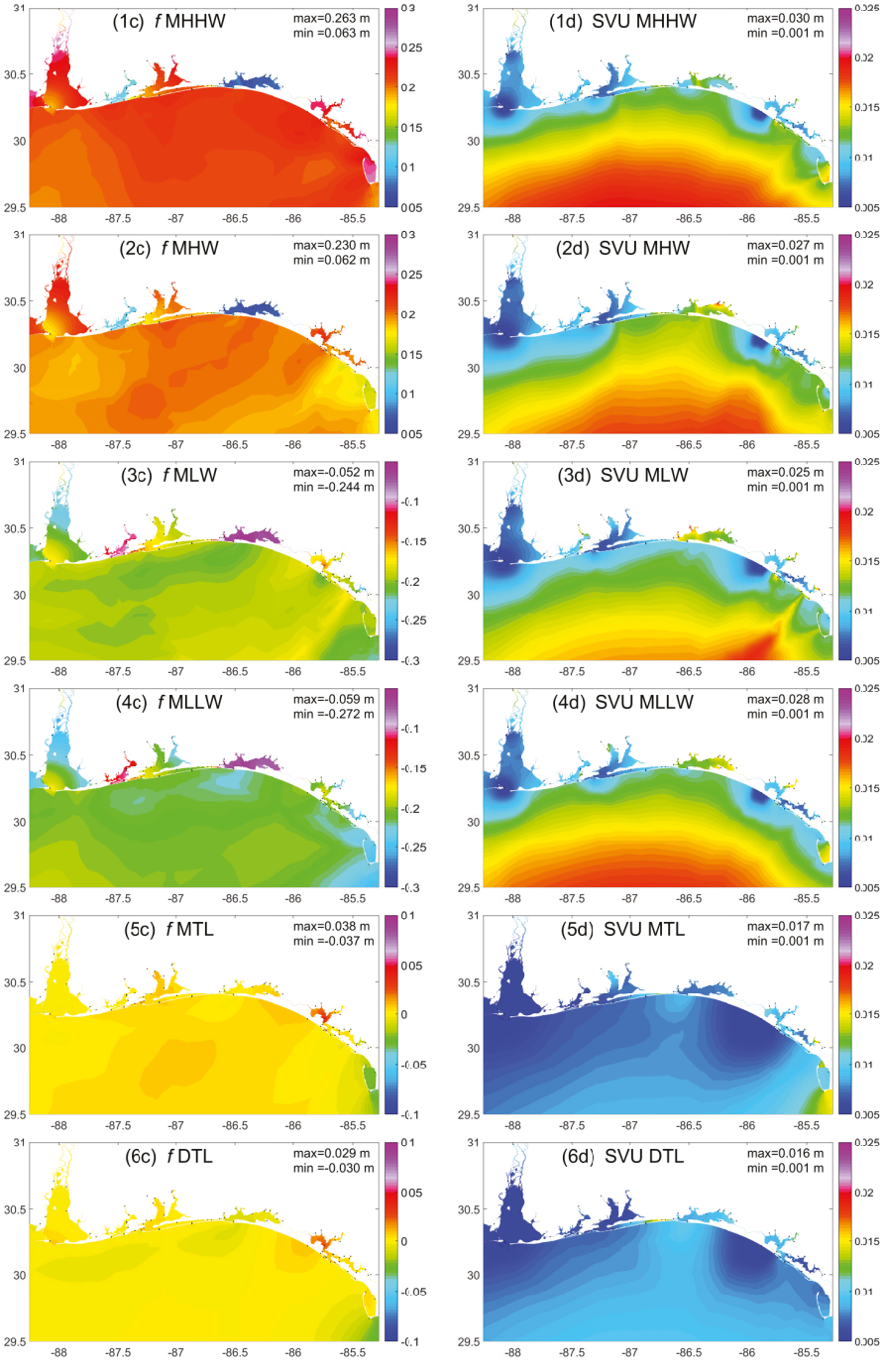

Figure 9. Datums products *f* and associated spatially varying uncertainty *Pa* in (**a**,**b**) computational domain and (**c**,**d**) VDatum region. Rows (**1**–**6**) are the six datums, MHHW, MHW, MLW, MLLW, MTL, and DTL, respectively.

Figure 9c,d show f and Pa in the VDatum region. The color scales in 9c and 9d were redesigned to show the local details. More details can be found in [40]. These results indicate:

(1) Along the coasts, large uncertainty can be seen in the southern portion of Saint Joseph Bay, Florida, for both MHHW and MLLW (Figure 9 panes 1d and 4d). The maximum uncertainty is 1.6 cm for MHHW. This is also the location that has the maximum MHHW and |MLLW|. Note that the MHHW-MHW and |MLLW-MLW| are also the largest among the stations in the VDatum region.

(2) For other bays, relatively local large uncertainties are found in the Choctawahatchee Bay, Florida (Figure 9 panes 2d and 3d). The maximum uncertainty ranges from 1.8 to 2.0 cm. Note that this group of tide stations inside the bay has the largest averaged measurement error even though their tidal ranges are quite small. The average measurement error is 2.7 cm inside the bay, while it is only 1.7 cm for stations in the domain.

(3) Some local large uncertainties are due to lack of measurements. Such examples include the upper stream of the Mobile River, Alabama. (1.9 cm maximum uncertainty), the Deer Point Lake, Florida, to the northern most of the Saint Andrew Bay (1.8 cm maximum uncertainty for MLLW).

(4) Large uncertainty can also be caused by the relatively large model errors. One example is the 1.9 cm maximum uncertainty and 4 cm model error for MLW at station 8728973 at Wetappo Creek, East Bay, Florida.

The above datum products and spatially varying uncertainty in VDatum region are then further interpolated and saved to five regularly spaced marine grids. Figure 10a shows the bounding polygons for the five marine grids revised by Hess in 2012 [42]. In this study, they have been further reconfigured as Figure 10b, to cover all the tide stations in the region as well as the newly-added intra-costal waterways. In addition, the bounding polygon for northwest Florida was also modified. The new polygons share the common interfaces with the adjacent polygons whenever possible, e.g., no overlaps between the polygons. By using the new polygons, new marine grids were generated for the five areas. The datum products and spatially varying uncertainty were then populated on to the new marine grids. Plots for each marine grid can be found in [40].

We next compared the VDatum values in the marine grid to the observations at the tide stations. The standard deviations range from 0.07 to 0.83 cm (Table 4). The maximum error is about 1 cm. Continuity of values across interfaces was then checked. As shown in Figure 10b, there are 11 interfaces: (1) New Orleans-NEGOM, (2) New Orleans-Mobile Bay, (3) Mobile Bay-NEGOM, (4) Mobile Bay-Pensacola Bay, (5) Pensacola Bay-NEGOM, (6) Pensacola Bay-St Andrews Bay, (7) St Andrews Bay-NEGOM, (8) St Joseph Bay-NEGOM, (9) Cedar Key-NEGOM, (10) St Joseph Bay-Cedar Key, and (11) St Andrews Bay-St Joseph Bay. Along boundary 9, the NEGOM-Cedar Key boundary, there was a maximum of 2.8-cm difference in MLW across the interface. The difference is due to the differing values produced by the ADCIRC models for the north-east Gulf of Mexico and for the Florida shelf. Hess also reported a similar large difference in MLW across the 9th interface from the previous version of the tidal model [42].

Table 4. Comparison of observations and interpolated values (Standard deviations, cm) from the marine grids for the five areas in the VDatum region.

REGION	No. of Tide Stations	MHHW	MHW	DTL	MTL	MLW	MLLW
FL_andrw03	26	0.61	0.67	0.46	0.69	0.67	0.66
FL_moble04	7	0.60	0.43	0.31	0.39	0.83	0.61
FL_negom04	4	0.42	0.57	0.36	0.5	0.75	0.65
FL_pcola03	43	0.65	0.65	0.44	0.55	0.68	0.62
FL_stjoe03	3	0.76	0.39	0.07	0.83	0.59	0.66

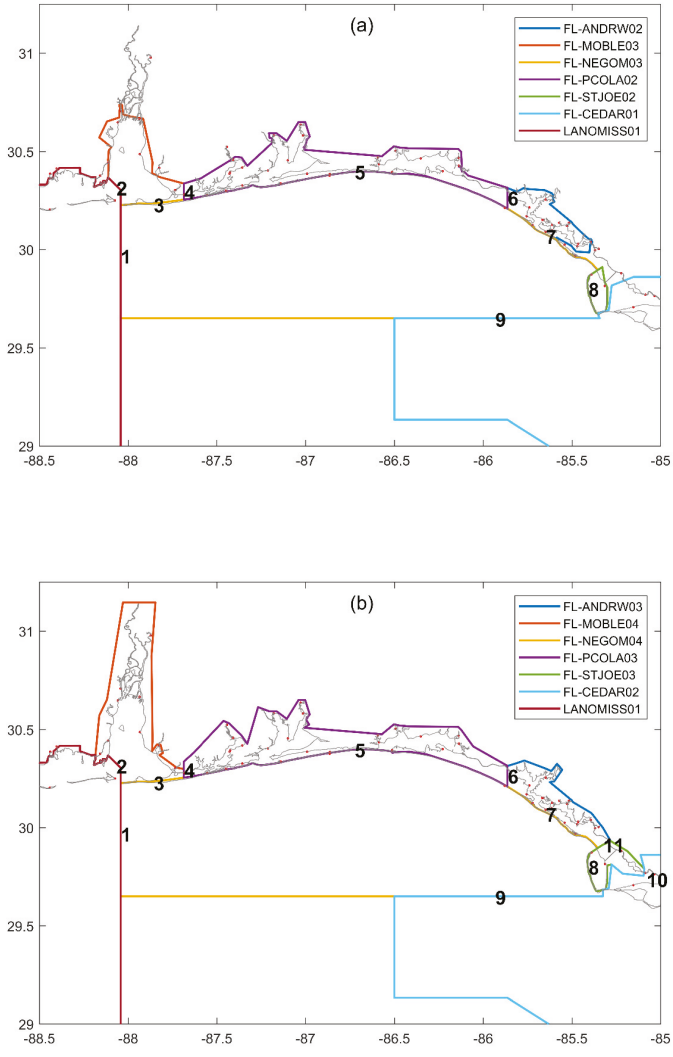

Figure 10. (**a**) 2012 and (**b**) 2018 revised bounding polygons. Dots indicate the locations of the tide stations.

4.3. Lessons Learned

In this section, we summarize lessons learned from the study to provide guidelines for future VDatum development. The modeled datums in this section refer to the original model results f_m computed from ADCIRC, i.e., before applying the spatially varying uncertainty method.

4.3.1. Sensitivity of Modeled Datums to Breakwaters

When we conducted the first test using the original 2008 model grid and input files, we obtained an over-prediction trend for stations inside Perdio Bay (Figure 11a). This is also reported by Dhingra et al. [12] in 2008, which resulted in the largest error in the Bay area. To address this issue, Dhingra et al. incorporated several changes, including extending the domain to include the

lower end of the Perdido River, adding a radiation boundary condition to the upstream end of the river, and refining the intracoastal water way that connects Perdido Bay to Pensacola Bay, Fla., etc. However, no major changes in the datums resulted [12]. By overlapping the model grid on Google Earth, we found that the two breakwaters at the entrance of Perdido Bay were missing from the 2008 model grid (Figure 10b). The next test we did was to pick up 9 nodes (the red circles in Figure 11b), aligned them with the breakwaters as in Figure 11d, and assigned a land value of −1 m. Figure 11c shows the updated model results: the Perdido Bay stations now nicely distribute on both sides of the solid line, e.g., no bias. The average model errors are also reduced. The above results point to the importance of including the breakwaters at the Perdido Bay entrance for model accuracy. The 170-m-wide narrow entrance formed by the breakwaters can limit the total amount of tidal wave energy that can propagate into the Bay, thus affecting the tidal range. The model grid must resolve such sudden changes in bathymetry and coastal geometry accurately.

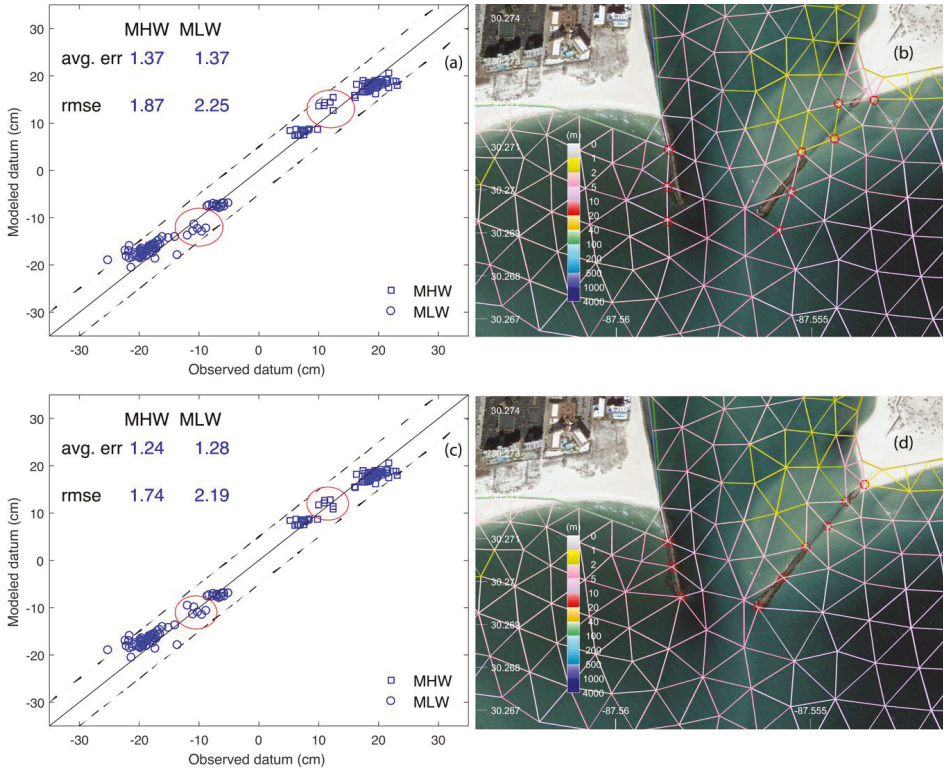

Figure 11. (**a**,**c**) Model data comparison at 74 stations in VDatum region (**b**) without and (**d**) with breakwaters at the entrance, respectively. Tide stations inside the Perdido Bay were within the red circle. Tests were conducted using the 2008 model grid. The dashed lines indicate the 5-cm error band.

4.3.2. Sensitivity of Modeled Datums to Offshore Boundary Conditions

Figure 12 compares the modeled datums using the (a) EC2001 and (b) EC2015 tidal databases [24,41]. The two tests were conducted with the same 2008 model grid with 74 tide stations in the VDatum region. The EC2015 tidal database reduced errors for both MHHW and MLLW, from 2.01 and 2.5 cm to 1.18 and 1.43 cm, respectively. These represent more than 40% reduction from the original errors. The EC2015 tidal database has incorporated the bathymetry data from the

VDatum tide models developed for U.S. East Coast [41]. It also has higher resolution in coastal area than the EC2001 database. Therefore, it likely has more accurate representation of the bathymetry data, particularly in shallow coastal regions. Note that the EC2015 tidal database reduced the underestimate/bais error mainly in the group 1 tide stations, which are either on the open coast or in less protected bays. Groups 2 and 3 stations in the two well-protected bays are not sensitive to the changes of offshore boundary conditions.

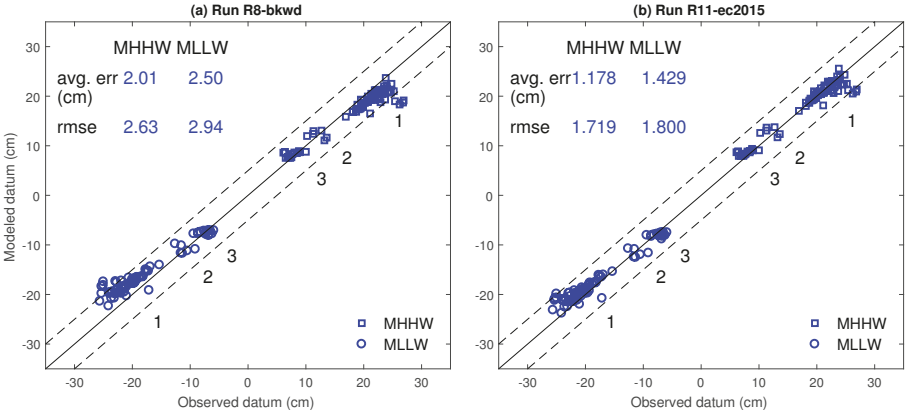

Figure 12. Sensitivity of modeled datums to offshore boundary conditions using (**a**) EC2001 and (**b**) EC2015 tidal data base. Tests were conducted using the 2008 model grid with breakwaters added to Perdido Bay. The dashed lines indicate the 5-cm error band.

4.3.3. Sensitivity of Modeled Datums to Water Depth

This study also shows that water depth in coastal area plays an important role on model accuracy. Two types of very large absolute model error (>10 cm) in datums were found due to inaccurate water depths: (1) an underestimate when the water depth is not deep enough and (2) an overestimate when the water depth is too deep. Figure 13a shows these two types of errors for stations outside the VDatum region at an early stage of testing.

The first type of error (large underestimate) usually is found at |MLLW| while it has little effect on MHHW. For example, Figure 13a shows that MLLW has greater average model error than MHHW. This is due to the underestimate for some stations at MLLW only (those stations above the 5 cm error bar at MLLW in Figure 13a). An examination on the model time series at those stations reveals that at MLLW, the model outputs a non-value due to the exposure of the shallow bottom. Using high resolution bathymetry data or adjusting the water depth around the stations deeper if such data are unavailable, e.g., making them slightly deeper to avoid the bottom exposure at MLLW, improved the model results as illustrated in Figure 13b. One example is the MLLW error for station 8728130 reduced from 21 cm underestimate to 1 cm.

The second type of error (large overestimate) can affect both |MLLW| and MHHW. This usually occurs at some river stations that are not only relatively far from the open coast but also have very shallow and narrow segments, and/or with expansion and then contraction of the river width. These river features result in much smaller tidal datums than those of the stations at open coast. For example, the MHHW at station 8728171 in Wakulla River, Fla., is 0.18 m, which is significantly smaller than the 0.51 m at the nearest station 8728151. This station 8728171 has the largest model error of 0.17 m (or 98%), which is plotted as the red diamond in Figures 6 and 13. Another example is the 0.38 m MHHW at station 8727989 (red plus in Figures 6 and 13) in Aucilla River, Florida, which is also quite smaller than the 0.50 m MHHW at nearby stations at the open coast.

The difficulty in modeling such outlier river stations is the lack of complete, high resolution bathymetry data that can accurately represent the change of depth along the river as well as on river cross section. Examples include: there is a bathymetry data gap between NOS bathymetry data and data collected by Howard T. Odum Florida Springs Institute in Wakulla River [38]; the single beam survey data for the Aucilla River did not capture the rock section in the river [40]; there is a mismatch in position between the NOS survey data in 1878 and current NGS shoreline data in Ochlockonee River, Florida, etc. For such locations, special adjustments were applied to the river depths and widths to reduce the error as much as possible. It is based on the modeler's best judgment, using available information from observation and bathymetry data, and Google Earth satellite imagery. Note that such adjustments are at locations within the model grid but far away from the VDatum region.

In this study, we did not tune the friction coefficient since the model accuracy in the VDatum region is already quite good. The model RMSE error for the four datums is only 1.6 cm, which is very close to the 1.7 cm averaged measurement error (RMSE) at stations. As to stations outside VDatum region with large model errors, we are in the process of obtaining more accurate bathymetry data. River LiDAR mapping projects have been conducted and proposed for Wakulla and Aucilla Rivers, respectively (personal communications with G. Cole, 2017). When those new data become available, we will redo the test for updating VDatum for those areas and evaluate the sensitivity to friction coefficients.

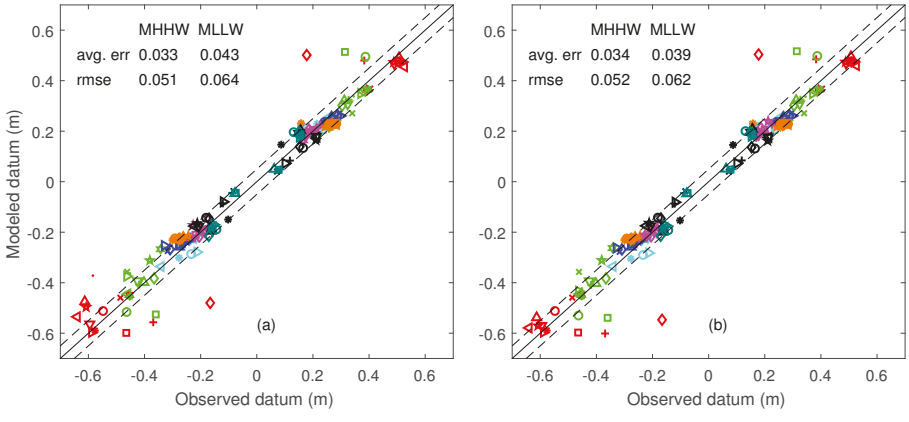

Figure 13. Sensitivity of modeled datum to water depth for stations outside VDatum region. (**a**) Two types of large model error at early stage of testing. (**b**) Increasing minimum water depth resolved the underestimate at MLLW. See Figure 6c for the final results. The dashed lines indicate the 5-cm error band.

4.3.4. Sensitivity of Spatially Varying Uncertainty to Model Error

Large model errors from tide stations can propagate as background uncertainty during spatially varying uncertainty computation. Figure 14a shows the spatially varying uncertainty for MLLW using the preliminary results with large model errors as in Figure 13a. As the model error was reduced as shown in Figure 6c, the spatially varying uncertainty is also reduced as in Figure 14b. The tests were conducted using the 144 tide stations with root mean squared error data. The above results point to the importance of improving model accuracy in order to reduce the spatially varying uncertainty.

4.3.5. Model Error at Intracoastal Waterway Station 8761678

For tide stations located in the Intracoastal Waterway (ICWW), additional attention needs to be paid to the multi-connecting channels. Such an example is station 8761678, Michoud substation, ICWW, Louisiana (Figure 15). The observed MHHW and MLLW are 0.21 m at the station. Figure 15 a shows

an early testing version of the grid around the station. It produces −8 cm error in both MHHW and |MLLW|. This is nearly double the −3 to −4 cm error in magnitude at the four nearby tide stations. After connecting the channel to Lake Borgne through station 8761529 (Figure 15b), the model error reduces to −4 cm for MHHW at 8761678. This is consistent with the error at the nearby tide stations. Note this reduction in error also improves the spatially varying uncertainty in the area for MHHW from Figure 15c to Figure 15d.

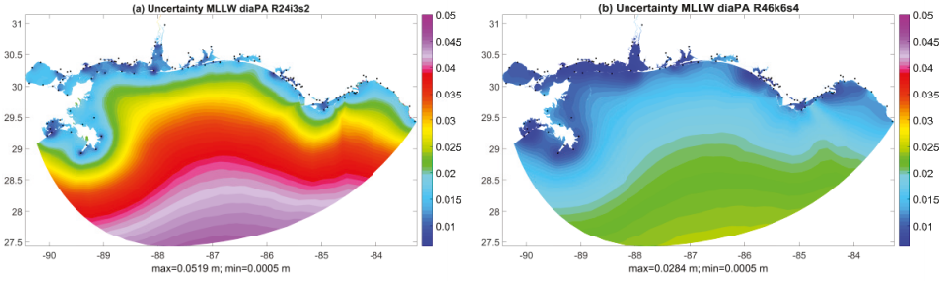

Figure 14. Sensitivity of spatially varying uncertainty to model error. (**a**) Before and (**b**) after error reduction (e.g., Figure 13a vs. Figure 6c). Tests were conducted using 144 tide stations with RMSE data. Unit for the color bar is in meter.

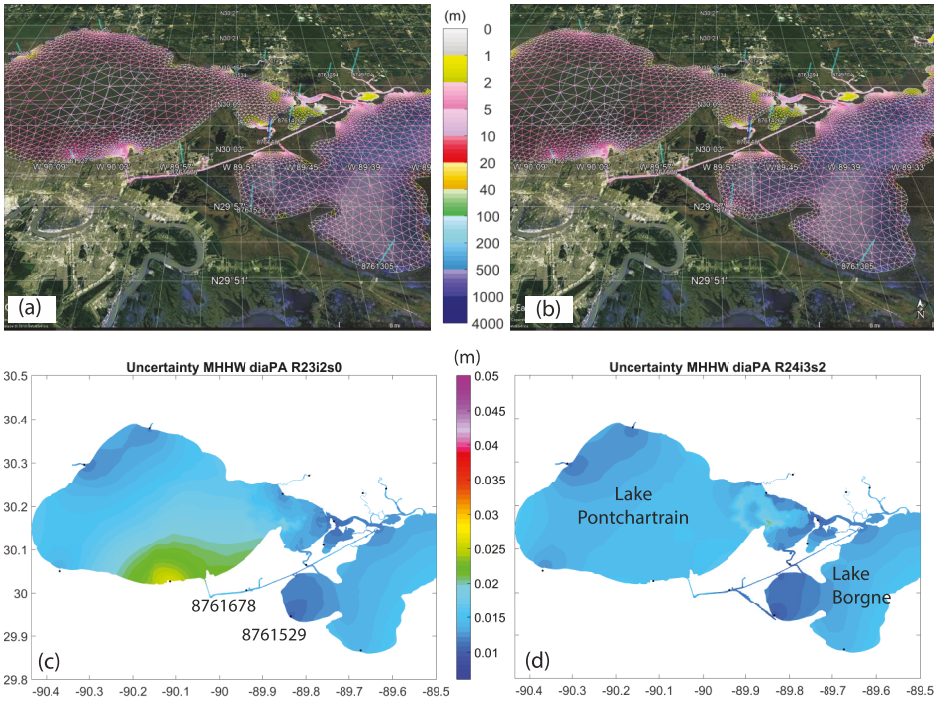

Figure 15. Sensitivity of spatially varying uncertainty to model error at intracoastal waterway station 8761678. (**a**) 8 cm and (**b**) 4 cm error at 8761678, Michoud substation, Intracoastal Waterway (ICWW), Louisiana. (**c**) and (**d**) Spatially varying uncertainty computed from the model grids in (**a**) and (**b**), respectively.

5. Summary and Conclusions

In this study, we highlight the creation of the tidal datum fields and associated spatially varying uncertainty for VDatum. The region of interest encompasses Mobile Bay, Ala., Perdido Bay, Ala. and Fla., Pensocola Bay, Choctawatchee Bay, St. Andrew Bay, St. Joseph Bay, and Cape San Blas, Florida, from the west to the east. We present the development, testing of the numerical model of tides in north-eastern Gulf of Mexico, and lessons learned.

In the VDatum region, the average model error is 1.2 cm (or 7.9%) for the four datums for the 83 tide stations, among which 95.5% of the modeled datums have errors within ± 3 cm. After applying the spatially varying uncertainty method, the maximum absolute error in the datum products at station locations is 1 cm and the maximum uncertainty in the VDatum region is 2.5 cm. Compared to the single value uncertainty for a region, the spatially varying uncertainty provides more accurate representation of the uncertainty for the datum products.

The study points out that large model errors, measurement errors, and lack of observations can contribute to large spatially varying uncertainty. Accurate water depth data with high resolution in coastal areas is essential for improving model accuracy. This is especially important for shallow and narrow rivers. The tide model also needs to resolve the narrow entrances with breakwaters for bays well. For tide stations located in the intracoastal waterway, additional attention needs to be made to the multi-connecting channels. As we extend VDatum coverage to rivers and intracoastal waterways, high-quality river bathymetry data such as river LiDAR mapping data are needed.

The spatially varying uncertainty will be provided to the tri-office VDatum team for decision-making on placement of new tide gauges of high precision. New tide gauge data can be used to address the issues of lack of observations and large measurement errors and, therefore, to further reduce the uncertainty in the VDatum products in the future.

Author Contributions: Writing-Original Draft Preparation, L.T.; Supervision and Resources, E.M.; Conceptualization and Methodology, L.S., E.M. and K.H.; Writing-Review and Editing, K.H. and E.M.; Tidal Datums Data and Analysis, A.C. and M.M.; Shoreline Data and Project Administration, S.W.; Bathymetry data, C.H.

Funding: This research was funded by NOAA.

Acknowledgments: The authors thank the three anonymous reviewers for their careful reading and many insightful comments which lead to the improvement of the manuscript. We also thank CSDL's Zizang Yang and Hongqiang Zhou for many thoughtful discussions and comments; Kurt Nelson at CSDL, Chris Libeau at Marine Chart Division, Juliet Kinney at NOAA/UNH Joint Hydrographic Center, Tim Carlile at Land and Sea Surveying Inc, Emily Taylor at Howard T. Odum Florida Springs Institute, and George Cole at Aucilla Research Institute for bathymetry data and discussion; CSDL's IT group for their supports. Liujuan Tang thanks Chang Zhao and Karen Ferebee at ERT, Julia Powell and Neeraj Saraf at CSDL for their administrative support; and Pacific Hydrographic Branch and Olivia Hauser for providing office accommodation and support to the project.

Conflicts of Interest: The authors declare no conflict of interest.

References

1. Parker, B. The integration of bathymetry, topography, and shoreline and the vertical datum transformations behind it. *Int. Hydrogr. Rev.* **2002**, *3*, 35–47.
2. Myers, E.P.; Wong, A.; Hess, K.; White, S.; Spargo, E.; Feyen, J.; Yang, Z.; Richardson, P.; Auer, C.; Sellars, J.; et al. Development of a national VDatum, and its application to sea level rise in North Carolina. In Proceedings of the U. S. Hydrographic Conference, San Diego, CA, USA, 29–31 March 2005.
3. USGS. National Elevation Dataset (NED)—The Long Term Archive. Available online: https://lta.cr.usgs.gov/NED (accessed on 9 October 2018).
4. Umbach, M.J. *Hyrographic Manual*, 4th ed.; NOAA Natioinal Ocean Service: Rockville, Maryland, 1976.
5. NOAA. NOAA/NOS' VDatum 3.9: Vertical Datums Transformation. Available online: https://vdatum.noaa.gov/ (accessed on 9 October 2018).
6. University Colloge London. Vertical Offshore Reference Frames. Available online: https://www.ucl.ac.uk/vorf (accessed on 9 October 2018).
7. SHOM. Data.Shom.Fr. Available online: https://data.shom.fr/ (accessed on 9 October 2018).

8. Keysers, J.H.; Quadros, N.D.; Collier, P.A. *Vertical Datum Transformations across the Littoral Zone*; Department of Climate Change and Energy Efficiency: Canberra, Australia, 2013; p. 110.
9. NOS. *Standard Procedures to Develop and Support NOAA's Vertical Datum Transformation Tool, VDatum*; Version 2010.08.03; National Ocean Service: Silver Spring, MD, USA, 2010.
10. Milbert, D.G.; Hess, K.W. Combination of topography and bathymetry through application of calibrated vertical datum transformations in the Tampa bay region. In Proceedings of the Second Biennial Coastal GeoTools Conference, Charleston, SC, USA, 8–11 January 2001.
11. CO-OPS. *Computational Techniques for Tidal Datum Handbook*; NOAA Special Publication NOS-OPS 2: Silver Spring, MD, USA, 2003; p. 98.
12. Dhingra, E.A.; Hess, K.W.; White, S.A. *VDatum for the Northeast Gulf of Mexico from Mobile Bay, Alabama, to Cap San Blas, Florida: Tidal Datum Modeling and Population of the Marine Grids*; NOAA Technical Memorandum NOS CS 14; Department of Commerce, National Oceanic and Atmospheric Administration: Silver Spring, MD, USA, 2008; p. 64.
13. Yang, Z.; Myers, E.P.; White, S.A. *VDatum for Eastern Louisiana and Mississippi Coastal Waters: Tidal Datums, Marine Grids, and Sea Surface Topography*; NOAA Technical Memorandum NOS CS 19; National Oceanic and Atmospheric Administration, National Ocean Service, Office of Coast Survey, Coast Survey Development Laboratory: Silver Spring, MD, USA, 2010; p. 56.
14. Xu, J.; Myers, E.P.; Jeong, I.; White, S.A. *VDatum for the Coastal Waters of Texas and Western Louisiana: Tidal Datums and Topography of the Sea Surface*; NOAA Technical Memorandum NOS CS 22; National Oceanic and Atmospheric Administration, National Ocean Service, Office of Coast Survey, Coast Survey Development Laboratory: Silver Spring, MD, USA, 2010.
15. Hess, K.W. Spatial interpolation of tidal data in irregularly-shaped coastal regions by numerical solution of Laplace's equation. *Estuar. Coast. Shelf Sci.* **2002**, *54*, 175–192. [CrossRef]
16. Hess, K.W.; Schmalz, R.A.; Zervas, C.; Collier, W.C. *Tidal Constituent and Residual Interpolation (TCARI): A New Method for the Tidal Correction of Bathymetric Data*; NOAA Technical Report NOS CS 4; National Oceanic and Atmospheric Administration: Silver Spring, MD, USA, 1999; p. 99.
17. Hess, K.W.; Spargo, E.A.; Wong, A.M.; White, S.A.; Gill, S.K. *VDatum for Central Coastal North Carolina: Tidal Datums, Marine Grids, and Sea Surface Topography*; Coast Survey Development Laboratory, National Ocean Services: Silver Spring, MD, USA, 2005.
18. NOAA. NOAA/NOS' VDatum: Estimation of Vertical Uncertainties in VDatum. Available online: https://vdatum.noaa.gov/docs/est_uncertainties.html (accessed on 9 October 2018).
19. Shi, L.; Myers, E.P. Statistical interpolation of tidal datums and computation of its associated spatially varying uncertainty. *J. Mar. Sci. Eng.* **2016**, *4*, 64. [CrossRef]
20. Fearnley, S.M.; Miner, M.D.; Kulp, M.; Bohling, C.; Penland, S. Hurricane impact and recovery shoreline change analysis of the Chandeleur Islands, Louisiana, USA: 1855 to 2005. *Geo-Mar. Lett.* **2009**, *29*, 455–466. [CrossRef]
21. Gill, S.K.; Schultz, J.R. *Tidal Datums and Their Applications*; NOAA Special Publication NOS CO-OPS 1; National Oceanic and Atmospheric Administration, Center for Operational Oceanographic Products and Services: Silver Spring, MD, USA, 2001; p. 111.
22. Luettich, R.A.; Westerink, J.J.; Scheffner, N.W. *Adcirc: An Advanced Three-Dimensional Circulation Model of Shelves, Coasts, and Estuaries, Report 1: Theory and Methodology of Adcirc-2ddi and Adcirc-3dl.*; Technical Report DRP-92-6; U.S. Department of the Army: Arlington County, VA, USA, 1992.
23. Luettich, R.A.; Westerink, J.J. Formulation and Numerical Implementation of the 2D/3D ADCIRC Finite Element Model Version 44.XX. 2004, p. 74. Available online: http://www.unc.edu/ims/adcirc/adcirc_theory_2004_12_08.pdf (accessed on 8 October 2018).
24. Mukai, A.Y.; Westerink, J.J.; Luettich R.A., Jr.; Mark, D. *Eastcoast 2001: A Tidal Constituent Database for the Western North Atlantic, Gulf of Mexico and Caribbean Sea*; Technical Report, ERDC/CHL TR-02-24; Coastal and Hydraulics Laboratory, US Army Engineer Research and Development Center: Vicksburg, MI, USA, 2002; p. 201.
25. Luettich, R.A.J.; Westerink, J.J. *Continental Shelf Scale Convergence Studies with a Barotropic Tidal Model*; American Geophysical Union Press: Washington, DC, USA, 1995; Volume 48, pp. 349–371.

26. Spargo, E.; Westerink, J.J.; Luettich, R.A.; Mark, D. Developing a tidal constituent database for the eastern north pacific ocean. In *Estuarine and Coastal Modeling VIII, Proceedings of the Eighth International Conference, Monterey, CA, USA, 3–5 November 2003*; American Society of Civil Engineers: Reston, VA, USA, 2004; pp. 217–235.
27. Hess, K.W.; White, S.A. *VDatum for Puget Sound: Generation of the Grid and Population with Tidal Datums and Sea Surface Topography*; NOAA Technical Memorandum NOS CS 4; National Oceanic and Atmospheric Administration, Coastal Survey Development Laboratory: Silver Spring, MD, USA, 2004; p. 27.
28. Michalski, M. *Tide station, Tidal Datum and Geodetic Datum Assessment for VDatum Project*; National Oceanic and Atmospheric Administration, Center for Operational Oceanographic Products and Services: Silver Spring, MD, USA, 2011.
29. Bodnar, A.N. *Estimating Accuracies of Tidal Datums from Short Term Observations*; Technical Report NOS CO-OPS 0074; National Oceanic and Atmospheric Administration, Center for Operational Oceanographic Products and Services: Silver Spring, MD, USA, 1981; p. 32.
30. National Geodetic Survey. National Geodetic Survey—NOAA Shoreline Data Explorer. Available online: https://www.ngs.noaa.gov/CUSP/ (accessed on 9 October 2018).
31. National Geodetic Survey. National Geodetic Survey Shoreline Products. Available online: https://geodesy.noaa.gov/RSD/shoredata/NGS_Shoreline_Products.htm (accessed on 9 October 2018).
32. Taylor, L.A.; Eakins, B.W.; Carignan, K.S.; Warneken, R.R.; Sazonova, T.S.; Schoollcraft, D.C.; Sharman, G.F. *Digital Elevation Model of Biloxi, Mississippi, 2008b: Procedures, Data Sources and Analysis*; NOAA Technical Memorandum NESDIS NGDC-9; National Oceanic and Atmospheric Administration, National Geophysical Data Center: Boulder, CO, USA, 2008.
33. Taylor, L.A.; Eakins, B.W.; Carignan, K.S.; Warneken, R.R.; Sazonova, T.; Schoollcraft, D.C.; Sharman, G.F. *Digital Elevation Model of Panama City, Florida, 2008: Procedures, Data Sources and Analysis*; NOAA Technical Memorandum NESDIS NGDC-8; National Oceanic and Atmospheric Administration, National Geophysical Data Center: Boulder, CO, USA, 2008; p. 27.
34. Love, M.R.; Amante, C.J.; Taylor, L.A.; Eakins, B.W. *Digital Elevation Models of New Orleans, Louisiana: Procedures, Data Sources and Analysis*; NOAA Technical Memorandum NESDIS NGDC-49; National Oceanic and Atmospheric Administration, National Geophysical Data Center: Boulder, CO, USA, 2011; p. 46.
35. Love, M.R.; Caldwell, R.J.; Carignan, K.S.; Eakins, B.W.; Taylor, L.A. *Digital Elevation Models of Southern Louisiana: Procedures, Data Sources and Analysis*; National Oceanic and Atmospheric Administration, National Geophysical Data Center: Boulder, CO, USA, 2010; p. 22.
36. Love, M.R.; Amante, C.J.; Carignan, K.S.; Eakins, B.W.; Taylor, L.A. *Digital Elevation Models of the Northern Gulf of Coast: Procedures, Data Sources and Analysis*; National Oceanic and Atmospheric Administration, National Geophysical Data Center: Boulder, CO, USA, 2010.
37. DeWitt, N.C.; Stalk, C.A.; Smith, C.G.; Locker, S.D.; Fredericks, J.J.; McCloskey, T.A.; Wheaton, C. *Single Beam Bathymetry Data Collected in 2015 from Grand Bay, Mississippi/Alabama*; United States Geological Survey: Reston, VA, USA, 2015.
38. The Howard, T. *Odum Florida Springs Institute. Wakulla Springs Baseline Ecosystem Assessment*; Florida Springs Institute: High Springs, FL, USA, 2016; p. 101.
39. AQUAVEO. Aquaveo: Water Resources Software and Engineering Consulting Services for Modeling Groundwater, Surface-Water, and Watershed Hydraulics & Hydrology. Available online: https://www.aquaveo.com/ (accessed on 9 October 2018).
40. Tang, L.; Myers, E.P.; Shi, L.; Hess, K.; Carisio, A.; Michalski, M.; White, S.A.; Hoang, C. *VDatum with Spatially Varying Uncertainty in the Northeast Gulf of Mexico from Mobile Bay, Alabama, to Cape San Blas, Florida*; NOAA Technical Report NOS CS; National Oceanic and Atmospheric Administration: Silver Spring, MD, USA, 2018; p. 79.
41. Szpilka, C.; Dresback, K.; Kolar, R.; Feyen, J.; Wang, J. Improvements for the western north atlantic, caribbean and gulf of mexico adcirc tidal database (EC2015). *J. Mar. Sci. Eng.* **2016**. [CrossRef]
42. Hess, K.W. Revised VDatum for the northeast gulf of Mexico. Unpublished work, 2012; p. 7.

Journal of
Marine Science and Engineering

MDPI

Article

A Hybrid Lagrangian–Eulerian Particle Model for Ecosystem Simulation

Pengfei Xue [1,2,*], David J Schwab [3], Xing Zhou [1], Chenfu Huang [1], Ryan Kibler [1] and Xinyu Ye [1]

1 Department of Civil and Environmental Engineering, Michigan Technological University, Houghton, MI 49931, USA; xingzhou@mtu.edu (X.Z.); chenfuh@mtu.edu (C.H.); rjkibler@mtu.edu (R.K.); xinyuy@mtu.edu (X.Y.)
2 Great Lakes Research Center, Michigan Technological University, Houghton, MI 49931, USA
3 Michigan Tech Research Institute, Michigan Technological University, Ann Arbor, MI 48105, USA; djschwab@mtu.edu
* Correspondence: pexue@mtu.edu; Tel.: +1-906-487-1837

Received: 15 August 2018; Accepted: 21 September 2018; Published: 26 September 2018

Abstract: Current numerical methods for simulating biophysical processes in aquatic environments are typically constructed in a grid-based Eulerian framework or as an individual-based model in a particle-based Lagrangian framework. Often, the biogeochemical processes and physical (hydrodynamic) processes occur at different time and space scales, and changes in biological processes do not affect the hydrodynamic conditions. Therefore, it is possible to develop an alternative strategy to grid-based approaches for linking hydrodynamic and biogeochemical models that can significantly improve computational efficiency for this type of linked biophysical model. In this work, we utilize a new technique that links hydrodynamic effects and biological processes through a property-carrying particle model (PCPM) in a Lagrangian/Eulerian framework. The model is tested in idealized cases and its utility is demonstrated in a practical application to Sandusky Bay. Results show the integration of Lagrangian and Eulerian approaches allows for a natural coupling of mass transport (represented by particle movements and random walk) and biological processes in water columns which is described by a nutrient-phytoplankton-zooplankton-detritus (NPZD) biological model. This method is far more efficient than traditional tracer-based Eulerian biophysical models for 3-D simulation, particularly for a large domain and/or ensemble simulations.

Keywords: property-carrying particle model; coupled models; ecosystem simulation; biophysical modeling; Sandusky Bay; Great Lakes

1. Introduction

Current numerical methods for simulating biogeochemical processes in aquatic environments are typically constructed as individual-based models (IBMs) using Lagrangian particles [1–3] or as grid-based concentration models in an Eulerian framework [4–6]. IBMs allow for a mechanistic description of individuals and of interactions among individuals, represented by an ensemble of particles. Each individual contains a set of state variables (e.g., age, size, and nutrient quota) with corresponding physiological traits and behavioral traits [3], and the population-level properties emerge as a result of the cumulative behavior of the individuals [7]. IBMs have rapidly gained popularity in ecological modeling, particularly when simulating complete life cycles, adaptive behavior, and intrapopulation variability in response to internal and external environmental conditions becomes essential [8,9]. Large computational demand has long been known as one of the hallmark problems for IBM [2,7,8]. This is still true even with increased computational resources and implementation of the strategic approaches for reducing the number of individuals explicitly simulated in the model such as introducing the super individual particles or representative spaces [2].

On the other hand, the traditional grid-based Eulerian approach is also widely used in coupled physical–biogeological modeling [6,7,10,11] in the inland water and ocean modeling communities [12–18]. Unlike the particle models in which mass is transported as discrete particles [19,20], the Eulerian (concentration) model assumes average properties (state variables) of a population within a control volume, and estimates the change of the property using mass balance and reaction equations [21]. It does not describe intrapopulation variability but focuses on characteristics of the population mean, which is appropriate when growth kinetics are formulated as a function of the external conditions [7].

In general, the Eulerian model employs finite difference or finite element schemes to solve the governing reaction-transport equations [4,6]. Equations for the time evolution of state variables of the biophysical model include advection and diffusion terms which depend on hydrodynamic variables, as well as source and sink terms representing growth, decay, and interaction with other biogeochemical variables [6,11,22]. The property concentration fields ($C_i, i = 1, 2, 3, \ldots$.) are often calculated using a set of advection–diffusion equations:

$$\frac{\partial DC_i}{\partial t} + \frac{\partial DuC_i}{\partial x} + \frac{\partial DvC_i}{\partial y} + \frac{\partial DwC_i}{\partial z} - \frac{1}{D}\frac{\partial}{\partial z}\left(K_h \frac{\partial C_i}{\partial z}\right) - DF_c = C_{i,source} - C_{i,sink} \quad (1)$$

where D is the total water depth, u, v, and w are the x, y, and z components of the water velocity, K_h is the vertical thermal diffusion coefficient, F_c is the horizontal diffusion term, and $C_{i,source}$ and $C_{i,sink}$ represents the sources and sinks of C_i, respectively, due to the biological processes which are typically described using a set of biological process equations.

However, even in the relatively simple, less computationally demanding Eulerian model, a major practical challenge is that the biological submodel often involves a large group of parameters for calibration and confirmation which requires a considerable amount of computational time to tune the model. As shown in Equation (1), tuning the simulation of biological processes (e.g., changes in parameterization, initial and boundary conditions) requires a complete time integration of the entire equation, although bio-physical coupled models can have different time steps for physical and biological process terms as they may have different time and space scales. However, biophysical processes are generally not two-way coupled. In other words, one can often assume that changes in biological processes (in our case, the resulting changes in nutrient-phytoplankton-zooplankton-detritus (NPZD) property concentration) do not affect the hydrodynamic condition (currents, temperature, mixing, etc.). This indicates that there may be a more computationally efficient approach to resolve the impact of hydrodynamics on the biological processes rather than explicit integration of Equation (1) for each biological component every time the biological submodel is tuned.

The property-carrying particle model (PCPM) is developed to test the feasibility of an alternative strategy to grid-based approaches for linking hydrodynamic and biogeochemical models in the Eulerian framework that may reduce the problems mentioned above, particularly in regions where advection–diffusion plays a key role in regulating biogeochemcal processes. Instead of grid-based, time-averaging of hydrodynamic variables, the hydrodynamic model is used to calculate the Lagrangian trajectories of a large number of current-following tracer particles; these trajectories become the linking mechanism between the hydrodynamic model and the biogeochemical model. In the hybrid Lagrangian–Eulerian PCPM, each current-following tracer particle carries with it a number of time-varying properties which correspond to the state variables of the Eulerian biogeochemical model. The PCPM also employs its own horizontal grid system or series of regions which is independent of the hydrodynamic model grid and is used to calculate local average values of the particle-based properties. These cell-based properties allow all particles within a PCPM cell to influence the properties of other particles within the same cell or region and allow for display and analysis of biogeochemical fields. PCPM also differs from typical IBMs in that the tracer particles in PCPM typically carry 'field' based properties like concentration, as opposed to properties associated with an individual organism.

PCPM uses a computational grid system which is independent of the grid system used to compute currents for particle trajectories. The PCPM computational cells are used to define regions in which the properties carried by the particles are allowed to interact with one another. In this respect, PCPM is conceptually similar to the classic particle-in-cell (PIC) method with PM (particle–mesh) interactions [23,24], popularly used in plasma simulation [24,25]. PIC methods can also be mesh-independent by allowing direct particle–particle (PP) interactions, or a combination of PM and PP [23–26]. In PCPM, a basic simplifying assumption is that only particles within a single PCPM cell are allowed to interact, such as the PIC–PM method. The advantage of this approach is that it is conceptually intuitive to implement and computationally efficient to program.

An alternative approach to implementing a PCPM would allow particle-based properties to influence particle trajectories, perhaps through buoyancy or sinking. In this case, the PCPM would have to be coupled directly with the particle trajectory calculation. In the initial implementation of PCPM in this paper, we consider only the uncoupled case.

To illustrate more clearly the type of application envisioned for PCPM, we constructed and applied a rudimentary biophysical model to an actual aquatic system, Sandusky Bay, where the physical transport of flow and nutrient loading from the Sandusky River has proven to be critical to the ecosystem [27,28]. Since the mid-1990s, harmful algal blooms (HABs) have become the new norm for summer months in the Lake Erie ecosystem [29]. Harmful algal blooms occur in the system when cyanobacteria are provided the right temperature, light, and nutrient conditions to proliferate [30]. When these blooms transpire, they have many adverse impacts. At the local ecosystem level, HABs result in depleted dissolved oxygen levels below the lake's surface threatening the survival of organisms living below the surface [31]. Additionally, some cyanobacteria species produce a toxin, such as microcystin, which affects the nervous system, liver, and kidney further impeding aquatic organisms and humans [31].

The colonial cyanobacterium Microcystis dominates the cyanobacterial community in the offshore waters of western Lake Erie; however, the filamentous cyanobacterium Planktothrix dominates the nearshore bays and tributaries [28], such as in Sandusky Bay [27,28,32]. Situated on Lake Erie's south-western coast, Sandusky Bay borders Ohio's Ottawa, Erie, and Sandusky counties (Figure 1). From a physical aspect, Sandusky Bay is relatively shallow bay with an average depth of roughly 2.6 m as well as occupying a relatively small area [32]. The primary draining watershed to Sandusky Bay originates from the Sandusky River at the west end of the bay. The Sandusky River drains a 1420 square mile area; of which, over 80% is dedicated to agricultural production [31]. This largely agricultural watershed leads to high nitrogen and phosphorus entering Sandusky Bay. Combining these high nutrient loads with the physical aspects leads to very high concentrations of nitrogen and phosphorus within Sandusky Bay, thus resulting in these cyanobacteria blooms (*Planktothrix agardhii*) [27,28,32].

The intent of this study is to test the feasibility of PCPM for biological–physical coupled modeling and examine its effectiveness and computational efficiency in practical application by implementing it in relation to HABs in Sandusky Bay. The remaining sections of this paper are organized as follows: details of PCPM and the design of numerical experiments are described in Section 2. The model results of idealized cases and the practical application to Sandusky Bay are presented in Section 3. A discussion and summary of the PCPM applications are included in Section 4.

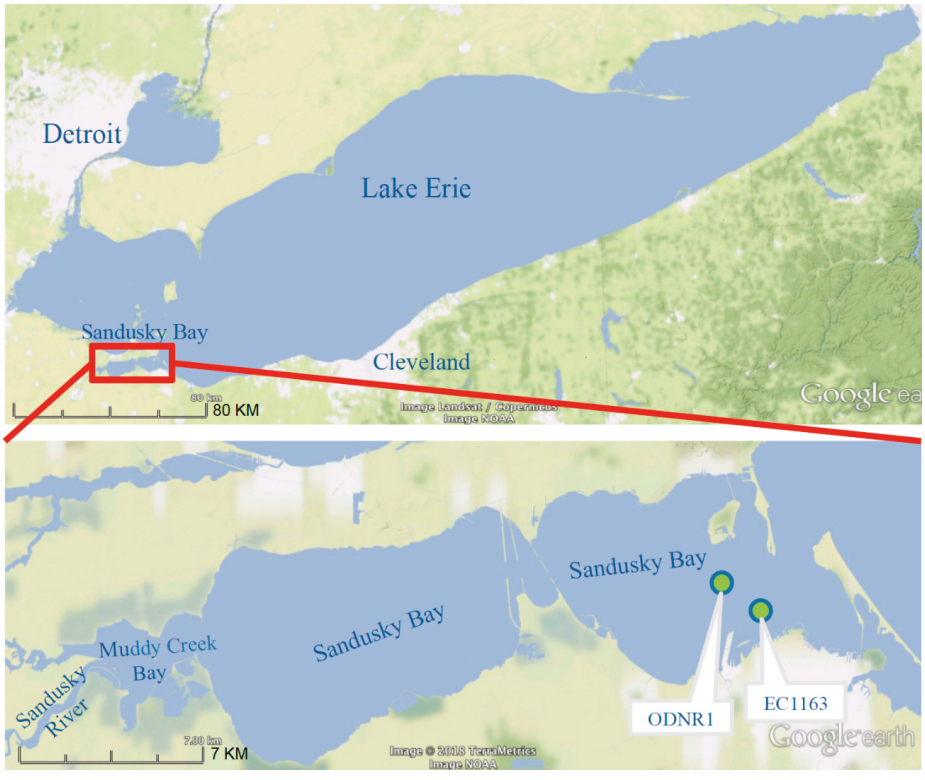

Figure 1. Sandusky Bay is situated on Lake Erie's south-west coast occupying a small portion of the Great Lake's coastline. Sandusky Bay is relatively shallow bay with an average depth of ~2.6 m. The primary draining watershed to Sandusky Bay originates from the Sandusky River on the west end of the bay. Sampling stations ODNR1 and EC1163 are denoted with green dots.

2. Methods

2.1. Property-Carrying Particle Model (PCPM)

In this implementation of PCPM, particle trajectories are pre-computed based on the output of a hydrodynamic model and are independent of the particle properties. An initial particle density (i.e., total number of particles/volume of computational domain) is selected and particles are randomly distributed throughout the computational domain. Particles are not allowed to leave the computational domain except at hydrodynamic outflows. At hydrodynamic inflows, new particles are introduced with the same density as the initial distribution. The total number of active particles is not strictly preserved, but if there is a net balance of hydrodynamic inflows and outflows, the total number of particles is approximately constant.

Any suitable method can be used to generate the Lagrangian particle trajectories. Typically, the trajectories are calculated from a time integration of the Lagrangian equations of motion:

$$\frac{dx}{dt} = u, \frac{dy}{dt} = v, \frac{dz}{dt} = w \tag{2}$$

where (x, y, z) is the particle's position in 3 dimensions, (u, v, w) is the local fluid velocity vector, and t is time. For the two idealized examples presented in this paper, the trajectories are calculated

semi-analytically from a simple, idealized flow field. The third, more realistic example, demonstrates the use of a full hydrodynamic model of a natural basin (i.e., Sandusky Bay) to compute currents and trajectories.

Each computational time step in the PCPM consists of six intermediate steps:

1. Read particle locations (x, y, z) and temperature. This step simply updates the location of each particle that is being used in the computation. Figure 2 is a conceptual representation of a PCPM computational cell, Particles (m_1, m_2, m_3, ...) move in and out of the cell at each PCPM time step based on their trajectories as computed from the hydrodynamic model. The total number of particles for a particular computation is assumed to be fixed for the duration of the computation, although some particles may enter or leave the PCPM domain during the computation. Water temperature or other physical properties from the hydrodynamic calculation can be stored along with the pre-computed particle trajectories and can be included as one of the properties ($P1$, $P2$, $P3$, ...) carried by the particle.
2. Determine the PCPM cell for each particle. In Figure 2, the PCPM cell is represented by the enclosing rectangle. The PCPM domain need not coincide with the domain that was used for the hydrodynamic simulation and computation of particle trajectories. It can be regular or irregular, as long as there is a prescribed method to calculate which PCPM cell contains a prescribed particle position (x, y, z). The PCPM cells are the volumes within which particle properties can interact, that is, during a single time step, all particles within a PCPM cell can influence the evolution of particle properties within that cell, but are independent of other cells.
3. Apply boundary conditions to any particle-based properties that require them. If there is a property (e.g., concentration of a dissolved nutrient) that needs to be specified as a boundary condition, then particles within the cell where the boundary condition needs to be applied will have that property adjusted to meet the boundary condition. For example, in a cell that is associated with an inflow to the domain, the properties that are being carried into the domain through the inflow are adjusted to take account of the change in that property for particles within that cell. Alternatively, if particles from the hydrodynamic-based trajectory calculation are entering a PCPM cell, the values of the associated properties for each particle need to be specified.
4. Calculate PCPM cell-based averages of each property. In this step, the averages of K_{th} property for cell n are calculated as:

$$\overline{PK_n} = \sum_{j=1}^{L} PK_{m_j}/L \tag{3}$$

where the summation includes all L particles (m_1, m_2,...m_L) currently within cell n. L is the number of particles within that cell. If no particles are present in a particular cell, PCPM uses the values of $\overline{PK_n}$ from the previous time step.

5. Calculate the time evolution of the cell-based properties (and particle-based properties if necessary) using the process equation defined for that property. The process equations can incorporate terms which depend on either particle-based or cell-based properties, or both, i.e.,

$$\overline{PK_n(t+\Delta t)} = FN\left(P1_M(t), P2_M(t), P3_M(t), \ldots \overline{P1_n}(t), \overline{P2_n}(t), \overline{P3_n}(t), \ldots\right) \tag{4}$$

Note that M indicates m_1, m_2,...m_L. The form of FN is completely general and depends on the problem being solved. For instance, in a NPZD model, the Pi, ($i = 1, 2, 3, \ldots$) would be N, P, Z, D, and water temperature, and the FN would be the process equations relating these properties. Since the cell-based averages have already been computed, the right-hand side of Equation (4) is independent of the left-hand side, so the computation of the evolution equations can be carried out in parallel. This is another key design feature of PCPM allowing it to take full advantage of multiprocessing computer environments, both symmetric multi-processing (SMP) and massively parallel processing (MPP).

6. Redistribute cell-based properties to particles within each cell by replacing the particle-based property with a weighted average of the cell-based property. After the evolution equations have been carried out (Step 5), particles within an individual cell most likely carry a range of different values of the various properties, which vary around the new cell-based average computed in Step 5, $\overline{PK_n(t+\Delta t)}$. PCPM provides an optional step to reduce the variance of the new particle-based properties within each cell. This optional step is applied as a 'nudging' term, i.e.,

$$PK_m(t+\Delta t) = (1-\alpha_i)PK_m(t) + \alpha_i\overline{PK_n(t+\Delta t)} \quad (5)$$

where $0 < \alpha_i < 1$ is the redistribution weight (i.e., nudging) factor. If $\alpha_i = 0$, no adjustment is carried out and the particle-based property remains unchanged. If $\alpha_i = 1$, then all particles within a cell are assigned the cell-based average of that property. This step can be useful to smooth results when limited particle density results in excessive within-cell variability.

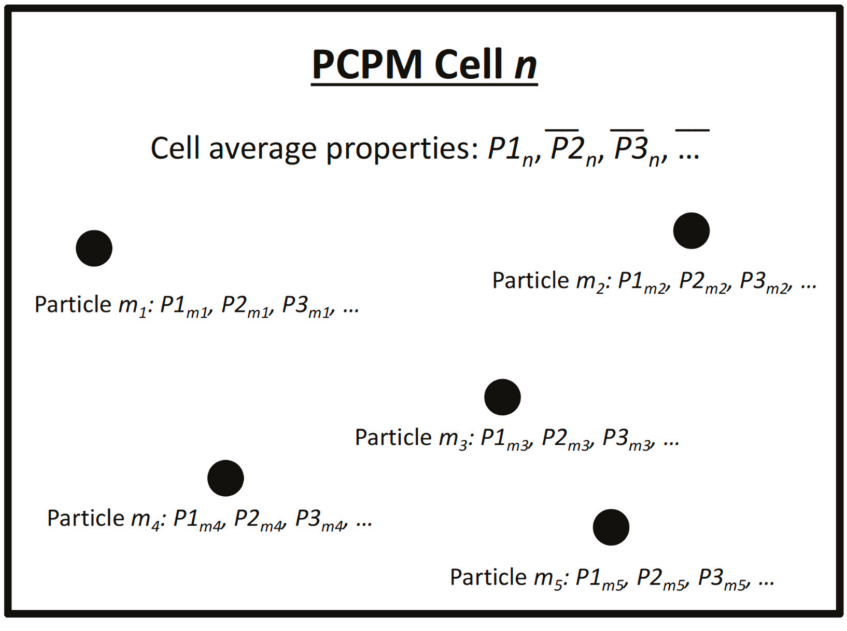

Figure 2. Conceptual representation of a property-carrying particle model (PCPM) computational cell n and particles (m_1, m_2, m_3, m_4, m_5 ...) within the cell n. PCPM cell-based average of each property ($\overline{P1_n}$, $\overline{P2_n}$, $\overline{P3_n}$, ...) is determined by the property values carried by the particles that have entered in this cell. After time evolution of PCPM properties using process equations, the updated PCPM cell-based properties ($\overline{P1_n}$, $\overline{P2_n}$, $\overline{P3_n}$, ...) are redistributed to particles with a weighted average. The particles then move around carrying the updated properties to different PCPM computational cells in the next cycle.

Note that all steps except 3 and 5 are independent of the specific problem, i.e., they will be carried out the same way no matter how many properties are attached to the particles or what those properties represent. More importantly, steps 1 and 2 only need to be run once regardless of modifications in biological processes at the later stage. These are two of the key designs of PCPM that contribute to enhanced computational efficiency.

2.2. Idealized Case 1: Advection–Diffusion Plume

In PCPM, diffusion is provided mainly by particle trajectories, although the cell-based averaging of particle properties and the (optional) redistribution of cell-based properties to particles within the cell can also act as diffusive terms. To demonstrate the effect of particle trajectory diffusion on particle properties, we constructed a 500 m wide × 2000 m long channel divided into 10 m square cells. Particles were introduced at random locations along the center 400 m section of the left edge of the channel at the rate of 100/s. The particles were assigned an along-channel velocity of 2 m/s. Horizontal diffusion was added using a random-walk perturbation to the particle trajectories of $2r\sqrt{2k_h\Delta t}$ in both cross-channel and long-channel directions. Here, r is a uniformly distributed random number in the range $[-1, 1]$, k_h is the horizontal diffusion coefficient (10 m^2/s in this experiment), and Δt is the time step for the particle trajectory calculation (1 s).

In this example, PCPM particles carry only one property, concentration ($P1 = C$), and there is no time evolution equation (step 5, above). The purpose of this example is to illustrate how PCPM simulates horizontal diffusion through a combination of the particle trajectories and the cell-based averaging in step 6. To simulate a concentration plume, particles introduced in the center of the left wall (-50 m $< y <$ 50 m) are assigned the initial condition $C = 1$. Particles entering the channel outside this region have an initial condition of $C = 0$.

2.3. Idealized Case 2: Vertical Settling

Since this implementation of PCPM does not allow the properties carried by the particles to influence particle trajectories, the question arises of how to simulate the vertical transport of a property when the vertical transport depends on the property itself, such as sediment settling or biologically generated buoyancy. In PCPM, the answer is simply to solve the vertical transport at the PCPM cell-based Eulerian framework in step 5 as a traditional cell-based method. Interaction of particle properties with adjacent cell averages is technically not allowed in the basic PCPM framework, but an exception is made in this case. The vertical advection–diffusion equation for sediment concentration is shown below:

$$\frac{\partial C}{\partial t} = w_s \frac{\partial C}{\partial z} + k_z \frac{\partial^2 C}{\partial z^2} \tag{6}$$

where w_s is the bulk settling velocity of the suspended material and k_z is the vertical diffusion coefficient.

Since vertical diffusion is already included in the particle trajectories, PCPM only needs to consider the first term on the right-hand side of (7) to account for the additional vertical transport that depends on the property itself. To implement this term in the PCPM, the process equation for a particle carrying a property C_m in vertical cell k looks like:

$$C_m(t + \Delta t) = C_m(t) + w_s \Delta t \left(\overline{C_{k-1}(t)} - \overline{C_k(t)} \right) \Delta z + (other\ process\ terms) \tag{7}$$

where $\overline{C_k(t)}$ is the average concentration in vertical cell k, $\overline{C_{k-1}(t)}$ is the average concentration in the next higher vertical cell, and Δz is the spacing between the centers of the cells. For particles in the top cell ($k = 0$), we set:

$$C_m(t + \Delta t) = C_m(t) - w_s \Delta t \overline{C_0(t)} \Delta z + (other\ process\ terms) \tag{8}$$

and for particles in the bottom cell ($k = kmax$), we set:

$$C_m(t + \Delta t) = C_m(t) - w_s \Delta t \overline{C_{kmax}(t)} \Delta z + (other\ process\ terms) \tag{9}$$

As a test case, we examine the vertical settling in a one-dimensional water column of depth d with particles moving vertically only through vertical diffusion. Particles are initially distributed randomly

in the column and then move with a random walk velocity of $2r\sqrt{2k_z\Delta t}$ where r is a uniformly distributed random number in the range $[-1, 1]$ and k_z is the vertical diffusion coefficient. Particles are not allowed to cross the surface or bottom boundaries. Thus, in this experiment, the number of particles is constant and the particles are always approximately uniformly distributed in the vertical due to vertical mixing.

For the experiment, we set $C = 1$ as the bottom boundary condition by assigning this value at the beginning of each time step to all particles in the lower half of the bottom cell. The initial condition in other cells is $C = 0$. For the test case, we set the number of particles to 1000, $d = 20$ m, $k_z = 10^{-4}$ m^{2}s^{-1}, and the redistribution parameter $\alpha = 0.1$. Three runs were made with 5, 10, and 20 vertical cells respectively. The PCPM is integrated in time with $\Delta t = 1$ h.

2.4. Sandusky Bay Model

The hydrodynamic model used in this study is FVCOM (finite volume community ocean model) [33]. FVCOM is an unstructured-grid, finite-volume, three-dimensional (3-D) primitive equation ocean model with a generalized, terrain-following coordinate system in the vertical and a triangular mesh in the horizontal. The unstructured grid can be designed to provide a customized variable resolution to both coastline and bathymetry. With the merits of ideal geometric fitting and local refinement of mesh resolution, FVCOM has been used in numerous applications to estuaries, coastal oceans, and the Great Lakes [34–40]. These characteristics make the model well suited for the study of Sandusky Bay.

Although this study focuses on Sandusky Bay, FVCOM is configured to simulate physical dynamics for all of Lake Erie including a high-resolution Sandusky Bay-FVCOM developed in this study, thus providing reliable representation of large-scale background circulation and the role of remote forcing impacting the water movement in the bay through the opening; additionally, this configuration avoids the impact of setting an artificial numerical boundary condition for our target region. The hydrodynamic model is well calibrated for the Lake Erie, based on the next-generation National Oceanic and Atmospheric Administration (NOAA) Lake Erie Operational Forecast System (LEOFS; see Kelley et al., [40] for detailed model validation), a real-time nowcast and forecast model that is built on the FVCOM. In the upgraded NOAA operational model for Lake Erie [40], the FVCOM model is developed with horizontal resolution ranging from 100 to 2500 m, and 21 uniform vertical sigma (terrain-following) layers for Lake Erie. The advantage of our model setting is that model resolution varies from 100–2500 m (coarse) in the open lake to 10–50 m (fine) in Sandusky Bay, affording a high degree of resolution across the 20 km × 3 km study site and adequately resolving the geographic complexity and coastal hydrodynamic conditions of that system (Figure 3). The model configuration yields a total of 73,000 grid elements (cells) in the horizontal plane with 50,000 of them resolving the bay.

In the PCPM implementation, 86,000 initial particles are randomly distributed throughout Sandusky Bay with a total water volume of 3.01×10^8 m^3. With PCPM cell resolution of 200 m × 200 m and the mean water depth of 2.6 m in Sandusky Bay, each PCPM cell contains 30 particles on average. New particles are introduced from the Sandusky River with the same density as the initial distribution. The number of new particles released from the river mouth varies greatly in accordance with the river flow rate. Table 1 presents the number of new particles released each month, based on the total water volume input from the Sandusky River. For example, 205,367 particles are released in March due to the highest river discharge in this month, which approximately equals the total number of particles (207,050) released from April to October.

Table 1. The number of new particles released and the total water volume input from the Sandusky River in each month.

Month	Monthly Discharge (10^8 m^3)	Particles (Number)
January	0.364	10,405
February	2.27	64,980
March	7.19	205,367
April	1.53	43,741
May	0.443	12,640
June	3.00	85,754
July	1.97	56,347
August	0.129	3680
September	0.089	2544
October	0.093	2654
November	0.133	3798
December	1.15	32,951

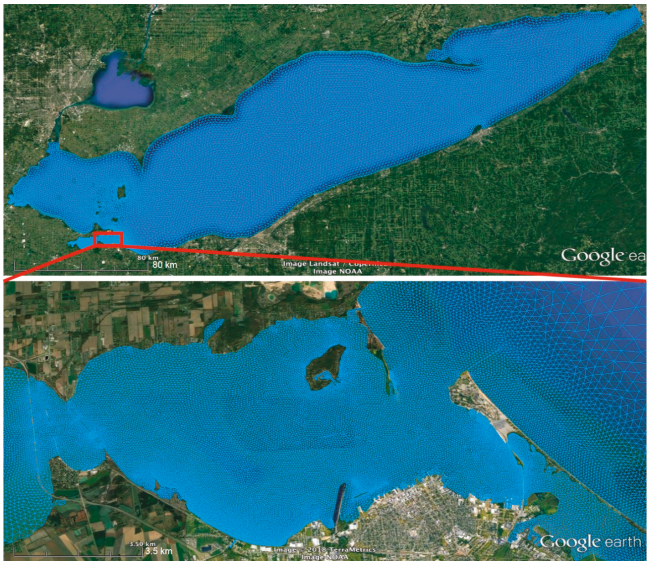

Figure 3. Finite volume community ocean model (FVCOM) model mesh for Lake Erie (**upper** panel) and linked with a high-resolution mesh for Sandusky Bay (**lower** panel). Only a portion of the Sandusky Bay mesh is displayed for a clear representation of the mesh's resolution.

2.5. Sandusky Bay Biological Model

The biological model used in this work is a general 3-D NPZD model [17]. As a common approach, the biological model is constructed by implementing 1-D NPZD models for each vertical column of PCPM cells that are distributed spatially across the 2-D domain to form a 3-D representation of the system. An exchange of properties between adjacent water columns occurs across their shared interface through advection and dispersion. Figure 4 displays the interactions among state variables in the NPZD model.

$$\begin{cases} \frac{dN}{dt} - \frac{\partial}{\partial z}(K_h \frac{\partial N}{\partial z}) - F_Z = -P(uptake) + Z(respiration) + P(respiration) + D(remineralization) \\ \frac{dP}{dt} - \frac{\partial}{\partial z}(K_h \frac{\partial P}{\partial z}) - F_P = P(uptake) - P(respiration) - ZP(grazing) + P(sinking) \\ \frac{dZ}{dt} - \frac{\partial}{\partial z}(K_h \frac{\partial Z}{\partial z}) - F_Z = ZP(grazing) - Z(respiration) - Z(mortality) \\ \frac{dD}{dt} - \frac{\partial}{\partial z}(K_h \frac{\partial D}{\partial z}) - F_D = P(mortality) + Z(mortality) - ZP(grazing) - D(remineralization) + D(sinking) \end{cases} \quad (10)$$

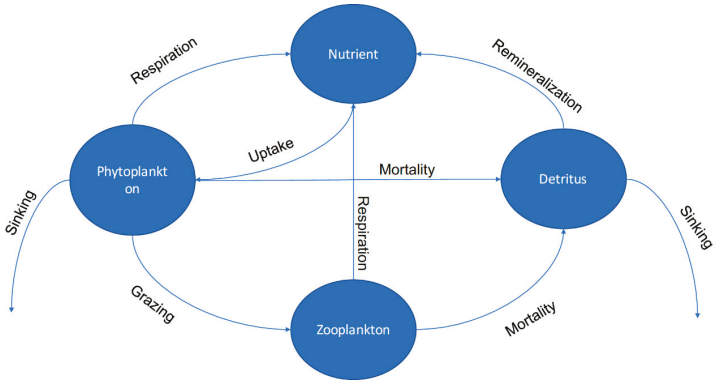

Figure 4. A schematic representation of the nutrient-phytoplankton-zooplankton-detritus (NPZD) model.

The governing equations for the model framework are based on Luo et al. [17], and the mathematical expressions for each term of the system of Equations (10) is presented in Appendix A. Several equations in the governing equations are modified for this study based on literature review. The light-limited, nutrient-limited, and temperature-limited functions $f(I), f(N), f(T)$, respectively, that contribute to the $P(uptake)$ are taken from Platt et al. [41] and Nicklisch et al. [42]. Also, the light attenuation functions are adjusted to Rowe et al. [18].

$$f(I) = (1 - e^{-\frac{\alpha_I I}{\mu max}})e^{-\frac{\beta_I I}{\mu max}} \tag{11}$$

$$f(N) = \frac{N - N_0}{K_s + N - N_0} \tag{12}$$

$$f(T) = \exp(-2.3(\frac{T_{opt} - T}{T_{opt} - T_{min}})^2) \tag{13}$$

$$I = I_0 \exp(-k_d h) \tag{14}$$

where α_I, β_I are the initial linear slope at low irradiance and the negative slope at the high irradiance that characterizes photoinhibition [43], μ_{max} is the maximum potential growth rate, and I is the light intensity. The nutrient threshold N_0 represents the pool of nutrient that was assumed to be biologically unavailable. T_{opt} and T_{min} are the optimal growth temperature and minimal growth temperature, respectively. k_d is the light attenuation coefficient that accounts for the impact of water turbidity, phytoplankton, and detritus on the light attenuation. Model parameterization is based on literature review [17,18,41,43] and subjective tuning for the Sandusky Bay simulation as there is no established NPZD model for the Sandusky Bay region. (See Table 2 for model parameterization).

3. Results

3.1. Idealized Case 1: Advection–Diffusion Plume

To illustrate the effect of the cell-based averaging (step 6), we show results of the first idealized case for four different values of the cell-based redistribution parameter (α = 0, 0.01, 0.1, 0.5) in Figure 5. In Figure 5, there are three panels for each value of α. The top panel shows the locations of particles after 720 time steps (12 min). The particles are colored using a blue-to-red scale for concentration values from 0 to 1. Particles with a concentration value of exactly 0 are colored light gray. The second panel shows the average concentration in each 10 m square cell with the same blue to red scale as the top

panel, except cells with $C = 0$ are black. The third panel compares concentration along the centerline of the plume from the second panel to the analytical solution for a diffusive plume [44,45], i.e.,

$$C(x) = \text{erf}([\frac{2}{3}\left(\left[1.4x + 1\right]^{0.833} - 1\right)]^{-0.5}\right) \quad (15)$$

where $C(x)$ is the centerline concentration x meters away from the channel entrance. erf represents Gauss error function, defined as: $\text{erf}(x) = \frac{2}{\sqrt{\pi}} \int_0^x e^{-t^2} dt$. In the case $\alpha = 0$, there is no cell-based redistribution of properties, so all particles retain their initial concentration values of either $C = 0$ (light gray in panel 1) or $C = 1$ (red in panel 1). As seen in the second and third panels, the random-walk diffusion in the particle trajectories does provide a rough approximation to the analytical solution by mixing of $C = 0$ and $C = 1$ particles in the PCPM cells. Of course increasing the number of particles in the simulation would provide a more accurate approximation, but would also increase the computational load. Setting the cell-based redistribution parameter to even the small value of $\alpha = 0.01$ provides a significant improvement in the solution with the same number of particles, particularly for $x > 500$ m. Now particles can have any value of C between 0 and 1. Increasing the redistribution parameter to $\alpha = 0.1$ further improves the solution for $x < 500$ m. Further increasing α to 0.5 does not significantly improve the solution in comparison to $\alpha = 0.1$.

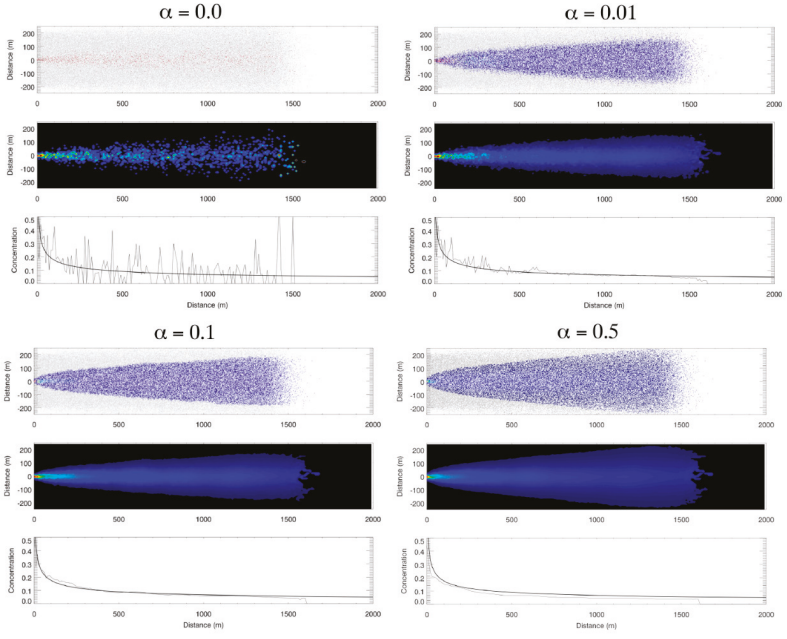

Figure 5. PCPM simulation of concentration plume in an idealized channel with four different values of the cell-based redistribution weight parameter ($\alpha = 0, 0.01, 0.1, 0.5$). There are three panels for each value of α. The **top** panel shows the locations of particles after 720 time steps (12 min). The **second** panel shows the average concentration in each 10 m square cell with the same blue to red scale as the top panel, except cells with $C = 0$ are black. The **third** panel compares concentration along the center line of the plume from the second panel to the analytical solution for a diffusive plume.

3.2. Idealized Case 2: Vertical Settling

The results at the end of 5000 time steps of the second idealized case are shown in Figure 6. In Figure 6, the dots represent the locations of the particles on the vertical axis and the value of

concentration they are carrying on the horizontal axis. The thin line is the cell average concentration. The thick line is the analytical solution,

$$C = e^{\frac{-w_s}{k_z}z} \tag{16}$$

As shown in Figure 6, the model properly simulates the change in concentration due to vertical settling and mixing while allowing the particles to remain approximately uniformly distributed in the vertical. The simulation accuracy increases with increased resolution of vertical layers. The model result with 20 vertical layers shows a close agreement with the analytical solution. Specifically, Figure 7 shows the evolution in time of the root mean square difference (RMSD) between the cell averages and the analytical solution for the three cases. While the RMSD in the simulation with 5 layers remains above 0.2 (the magnitude of initial error) over the entire simulation, the RMSD decreases quickly to 0.02 after 500 time steps and remains stable at this level when vertical resolution is increased to 20 layers.

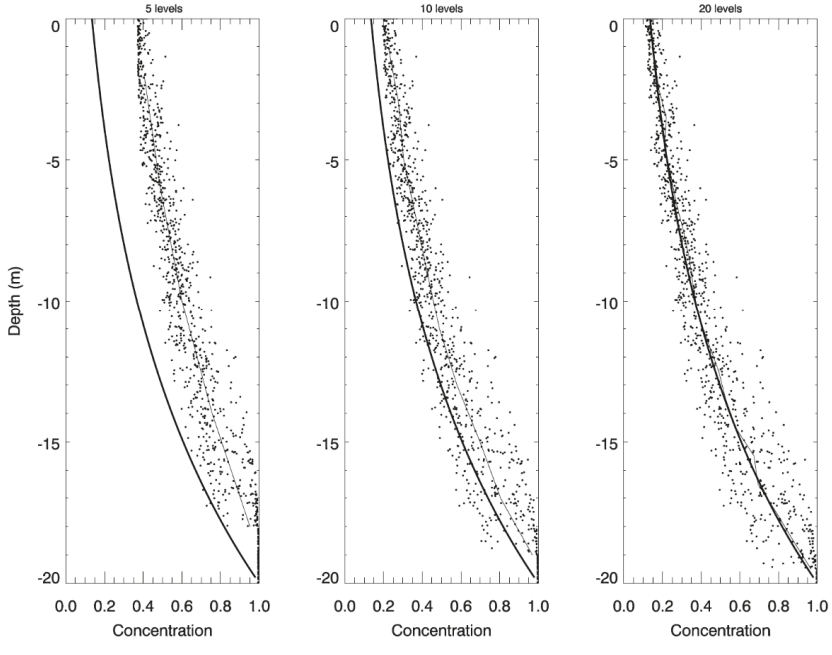

Figure 6. The PCPM simulation of vertical settling in comparison to the analytical solution at the end of 5000 time steps. Three runs were made with 5 (**left** panel), 10 (**middle** panel), and 20 (**right** panel) vertical cells, respectively. The dots represent the locations of the particles on the vertical axis with their respective concentration on the horizontal axis. The thin line represents the cell average concentration and the thick line represents the analytical solution.

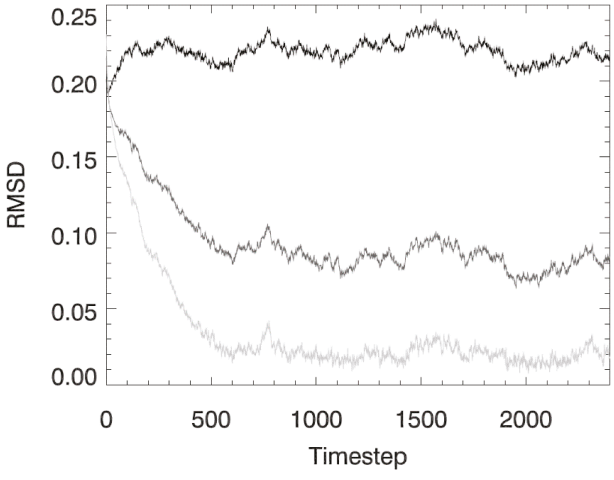

Figure 7. The time evolution of the root mean square difference (RMSD) between the cell averages and the analytical solution for the three cases presented in the Figure 3 (dark line for 5 cells, medium line for 10 cells, and light line for 20 cells).

3.3. Application to Sandusky Bay

To ensure the validity of the 1-D NPZD biological model, it was configured to duplicate several scenarios (not shown) from Edwards et al. [46]. The model demonstrated the expected linear stability of a vertically-distributed, NPZ ecosystem model when it was used in the scenarios that incorporate the impact of vertical mixing on biological dynamics. Scenarios include stable profiles, damping oscillatory dynamical trajectories, and vertically phase-locked systems, depending on the depth and choice of parameters and strength of vertical diffusion, which can be discerned from the eigenvalues in linear stability analysis [46]. The 1-D NPZD model used in this study reproduced all of these cases almost identically.

Before examining the impact of physical transport on the biological dynamics in Sandusky Bay, we first tested the ability of PCPM to simulate the advection–diffusion using a conservative soluble tracer in a natural setting. The Sandusky River plume is simulated using the conventional soluble-tracer model based on the advection-diffusion equation and compared to the result of PCPM approach in Figure 8. It is clear that the plumes simulated using the two methods show a very similar pattern, indicating the validity of the PCPM. Upon closer review, the plume simulated with soluble-tracer model shows a smoother evolution and sharper gradient near the plume front. We speculate this is partly due to the constant random-walk scale (10 m^2/s) used in the current particle-tracking model configuration. Nonetheless, the attractiveness of PCPM is its computational efficiency; it runs ~100 times faster than the soluble-tracer model which will be discussed in detail in the following section and Table 2.

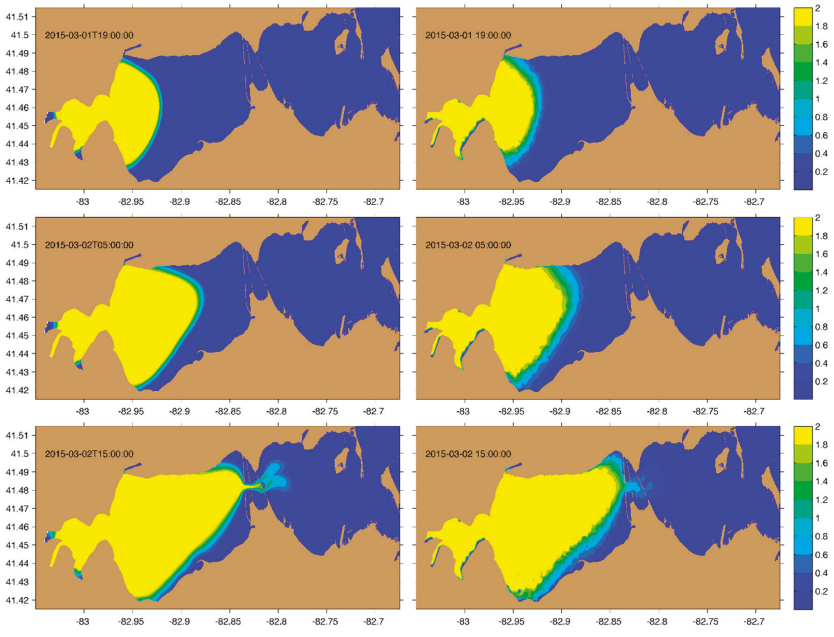

Figure 8. River plumes at selected times (labelled in each panel) simulated with conventional soluble-tracer model (**left** panels) and PCPM model (**right** panels). The color scale represents the tracer concentration.

To aid in model development, several datasets are gathered from literature as well as data acquisition organizations. Sandusky River daily discharge and nitrogen concentration are available from the National Center for Water Quality Research (https://ncwqr.org/monitoring/data/, accessed on 12 July 2018). Nitrogen, Chlorophyll concentration, and in-situ temperature data are available from two observational sites (ODNR1 and EC1163) in the eastern bay from May–October 2015, sampled by Bowling Green State University [28].

Using the PCPM-NPZD model, the importance of physical transport is demonstrated by comparing model results between the PCPM-NPZD-NOADV (no advection) simulation and the realistic PCPM-NPZD-REAL simulation. In the PCPM-NPZD-NOADV simulation, the model is configured the same as the PCPM-NPZD-REAL, except the movement of particles is driven only by turbulent diffusion without including advective processes due to the Sandusky River and wind field. Each simulation consists of three cases that use a high initial nutrient concentration of 9 mg N/L in June (case 1), medium initial concentration of 0.46 mg N/L averaged from July to September (case 2), and low initial concentration of 0.0075 mg N/L in August (case 3), respectively. The concentration values are estimated as total nutrient loading from the Sandusky River to the Bay (https://ncwqr.org/monitoring/data/,accessedon12July2018) divided by the total water volume of the bay. The comparison of model results is presented in Figure 9. The simulation of PCPM-NPZD-NOADV without resolving the advective transport processes shows a significant discrepancy from observational data (Figure 9, upper panels). The model fails to capture both the timing and magnitude of the blooms in all three cases, and model results are sensitive to the initial nutrient concentration.

On the other hand, after the impact of advective processes is resolved in the PCPM-NPZD-REAL simulation, the model accurately depicts the magnitude of the chlorophyll peak in mid-August (Figure 9, lower panels), and model results are insensitive to the initial condition, but determined by Sandusky River discharge and its nutrient loading. Three cases show nearly identical results. Results also support the field sampling study in Salk et al. [28]. Their study finds a strong, non-linear

connection between the bloom occurrence and the hydraulic residence time of the bay, which varies dramatically from 8 days to several months depending on the Sandusky River flow rate in the physical transport process. Although further development of the NPZD is undoubtedly necessary to resolve the onset and variability of the algal blooms by refining the structure of the biological model and improving the model parameterization, it is beyond the scope of this work in which we focus on demonstrating the feasibility of linking hydrodynamic effects and biological processes through the PCPM in a Lagrangian/Eulerian framework. Further development of the biological model and its application to the study of mechanisms responsible for the HABs in Sandusky Bay will be presented in another paper.

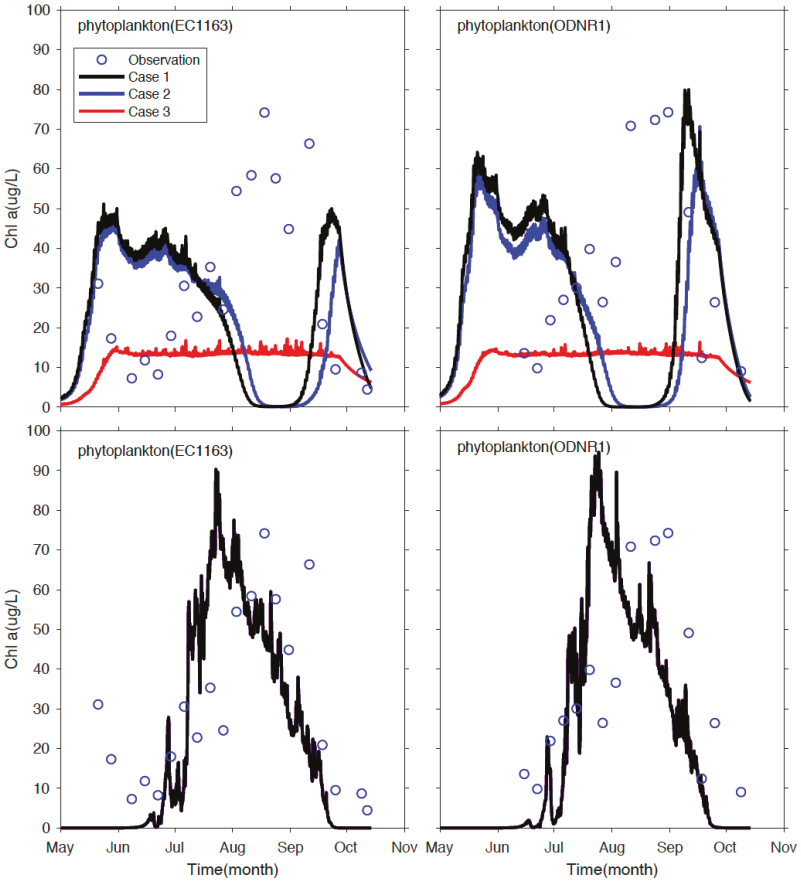

Figure 9. Observed and model simulated chlorophyll concentration at the sampling stations EC1163 (**left** panels) and ODNR1 (**right** panels). The upper panels are results from the PCPM-NPZD-NOADV (no advection) model simulations; the lower panel are the results from the realistic PCPM-NPZD model simulations where the three cases show nearly identical results, so only one result is plotted.

4. Summary and Conclusions

In this paper, we describe a novel method by integrating a property-carrying particle model (PCPM) and an Eulerian concentration biological model for ecosystem modeling. The model is tested in idealized cases and its utility is demonstrated in a practical application to Sandusky Bay. The novelty of this new technique lies in its integration of hydrodynamic effects via the property-carrying particle

tracking model and Eulerian grid-based biological modeling approach. Overall, there are several advantages of the PCPM over traditional Eulerian-based tracer approaches. The PCPM is simpler to implement and more efficient as it does not need to solve the advection–diffusion equation. Instead, the PCPM uses pre-computed particle trajectories to resolve the hydrodynamic condition based on currents from a hydrodynamic model. This means that the hydrodynamic model only needs to be run once giving one the ability to run different biological scenarios for the same physical characteristics; ultimately saving significant computational time.

As summarized in Table 2, a 30-day hydrodynamic simulation for the Lake Erie–Sandusky Bay FVCOM model takes 15 h to complete using 64 central processing units (CPUs). This step is necessary for both the PCPM-NPZD model and the traditional Eulerian, grid-based biophysical model. Once the hydrodynamic simulation is complete, PCPM-NPZD needs to calculate the Lagrangian trajectories of a large number of current-following tracer particles; it takes 1.5 h using a single CPU to track ~290,000 particles in the domain in March, which tracks the largest number of particles in the bay within a single month. The PCPM-NPZD model simulation using the particle trajectories as input completes a 30-day simulation within 5 min using a single CPU while it takes 5 h for a traditional Eulerian, grid-based biophysical model to complete the same simulation using 32 CPUs. If compared with the same computational power (e.g., single CPU), the PCPM-NPZD approach runs ~100 times faster for the biophysical modeling (Table 2; Scenario 1).

More importantly, in the PCPM framework, the hydrodynamics and associated water transport and mixing represented by particle trajectories are "reserved" and not affected by biochemical properties. In other words, it only takes another 5 min to run the PCPM-NPZD for a different set of parameters and property configurations. This is extremely useful during the model calibration and or ensemble simulations. The PCPM-NPZD would take 11.5 h to complete 100 runs using a single CPU, while the traditional method would require 500 h simulation using 32 CPUs (Table 2; Scenario 2). Such a high level of efficiency is not available from tracer-based models because one will have to re-run the Eulerian-based biological model for any change in parameter configuration or estimation of different property concentration. Also, the PCPM is capable of providing comparable simulation results to the soluble-tracer model, although the global and local mass conservation is not strictly preserved with finite particles. Above all, it is the PCPM's computational efficiency and coupling flexibility which makes it an attractive alternative method to the traditional approach.

Table 2. The comparison of total run time using the method developed in this study (new method) and the grid-based Eulerian method (traditional method) in two scenarios. Scenario 1: conduct coupled biophysical model only once; Scenario 2: run ensemble simulation of the coupled biophysical model for 100 simulations with different biological parameterization.

	Simulation Period (day)	Number of Central Processing Units (CPUs)	Time Per Run (Hour)	Scenario 1		Scenario 2	
				Required Runs	Total Time	Required Runs	Total Time
Hydrodynamic simulation (required for both methods)	30	64	15	1	15 h	1	15 h
Biological simulation							
New Method							
Particle trajectory model	30	1	1.5	1	1.6 hrs (1 CPU)	1	11.5 hrs (1 CPU)
PCPM-NPZD	30	1	0.1	1		100	
Traditional Method							
Eulerian, grid-based simulation	30	32	5	1	5 hrs (32 CPUs)	100	500 hrs (32 CPUs)

Author Contributions: Conceptualization, P.X. and D.J.S.; Formal analysis, X.Z., C.H., R.K. and X.Y.; Project administration, P.X.; Validation, X.Z.; Visualization, X.Z., C.H. and X.Y.; Writing—original draft, P.X. and D.J.S.; Writing—review and editing, P.X., D.J.S., R.K.

Funding: Xue's work is partly supported by the Ohio Department of Natural Resources, Sandusky Bay Initiative.

Acknowledgments: This is the contribution 57 of the Great Lakes Research Center at Michigan Technological University. The Michigan Tech high performance computing cluster, *Superior*, was used in obtaining the modeling results presented in this publication. We thank George Bullerjahn, Robert McKay and Timothy Davis (Bowling Green State University) for access to their Sandusky Bay water quality data.

Conflicts of Interest: The authors declare no conflict of interest.

Appendix A

Table A1. Biological model formulation and parameters; the original value of the parameters is provided in ( ) if tuned value was used.

Parameters	Description	Units	Value Used	References
k_s	Half-Saturation constant	μmol N/L	3 (0.6)	[17]
No	Nutrient threshold	μmol N/L	0 (1.4)	[18]
α_I	Initial linear slope at low irradiances	$\frac{\text{mgC}\cdot\text{m}^2}{\text{mgChl}\cdot\text{Einst}}$	7	[18]
β_I	Negative slope at high irradiances	$\frac{\text{mgC}\cdot\text{m}^2}{\text{mgChl}\cdot\text{Einst}}$	0	[43]
u_{max}	Maximum potential growth rate	$\frac{\text{mgC}}{\text{mgChl}\cdot\text{h}}$	2.4	[43]
T_{opt}	Optimum temperature	°C	27.2	[42]
T_{min}	Minimum temperature	°C	5.5	[42]
$u_{p(max)}$	Maximum growth rate for P	day^{-1}	1.1	
γ_p	Phytoplankton respiration coefficient	day^{-1}	0.01	[17]
γ_T	Exponential for Temperature forcing	dimensionless	0.07	[17]
γ_d	Remineralization rate of detritus	day^{-1}	0.015	[17]
G_{max}	Maximum P grazing rate by Z	day^{-1}	0.4	[17]
σ_P	Preference coefficient of Z on P	$\left(\text{mmol C m}^{-3}\right)^{-1}$	0.5	[17]
σ_D	Preference coefficient of Z on D	$\left(\text{mmol C m}^{-3}\right)^{-1}$	0.1	[17]
ϵ_p	Mortality rate of P	day^{-1}	0.005 (0.01)	[17]
ϵ_Z	Mortality rate of Z	day^{-1}	0.2 (0.01)	[17]
W_P	Sink velocity of P	m/day	0.6	[17]
W_D	Sink velocity of D	m/day	0.6	[17]
a_w	Water attenuation coefficient	m^{-1}	0.07	[18]
a_p	Phytoplankton attenuation coefficient	$\text{mgChl}^{-1}\ \text{m}^2$	0.03	[18]
a_d	Detritus attenuation coefficient	g detritus $\text{C}^{-1}\ \text{m}^2$	0.2	[18]

The mathematical expressions for the biological terms in the system of Equation (10) are listed below, where the definition and value of each parameter in the equations is above.

$$P(uptake) = u_{p(max)} \cdot f(T) \cdot f(I) \cdot f(N) \cdot P \tag{A1}$$

$$P(respiration) = \gamma_p \cdot P\Delta exp(\gamma_T \cdot T) \tag{A2}$$

$$Z(respiration) = \gamma_z \cdot \text{Zexp}(\gamma_T \cdot \text{T}) \tag{A3}$$

$$D(remineralization) = \gamma_d \Delta \text{D} \cdot \exp(\gamma_T \cdot \text{T}) \tag{A4}$$

$$ZP(grazing) = G_{max} \frac{\sigma_P P}{1 + \sigma_P P + \sigma_D D} Z \tag{A5}$$

$$ZD(grazing) = G_{max} \frac{\sigma_D D}{1 + \sigma_P P + \sigma_D D} Z \tag{A6}$$

$$P(mortality) = \epsilon_p P^2 \tag{A7}$$

$$Z(mortality) = \epsilon_z Z \tag{A8}$$

$$P(sinking) = -W_P \frac{\partial P}{\partial Z} \tag{A9}$$

$$D(sinking) = -W_D \frac{\partial D}{\partial Z} \tag{A10}$$

$$f(I) = (1 - e^{-\frac{\alpha_I I}{\mu max}}) e^{-\frac{\beta_I I}{\mu max}} \tag{A11}$$

$$f(N) = \frac{N - N_0}{K_s + N - N_0} \tag{A12}$$

$$f(T) = \exp(-2.3\left(\frac{T_{opt} - T}{T_{opt} - T_{min}})^2\right) \tag{A13}$$

$$I = I_0 \exp(-k_d h) \tag{A14}$$

$$k_d = a_w + a_p P_{chl} + a_d D \tag{A15}$$

References

1. Woods, J.D. The Lagrangian Ensemble metamodel for simulating plankton ecosystems. *Prog. Oceanogr.* **2005**, *67*, 84–159. [CrossRef]
2. Hellweger, F.L.; Bucci, V. A bunch of tiny individuals—Individual-based modeling for microbes. *Ecol. Model.* **2009**, *220*, 8–22. [CrossRef]
3. DeAngelis, D.L.; Grimm, V. Individual-based models in ecology after four decades. *F1000prime Rep.* **2014**, *6*, 39. [CrossRef] [PubMed]
4. Chapra, S.C. *Surface Water-Quality Modeling*; McGraw-Hill: Boston, MA, USA, 1997.
5. Franks, P.J. NPZ models of plankton dynamics: Their construction, coupling to physics, and application. *J. Oceanogr.* **2002**, *58*, 379–387. [CrossRef]
6. Butenschön, M.; Clark, J.; Aldridge, J.N.; Allen, J.I.; Artioli, Y.; Blackford, J.; Lessin, G. ERSEM 15.06: A generic model for marine biogeochemistry and the ecosystem dynamics of the lower trophic levels. *Geosci. Model Dev.* **2016**, *9*, 1293–1339. [CrossRef]
7. Hellweger, F.L.; Kianirad, E. Individual-based modeling of phytoplankton: Evaluating approaches for applying the cell quota model. *J. Theor. Biol.* **2007**, *249*, 554–565. [CrossRef] [PubMed]
8. Hellweger, F.L.; Kravchuk, E.S.; Novotny, V.; Gladyshev, M.I. Agent-based modeling of the complex life cycle of a cyanobacterium (Anabaena) in a shallow reservoir. *Limnol. Oceanogr.* **2008**, *53*, 1227–1241. [CrossRef]
9. Grimm, V.; Berger, U.; DeAngelis, D.L.; Polhill, J.G.; Giske, J.; Railsback, S.F. The ODD protocol: A review and first update. *Ecol. Model.* **2010**, *221*, 2760–2768. [CrossRef]
10. Bruggeman, J.; Bolding, K. A general framework for aquatic biogeochemical models. *Environ. Model. Softw.* **2014**, *61*, 249–265. [CrossRef]
11. Chai, F.; Dugdale, R.C.; Peng, T.H.; Wilkerson, F.P.; Barber, R.T. One-dimensional ecosystem model of the equatorial Pacific upwelling system. *Part I: Model development and silicon and nitrogen cycle. Deep Sea Res. Part II Top. Stud. Oceanogr.* **2002**, *49*, 2713–2745.
12. Fennel, K.; Wilkin, J.; Levin, J.; Moisan, J.; O'Reilly, J.; Haidvogel, D. Nitrogen cycling in the Middle Atlantic Bight: Results from a three-dimensional model and implications for the North Atlantic nitrogen budget. *Glob. Biogeochem. Cycles* **2006**, *20*. [CrossRef]
13. Edwards, K.P.; Barciela, R.; Butenschon, M. Validation of the NEMO-ERSEM operational ecosystem model for the North West European Continental Shelf. *Ocean Sci.* **2012**, *8*, 983–1000. [CrossRef]
14. Rodrigues, M.; Oliveira, A.; Queiroga, H.; Fortunato, A.B.; Zhang, Y.J. Three-dimensional modeling of the lower trophic levels in the Ria de Aveiro (Portugal). *Ecol. Model.* **2009**, *220*, 1274–1290. [CrossRef]
15. Xue, P.; Chen, C.; Qi, J.; Beardsley, R.C.; Tian, R.; Zhao, L.; Lin, H. Mechanism studies of seasonal variability of dissolved oxygen in Mass Bay: A multi-scale FVCOM/UG-RCA application. *J. Mar. Syst.* **2014**, *131*, 102–119. [CrossRef]
16. Chao, X.; Jia, Y.; Shields Jr, F.D.; Wang, S.S.; Cooper, C.M. Three-dimensional numerical simulation of water quality and sediment-associated processes with application to a Mississippi Delta lake. *J. Environ. Manag.* **2010**, *91*, 1456–1466. [CrossRef] [PubMed]

17. Luo, L.; Wang, J.; Schwab, D.J.; Vanderploeg, H.; Leshkevich, G.; Bai, X.; Wang, D. Simulating the 1998 spring bloom in Lake Michigan using a coupled physical-biological model. *J. Geophys. Res. Oceans* **2012**, *117*. [CrossRef]
18. Rowe, M.D.; Anderson, E.J.; Vanderploeg, H.A.; Pothoven, S.A.; Elgin, A.K.; Wang, J.; Yousef, F. Influence of invasive quagga mussels, phosphorus loads, and climate on spatial and temporal patterns of productivity in Lake Michigan: A biophysical modeling study. *Limnol. Oceanogr.* **2017**, *62*, 2629–2649. [CrossRef]
19. Wong, K.T.; Lee, J.H.; Choi, K.W. A deterministic Lagrangian particle separation-based method for advective-diffusion problems. *Commun. Nonlinear Sci. Numer. Simul.* **2008**, *13*, 2071–2090. [CrossRef]
20. Dimou, K.N.; Adams, E.E. A random-walk, particle tracking model for well-mixed estuaries and coastal waters. *Estuar. Coast. Shelf Sci.* **1993**, *37*, 99–110. [CrossRef]
21. Zhang, X.Y. Ocean Outfall Modeling—Interfacing Near and Far Field Models with Particle Tracking method. Ph.D. Thesis, MIT, Cambridge, MA, USA, 1995.
22. Xue, P.; Schwab, D.J.; Sawtell, R.W.; Sayers, M.J.; Shuchman, R.A.; Fahnenstiel, G.L. A particle-tracking technique for spatial and temporal interpolation of satellite images applied to Lake Superior chlorophyll measurements. *J. Great Lakes Res.* **2017**, *43*, 1–13. [CrossRef]
23. Harlow, F.H. The Particle-in-Cell Computing Method for Fluid Dynamics. *Methods Comput. Phys.* **1964**, *3*, 319–343.
24. Tskhakaya, D. The Particle-in-Cell Method. In *Computational Many-Particle Physics. Lecture Notes in Physics*; Fehske, H., Schneider, R., Weiße, A., Eds.; Springer: Berlin/Heidelberg, Germany, 2008; Volume 739.
25. Hockney, R.W.; Eastwood, J.W. *Computer Simulation Using Particles*; McGraw-Hill: New York, NY, USA, 1981.
26. Grigoryev, Y.N.; Vshivkov, V.A.; Fedoruk, M.P. *Fedoruk Numerical "Particle-in-Cell" Methods: Theory and Applications*; De Gruyter VSP: Utrecht, The Netherlands; Boston, MA, USA, 2002; 249p.
27. Conroy, J.D.; Kane, D.D.; Quinlan, E.L.; Edwards, W.J.; Culver, D.A. Abiotic and biotic controls of phytoplankton biomass dynamics in a freshwater tributary, estuary, and large lake ecosystem: Sandusky Bay (Lake Erie) chemostat. *Inland Waters* **2017**, *7*, 473–492. [CrossRef]
28. Salk, K.R.; Bullerjahn, G.S.; McKay, R.M.L.; Chaffin, J.D.; Ostrom, N.E. Nitrogen cycling in Sandusky Bay, Lake Erie: Oscillations between strong and weak export and implications for harmful algal blooms. *Biogeosciences* **2018**, *15*, 2891. [CrossRef]
29. Stumpf, R.P.; Wynne, T.T.; Baker, D.B.; Fahnenstiel, G.L. Interannual variability of cyanobacterial blooms in Lake Erie. *PLoS ONE* **2012**, *7*, e42444. [CrossRef] [PubMed]
30. Chaffin, J.D.; Bridgeman, T.B.; Bade, D.L. Nitrogen constrains the growth of late summer cyanobacterial blooms in Lake Erie. *Adv. Microbiol.* **2013**, *3*, 16. [CrossRef]
31. U.S. EPA. U.S. Action Plan for Lake Erie. 10 August 2017. Available online: https://www.epa.gov/sites/production/files/2017/08/documents/us_dap_preliminary_draft_for_public_engagement_8-10-17.pdf (accessed on 15 May 2018).
32. Davis, T.W.; Bullerjahn, G.S.; Tuttle, T.; McKay, R.M.; Watson, S.B. Effects of increasing nitrogen and phosphorus concentrations on phytoplankton community growth and toxicity during Planktothrix blooms in Sandusky Bay, Lake Erie. *Environ. Sci. Technol.* **2015**, *49*, 7197–7207. [CrossRef] [PubMed]
33. Chen, C.; Liu, H.; Beardsley, R.C. An unstructured grid, finite-volume, three-dimensional, primitive equations ocean model: Application to coastal ocean and estuaries. *J. Atmosp. Ocean. Technol.* **2003**, *20*, 159–186. [CrossRef]
34. Yang, Z.; Wang, T.; Copping, A.E. Modeling tidal stream energy extraction and its effects on transport processes in a tidal channel and bay system using a three-dimensional coastal ocean model. *Renew. Energy* **2013**, *50*, 605–613. [CrossRef]
35. Xue, P.; Schwab, D.J.; Hu, S. An investigation of the thermal response to meteorological forcing in a hydrodynamic model of Lake Superior. *J. Geophys. Res. Oceans* **2015**, *120*, 5233–5253. [CrossRef]
36. Anderson, E.J.; Bechle, A.J.; Wu, C.H.; Schwab, D.J.; Mann, G.E.; Lombardy, K.A. Reconstruction of a meteotsunami in Lake Erie on 27 May 2012: Roles of atmospheric conditions on hydrodynamic response in enclosed basins. *J. Geophys. Res. Oceans* **2015**, *120*, 8020–8038. [CrossRef]
37. Xue, P.; Pal, J.S.; Ye, X.; Lenters, J.D.; Huang, C.; Chu, P.Y. Improving the Simulation of Large Lakes in Regional Climate Modeling: Two-Way Lake–Atmosphere Coupling with a 3D Hydrodynamic Model of the Great Lakes. *J. Clim.* **2017**, *30*, 1605–1627. [CrossRef]

38. Khangaonkar, T.; Nugraha, A.; Xu, W.; Long, W.; Bianucci, L.; Ahmed, A.; Pelletier, G. Analysis of Hypoxia and Sensitivity to Nutrient Pollution in Salish Sea. *J. Geophys. Res. Oceans* **2018**. [CrossRef]
39. Ye, X.; Anderson, E.J.; Chu, P.Y.; Huang, C.; Xue, P. Impact of Water Mixing and Ice Formation on the Warming of Lake Superior: A Model-guided Mechanism Study. *Limnol. Oceanogr.* **2018**. [CrossRef].
40. Kelley, J.G.W.; Chen, Y.; Anderson, E.J.; Lang, G.A.; Xu, J. Upgrade of NOS Lake Erie Operational Forecast System (LEOFS) To FVCOM: Model Development and Hindcast Skill Assessment. *NOAA Tech. Memo. NOS CS* **2018**, *40*, 92.
41. Platt, T.G.C.L.; Gallegos, C.L.; Harrison, W.G. Photoinhibition of photosynthesis in natural assemblages of marine phytoplankton. *J. Mar. Res.* **1981**, *38*, 687–701.
42. Nicklisch, A.; Shatwell, T.; Köhler, J. Analysis and modelling of the interactive effects of temperature and light on phytoplankton growth and relevance for the spring bloom. *J. Plankton Res.* **2007**, *30*, 75–91. [CrossRef]
43. Fahnenstiel, G.L.; Chandler, J.F.; Carrick, H.J.; Scavia, D. Photosynthetic characteristics of phytoplankton communities in Lakes Huron and Michigan: PI parameters and end-products. *J. Great Lakes Res.* **1989**, *15*, 394–407. [CrossRef]
44. Stacey, M.T.; Cowen, E.A.; Powell, T.M.; Dobbins, E.; Monismith, S.G.; Koseff, J.R. Plume dispersion in a stratified, near-coastal flow: Measurements and modeling. *Cont. Shelf Res.* **2000**, *20*, 637–663. [CrossRef]
45. Kim, T.; Khangaonkar, T. An offline unstructured biogeochemical model (UBM) for complex estuarine and coastal environments. *Environ. Model. Softw.* **2012**, *31*, 47–63. [CrossRef]
46. Edwards, C.A.; Powell, T.A.; Batchelder, H.P. The stability of an NPZ model subject to realistic levels of vertical mixing. *J. Mar. Res.* **2000**, *58*, 37–60. [CrossRef]

Journal of
Marine Science and Engineering

MDPI

Article

Modeling the Transport and Fate of Sediments Released from Marine Construction Projects in the Coastal Waters of British Columbia, Canada

David B. Fissel * and Yuehua Lin

ASL Environmental Sciences Inc., #1-6703 Rajpur Place, Victoria, BC V8M 1Z5, Canada; alin@aslenv.com
* Correspondence: dfissel@aslenv.com; Tel.: +1-250-656-0177 (ext. 112)

Received: 2 August 2018; Accepted: 27 August 2018; Published: 6 September 2018

Abstract: Major marine construction projects, resulting in the release of sediments, are subject to environmental assessment and other regulatory approval processes. An important tool used for this is the development of specialized numerical methods for these marine activities. An integrated set of numerical methods addresses four distinct topics: (1) The near-field release and mixing of suspended sediments into the water column (i.e., the initial dilution zone); (2) the transport of the suspended sediments under the influence of complex ocean currents in the far-field; (3) the settling of the transported suspended sediments onto the seabed; and (4) the potential for resuspension of the deposited sediments due to sporadic occurrences of unusually large near-bottom currents. A review of projects subjected to environmental assessment in the coastal waters of British Columbia, from the year 2006 to 2017, is presented to illustrate the numerical models being used and their ongoing development. Improvements include higher resolution model grids to better represent the near-field, the depiction of particle size dependent vertical settling rates and the computation of resuspension of initially deposited sediments, especially in relation to temporary subsea piles of sediments arising from trenching for marine pipelines. The ongoing challenges for this numerical modeling application area are also identified.

Keywords: British Columbia; environmental assessment; marine construction; circulation; numerical model; sediment model; tidal current; wind-driven current; stratification; initial dilution zone

1. Introduction

In this paper, we present an overview of the development and applications of advanced numerical modeling of sediment transport and fate resulting from marine construction. This modeling is a useful tool to quantify the effects of these activities on the receiving environment. The modeling applications address a wide range of marine construction activities including: Dredging for the expansion of ports and harbors; disposal at sea of dredgates; trenching and backfilling for marine pipelines in shallow waters in approaching the coastline; and the removal and installation of underwater electrical cables.

In particular, we provide an overview of the modeling methods for their application in addressing environmental assessment and review issues. We present examples of the models for environmental assessment for port development and for construction of marine pipelines in the jurisdiction of British Columbia, Canada.

2. Physical Setting of British Columbia Coastal Waters

The British Columbia coastal waters extend over a distance of more than 900 km from the Canadian—United States border in the south, near the Port of Vancouver to the northern border between Alaska (U.S.) and British Columbia (Canada) in the north (Figure 1). The water depths range from up to 1800 m in the offshore continental margin to shallow waters in the inland seas such as

Chatham Sound and the Strait of Georgia, with larger water depths in the deep inland fjords extending into the mainland. The physical forces acting on the ocean waters can be highly energetic [1] due to: Seasonally large winds (fall and winter); large tides, especially in the northern British Columbia (BC) waters; and major fresh water discharges, including the Fraser, Skeena and Nass Rivers (Figure 1).

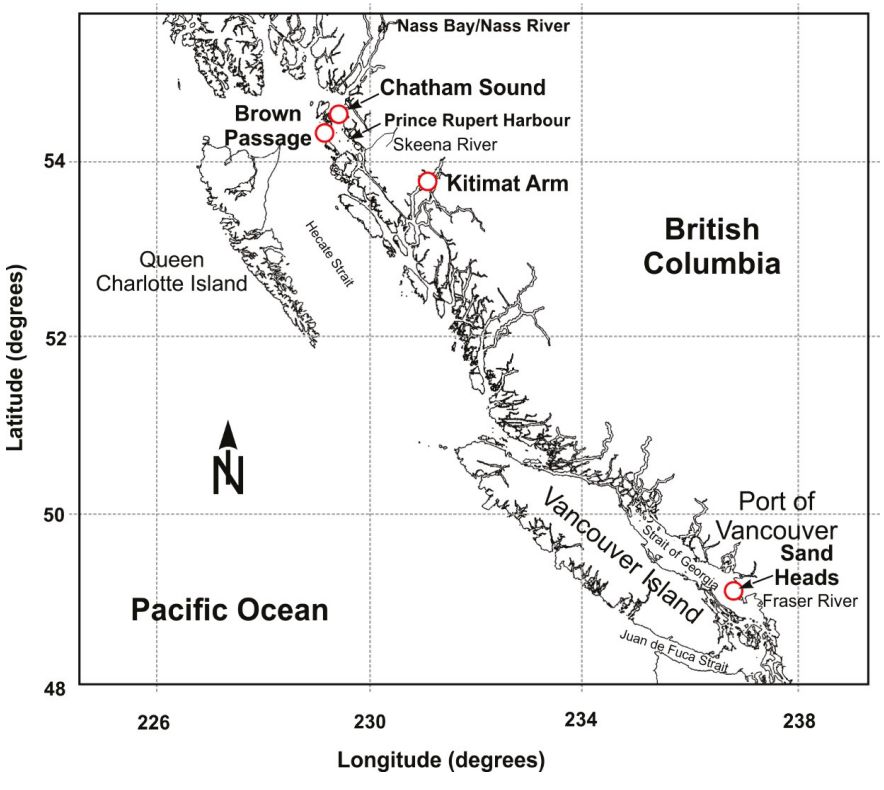

Figure 1. A map of the British Columbia coast highlighting the areas where numerical modeling of sediment transport from marine construction has been carried out, from the Port of Vancouver in the south to Prince Rupert and Kitimat Harbors in the north as well as the Nass River Estuary in Northern British Columbia.

The large river discharges result in a high degree of density stratification of the water column which necessitates the use of 3-dimensional (3D) numerical models required to represent the vertical variations in ocean currents and other water properties such as temperature, salinity and density.

3. Environmental Assessment of British Columbia Marine Construction Projects

Marine construction projects have undergone more detailed levels of environmental reviews and assessments in recent decades to the point where environmental issues can present the greatest challenge in the project development process [2]. All marine construction results in environmental change and some of these changes may have negative consequences for some of the stakeholders who may be affected by the dredging project.

Environmental changes resulting from marine construction which are typically addressed include potential increases in suspended sediments in the water column, which can: Reduce visibility within the water column for fish and other animals that are seeking food prey; and decrease the penetration of sunlight available to marine vegetation. Increased suspended sediments can also detract from human

usage of the marine areas for recreational purposes. Another environmental parameter of interest is an increase in the deposition of sediments to the seabed which may impact benthic communities and fish spawning usage of the seabed. In addition, sediment bound contaminants, if present in the marine construction area, may be released into the water column through the construction activities and may be subsequently be deposited at other locations. Guidelines for acceptable levels of increases in suspended sediment concentrations and sediment deposition are provided in the Canadian Council of Minister of the Environment (CCME) Canadian Water Quality Guidelines for the Protection of Aquatic Life [3]. Another aspect of environmental changes related to marine construction is the erosion of bottom sediments, which have been initially deposited due to marine construction, by unusually large near-bottom currents and their transport and fate in the marine environment. The changes in the sediment regime related to marine construction activities can be computed and quantified using numerical modeling methods presented below.

Major marine construction projects are subject to environmental reviews by governments through an environmental regulatory and permitting system. For projects in the province of British Columbia (BC) in Canada, the environmental regulatory system is shown as an organizational chart in Figure 2. The lead government environmental agency, usually the British Columbia Environmental Assessment Office (BCEAO), considers the inputs from many other government agencies, as well as from stakeholder groups including First Nations organizations and environmental non-governmental organizations, as well as private citizens, industry associations and others. For some projects, the federal government takes the lead role in the environmental assessment through the Canadian Environmental Assessment Agency (CEAA). In all cases, federal and provincial government agencies are involved in the expert review of evidence presented by the Proponent and its consultants in the application for the project.

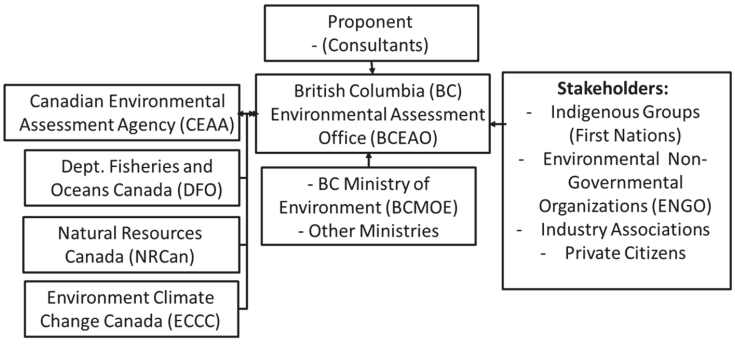

Figure 2. An organizational chart for the Environmental Assessment Regime in British Columbia, Canada.

Following the first environmental review and assessment of the project, the construction phase of the project is required to follow the project plan and to address any conditions stipulated in the environmental review, including environmental monitoring during construction, and in some cases, following the completion of construction.

The environmental assessments of marine construction typically involve key government departments including Environment and Climate Change Canada (ECCC), the Canadian Department of Fisheries and Oceans (DFO) and the British Columbia Ministry of the Environment (BCMOE). For sediment transport and disposal issues in these assessments, ECCC and BCMOE have developed guidelines and in-house expertise that are specific to marine sediments including Disposal at Sea [4–6] and contaminated sediments [7].

4. Approaches to Numerical Modeling of Sediments Released from Marine Construction Activities

The advantage of using numerical modeling methods for sediment releases from marine construction projects is that the distribution of the released sediments can be quantified in considerable detail in terms of: (a) The time-varying distribution of the construction-released suspended sediments in the water column with location over the receiving area of the marine environment; (b) the spatial distribution of the construction-released sediments deposited onto the seabed; and (c) the potential for resuspension of these deposited sediments and their subsequent transport and fate for times of very strong ocean bottom currents. To ensure the validity of the highly detailed model outputs, the numerical models are subjected to calibration and verification analysis through comparison with field data.

An overview of the high level modeling approach for addressing the transport and fate of construction-released sediments, as used for environmental assessment purposes, is presented in Figure 3.

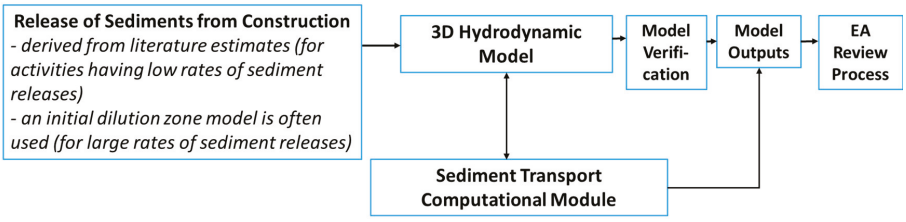

Figure 3. An overview of modeling methods for addressing environmental assessment (EA) issues.

4.1. 3D Hydrodynamic Models

The 3D hydrodynamic model is at the core of the integrated numerical modeling approach to simulating sediment transport and fate. These advanced numerical models compute the 3D circulation and densities of the receiving waters into which the sediments from marine construction activities are released. The hydrodynamic model provides a computational fluid dynamics approach to the study of river, estuarine and coastal circulation regimes. These hydrodynamic models apply the full three-dimensional basic equations of shallow water hydrodynamics and conservative mass transport and solves for time-dependent, three-dimensional velocities, salinity, temperature, kinetic energy and mixing length and water surface elevation. The model is calibrated against field observations with adjustments made to some of the model parameters to improve the model performance. The most common adjustments are to horizontal and vertical diffusivity values, seabed bottom roughness and parameters determining the bottom friction.

Hydrodynamic models require extensive data inputs to force the computation of the ocean circulation and other dynamical properties within the 3D coordinates encompassing the model domain, i.e., within the model area and over the included water depths. The key data inputs are: Surface winds, provided as a surface boundary condition (SBC) in the model; tidal height data at the open boundary conditions (OBC) of model domain which allow the model to compute tidal heights and tidal currents within the model domain; and the volume of freshwater from major rivers entering the model domain on the appropriate open boundary condition of the model. The bottom boundary of the model is provided by bathymetric data which represents the depth of the seabed below the mean water surface level at each model grid. The variations in the water density, determined from ocean temperatures and salinities, within the model domain is also provided as data inputs to the model through specifying these values at OBC's and as initial conditions within the model domain. Thus, surface heat flux (shortwave radiation, longwave radiation, latent, and sensible heat flux) and freshwater flux (evaporation, precipitation, and river runoff) may need to be considered in certain numerical studies. For some model applications, ocean waves within the model domain

are also computed arising from the surface winds and by representing the incoming waves as open boundary conditions. Another dynamical factor affecting surface momentum and heat flux is sea-ice, although sea-ice is not present in most BC coastal modeling projects.

The horizontal grid system varies among the various available hydrodynamic models. Many of the models make use of a finite-difference rectangular grid system with some of these allowing for higher resolution representation of the circulation in sub-areas of the model domain through the use of nested horizontal grid systems. For the projects of the present study we have used two 3D hydrodynamics models.

The first approach, COastal CIRculation and SEDiment transport Model (COCIRM-SED) (Figure 4), is a highly-integrated, three-dimensional, free-surface, finite-difference numerical model code for use on rivers, lakes, estuaries, bays, coastal areas and seas [8–11] and consists of the circulation or hydrodynamic model as well as sub-modules which including multi-category sediment transport, morphodynamics, water quality and particle tracking, as discussed further below. It also includes wetting/drying and nested grid schemes, capable of incorporating tidal flats, jet-like outflows, outfall mixing zone and other relatively small interested areas. The gridding scheme in COCIRM uses:

- in the vertical, either z layers (fixed size vertical layers which extend across the model domain) or sigma layers (a fixed number of vertical layers for each horizontal grid which is scaled according to the water depth in that grid), typically 10–30 layers.
- and a rectangular horizontal grid size, typically ranging in size from 10–100 m.

The second approach is the well-known Delft3D model which supports a more flexible model gridding system than the finite difference grid. In particular, curvilinear orthogonal grids can be used to provide a high grid resolution in the area of interest and a low resolution elsewhere, thus saving computational effort. Delft3D [12] is an advanced suite of integrated numerical model components Figure 5), or modules, which can be combined with the Delft3D-Flow hydrodynamic model. Delft 3D is one of a handful of advanced deterministic (process-based) coastal ocean models, which are routinely used for this purpose [13].

More recently, the use of the unstructured Finite-Volume, primitive equation Community Ocean Model (FVCOM) model, which allows much higher horizontal resolution in the immediate vicinity of the construction activity, has been under development. FVCOM is a predictive, unstructured-grid, finite volume, free-surface Community Ocean Model, solving the 3-D equations of shallow water hydrodynamics and conservative mass transport [14], which provides modules to compute sediment transport and fate that are applicable to marine construction model applications. This very flexible gridding approach allows for very high resolution, i.e., small volume elements in the immediate vicinity of the construction activity where the sediments are being released, as well as providing much greater flexibility for representing very narrow ocean channels adjoining much larger water bodies connecting these channels to offshore areas. An example of the highly variable gridding system which can be used in FVCOM for the area around the Port of Prince Rupert is shown in Figure 5.

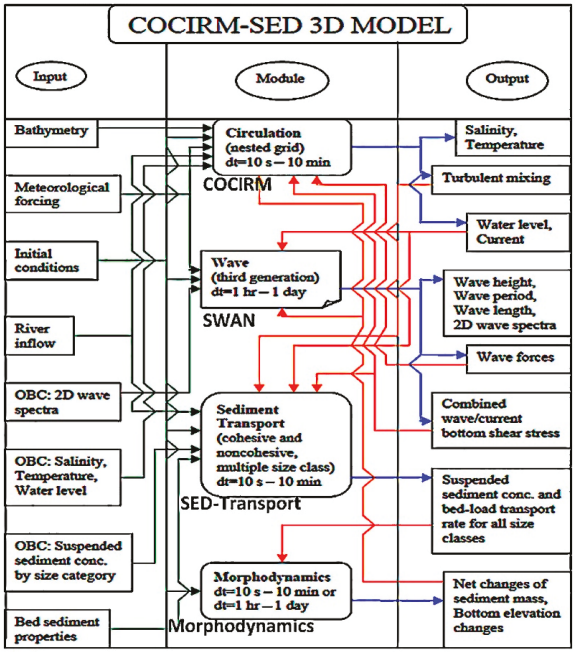

Figure 4. Schematic diagram of the COastal CIRculation and SEDiment transport Model (COCIRM-SED) numerical model. OBC represents Open Boundary Conditions, SWAN is the Simulating WAves Nearshore ocean wave model [12] and dt is the user-selectable time scale range for which bottom elevations are adjusted in the Morphodynamics module.

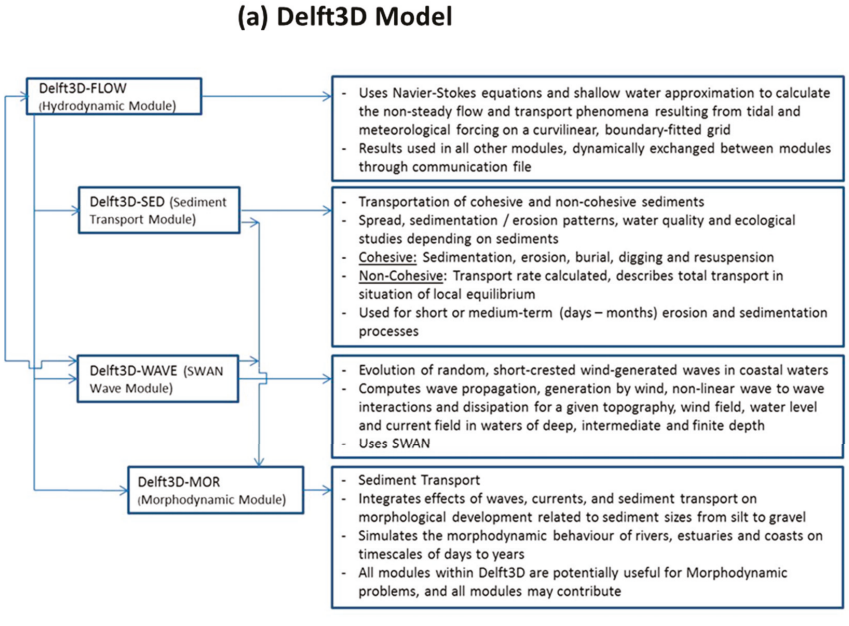

Figure 5. *Cont.*

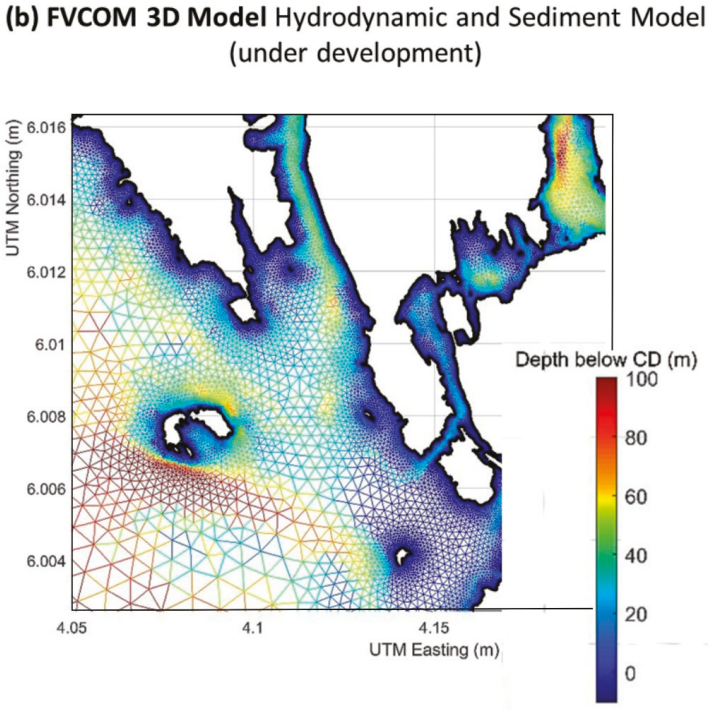

Figure 5. (**a**) Schematic diagram describing the major modules of the Delft-3D model which uses the same inputs and outputs as the COCIRM-SED model system presented in Figure 4; and (**b**) an example of a Finite-Volume, primitive equation Community Ocean Model (FVCOM) for the Port of Prince Rupert which is presently under development.

4.2. Release of Sediments from Construction

The release of sediments arising from marine construction activities is derived from technical documents on specific marine construction activities which are publicly available and from information provided by the marine construction operators and their equipment suppliers. Sediment releases are derived from the time varying rates of the mass and/or volumes of sediments arising from the construction activity which enter the marine receiving waters.

The nature of the sediments released into the receiving waters vary considerably according to the type of construction activity being much different for the mass and volumetric quantities of sediments released, and the rate of release. For example, for disposal at sea from large barges, this activity consists of very high volumes of materials being released, typically 2000 m^3, with nearly 100% release of the sediments into the ocean through the bottom of the barge (Figure 6), over a short period of time of a few minutes. In contrast, the rate of release of sediment mass or volume into the receiving waters is much smaller, by three to four orders of magnitude, for mechanical dredging of the seabed as discussed below.

The particle size distribution of the sediments being discharged is an essential input to determine the rate and transport of the sediments within the water column. The particle size distribution is determined through laboratory analyses of surficial and sub-surficial sediment samples obtained in the vicinity of the marine construction activities where sediments are initially moved. Other key sediment properties are the density or specific gravity and the settling velocity of each sediment type. Density is determined from laboratory measurements and settling velocity, by each particle size, is determined from published tables which in some projects is augmented by laboratory measurements of collected

sediment samples. All of these parameters are required by the Sediment Transport Computational Module (Figure 3) for each grid element of the Hydrodynamic Model which receives the released sediments at the model time steps in which the releases occur.

Figure 6. Examples of marine construction equipment: (**a**) A clamshell bucket grab; (**b**) a barge-mounted backhoe; (**c**) a cutter suction head and support vessel; and (**d**) a split hull barge used for disposal at sea.

Dredging construction activities take many different forms which generally fall within two general categories of mechanical dredging and hydraulic dredging [15]. Mechanical dredgers use a grab or a bucket to loosen the in-situ material on the seabed and raise it to the surface (Figure 6). These come in different types with the most common types being bucket dredgers, grab dredgers and backhoe dredgers. Hydraulic dredging involves raising the loosened materials from the seabed in suspension through a pipe system connected to a centrifugal pump. Hydraulic dredging systems also have different types including: A suction dredger, a cutter suction dredger and a trailing suction dredger (Figure 6). Ongoing improvements in dredging systems are being realized to make the dredging operations more efficient [16] and more effective in reducing the loss of materials during handling and transport of the materials. The dredged materials can be loaded onto the ship from which the dredge is suspended and then later offloaded, or in the case of the cutter suction dredge, the materials can be discharged through a pipe to an ocean disposal area.

Trenching and backfilling of marine pipelines or underwater electrical cables represents a different marine construction activity in which sediments are released into the ocean receiving waters. Burial of the pipe or cable first requires trenching of the seabed which can be done by three different methods: Water-jetting, mechanical cutting or ploughing [17]. Once installed, the pipeline or cable can be backfilled in order to provide protection through either natural infilling or by artificial methods [18].

The key release parameters of mass and volume discharged, the rate of releases and the spatial distribution of the released sediments within the receiving water column has a very large range of possible values. As an example, for mechanical dredging, Hayes et al (2007) [19] suggest that the rate and mass of sediment resuspended during standard clamshell bucket dredging varied from 0.16 to 0.88% based on 5 field studies for estuarine and freshwater river environments. Burt et al (2007) [20] provide a higher range of estimated release rates for a specific dredging operation in a river with normal values being 3.35% but larger values of 5–6% were reported, and even very large transient values of 10% or more were noted. Given the large range in reported sediment release values from these mechanical dredging activities, the sediment release rate needs to be examined for each specific dredging operation according to the type of dredging operation being conducted in terms of the equipment in use, the physical and geotechnical properties of the bottom materials to be excavated and the operating conditions while dredging is underway.

4.3. Representing Sediments in the Numerical Models

The representation of the initial released sediments into the model must specify the fundamental properties of the sediments within the initial receiving volume of the model grid elements including particle size distribution, specific gravity and the settling velocities for each particle size. For subsequent model time steps, the model computes the changing suspended sediment concentrations within each grid volume element under the influence of horizontal transport by the local ocean currents and the vertical settling of the sediments, for each particle size category.

The models use high resolution grid sizes, relative to the requirements for the representation of ocean current, water level and water density features, of a few tens of meters, or smaller. This model horizontal resolution, combined with typical model time steps of a few to several seconds, allows the initial release of the discharged sediments to be initially diluted within a volume of one to a few model grid cells in the horizontal and over all or a subset of the model grid elements in the vertical within this horizontal subarea of the model. This simplifies, and in some cases, avoids altogether the need for initial mixing or dilution zone models (discussed below). For very small release rates, the representation of the released suspended sediment concentration (SSC) is correct as an average value over the full area and volume of the receiving grid element, although it does not identify the peak value of the sediment concentration within the grid element. As the suspended sediments further mix under the influence of ambient diffusion, negative buoyant spreading and advection by the ambient currents, the model representation of the peak SSC values tends to better represent the actual peak SSC values over mixing time scales of many minutes to a few hours.

The initial area and volume over, which the suspended sediments from construction activities occurs varies greatly, according to the type of construction activity being conducted. As an example, for mechanical dredging, having small release rates, the initial release typically extends over an initial release zone (IRZ), with has typical horizontal distances of one to a few tens of meters. The horizontal model resolution should match the distance scale of the IRZ. However, the size of this zone, especially for simulations of construction with small release rates such as mechanical dredging, is typically more uncertain than the rate of release of sediment mass or volume from the construction activity. Should the uncertainties in the IRZ distance scales result in the horizontal model grid size being larger than the IRZ size, the SSC values will be initially underestimated by the ratio of the horizontal grid size to the near-field zone distance scale. For the opposite case of the IRZ distance being somewhat being larger than one model grid size, the initial SSC values will be overestimated within the model grid receiving the sediment release. The effect of this uncertainty for the size of the IRZ to the horizontal model grid size is largest in the immediate vicinity of the construction activity; this is a very small area, that is highly disturbed from normal conditions due to the physical presence of the marine construction equipment and the associated acoustic noise in air and in the water.

For assessment of environmental effects from sediment releases, the changes in SSC and sediment deposition are more important in areas beyond the IRZ of the marine construction. Over the near-field zone consists of the plume area dominated by rapid settling velocities and large changes in SSC and sediment load. These changes are dominated by gravity settling with advection and diffusion also being important. The dimension of the near-field zone is typically occurring over a distance of about 100 m from the IRZ with associated time scales of up to one hour [21]. Within the near-field zone, the expansion of the area of the released sediments results in multiple additional horizontal model grid elements containing the released sediments, and a corresponding reduction in the SSC levels within the individual grid elements. As the vertical settling and advection-diffusive mixing proceeds through the near-field zone, the uncertainties in the model representation of the SSC values tends to decrease from the uncertainties in the IRZ. Beyond the near-field zone, the released sediments enter the far-field zone in which the plume varies more slowly, and advective-diffusive processes are as important as vertical settling.

In the examples presented below, the horizontal model grid size is selected to approximately match the estimated distance scale of the IRZ. The emphasis in the presented model outputs are on

the changes in SSC and sediment deposition values beyond the immediate vicinity of the disturbed construction zone and the near-field zone. Often, the model output display results are presented and discussed for areas at distances from the construction zone of 100 to 300 m and beyond.

In contrast to mechanical dredging, the volume of the rates of sediment releases for disposal at sea from large barges, or high volume pipe discharges from cutter section dredging is typically much larger and can extend over many model grid elements. For these applications, an additional numerical model, in the form of an initial dilution zone (IDZ) model, is used to compute the initial SSC values and particle size distributions, which are then applied to the specification of sediments within the volume elements of the hydrodynamic model. For other types of sediment releases involving much high higher mass and volumes being released and much higher discharge rates, a 3D IDZ model is required. IDZ models are important especially with application to the disposal at sea of large volumes of marine dredgates from large barges or from pipe discharges with large volume fluxes, such as pipe discharges of dredgates from cutter suction dredging operations. Representing the release of large volumes of sediments can be addressed through specialized 3D models developed for this purpose. The IDZ models used in this paper are derived from two models which are part of the Automated Dredging and Disposal Alternatives Modeling System (ADDAMS) developed by the U.S. Army Corps of Engineers [22]. The Short Term FATE (STFATE), is a short-term fate model of sediment disposal, which is accepted by the U.S. Environmental Protection Agency [23]. The STFATE model can be used to simulate the short-term fate and near-field distribution of the disposal material released from large marine barges immediately following each disposal operation. The STFATE operates on the actual bathymetry using an identical or smaller model mesh to match the 3D hydrodynamic model grid, and typically is run over the initial tens of minutes of the disposal operation. STFATE simulates the dilution and dispersion of released sediments due to the gravitational descent, horizontal transport due to the ocean currents and turbulent diffusion and the rapid deposition of most coarse sediments with size larger than medium sand. The STFATE output provides the required information on the sediment releases to the 3D model hydrodynamic and sediment transport models, as well as the initial bottom accumulation in the immediate vicinity of the barge.

For discharges of released sediments through pipes, generated by hydraulic dredging methods, a different ADDAMS model, Continuous Discharge FATE (CDFATE) is used to simulate the initial dilution zone [24]. CDFATE is operated to simulate the distribution of suspended and deposited sediments for the pipe slurry discharge over a time frame of one hour or less under varying water depths and ocean current conditions. CDFATE delineates the horizontal spatial extent of the initial zone in which released sediments are present and the concentrations of the suspended sediments within this zone. To compute the vertical distribution of the sediment slurry from the pipe, and the amount of direct deposition during the initial 45 min of sediment disposal, the STFATE model was applied to the CDFATE results. The combination of CDFATE and STFATE simulations, where CDFATE provides the horizontal distribution and STFATE provides the vertical distribution (including direct deposition) provides a complete 3D representation of the SSC distribution for the initial dilution zone over the water column.

Other requirements for the computation of the transport and fate of sediments released from marine construction includes the representation of mitigation measures that can be conducted to limit the spatial extent of the SSC and deposition to the seabed in order to reduce environmental impacts. Two of these mitigative measures are the use of silt curtains and sheet piles located in the immediate vicinity of the marine construction activity. Realistic simulation of the effects of these mitigation measures requires the use of horizontal grids having horizontal grid dimensions of 20 m or less. Even for such fine grid sizes, the location of silt curtains may be displaced by a distance of a few to several meters from their actual location relative to the construction activity.

4.4. Sediment Transport Computational Module

The sediment transport computation module simulates the sediment dynamics of the released suspended sediments, separately for a set of discrete sediment particle size categories, typically numbering from 3–8. In the COCIRM-SED modeling framework, for fine-grained sediments with particle sizes less than 32–62 μm (clay–silt range), modeling of cohesive sediment transport is applied, while for coarse sediments with particle sizes of 32–62 μm (coarse silt, sand, granule and fine pebble), modeling of non-cohesive sediment transport is used. The vertical settling velocities for each sediment particle size category are derived according to laboratory and textbook results. Two separated parts are involved in coarse sediment transport, namely suspended-load and bed-load. The deposition of suspended sediments onto the seabed and the erosion of the deposited sediments off the seabed are also represented according to turbulent sediment dynamical methods derived from laboratory and widely accepted sediment-related hydraulic engineering methods. The morphological or morphodynamic module solves for the bottom elevation variations due to sediment deposition and erosion over the duration of the modeling.

The details of these computations for the modeling systems used in the present study are described in detail in References [10,12]. Evaluation of the environmental effects derived from the outputs from the modeling of the sediments released from marine construction activities are facilitated by comparisons with the SSC, and sediment deposition rates under natural conditions for the study area. The sediment regime of the natural environment can be represented through SSC and sediment deposition rates realized from observations or from sediment background models which use similar methods to those of the present study (e.g., Reference [25]).

5. Examples of Numerical Modeling of Sediments Released from Marine Construction Activities

A partial list of numerical modeling studies conducted in support of the environmental assessment for major marine construction projects proposed for the coastal waters of British Columbia from the year 2006 to 2017, is presented in Table 1. These eight studies illustrate the diversity of the marine construction activities, in terms of the type of construction activity simulated, the attributes of the 3D model used and the Initial Dilution Zone (IDZ) models that were applied. In all of these studies, numerical modeling of sediment releases played a key role in quantifying the effects on the marine environment.

Table 1. A list of selected sediment modeling projects for the transport and fate of sediments released from marine construction projects off the coast of British Columbia conducted over the years 2006 to 2017.

Geographical Area	Marine Construction Activity	3D Model, Grid Size (#Vertical Layers)	IDZ Model	Literature References
Roberts Bank, Strait of Georgia, BC	Vancouver Island Transmission Reinforcement (VITR) Project: trenching of underwater electrical cables	COCIRM-SED, 10 m/50 m (13)	STFATE	[9]
Kitimat Harbor, BC	Dredging of marine berths at proposed oil export marine terminal for an oil export project	COCIRM-SED, 20 m/100 m (20)	-	[26]
Prince Rupert Harbor, BC	Dredging in Harbor, Disposal at Sea	COCIRM-SED, 100 m (22)	STFATE, CDFATE	[27]
Brown Passage	Disposal at Sea of marine dredgates from marine construction in Prince Rupert	COCIRM-SED, 100 m (22)	STFATE	[10,28,29]
Porpoise Channel near Prince Rupert	Dredging of Materials Offloading Facility (MOF) for a Liquified Natural Gas (LNG) Project	COCIRM-SED, 30 m/210 m (12)	-	[28]
Casey Cove, Prince Rupert	Dredging of Marine Berths & Materials Offloading Facility (MOF) for a LNG Project	COCIRM-SED, 30 m/210 m (13)	-	[30,31]
Kitimat Harbor	Dredging for a LNG marine terminal	COCIRM-SED, 20 m/100 m (20)	-	[32]
Nass Bay and Iceberg Bay	Trenching and backfilling for a marine gas pipeline	Delft3D-SED, 10 m/35 m (10)	-	[33]

In the remainder of this section, for three of these studies, we present descriptions of the modeling approach used and examples of the model outputs which were used to inform the environmental assessment of the projects.

5.1. Marine Dredging in Porpoise Channel of Chatham Sound

The first example is from the BC North Coast in the vicinity of the Port of Prince Rupert within the extended area managed by the Prince Rupert Port Authority. This dredging operation was simulated to occur over a period of 153 days from January to June. The model domain includes southern and central Chatham Sound, a shallow inland sea, with the construction type being dredging the sea bed in Porpoise Channel off Lelu Island, in order to build a marine offloading facility for a proposed Liquified Natural Gas (LNG) project on Lelu Island. This involves dredging of 615,000 m^3 of bottom materials for construction of a materials offloading facility in Porpoise Channel, the resolution of the COCIRM-SED model [28] is 30 m in the vicinity of the dredging area including Porpoise Channel and adjoining areas, within a 210 m horizontal grid over the remainder of the model domain Figure 7. The vertical resolution was 12 z-layers. Z-layers rather than sigma layers were used for this model application because of the high degree of vertical stratification within the water column in the model domain due to the direct discharges of the Skeena River. This high level of vertical stratification could result in instabilities to the model computations, especially near open boundaries, if using sigma layers in such a highly stratified hydrodynamic regime.

The COCIRM-SED model was forced at the open boundary conditions by tidal levels. The Skeena River discharge was specified as an input to the southeast open boundary of the model. Wind forcing is applied through the surface boundary condition and the stratified water properties within the model are determined from historical DFO conductivity temperature depth (CTD) water properties data sets. Both COCIRM-SED models were calibrated and validated using comparisons to DFO current meter data sets (locations shown in Figure 7) with overall good agreement between the model and observed currents [28].

In this simulation, the loss rate was taken to be 1% so as to be on the conservative side based on studies by [18] for releases from a bucket dredge. These releases were represented as one-half of the total loss occurring within 5 m of the bottom due to a combination of: Capturing the sediment, expulsion of sediments when closing the bucket, and during the initial raising of the bucket through the water column. The remaining 50% of the losses are assumed to be evenly distributed through the upper water column. The mass discharge rate of the released sediments, as computed individually for each of six particle size categories, were input directly into the z-layers of the 30 m horizontal grids that were occupied by the dredging unit.

The model outputs provided for the environmental assessment process included the predicted distribution of Suspended Sediment Concentration (SSC) during the course of the dredging operations (see an example of the model derived SSC values for a large flood and large ebb tidal flow in Figure 8) and the deposition of the sediments released by dredging onto the seabed, as shown in Figure 9. The highest SSC's of 16–17 mg/L are in the immediate vicinity of the dredging, within 200 m, while the adjoining areas within about 1 km have SSC levels of 1–5 mg/L. Otherwise, the SSC values are below 1 mg/L which is well below natural background levels.

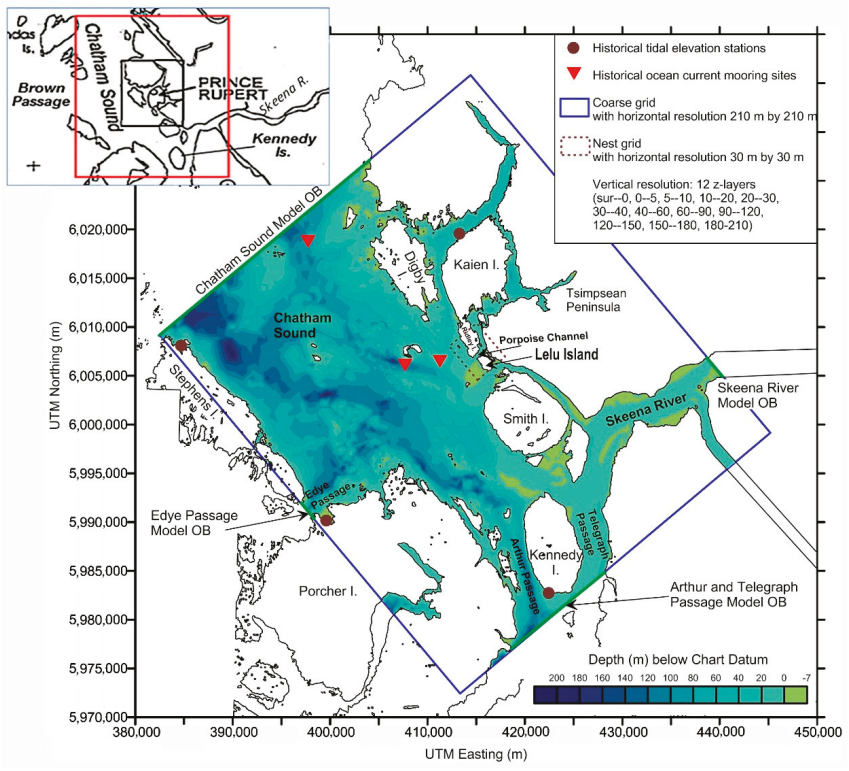

Figure 7. The model domain, open boundaries (OB), water depths and locations of current meter data sets used in model verification for the numerical sediment transport model for dredging in Porpoise Channel.

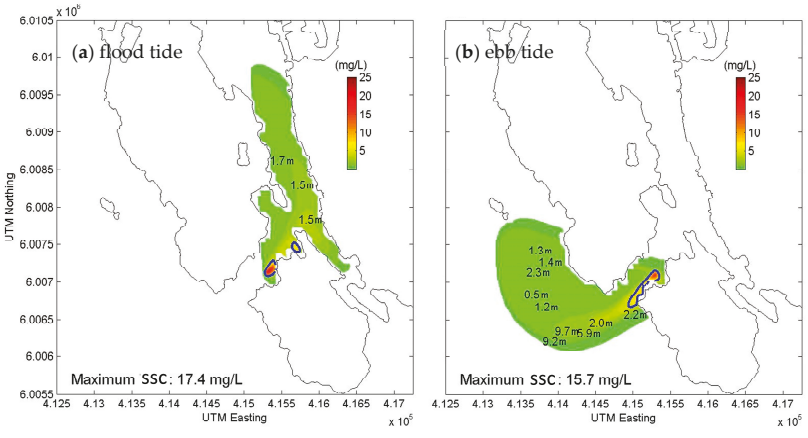

Figure 8. Model-derived suspended sediment concentration (SSC) (mg/L above background, maximum value in the water column) for (**a**) a flood tide and (**b**) and ebb tide. Numbers mark depths (above seabed) of maximum values in vertical column. Blue contours present the areas of SSC greater than 5 mg/L.

The sediment models are also used to compute the net deposition resulting from the 30 days of dredging (Figure 9). Here we see that the maximum deposition is 0.11 m, which is confined to within 50 m of the immediate vicinity of the disturbed dredging area. Outside of the immediate area of dredging the sediment depositions amount to 0.01–0.025 m in the confined areas of Porpoise Channel, extending inland to the mainland coast. Otherwise, deposition levels are very low at less than 0.002 m (or 2 mm) which are well below background levels which are related to deposition from the Skeena River sediments and natural transport of sediments.

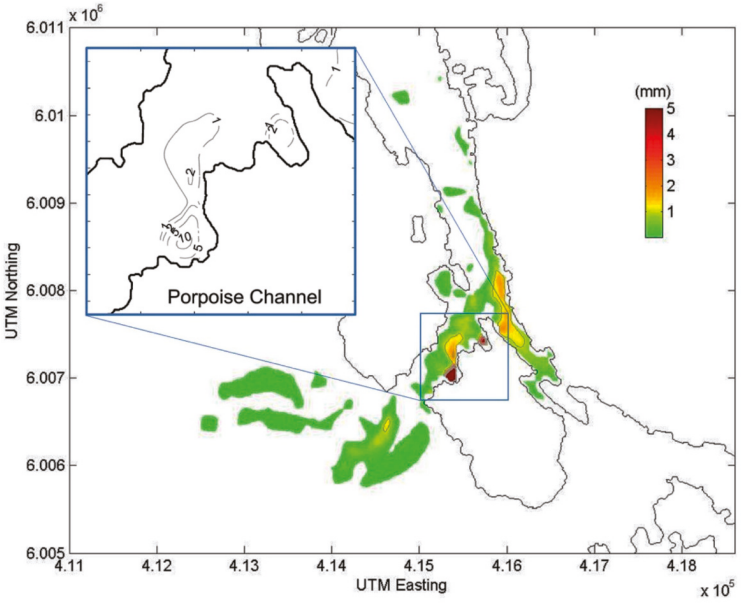

Figure 9. Model derived deposition onto the seabed in Porpoise Channel and the surrounding area after 30 days of dredging activity in January. The line contours are for values of 1, 2 and 5 mm.

5.2. Disposal at Sea of Dredged Sediments in Brown Passage

This example of numerical modeling of sediment transport is from Brown Passage, which connects the inland sea of Chatham Sound to the deeper Pacific Waters of Hecate Strait and Dixon Entrance [29]. The construction activity simulated is for ocean dumping from barges for disposal of dredged sediments at a proposed site in approximately 200 m water depth (Figure 10). The disposal from the barge has a volume of 2400 m^3 which occurs over a 2 min duration, with barge disposals being repeated every 8 h and 43 min.

The COCIRM-SED finite difference model was used over the domain shown in the map and with a horizontal resolution of 100 m and a vertical resolution of 22 sigma layers [25]. The use of sigma layers was suitable for this model application because the density stratification of the water column within the model domain was smaller than for model domains which include direct inputs from major river discharges. The model was forced at tidal height elevations spanning four open boundaries and by hourly surface winds. The four model open boundaries include the four adjoining sides of Brown Passage (Figure 10). Tidal elevations at these four open boundaries were derived from 7 major tidal height constituents (O1, P1, K1, N2, M2, S2, K2) using the DFO standard tidal prediction program. Wind forcing is applied through the model surface boundary conditions using wind data measurements at the nearby Lucy Island weather station. The initial temperature and salinity distribution within the model domain are derived from DFO historical CTD measurements [29].

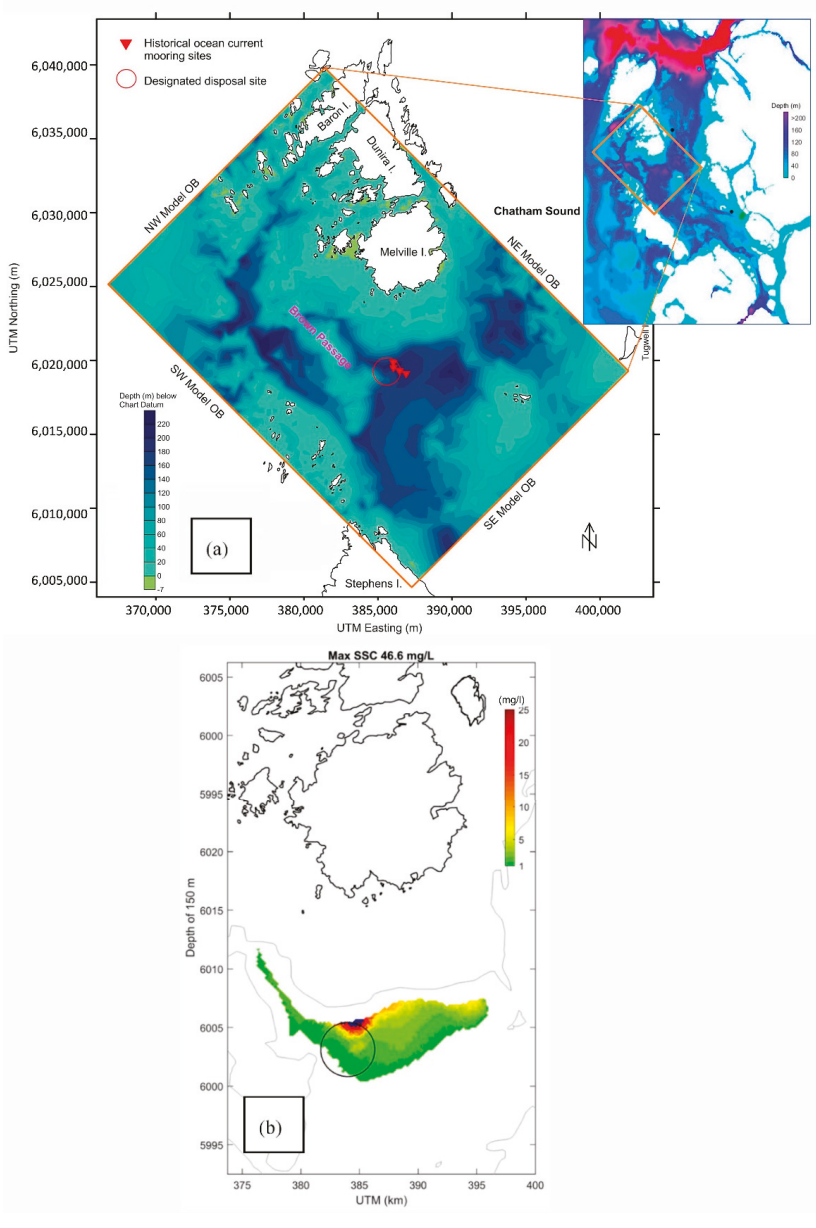

Figure 10. (**a**) The Brown Passage model domain and its water depths and (**b**) a sample of the model results for the sediment plume at 150 m depth realized from the disposal at sea operations. Areas with SSC greater than 25 mg/L are marked by blue color. The black circle marks a previously used ocean disposal site (1 nautical mile in diameter).

The STFATE IDZ model was used to represent the short term distribution of the sediment releases as input to the 3D hydrodynamic model. The STFATE model results show that during the initial 45 min of each disposal trip, the sand settles more quickly than clay or silt. The suspended sediment is mostly concentrated within 10 m of the bottom. Moderately high levels of clay and silt (50 mg/L) are

predicted at depths around 150 m above the seabed (i.e., at 50 m water depth), and moderately high levels of sand (70 mg/L) are predicted from approximately 20–80 m above the seabed (i.e., at 120 to 180 m depth).

One snapshot of the sediment transport model results for SSC is shown at 150 m depth (Figure 10). Here we see maximum SSC value of 46.6 mg/L in the immediate vicinity, within 500 m, of the barge disposal location. The SSC values extend in the form of a subsurface plume eastward from the previously used disposal site to a distance of a few kilometers with SSC values that are generally less than 5 mg/L.

5.3. Trenching for a Marine Pipeline in Nass Bay

This example of sediment transport modeling is for trenching conducted for a marine pipeline project in the shallow waters of Nass Bay of the Nass River Estuary in northern BC [33]. Here we see (Figure 11) the water depths in the model domain (left) and the horizontal grids in the Delft3D-SED model with 35 m resolution except for a higher resolution of 10 m in the pipeline corridor along southern side of Nass Bay. In the vertical, 10 sigma layers were used. For this model application, sigma layers were found to be suitable even with the direct input of freshwater from the Nass River into Nass Bay, because the water depths in Nass Bay are comparatively shallow which allows sigma the absolute depths of the sigma layers to vary less than would be the case where there is a large range in the total water depth within the receiving waters of the low density river water inputs. The forcing for the Delft3D hydrodynamic model is tidal heights and salinities obtained from time series measurements at the single open boundary at the Nass Bay entrance to Portland Inlet. The discharge from the Nass River obtained daily river data from Station 'Nass River above Shumal Creek (08DB001)', recorded by the Environment Canada and available online, is used for the eastern open boundary of the model. Salinity conditions required to initialize the model were obtained using transect data from boat-based CTD profile data across the mouth of Nass Bay as well as at interior locations in Nass Bay and Iceberg Bay. Winds forcing was provided by the Environment Canada Meteorological Service (ECMSC) using the High Resolution Deterministic Prediction System (HRDPS). The Delft3D hydrodynamic model was validated using ocean current observations obtained from an Acoustic Doppler Current Profiler (ADCP) instrument mounted on a subsurface mooring located at 22.5 m water in southwestern Nass Bay during a model verification run for a 25-day period in November 2015 [33].

The sediments released from the trenching operation were derived for the case of two mechanical bucket dredges operated simultaneously from the center of the marine pipeline corridor moving in opposite directions. The total width of the trench is taken as 33 m with 1:5 sloping sides spanning 15 m on either side plus a flat segment of 3 m width. Handling losses as the sediment is trenched and then dumped either onto a spoil pile directly or in intermediate locations are taken as 3% for each time the material is moved. The 3% release rate is at the large end of the possible range of release rates so as to avoid any possibility of underestimation of sediment releases in the absence of a definitive design for this construction activity. This release rate is applied over the full water column since water depths relative to the low tide water levels are small being about 1 m or over nearly all of the pipeline route.

A representative example of the sediment model results is provided a snapshot of the SSC values at the end of flood tide (Figure 12). Here, the highest SSC values occur within 50 m of the two dredging barges reaching values of up to 66 mg/L. These large SSC values were limited to areas within 50 m of the dredging barges with much lower values of 1–5 mg/L extending to distances of 100–200 m, beyond which the SSC values were very small at <1 mg/L. In the areas beyond 50 m from the dredging barges, the SSC values are generally considerably less than the natural background SSC values in Nass Bay associated with the high turbidity of the Nass River waters within Nass Bay and the natural episodes of bottom sediment resuspension associated with very large tidal currents in the shallow waters of Nass Bay [33].

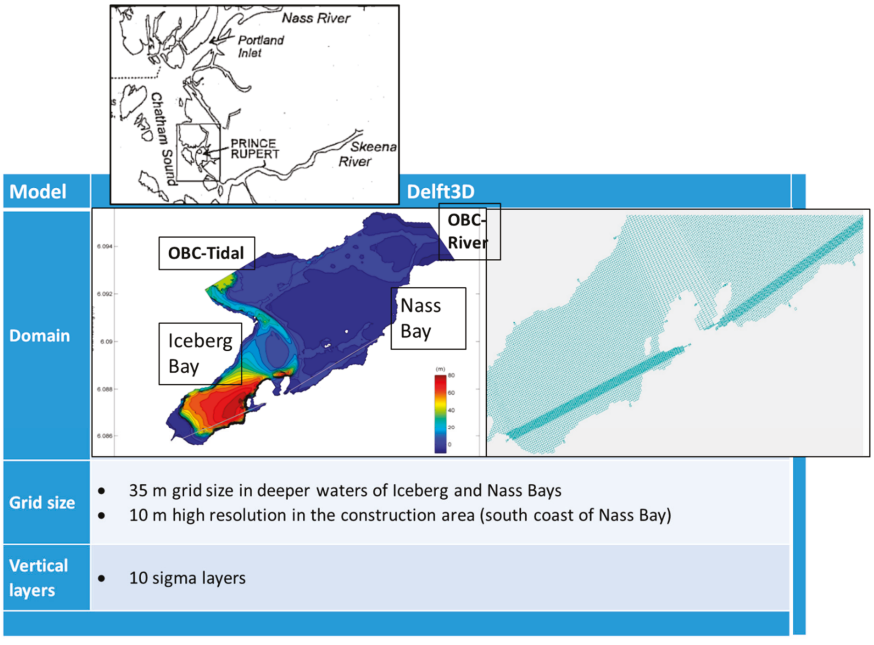

Figure 11. The model domain, including water depths and the horizontal grids, for the Delft3D sediment transport model used to simulate the fate and transport of sediments from trenching and backfilling for marine pipeline construction in Nass Bay.

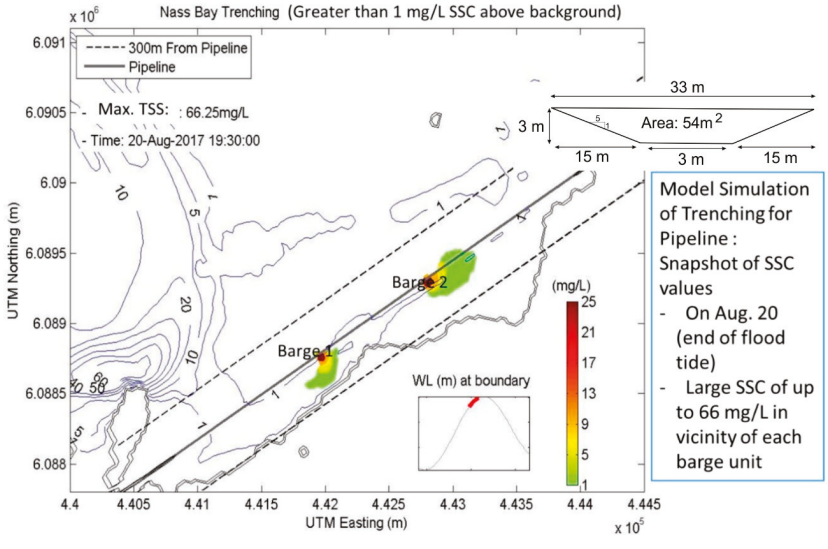

Figure 12. Model derived simulations of suspended sediment concentrations for trenching of the Nass Bay pipeline by two clamshell dredge units.

6. Summary and Discussion

The use of integrated 3D sediment transport models provides a useful method to simulate the suspended sediment concentrations and deposition onto the seabed of sediments released from

marine construction activities. The 3D models have horizontal grid resolutions of typically 10–30 m (for dredging and for marine pipeline construction) and 100 m (for ocean disposal at sea) with vertical resolution of 10–30 layers over the water column.

The sediment transport modeling provides quantitative and highly detailed depictions of the SSC distributions in all three dimensions under time varying forcing by tides, winds and river discharges. It also provides detailed two dimensional maps of the deposition of the released sediments resulting from the marine construction activity. These model outputs inform the environmental assessments of the marine construction project by allowing the effects of the marine construction to be estimated on the natural marine ecosystem, including marine vegetation, benthic communities and fishing activities.

The results of the sediment transport models can be used to develop more environmentally effective and efficient marine construction plans and to test the effect of mitigative measures such as sheet piles and silt curtains. The effects of mitigative measures is carried out by operating the model with and without the mitigative measures. The effect of silt curtains was tested through model runs for the two projects conducted in Kitimat Harbor (Table 1) and the model results provided information on the reductions of, and areal extent for, the SSC and deposition values resulting from the use of silt curtains. 3-D modeling is useful in quantifying the effects of mitigative measures and in optimizing the results achieved from these measures. In a similar fashion, variations in the way the construction activity is conducted can be simulated through model runs by computing the effect of changes in the construction plan on the resulting SSC and sediment deposition.

Further progress for this type of sediment transport and fate modeling can be achieved through the use of even higher resolution models through variable grid sizes which would allow very high resolution in the immediate vicinity of the marine construction activity where the sediments are released. The improvement in horizontal resolution reduces the reliance on the use of initial dilution zone models which have their own uncertainties and increase the effort for the overall modeling process. The use of unstructured finite volume models represent an approach to achieving the very high resolution being sought.

Another area of improvement would be to have more accurate inputs to the models on the sediment releases from construction activities, including more data on wider range of construction activities and the evolving equipment and operations within each type of construction activity. The improved sediment release information could be achieved by in-situ and laboratory-derived measurements of sediment releases during the operation of the equipment in the marine environment. The in-situ studies would include measurements of the mass and volumetric rates of sediment release, the areas and volumes of the receiving waters over which the sediment releases from the equipment extend initially in the first several seconds, following the release and differences in the released sediments rates by sediment particle size categories. Laboratory studies would involve the use of controlled physical models of the construction activity, including the actual sediments that are being handled, to make similar measurements as described above for the in-situ measurements.

Finally, improvements in the computation of sediment transport and fate in the far-field is needed to improve on the use of present understandings which are derived from general references to the engineering literature and generalized laboratory studies. In some cases, improvements could be realized through the use of laboratory studies and in-situ measurements for the specific area and sediments which apply to the particular marine construction project being assessed. The key processes which should be addressed are to better represent the variability in: Settling velocities for each particle size category and the resuspension of deposited sediments under episodic occurrences of large near-bottom currents. The use of project-specific field and laboratory studies provide testing and validation of understandings applied in the sediment transport and fate computational module which are derived from engineering literature references and generalized laboratory studies. This approach would increase the confidence in the sediment transport and fate modeling results.

Author Contributions: Conceptualization, D.B.F. and Y.L.; Methodology, D.B.F. and Y.L.; Model Development and Validation, Y.L. and D.B.F.; Formal Analysis, Y.L.; Writing-Original Draft Preparation, D.B.F.; Writing-Review & Editing, D.B.F. and Y.L.; Project Administration, D.B.F.

Funding: This research, which primarily addresses developing methodology and approaches to sediment transport and fate modeling, received no external funding. For the examples of the model outputs presented, partial funding was provided towards specific model runs by various clients of ASL Environmental Sciences Inc.

Acknowledgments: The contributions of ASL Environmental Sciences Inc.'s personnel who assisted in the operation of the models are Alison Scoon and Ryan Clouston. We also acknowledge the contribution to the early development of the modeling methodology and approaches of Jianhua Jiang, formerly with ASL (until 2012) and presently with Alberta Energy Regulator (AER).

Conflicts of Interest: The authors declare no conflict of interest.

References

1. Thomson, R.E. *Oceanography of the British Columbia Coast*; Canadian Special Publication of Fisheries and Aquatic Sciences 56; Fisheries and Oceans Canada: Ottawa, ON, Canada, 1981; p. 291. Available online: http://waves-vagues.dfo-mpo.gc.ca/Library/487.pdf (accessed on 16 July 2018).
2. International Association of Dredging Companies (IADC); International Association of Ports and Harbors (IAPH). *Dredging for Development*, 6th ed.; Bray, N., Cohen, M., Eds.; International Association of Dredging Companies (IADC): The Hague, The Netherlands, 2011; p. 86.
3. Canadian Council of Ministers of the Environment. Canadian Water Quality Guidelines for the Protection of Aquatic Life—Total Particulate Matter. 2002. Available online: http://ceqg-rcqe.ccme.ca/download/en/217 (accessed on 16 July 2018).
4. Environment Canada. *Technical Guidance for Physical Monitoring at Ocean Disposal Sites*; Marine Environment Division; Environment Canada: Fredericton, NB, Canada, 1998; p. 49. Available online: http://publications.gc.ca/collections/collection_2014/ec/En14-186-1998-eng.pdf (accessed on 16 July 2018).
5. Environment and Climate Change Canada. Appendix C: Guidance for Disposal Site Selection. 2013. Available online: https://www.ec.gc.ca/iem-das/default.asp?lang=En&n=8E789D01-1&toc=show (accessed on 16 July 2018).
6. Environment and Climate Change Canada. Disposal at Sea Permit Application Guide: Disposal Site Selection, Assessments. 2018. Available online: https://www.canada.ca/en/environment-climate-change/services/disposal-at-sea/permit-applicant-guide/applicant-guide-permit-site-selection/assessments.html (accessed on 16 July 2018).
7. McDonald, D.D.; Ingersoll, C.G. A Guidance Manual to Support the Assessment of Contaminated Sediments in Freshwater, Estuarine, and Marine Ecosystems in British Columbia. Volume IV—Supplemental Guidance on the Design and Implementation of Detailed Site Investigations in Marine and Estuarine Ecosystems. Report for British Columbia Ministry of Environment, Lands, and Parks. 1998; p. 85. Available online: https://www2.gov.bc.ca/assets/gov/environment/air-land-water/site-remediation/docs/technical-guidance/x19_v4.pdf (accessed on 16 July 2018).
8. Jiang, J.; Fissel, D.B.; Topham, D. 3D numerical modeling of circulations associated with a submerged buoyant jet in a shallow coastal environment. *Estuar. Coast. Shelf Sci.* **2003**, *58*, 475–486. [CrossRef]
9. Jiang, J.; Fissel, D.B.; Borg, K. Sediment Plume and Dispersion Modeling of Removal and Installation of Underwater Electrical Cables on Roberts Bank, Strait of Georgia, British Columbia, Canada. In *Estuarine and Coastal Modeling*; Spaulding, M.L., Ed.; American Society of Civil Engineers: Reston, VA, USA, 2008; pp. 1019–1034.
10. Jiang, J.; Fissel, D.B. Modeling Sediment Disposal in Inshore Waterways of British Columbia, Canada. In *Estuarine and Coastal Modeling*; Spaulding, M.L., Ed.; American Society of Civil Engineers: Reston, VA, USA, 2012; pp. 392–414.
11. Lin, Y.; Fissel, D.B. The Ocean Circulation of Chatham Sound, British Columbia, Canada: Results from Numerical Modeling Studies Derived Using Historical Data Sets. *Atmos.-Ocean* **2018**. [CrossRef]
12. Deltares. Software Simulation Products and Solutions. 2015. Available online: https://oss.deltares.nl/web/delft3d (accessed on 16 July 2018).
13. Amoudry, L.O.; Souza, A.J. Deterministic coastal morphological and sediment transport modeling: A review and discussion. *Rev. Geophys.* **2011**, *49*, RG2002. [CrossRef]

14. Chen, C.; Liu, H.; Beardsley, R.C. An unstructured, finite-volume, three-dimensional, primitive equation ocean model: Application to coastal ocean and estuaries. *J. Atmos. Oceanic Technol.* **2003**, *20*, 159–186. [CrossRef]
15. European Dredging Association, Types of Dredgers. 2018. Available online: https://www.european-dredging.eu/Types_of_dredger (accessed on 16 July 2018).
16. Randall, R.; Drake, A.; Cenac, W., II. Improvements for Dredging and Dredged Material Handling. In Proceedings of the WEDA XXXI Technical Conference and TAMU 42 Dredging Seminar, Nashville, TN, USA, 5–8 June 2011; Available online: https://www.westerndredging.org/phocadownload/ConferencePresentations/2011_Nashville/Session2A\protect\discretionary{\char\hyphenchar\font}{}{}AdvancesInDredging/2%20-%20Randall,%20Drake,%20Cenac%20-%20Improvements%20for%20Dredging%20and%20Dredged%20Material%20Handling.pdf (accessed on 16 July 2018).
17. Braestrup, M.W. (Ed.) *Design and Installation of Marine Pipelines*; Blackwell Press: Oxford, UK, 2005; p. 342. Available online: http://marineman.ir/wp-content/uploads/2015/06/M.W.-Braestrup-Design-And-Installation-Of-Marine-Pipelines-Blackwell-Science-2005.pdf (accessed on 16 July 2018).
18. Finch, M.; Fisher, R.; Palmer, A.; Baumgard, A. An Integrated Approach to Pipeline Burial in the 21st Century. In Proceedings of the Deep Offshore Technology 2000 Conference, New Orleans, LA, USA, 7–9 November 2000.
19. Hayes, D.F.; Borrowman, T.D.; Schroeder, P.R. Process-Based Estimation of Sediment Resuspension Losses during Bucket Dredging. In Proceedings of the WEDA XVIII World Dredging Congress, Lake Buena Vista, FL, USA, 27 May–1 June 2007.
20. Burt, N.; Land, J.; Otten, H. Measurement of sediment release from a grab dredge in the River Tees, UK, for the calibration of turbidity prediction software. In Proceedings of the WODCON 2007 Conference Proceedings, Orlando, FL, USA, 25–29 April 2007; pp. 1173–1190.
21. Bridges, T.S.; Ellis, S.; Hayes, D.; Mount, D.; Nadeau, S.C.; Palermo, M.R.; Patmont, C.; Schroeder, P. *The Four Rs of Environmental Dredging: Resuspension, Release, Residual and Risk*; US Army Corps of Engineers Report ERDC/EL TR-08-4; US Army Corps of Engineers: Vicksburg, MS, USA, 2008; p. 64. Available online: http://citeseerx.ist.psu.edu/viewdoc/download?doi=10.1.1.466.3020&rep=rep1&type=pdf (accessed on 16 July 2018).
22. Schroeder, P.R.; Palermo, M.R.; Myers, T.E.; Lloyd, C.M. *The Automated Dredging and Disposal Alternatives Modeling System (ADDAMS)*; ERDC TN EEDP-06012; U.S. Army Engineering Research and Development Centre: Vicksburg, MS, USA, 2004; Available online: http://el.erdc.usace.army.mil/eedp (accessed on 16 July 2018).
23. EPA and USACE. Appendix C Evaluation of Mixing. In *Evaluation of Dredged Material Proposed for Discharge in Waters of the U.S.—Testing Manual (Inland Testing Manual)*; Environmental Protection Agency and United States Army Corps of Engineers: Washington, DC, USA, 1998; p. iv + 80. Available online: http://sdi.odu.edu/mbin/addams/stfate/STFATE_inlandc.pdf (accessed on 16 July 2018).
24. Chase, D. *CDFATE User's Manual*; U.S. Army Engineering Research and Development Centre: Vicksburg, MS, USA, 1994; p. 60. Available online: https://dots.el.erdc.dren.mil/elmodels/pdf/cdfate.pdf (accessed on 16 July 2018).
25. Dunn, R.J.K.; Zigic, S.; Burling, M.; Lin, H.-H. Hydrodynamic and sediment modelling within a macro tidal estuary: Port Curtis Estuary, Australia. *J. Mar. Sci. Eng.* **2015**, *3*, 720–744. [CrossRef]
26. Fissel, D.; Jiang, J.; Borg, K. *Spatial Distributions of Suspended Sediment Concentrations and Sediment Deposition from Marine Terminal Dredging Operations*; Unpublished Report; Jacques Whitford Ltd.: Burnaby, BC, Canada; ASL Environmental Sciences: Sidney, BC, Canada, 2006; p. vi + 24. Available online: https://www.ceaa.gc.ca/050/documents_staticpost/cearref_21799/2424/marine_fish_and_fish_habitat.pdf (accessed on 16 July 2018).
27. Jiang, J.; Fissel, D. 3D Numerical Modeling of Canpotex Dredging disposal off Prince Rupert. In *Stantec, Proposed New Disposal at Sea Sites*; Unpublished Report; Stantec Ltd.: Burnaby, BC, Canada; ASL Environmental Sciences Inc.: Victoria, BC, Canada, 2011; p. 40. Available online: https://www.ceaa.gc.ca/050/documents_staticpost/47632/53481.pdf (accessed on 16 July 2018).
28. Lin, Y.; Fissel, D. *Sediment Modeling of Dredging off Lelu Island, Prince Rupert, BC Canada, and Disposal of Dredgate at Brown Passage*; Unpublished Report; Stantec Ltd.: Burnaby, BC, Canada; ASL Environmental Sciences Inc.: Victoria, BC, Canada, 2013; p. 29. Available online: http://www.ceaa-acee.gc.ca/050/documents/p80032/98724E.pdf (accessed on 16 July 2018).

29. Lin, Y.; Fissel, D.B.; Mudge, T.; Borg, K. Baroclinic Effect on Modeling Deep Flow in Brown Passage BC Canada. *J. Mar. Sci. Eng.* **2018**. submitted for publication.
30. Fissel, D.B.; Lin, Y.; Mudge, T. Challenges and Advancements in Sediment Transport Modelling of Dredging for Complex Coastal Conditions. In Proceedings of the Western Dredging Summit and Expo, Norfolk, VA, USA, 25–28 June 2018; Available online: https://www.westerndredging.org/phocadownload/2018_Norfolk/Proceedings/4b-5.pdf (accessed on 16 July 2018).
31. Scoon, A.; Lin, A.; Clouston, R.; Fissel, D.B. *Aurora LNG Project: MOF and Terminal Dredge Modelling*; Unpublished Report; Stantec Ltd.: Burnaby, BC, Canada; ASL Environmental Sciences Inc.: Victoria, BC, Canada, 2016; p. 79. Available online: https://projects.eao.gov.bc.ca/api/document/58923172b637cc02bea163e7/fetch (accessed on 16 July 2018).
32. Environmental Assessment Office. LNG Canada Export Terminal Project Assessment Report. 2015, p. 361. Available online: https://www.ceaa-acee.gc.ca/050/documents/p80038/101852E.pdf (accessed on 16 July 2018).
33. Fissel, D.B.; Lin, A.; Lim, J.; Scoon, A.; Lim, J.; Brown, L.; Clouston, R. The variability of the sediment plume and ocean circulation features of the Nass River Estuary, British Columbia. *Satell. Oceanogr. Meteorol.* **2017**, *2*, 316. [CrossRef]

MDPI
St. Alban-Anlage 66
4052 Basel
Switzerland
Tel. +41 61 683 77 34
Fax +41 61 302 89 18
www.mdpi.com

Journal of Marine Science and Engineering Editorial Office
E-mail: jmse@mdpi.com
www.mdpi.com/journal/jmse

MDPI
St. Alban-Anlage 66
4052 Basel
Switzerland

Tel: +41 61 683 77 34
Fax: +41 61 302 89 18

www.mdpi.com

ISBN 978-3-03921-270-5